Structure-property correlations in novel spin crossover materials

Amber L. Thompson

Structure-Property Correlations in Novel Spin Crossover Materials

Amber L. Thompson

A Thesis presented for the degree of

Doctor of Philosophy

Chemical Crystallography Group
Department of Chemistry
University of Durham
England

May 2004

Dedicated to

My Dearest Chris.

Structure-Property Correlations in Novel Spin Crossover Materials

Amber L. Thompson

Submitted for the degree of Doctor of Philosophy

May 2004

Abstract

In complexes where the energy difference between the high and low spin state of the metal is of the order of k_bT, temperature can be used to induce a spin crossover transition (SC). In some cases, at very low temperatures, irradiation can induce excitation to a meta-stable high spin state. At low temperatures, this Light-Induced Excited Spin-State Trapped (LIESST) state is generally long lived, enabling structural examination.

The results presented herein refer to a wide range of iron(II) spin crossover materials which have been structurally studied in both thermal and light induced states. These fall into three categories; mononuclear, dinuclear and polymeric. The mononuclear complexes studied include FeL[$H_2B(Pz)_2]_2$ L = 2,2′-bipyridine (**1**) and 1,10-phenanthroline (**2**), of which **2** was found to undergo a change in symmetry in addition to the change in spin state, leading to a novel light induced polymorphism that has not been previously seen.

Two dinuclear compounds with step transitions have been examined. While $\{[N(CN)_2](FeBpl)_2\}(PF_6)_3$ undergoes a gradual transition, the transitions in $[Fe(Btz)(NCS)_2]_2$Bpmd are abrupt and the latter also undergoes LIESST but with a rapid relaxation that has not been observed previously with any other technique. While the origin of this relaxation is uncertain, the structure of this excited state has been studied under constant irradiation.

The largest structural study of three dimensional SC materials has been carried out, including bimetallic polymers with $[Au(CN)_2]^-$, $[Ag(CN)_2]^-$, $[Ag_2(CN)_3]^-$ and $[Pd(CN)_4]^{2-}$ bridging ligands. These anionic bridges have been shown to enhance cooperativity between iron centres leading to abrupt transitions and hysteresis. These materials have been shown to undergo LIESST, crystalline state allosterism, and thermo-chromism. Such multi-property materials have a high potential for technological applications.

Declaration

The work in this thesis is based on research carried out at the Chemical Crystallography Group, Department of Chemistry, University of Durham, England. No part of this thesis has been submitted elsewhere for any other degree or qualification and it is all my own work unless referenced to the contrary in the text.

Acknowledgements

First and foremost, I must thank my collaborators. Primarily, this includes Prof. José Real and Dr. Carmen Muñoz (Universitat de València and Universitat Politècnica de València) who together with their students, provided these fascinating spin transition materials and the corresponding magnetic susceptibility data — ¡Muchas Gracias!

For collaboration on work not discussed here in detail, thanks also to Drs. Roberto Mercader and Alejandro Ayala and their students as well as the chemists in Durham in particular Keith Dillon and Andy Beeby together with their students Stéphanie Cornet, Sylvia Bettington and Simon Rutter.

There is Jim Hodgson, and Andy (who gets a double mention), for their sterling work when designing and building the laser mounts. Thanks also to all the technical and cleaning staff in the department, who keep the place running.

Next, there's all my crystallography colleagues, both within the lab in Durham and further afield including those at ISIS and the Institut-Laue Langevin. Their help and support has been invaluable — you know who you are.

Then there's my friends and family, again there is no real need to mention names, but in particular, thanks to Sylvia and Chris for their support and help.

Thanks also the EPSRC for funding me through three of the best years of my life.

Finally, my deepest thanks go to my two supervisors — Prof. Judith Howard and Dr. Andrés Goeta. Judith has been fantastic throughout, offering help and support wherever and whenever she could and undertaking the not inconsiderable task of proofreading. Andrés on the other hand has always been there when he's wanted and never when he's not. Not only has he taught me everything I know, but his complete and total faith has given me confidence to try to do the impossible. His respect and trust have been invaluable. A student couldn't wish for better supervisors.

Contents

V Appendices

List of Figures

List of Tables

Abbreviations and Notes

ADP	Atomic Displacement Parameter
Bu	Butyl, C_4H_9–
CIF	Crystallographic Information File
CCR	Closed Cycle Refrigerator
CFT	Crystal Field Theory
DSC	Differential Scanning Calorimetry
EPR	Electron Paramagnetic Resonance Spectroscopy
esd	Estimated Standard Deviation
ESR	Electron Spin Resonance Spectroscopy
ESRF	The European Synchrotron Radiation Facility
Et	Ethyl, C_2H_5–
EXAFS	Extended X-ray Absorption Fine Structure
GSAS	Generalised Structure Analysis System
HS	High Spin
ISC	Intersystem Crossing
L	Generic Ligand
LAMP	Large Array Manipulation Program
LIESST	Light-Induced Excited Spin-State Trapping
LS	Low Spin
M	Generic Metal
Me	Methyl, CH_3–
MRI	Magnetic Resonance Imaging

NIR	Near Infrared
NLO	Non-linear Optics/Non-linear Optical
NMR	Nuclear Magnetic Resonance
NPD	Neutron Powder Diffraction
NSXD	Neutron Single Crystal Diffraction
Ph	Phenyl, C_6H_5-
Pr	Propyl, C_3H_7-
PSD	Position Sensitive Detector
SA	Simulated Annealing
SC	Spin Crossover
SG	Space Group
SQUID	Superconducting Quantum Interference Device
T_c	Critical Temperature of a Transition
ToF	Time-of-Flight
TGA	Thermogravimetric Analysis
TMP	Turbomolecular Pump
V	Unit Cell Volume
VSM	Vibrating Sample Magnetometer
VT	Variable Temperature
X	Generic Counter Ion or Solvent
Y	Generic Counter Ion or Solvent
XANES	X-Ray Absorption Near Edge Structure
XAS	X-Ray Absorption Spectroscopy
XRD	X-ray Diffraction
XRPD	X-ray Powder Diffraction
XRSXD	X-ray Single Crystal Diffraction

1D	One Dimensional
2D	Two Dimensional
3D	Three Dimensional

Ligand Abbreviations

Bpe	Trans-1,2 bis(4-pyridyl)-ethylene	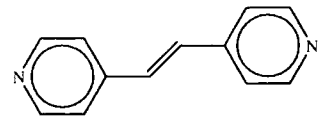
Bpl	*N*-benzyl-*N*-pyridin-2-ylmethyl-*N'*-(2-pyridin-2-yl-1-pyridin-2-ylmethyl-ethyl)-ethane-1,2-diamine	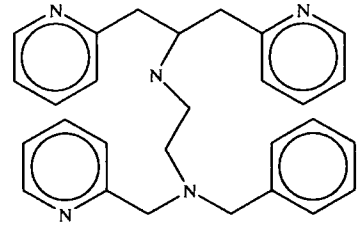
Bpmd	2,2′-Bipyrimidine	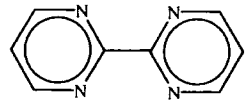
Bppm	Biphenyl-4-yl[1-pyridin-2-yl-methylidine]-amine	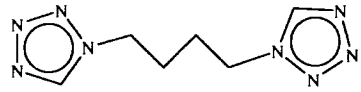
Bpyd	2,2′-Bipyridine	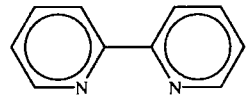
Bpyn	4,4′-Bipyridine	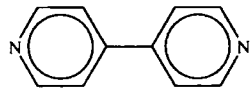
Bta	2,2′-Bi-4,5-dihydrothiazine	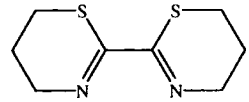
Btrz	4,4′-Bis-1,2,4-triazole	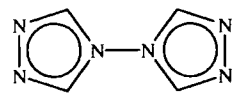
Btrzp	1,2-Bis(tetrazole-1-yl)propane	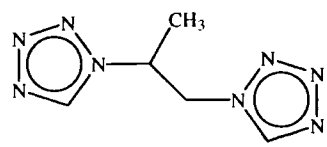

Bttzb	1,4-Bis(tetrazole-1-yl)butane	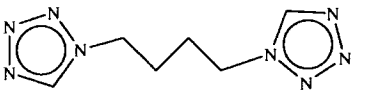
Btz	2,2′-2-Bithiazoline	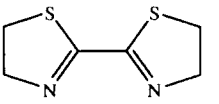
Cbs	4-Chlorobenzylsulphonate	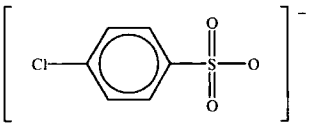
Cp	Cyclopentadiene	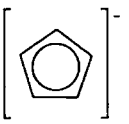
Cp*	Pentamethyl-cyclopentadiene	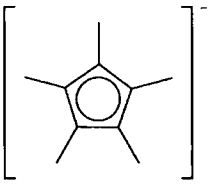
Dpa	2,2′-Dipyridylamine	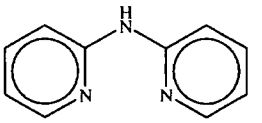
Dppen	1,2-Bis-(diphenylphosphinato)ethylene	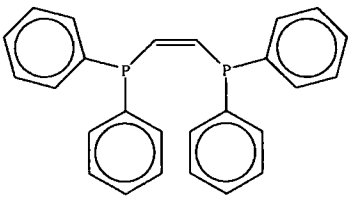
Etrz	4-Ethyl-1,2,4-triazole	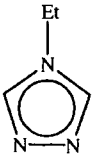

Hbpz	Di(hydro)bis(1-pyrazolyl)borate	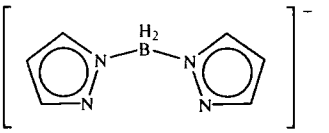
Htrz	4-(3′-Hydroxypropyl)-1,2,4-triazole	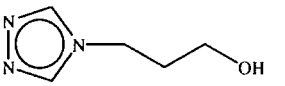
Mtz	1-Methyltetrazole	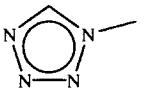
Pdz	Pyridazine	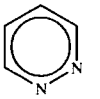
Pdzm	Octaaza-tricyclo-hexacosa-decaene	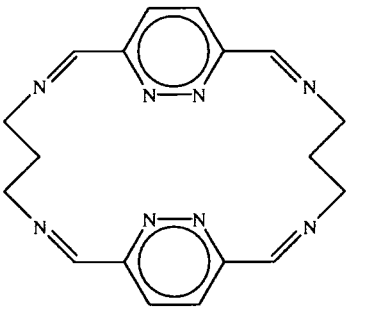
Phen	1,10-Phenanthroline	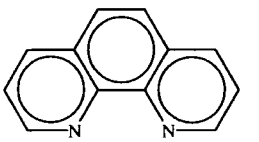
Pic	2-Picolylamine	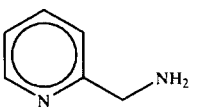
Pmd	Pyrimidine	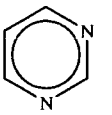

Ptz	1-Propyltetrazole	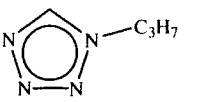
Pyd	Pyridine	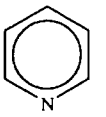
Pyim	2-(2-Pyridyl)imidazole	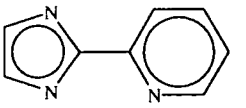
Pyz	Pyrazine	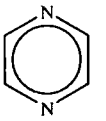
Pz	Pyrazole	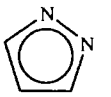
*R*tz	1-Alkyltetrazole	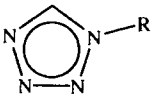
Sal	1,12-Di(2-oxy-5-nitro-benzyl)-2,5,8,11-tetraaza-dodecane	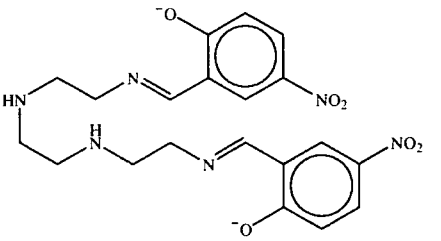
Terpyridine	[2,2′;6′,2″]Terpyridine	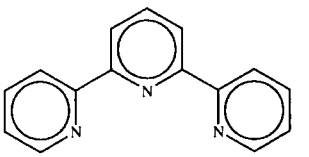

Terpyridol	1′*H*-[2,2′;6′,2″]Terpiridin-4'-ol	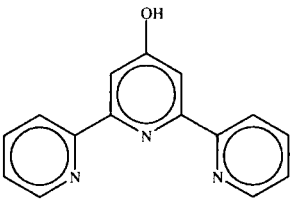
Terpyridone	1′*H*-[2,2′;6′,2″]Terpiridin-4'-one	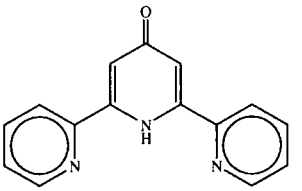
Tos	Tosylate, *p*-tolylsulphonate	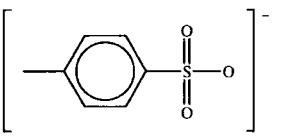
Trf	Triflate, trifluoromethyl-sulphonate	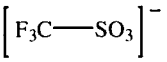
Trz	1,2,4-Triazole	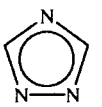
Trzt	4-(*p*-Tolyl)-1,2,4-triazole	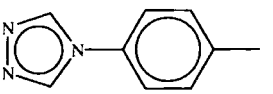
Ttz	Tetrazole	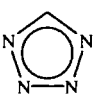

Graphics

Unless otherwise specified the following atom colours apply:

Hydrogen	Green	Iron	Red
Boron	Orange	Cobalt	Blue
Carbon	Grey	Nickel	Green
Nitrogen	Blue	Copper	Cyan
Oxygen	Red	Zinc	Green
Fluorine	Green	Palladium	Green
Phosphorus	Purple	Silver	Purple
Sulphur	Yellow	Iodine	Purple
Chlorine	Green	Platinum	Purple
Chromium	Purple	Gold	Orange
Manganese	Cyan		

In general, thermal ellipsoids are drawn at 50% probability and where pictures of structures from the literature are given, the details were obtained from the Cambridge Structural Database[1] using the ConQuest software.[2]

Compounds

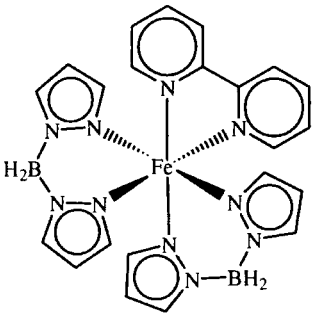

Compound **1** - FeBpyd$[H_2B(Pz)_2]_2$

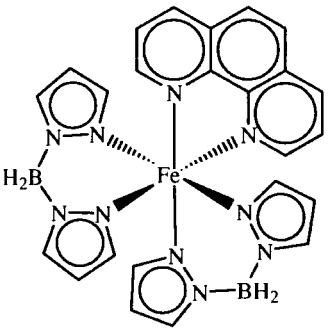

Compound **2** - FePhen$[H_2B(Pz)_2]_2$

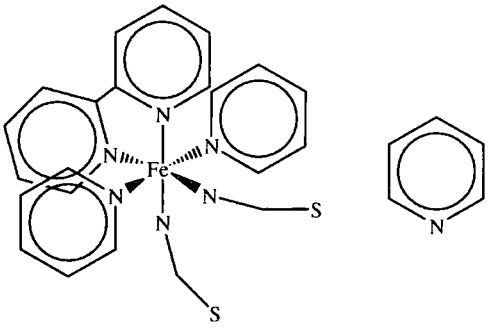

Compound **3** - $[Fe(Bpyd)Pyd_2(NCS)_2]Pyd_{0.225}$

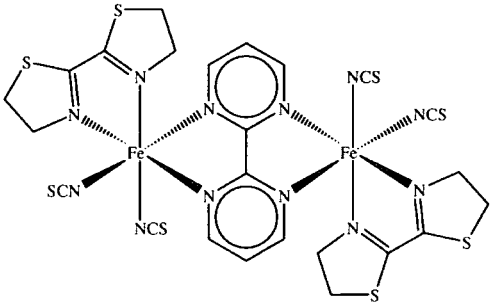

Compound **4** - $[Fe(Btz)(NCS)_2]_2Bpmd$

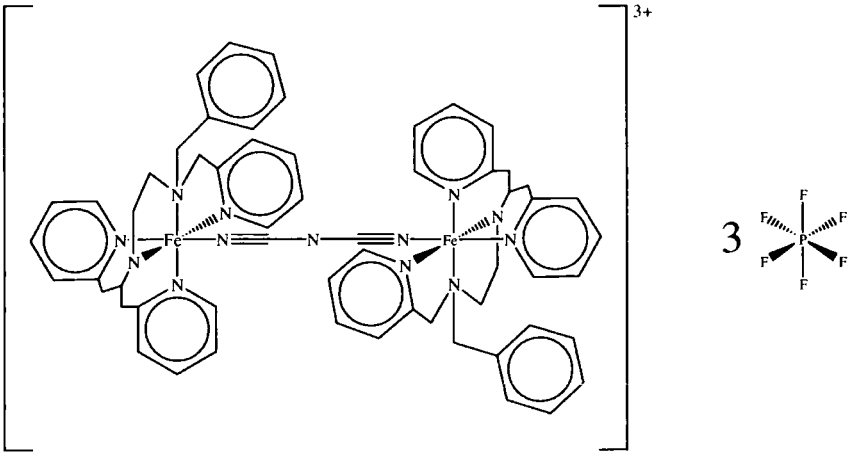

Compound **5** - $\{[N(CN)_2](FeBpl)_2\}(PF_6)_3$

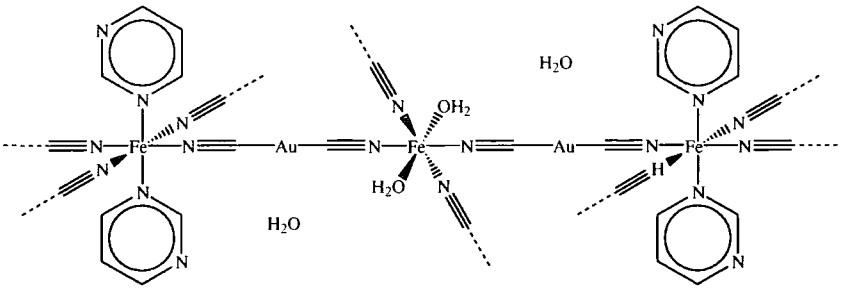

Compound **6** - $\{Fe(Pmd)_2Fe(H_2O)_2[Au(CN)_2]_4\}.H_2O$

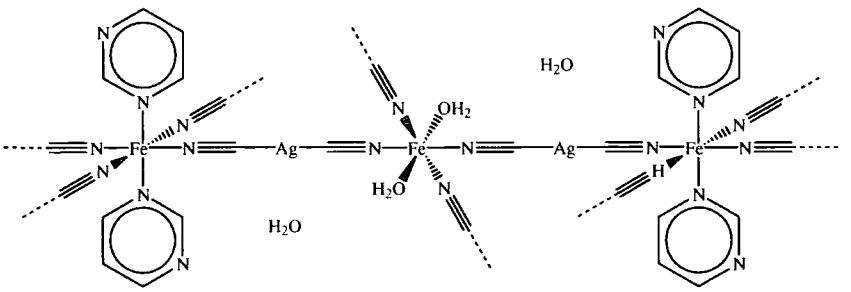

Compound **7** - $\{Fe(Pmd)_2Fe(H_2O)_2[Ag(CN)_2]_4\}.H_2O$

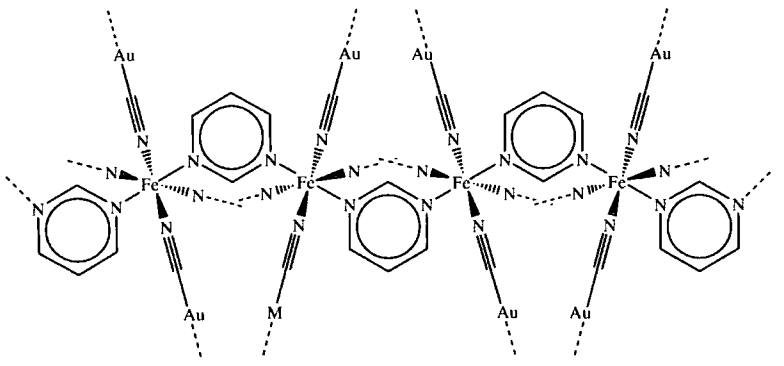

Compound **8** - $\{Fe(Pmd)_2[Au(CN)_2]_4\}$

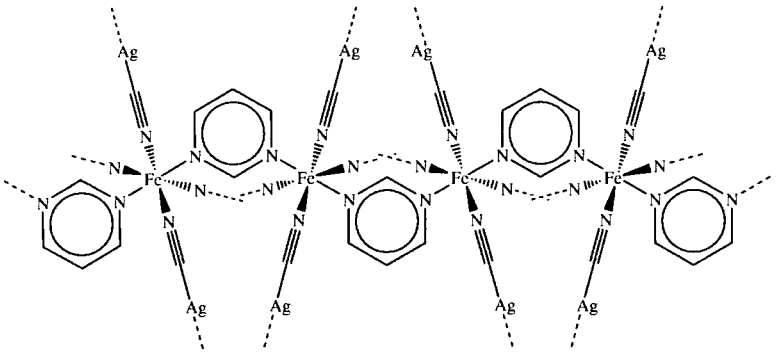

Compound **9** - $\{Fe(Pmd)_2[Ag(CN)_2]_4\}$

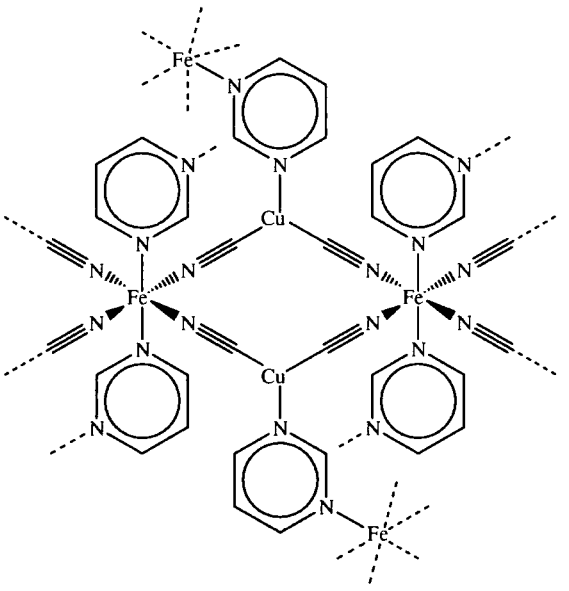

Compound **10** - $\{Fe(Pmd)_2[Cu(CN)_2]_2\}$

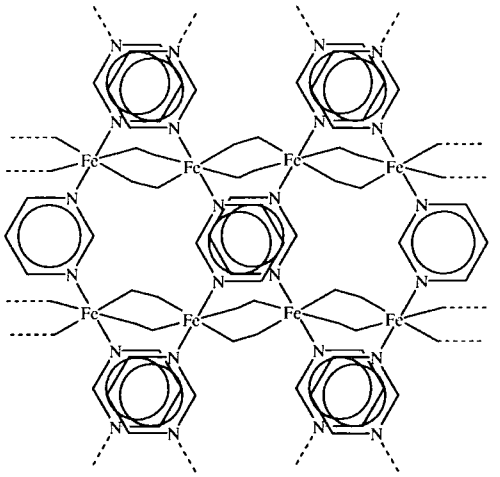

Compound **11** - $\{Fe(Pmd)[Ag(CN)_2][Ag_2(CN)_3]\}$

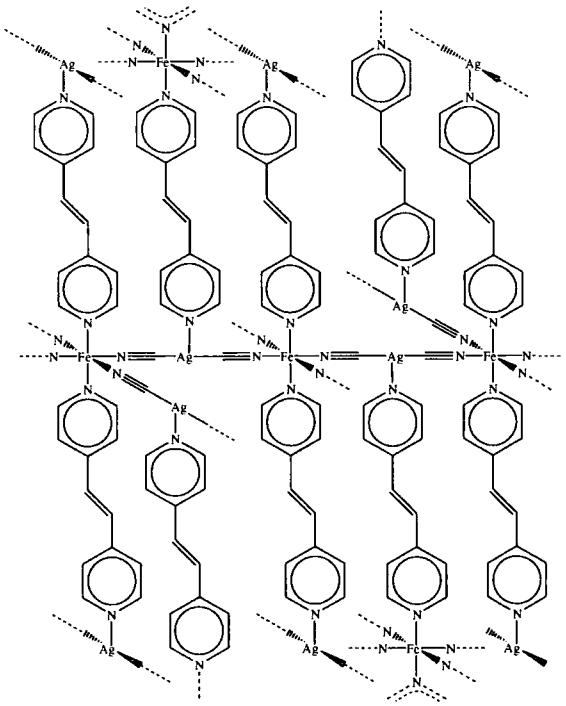

Compound **12** - $\{Fe(Bpe)[Ag(CN)_2]_2\}$

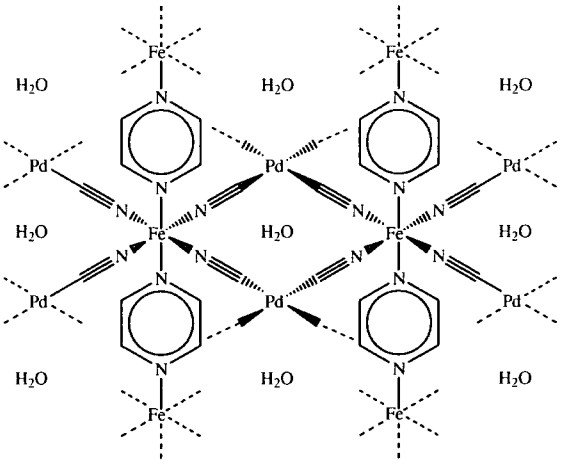

Compound **13** - $\{FePz[Pd(CN)_4]\}.2H_2O$

Full crystallographic data tables for the structures of compounds **1** to **13** are included on the accompanying compact disc, along with some additional material. The copyright of this thesis extends to the contents of the CD and as such no quotations from it should be published without the author's prior written consent and information derived from it should be acknowledged.

Part I

Introduction

Chapter 1

Structure Property Correlations and Spin Crossover

1.1 Structure Property Correlations

Structural studies and in particular crystallographic studies are vitally important to the area of materials science as they are the only way to unequivocally 'see' the atomic arrangement within a material. This 'vision' leads to an understanding of a material's properties and behaviour, without which we cannot make improvements and/or predictions. One of the key areas of materials science where this approach is indispensable, is the study of materials that undergo some sort of change when influenced by an external stimulus. Such changes are known as phase transitions.

1.1.1 Phase Transitions

Many materials undergo phase transitions and a considerable amount of time is dedicated to their study and their potential technological applications. Possible uses include key components of electronic displays, batteries, switches, information storage systems etc.. Phase transitions can either be structural in nature or involve a change in physical properties. However, the most interesting phase transitions are those where a change in the physical properties is accompanied by a structural change. The study of these transformations can give useful insight into the mechanism of the transition and also into the nature of the physical property. Understanding the behaviour of a material and the mechanism

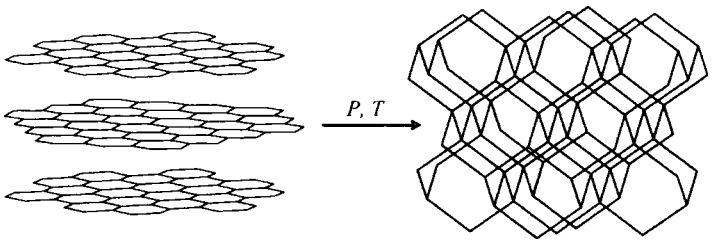

Figure 1.1: Graphite and diamond. The hexagons that make up the graphite sheets are shown (left) together with the continuous array of tetrahedra in diamond (right). To convert graphite to diamond high temperatures and pressures are required.

for a phase change is the first step towards the design of new materials possessing enhanced properties.

Characteristics of Phase Transitions

There are two major types of structural phase transition: Displacive and Reconstructive. Displacive transitions have low activation energies and involve only small structural distortions. In contrast, reconstructive transitions involve bonds breaking and reforming. These often require extreme conditions as they have higher activation energies. For example, there are two structures (or allotropes) of carbon that are stable at room temperature: graphite and diamond. In order to induce a transition between these two states, very high pressure and temperature is required as the transition is highly reconstructive (Figure 1.1). These transitions are also often slow and there is no inherent symmetry or structural relationship between the two phases. In contrast, spin transitions are generally displacive in nature (see below).

First and Second Order Transitions

Transitions can also be classified by considering the behaviour of thermodynamic quantities on passing from one polymorph (or phase) to another. At the equilibrium temperature or pressure, the Gibbs free energies of the two phases are equal, therefore $\Delta G = 0$ (therfore $\Delta H = T\Delta S$, from equation 1.1). Although there is no discontinuity or change in the free energy on passing between two phases, there may be a discontinuity in a *derivative* of the

free energy.[3]

The first derivatives of the free energy with respect to pressure (P) and temperature (T) correspond to volume (V) and entropy (S, equations 1.1 to 1.4). These can be measured using dilatometry and differential scanning calorimetry (DSC) respectively. Dilatometry is generally used to measure a change in volume, though this can sometimes be seen visually e.g. when a crystal shatters as a result of a sudden increase in the rate expansion or contraction. In crystalline materials however, expansion or contraction rates can also be measured using diffraction, where cell parameters recorded as a function of temperature can be used to identify phase transitions.

DSC on the other hand, involves taking a small quantity of sample and heating it, simultaneously comparing its enthalpy with that of a known reference. Although this is probably the easiest way to test for a phase transition, not all transitions are visible with DSC. In some transitions there is no change in the first differential, only in the second differential. These second order transitions are more difficult to see as the changes involved are usually much smaller, but they can be characterised by changes in the heat capacity C_p, thermal expansion α, and compressibility β (equations 1.5 to 1.7).

$$\Delta G = \Delta H - T\Delta S \tag{1.1}$$

$$H = U + PV \tag{1.2}$$

$$\frac{\partial G}{\partial P} = V \tag{1.3}$$

$$\frac{\partial G}{\partial T} = -S \tag{1.4}$$

$$\frac{\partial^2 G}{\partial T_P^2} = -\frac{\partial S}{\partial T_P} = -\frac{C_P}{T} \tag{1.5}$$

$$\frac{\partial^2 G}{\partial P \partial T} = \frac{\partial V}{\partial T_P} = V\alpha \tag{1.6}$$

$$\frac{\partial^2 G}{\partial P_T^2} = \frac{\partial V}{\partial P_T} = -V\beta \tag{1.7}$$

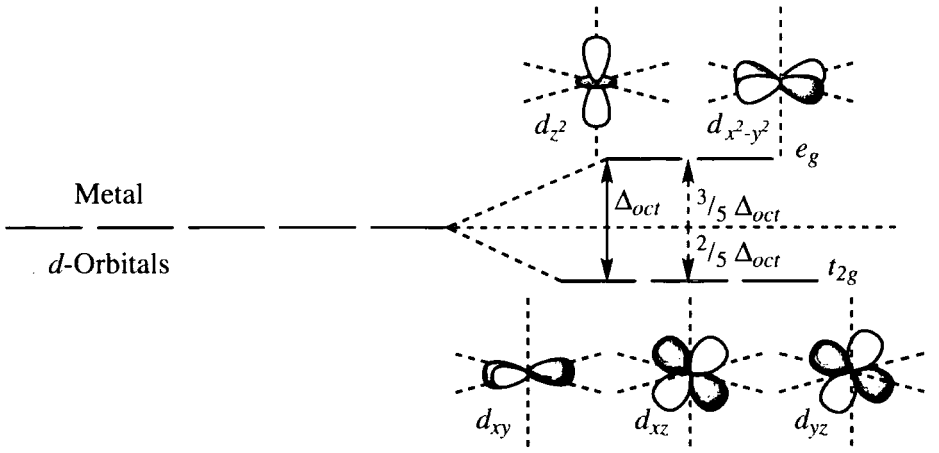

Figure 1.2: Schematic of octahedral splitting in transition metals.

1.2 The Spin Crossover Phenomenon

An important area of phase transition research is that of Spin Crossover (SC). These materials undergo an electronic transition in response to a number of stimuli, including temperature, pressure and light.[4] These transitions are generally displacive in nature and tend to result in a small structural change around a metal atom, usually a change in bond lengths and angles, but can also include more dramatic structural changes, for example, loss of symmetry. SC is usually most apparent in magnetic susceptibility data, but can often also be seen with many other techniques including Mössbauer spectroscopy, crystallography, light absorption spectroscopy, differential scanning calorimetry and X-ray absorption spectroscopy. In addition, there is sometimes a colour change, making these materials a particular target for data display technology, but they have many other potential uses including data storage.

1.2.1 High Spin and Low Spin

When a transition metal is ligated, the energy of the five d-orbitals is no longer the same. This loss of degeneracy or splitting, depends on the field caused by the ligands and the metal centre, resulting in either a tetrahedral or an octahedral geometry. Where there is octahedral coordination, the $d_{x^2-y^2}$ and d_{z^2} orbitals have a higher energy than the d_{xy}, d_{xz} and d_{yz} orbitals (Figure 1.2). In tetrahedral coordination, this arrangement is reversed.

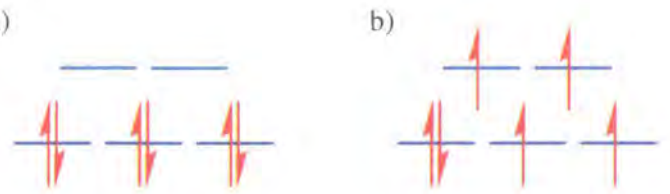

Figure 1.3: Schematic of low spin and high spin Fe^{2+} (a and b respectively).

Crystal Field Theory (CFT)

Crystal Field Theory is used to explain the loss of degeneracy in the d orbitals of a metal complex.

In an octahedral complex, the energy separation between the e_g and t_{2g} energy levels is known as Δ_{oct}, Δ_o or $10Dq$ and it depends on a number of factors including the metal and its oxidation state as well as the type, geometry and number of ligands. It is possible to list both the ligands and the metals in order of increasing field strength, i.e. the order that increases Δ_{oct}, which is called the spectrochemical series:[5,6]

Low Δ_{oct} $I^- < Br^- < S^{2-} < NCS^- < Cl^- < N_3^-, F^- < HO^- < O^{2-} < H_2O < SCN^-$
$< Pyd, NH_3 < Bpyd, Phen < ON^{2-} < CN^- < CO$ **High** Δ_{oct}

Low Δ_{oct} $Mn^{2+} < Ni^{2+} < Co^{2+} < Fe^{2+} < V^{2+} < Fe^{3+} < Cr^{3+} < V^{3+} < Co^{3+} < Mn^{3+}$ **High** Δ_{oct}

Electronic Configurations in Octahedral Complexes

For transition metals which have between four and seven electrons in the d-shell there are two possible electronic configurations. For example, Fe^{2+} has six electrons in the d-shell, which can be arranged in two ways: low spin and high spin (Figure 1.3).

Which one of these spin states is preferable depends on the overall energy, which comes down to a balance between unfavourable 'Pairing Energy' of the electrons and the benefit of the lower energy t_{2g} orbital.

Increasing the octahedral splitting Δ_{oct}, increases the energy difference between the t_{2g} and the e_g levels which means more energy is saved by using the lower, t_{2g} level. This splitting depends on the metal and the ligands and hence the spectrochemical series. The first three electrons singly fill each of the three t_{2g} orbitals, but the energy gained

from putting the next electron into the lower level is opposed by the unfavourable Pairing Energy. Thus the electronic configuration depends on this energy balance ($t_{2g}^4\, e_g^0$ versus $t_{2g}^3\, e_g^1$).

The Pairing Energy is made up of two components; the Coulombic Repulsion and the Exchange Energy. The Coulombic Repulsion is caused by pushing two electrons together into the same orbital. Heavier metals have more diffuse orbitals, so this term gets smaller. Consequently, second and third row transition metals, where this term is very small are almost always low spin. The Exchange Energy is proportional to the number of parallel electrons i.e. those with their spin in the same direction. The greater this is, the more difficult it is to pair electrons. Consequently, d^5 compounds (for example Fe^{3+} and Mn^{3+}) are mostly high spin.

Structural Differences

Crystallographically, high spin materials can be distinguished from low spin using diffraction techniques, by comparison of bond lengths. In iron(II) complexes, the metal to ligand distances are usually about 0.2 Å longer for high spin structures than low spin materials.[4] This is because electrons are removed from the anti-bonding e_g orbital and placed in the bonding t_g orbital. This leads to a strengthening of the metal–ligand bonds which is manifested in a shortening of the bond in the low spin state and an associated change in the vibrational frequencies.

A search of the Cambridge Structural Database[1] clearly shows the bimodal distribution for iron–nitrogen ligands (Figure 1.4). However, in contrast to the nitrogen ligands most iron–oxygen ligand complexes are clearly high spin (Figure 1.5).* This is because the oxygen bound ligands generally confer a much weaker ligand field than nitrogen bound ligands. For example, iron(II) hexahydrate salts are generally high spin compared with iron(II) hexacyanate salts which are low spin.[7] For intermediate strength ligand fields, the

*Searches were carried out for Fe–N fragments and Fe–O fragments and in both cases the search criteria specified that the iron was six-coordinate. Polymeric and disordered structures were excluded and only structures with no errors and R-factors $< 10\%$ were accepted.

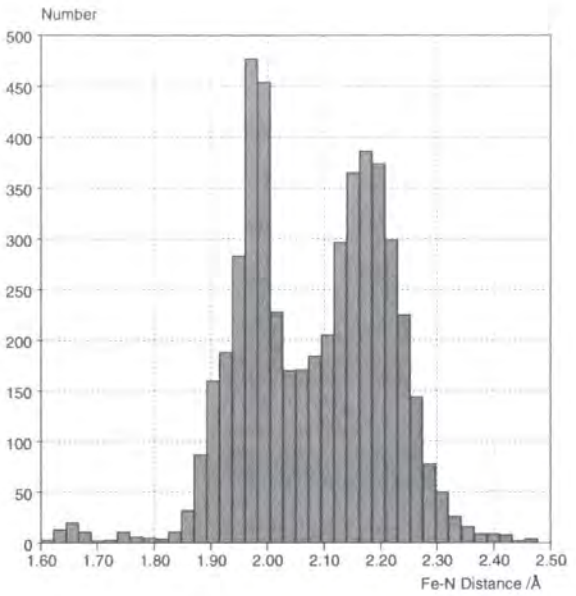

Figure 1.4: Histogram of Fe–N bond lengths.

energy difference between the two states is of the order of k_bT[†] and a change in pressure or temperature can induce a transition between the two states. This is known as a spin transition or spin crossover (SC).

Spin Transitions

So, in complexes where the difference in energy between the high spin and low spin states is of the order of k_bT, temperature can be used to induce a transition between the spin states. Thus cooling a high spin sample *can* result in the low spin species and vice versa.

Since there is a change in volume associated with spin crossover, transitions can also be pressure induced with high pressure generally favouring the low spin state and in general increasing the temperature of the transition. One example of this is the triazole derivative $[Fe(Htrz)_3]Cbs_2.H_2O$ which has a sharp transition at about 180 K with a 5 K hysteresis.[8] Applying a pressure of 5.9 kbar increases the transition temperature to 324 K. In some cases irradiating with light also induces a transition, which is known as the LIESST effect

[†] k_b is the Boltzmann constant and T is the temperature (K).

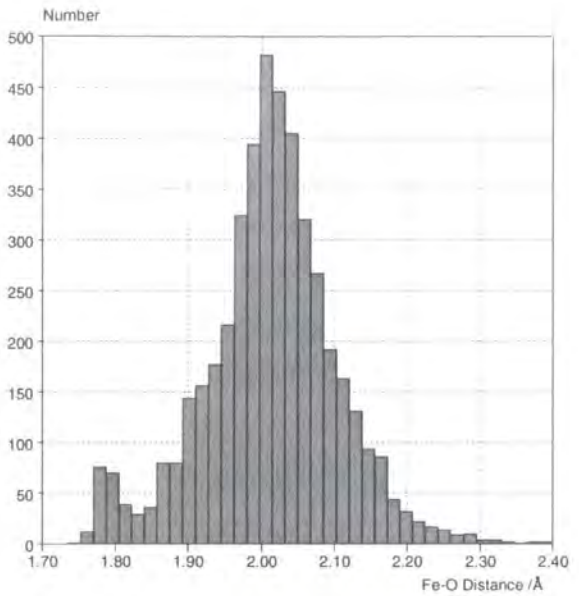

Figure 1.5: Histogram of Fe–O bond lengths.

(see Section 1.2.3). In all these cases, the communication between molecules is critical to the way the transition is passed from one SC centre to the next.

1.2.2 Cooperativity

The concept of cooperativity is an important one when discussing SC and it refers to the way that SC centres 'communicate' through a material. This 'communication' is important as it explains how the transition spreads throughout the structure, and indeed cooperative effects constitute the basic mechanism for the spin crossover transition.

Weak Interactions in the Solid State

In the solid state, a molecule interacts with the surrounding molecules. As such, molecules cooperate all the time in the solid state through weak interactions like hydrogen-bonding and π–π interactions. Hence, these types of interactions are critical in spin crossover as they provide a path for cooperativity. A key example is the series of compounds based on $Fe(L)_2(NCS)_2$ where L can be one of three different bidentate ligands, 2,2′-bi-4,5-dihydrothiazine (Bta), 1,10-phenanthroline (Phen) and dipyrido[3,2-a:2′3′-c]phenazine (Dpp) (Figure 1.6).[9–11] From the crystal packing diagrams it is clear that the Dpp ligands

overlap allowing a considerable π–π stacking interaction. This can be compared with the minimal overlap of the Bta ligands and the intermediate overlap of the Phen ligands. Thus, the ligand overlap and therefore the π–π stacking interactions make a vast difference to the cooperativity, which is most obvious in the nature of the transition (Figure 1.6).

Abrupt Transitions and Hysteresis

In the Bta compound, the transition takes place over a large temperature range because there is little cooperativity. The increased cooperativity in the Phen compound means that the transition takes place over a much smaller temperature range and is therefore described as abrupt. This is one of the key ways of identifying cooperative systems — by the sharpness of the transition. Sharp transitions are caused by increased cooperativity which allows the spin transition to be communicated rapidly through the structure over a small temperature range. SC transitions take place as a result of coupling between the metal centres and crystal lattice, which takes place through the metal–ligand bond vibrations. Consequently, the transition proceeds though the formation of domains of molecules with the same spin and these in turn spread throughout the sample. The stronger the metal–lattice coupling, the faster the domains spread and the more abrupt the transition. Since the metal–ligand vibrations depend upon the bond length, larger metal–ligand contractions generally give sharper transitions.

Increasing the ligand overlap by substituting the Phen ligand with the Dpp ligand leads to increased cooperativity which is apparent in the abrupt transition which takes place with hysteresis. Hysteresis is where the transition occurs at a lower temperature when cooling than when heating. This is caused by a kind of inertia, where the system opposes the transition as long as possible until all the molecules can make the transition at almost the same time. All these effects are most easily seen by looking at magnetic susceptibility data (see pages 15–18).

Dilute and Solution Based Systems

In contrast, spin crossover systems in solution are much more gradual, following the prediction of the Boltzmann distribution between two vibronic manifolds. Similarly, in systems where the spin crossover centre has been "diluted" by doping with a different metal centre

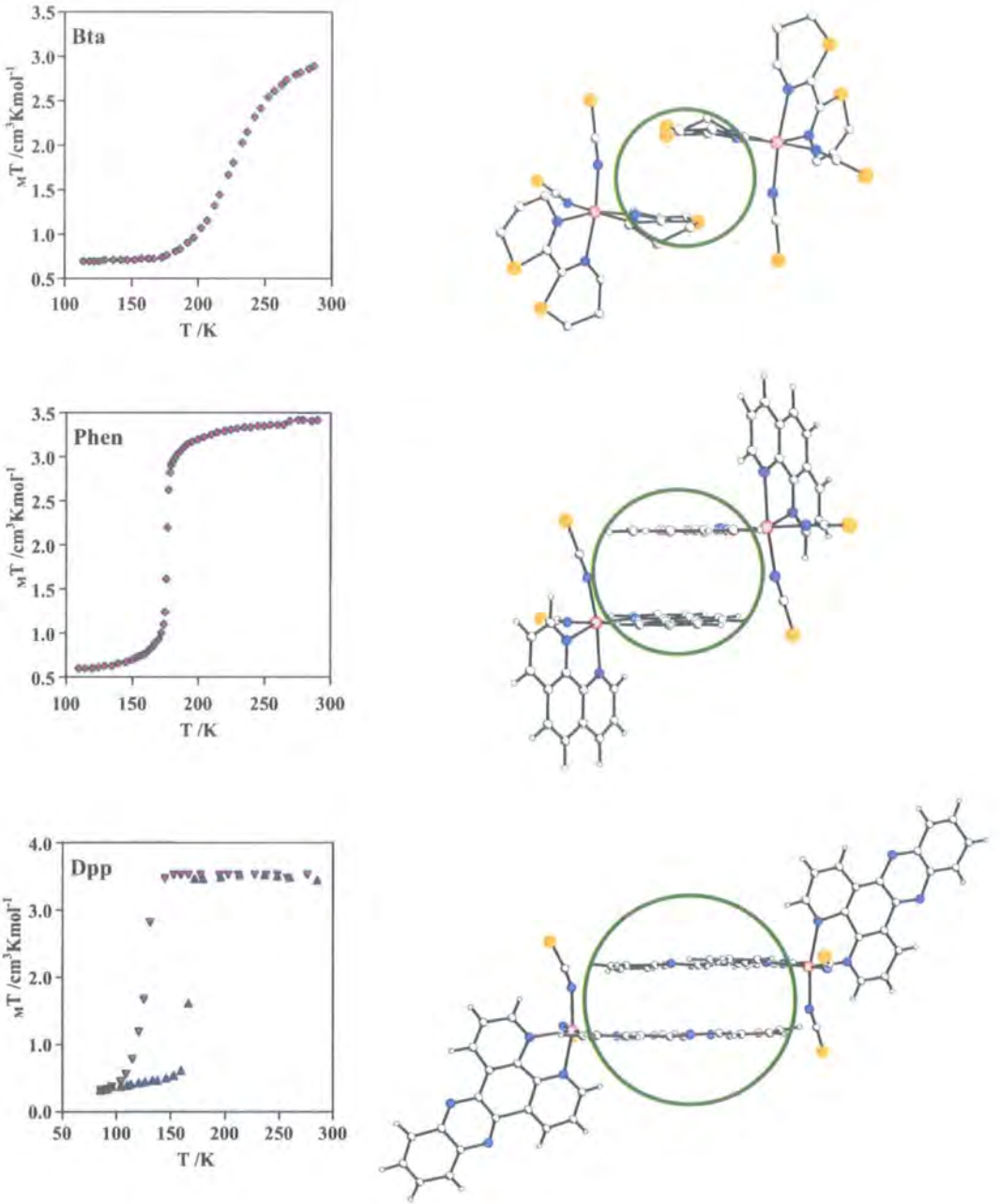

Figure 1.6: Ligand overlap in Bta, Phen and Dpp complexes (top, middle and bottom respectively).[9–11] The increased ligand overlap (circled) leads to increased π–π stacking interactions and therefore cooperativity, which can be seen initially in the increased abruptness in the Phen complex and in the hysteresis in the Dpp complex as shown by the magnetic susceptibility data.

(iron is often diluted with zinc as they have a similar volume), the cooperativity is reduced and the transition becomes less abrupt. Interestingly, the increased cooperativity seen in pure or neat spin crossover compounds leads to a strongly accelerated relaxation of any meta-stable excited state.[12]

1.2.3 Light-Induced Excited Spin-State Trapping (LIESST)

In the course of their work on the $[Fe(Rtz)_6](X)_2$ series of compounds (see page 26), Gütlich and co-workers studied $[Fe(Ptz)_6](BF_4)_2$ and discovered an hitherto unreported phenomenon, now known as LIESST.[13]

$[Fe(Ptz)_6](BF_4)_2$

In 1984 Decurtins *et al.* reported that by using a xenon arc lamp to irradiate the low temperature low spin $[Fe(Ptz)_6](BF_4)_2$, the high spin state could be repopulated, a process which they followed using Mössbauer spectroscopy.[13]

Initially, they cooled the sample below the transition temperature (which takes place at approximately 135 K), where the sample contained only low spin Fe^{2+}. The sample was then irradiated at 15 K yielding the pure high spin state with spectra comparable to those recorded at room temperature. They then warmed the sample to approximately 50 K and then cooled it back to 15 K, yielding the spectra of an HS/LS mixture. From the integrated areas, they found that this mix was 46% low spin and 54% high spin. However, repeating the warming to 50 K and cooling back to 15 K process, increased the amount of HS in the sample to 70%. Finally raising the temperature to 97 K, the Mössbauer spectra indicated that the sample was pure LS and on warming through the transition at 135 K the sample returned to the original pure HS state.

They called the formation of this meta-stable high spin state Light-Induced Excited Spin-State Trapping or LIESST.

Following this excitation of a low spin state to give the meta-stable high spin species, Decurtins *et al.* also tried the reverse experiment.[14] A single crystal of $[Fe(Ptz)_6](BF_4)_2$ was trapped in the meta-stable high spin state then irradiated with infrared light ($\lambda > 700$ nm). This led to the regeneration of the low spin species which was characterised using absorption spectroscopy. They called this process "Reverse-LIESST".

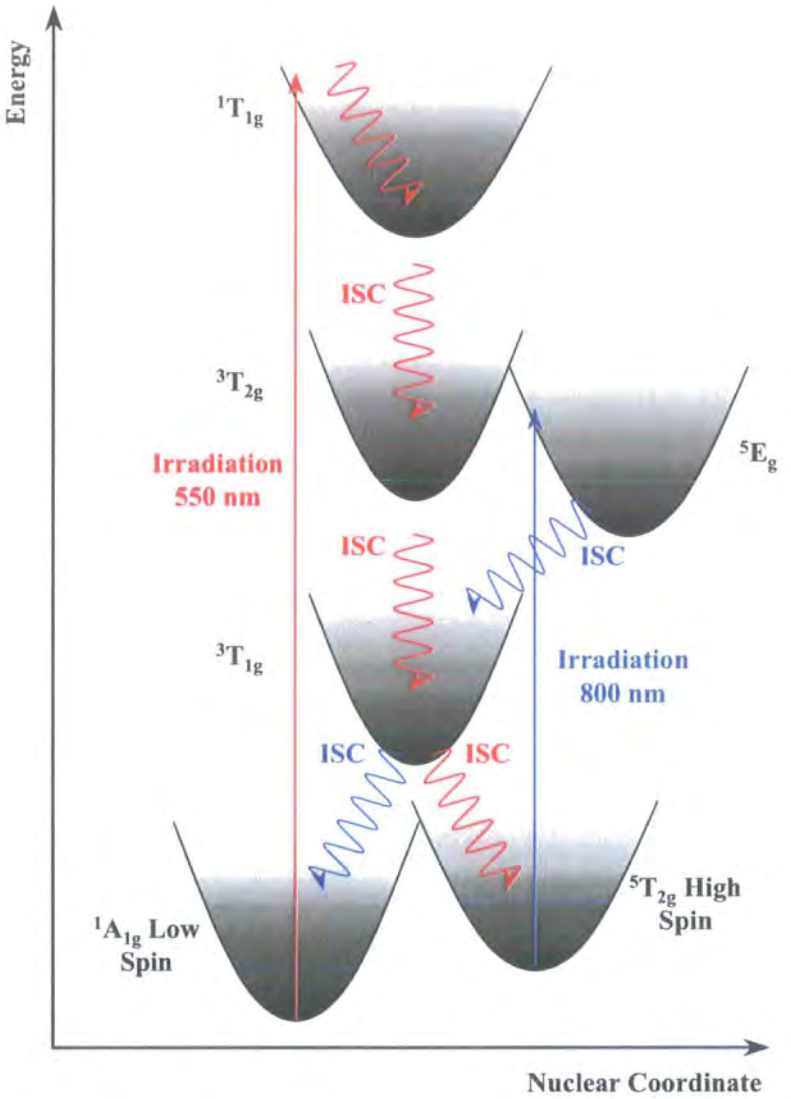

Figure 1.7: A schematic of the mechanism of the LIESST process in Fe^{II} complexes. Irradiation of the low spin $^1A_{1g}$ leads to the formation of the $^1T_{1g}$ state, which then relaxes via intersystem crossing (ISC) to the meta-stable high spin $^5T_{2g}$ state (shown in red). Irradiation of the high spin $^5T_{2g}$ state followed by ISC is also shown (blue).[15]

Theory

Further to their experimental work, Decurtins *et al.* proposed a mechanism for the LIESST process (Figure 1.7).[14] They proposed that during excitation with green light, the complex is excited from its low spin $^1A_{1g}$ state to a $^1T_{1g}$ state which is spin allowed. The $^1T_{1g}$ state typically possesses a lifetime of a few nanoseconds and relaxation takes place through intersystem crossing (ISC) via the $^3T_{1g}$ to the meta-stable high spin $^5T_{2g}$ state. If the temperature is sufficiently low this meta-stable state is trapped and has an effectively infinite lifetime that is progressively reduced on warming. An alternative LS→HS route is sometimes possible by irradiating with infrared light (λ = 980 nm), which leads to excitation from the $^1A_{1g}$ state to the $^3T_{1g}$ state followed by ISC to the HS $^5T_{2g}$ state.[15]

The reverse-LIESST process occurs on irradiating the high spin $^5T_{2g}$ state with infrared radiation ($\lambda \approx 820$ nm), leading to excitation into the ^5E_g band followed by ISC.

1.2.4 Technological Applications of Spin Crossover Materials

Cooperativity is vital if these materials are to be used in technological devices such as molecular switches or temperature sensors. For a material to be used in these ways, the transition must be sharp. Another potential use is in memory or data storage devices. In this case, cooperativity is vital, but is not the only consideration. In addition to a large hysteresis and a sharp phase transition, the transition should take place as close as possible to room temperature, ideally with the centre of the hysteresis at ambient conditions. Where the material is highly coloured it is also possible to differentiate between two samples at room temperature, one of which has been heated and one cooled, since the sample that has been heated will be high spin, while the sample that has been cooled will be low spin and their colours different. This ability to tell what has happened to the sample is known as the memory effect.

It is also possible to use materials with a dramatic colour change in electronic displays.[16,17] The spin crossover material can be dispersed within a resin and layered on top of an alumina plate that contains resistive dots and conductive electrodes. When a current is applied to the resistive dots, they heat up causing a spin transition in the material in the resin above and a corresponding colour change. The system can then be cooled down to reverse the spin transition. This heating and cooling can be induced using a system of

Peltier elements.[18]

More recently work has been performed on spin crossover materials as potential 'Intelligent Contrast Agents' for Magnetic Resonance Imaging (MRI). MRI is based on the same phenomenon that is widely used for chemical analysis, Nuclear Magnetic Resonance (NMR). In 1971 Raymond Damadian showed that the nuclear magnetic relaxation times of tissues and tumors differed,[19] thus motivating scientists to consider magnetic resonance imaging for the detection of disease. In iron(II) spin crossover materials the MRI (or NMR) signal is dominated by the paramagnetism when the material is high spin, leading to a broadening of the signal. One idea is that this effect could be used in monitoring a tumor during hypothermia treatment.[20]

1.2.5 Characterisation Techniques

A wide range of techniques and equipment has been used to study the spin crossover phenomenon. However, none give a complete picture of the process and in order to characterise the transitions fully, a combination of techniques are needed.

Magnetism

Ions with unpaired electrons (paramagnetic ions) have a net magnetic moment, while those with paired electrons (diamagnetic ions), have none. Since the spin crossover phenomenon involves a change in the number of unpaired electrons, there is a corresponding change in the magnetic susceptibility which can be measured using a number of different pieces of equipment, including Faraday Balances,[‡] Vibrating Sample Magnetometers (VSMs) and Superconducting Quantum Interference Devices (SQUIDs). The use of these instruments can give vital information on the nature and temperature of electronic transitions.

Types of Transition

There are a number of different characteristics that can be inferred from variable temperature magnetic susceptibility data. If there is a slow change in the magnetic susceptibility

[‡]Also known as Thermal Magnetization Analyzers (TMAs).

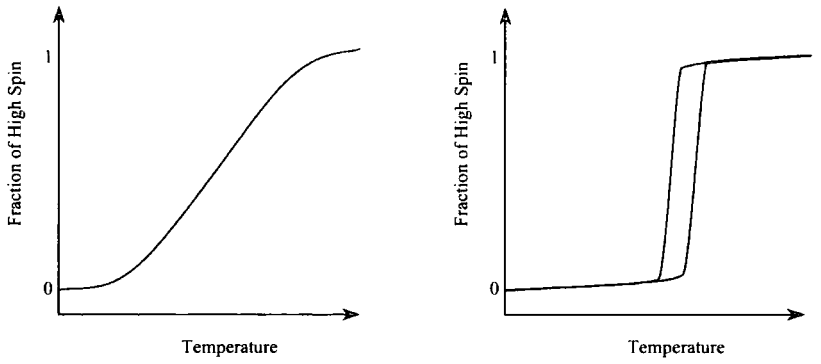

Figure 1.8: Schematic of a gradual transition (left) and an abrupt transition with hysteresis (right). The cooling curve is shown in blue with warming curve in red.

with respect to temperature then the transition is described as gradual or smooth. On the other hand, if there is a rapid change the transition is described as abrupt (Figure 1.8). This is an important characteristic as more abrupt transitions indicate strong cooperativity which is vital for potential applications. Strongly cooperative materials also have a hysteresis where the transition does not follow the same path on heating and cooling (Section 1.2.2). Transitions with a hysteresis are also described as discontinuous.

Not all SC transitions go to completion and in some cases there is residual low spin at high temperature. This occurs because the spin crossover phenomenon is statistical in nature and although the ligand field is strong, it is not strong enough to enable complete conversion, leaving a small percentage of residual high spin. Transitions where there is residual low spin at high temperature (or vice versa) are known as incomplete transitions.

Step Transitions

Another feature that is sometimes seen in magnetic susceptibility data is a step or plateau, where there is an intermediate species that is exists, usually half way between the two extreme states. Sometimes this is because there is more than one iron centre and the intermediate has half the iron centres in the high spin configuration and half in the low spin configuration. However, often it is because the high and low spin centres are averaged

out over the structure. In such cases, it is possible that there is long range ordering, but usually the super lattice reflections are so weak that they are impossible to see under laboratory conditions. The first material where super lattice reflections have been observed that are solely due to HS/LS ordering is $[Fe(Pic)_3]Cl_2.EtOH$.[22]

$[Fe(Pic)_3]Cl_2.EtOH$

The iron(II) picolylamine (Pic) complexes are one of the oldest series of spin crossover complexes, first reported by Renovitch and Baker in 1967 (Section 1.3.3).[23] One of these complexes, $[Fe(Pic)_3]Cl_2.EtOH$, undergoes an abrupt spin transition at approximately 120 K on cooling. In addition, optical and magnetic susceptibility data together with unit cell parameters, indicate that there is an intermediate phase between 114 K and 122 K.[24]

Initial structural studies of this iron complex confirmed that the intermediate phase together with the high and low spin phases has a single iron atom in the asymmetric unit.[25] All three phases were found to be isostructural except for minor changes in the disorder and location of the chloride counter ions and ethanol solvent. However, more recently, single crystal diffraction data have been collected using BM1A (Swiss-Norwegian Beamline) at the ESRF where additional Bragg reflections were found, indicating the presence of a superstructure caused by the separation of the single iron centre into two.[22] The percentage of high spin iron atoms on each site was refined to 85% on one and 13% on the other.

Hexadentate Salicylaldehyde Iron(II) Derivative

Another complex that undergoes a step transition is an iron(II) centre caged by a ligand formed through the condensation of nitrosalicylaldehyde with tetraazadecane (Sal).[26,27] Unusually, Fe(Sal) is a monomeric iron centre bound by four nitrogen and two oxygen atoms of the Sal ligand which form a complex cage (Figure 1.9). Like $[Fe(Pic)_3]Cl_2.EtOH$, the compound undergoes a two step spin crossover that occurs concurrently with two crystallographic phase changes. During the first step, the structure remains monoclinic, but looses a c-glide plane, changing from $\mathbf{P2}/c$ with half a molecule in the asymmetric unit at 292 K to **P2** at 153 K, where there are two crystallographically unique half molecules. The second step involves a further change in space group at 103 K apparently to **P1**

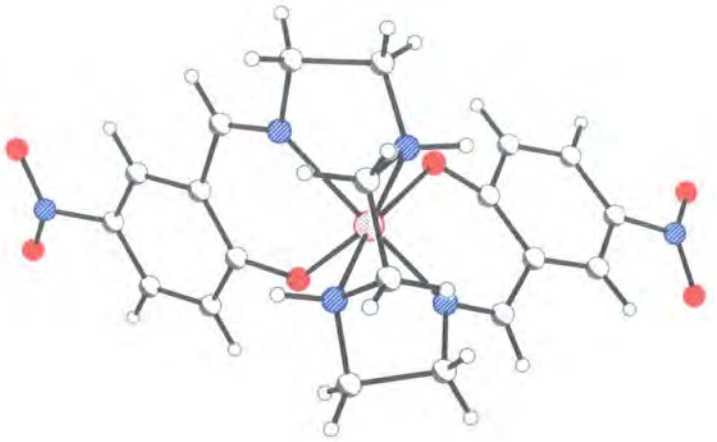

Figure 1.9: The monomeric Fe(Sal) consisting of a single iron centre bound by four nitrogen and two oxygen atoms of the Sal ligand which forms a complex cage.

where there are two entire unique molecules, though the refinement was destabilised by a large degree of correlation and a shortage of data. In this case however, the bond lengths for the intermediate structure indicate that both iron centres are between high and low spin, suggesting that in this case at least, the intermediate phase is truly HS/LS disordered. The possibility remains however, that this picture is incomplete and without further investigation it is not possible to ascertain whether or not there is HS/LS ordering in the intermediate phase.

Spectroscopic Methods and Other Useful Techniques

A number of spectroscopic methods have been used to characterise the SC phenomenon, some commonly available, some more unusual.

In infrared spectroscopy for example, a shift of 150 cm^{-1} from about 250 cm^{-1} for high spin iron complexes to approximately 400 cm^{-1} for comparable low spin species is typically seen (an approximate energy change of 0.02 eV).[28] Changes in spin state can also induce a smaller shift in the frequency modes seen within the ligands. For example, cyanide frequency modes have been shown to shift 40 cm^{-1} in iron thiocyanate and iron selenocyanate complexes.[29]

The information obtained from Raman spectroscopy is similar in nature to that ob-

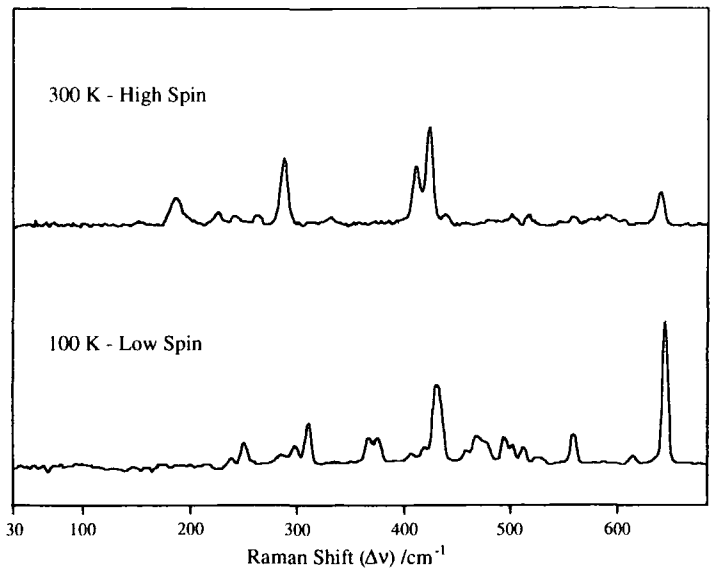

Figure 1.10: Raman spectra for $Fe(Phen)_2(NCS)_2$ at 300 K and 100 K.[30]

tained from infrared spectroscopy. In terms of spin crossover, the transition can be followed by observing the characteristic peaks due to the different spin states (Figure 1.10).[30] A general shift to higher frequency can be seen as the metal atom changes from high spin to low spin. This is in keeping with infrared spectroscopy where there is a similar shift caused by the shortening and strengthening of the Fe–N bonds.

One of the most useful techniques used in the study of spin crossover is Mössbauer spectroscopy. As the majority of spin crossover materials are iron compounds and the most commonly used nuclei for Mössbauer Spectroscopy is ^{57}Fe, the two are ideally suited. Changing the spin state leads to small changes in the absorption energies, which can easily be seen with Mössbauer spectroscopy. For example, the high spin spectra of $[Fe(Ptz)_6](BF_4)_2$ has two bands while the low spin spectra consists of one band only (Figure 1.11).[7] The integrated intensity of the bands seen with Mössbauer spectroscopy are proportional to the fraction of molecules in the spin state, which makes variable temperature Mössbauer spectroscopy an important characterisation technique. However, while iron(II) compounds give sharp, well defined spectra, iron(III) spectra are much broader making data analysis more difficult.

Since bond length is a key indicator of spin state, Extended X-ray Absorption Fine

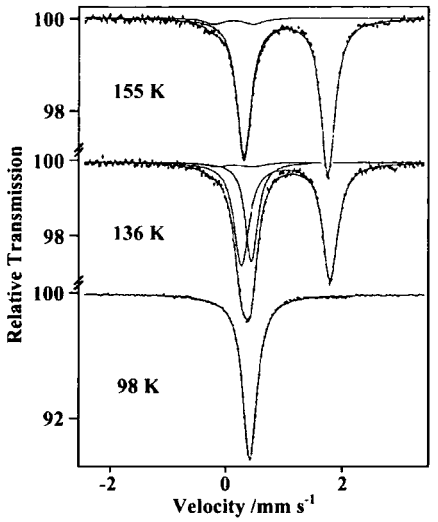

Figure 1.11: Temperature dependent ^{57}Fe Mössbauer spectra for $[Fe(Ptz)_6]((BF_4)_2)$.[7] While the complex is high spin at 155 K and low spin at 98 K, both states are present at 136 K.

Structure (EXAFS) and X-ray Absorption Near Edge Spectroscopy (XANES) are also used to characterise SC materials. The main advantage of both XANES and EXAFS over diffraction methods is that since they do not rely on long range order, they can be used on amorphous materials or where crystallinity is poor and even on liquids and gases. However, little or no information can be derived for anything further than three or four angstroms away from the metal centre, which means X-ray absorption spectroscopy cannot be used to see the 'bigger picture'. Thus it is not possible to see other structural features (like solvent or counter ion disorder, hydrogen bonding or π–π interactions) making it more difficult to correlate structural changes with physical properties. In addition, if there is more than one distinct type of iron centre within a sample, the spectra are considerably more complicated hence obtaining information is more difficult.

Finding a phase transition can often be a problem as many of the methods detailed above are time consuming or expensive. So efficient methods like Dilatometry,[§] Differential

[§]Dilatometry is also known as Thermomechanical Analysis.

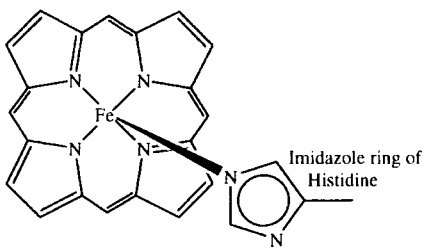

Figure 1.12: The iron environment in a hæm unit. The substituents of the porphyrin and part of the histidine are omitted for clarity.

Scanning Calorimetry (DSC),[¶] and Thermogravimetric Analysis (TGA) are invaluable for diagnosing the presence and location of a phase transition.

1.3 Some Important Spin Crossover Materials

A wide variety of materials undergo spin crossover, from proteins to small molecules. Understanding the mechanism of these processes is often key to understanding why SC occurs. So, studying the structures of these materials and correlating them with their properties is vital in aiding this understanding.

1.3.1 Spin Crossover in Nature

Iron is abundant in nature and is probably most important in oxygen transport and storage in mammal circulation systems, in which SC plays a crucial role.

Myoglobin and Hæm Units

Myoglobin is a protein, consisting of one hæm unit and 153 amino acid residues, that is found in muscle tissue where it is used to store oxygen. The hæm unit is where the active site resides and consists of a five coordinate iron(II) centre ligated by four nitrogen atoms from a porphyrin ring system and the nitrogen atom from a histidine amino acid group from another part of the protein (Figure 1.12). This iron centre binds reversibly with oxygen,

[¶]Differential Scanning Calorimetry is also known as Differential Thermal Analysis (DTA).

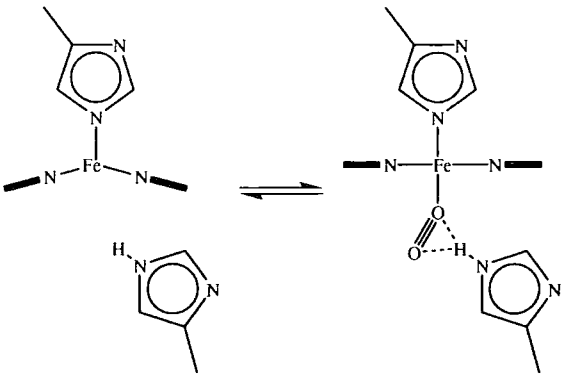

Figure 1.13: Schematic of oxygen binding to a hæm unit. The iron moves from the out of plane position to the centre of the plane with a corresponding shortening of the Fe–N bond lengths and undergoes spin crossover.

changing from high spin to low spin. This spin crossover causes a change in geometry round the iron atom. Thus, the distorted square pyramidal type arrangement changes to an octahedral geometry with the oxygen binding to the iron at an angle. Initially, in the deoxygenated form, the porphyrin is slightly domed with the iron sitting slightly out of the plane in the histidine direction. When the oxygen binds, the Fe–N bond lengths shorten allowing the porphyrin to flatten out and the iron to move into the centre of the porphyrin plane, pulling the histidine amino acid about 0.5–0.6 Å closer to the porphyrin. The oxygen binds to the iron at an angle, in the bent η^1 mode and forms hydrogen bonds with another histidine on the other side of the porphyrin ring (Figure 1.13).[31]

Cooperativity in Hæmoglobin

Hæmoglobin, the protein used to transport oxygen round the body, also contains hæm units like myoglobin. However, while myoglobin consists of a single chain of amino acids with one hæm unit, hæmoglobin has four chains each with their own hæm unit. These chains are of two different types known as α and β and there are two of each type.[32]

While the binding of oxygen to myoglobin is a relatively simple bimolecular process, in hæmoglobin the coordination of oxygen is a cooperative process, with the α and β chains involved in changing the shape of the overall protein by adjusting the access to the iron centres. This cooperative behaviour aids rapid respiratory transport of oxygen

in mammals. The uptake and release of oxygen takes place over the relatively narrow partial pressure range, thus absorption and desorption take place according to the slight difference in pressure between the lungs and muscle tissue.[32]

1.3.2 Spin Crossover — Discovery and History

Although spin crossover has always existed, it was only discovered in the 1930s. Cambi and co-workers[33–35] were studying the magnetism of derivatives of iron(III) tris-dithiocarbamates (which have since been studied structurally by Leipoldt and Coppens).[36,37] Cambi and co-workers observed electronic states whose population was strongly dependant on temperature, an anomaly they assigned to a rearrangement of the electrons in the *d*-orbitals as the temperature was decreased. Despite this discovery, it took another thirty years before the thermal spin crossover complexes, $[Fe(Phen)_2(NCS)_2]$, $[Fe(Phen)_2(NCSe)_2]$ and $[Fe(Bpyd)_2(NCS)_2]$ were first reported by Baker and Bobonich in 1964.[38]

$[Fe(Phen)_2(NCS)_2]$

Baker and Bobonich studied the magnetic moments at different temperatures of a series of 1,10-phenanthroline complexes of the form $[Fe(Phen)_2X_2]$ where $X = Cl^-$, Br^-, I^-, N_3^-, NCS^- and $NCSe^-$ together with the related bipyridine complex $[Fe(Bpyd)_2(NCS)_2]$.[38] They found that while the magnetic moment was slightly lower than expected, it was essentially independent of temperature for the chloride, bromide, iodide and azide complexes. However, in the case of the NCS^- and $NCSe^-$ compounds, between room temperature and 100 K there was a dramatic decrease from approximately 5 BM to about 1.4 BM. König and Madeja explained that two magnetically different $[Fe(Phen)_2X_2]$ complexes could be prepared, dependant on the ligand field strength of X.[39] They concluded that the effect seen in the thiocyanate and selenocyanate complexes where the ligand strength is close to the crossover point, was that of a spin state equilibrium.

Since 1964, $[Fe(Phen)_2(NCS)_2]$ has become one of the most widely studied SC complexes, with a wide range of techniques employed. These include infrared spectroscopy,[28,40] Mössbauer spectroscopy,[41] Raman spectroscopy,[30] NMR,[42] ESR,[41] calorimetry,[43] and muon spin resonance[44] as well as structural studies.[9]

	293 K	130 K	293 K, 1.0 GPa	30 K, Irr.
Fe–N1	2.199(3) Å	2.014(4) Å	2.003(7) Å	2.177(4) Å
Fe–N2	2.213(3) Å	2.005(4) Å	1.975(8) Å	2.184(4) Å
Fe–N20	2.057(4) Å	1.958(4) Å	1.954(7) Å	2.006(5) Å

Table 1.1: Fe–N bond lengths for $[Fe(Phen)_2(NCS)_2]$ under different conditions. N1 and N2 are part of the Phen ligand, while N20 is part of the thiocyanate.

One of the most interesting things about this compound is the fact that exhaustive studies have shown that it not only undergoes thermally induced spin crossover, but also light and pressure induced transitions, all of which have been studied crystallographically.[9,45,46]

The SC transition takes place at around 176 K and the sharp transition that takes place over a temperature range of only 5 K indicates that it is cooperative in nature, although any hysteresis is small, less than 1 K in magnitude (Figure 1.6, Section 1.2.2). The structure is orthorhombic (**P***bcn*) with one half molecule in the asymmetric unit, with the iron centre sitting on a two-fold rotation axis (Figure 1.14). Structural studies carried out by Gallois *et al.* on $[Fe(Phen)_2(NCS)_2]$ above and below the transition (at 293 K and 130 K respectively), show that while there is no change in symmetry, the FeN_6 octahedron becomes more regular for the LS state and the Fe–N bond lengths are between 0.1 Å and 0.2 Å shorter (Table 1.1).[9] It is interesting to note that the shortest Fe–N bond length is to the thiocyanate ligand which also undergoes the least contraction. This reduced contraction is thought to be because thiocyanate is a weaker π-electron acceptor than Phen, so the Fe–N bond shortens less in the low spin state.[9]

Spin crossover is also seen on the application of pressure to the sample at 293 K, indicating that the temperature of the transition is increased by at least 115 K at 1.0 GPa pressure.[45] A similar degree of shortening is seen in the pressure induced LS state compared to that under seen on cooling (Table 1.1).

$[Fe(Phen)_2(NCS)_2]$ also undergoes Light-Induced Excited Spin-State Trapping (LIESST) and the structure of the meta-stable high spin state was presented in 2002 by Marchivie *et al.*.[46] It is noticeable however, that all three Fe–N bond lengths are shorter than those seen at room temperature (Table 1.1).

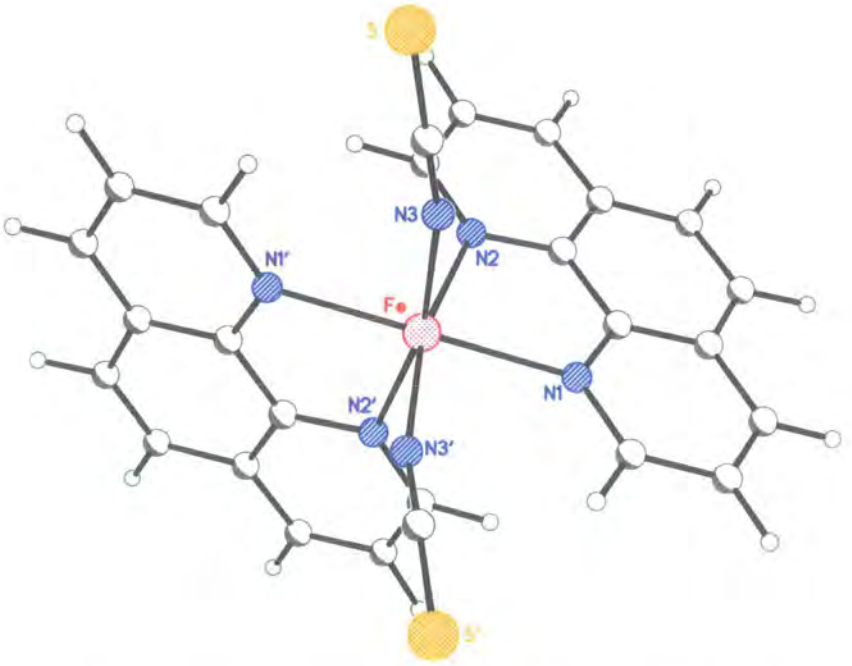

Figure 1.14: $[Fe(Phen)_2(NCS)_2]$ viewed down the two-fold rotation, with the symmetry equivalents primed.

Polymorphism is a phenomenon that has also been seen in $[Fe(Phen)_2(NCS)_2]$. The second polymorph has one molecule in the asymmetric unit and a cell of approximately double that of the first.[9,47] EXAFS data indicate that the average change in bond length for this polymorph is 0.24 Å compared with 0.16 Å (Table 1.1). This larger change in bond lengths leads to a larger increase in the frequency of the vibration of the Fe–N bonds, which leads to stronger iron–lattice coupling. This is reflected in the spin transition, which is sharper for the second polymorph, than for the first polymorph.

Thiocyanate Ligands

It is interesting to note, that while $[Fe(Phen)_2(NCS)_2]$ undergoes spin crossover, $[Fe(Phen)_3]X_2$ is low spin irrespective of the anion.[37] While this may be partly due to the cationic nature of the complex, the thiocyanate ligand clearly has a large effect. Consequently, a considerable portion of the literature has focussed on the use of thiocyanate ligands as they cause a marked weakening of the ligand field allowing SC transitions to take place that otherwise would not be possible. Thus thiocyanate ligands have been used in the design of a number of other SC materials of the type $[Fe(L)_2(NCS)_2]$. The bidentate ligands used include 2,2′-bipyridine (Bpyd),[48,49] 2,2′-bis-4,5-dihydrothiazine (Bta),[10,50] 2,2′-bis-2-thiazoline (Btz)[51] and the more complex biphenyl-4-yl[1-pyridin-2-yl-methylidine]-amine (Bppm)[52] amongst many others (Figure 1.15).

1.3.3 Notable Spin Crossover Complexes

Although spin crossover has been seen in all first row transition metals that have the appropriate electronic configurations, it is most common in iron and cobalt.

Tetrazole, Triazole and Oxazole

A fertile area of spin crossover research has been centred around complexes of the form $[Fe(L)_6](X)_2$ where the ligands are cyclopentene derivatives, like tetrazole,[55] triazole[56] and oxazole.[57] By far the most widely studied of these materials is the tetrazole based, $[Fe(R\text{tz})_6](X)_2$ series of complexes and consequently it includes a number of particularly interesting examples.

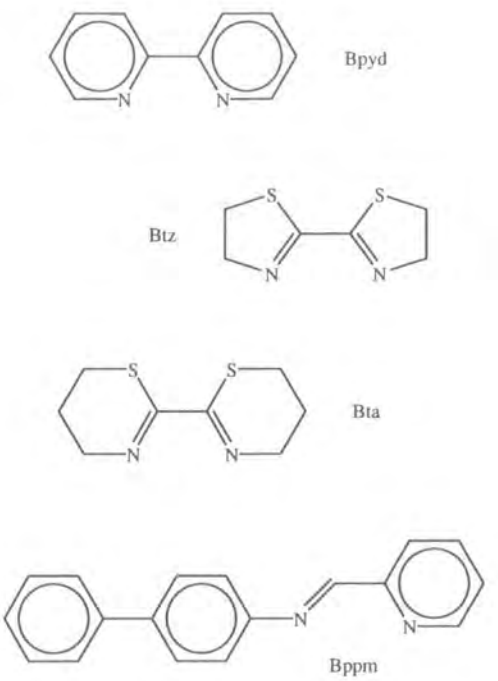

Figure 1.15: A selection of the bidentate ligands used in $[Fe(L)_2(NCS)_2]$ spin crossover complexes.

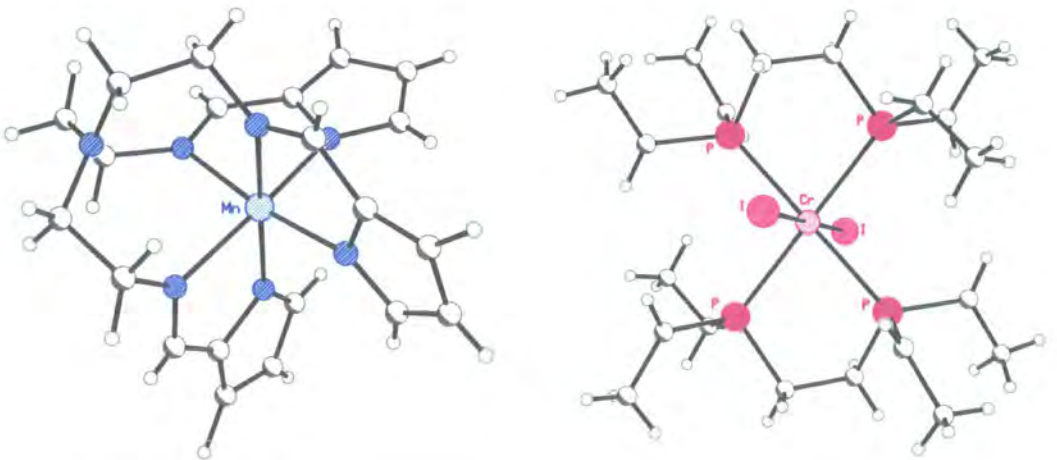

Figure 1.16: The first manganese and chromium spin crossover complexes.[53,54]

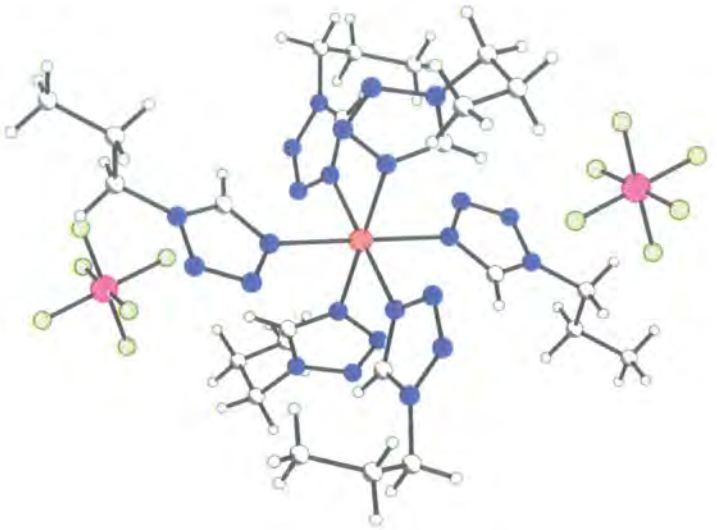

Figure 1.17: Low spin $[Fe(Ptz)_6](PF_6)_2$ at 130 K showing the ordered PF_6^- counter ions.[58]

$[Fe(Ptz)_6](PF_6)_2$

$[Fe(Ptz)_6](PF_6)_2$ is one of the first of these complexes, with a cooperative, highly abrupt transition at approximately 74 K and no appreciable hysteresis. This transition temperature has been studied as a function of pressure and found to increase to 102 K at 1 kbar.[58] Structural studies of the high and low spin complexes indicate that there is no change in symmetry, with both structures triclinic ($\mathbf{P\bar{1}}$) and the iron atom on an inversion centre. The PF_6^- ion is ordered at low temperature and modelled as rotationally disordered over three positions at room temperature, suggesting that the counter ion is tumbling due to thermal effect. This type of counter ion disorder–order transition is not uncommon in these types of system and the solvent and counter ions often make a huge difference to the nature or indeed presence of a transition.

$[Fe(Ptz)_6](BF_4)_2$

Another extensively studied compound in this series is $[Fe(Ptz)_6](BF_4)_2$. In contrast with many spin crossover complexes, the spin transition is coupled with a crystallographic phase change from rhombohedral ($\mathbf{R\bar{3}}$) to triclinic (believed to be $\mathbf{P\bar{1}}$).[59,60] The transition takes place at approximately 130 K with a 7 K hysteresis.[55] Interestingly, the high temperature

structure can be trapped by super-cooling, but the spin crossover is retained. The fact that this quench trapped low spin state has no hysteresis suggests that the hysteresis is due to the presence of the crystallographic phase change. Studies on $[Fe(Ptz)_6](BF_4)_2$ doped with the isostructural $[Zn(Ptz)_6](BF_4)_2$ support the conclusion that doping reduces the cooperativity, with the transition becoming more gradual.[61–63]

In addition to this, $[Fe(Ptz)_6](BF_4)_2$ was also the first compound shown to undergo both LIESST and reverse-LIESST (see page 12)[7] and the light induced transitions have also been found in samples diluted with $[Zn(Ptz)_6](BF_4)_2$.[64] These show a gradual decrease in the abruptness of the transition as the dilution is increased.

$[Fe(Mtz)_6](BF_4)_2$

Crystallographic data collected at 157 K and 113 K indicate that the structure of $[Fe(Mtz)_6](BF_4)_2$ is monoclinic with two crystallographically independent iron centres related to each other by a pseudo mirror plane.[60] Although the geometries around the iron centres are nearly identical, there is a clear distinction in the anisotropic thermal displacement parameters. Mössbauer spectroscopy confirms that the two iron sites are indistinguishable above the transition (approximately 160 K), but behave differently.[65] One site (Fe_A) undergoes SC, while the other remains high spin down to at least 4.2 K (Fe_B). Irradiating with a xenon arc lamp (350 nm $< \lambda <$ 650 nm) or a green argon ion laser (λ = 514 nm) at 20 K, leads to the light induced trapping of Fe_A in a meta-stable high spin state of practically infinite lifetime below 40 K. More unusually, irradiating with a red light ($\lambda >$ 700 nm) or a diode laser (λ = 820 nm) at 20 K, leads to the light induced trapping of Fe_B in a meta-stable low spin state from which relaxation to the high spin state occurs only above approximately 50 K. This behaviour is of particular consequence as the meta-stable low spin state is not reachable thermally.[66]

In most Fe(II) SC complexes, the minimum energy of the low spin $^1A_{1g}$ state lies approximately 500 cm^{-1} below that of the high spin $^5T_{2g}$ level (Figure 1.7), thus there is a temperature where the low spin state is thermodynamically favourable. Where the energy difference is considerably less than 500 cm^{-1}, the compound prefers to remain high spin. This is because a transition to the low spin state is only energetically favourable at *much* lower temperatures and at such low temperatures there is not enough thermal

energy in the system to overcome the energy barrier between the states. Similarly, if the energy potential of the high spin $^5T_{2g}$ lies below that of the low spin $^1A_{1g}$ potential, then the complex will remain high spin at all temperatures and the low spin will be thermally inaccessible. Hauser first suggested that it may be possible to trap the meta-stable low spin state in a process that corresponds with the original LIESST effect. Thus, irradiating the high spin ground state of Fe_B in compound $[Fe(Mtz)_6](BF_4)_2$ leads to a process that is analogous to the 'normal' LIESST that occurs for Fe_A.

Picolylamine Complexes

Picolylamine (Pic) is a pyridine derivative, consisting of an aromatic ring with a pendent methylamine group. As a bidentate ligand, it forms the basis of another of the most studied series of spin crossover compounds, $[Fe(Pic)_3]X_2.Y$ (where X = counterion and Y = uncoordinated solvent). $[Fe(Pic)_3]X_2$.EtOH was reported first by Renovitch and Baker in 1967, who investigated the chloride, bromide and iodide using both Mössbauer spectroscopy and magnetic moment measurements.[23] Renovitch and Baker showed that while the transitions in the chloride and bromide salts are incomplete, iodide salt has no transition and is a mixture of HS and LS at both room temperature and at 4.2 K. However, the magnetic data suggest that there may be a transition just above 300 K. Further examination of the bromide and chloride by Gütlich and co-workers, indicated that they both undergo step transitions, but the bromide transition has a much less pronounced plateau and the HS-Intermediate step also has a marked hysteresis.[24,67] Crystallographic studies of the chloride and bromide salts indicate that there are no symmetry changes with the spin transitions.[25,67] In the chloride however, there is clear rotational disorder in the ethanol solvent molecule in the high spin state that is not present in the low spin state, nor seen at all in the bromide salt. This comparison of the picolylamine halide salts demonstrates the importance to the nature of the transition, of uncoordinated counter ions and solvent, some distance from a spin crossover centre. This can be rationalised as due to cooperative interactions.

Over the last thirty-five years $[Fe(Pic)_3]Cl_2$.EtOH together with the hydrate, dihydrate and methanol solvate have all been studied extensively, including a comparison of the compounds which was carried out by Sorai *et al.* using Mössbauer spectroscopy.[37,68] They

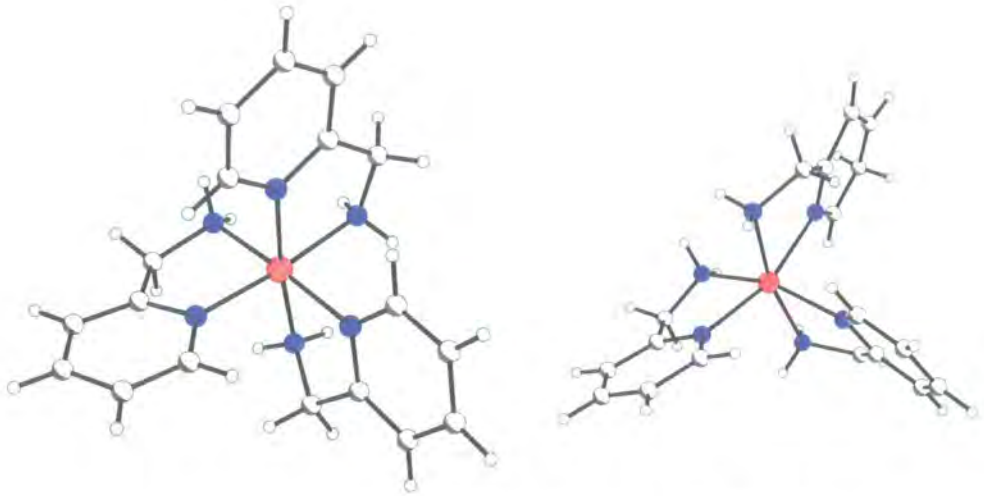

Figure 1.18: *mer*-$[Fe(Pic)_3]^{2+}$ (left) and *fac*-$[Fe(Pic)_3]^{2+}$ (right).

showed that the solvent is also important to the nature of the transition, with the ethanol and methanol adducts behaving in a very different manner to the hydrate (which has a 90 K hysteresis) and the dihydrate (which is low spin). The reason for some of this difference probably stems from the ligand arrangement around the iron centre.[25,67,69–71] Both the ethanol and methanol solvates have the ligands arranged in a meridonal arrangement, whereas the dihydrate is facial (Figure 1.18).

Irradiation of $[Fe(Pic)_3]Cl_2.EtOH$ crystals below a temperature of approximately 25 K, yields a change in colour, a result consistent with the LIESST effect.[14] Further to this, $[Fe(Pic)_3]Cl_2.EtOH$ has also been examined using proton NMR[42] and ESR.[41]

$[FeL_2]X_n$ Complexes

These complexes consist of a single iron centre bound by two heterocyclic tridentate ligands, *L*. The first of this type of ligand is [2,2′;6′,2″]terpyridine, which together with its derivatives have been shown to complex a variety of metals leading to the formation of materials with a range of potential biological, photochemical and magnetic properties.[72] The ligand consists of three pyridine rings positioned such that a small distortion allows easy terdentate binding to a metal centre (Figure 1.19).

Although $Fe(Terpy)_2^{2+}$ compounds are generally low spin,[73] both iron and cobalt complexes of terpyridine derived ligands have been shown to exhibit SC behaviour.[7,74,75]

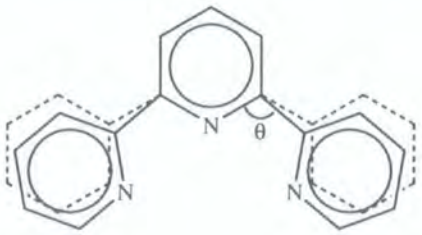

Figure 1.19: The distortion of the terminal rings of terpyridine on forming a complex. The C–C–N angle (θ) typically decreases from approximately 117° in the free ligand to 114° in the complex.[72]

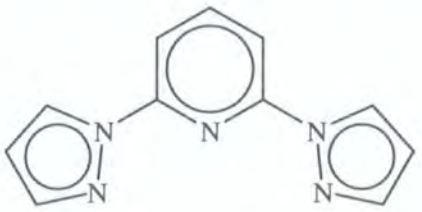

Figure 1.20: 2,6-dipyrazol-1-yl-pyrazine.

Other chelating ligands include 2,6-dipyrazol-1-yl-pyrazine ligands which are closely related to the terpyridine ligands, where the pendent pyridine groups are replaced with pyrazole groups leading to a slight increase in the natural bite angle (Figure 1.20).

Wide ranging studies of iron(II) dipyrazolylpyridine derivatives have demonstrated how minor changes to the ligand together with changes to the counter ion, can have an enormous effect on the magnetic properties.[76–78] This effect has also been seen in iron(II) complexes of the bidentate 2-(2′-pyridyl)benzimidazole where a range of compounds were studied including BPh_4^-, BF_4^-, PF_6^-, NO_3^-, Br^-, I^- and ClO_4^- salts together with the neutral species (caused by deprotonation of the imidazole).[79–82] This ligand has also been extended to give the tridentate 2,6-bis(benzimidazole-2′-yl)pyridine which has been used to form iron(II) complexes.[81,83]

The key problem with $[FeL_2]X_n$ compounds is that since the tridentate ligands form such stable ML_2^{n+} complexes, it is not possible to generate a range of materials by simple ligand substitution. However, functionalisation of the ligands has proven to be a fertile

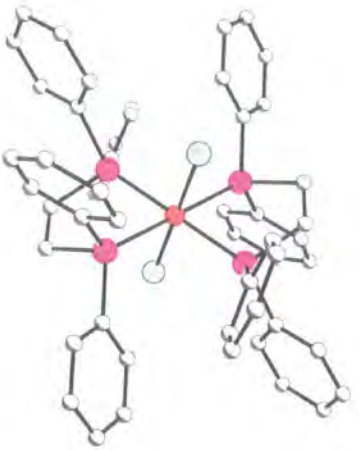

Figure 1.21: $[Fe(Dppen)_2]Cl_2.2Me_2CO$ at 130 K.[84] The hydrogen atoms and solvent are omitted for clarity.

field of research, as has changing the counter ion.

Iron Phosphine Complexes

Almost all the complexes discussed so far have involved nitrogen bound ligands, but this is not a requirement for spin crossover in iron(II) complexes. An example of this is $[Fe(Dppen)]_2Cl_2.2Me_2CO$, which has two phosphorus binding bidentate ligands and two chloride ligands. From magnetic susceptibility measurements, XRPD data and Mössbauer spectroscopy, the spin transition has been found to be centred around 240 K, but is gradual with a range of approximately 60 K.[84,85]

Structural studies both above and below the spin transition (room temperature and 130 K) show that it is not coupled with a crystallographic change.[84] The iron atom resides on an inversion centre which means the iron and Dppen ligands are rigorously co-planar with the chloride ligands in a *trans* geometry (Figure 1.21). Interestingly, while some of the largest Fe–L bond length changes are seen to take place in the average Fe–P distance (0.284(8) Å), the Fe–Cl changes by only 0.034(8) Å, which is possibly statistically indistinguishable from the HS state.

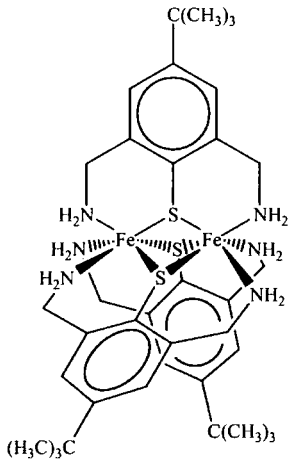

Figure 1.22: The proposed structure of a thiolate bridged, dinuclear iron(III) spin crossover complex.[86]

Dinuclear Spin Crossover Complexes

Dinuclear compounds are complexes that have two spin crossover active centres and are surprisingly rare. One example of this is the thiolate bridged dinuclear iron(III) complex discussed by Kersting *et al.* in 1998.[86] Although the complex has not been characterised structurally, strong antiferromagnetic coupling between the iron centres means the compound is diamagnetic at room temperature and has been studied using ^{1}H NMR spectroscopy leading to a proposed structure (Figure 1.22). ^{57}Fe Mössbauer spectroscopy indicates the transition is gradual, but otherwise the data is inconclusive.

The reason for particular interest in these materials is the fact that they often show interesting magnetic properties like step transitions, giving an insight into the cooperative mechanisms behind the spin crossover process.

Bipyrimidine Bridged Complexes

Bipyrimidine bridged complexes of the form $[Fe(Bpmd)(NCX)_2]_2(Bpmd)$ (where X = S or Se), have been investigated by Real and co-workers, although only the sulphide has been characterised structurally and then only at room temperature (Figure 1.23).[87,88] Under ambient conditions and on cooling, $[Fe(Bpmd)(NCS)_2]_2(Bpmd)$ remains HS down to at least 4 K, but the selenide undergoes a single SC transition at approximately 120 K.

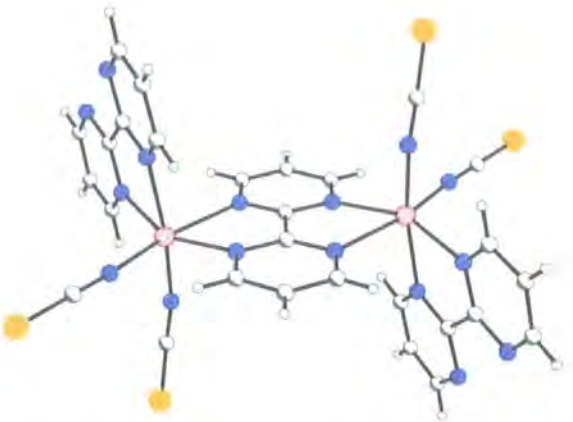

Figure 1.23: The dinuclear compound $[Fe(Bpmd)(NCS)_2]_2(Bpmd)$.

Thus, the sulphide is paramagnetic with intramolecular antiferromagnetic coupling. This behaviour remains when pressure up to 3.8 kbar is applied.[88] Increasing the applied pressure to 6.3 kbar induces a 50% spin crossover transition at approximately 100 K with a thermal hysteresis of 5 K. Magnetic susceptibility data collected during slow cooling, indicates that the antiferromagnetic coupling between the remaining HS centres is retained at 6.3 kbar. Increasing the pressure to 8.9 kbar not only raises the transition temperature to approximately 150 K, but also leads to the loss of the antiferromagnetic coupling. 11 kbar increases the transition temperature further, to 200 K.

In contrast, the application of a pressure of 5.8 kbar to the spin transition in the selenide, starts the development of a secondary transition.[88] This second step of the transition becomes more pronounced on increasing the pressure until 10.3 kbar. At 10.3 kbar the intermediate plateau begins to smear out suggesting the transition is being converted into a single step transition. Thus, the application of pressure in both the thiocyanate and the selenocyanate, has been shown to induce and modify the nature of the SC transition.

The related compound $[Fe(Dpa)(NCS)_2]_2(Bpym)$ is believed to adopt a similar molecular structure to the Bpmd analogue (although it has not been characterised structurally).[89] Magnetic and Mössbauer data indicate that there is a gradual, single step transition centred at approximately 245 K, without the application of pressure. It is possible that this is due to the presence of hydrogen bonding between the Dpa ligand and the thiocyanate ligands, but without structural data it is not possible to draw any definite conclusions.

Ligand	Counter Ion	Solvent	Spin State
4 H_2O	4 ClO_4^-	-	High Spin
4 H_2O	2 $S_2O_6^{2-}$	4 H_2O	High Spin
2 N_2^-	4 ClO_4^-	-	High Spin
3 OCN^-	1 ClO_4^-	-	High Spin
2 NCS^- & 2 SCN^-	-	-	Spin Crossover
2 MeCN	4 ClO_4^-	-	Spin Crossover
2 Cl^-	4 ClO_4^-	-	Low Spin

Table 1.2: Cobalt macrocyclic compounds.

Cobalt Macrocycles

In 2002, Brooker *et al.* reported an interesting structural and magnetic study of a range of dinuclear macrocyclic cobalt complexes.[90] The series was based on an octadentate pyridazine-containing Schiff-base macrocycle with two natural binding sites (Pdzm). Seven complexes were studied, each possessing different subsidiary axial donor ligands, counter ions and solvent, and which exhibited a range of magnetic properties from high spin, to low spin to spin crossover (Table 1.2). In most of these complexes, the Pdzm ligand occupies a pseudo square planar geometry with the subsidiary ligands occupying the axial site. The only exceptions to this are the chloride complex for which the structure has not been determined and the isocyanate complex where the ring occupies a buckled conformation caused by the bridging isocyanate ligand (Figure 1.24). One of the most interesting things about these materials is that weak antiferromagnetic exchange via the pyridazine bridges is seen in all the compounds, but is considerably weakened in the isocyanate complex due to reduced overlap between the Co(II) $d_{x^2-y^2}$ orbital and the pyridazine p-orbital. Also, the thiocyanate and acetonitrile compounds were the first dicobalt complexes to exhibit spin crossover and exchange coupling.[91]

Mixed Compounds

The mixed mononuclear/dinuclear spin crossover compound $[Fe_2(Trzt)_5(NCS)_4]_2$-$[Fe(Trzt)_2(NCS)_2(H_2O)_2]$ consists of two iron centres bridged by three triazole ligands in a 1,2-arrangement (Figure 1.25).[92] These dinuclear units are connected together through the mononuclear centre by hydrogen bonding interactions. Magnetic susceptibility data

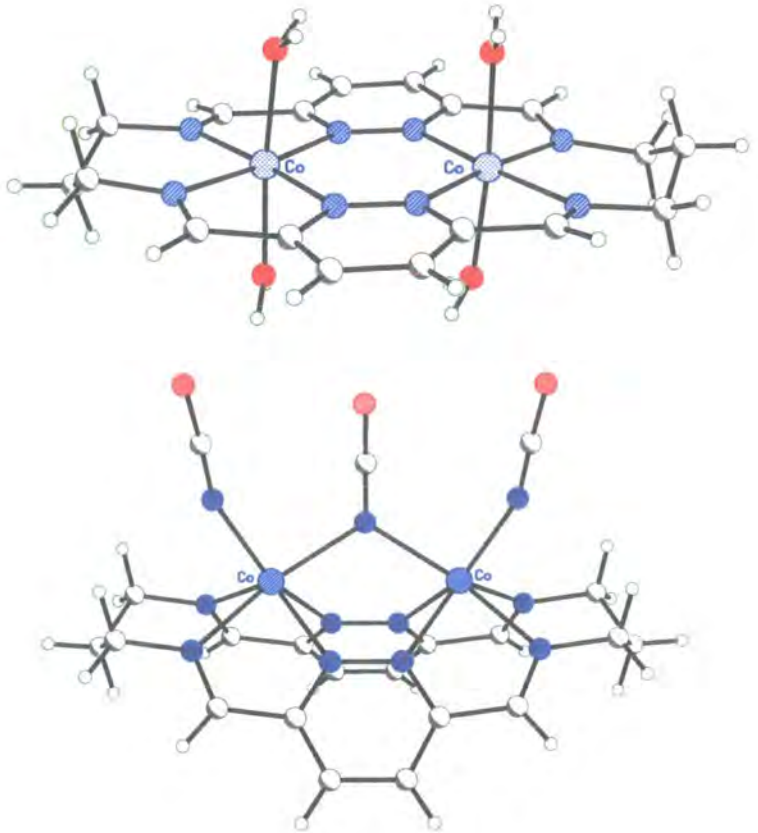

Figure 1.24: Two dinuclear cobalt macrocyles showing the different conformations occupied by the Pdzm ligand in the water complex (top) and the isocyanate complex (bottom).

and Mössbauer spectroscopy indicate that the transition takes place from three high spin centres to two LS and one HS at about 111 K. The transition is sharp, indicating a high degree of cooperativity, but with no appreciable hysteresis.

Although similar dimeric triazole-bridged, species have been known,[93,94] this mononuclear/dinuclear compound has the Trzt units in a *trans* arrangement. This allows the formation of the hitherto unknown pentanuclear motif which is the first species of this type known to undergo spin crossover. The concept of one centre remaining high spin is not uncommon and the effect can be viewed as similar to that of doping with a metal that does not undergo a transition. Doping in this way has been carried out by formal, partial replacement of iron with zinc (see pages 10 & 28), but has also been carried out in other cases. For example, the dinuclear iron(II)-chromium(III) spin crossover complex, (bis(pyridinyl)pyrazolate)-(bis(pyridylmethyl)ethane-diamine)-(nitrilotriacetato)-chromium(III)-iron(II) tetrafluoroborate (Figure 1.26) has a very gradual spin transition.[95] Since dilution generally decreases cooperativity, considering this system in terms of an iron complex 50% doped with chromium, leads to the conclusion that if both nuclei were iron(II) and underwent SC, the transition might become more abrupt.

A Binuclear Iron Helicate

There are many solution based spin crossover complexes, but since the transitions essentially take place in isolation, there is little interaction between the individual molecules and cooperativity effects are minimal. Telfer *et al.* have reported a novel binuclear helicate (Figure 1.27) which undergoes SC.[96,97] The transition is gradual as would be expected in a solution based system since the transition is essentially a thermal Boltzmann distribution of all the vibrational energy levels of both states. However, in the case of this dinuclear species, a single equilibrium constant could not be fitted suggesting that it, like many of the solid state dinuclear complexes, undergoes a step transition.

Trinuclear Spin Crossover

Building on triazole complexes, $[Fe(Etrz)_2(H_2O)_2]_3(Trf)_6$ is a linear trinuclear unit with bridging triazole ligands (Figure 1.28).[98,99] Structural studies above and below the tran-

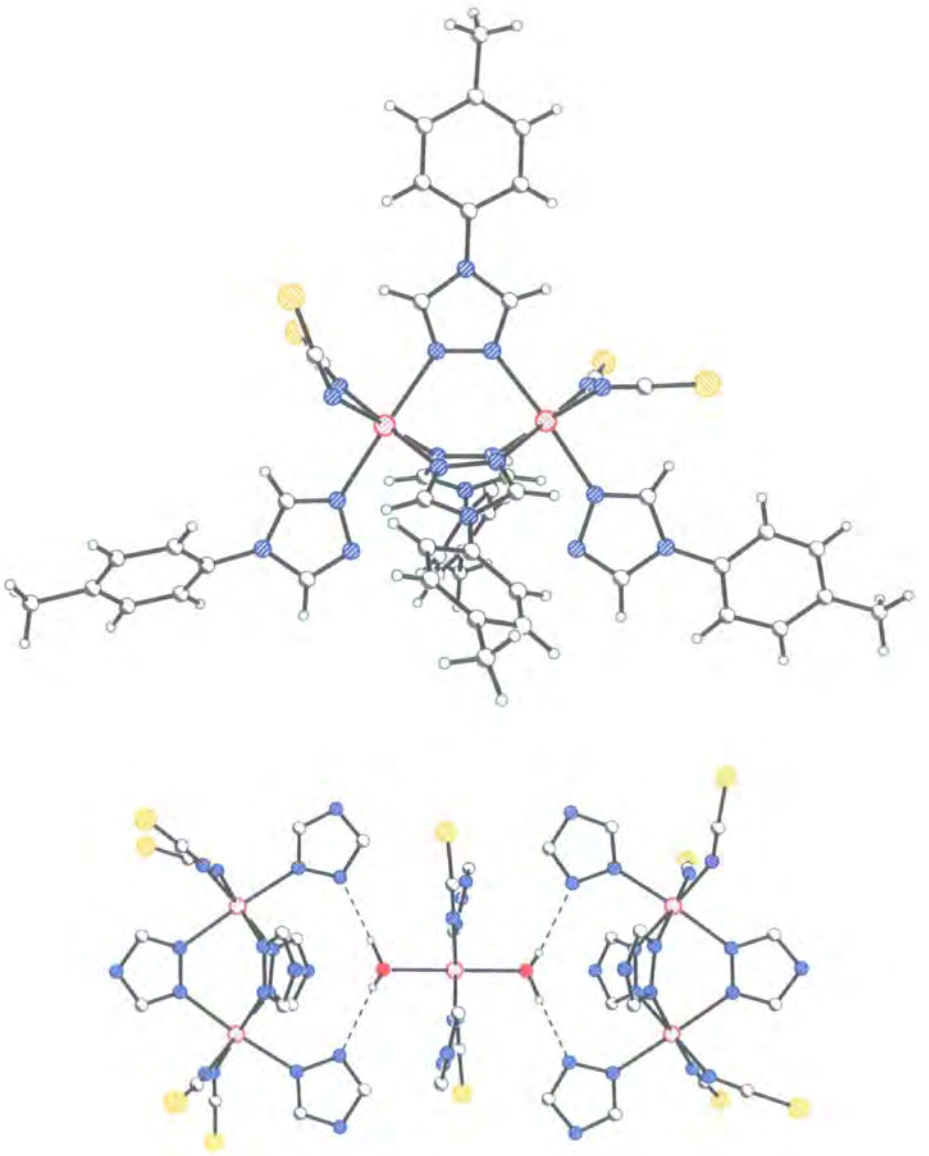

Figure 1.25: An unusual mixed mononuclear/dinuclear spin crossover complex, $[Fe_2(Trzt)_5(NCS)_4]_2$-$[Fe(Trzt)_2(NCS)_2(H_2O)_2]$. The dinuclear unit is shown (top) together with the unusual pentanuclear motif (bottom).

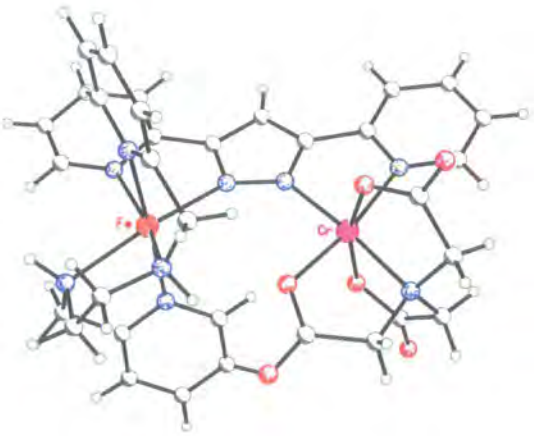

Figure 1.26: A heterometallic dinuclear iron(II)-chromium(III) complex.

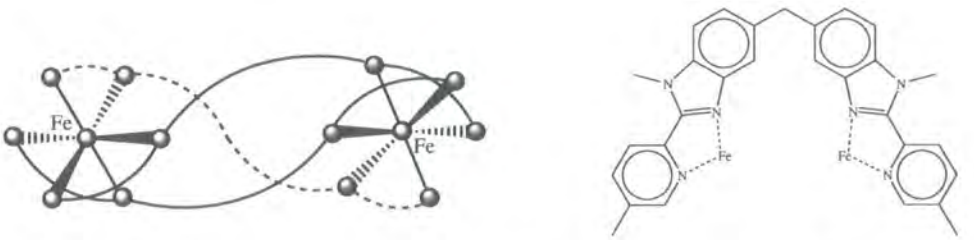

Figure 1.27: A binuclear spin crossover iron(II) helicate. A schematic of the structure is shown (left) together with the ligand (right) The ligand is tetradentate, binding twice to both iron centres (shown with broken lines). Three ligands, each binding in a bidentate arrangement round the two iron centres, combine to make the helical complex.

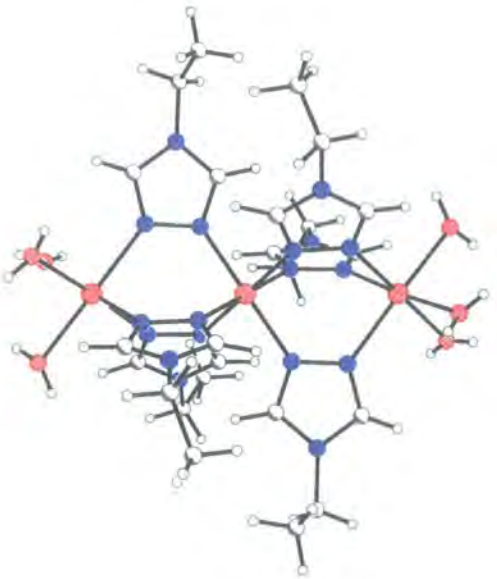

Figure 1.28: $[Fe(Etrz)_2(H_2O)_2]_3^{6-}$. Note the eclipsing interactions of neighbouring Etrz ligands, which cause the triazole ligands to slightly change orientation when changing from HS to LS.[98,99]

sition (room temperature and 105 K) show that the central iron(II) atom undergoes SC while the outer atoms remain high spin. This result is supported by magnetic susceptibility and Mössbauer data, which show the compound undergoes a gradual transition between 230 K and 190 K. Due to the shortening of the Fe–N distances caused by the SC transition, the triazole ligands undergo a subtle change in orientation.

Tetranuclear Spin Crossover

Self assembly synthetic techniques have yielded another solution based complex of particular note. In this case, the spin crossover transition also takes place in the solid state.[100] Structure determination shows that the complex consists of a 2×2 iron(II) grid together with eight perchlorate counter ions and several disordered solvent molecules of acetonitrile and water (Figure 1.29). However, magnetic measurements reveal that the transition is extremely gradual suggesting that it is virtually non-cooperative. Single crystal data at 293 K and 100 K show how the transition proceeds, with three high spin centres and one intermediate spin centre at room temperature, changing to one high spin and three

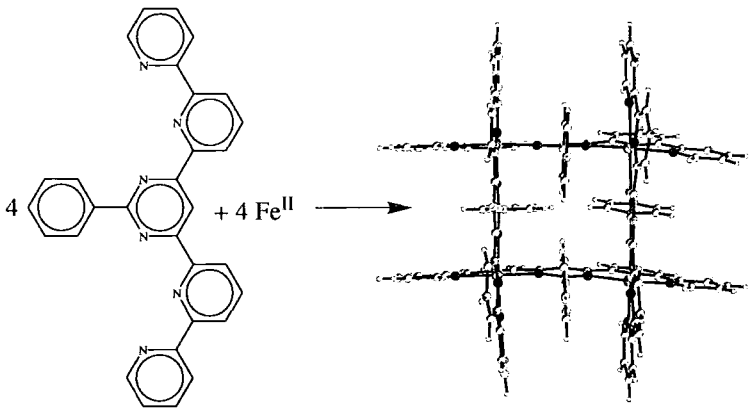

Figure 1.29: The formation of a spin crossover 2 × 2 iron(II) grid.

intermediate centres at low temperature. The nature of the intermediate centres has not been explored, but it is possible that they result from HS/LS static disorder.

1.3.4 Coordination Polymers

"Coordination polymer" is a term used to describe metal-organic framework compounds that extend in one, two or three dimensions through strong covalent bonds forming infinite chains or networks. They contain metal centres which are connected through bridging organic ligands. The bridging ligands allow a large diversity of networks leading to a wide range of structures and physical properties. Coordination polymers have been investigated as possible luminescent, non-linear optical and conductive materials.[101] In addition, the porous nature of many of these compounds also makes them ideal candidates for catalysis. Despite the obvious interest in these compounds in their disparate fields, considerably fewer spin crossover coordination polymers have been studied than monomeric SC compounds.

Triazole and Tetrazole Bridged Polymers

One of the first one dimensional (1D) polymers that exhibited SC was the iron(II) $[Fe(Trz)_3](X)_2.xH_2O$ system, which was first reported by Lavrenova *et al.* in 1986.[102] The structure was studied using EXAFS and is thought to consist of chains of iron atoms each connected by three bridging triazole ligands, very similar in nature to the trinuclear

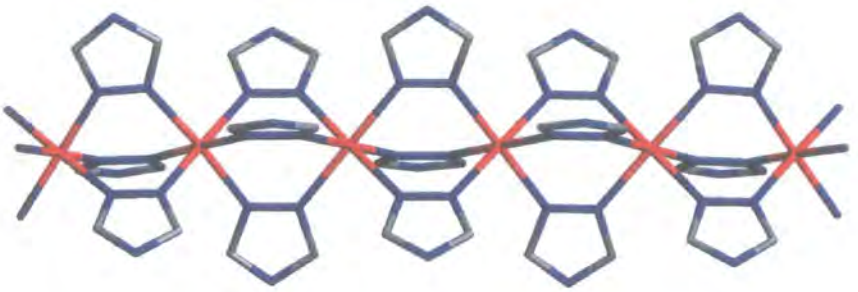

Figure 1.30: The $[Fe(Trz)_3]_\infty$ polymer chain.

species $[Fe(Etrz)_2(H_2O)_2]_3(Trf)_6$, reported in 1984 by Vos *et al.* (Figure 1.30).[17,98,99]

A large number of this family of materials have been explored by varying the substituent on the free nitrogen of the triazole ring (Trz), changing the counter ion and modifying the uncoordinated solvent.[103–105] These changes dramatically alter the nature of the spin transition, resulting in a range of types, including very abrupt transitions and continuous transitions. For example, $[Fe(Trz\text{-}NH_2)_3](NO_3)_2$ has a very sharp transition, with a 35 K hysteresis (T_c = 313 K on cooling and 348 K on warming), whilst $[Fe(Trz\text{-}NH_2)_3](BF_4)_2.H_2O$ has a more gradual transition that takes place at 255 K with a hysteresis of only 7 K.[103] In contrast, the spin crossover behaviour of $[Fe(Trz\text{-}NH_2)_3](Tos)_2.2H_2O$ is coupled with a dehydration-rehydration process.[104] As the sample is heated, the uncoordinated water is lost, followed by an extremely abrupt transition at 361 K from the meta-stable low spin $[Fe(Trz\text{-}NH_2)_3](Tos)_2$, to the high spin state. The transitions in this dehydrated compound following the dehydration-SC are more gradual and take place at a much lower temperature (T_c = 279 K on cooling and 296 K on warming). In this case, the dehydrated phase is hygroscopic and reabsorbs water under normal atmospheric conditions, however in some cases, the complexes are air stable.

The first polymer to be fully characterised structurally was $[Fe(Btrzp)_3](ClO_4)_2$ which is hexagonal ($\mathbf{P\bar{3}}c1$) with iron chains running along the c-axis forming channels in which the ClO_4^- counter ions reside (Figure 1.31).[106] The transition is gradual and incomplete, taking place over a temperature range of over 100 K centred at approximately 150 K. Structural data recorded at 100 K and 200 K indicate a shortening of the Fe–N distances from 2.164(4) Å to 2.038(4) Å, coupled with a shortening of the Fe$\cdots$Fe distance along

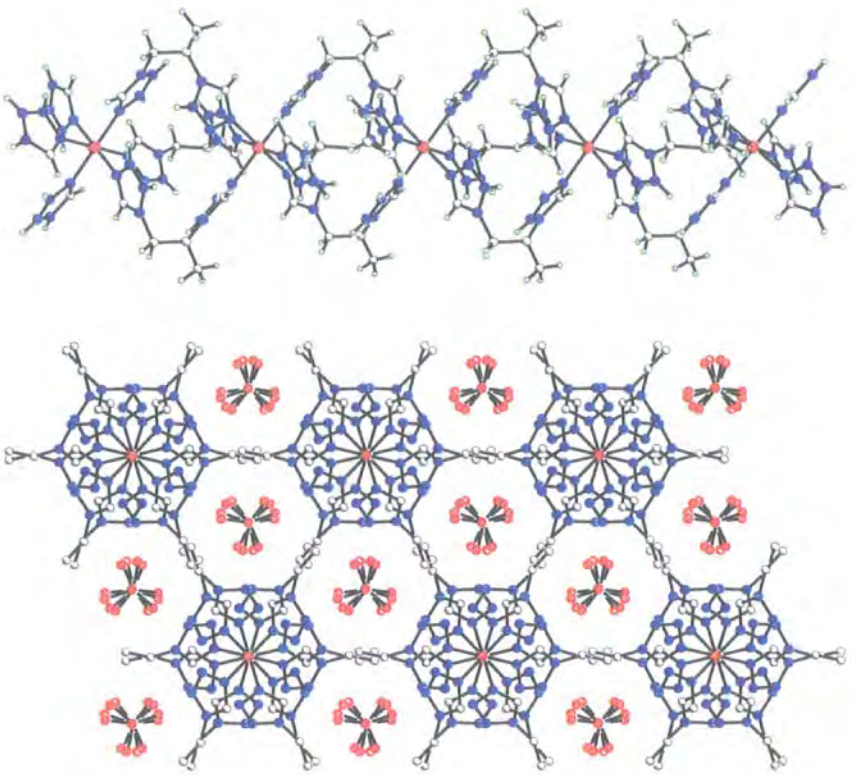

Figure 1.31: $[Fe(Btrzp)_3](ClO_4)_2$ at 100 K. The chain structure is clearly shown (top) along with the channels (bottom, hydrogen atoms are omitted for clarity).

the chain from 7.422(3) Å to 7.273(3) Å.

Following the triazole polymers, a number of bis-tetrazole bridged polymers were studied including the linear, 1,2-bis(tetrazol-1-yl)propane bridged, iron(III) SC complex.[107] This structure is also hexagonal with iron chains similar to those seen in $[Fe(Btrzp)_3](ClO_4)_2$ and the transition (centred at approximately 140 K), is also gradual and incomplete, though the residual high spin is only 7%. Structural data have been recorded at 150 K and 200 K as well as above the transition and below the transition, at 296 K and 100 K. The Fe–N distances clearly show the change from HS to LS, coupled with a shortening of the Fe$\cdots$Fe distance along the chain from 7.477 Å, to 7.461 Å at 200 K, 7.376 Å at 150 K and 7.293 Å at 100 K.

The gradual nature of the transitions in these compounds is thought to be caused by the flexibility in the ligand because the central unit acts like a kind of shock-absorber,

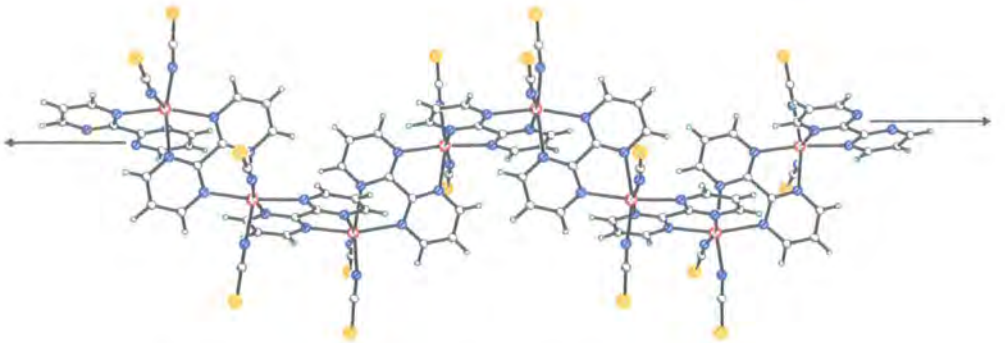

Figure 1.32: The chiral polymer $[Fe(Bpmd)(NCS)_2]_\infty$.

preventing the transmission of elastic interactions along the iron chains.[108]

A Bipyrimidine Bridged Polymer

Based on the bipyrimidine bridged dinuclear complexes, De Munno *et al.* developed the polymer $[Fe(Bpmd)(NCS)_2]_\infty$.[109] This polymer crystallises in the tetragonal space groups $\mathbf{P}4_1$ and $\mathbf{P}4_3$, forming chiral chains of iron(II) centres successively bridged by Bpmd ligands (Figure 1.32). Similar to the dinuclear complex, under ambient conditions and on cooling to as low as 4 K, there is antiferromagnetic coupling between the high spin iron centres. Also like its dinuclear counterpart, under a pressure of 11.8 kbar, the polymer undergoes spin crossover which takes place between 100 K and 150 K to around 40–50% completion.[88]

A Bipyridine Bridged Polymer

A much more recent example of a polymeric spin crossover material is the bipyridine (Bpyn) bridged polymer $[Fe(Pyim)_2(Bpyn)](ClO_4)_2.2C_2H_5OH$ which was reported by Matouzenko *et al.* in 2003.[110] Magnetic and Mössbauer data indicate that the compound has an abrupt transition at approximately 205 K with no noticeable hysteresis. It consists of iron(II) centres which are ligated by two bidentate pyridyl-imidazole ligands and also by two different Bpyn molecules in a *cis* conformation. The former come together with the Bpyn ligands forming a bridge between iron centres leading to chains which adopt a zig-zag arrangement (Figure 1.33). In addition to the iron centre (which sits on a two-fold rotation

Figure 1.33: The unusual zig-zag chains in the spin crossover polymer $[Fe(Pyim)_2(Bpyn)](ClO_4)_2.2C_2H_5OH$.

Figure 1.34: The disordered perchlorate in $[Fe(Pyim)_2(Bpyn)](ClO_4)_2.2C_2H_5OH$ showing the disorder in the high spin and low spin states (left and right respectively).

axis), there are also a perchlorate counter ion and ethanol solvent. At room temperature the ethanol is well ordered, but the perchlorate ion is disordered and was modelled with two components rotationally disordered about the chlorine centre. At 173 K, the disorder over the two sites is retained, but the two tetrahedra now occupy positions where one face (and therefore three of the oxygen atoms) are coincident (Figure 1.34). Interestingly, while the ethanol is ordered in the high spin state, it is disordered below the transition and is modelled with a minor component of 30%. This material is a good example of how the counter ion and solvent are very important to the nature of transition. This effect is not uncommon, but clearly demonstrates that cooperativity can take place through weak intermolecular interactions, in this case involving C–H$\cdots$O hydrogen bonding between the ligands and the perchlorate counter ion.

Despite these interesting results, there are still relatively few one dimensional coordination polymers to date and attention has focused on materials with higher dimensionality.

Two Dimensional Layered Materials

Moving from one dimensional to two dimensional SC materials has had a profound effect on the field of spin crossover research, leading to the development of bimetallic polymers as SC materials.

Bimetallic polymers use metal containing anions as multidentate bridging ligands. Historically, extensive work has been carried out on two dimensional coordination polymers of this type as they can form stable networks with high dimensionality.[111] In particular, a considerable amount of work has been done on the square planar cyanometallates $[Pt(CN)_4]^{2-}$ and $[Ni(CN)_4]^{2-}$ including the Hofmann clathrates.[112] However, despite all this, very little work has been carried out on two dimensional systems with spin crossover transitions and to date the research has been limited to a small number of two dimensional SC materials.

The first two dimensional spin crossover material was reported in 1990 by Vreugdenhil *et al.* and was an extension of the triazole polymers.[113]

Water Controlled Cooperativity

Using bis-triazole ligands (Btrz) enabled the formation of the 2D compound $[Fe(Btrz)_2(NCS)_2].H_2O$ (Figure 1.35), which has been studied using EPR and Mössbauer spectroscopy.[113] It has been found to have a very abrupt transition at approximately 130 K with a 20 K hysteresis. On heating $[Fe(Btrz)_2(NCS)_2].H_2O$ to 240 °C the solvent water is lost. The resulting complex is high spin and does not undergo SC which suggests that the water is critical to the transition. Structural studies of the compound indicate that the water hydrogen-bonds to the non-coordinating nitrogen atom of the Btrz ligands forming a bridge between the $[Fe(Btrz)_2(NCS)_2]$ layers.

One of the most interesting aspects of the hydrated compound $[Fe(Btrz)_2(NCS)_2].H_2O$, is its unusual behaviour under pressure.[114] Initially, applying pressure to the compound leads to a broadening of the hysteresis, increasing the temperature of the warming mode. At 3.0 kbar the transition is noticeably more gradual, with a dramatic increase in the

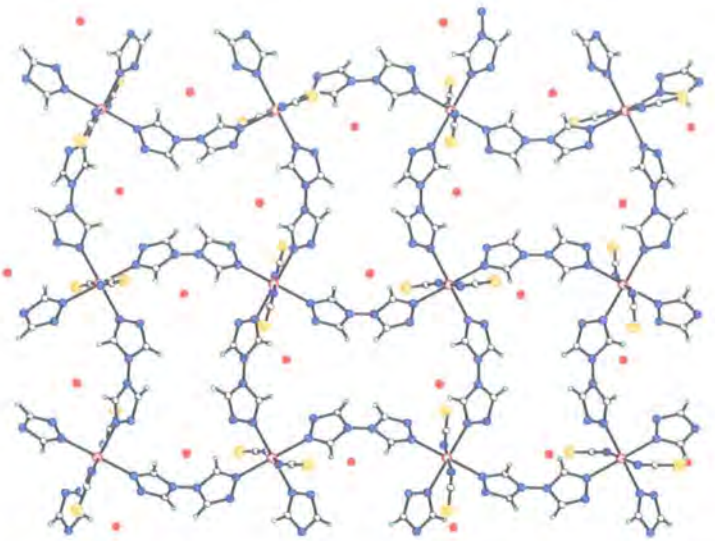

Figure 1.35: A sheet of $[Fe(Btrz)_2(NCS)_2].H_2O$.

amount of residual high spin as the pressure is increased to 6.7 kbar. By 10.5 kbar, the transition is no-longer visible with the high spin state stabilised throughout the temperature range. After releasing the pressure, the shift in the transition temperature is partially maintained and remains 7 K below that under normal, ambient conditions. The hysteresis also remains enlarged at 32 K and the transition remains incomplete, though after approximately 175 hr the amount of residual high spin relaxes to about 30%. Although unconfirmed, this unusual behaviour is thought to result from a pressure induced structural transition.

Other two dimensional materials of this type have been studied by Real and co-workers, using 1,2-bis(4-pyridyl)ethylene and 1,4-bis(4-pyridyl)butadiyne to link the iron(II) centres into continuous sheets.[115,116]

Hofmann Type Networks

The first of the Hofmann clathrates, $\{[Ni(CN)_2]NH_3.C_6H_6\}$, was accidentally discovered in 1897, when the German chemist Hofmann treated a nickel hydroxide solution with laboratory fuel (coal) gas.[112] Deliberate synthesis of this and related compounds followed by mixing ammonia solutions of nickel cyanide with benzene, thiophene, pyrrole and furan. It was over fifty years later however, that Powell and Rayner solved the structure of the

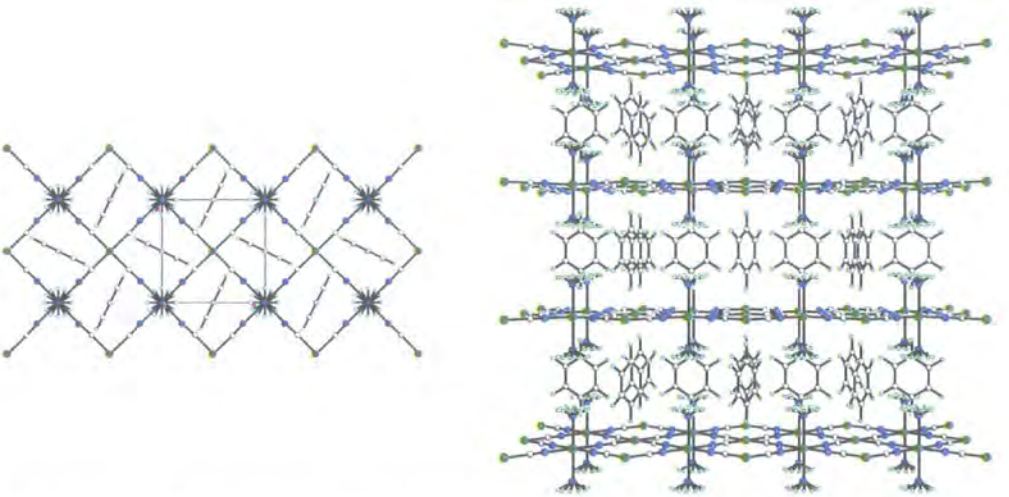

Figure 1.36: The benzene Hofmann clathrate.[119] The square planar nickel centres form sheets (left, viewed down the *c*-axis). The sheets stack directly above each other and provide layers between which the benzene guest molecules sit.

benzene Hofmann clathrate as a continuous array of square planar $[Ni(CN)_4]^{2-}$ ions with a central nickel(II) ion coordinated by the carbon end of the cyanide ligands.[117,118] These $[Ni(CN)_4]^{2-}$ ions form bridges between six coordinate nickel(II) centres which are ligated in a square planar manner by the four nitrogen atoms of the $[Ni(CN)_4]^{2-}$ ions and capped by two ammonia ligands (Figure 1.36). These sheets stack directly above each other forming channels between the four coordinate nickel atoms and additional cavities between the ammonia ligands which guest molecules (in this case benzene) can occupy.

These Hofmann clathrates have a low stability, with solvent loss a key problem and in the presence of water, they are readily hydrated. However, they led the way to a whole family of modified Hofmann-type clathrates, including the first two dimensional SC material (although its spin crossover transition was not recognised until much later).[120]

$\{Fe(Pyd)_2[M(CN)_4]\}$

Replacing the octahedral nickel with iron gives the Hofmann-type clathrate $\{Fe(NH_3)_2[Ni(CN)_4].2C_6H_6\}$ which is high spin.[120] However, replacing the ammonia with pyridine gives a new Hofmann-related, spin crossover material. Although $\{Fe(Pyd)_2[Ni(CN)_4]\}$ was first reported in 1973,[121] its spin crossover nature wasn't discov-

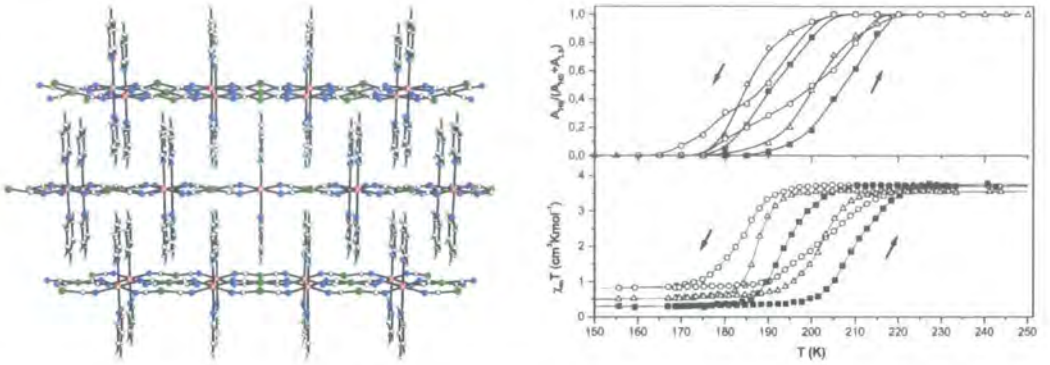

Figure 1.37: The structure of $Fe(Pyd)_2[Ni(CN)_4]$ (left), the Pyd–Pyd distance is approximately 3.7 Å. The effect on the spin transition of isotopic substitution (right) includes unsubstituted data (■), the deuterated species (△) and the ^{15}N data (○). The temperature dependence of the Mössbauer ratio and the magnetic susceptibilities are shown (top and bottom respectively).[122]

ered until 1996 when it was studied using Mössbauer spectroscopy which showed that the iron(II) centres undergo a highly cooperative transition just below 200 K with a 15 K hysteresis.[120] The structure which is related to the Hofmann clathrates, has slipped layers so that the pyridine rings from adjacent layers interdigitate, leading to weak π–π interactions (Figure 1.37).

One of the most interesting aspects of this material was reported more recently by Kitazawa and co-workers, who investigated the effects of isotopic substitution on the SC transition.[122] Kitazawa and co-workers compared the magnetic behaviour on deuteration of the Pyd ring and replacement of the cyanide nitrogen atoms with ^{15}N. Previous isotopic studies on $[Fe(Pic)_3]Cl_2$.EtOD, $[Fe(Pic)_3]Cl_2$.MeOD and FeSal generally indicated stabilisation of the low spin state i.e. the transition temperature was increased, although the overall shape of the transition curves were retained.[37,123,124] These isotope effects were interpreted as causing an increase in the energy gap between the two states due to modifications in the ligand field caused by changes in the hydrogen bonding network and the mass effect on the zero-point vibrational energies.

$\{Fe(Pyd)_2[Ni(CN)_4]\}$ is very different to the previously studied materials as there is no hydrogen bonding network and instead it consists of a true two dimensional polymeric structure. On isotopic replacement there is a marked decrease in the transition tem-

Compound	T_c (Cooling)	T_c (Warming)	Hysteresis
{Fe(Pyd)[Ni(CN)$_4$]}	186 K	195 K	11 K
{Fe(Pyd)[Pd(CN)$_4$]}	208 K	213 K	5 K
{Fe(Pyd)[Pt(CN)$_4$]}	208 K	216 K	8 K

Table 1.3: Transition temperatures for {Fe(Pyd)$_2$[M(CN)$_4$]}.

perature and Mössbauer spectroscopy has revealed additional low frequency vibrational modes that decrease on substitution. This effect has been put down to the vibrational contribution to the entropy.[122]

{Fe(Pyd)[Pt(CN)$_4$]} and {Fe(Pyd)[Pd(CN)$_4$]} have also been reported and show similar characteristics when compared with the parent bimetallic nickel complex. The transitions are similarly sharp, taking place at a slightly higher temperature with a slightly reduced hysteresis (Table 1.3).[125]

Expanding 2D to 3D

The advent of the three dimensional, spin crossover, coordination polymer is very recent with the first reported example in 1999 by García *et al.*.[126] This first material, [Fe(Btrz)$_3$](ClO$_4$)$_2$, is derived from the two dimensional network material [Fe(Btrz)$_2$(NCS)$_2$].H$_2$O by replacing the two anionic thiocyanate ligands with another bridging bis-triazole ligand. This transforms the polymer from a two dimensional system to a three dimensional cationic network that is charge-balanced by the perchlorate anions (Figure 1.38).[126]

This polymeric system has a two-step spin transition, the reason for which is the existence of two crystallographically inequivalent iron(II) sites. These are thought to have a slightly different ligand field strength and, consequently, different critical temperatures leading to two transitions approximately 40 K apart.[126]

In a similar manner, Konisbruggen *et al.*[127] generated the three dimensional network [Fe(Bttzb)$_3$](ClO$_4$)$_2$ from the related two-dimensional polymeric material.

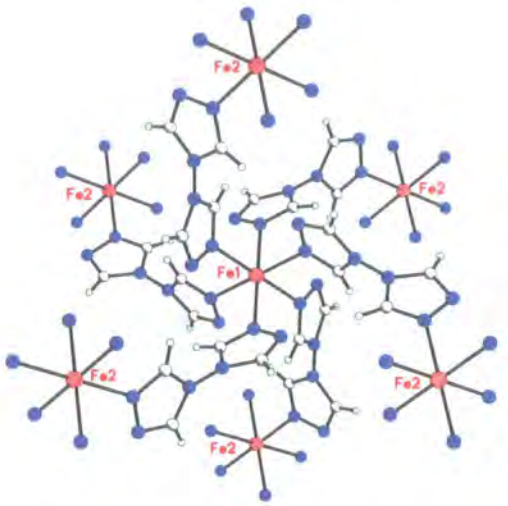

Figure 1.38: A section of the first three dimensional spin crossover network, $[Fe(Btrz)_3](ClO_4)_2$ at 260 K.[126] The alternating iron centres can be clearly seen with the bridging Btrz ligands. The perchlorate counter ions are omitted for clarity.

Hofmann-Type Bimetallic 3D Networks

Likewise, extending the same ideas to the two dimensional Hofmann-type networks $\{Fe(Pyd)[M(CN)_4]\}$, three dimensional materials have been designed. In this case, replacing the pyridine ring with a pyrazine ring (Pyz), led to a cross-linking of the layers forming the three-dimensional clathrate-type network $\{Fe(Pyz)[M(CN)_4].2H_2O\}$ (Figure 1.39).[125] In these materials, the $[M(CN)_4]^{2-}$ anions ligate iron(II) centres in a square planar arrangement forming sheets. These sheets are connected by pyrazine (Pyz) which ligates two otherwise independent iron centres at the apical site, thus bridging the gap between the layers. In contrast to the two dimensional materials, these layers lie directly above each other with their positions fixed by the Pyz bridging rings.

These compounds have a noticeably larger hysteresis and higher transition temperatures than their two dimensional analogues. This effect has not been put down to ligand field effects since Pyd is stronger than Pyz. Instead it has been explained in terms of increased internal pressure caused by the more rigid three dimensional structure giving a stronger effective field at the iron centre.

Raman studies of these compounds have shown that at room temperature the

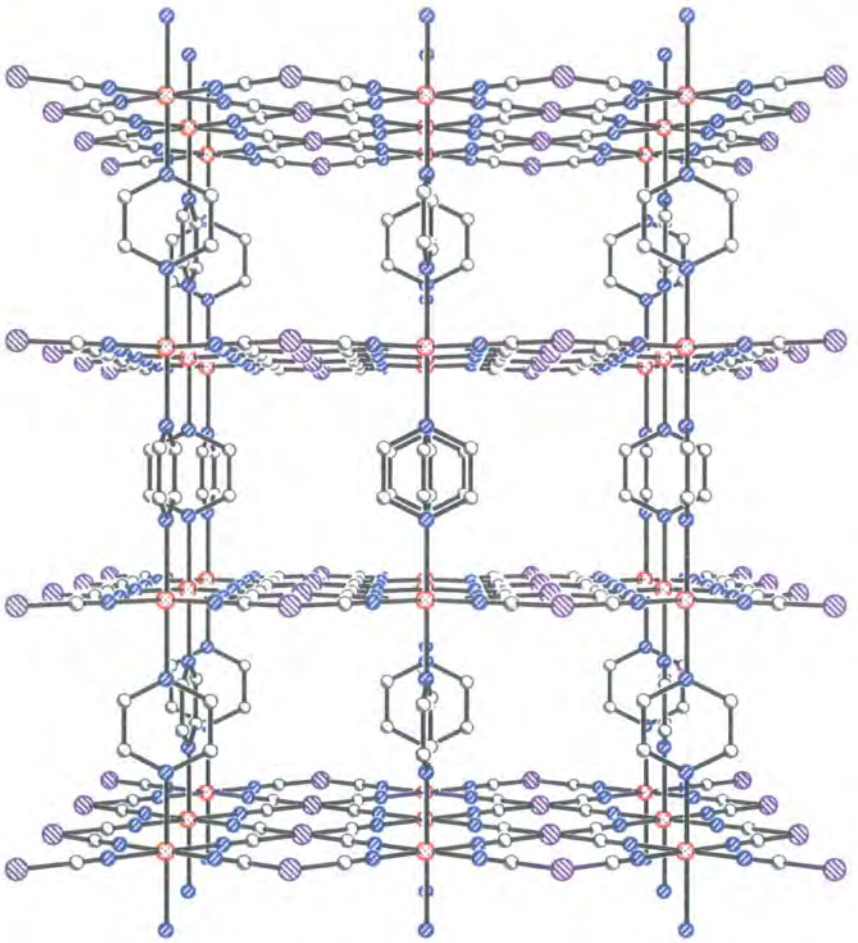

Figure 1.39: $Fe(Pyz)[Pt(CN)_4].2H_2O$ showing the Fe–$[Pt(CN)_4]$ layers. The Pyz ligands that link the layers are disordered, but only one component is displayed here for clarity. Iron is shown in red with platinum in purple.

transitions can be induced by the application of pressure.[128] Indeed, although the transition does not go to completion, the application of 1.35(5) kbar induces SC in $\{Fe(Pyz)[Ni(CN)_4].2H_2O\}$ that is not reversed until the pressure is reduced to below 0.65(5) kbar, making this the first example of piezo-hysteresis. In contrast, the palladium analogue also undergoes pressure induced SC, but the pressure required is higher (1.80(5) bar) and the transition is more gradual so the presence of a hysteresis could not be confirmed. Considerably higher pressure is required to induce a transition in $\{Fe(Pyz)[Pt(CN)_4].2H_2O\}$, but due to the equipment used, the exact pressure could not be determined and in both the palladium and platinum complexes, it is possible that the SC is competing with an additional structural change.

1.4 Conclusion

A wide range of spin crossover complexes have been reviewed, but while this introduction covers the majority of the most important and relevant materials, it only touches the tip of the iceberg and there are a considerable number of materials that have not been included. Like the original $[Fe(Phen)_2(NCS)_2]$ and the picolylamine complexes, some of the materials discussed here have been exhaustively studied. Others have been developed much more recently and therefore have been studied to a lesser degree. Perhaps some of the most interesting materials are the relatively new polymeric compounds, which due to their often high degree of cooperativity, strong thermochromism and tunability, appear to have many potential technological applications making this an exciting new and novel area for further research.

In all the cases discussed however, studying the structure has given a key insight into why the materials behave the way they do. For example, in the case of the mixed $[Fe_2(Trzt)_5(NCS)_4]_2$-$[Fe(Trzt)_2(NCS)_2(H_2O)_2]$ complex it would not have been possible to discover which iron atom remains low spin below the transition.[92] Without structural studies, it would not have been possible to discover that the difference between the facial and meridonal organisation of the ligands in the picolylamine solvates makes the dihydrate low spin.[25,67,69–71] The literature contains many such examples and it is clear that this valuable tool has furthered material development, giving an insight into how and why spin crossover transitions take place.

Chapter 2

Experimental

2.1 Introduction

X-ray diffraction is a very powerful technique used to discover and study the atomic arrangement in crystalline solids. This is possible because a periodic array of atoms behaves like a diffraction grating, the wavelength of X-rays being comparable to the interatomic spacings. Single crystal diffraction is the key structure solution technique in use today. In this context, a single crystal is a continuous, periodic array of repeat units. These repeat units are known as unit cells, each of which consists of one or more asymmetric units which are related to each other by symmetry. These symmetry operations combine to form one of 230 space groups (SG).

Single crystals are different from a crystalline powder, which is a collection of randomly oriented, "continuous, periodic arrays of unit cells". Each array is called a domain. Most of the characterisation was carried out by X-Ray Diffraction (XRD). Two techniques were used — Single Crystal X-Ray Diffraction (XRSXD) and Powder X-Ray Diffraction (XRPD).

2.2 X-ray Single Crystal Diffraction (XRSXD)

Early in the twentieth century, Lawrence Bragg suggested that a crystal could be thought of as containing an infinite amount of imaginary parallel planes, which behave like mirrors. This gave rise to "Bragg Reflections" and "Bragg's Law" (Figure 2.1), which explains that

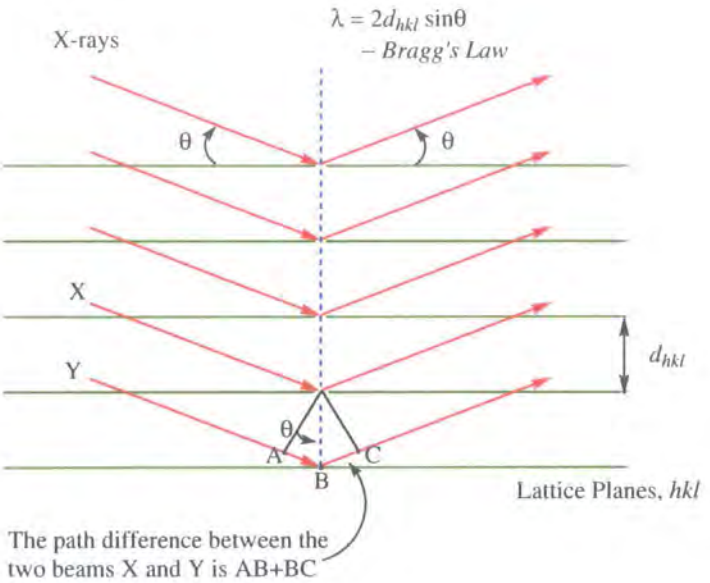

Figure 2.1: Schematic showing Bragg's Law.

each series of planes only diffracts when the scattered beams combine to give constructive interference i.e. when the path-length difference is an integer number of wavelengths. This is dependent on the wavelength of the beam (λ) and on the angle of incidence (θ). This means that by moving the detector and the crystal it is possible to measure a wide range of reflections.

2.2.1 Crystal Selection and Mounting

The crystals used were carefully selected such that they were 0.1–0.5 mm in all dimensions and were centred by eye using a microscope, so that the X-ray beam would hit the sample in the middle and bathe the whole of the crystal. This is important as the absorption varies with the amount of sample in the beam. The nature of the material also significantly affects the absorption as heavy atoms absorb more than lighter atoms.

In general, the crystals that were chosen were well shaped and free from growths and inclusions (Figure 2.2). Single crystals that were clear were also tested for extinction under polarised light, as a method of confirming crystallinity.

At room temperature, atoms have much increased thermal motion (with respect to low temperature) and sometimes tend to disorder. So in general, the majority of data were

Figure 2.2: Good quality crystals and poor quality crystals. The sample on the left consists of well shaped crystals free from intergrowths and inclusions. The sample on the right has no clear faces and may contain a number of crystalline components.[129]

Figure 2.3: Mounting crystals using the 'oil drop' method.[132]

recorded at as low a temperature as possible. In such cases, crystals were bathed in oil and frozen onto a hair (Figure 2.3). In addition to facilitating mounting, this method also helps to prevent chemical degradation in crystals that are air or moisture sensitive. The temperature was controlled using an Oxford Cryostream N_2 low temperature device,[130] which was used for routine data collections. An Oxford Cryosystems HeliX[131] could also be used if temperatures below 90 K were required. Where data were required above 230 K, crystals were mounted either on a hair or a glass fibre with either epoxy glue or nail polish.

Initially, a small set of frames were collected in order to find the unit cell parameters and assess the crystal quality (Figure 2.4). This routine allows the software to establish the "orientation matrix", which can be used to relate the position of all the reflections with the angles of the diffractometer. Finally, before each collection, a "dark" frame was recorded which was used to subtract the background from the data collected.

2.2.2 Bruker SMART-CCD 1000

The main instrument used was a 3-circle Bruker SMART-CCD 1000 diffractometer equipped with a molybdenum Kα, fine-focus sealed X-ray tube and a graphite monochromator, $\lambda = 0.71073$ Å (Figure 2.5). The detector is a charge coupled device area detector (CCD) and in general, measurements were recorded using ω scans at different ϕ settings.

2.2.3 Bruker SMART-CCD 6000

A similar instrument to the SMART-CCD 1000, the SMART-CCD 6000 is a more recent model and is also fitted with a molybdenum X-ray source. The main difference is the much larger area detector. In addition, the Bruker SMART-CCD 6000 has a digital video camera used to centre crystals. The camera was particularly useful with materials that undergo a colour change, making it possible to record crystal colours at various temperatures.

2.2.4 Bruker Proteum M

This instrument is a Bruker Proteum M diffractometer with an Apex detector. However, the source is a Bede Microsource®[133,134] and is the first of its type to have a molybdenum target.

The Microsource® is designed as a compact, low power, high brightness, microfocus X-ray source. X-rays are generated using an electron beam that is electromagnetically focused and positioned on the target.[133] In contrast with a conventional X-ray tube where the electron beam current is controlled by the current supply to the filament, in the Microsource® the beam current is controlled by a potential difference between the cathode and an intermediate electrode. This means the operating current is considerably lower (1.2 mA compared with 40 mA), resulting in a much lower power (60 W compared with 2000 W). This is in huge contrast to the *Fddd* diffractometer which has a 15 kW rotating anode.[135]

The X-rays generated can be focused leading to a more intense beam at the sample. This is done using either a Micromirror® optic[134] or a polycapillary optic (as in Durham).

Despite the obvious differences, in practice, the Bruker Proteum M with Bede Microsource® is used in a very similar fashion to the conventional Bruker SMART-CCD diffractometers.

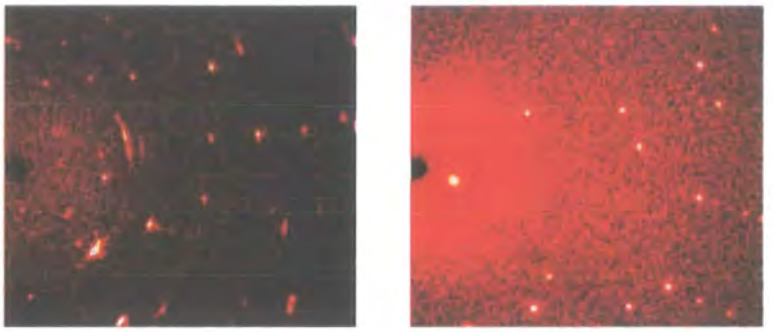

Figure 2.4: Frames of Bragg diffraction of varying quality. Poor diffraction is shown (left), where the reflections are split and smeared indicating poor crystallinity or diffraction from more than one crystal. Good diffraction is shown (right), where the reflections are well defined and continue to a high angle, indicating a high quality, single crystal.

Figure 2.5: The Durham SMART-CCD 1000.

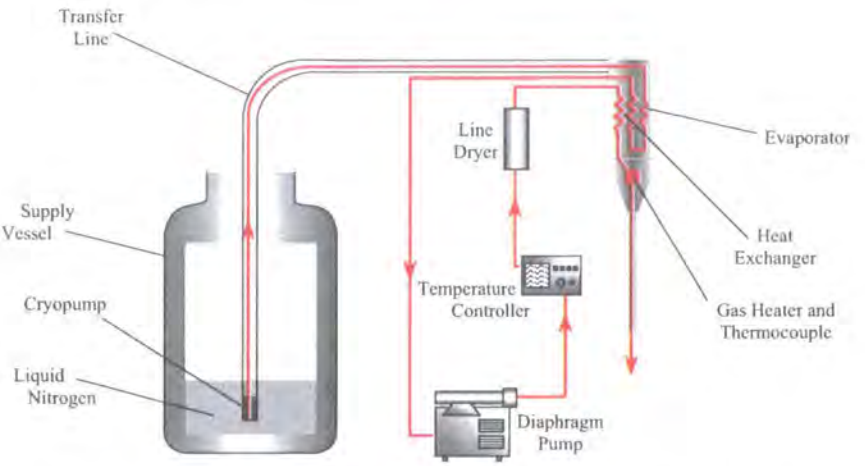

Figure 2.6: Schematic of the Oxford Cryosystems Cryostream.

2.2.5 Temperature Control

Two low temperature devices were used, the Oxford Cryosystems Cryostream and the Oxford Cryosystems HeliX.[130,131]

Oxford Cryosystems Cryostream

Two different versions of the Oxford Cryostream[130] were used: 600 Series and 700 Series Cryostream Coolers. In essence, both function the same way. A diaphragm pump draws liquid nitrogen from a Dewar vessel into the cold head. Here the nitrogen is evaporated and the vapour flows along one path of the heat exchanger and through the temperature controller, the pump and a line drier. When it returns to the cold head, it is cooled further when it passes along the second path of the heat exchanger. The temperature of this gas at the sample is controlled using a heater before it leaves the nozzle and comes into contact with the sample (Figure 2.6).

There are two minor differences between the two systems. The 700 series has a slightly larger range, 80–400 K (compared with 80–360 K) and has a turbo setting, which increases the nitrogen flow at low temperature, making it quicker to achieve lower temperatures. Two consequences of the increased flow however, are increased vibration at the sample and a less stable base temperature. Consequently, the turbo setting is not usually used during data collection.

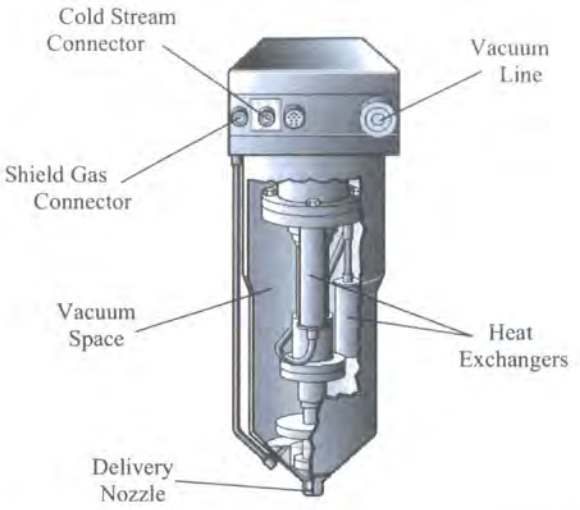

Figure 2.7: Cutaway diagram of the Oxford Cryosystems HeliX.[131]

Oxford Cryosystems HeliX

The Oxford Cryosystems HeliX[131] has a base temperature of 28 K with a stability of 0.3 K. It works by passing helium gas from a standard gas cylinder through heat exchangers mounted on a Closed Cycle Cryo-Refrigerator (CCR). The CCR is mounted within the HeliX and recycles compressed helium gas, which is water cooled. A Turbomolecular Pump (TMP) is used to maintain a vacuum space within the HeliX ($< 10^{-4}$ mbar), to minimise heat loss.

2.2.6 Irradiation

In some cases, samples could be excited to a different spin state using laser light. In these cases, the samples were mounted as described previously and cooled to 30 K using the HeliX.[131] The samples were then irradiated for between 2 and 10 mins with a laser. A number of lasers were available for use, including a diode near infrared laser (NIR) $\lambda = 830$ nm (4 mW power output), two red Helium-Neon lasers (HeNe) with $\lambda = 633$ nm (25 mW and 15 mW) and a green Nd:YAG laser $\lambda = 532$ nm (10 mW). The laser was directed using either mirrors or prisms or a combination of both, which were used to align the beam by eye on the sample (Figure 2.8).

Figure 2.8: Picture of the SMART-CCD 1000 with the red laser. The thin red line gives an idea of the beam path.

2.2.7 Data Collection, Analysis and Manipulation

In general, all the data manipulation was performed using the Bruker SAINT-PLUS suite of programs[136] and the SHELXTL V5.1 software.[137] Initially, a few frames were collected for indexing and the orientation matrix was obtained using the built-in auto-indexing routine in the SMART software.[138]

Given sensible cell parameters a full data collection was then recorded, using the SMART software.[138] In general, several series of narrow ω scans (0.3°) were carried out at different ϕ settings in such a way as to collect a sphere of data to a maximum resolution between 0.70 and 0.77 Å. Usually frames were collected for between 10 and 30 seconds per frame, depending on the size and diffraction of the crystal. A background (or dark) frame was recorded before the collection and automatically subtracted from each frame by the software.

The cell parameters were then refined using strong reflections above a suitable threshold to get more accurate values. This done, the raw frame data were integrated using these cell parameters and the corresponding orientation matrix, using the SAINT software.[136] File preparation was carried out using XPREP and the structure solved using XS.[137]

Structure Solution and the Phase Problem

Experimentally it is possible to measure the intensity of the reflections (I), but not the phase (Equation 2.1). In order to determine the electron density, we need both the amplitudes, $|F(h)|$ and the phases, $\exp(i\phi(h))$ (Equation 2.2). Nature has been very cruel because the phases give more structural information than the intensity. However, it is possible to get information about the phases from the intensities using constraints. For example, using the fact that electron density cannot be negative and a structure is composed of discrete atoms leads to a series of inequalities. These make it possible to assign some starting phases, which can be used as a basis for structure refinement. This process is known as 'Direct Methods'.

$$\sqrt{I} = F(h) = |F(h)| \times \exp(i\phi(h)) \tag{2.1}$$

$$\rho(xyz) = \frac{1}{V}\sum_{hkl} F(hkl)\exp[-2\pi i(hx + ky + lz)] \tag{2.2}$$

Since one of the assumptions made is that all atoms are discrete, randomly distributed and have equal scattering factors, in theory, this technique is not appropriate for organometallic compounds. However, in all cases, direct methods were used initially as modern software is often more tolerant. Where this was unsuccessful, the Patterson method was tried.

The Patterson method was first discovered by A. L. Patterson in 1934.[139] It can be best explained by considering the scattering factors as complex numbers with the amplitude as the real part and the phase as the imaginary part. Multiplying the complex number by its complex conjugate gives a real number equivalent to the square of the real component with the imaginary parts cancelling out (Equation 2.3). This leads to something closely related to the electron density. Peaks in the Patterson map correspond to vectors between pairs of atoms in the structure. For each pair of atoms there are two peaks, because a Patterson map is inherently centrosymmetric. Given the number of peaks, there is considerable overlap, but the height of the peaks is proportional to the product of the number of electrons in the two atoms. For this reason, vectors between two heavy atoms stand out

clearly compared to vectors between smaller atoms. Thus, the Patterson solution method can only be used for structure solution where there are a few heavy atoms present.

$$P(uvw) = \frac{1}{V}\sum_{hkl}|F(hkl)|^2\cos[2\pi(hu+kv+lw)] \tag{2.3}$$

Structure Refinement and Completion

The structures were refined using full-matrix least squares on F^2 using XL[140] from the SHELXTL software.[137] The software includes a difference fourier synthesis routine which substitutes $|F_{obs}| - |F_{calc}|$ for the structure factor (in Equation 2.2) making the residual electron density peaks stand out. This was used to locate any atoms not found at the solution stage.

Once all the atoms had been located, the thermal parameters were fully refined until the structure refinement was satisfactory with any disorder modelled appropriately. The weighting scheme was then adjusted and the refinement continued until the maximum shift/esd was less than 0.005.

Final solutions were viewed and checked using ATOMS V5.1,[141] XP,[137] ORTEP3,[142] Mercury[2] or similar and Crystallographic Information Files (CIFs) prepared and checked for publication using enCIFer[143] and CheckCif.[144]

Absorption

Absorption is an increased problem when working with heavy elements. Symptoms of absorption include poorly shaped thermal ellipsoids, high residual electron density and non-positive definite thermal parameters. However, it can be fairly straight forward to correct for absorption once the composition is known.

In general, efforts were made to index the crystal faces as this enables a more accurate absorption correction. This involves indexing the crystal faces and measuring the distance from them to the centre of the crystal.[137] If this was not possible, an empirical absorption correction from multiple measurements of equivalent reflections was applied to the data using SADABS.[145]

SADABS operates in three stages. Firstly, it determines scaling and absorption parameters by fitting individual intensities (I_o) to the mean corrected intensities averaged over all equivalents (Equation 2.4). This is done by alternately refining a scale factor for each frame ($S(n)$) and an absorption factor for the diffracted beam ($P(u,v,w)$). S and P are refined to minimise the $\sum[w(< I_c > -I_c)^2] + \sum[(\frac{1}{\sigma})^2(S_N - S_{N+1})]$ where $< I_c >$ is the mean for a group of equivalents, σ is the estimated standard deviation (esd) and S_N and S_{N+1} are scale factors for adjacent frames. The values of scale factors in adjacent frames are related by linear interpolation (equations 2.5 and 2.6).

Next, a small number of outliers are rejected, including those partially blocked by the beam stop or clipping the edge of the detector *etc.*. Finally an error model is generated for the remaining reflections by adjusting values for the scale factors k and g, so that χ^2 is fitted to unity which puts $\sigma(I)$ onto an absolute scale (Equation 2.7).

$$I_c = I_o S(n) P(u,v,w) \tag{2.4}$$

$$S_n = (1-x)S_N + xS_{N+1} \tag{2.5}$$

$$x = n - N \quad (N \textit{ integer},\ 0 < x < 1) \tag{2.6}$$

$$\sigma^2(abs) = k[\sigma^2(raw) + (g < I_c >)^2] \tag{2.7}$$

SADABS assumes the crystal is isotropic, which is rarely entirely true. However, in general it is fairly effective, but does not always work with crystals that are thin plates or long needles or where there is a shortage of data.

Twinning

Some of the crystals studied were found to exhibit twinning. A twinned 'crystal' is one which is not truly single, but consists of two or more intergrown crystals whose orientations are related by some symmetry operation. Twinning most often occurs when the lattice

symmetry is higher than the crystal symmetry, for example in monoclinic crystals where β is close to 90°. Twinned crystals can be divided into two categories: merohedral and non-merohedral. Non-merohedral twinning is usually identified when a well formed crystal that scatters strongly and cleanly either doesn't index or only indexes with a fraction of the reflections. Typically, it is then usually possible to index the rejected reflections with the same unit cell, but a different orientation matrix. Thus, when non-merohedral twinning is present, the reflections belonging to the different crystal orientations do not completely overlap (thought they may do so partially). Merohedral twins however, often index well, but either do not solve or refine badly. In this situation, reflections from the different orientations overlap, affecting the relative value of the intensities. In such cases, a matrix that relates the twin components can be included in the refinement and a twin ratio refined. In some cases, this twin matrix is apparent on considering the lattice symmetry, but where this is not obvious, software like ROTAX[146] is available to help determine twin laws (the symmetry operation(s) relating the twin components, written as a matrix). This method can also be used to refine structures where the crystal is a non-merohedral twin, but the partial overlap of reflections from the second twin component has been ignored. Ideally however, the second twin component in non-merohedrally twinned crystals should be included, by integrating all the data from all components using software like GEMINI.[147]

Data Quality Assessment

The quality of the data and refinement were assessed in a number of ways. Before data collection, the matrix frames were examined visually to look for twinning and to check that the cell fitted the data well. The quality of the indexing was also used to assess the validity of the experiment. However, given the durability of modern techniques and software, poor data do not always lead to poor results, so substandard data wasn't always rejected out of hand if it indexed reasonably well.

On the whole, the quality of the data therefore was assessed by the quality of the results, which were quantified in a number of ways. Firstly, the structure itself was examined and bond lengths and angles were checked to ensure they made chemical sense. Next, the difference map was studied. This was used to make sure there were no atoms missed

or incorrectly assigned. Where a metal was present, special care was taken as ripples in the fourier map were often visible. These are caused by data that isn't 100% complete. This effect is theoretically present for all atoms, but since the X-ray scattering factor is proportional to the number of electrons, the effect is much stronger for heavy metals than for lighter elements.

Thermal parameters were also used as a key indicator of the quality of a structure. Initially, all thermal parameters were refined as isotropic, with one parameter describing the thermal motion as a sphere. The magnitude of this parameter was used to give an indication of thermal motion (for example in a PF_6^- counter ion) and whether atom assignment was correct.

In most cases, in the final model, non-hydrogen thermal motion was described as an ellipse using six anisotropic displacement parameters. Not only did this give more information about the thermal motion, but it also gave a better idea of the quality of the model and the data. For example, elongated thermal ellipses for a CF_3 group could indicate disorder, but where this could not be the case or where many atoms were affected, absorption could be causing a problem.

In extreme cases, poor data, a poor model or disorder led to the situation where the ADPs no longer described an ellipse and one of the thermal parameters was non-positive definite. In such cases, the data was either rejected or efforts were made to solve the problem by applying or improving the absorption correction. Where absorption was not the problem, for example in the minor component of a disordered system, thermal motion was modelled as isotropic.

Another important quality assessment tool used were the figures of merit generated by the software. There were a number of these used during the space group selection and structure solution processes, which were used to help choose a sensible model. More important than these are those used to assess the data (equations 2.8 and 2.9) and the final model (equations 2.10 to 2.12). These are generally based on the difference between the observed and calculated structure factors (F_{obs} and F_{calc}) and in the case of $GooF$, the number of observations and parameters (n and p). The lower the value for these statistical measures, the better the data or the more reliable the model. However, these values are not wholly reliable, so were never used without the other assessment techniques detailed

R-Factor	Guideline
R_{int}	<10%
R_{sigma}	<20%
R_1	<5%
wR_2	<12%
$GooF$	0.95<S<1.05

Table 2.1: Guidelines for acceptability of figures of merit.

previously. Despite this, guidelines of acceptability are often used (Table 2.1).

The final stage of the refinement involved adjusting the weighting scheme (equation 2.13). In general a two parameter weighting scheme was used. During the early stages of the refinement, $a = 0.1, b = 0$ was used, but once the structure was satisfactory, these values were effectively refined. One consequence of this is the artificial improvement of the 'goodness of fit' ($GooF$) and the weighted R-factor (wR_2), so these values, like the other statistics, were never relied upon and only used as a guide.

$$R_{int} = \frac{\sum |F_{obs}^2 - \overline{F}_{obs}^2|}{\sum [F_{obs}^2]} \tag{2.8}$$

$$R_{sigma} = \frac{\sum [\sigma(F_{obs}^2)]}{\sum [F_{obs}^2]} \tag{2.9}$$

$$R_1 = \frac{\sum ||F_o| - |F_{calc}||}{\sum |F_{obs}|} \tag{2.10}$$

$$wR_2 = \sqrt{\frac{\sum [w(F_{obs}^2 - F_{calc}^2)^2]}{\sum w(F_o^2)^2}} \tag{2.11}$$

$$GooF = S = \sqrt{\frac{\sum [w(F_{obs}^2 - F_{calc}^2)^2]}{n - p}} \tag{2.12}$$

$$w = \frac{1}{\sigma^2(F_{obs}^2) + (aP)^2 + bP} \tag{2.13}$$

$$P = \frac{2F_{calc}^2 + Max(F_{obs}^2, 0)}{3} \tag{2.14}$$

2.3 X-ray Powder Diffraction (XRPD)

In a powder, the individual crystallites are randomly oriented, so compared with single crystal X-ray diffraction (XRSXD), in XRPD the individual reflections become a series of concentric intensity cones. This means there is increased peak overlap and a corresponding loss of information, making it very difficult (though not impossible) to solve molecular structures. However, powder diffraction data can still be used to *refine* a known structure and this is the primary use for XRPD.

2.3.1 Siemens D5000 Diffractometer

The Siemens D5000 Diffractometer is fitted with a copper fine-focus sealed tube source. The optical system employed includes 1° fixed or variable divergence slits, antiscatter slits and a 0.2 mm fixed detector slit (Figure 2.9). The detector setup is a scintillation counter preceded by a graphite (001) diffracted beam monochromator $K\alpha_1$ $\lambda = 1.54060$ Å, $K\alpha_2$ $\lambda = 1.54439$ Å and $\overline{\lambda} = 1.5418$ Å. The machine was generally used with a sample changer, enabling many samples to be run without constant maintenance. The hardware was controlled by Bruker propriety software, DiffracPlus EditJob V.4.0[148] and the data were qualitatively examined using EVA.[149]

2.3.2 Bruker D8 Advance

Like the Siemens D5000 Diffractometer, the Bruker D8 Advance also has a copper sealed tube source, but is fitted with a germanium (111) primary beam monochromator, which eliminates $K\alpha_2$ radiation giving a monochromatic wavelength of $\lambda = 1.540598$ Å. In general, a Braun Position Sensitive Detector (PSD) is used which enables enhanced data acquisition. The PSD is essentially an anodic wire with pulse generating electronics at each end which gives feedback to the controller. This allows the detector to scan a range of approximately 12°, effectively increasing the intensity by increasing the time spent at each 2θ point.

Not only can the Bruker D8 Advance be operated in capillary and flat plate modes, it also has facilities for environmental control. There are three environmental chambers: Anton Paar HTK1200,[150] Anton Paar TTK450[151] and the Oxford Cryosystems PheniX.[152]

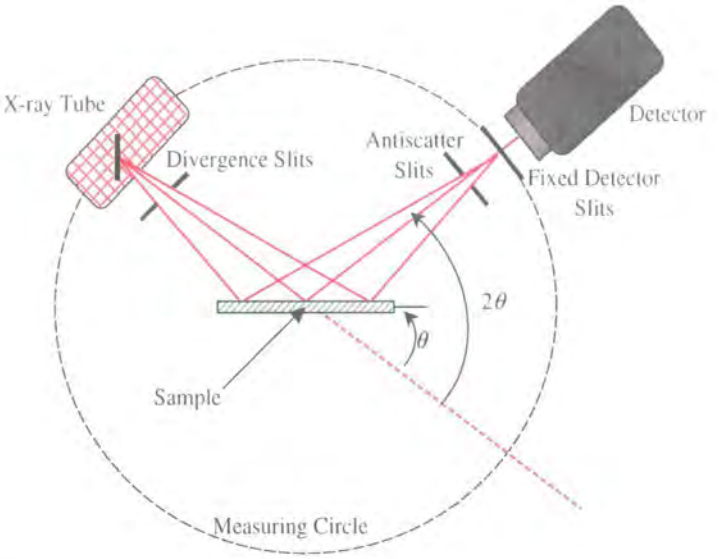

Figure 2.9: Schematic of the Siemens D5000 Diffractometer, a powder diffractometer.

Anton Paar HTK1200

The Anton Paar HTK1200 is a furnace type environmental chamber (Figure 2.10).[150] Temperature control is via heating elements and a thermocouple located underneath the sample which allows feedback to the temperature controller (Figure 2.11). This attachment allows temperature variation from room temperature to over 1000 °C.

The sample holder is a sintered alumina (alsint) crucible, which can be used to hold samples in three ways. Most simply, it can be packed with powder, but with temperature changes and the corresponding sample expansion, this can result in the sample falling out. Secondly, pellets can be pressed and fitted into the holder. However, the most frequently used method was a sample mounted on a fused silica disc. This disc was lightly greased with vaseline and sprinkled with powdered sample using a fine mesh.

Anton Paar TTK450

In contrast to the HTK1200, the Anton Paar TTK450 cryofurnace is a conduction based system.[151] Using this attachment, a sample can be studied from 90 K to over 700 K. Liquid nitrogen is used to achieve temperatures below ambient. Since this is stored in a Dewar vessel inside the diffractometer cabinet, its size and the amount it can hold are

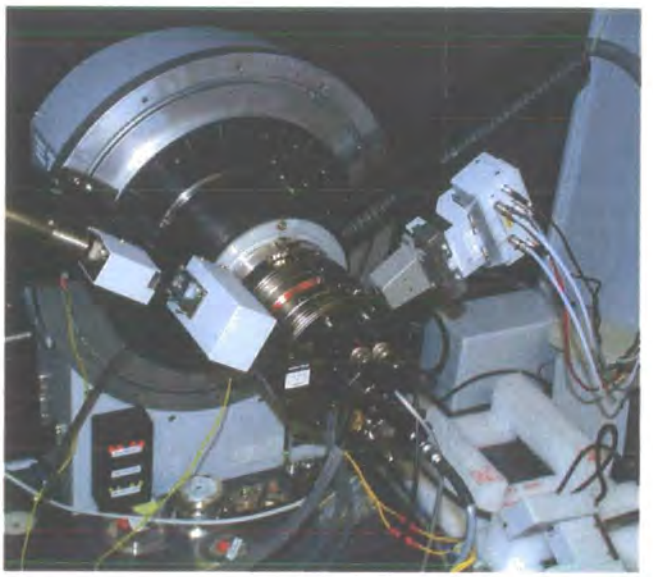

Figure 2.10: Picture of the Bruker D8 with the Anton Paar HTK1200 furnace attachment. The Braun position sensitive detector can be seen on the right hand side of the picture.[153]

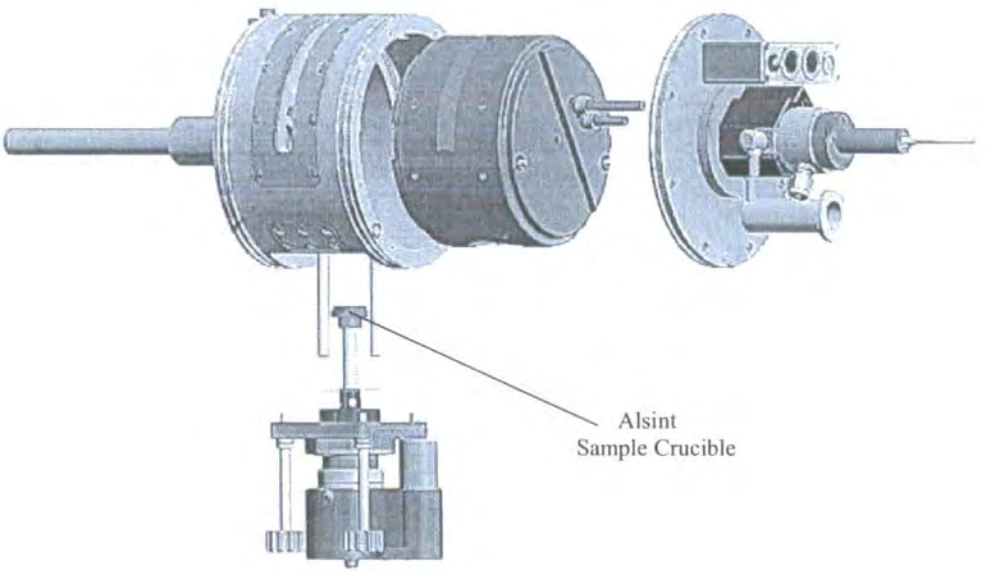

Figure 2.11: Cutaway diagram of the Anton Paar HTK1200 furnace attachment for the Bruker D8.[154]

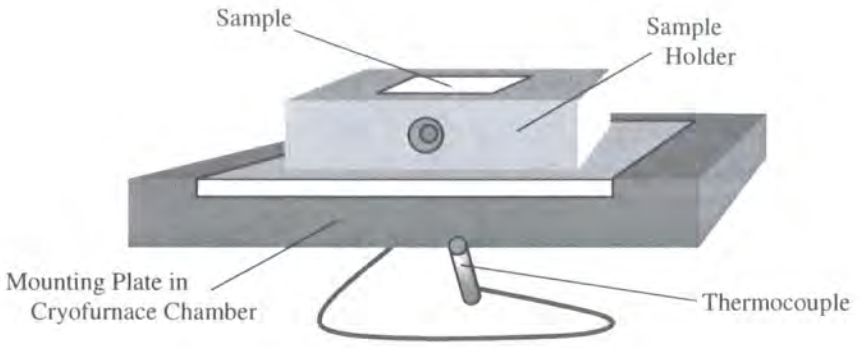

Figure 2.12: Diagram of the TTK450 cryofurnace sample holder.

limited, with the experimental time restricted accordingly.

The powdered samples are pressed into a stainless steel sample holder which slides into a socket within the attachment. Since the temperature is controlled via conduction, this connection is greased with conducting paste. However, it was found that the thermal conduction of most samples is poor, creating a thermal gradient thus giving erroneous results. So, rather than fill the stainless steel holder, an aluminium plate was made to fit the hole. The samples can be mounted on this in the same way as on the fused silica disc in the HTK1200 (Figure 2.12). The aluminium plate is set into the holder with the contacts greased with paste, which both aids conduction and helps to prevent the plate falling out of the holder at high angles. The disadvantage with this technique is the presence of aluminium peaks in the background. Since it is machined aluminium, it is no simple task to fit the peaks, though this can be done. In such cases, the aluminium can be considered as an internal standard and used to calibrate the temperature.

All scans were run under vacuum, to prevent the build-up of condensation and ice in the chamber at low temperature.

Oxford Cryosystems PheniX

Like the Anton Paar TTK450,[151] the Oxford Cryosystems PheniX[152] relies on conduction. Consequently, the aluminium sample plate was greased and sprinkled with sample in the same way as for the Anton Paar attachments. The sample plate is then *screwed* into the chamber and covered first with a heat shield, then with an outer cover. This cumbersome

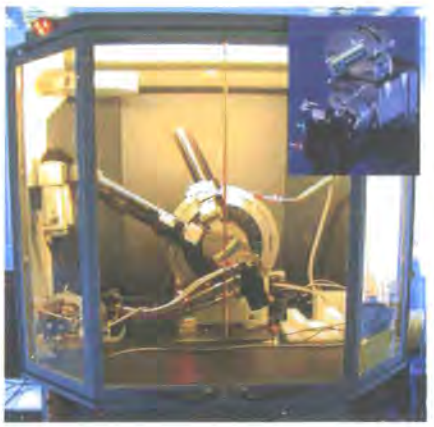

Figure 2.13: The Oxford Cryosystems PheniX mounted on the Bruker D8 Advance with a closeup of the PheniX opened showing the heat shield (inset).[155]

layered feature could cause a problem with so called 'dead areas' where something either obscures the incident or the scattered beams. However, a really clever part of the PheniX design, is the way the whole chamber moves with the goniometer (and therefore also with the sample), preventing loss of data (Figure 2.13).

There are two key advantages the Oxford Cryosystems PheniX has over the Anton Paar TTK450. Firstly, it has a closed cycle refrigerator (CCR), so it is far more efficient and there is no practical limit to the length of time taken to record data (low temperatures are achieved using liquid nitrogen with the TTK450, which is stored in a Dewar vessel inside the cabinet giving a maximum experiment time of about 16 hr). Secondly, the PheniX reaches temperatures as low as 17 K, compared to 90 K with the TTK450. However, as the PheniX has no heating facility, the maximum temperature it can reach is room temperature. Like the TTK450, data collections are carried out under vacuum to prevent buildup of ice.

2.3.3 Data Collection, Analysis and Manipulation

Data were collected using $\theta/2\theta$ coupled scans and the instruments were controlled by the proprietary Bruker software.[148] Scans were monitored using an online status display and on completion examined using EVA[149] where impurities could be identified using the integrated PDF-2 database.[156] Data were converted to a suitable format using the XCH

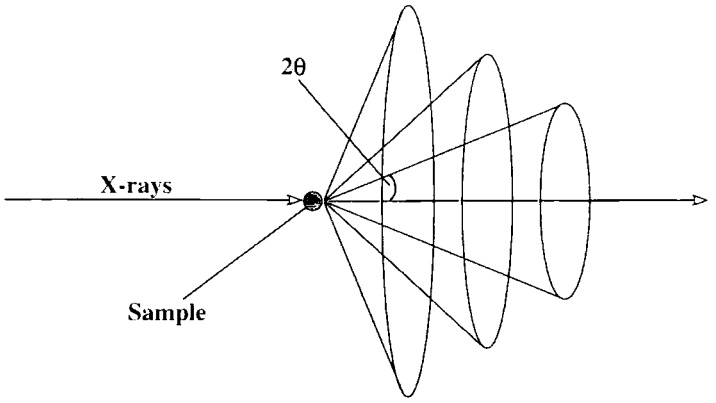

Figure 2.14: Schematic of powder diffraction. Single crystal diffraction leads to diffraction 'spots', powders are like many tiny single crystals, so the diffraction is smeared into cones.

software.[157] The General Structure Analysis System suite of programs (GSAS),[158] was used for Rietveld and Le Bail refinements. Both the UNIX® version and the Windows® version within the EXPGUI environment[159] were used, though this made little or no difference to the refinement results.

Rietveld Refinements

Rietveld refinement was developed by Hugo Rietveld in the late 1960s[160–162] and since then has been the primary tool in structure analysis using powder diffraction. The key problem with powder data is the loss of information in compressing individual reflections into cones of data (Figure 2.14). So, unlike single crystal diffraction, it is difficult to extract data in the form of *hkl* and intensity as there is considerable overlap. The idea Rietveld proposed was to compare calculated intensities ($y_{i(calc)}$) and observed intensities ($y_{i(obs)}$) at each data point, effectively fitting the data to the whole pattern instead of just to each individual reflection. Thus, the initial structure model is refined by least squares to produce a best fit model that minimises the residual, S_y. This residual is dependent on the 'weighting' (w_i) and the difference between the observed and calculated values (Equation 2.15). The function of the residual can be described as a three-dimensional hyper-surface with minima and maxima and the correct model is found at the lowest point.

Since many Bragg reflections contribute to the observed intensities of a powder pattern, this method avoids allocating intensities to particular Bragg reflections and the necessity of resolving overlapping peaks. Instead, the calculated intensity at any step, $y_{i(calc)}$, is predicted from the structural model. It is the quality of this model that the best-fit ultimately depends upon and it is important that the final result is the global minimum rather than a local or 'false' minimum.

$$S_y = \Sigma w_i (y_{i(obs)} - y_{i(calc)})^2 \tag{2.15}$$

In general, a background function is fitted first, as this is straight forward and relatively independent of the structure. The next set of variables refined, are those that govern the peak shape. Once the refinement is stable, more structure dependent variables are included; first the lattice parameters, then the atom positions and finally the temperature factors.

The measures used to assess the reliability of the refinement are a set of "Figures of Merit" including the structure R-factor, R_F; the Bragg R-factor, R_{Bragg} or R_{F^2}; the profile R-factor, R_p and the weighted R-factor, ${}_wR_p$ (equations 2.16–2.19). However, in a similar way to single crystal data, these figures of merit can be misleading, so the best measure of the quality of a refinement is the fit. In the case of powder data this can be studied by eye, looking at both the fit and the difference curve.

$$R_F = \frac{\sum \left| (I_{KCalc})^{\frac{1}{2}} - (I_K)^{\frac{1}{2}} \right|}{\sum (I_K)^{\frac{1}{2}}} \tag{2.16}$$

$$R_{F^2} = \frac{\sum \left| (I_{KCalc}) - (I_K) \right|}{\sum (I_K)} \tag{2.17}$$

$$R_p = \frac{\sum \left| (y_{iCalc}) - (y_i) \right|}{\sum (y_i)} \tag{2.18}$$

$${}_wR_p = \sqrt{\frac{\sum w_i \left((y_{iCalc}) - (y_i) \right)^2}{\sum w_i (y_i)}} \tag{2.19}$$

$$\chi^2 = \frac{\sum w_i (F^2_{Obs} - F^2_{Calc})^2}{(n-p)} \tag{2.20}$$

where I_K is the observed intensity of reflection K,
I_{KCalc} is the calculated intensity of reflection K,
y_i is the observed intensity at point i,
y_{iCalc} is the calculated intensity at point i,
F_{Obs} is the observed structure factor,
F_{Calc} is the calculated structure factor,
n is the number of observations,
and p is the number of parameters.

2.3.4 Profile Fitting

In some cases, where the structure is unknown, it is desirable to refine cell parameters without structural information. There are two techniques available, the Pawley method and the Le Bail method.

Pawley Fitting

The Pawley method was first developed in 1981 when it was used to refine the cell parameters of decafluorocyclohexene, with the final intention of extracting intensities for structure solution and refinement.[163]

Since Pawley fitting refines the intensity for each *hkl*, it is computationally intensive and in the early years had a reputation for being unstable and relatively difficult to control. However, in more recent years, techniques have improved so that the Pawley method is once more a going concern, but most current software that utilise this technique are commercial in nature or have restricted access, correspondingly reducing the availability.

Le Bail Fitting

The idea behind the Le Bail method came during a "long and lonesome night experiment at ILL" in July 1987.[164] Armel Le Bail considered how, at the end of a Rietveld refinement,

the so called '$|F_{obs}|$' are extracted and used to calculate the Bragg R-Factor.* He realised that these 'observed structure factors' could be recycled back into the refinement and used for the next cycle. In this way, the refinement proceeds without any reliance on the model. Thus, in practice, this allows the refinement of lattice parameters, peak shapes and sample height while effectively fitting the intensities.

Since the Le Bail method is computationally inexpensive and has been easy to integrate within Rietveld software, it has been incorporated into a lot of programs that are freely available to the academic community, such as GSAS and FullProf.[158,166] As a result, the technique is widely used and although it was first used to extract observed peak intensities for the structure solution and refinement of $LiSbWO_6$,[167] it is now also a valuable tool for comparing powder data without having to complete a full structural refinement.

Within GSAS, changing from a normal Rietveld refinement to Le Bail fitting is very straightforward as it is a function integrated into the program. GSAS also makes two options available at the start of the refinement. Not only is it possible to set the initial intensities as equal, in cases where the structure is known, the starting intensities can also be based on a model.

Structure Solution by Simulated Annealing (SA)

Simulated Annealing (SA) is a full profile fitting technique that can be used to solve powder structures.[168] Both Rietveld refinement and SA are used to probe a three dimensional hypersurface of potential solutions with the correct solution located at the global minimum. In addition to the global minimum there are many local or 'false' minima. Rietveld refinement is reliant on the starting structure being sufficiently close to the true structure that refinement will lead 'downhill' to the correct solution.

SA on the other hand, searches the hypersurface by moving a molecular fragment within the unit cell space. In each case, the goodness of fit is recorded and models are accepted or rejected accordingly. However, the rejection criterion depends on the 'temperature'. Initially, during structure solution by SA, a high temperature is used, which allows a large amount of 'uphill' movement. During the 'annealing', this 'temperature' is

*The '$|F_{obs}|$' are biased according to the F_{calc}, hence the quotes.

gradually reduced, which applies more stringent rejection criteria. In this way it is possible to search the hypersurface without getting stuck in a false minimum.

Part II

Spin Crossover in Mononuclear and Dinuclear Complexes

Chapter 3

Thermal and Light Induced Spin Crossover Transitions in Di(hydro)bis(1-Pyrazolyl)Borate Iron Complexes

3.1 Introduction

Work carried out by Hutchinson *et al.* showed that the tridentate (hydro)tris(1-pyrazolyl)borate ligand ($[HB(Pz)_3]^-$) promotes spin crossover.[169–171] Compounds **1** and **2** contain two related bidentate dihydrobis(1-pyrazolyl)borate ligands ($[H_2B(Pz)_2]^-$ or Hbpz) together with one other bidentate ligand each, yielding two compounds of the type $Fe(Hbpz)_2L$ (Figure 3.1). The problem with $[HB(Pz)_3]^-$ is that as a tridentate ligand, it readily forms very stable octahedral iron complexes leaving no room for generating new compounds by ligand substitution. As a bidentate ligand $[H_2B(Pz)_2]^-$ is a better candidate in this respect, and together with 2,2′-bipyridine (Bpyd) and 1,10-phenanthroline (Phen) makes two neutral mononuclear molecular complexes (compounds **1** and **2**).

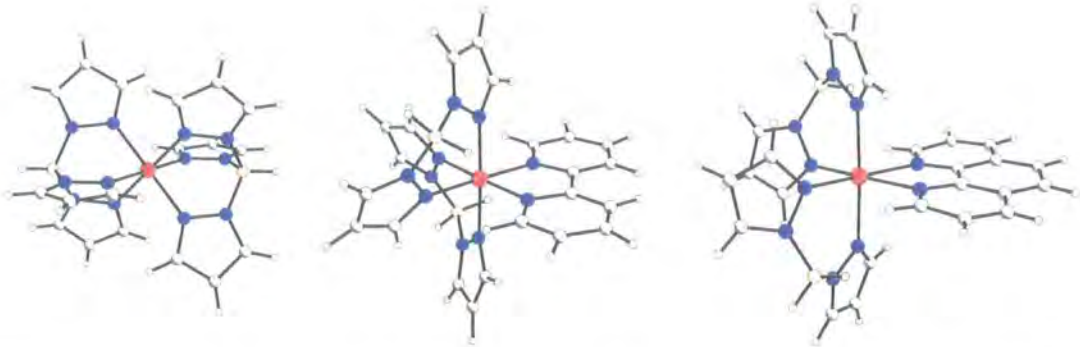

Figure 3.1: Three pyrazolyl-borate complexes — $Fe[HB(Pz)_3]_2$ (left),[169] $Fe(Bpyd)[H_2B(Pz)_2]_2$ (compound **1**, centre) and $Fe(Phen)[H_2B(Pz)_2]_2$ (compound **2**, right).[172]

3.1.1 Magnetic Susceptibility Data

SQUID magnetic susceptibility measurements indicate that both materials undergo a reasonably sharp spin crossover transition. Compound **2** exhibits an abrupt transition between 165 K and 155 K with a thermal hysteresis of approximately 4 K. Compound **1** behaves in a similar fashion, but the transition, which is centred around 160 K, is more gradual and there is no noticeable hysteresis (Figure 3.2).[172]

In addition, photomagnetic studies indicate that for both compounds, there is a complete conversion from low spin to high spin on irradiation at 10 K with a red laser ($\lambda = 647.1 - 676.4$ nm). The critical LIESST temperatures are 52 K and 44 K for compounds **1** and **2** respectively (Figure 3.3).[173]

3.1.2 Spectroscopy

Mössbauer spectroscopy has also been carried out on both compounds **1** and **2**. These results suggest that there is almost complete spin conversion at low temperature, while at room temperature there is 9.5% and 15% residual low spin for compounds **1** and **2** respectively.[173] In addition, Raman spectroscopy has been carried out on compound **2** above and below the spin transition.[173] The Raman results indicate the significant changes in the position of several of the low frequency modes that are generally associated with spin crossover.

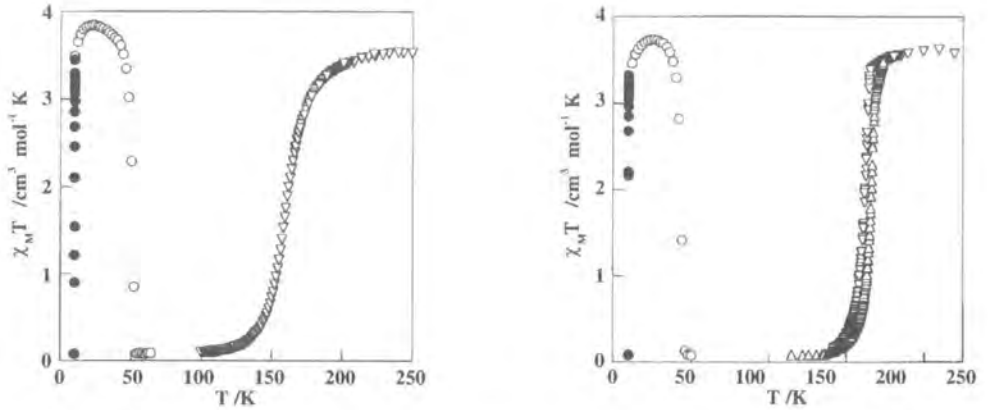

Figure 3.2: Magnetic susceptibility data for compounds **1** (left) and **2** (right).[173] Cooling and warming cycles show the 4 K hysteresis for compound **2** (▽ and △). Irradiation at 10 K for one hour (•) was followed by warming at 0.3 K/min (○).

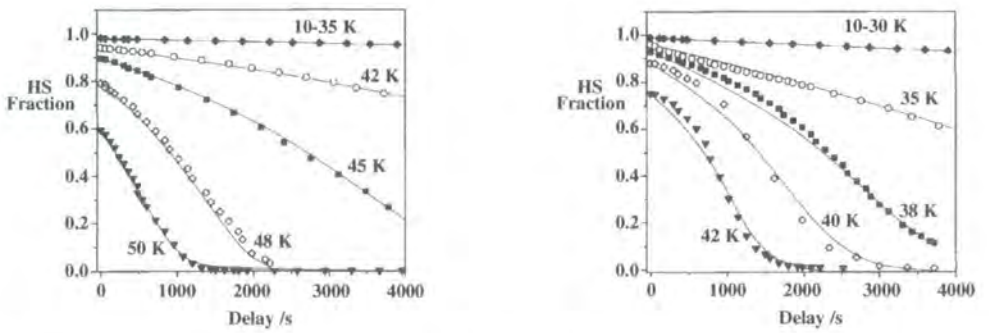

Figure 3.3: Time dependence of the high spin molar fraction generated by light irradiation for compounds **1** (left) and **2** (right).[173]

3.2 Single Crystal Diffraction Experiments

Samples of both compounds* were crystalline, consisting of crystals of varying quality, but in both cases, there were crystals suitable for single crystal X-ray diffraction experiments.

3.2.1 Data Collection

Initially, the very abrupt transition in compound **2** caused considerable difficulties when attempting to collect data on the low spin state. Crystals of compound **2** suffered severe destructive strain, which was initially thought to result from the sudden nature of the change from high to low spin, causing cracking and loss of crystallinity. These effects were not seen in compound **1** however.

$Fe(Bpyd)[H_2B(Pz)_2]_2$ (Compound 1)

A suitable red-brown crystal of compound **1** was selected, mounted in oil and quenched to 200 K using the Oxford Cryosystems Cryostream 600 on the Bruker SMART-CCD 1000 diffractometer.

A matrix collection was recorded and indexed giving cell parameters in keeping with those for the room temperature structure given in the literature.[172] A hemisphere of data was collected at 200 K with 7 s/frame. The crystal was then cooled to 120 K at 240 K/hr where a matrix collection indicated that the cell volume had contracted by over five percent, so a second hemisphere was collected, as at 200 K. On completion, the crystal was warmed to 200 K at 180 K/hr, then to 290 K at 360 K/hr and removed.

The cryostream was replaced with the HeliX[131] and the crystal returned to the diffractometer at 300 K and cooled in stages to 30 K (120 K/hr to 270 K, 240 K/hr to 200 K, 180 K/hr to 120 K and 360 K/hr to 30 K). At 30 K a matrix collection indexed satisfactorily, so a short hemisphere dataset was collected with 0.9° frames and 10 s/frame. On completion, the crystal was irradiated for approximately 15 mins with the 25 mW red laser (λ = 633 nm), followed by a matrix collection which indicated an increase in cell

*Crystals courtesy of Prof. José A. Real, Dr. M. Carmen Muñoz and Ms. Ana G. Galet Domingo (Valencia).

volume. A further 15 mins of irradiation yielded little further change in volume, so data were collected as at 200 K and 120 K.

$Fe(Phen)[H_2B(Pz)_2]_2$ (Compound 2)

Initially, cooling at 60 K/hr was attempted, but as the strain resulted in the crystal falling apart, cooling at 120 K/hr, 360 K/hr and quench cooling were tried. Although matrices collected at below the transition gave cell parameters that suggested the crystals had undergone spin crossover, cooling the crystal at 360 K/hr yielded the best data.

Crystal mounting proved to be the largest problem however, with larger crystals mounted in oil, epoxy resin (Araldite® 5 min mix) and nail-polish, all suffering damage. In the most extreme cases this resulted in the crystal splitting into two or more fragments or completely disintegrating. The best result was obtained using a small crystal mounted using epoxy resin which wasn't allowed time to harden. Once cold and in a nitrogen or helium stream, the rate of reaction was slowed significantly, preventing further hardening, so that the adhesive retained its elastic properties. This was of particular use, as it allowed the crystal to undergo larger structural changes without introducing additional strain, thus preventing fracturing.

Data were collected using a crystal (0.28 × 0.10 × 0.02 mm) mounted in this manner with the Oxford Cryosystems Cryostream[130] on the SMART-CCD 6000 diffractometer. The crystal was quenched to 200 K where a matrix was collected followed by a hemisphere of data (1200 frames, 20 s/frame). The crystal was then cooled through the transition at 360 K/hr to 100 K where a second matrix was followed by a data collection (1500 frames, 20 s/frame). On completion, the crystal was warmed back to 200 K, where a repeat matrix was in keeping with that recorded previously at 200 K. A subtle colour change was observed between 170 K and 160 K on cooling, with the crystal becoming a deeper, darker shade of red (Figure 3.4). The effect was reversed on warming, with the transition taking place at a temperature a few degrees higher than on cooling.

A second, slightly smaller crystal (0.15 × 0.12 × 0.08 mm) was selected and data were collected using the Bruker Proteum M diffractometer and the Oxford Cryosystems HeliX.[131] The crystal was mounted in epoxy resin and quenched to 200 K where a matrix collection was followed by a short data collection of 180, 3° frames at 40 s/frame. The

Figure 3.4: A crystal of compound **2** at 200 K (left) and 100 K (right).

crystal was then cooled at 360 K/hr to 100 K where a matrix was collected. This was followed by further cooling at 360 K/hr to 30 K where a matrix was followed by a hemisphere of data at 20 s/frame. On completion, the crystal was irradiated using a red laser (25 mW, $\lambda = 633$ nm) for approximately 90 s while constantly rotating ϕ for a more uniform irradiation. A matrix was collected and the data collection at 30 K was repeated. Severe icing was experienced throughout the low temperature part of the experiment, with problems increasing over time. No crystal colour change was observable at any stage, partly as a result of the icing, but also because the sample environment limits the amount of light at the sample, making the crystal much more difficult to see.

3.2.2 Data Analysis

Fe(Bpyd)[$H_2B(Pz)_2]_2$ (Compound 1)

The data generally indexed and integrated well, with the transitions making very little difference to the crystal quality. The structure was solved from the 200 K data in **C**2/c and SADABS[145] was used to apply a linear absorption correction.

Fe(Phen)[$H_2B(Pz)_2]_2$ (Compound 2)

The data collected at 200 K indexed with a monoclinic **C**-centred cell of a=17.3607(16) Å, b=16.0397(14) Å, c=10.5614(9) Å, β = 121.617(3)°, V = 2504.4(4) Å^3 (**C**2/c). At 100 K however, the data indexed with a smaller primitive cell of a=11.0458(13) Å, b=11.6730(13) Å, c=10.5651(12) Å, α = 109.777(3)°, β = 69.520(3)°, γ = 93.368(3)°, V = 1198.1(3) Å^3, which is related to the monoclinic cell by the matrix:

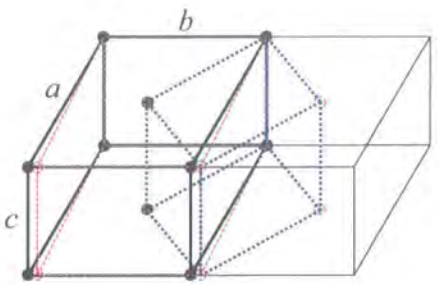

Figure 3.5: Schematic of the change from **C**-centred to primitive in compound **2**. The 200 K, high spin cell is shown in bold, with the distorted equivalent cell in red and the primitive cell in blue.

$$\begin{pmatrix} 0.5 & 0.5 & 0 \\ -0.5 & 0.5 & 0 \\ 0 & 0 & -1 \end{pmatrix}$$

Similarly, transforming the smaller 100 K primitive cell by the inverse matrix:

$$\begin{pmatrix} 1 & -1 & 0 \\ 1 & 1 & 0 \\ 0 & 0 & -1 \end{pmatrix}$$

gives the cell a=16.5354(14) Å, b=15.5923(13) Å, c=10.5651(12) Å, α = 89.688(4)°, β = 118.202(3)°, γ = 93.168(3)°, V = 2396.2(3) Å^3 which deviates significantly from monoclinic symmetry, particularly in γ. The two cells are related by a rotation around the c-axis (Figure 3.5).

The 30 K data indexed with similar cells, both before and after irradiation (where the cell volume increased, but the distortion remained). All three sets of data were examined in **C**2/c in case the change in angles was due to structural damage caused by the transition, but none solved and refinements of the 200 K structure gave very poorly shaped thermal ellipsoids, some of which were non-positive definite. Changing the symmetry to **P**$\bar{1}$ using the smaller primitive cell, resulted in a structure that not only solved, but also refined satisfactorily with sensible thermal parameters that were stable when refined as anisotropic ADPs.

Crystal faces had been indexed based on both the monoclinic and triclinic cells, so absorption corrections were carried out accordingly.

3.2.3 Structure Refinement

All the data discussed were of a generally high quality, which is reflected in the esds and statistics, resulting in reliable refinements.

Fe(Bpyd)[$H_2B(Pz)_2]_2$ (Compound 1)

All non-hydrogen atoms were refined as anisotropic in all four structures including the short data collection at 30 K. The hydrogens were all located in the difference map and refined satisfactorily.

Fe(Phen)[$H_2B(Pz)_2]_2$ (Compound 2)

Like compound **1**, in general, all non-hydrogen atoms were refined as anisotropic and the hydrogens were located in the difference map and refined accordingly.

In the case of the structure recorded at 100 K, the angles made by two of hydrogen atoms with the phenanthroline ring were unrealistic, so these were improved by the addition of restraints. This, together with the slight deterioration in the figures of merit suggest that there may have been damage to the crystal during the transition, though the quality of the refinement indicates that this was small.

The short data collection at 200 K gave satisfactory results consistent with those seen in the full data collection, apart from thermal ellipsoids that are slightly prolate and lower figures of merit - all problems that could result from the reduced quality of the data that were collected with wide frames.[†] Similarly, the 30 K results were in keeping with those at 100 K. The thermal parameters for the hydrogen atoms were not reliable however, so they were not refined.

[†]The data collected at 200 K with wide frames were recorded for structure confirmation and completion, but bond lengths, angles and other parameters discussed herein refer to the full dataset at 200 K collected with the Oxford Cryosystems Cryostream,[130] unless indicated otherwise.

The data collected after irradiation suffered from severe icing problems, so initially only the first run was used for the refinement. The shortage of data meant the thermal ellipsoids were all very prolate, with a distinct directionality. This was considerably improved by the addition of part of the second run, but although the hydrogen atoms were clearly visible in the difference map, the refinement became unstable, so the hydrogen atoms were added geometrically and refined using a riding model.

The program IVTON[174] was used to calculate the mean Fe–N bond lengths and the volumes for the iron octahedra in compounds **1** and **2**.

3.3 Discussion

Chemically, compounds **1** and **2** are very similar, the only difference being in the extra two carbon atoms in the phenanthroline ligand. These two carbons are very significant however, as the increased aromaticity confers an additional rigidity on the ligand as well as potentially increasing the degree of π–π overlap.

3.3.1 Structural Analysis

Structurally, compounds **1** and **2** are very similar. At 200 K, both structures are monoclinic ($\mathbf{C}2/c$), with the two halves of the molecule related by symmetry (Figure 3.6).

π–π Interactions in $\mathbf{Fe}L[\mathbf{H_2B(Pz)_2}]_2$

The iron centre in both compounds sits on the two fold rotation axis which runs through the middle of the Bpyd and Phen ligands and the iron centre. As well as generating one half of the bipyridine/phenanthroline groups, it also relates the two $[H(Pz)_3]^-$ ligands.

Neither structures have any hydrogen bonding interactions between molecules, but there are π–π stacking interactions in both complexes. In compound **1**, these take place between the Bpyd ligands of adjacent molecules which lead to the formation of chains. These chains form a staircase motif, with the molecules alternating their direction (Figure 3.7). Similarly, in compound **2**, π–π stacking interactions take place between symmetrically equivalent Phen ligands, but the amount of overlap is increased, effectively from one phenyl ring to two, due to the extra aromatic ring.

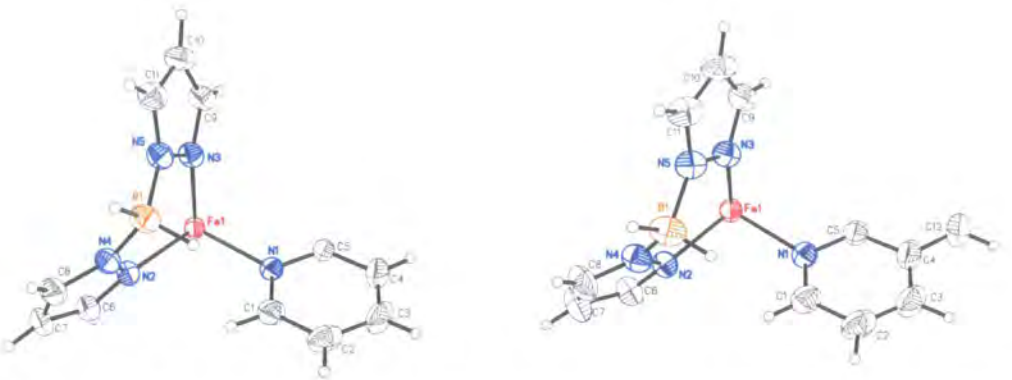

Figure 3.6: The asymmetric units at 200 K for compounds **1** (left), a = 16.2215(15) Å, b = 15.0254(15) Å, c = 11.0397(11) Å, β = 114.858(4)°, V = 2441.5(4) Å^3 (**C2**/c) and **2** (right) a = 17.3607(16) Å, b = 16.0397(14) Å, c = 10.5614(9) Å, β = 121.617(3)° V = 2504.4(4) Å^3 (**C2**/c).

	Compound 1	**Compound 2**
a	16.2215(15) Å	17.3607(16) Å
b	15.0254(15) Å	16.0397(14) Å
c	11.0397(11) Å	10.5614(9) Å
β	114.858(4)°	121.617(3)°
Volume	2441.5(4) Å^3	2504.4(4) Å^3

Table 3.1: Cell parameters for compounds **1** and **2**.

Although there is an increase in the number of overlapping rings in the Phen complex, the strength of the interaction is reduced, with the interplanar distance increasing from 3.691(6) Å in the Bpyd complex to 3.886(6) Å. This is presumably due to the change in the nature of the π–π interaction. In the case of the Phen complex, the overlapping ligands (and therefore the iron centres) are shifted away from each other and sideways slightly, increasing the Fe$\cdots$Fe distance from 8.8388(9) Å (in compound **1**) to 9.3293(9) Å (in compound **2**). This change is reflected in the cell parameters, which show that there is an increase in the a and b-axes and a contraction in the c-axis (Figure 3.8, Table 3.1).

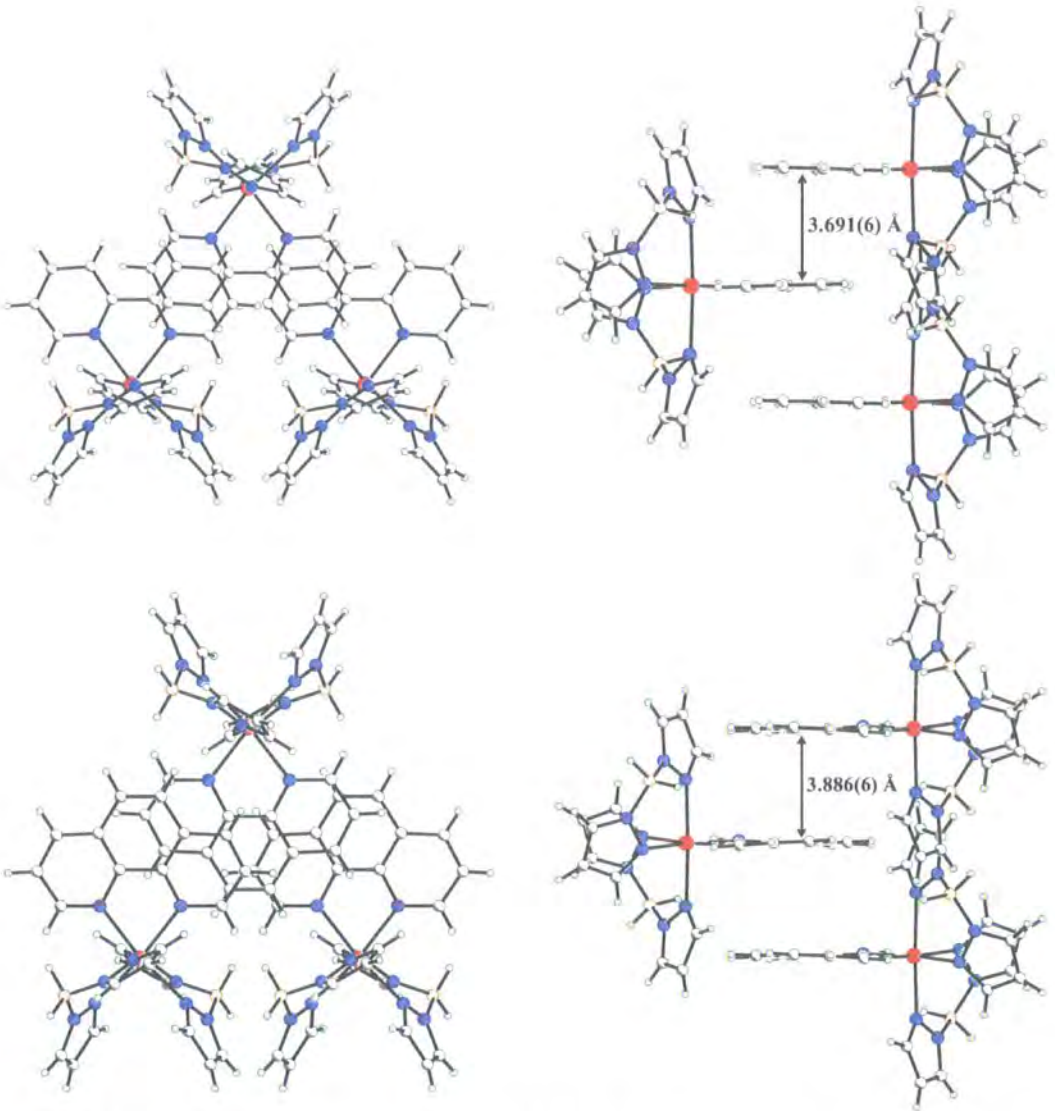

Figure 3.7: The π–π stacking in compound **1** (top) and compound **2** (bottom) at 200 K. Both compounds are shown without perspective, so that the overlap can clearly be seen. Although there is a reduction in the π–π distance, compound **2** packs more tightly because the interdigitating stacks of molecules are closer together. This tighter packing is reflected in the density, which is 1.406 Mg/m^3 for compound **2** compared with 1.377 Mg/m^3 for compound **1**.

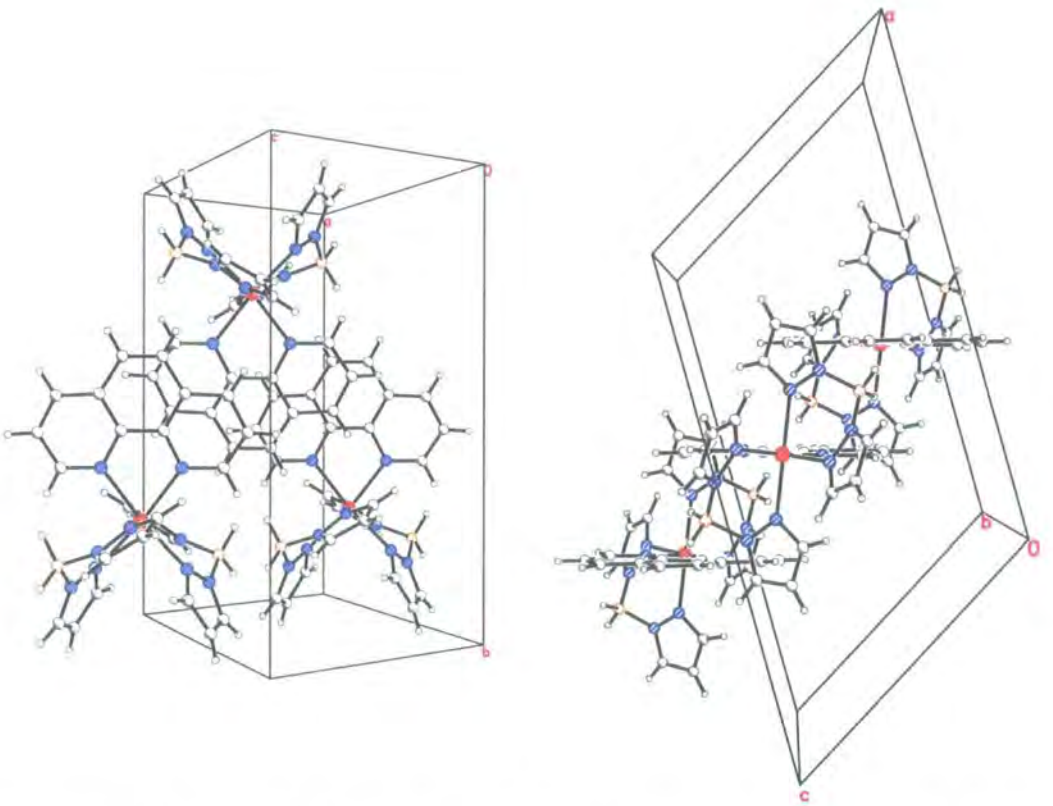

Figure 3.8: Compound **2** showing the unit cell. Three molecules of a chain are shown viewed perpendicular to the Phen ligands (left) and at 90°, down the b-axis (right). As the extra ring in the Phen ligands push the molecules apart, there is an increase in the length of the b-axis, while increasing interplanar L–L distances and a sideways shift, lead to an increase in a and a decrease in c.

Fe–N Distances

From the iron–nitrogen distances, at 200 K both compounds **1** and **2** are high spin, with average Fe–N distances of 2.183(1) Å and 2.180(1) Å respectively. The Fe–N distances are slightly shorter for the pyrazole rings than for the bipyridine and phenanthroline ligands (Table 3.2), which is probably due to steric effects. Both the bipyridine and phenanthroline ligands have a larger bite angle because they form a five membered ring when they ligate compared with the six membered rings formed by the Hbpz ligands. This results in a smaller N–Fe–N angle at the iron centre for the Bpyd and Phen ligands.

It is interesting to note that all the Fe–N distances in compound **2** are shorter than those in compound **1**, making the bite angles approximately 2° larger. This could explain why the transition takes place at a higher temperature, with the subtly stronger ligand field created by the Phen ligand reflected in the Fe–N distances and angles. However, the Mössbauer spectroscopic data indicate that there is 9.5% and 15% residual low spin at room temperature for compounds **1** and **2** respectively.[173] This would have the effect of reducing the apparent Fe–N distances, an effect that would be increased in the Phen complex, making the Fe–N distances shorter in a pure high spin Bpyd complex than in a pure HS Phen complex.

3.3.2 Low Spin

On cooling, both complexes clearly undergo a transition with a large unit cell contraction. The cell volume of compound **1** contracts from 2441.5(4) $Å^3$ at 200 K to 2334.5(2) $Å^3$ at 120 K, a change of over 100 $Å^3$, which corresponds to a contraction of nearly 4.4%. Compound **2** undergoes an additional structural phase change from **C**-centred monoclinic to primitive triclinic with an associated halving of the unit cell volume. Taking into account this change in cell volume, there is an additional contraction caused by the SC transition, which is comparable to that seen in compound **1**.

Fe–N Distances

In both compounds, the contraction is caused by changes in ligand–metal bond lengths in the way that is usually associated with spin crossover materials. In the case of compounds **1** and **2**, the change is approximately 0.18 Å. However, it is interesting to note that the Fe–N

	Compound 1		Compound 2	
Temperature	**200 K**	**120 K**	**200 K**	**100 K**
Fe–N1	2.2083(17) Å	1.9762(17) Å	2.2052(17) Å	1.977(3) Å/1.976(3) Å
Fe–N2	2.1621(17) Å	2.0195(18) Å	2.1562(17) Å	2.007(3) Å/2.002(3) Å
Fe–N3	2.1811(17) Å	2.0153(17) Å	2.1798(17) Å	2.024(3) Å/2.003(3) Å
Average	2.183(1) Å	2.004(9) Å	2.180(1) Å	1.998(6) Å
Average Change	0.179(9) Å		0.182(6) Å	
Bpyd	73.62(9)°	81.22(10)°	-	
Phen	-		75.01(9)°	82.38(12)°
Hbpz	88.91(7)°	91.58(7)°	90.40(6)°	92.88(11)°/92.59(11)°

Table 3.2: Fe–N distances and ligand bite-angles for compounds **1** and **2**.

bonds to the Bpyd and Phen ligands, which at 200 K were longer than those to the Hbpz ligands, are noticeably shorter in the low spin structures. Also, the average Fe–N distance at 100 K for compound **2** is shorter than for compound **1** at 120 K.

Structural Changes in Compound 2

The Phen complex undergoes a symmetry loss coupled with the spin transition. This loss of symmetry is clearly primarily due to the change in the γ angle from 90° to 93.368(3)°. A consequence of this is the loss of the C_2 molecular symmetry, resulting in a doubling of the number of atoms in the asymmetric unit. Overlaying a molecule rotated by 180° shows the loss of symmetry clearly (Figure 3.9).

3.3.3 LIESST

The photomagnetic data clearly indicate that both compounds should form a meta-stable light induced high spin excited state, so both compounds were irradiated using a red laser, which led to an increase in cell volume in both cases.

$Fe(Bpyd)[H_2B(Pz)_2]_2$ (Compound 1)

An increase in the average Fe–N bond length from 2.007(8) Å at 30 K to 2.187(2) Å on irradiating, indicates that a light induced transition took place. The fact that the meta-stable state remained high spin for the duration of the data collection, indicates that, as

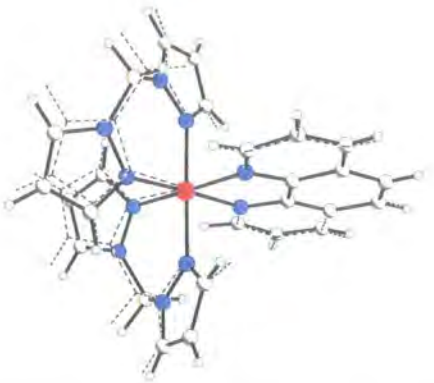

Figure 3.9: Overlay showing the loss of C_2 symmetry in compound **2** at 120 K, generated by mapping opposite halves of the phenanthroline ligands

in other cases, at 30 K the lifetime is long.

A comparison of parameters other than the Fe–N distances indicates that the excited state is comparable to the high spin state at 200 K, as with other known compounds.

Fe(Phen)$[H_2B(Pz)_2]_2$ (Compound 2)

On irradiation, compound **2** undergoes an increase in cell volume from 1192.9(4) Å^3 to 1231.0(13) Å^3 (3.2%) indicating that there is a light induced transition. However, converting the excited state cell to the monoclinic equivalent, indicates that the γ angle does not return to 90°. Structure solution confirms that the structure remains triclinic, but an average Fe–N distance of 2.171(8) Å indicates that the structure is definitely high spin.

So, unlike the Bpyd analogue, the light induced state is not equivalent to the high spin state at 200 K for the Phen complex. Presumably, the high spin monoclinic structure is energetically favourable, as that is the structure type that crystallises for both the Bpyd and Phen compounds under ambient conditions. Despite this however, the excitation with a red laser leads to a high spin state that retains the primitive triclinic structure. Although this effect has apparently not been recorded in the literature, on consideration, it is apparent why it occurs in this case. For a structure to undergo major changes, a considerable amount of energy is required. Clearly, sufficient thermal energy is available at 200 K, but at temperatures as low as 30 K there is not enough thermal energy for the structure to overcome the energy barrier and complete the structural change. On the

other hand, there is enough energy provided by the laser to enable the electronic transition from the low to high spin. Thus, the thermally induced transition consists of a structural transition coupled with an electronic transition, while the light induced transition is only electronic in nature.

3.3.4 Spin Crossover Transitions

So both compounds undergo thermal and light induced transitions, but only compound **2** has a thermally induced transition that is associated with a symmetry change.

Fe–N Distances, Octahedral Volumes and Distortion

While changes in the Fe–N distances give information on the presence of transitions, a better way of following changes in the spin state is to look at the octahedral volumes, where the changes in Fe–N distances are magnified (Table 3.3).

Overlaying the structure of the low and high spin states of compound **1**, shows that there is a reorganisation on spin crossover and the high spin core is more distorted than in the low spin structure (Figure 3.10). This result was first observed in compound **1** by Real *et al.*,[172] but this is not a new phenomenon and was discussed in detail by Guionneau *et al.*.[175] Guionneau *et al.* discussed the distortion around the iron centre in terms of a parameter Σ (Equation 3.1) for which they give characteristic values of approximately 85° and 50° for high and low spin structures respectively. The exception to this in the compounds they discuss is $[Fe(Phen)_2(NCS)_2]$, where there is a smaller distortion, thought to result from rigidity conferred by the molecular symmetry.

$$\Sigma = \sum_{i=1}^{12} |90 - \theta_i| \tag{3.1}$$

In compounds **1** and **2**, the N–Fe–N ligand bite-angles indicate that the octahedral centre is closer to regular in the low spin state. However, a comparison of Σ values indicates that the distortion in the HS state is not as great as that seen in the compounds studied by Guionneau *et al.* (Table 3.3). This effect could be because compounds **1** and **2** are of the form FeL_3, whereas those discussed by Guionneau *et al.* are of the form

Compound/ Temperature/ Conditions	Average Fe–N	Octahedral Volume	Ideal Volume	Distortion as a Percentage	Σ
Compound **1**					
200 K	2.183(1) Å	13.67(2) Å^3	13.87(5) Å^3	1.51%	48(1)°
120 K	2.004(9) Å	10.65(2) Å^3	10.73(5) Å^3	0.79%	40(1)°
30 K	2.007(8) Å	10.69(2) Å^3	10.78(5) Å^3	0.82%	40(1)°
30 K - Irr.	2.187(2) Å	13.74(2) Å^3	13.95(5) Å^3	1.33%	47(1)°
Compound **2**					
200 K	2.180(1) Å	13.63(2) Å^3	13.81(5) Å^3	1.33%	42(1)°
100 K	1.998(6) Å	10.56(2) Å^3	10.63(5) Å^3	0.69%	32(1)°
30 K	1.996(9) Å	10.53(2) Å^3	10.63(5) Å^3	0.72%	38(1)°
30 K - Irr.	2.171(8) Å	13.44(3) Å^3	13.64(5) Å^3	1.54%	42(1)°

Table 3.3: Fe–N distances and angles for compounds **1** and **2**.

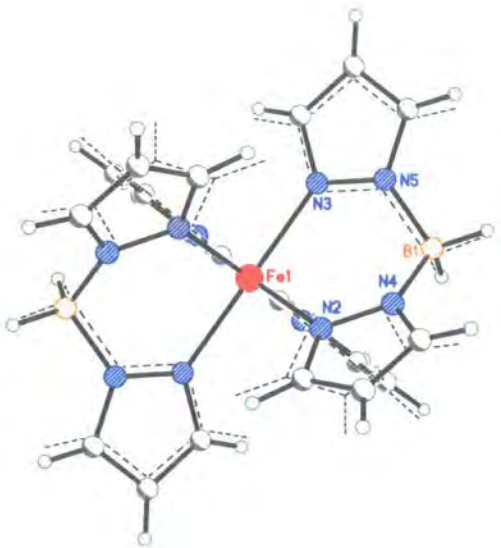

Figure 3.10: Overlay of compound **1** at 200 K and 120 K, showing the change in angle of the Hbpz ligands and the contraction of the Fe–N bond lengths. The low spin structure (120 K) is shown as a broken line and the iron and Bpyd nitrogen atoms were used to provide the fit.

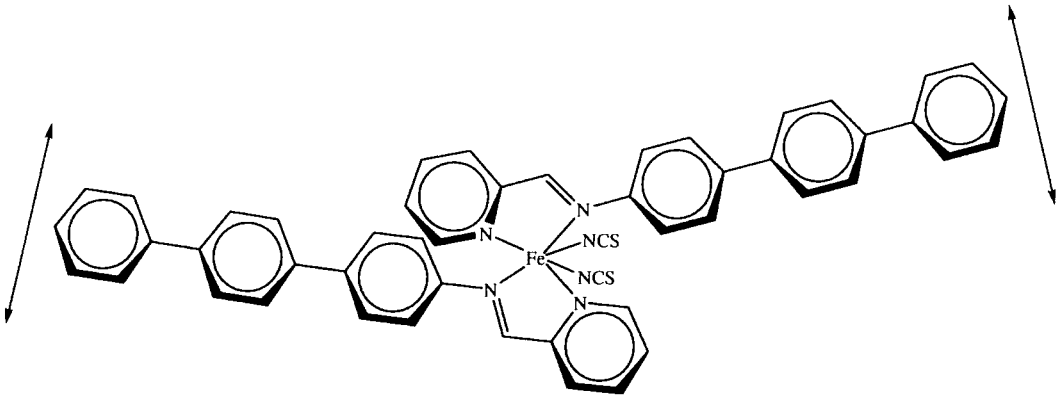

Figure 3.11: Schematic of the possible lever type effect in the compounds studied by Guionneau *et al.*. The arrows show how a small amount of packing force towards the end of the long ligands could lead to a distortion at the iron core.

FeL_2(NCS)$_2$ (L is a bidentate ligand). It is possible that the FeL_3 complexes have less flexibility than the FeL_2(NCS)$_2$ complexes, as there are three bidentate ligands rather than two and bidentate ligands add restraints to the geometry. Another possibility is that the nature of the ligand L is important. The ligands used in the study by Guionneau *et al.* are generally long ligands consisting of three or more phenyl rings. Packing forces on the end of these ligands could be leading to a lever-type effect causing a distortion of the iron core (Figure 3.11). In fact, the true cause is probably a combination of both of these effects, although it is almost certain that this explanation is still incomplete.

Another way of seeing the octahedral distortion is to compare the octahedral volumes (calculated using IVTON)[174] with the ideal volumes calculated from the average Fe–N distances.[‡] Any deviation from regularity should result in a reduction of the octahedral volume, with the smallest volumes for the most distorted octahedra. In the cases of compounds **1** and **2**, there is clearly a considerable deviation in the high spin state, which is still present (though reduced by nearly half) in the low spin state (Table 3.3). It is interesting to note that the deviation from regular (assessed by comparing octahedral

[‡]The volume of a regular octahedron can be defined as twice the volume of the component square based pyramid, thus $V = \frac{4}{3}r^3$, where V is the volume and r is the average Fe–N distance.

volumes or Σ values) is larger for the Bpyd complex than for the Phen complex, suggesting that the irregularity does not contribute to the cooperativity in this system.

Looking again at the octahedral volumes, it is clear that the values for compound **1** in the low spin state are approximately 0.1 $Å^3$ larger than those for compound **2**. This is possibly due to a small amount of residual high spin, but this was not seen in the Mössbauer spectroscopy or magnetic susceptibility measurements.[173] It could also be due to a stronger ligand field created by the Phen ligand, but this would also be visible in the high spin state and the octahedral volumes are very similar at 200 K. The Mössbauer spectroscopy indicates the presence of a larger amount of residual low spin in compound **2** than **1**. Thus, it is probable that a theoretical 100% high spin compound **2** would have a larger octahedral volume than a theoretical 100% compound **1**. This means that the change in Fe–N distances would have to be larger for the Phen complex than for the Bpyd complex. Since the cooperativity of a system is dependent on the coupling between the iron centre and the lattice vibrations via the metal–ligand bonds, larger Fe–N distance change compared with compound **1** is reflected in increased cooperativity for compound **2**.

π–π Stacking

On conversion to the low spin state, the intermolecular π–π stacking distance decreases in both compounds **1** and **2**. At 200 K, the Bpyd–Bpyd distance is 3.691(6) Å, which contracts to 3.560(6) Å at 120 K and 3.549(7) Å at 30 K. In the high spin state at 200 K, the Phen–Phen distance is larger at 3.886(6) Å, but the symmetry change leads to two distances in the low spin structure, 3.657(9) Å and 3.528(9) Å. The 30 K structure shows the expected thermal contraction to 3.640(7) Å and 3.507(7) Å. A comparison of the contractions shows that while compound **1** contracts by 0.14(1) Å between 200 K and 30 K, compound **2** contracts by 0.25(1) Å and 0.38(1) Å over the same temperature range, an average of 0.31(1) Å. This increased contraction possibly reflects the increased cooperativity caused by the increased overlap in the π system.

Irradiating compound **1** leads to an increase in the Bpyd–Bpyd distance to 3.634(8) Å, which although slightly smaller than that for the thermal HS structure, is consistent with the return to the high spin state as seen in the changes to the Fe–N distances and the octahedral volume. On irradiating compound **2**, the splitting of the distances into two caused

by the loss of symmetry seen at 100 K and 30 K, is not only retained, but enhanced. Not only is there an increase in the average Phen–Phen distance (from 3.574(18) Å to 3.726(21) Å), this increase is also noticeably larger than for compound **1** (0.15(1) Å compared with 0.09(1) Å). A comparison of the low spin π–π distances at 30 K with those when irradiated indicates that while one experiences no change (3.638(10) Å compared with 3.640(7) Å at 30 K) the second π–π distance increases by 0.31(1) Å from 3.507(7) Å to 3.813(11) Å. Presumably this is because while the preferred distance is that of the thermal HS state, this is not attainable due to the structural changes.

Fe···Fe Distances

In the high spin state, each iron centre in compounds **1** and **2** is surrounded by three pairs of symmetry related iron centres, 7 Å to 10 Å away (Figure 3.12). On cooling compound **1** to the low spin state, these pairs are retained, but in compound **2**, due to the space group change, the symmetric relationship is lost and there are six independent distances. Since the low spin and LIESST structures are isostructural for both compounds, on excitation there are six independent distances for compound **2**, but only three for compound **1**.

Comparing the Fe···Fe distances for the high spin and low spin compound **1** shows that there is a contraction in distances 2 and 3, while distance 1 expands. The effect in compound **2**, is different. The average of distance 1 contracts or remains the same (within error) while distances 2 and 3 show a marked split with one component contracting more. The behaviour of the Fe···Fe distance 2 reflects the difference between the Bpyd and Phen ligands and the decrease in the π–π distance associated with the spin transition. The behaviour of distances 1 and 3 between compounds **1** and **2** is less easy to rationalise, but looking carefully at the view down the *c*-axis gives an indication of why this might be the case (Figure 3.12). There is a slight, but definite change in the orientation of the Hbpz ligands, that can be more clearly seen by looking at the overlay of the two molecules (Figure 3.13). This change reflects the way compound **2** is closer to ideal than compound **1**, which is probably related to the ligand field strengths and the different flexibilities of the Bpyd and Phen ligands.

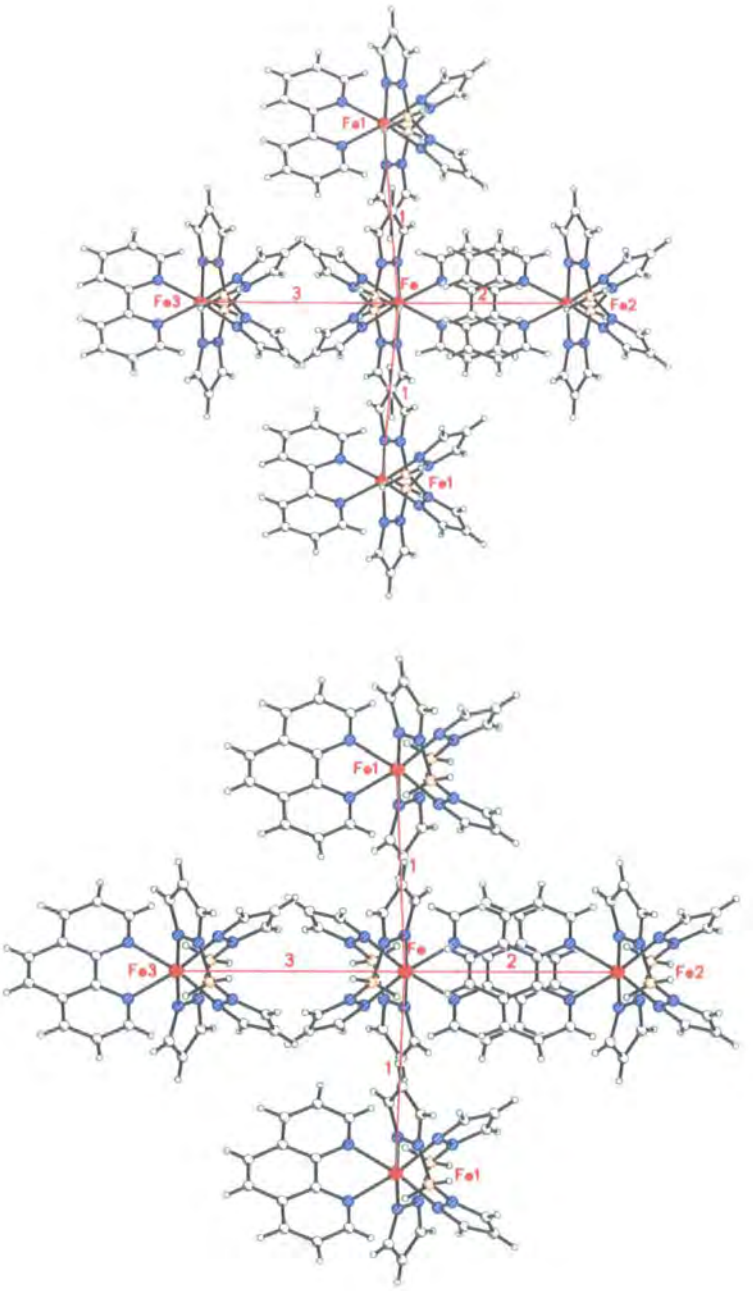

Figure 3.12: Fe$\cdots$Fe distances for compounds **1** and **2** at 200 K. Four distances are shown, 2×1, 2 and 3 with the symmetric equivalents of 2 and 3 hidden behind 2 and 3. Viewed down the *c*-axis.

Compound/	Fe···Fe Distance		
Temperature/Conditions	**1**	**2**	**3**
Compound **1**			
200 K	7.6801(7) Å	8.8388(9) Å	9.8203(10) Å
120 K	7.7167(4) Å	8.5985(8) Å	9.6009(8) Å
30 K	7.6971(5) Å	8.5997(10) Å	9.5849(10) Å
30 K - Irradiated	7.5963(4) Å	8.8372(10) Å	9.7540(11) Å
Compound **2**			
200 K	7.4252(7) Å	9.3293(9) Å	9.8787(9) Å
120 K	7.3998(12) Å/7.4524(12) Å	9.0493(12) Å/9.1478(12) Å	9.6501(12) Å/9.8343(12) Å
30 K	7.3853(12) Å/7.4267(12) Å	9.0346(13) Å/9.1377(13) Å	9.6471(14) Å/9.8301(13) Å
30 K - Irradiated	7.3743(37) Å/7.4369(39) Å	8.9892(38) Å/9.3709(41) Å	10.3681(25) Å/9.6240(41) Å

Table 3.4: Fe···Fe distances for compounds **1** and **2**.

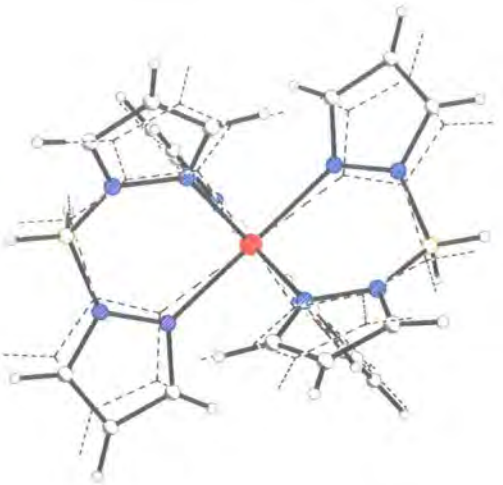

Figure 3.13: Overlay of compounds **1** and **2** at 200 K, showing the change in angle of the Hbpz ligands. The phenanthroline complex (compound **2**) is shown as a broken line and the iron and Bpyd/Phen nitrogen atoms were used to provide the fit.

3.4 Conclusion

Weak intermolecular forces such as hydrogen bonds and π–π interactions have been shown to be critical to cooperativity and these compounds corroborate this. Although there are no conventional hydrogen-bonds, there are weak π–π type stacking interactions. The extra two carbon atoms in the phenanthroline ligand introduce an additional aromatic ring which increases the amount of π–π overlap from effectively one ring to two. This increased interaction leads to increased cooperativity which can clearly be seen by the sharper, more abrupt transition in compound **2** than in compound **1**, which takes place with hysteresis.

In this pair of compounds however, things are not so simple. Crystals of the Bpyd complex (compound **1**) undergo spin crossover with very little damage, the crystal lattice flexing to accommodate the changes in bond lengths around the iron centre. The transition in the Phen complex however, is potentially far more destructive, with the crystal structure suffering a major loss of symmetry. This symmetry change from monoclinic ($\mathbf{C}2/c$) to a smaller triclinic cell ($\mathbf{P}\overline{1}$), caused major problems, with mounting methods and cooling rates exacerbating the crystal damage. In this case, these problems were largely eliminated

by rapid cooling and mounting in a flexible medium, which resulted in data of a high enough quality to locate and refine hydrogen atoms.

The lowering of the Laue symmetry leads to a doubling of the asymmetric unit with a loss of the C_2 molecular symmetry as well as the loss of symmetry relating molecules. This affects the vital π–π stacking distances as well as the other intermolecular distances, including the distances between the iron centres.

The size and quality of crystals can seriously affect the spin crossover properties, but assuming that the Mössbauer data is applicable to the samples studied here, the high spin Phen complex has more residual LS at room temperature than the Bpyd complex, while at low temperature both SC transitions are complete. This suggests that the change in Fe–N bond lengths around the iron centre for compound **1** is less than that for compound **2**. Since the cooperativity is thought to rely on the transmission of the transition from the iron centre to the lattice phonon system through the Fe–N vibrations, this larger change would be expected to increase the cooperativity, explaining the sharper transition seen in the Phen complex.

Both complexes can also be converted to a meta-stable HS state by irradiation with red light. While the Bpyd LIESST state is isostructural with the HS complex at 200 K, the Phen complex is not. Due to the symmetry change, when irradiated at 30 K a new HS structure is generated based on the triclinic low spin phase. It is thought that the structure is unable to change back to the monoclinic HS structure because there is not enough thermal energy available at 30 K.

As has been shown previously, the high spin iron octahedra are highly distorted with respect to the low spin centres in compound **1**. This distortion has been quantified by comparison with the idealised octahedral volume, which has shown how the distortion in the thermal high spin octahedra is slightly more than that seen in the light induced structure. Further comparison with the Phen complex shows that the distortion is slightly less than that seen in the Bpyd compound, in all three states.

The comparison of compounds **1** and **2** has given a key insight into why the magnetic susceptibilities are different. The increased π–π overlap explains why the cooperativity is increased in the phenanthroline complex and the changes in Fe$\cdots$Fe distances caused by the reduction in octahedral distortion, ultimately lead to subtle changes in the crystal

packing.

The sudden structural change that is coupled with the SC transition indicates why collecting good quality data was initially so difficult. This transition leads to a splitting of the π–π chains into pairs, an effect that is accentuated on irradiation, where the low symmetry is retained, giving rise to a new phase. This "light induced polymorphism" is an effect, that to our knowledge, has not been seen before in the literature.

Chapter 4

Cooperativity in $[Fe(Bpyd)Pyd_2(NCS)_2]Pyd_{0.225}$

4.1 Introduction

Since the discovery of the spin crossover materials $[Fe(Phen)_2(NCS)_2]$, $[Fe(Phen)_2(NCSe)_2]$ and $[Fe(Bpyd)_2(NCS)_2]$ reported by Baker and Bobonich in 1964,[38] there has been considerable interest in these and other thiocyanate and thioselenate complexes.[10,46,50–52]

Compound **3** is a similar thiocyanate spin crossover complex, consisting of an octahedral iron(II) centre surrounded by one bidentate Bpyd ligand, two monodentate Pyd ligands and two anionic thiocyanate ligands.

4.1.1 Magnetic Susceptibility Data

From the SQUID magnetic susceptibility data, a very abrupt transition from the high spin to the low spin state can be seen at approximately 114 K (Figure 4.1).[176] In addition to the sharp transition, there is a clear hysteresis, indicating a high degree of cooperativity. Compound **3** is also thought to undergo Light-Induced Excited Spin-State Trapping on irradiation at 30 K.[176]

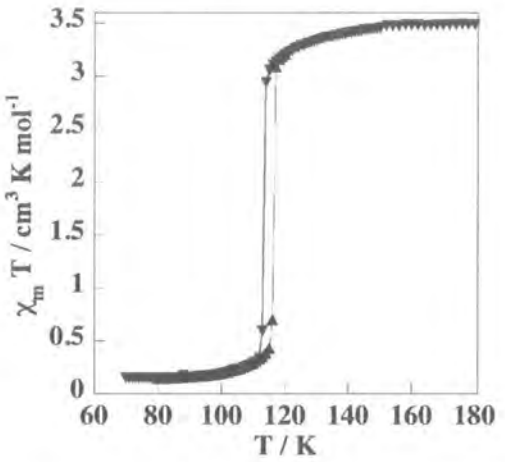

Figure 4.1: Magnetic susceptibility data for compound **3**.[176] Cooling (▼) and warming (▲) are shown, so that the hysteresis can be seen.

4.2 Single Crystal Diffraction Experiments

Compound **3** forms metallic black crystals of monoclinic habit. Although the crystals* cannot be seen to extinguish because of their opacity, when viewed in reflection it is possible to see any flaws on their surface. This gives a good indication of the crystal quality, but has limitations as it does not give any indication of internal quality.

4.2.1 Data Collection

A characteristic crystal was mounted on a hair with oil on the SMART-CCD 1000 and quench cooled to 160 K where a matrix collection gave a tetragonal **I**-centred cell of $a = 18.031(5)$ Å, $c = 28.984(2)$ Å, $V = 9423(2)$ Å^3.

*Crystals courtesy of Prof. José A. Real, Dr. M. Carmen Muñoz and Dr. Ana B. Gaspar Pedrós[177] (Valencia).

Low Temperature Data

The matrix data collection at 160 K was followed by a hemisphere data collection at 10 s/frame. On completion, the crystal was cooled to 100 K where another matrix was recorded. This gave a similar cell with a reduced volume of 9039(4) $Å^3$. This was followed by the same hemisphere data collection also at 10 s/frame, after which the crystal was warmed to 160 K at 120 K/hr.

After six months, the crystal was returned to the SMART-CCD 1000 and a matrix was recorded at room temperature, after which another hemisphere was collected at 20 s/frame. On completion, a second matrix was collected after which the crystal was removed.

Irradiation

The crystal was returned to the Bruker SMART-CCD 1000 with the Oxford Cryosystems HeliX[131] and cooled at a rate of 120 K/hr to 30 K, where another matrix was collected before the sample was irradiated successively and repeatedly with the 25 mW red laser (λ = 633 nm), the green laser (λ = 532 nm) and the NIR laser (λ = 830 nm). Matrices collected after each irradiation step indicated no appreciable change in unit cell volume. The only noticeable change appeared to be a reduction in the number of reflections yielded from the matrix collections, so data were not collected and the crystal was returned to room temperature at 120 K/hr and removed.

Irradiation During Data Acquisition

It was thought that the first frame of the matrix collections after irradiation appeared to have spots in slightly different positions to those prior to irradiation, suggesting that either the sample was relaxing very rapidly, or relaxation was stimulated by the X-rays. In order to test this theory, a new laser mounting device was designed in order to irradiate the sample during data collection (Figure 4.2). The device was mounted on the back of the detector, using a combination of mirrors and prisms mounted on the front of the detector to target the crystal. The approach angle of the laser beam means that the laser remains centred on the sample regardless of the crystal orientation. In addition, the equipment can remain in place as a permanent feature, so that minimal alignment is necessary before use.

Figure 4.2: Irradiating a crystal on the Bruker Proteum M diffractometer. The laser beam approaches the crystal from underneath the front of the detector.

Figure 4.3: Irradiation of a crystal of compound **3** with green light. The video camera used for centering the crystal can also be used for aligning the laser.

Although the original crystal indexed well at 210 K, the crystal was too weak to continue, so a new crystal with similar size and morphology to the first was selected and mounted in oil. This sample was mounted on the Bruker Proteum M fitted with the Oxford Cryosystems HeliX[131] and quenched to 210 K. Matrix collections at 150 K, 90 K and 30 K gave cells consistent with a transition at 114 K. Irradiating with a red laser for 5 mins at 30 K prior to a matrix collection and during a matrix collection gave cells with comparable volumes. Irradiating during collection with the green laser however (Figure 4.3), indicated a unit cell contraction from 8979(3) Å^3 at 30 K to 8932(11) Å^3 (a change >0.5%). A matrix collection started approximately 2 mins after the irradiation was terminated indicated that the crystal had returned to the state prior to irradiation with no noticeable contraction (V = 8978(3) Å^3).

4.2.2 Data Analysis

The data indexed well at both 160 K and 100 K with the crystal clearly suffering little or no structural damage. The data were integrated according to usual procedures to a resolution of 0.73 Å. The structure was solved using direct methods from the 160 K data. Since the faces were clean and had been indexed, absorption corrections were carried out accordingly.

4.2.3 Structure Refinement

It was clear that in addition to the complex, there is solvent of crystallisation present, sitting along the 4_1 screw axis. Given the location and nature of the solvent, it is clearly inherently disordered.

At both 160 K and 100 K all non-hydrogen atoms in the complex were refined with anisotropic displacement parameters and the hydrogen atoms were located in the difference map. Refinement of hydrogen positions led to an unreliable model, so the hydrogen atoms were removed, added geometrically and refined using a riding model. The program IVTON[174] was used to calculate the mean Fe–N bond lengths and the volumes for the iron octahedra in compound **3**.

Disordered Pyridine Solvent

From a study of the Fourier maps, it quickly became clear that there was solvent of crystallisation present in addition to the $Fe(Bpyd)Pyd_2(NCS)_2$ complex. Chemically, pyridine made most sense and crystallographically, disordered pyridine fitted the data. The disorder was caused by the proximity of the 4_1 screw axis, which generated three additional atoms for every one located. For this reason, the occupancy was initially assigned as 25%.

For the refinement to remain stable, it was necessary to apply constraints to fix the ring in a regular arrangement and hydrogens were added geometrically and refined using a riding model. In order to locate the position of the nitrogen atom, thermal parameters were studied and several positions were tried and the best selected. It is probable that there is some additional disorder in the location of the nitrogen, but only one position is used in the model given the complexity of the disorder.

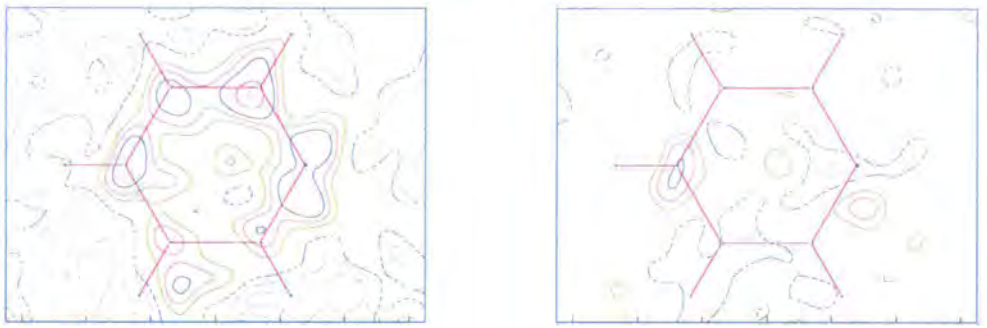

Figure 4.4: Electron density Fourier maps for the disordered pyridine solvent in compound **3**. An F_{obs} map with one symmetric equivalent of pyridine overlayed is shown (left), together with the $F_{obs} - F_{calc}$ map (right). In both cases, contours are drawn every 0.2 e^- between 0.2 e^- and 1.2 e^- and -0.2 e^- and -0.8 e^- with the negative electron density shown in broken lines. The symmetry related components of the disordered solvent are omitted for clarity.

Initially, the thermal parameters were thought to be relatively large so the occupancy at 100 K was refined. This gave a value of 22.5%, which though not entirely reliable due to the correlation between the occupancy and thermal parameters, considerably improved the statistics. In order to avoid correlation during the refinement, the occupancy was fixed to 22.5%, which established the structural formula of compound **3** as $[Fe(Bpyd)Pyd_2(NCS)_2]Pyd_{0.225}$. In the final refinement, the non-hydrogen thermal parameters were modelled as isotropic and restrained as equal for stability. The final difference map shows how inclusion of the solvent considerably improves the refinement (Figure 4.4).

Twinning

A twin refinement was carried out using the matrix

$$\begin{pmatrix} 0 & 1 & 0 \\ 1 & 0 & 0 \\ 0 & 0 & -1 \end{pmatrix}$$

but although it accounted for the very few systematic absence violations, the twin fraction refined to zero and there was no change to the statistics, indicating that any twin component present was very small.

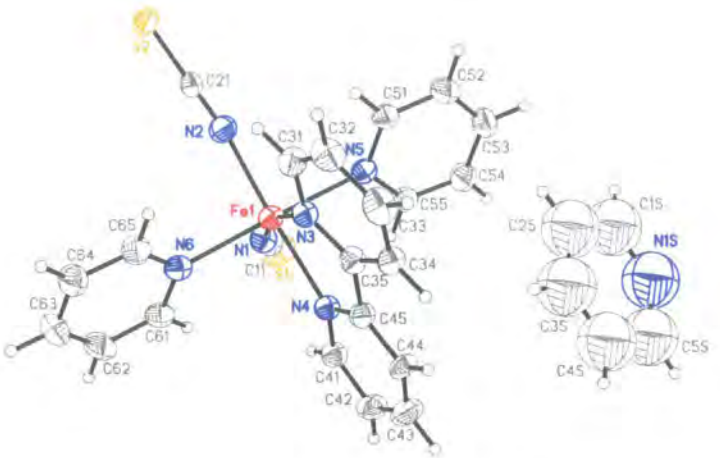

Figure 4.5: The asymmetric unit for compound **3** at 160 K, $a = b = 18.0482(5)$ Å, $c = 28.9962(10)$ Å, $V = 9445.2(5)$ Å^3 ($\mathbf{I4_1}/a$).

4.3 Discussion

At 160 K, the structure is tetragonal, $\mathbf{I4_1}/a$ (Laue group $4/m$), with one molecule of complex and one molecule of solvent (22.5% occupied) in the asymmetric unit (Figure 4.5).

4.3.1 Structural Analysis

The two NCS^- ligands sit in the equatorial plane together with the bidentate bipyridine ligand (Bpyd). The iron(II) octahedron is capped by two pyridine ligands sitting *trans* to each other, in a very slightly twisted conformation with an angle of 13.4(2)° between the two rings (Figure 4.6).

Fe–N Bond lengths

At 160 K, the complex is clearly high spin with an average Fe–N bond length of 2.17(5) Å. A comparison of the individual Fe–N bond lengths show that there is a larger range than that seen in many other complexes, for example compounds **1** and **2**, where all the Fe–N distances fall within a range of 0.05 Å. In the case of compound **3** the range is over 0.15 Å, from 2.075(2) Å to 2.229(2) Å. On close inspection it becomes clear that the Fe–N bond lengths can be split into two categories: short and long. Fe1–N1 and Fe1–N2 (2.075(2) Å

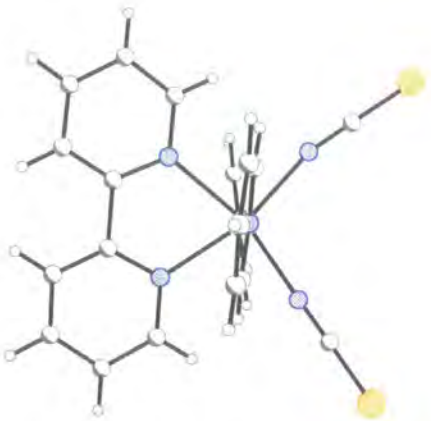

Figure 4.6: The Fe(Bpyd)$Pyd_2(NCS)_2$ complex at 160 K, showing the slight twist in the Pyd rings.

and 2.095(2) Å) fall into the category of short, while Fe1–N3, Fe1–N4, Fe1–N5 and Fe1–N6 can all be classified as long (2.215(2) Å, 2.219(2) Å, 2.229(2) Å and 2.217(2) Å). The short Fe–N distances are to the thiocyanate ligands, which reflects the ionic nature of the ligands and are comparable in length to those for the related complex, $[Fe(Phen)_2(NCS)_2]$, at 290 K.[9]

C–H$\cdots$S Interactions

There are no conventional hydrogen bonding interactions and the most interesting short contacts are a number of C–H$\cdots$S interactions between the NCS^- ligands and the Bpyd and Pyd ligands (Figure 4.7). Two of the six C–H$\cdots$S interactions form a connection between two molecules. Both sulphur atoms are involved, with separate C–H$\cdots$S contacts to the same half of a Bpyd in a neighbouring molecule. Similar interactions from sulphur atoms of the neighbouring molecule lead to the formation of chains of Fe(Bpyd)$Pyd_2(NCS)_2$ complexes connected together by the C–H$\cdots$S close contacts.

4.3.2 Spin Crossover Transitions

There is no change in symmetry on cooling from 160 K to 100 K, and like the 160 K structure, at 100 K the compound is still tetragonal ($I4_1/a$) with one molecule of complex in the asymmetric unit; a total of sixteen molecules in the unit cell.

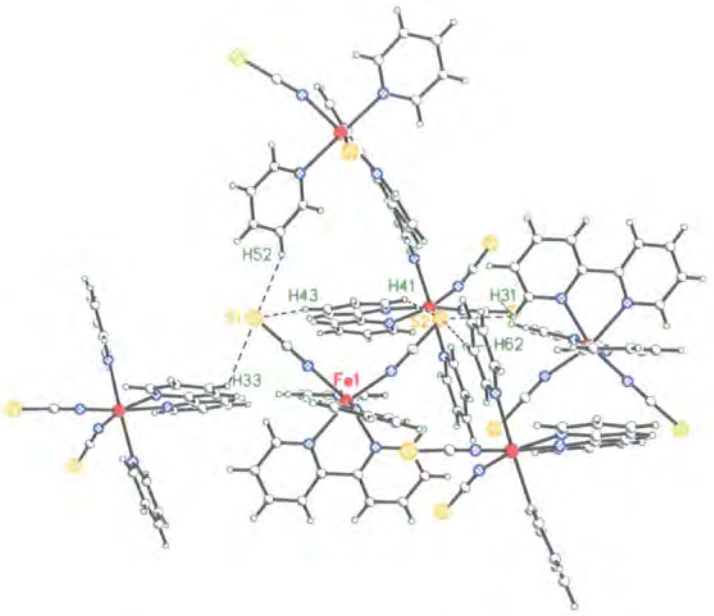

Figure 4.7: C–H···S interactions for compound **3**.

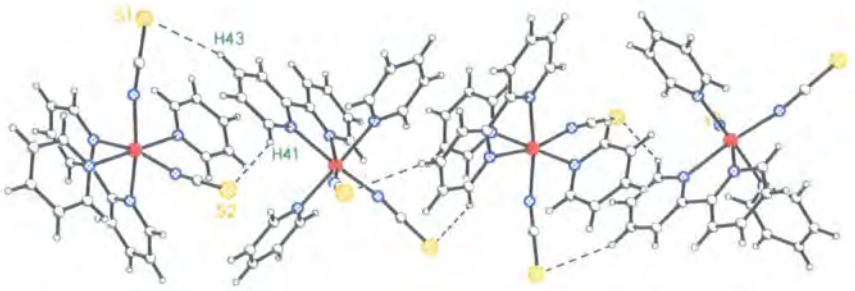

Figure 4.8: Chains of $Fe(Bpyd)Pyd_2(NCS)_2$ complexes, connected by C–H···S close contacts. The S1···H43 distance is the longer of the two at 3.023(7) Å compared with 2.757(7) Å for the S2···H41 contact.

Fe–N distances, Octahedral Volumes and Octahedral Distortion

Although there is no visible colour change on cooling, the change in unit cell volume and average Fe–N bond length from 2.17(5) Å at 160 K to 1.98(3) Å at 100 K indicate the presence of a spin transition.

The contraction in the Fe–N distance for the thiocyanate ligand is considerably less than that for the Pyd and Bpyd ligands. This effect has been seen before in thiocyanate SC complexes with a contraction of only 0.099(4) Å for the Fe–NCS distances in $[Fe(Phen)_2(NCS)_2]$ compared with 0.185(4) Å and 0.208(4) Å for the phenanthroline ligands.[9] In the case of compound **3**, all the contractions are larger than for $[Fe(Phen)_2(NCS)_2]$ suggesting that there is increased coupling between the iron centres and the lattice vibrations increasing the cooperativity.

At 160 K, the Fe–N bond lengths were grouped into two categories, short and long. At 100 K, in addition to the contraction, the Fe–N bond lengths are split into three categories. In the high spin state, there are clearly two short Fe–N bonds and four long bonds. At 100 K, the difference between the short thiocyanate Fe–N bond lengths and the others is reduced and the four Bpyd/Pyd Fe–N distances separate into two groups so that there is 0.046 Å between the longer Fe–Pyd bond lengths and the intermediate Fe–Bpyd distances (Table 4.1). Indeed, the Fe–Bpyd bond lengths are now closer to the shorter Fe–NCS distances (a difference of less than 0.02 Å). This reflects the change from the distorted HS iron atom to the relatively regular LS iron(II).

This distortion is roughly quantified by a comparison of the actual and ideal octahedral volumes (in the same way as for compounds **1** and **2**). In the case of compound **3**, although there is a slight increase in the angular distortion (compared with compounds **1** and **2**), the distortion is largely due to the difference in Fe–N bond lengths. The largest deviation from 90° in compound **3** is in the N3–Fe1–N4 angle and is caused by the strain in the Bpyd ligand. This deviation is similar to that seen in the Bpyd and Phen ligands in compounds **1** and **2** (73.26(8)° compared with 73.62(9)° and 75.01(9)° for the Bpyd and Phen ligands in compounds **1** and **2** at 200 K). In compounds **1** and **2** there are three such bidentate ligands introducing considerable distortion. In contrast, compound **3** has four monodentate ligands, which have primarily steric interactions governing the N–Fe–N angles. However, the distortion is increased by the wide range of Fe–N bond lengths, and

	160 K	100 K	Difference
Fe1–N1	2.075(2) Å	1.950(2) Å	0.125(4) Å
Fe1–N2	2.095(2) Å	1.953(2) Å	0.142(4) Å
Fe1–N3	2.215(2) Å	1.970(2) Å	0.245(4) Å
Fe1–N4	2.219(2) Å	1.971(2) Å	0.248(4) Å
Fe1–N5	2.229(2) Å	2.017(2) Å	0.212(4) Å
Fe1–N6	2.217(2) Å	2.015(2) Å	0.202(4) Å
N1–Fe1–N2	103.49(9)°	91.31(9)°	+12.2(2)°
N3–Fe1–N4	73.21(8)°	81.15(9)°	+7.9(2)°
N5–Fe1–N6	177.86(8)°	178.57(9)°	+0.7(2)°
N1–Fe1–N4	91.27(9)°	93.56(9)°	−2.3(2)°
N2–Fe1–N3	92.06(9)°	94.02(9)°	−2.0(2)°
N2–Fe1–N6	88.85(9)°	88.02(9)°	−0.8(2)°
N3–Fe1–N6	93.37(8)°	93.53(9)°	−0.2(2)°
Average Fe–N	2.17(5) Å	1.98(3) Å	0.19(4) Å
Octahedral Volume	13.44(4) Å^3	10.28(4) Å^3	3.16(4) Å^3
Ideal Volume	13.62(8) Å^3	10.33(8) Å^3	-
Distortion	1.4%	0.5%	-
Σ	53(1)°	33(1)°	-

Table 4.1: Fe–N bond lengths, selected N–Fe–N angles and octahedral volumes for compound **3**. Where the change in angle brings the octahedron closer to regular on cooling to 100 K, the sign is given as positive.

the effect the bidentate Bpyd ligand has on the coplanar thiocyanate ligand angles. Thus, the LS FeN_6 octahedron is considerably more regular than the HS FeN_6 octahedron largely due to a reduction in the distribution of the Fe–N distances as well as changes in the Bpyd and thiocyanate angles (Figure 4.9, Table 4.1).

C–H···S Interactions

On cooling through the spin transition there is very little change in the six H···S distances (Table 4.2). However, it is noticeable that all H···S1 distances show a slight decrease on cooling while the H···S2 distances all increase or remain unchanged. Clearly, on cooling through the spin transition, if the structural change only involved the Fe–N distances, the H···S distances should increase. However, the contraction within the molecule leads to a

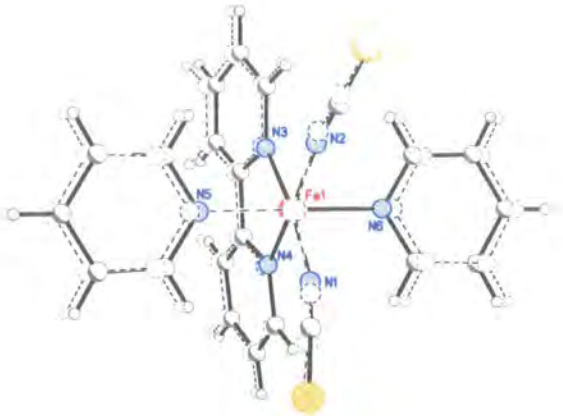

Figure 4.9: Overlay of the high spin and low spin states of compound **3**. The named atoms were used for the overlay.

			160 K	100 K
S1	H33	1	2.955(7) Å	2.903(7) Å
	H43	2	3.083(7) Å	3.022(7) Å
	H52	3	2.984(7) Å	2.941(7) Å
S2	H31	4	2.900(7) Å	2.957(7) Å
	H41	5	2.725(7) Å	2.757(7) Å
	H62	6	2.774(7) Å	2.771(7) Å

Table 4.2: H···S distances for the C–H···S close contacts in compound **3**.

contraction in the unit cell volumes, demonstrating how the transition affects more than just the iron core. Thus, the whole structure is modified, which is reflected in the changes in the C–H···S interactions.

Solvent of Crystallisation

In common with many examples of this type of material, there is solvent of crystallisation present, in this case pyridine. At 160 K the pyridine ring occupies a position with the four-fold screw axis running in the plane of the molecule, generating the other disordered components. These components consist of two pairs of rings at right angles to each other. On cooling through the transition however, the relative position of the components of the disordered solvent change. There is a reduction in the disorder reflected in the reduction

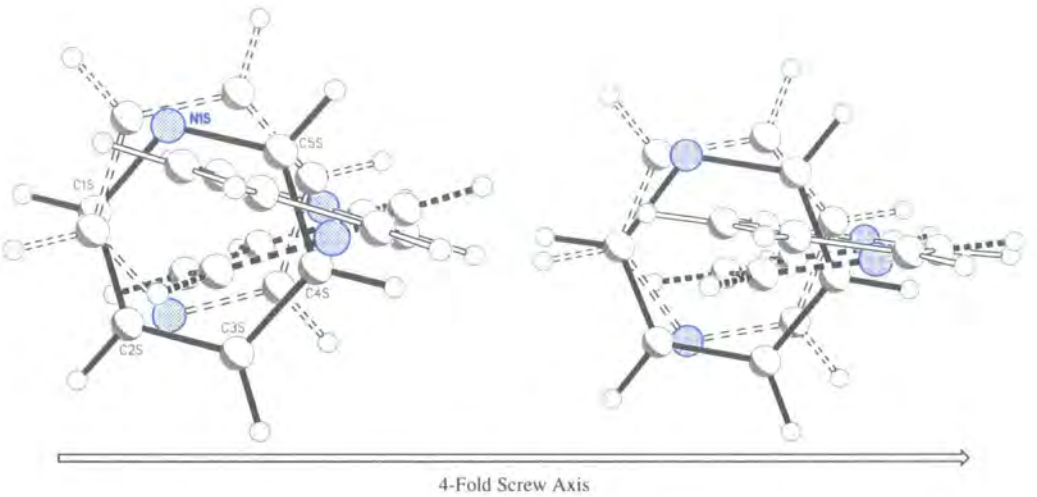

Figure 4.10: Disordered solvent in compound **3**. The pyridine is modelled as disordered around the 4_1 screw axis, with a 22.5% occupancy in each of the four positions. On cooling through the spin transition (from left to right), the disorder is reduced, with C1s moving closer to the 4_1 screw axis.

of thermal motion, but this is coupled with a reduction in the separation of the pairs of rings together with a separation of the two components at right angles to each other (Figure 4.10).

Fe···Fe Distances

At 160 K there are nine Fe···Fe distances that are less than 10.5 Å, four pairs related by symmetry (1, 3, 4 and 5) and one unpaired (2, Table 4.3). All short Fe···Fe distances are between molecules connected by C–H···S interactions, with the shortest distance connected through the two C–H···S interactions (2 & 5) via the Bpyd ligand, which forms chains (Table 4.3). Interestingly, the second shortest C–H···S interaction is 6 (after 5), which also leads to the second shortest Fe···Fe distance. There appears to be little or no further connection between the Fe···Fe distance and C–H···S distance.

The majority of the Fe···Fe distances undergo little or no change on SC. The exceptions to this are distances 4, and to a lesser degree, 5 and 2 (Table 4.3). On SC, the change in distance 4 is a contraction of 0.4130(6) Å, which is four times larger than the

	160 K	100 K	Difference	C–H···S Interaction
1	7.3053(2) Å	7.3123(2) Å	+0.0070(2) Å	2 & 5
2	8.3685(6) Å	8.3065(6) Å	−0.0620(6) Å	6
3	9.6026(7) Å	9.6152(7) Å	+0.0126(7) Å	4
4	10.1147(6) Å	9.7017(6) Å	−0.4130(6) Å	1
5	10.4502(4) Å	10.3497(4) Å	−0.1005(4) Å	3

Table 4.3: Fe···Fe distances for compound **3**.

second largest and up to seven times the magnitude of the remaining three. On close inspection, this distance is between iron centres around the Pyd solvent of crystallisation (Figure 4.11). It is possible that the change in position of the components of the disordered solvent could be responsible for the change in Fe···Fe distance 4 (Figure 4.11 and Table 4.3).

Irradiation

Irradiating the crystal with red light did not induce excitation to the LIESST state in the crystal that were tried. However, although the esds were large, irradiating with green light led to a unit cell volume contraction of approximately 0.5%. Exactly why this happened is unclear, but it is possible that at 30 K there is a small amount of residual high spin present. If this is the case, it is possible that irradiation of the sample is inducing a process analogous to reverse-LIESST, converting the residual HS to LS. From the matrix collection after irradiation, it appears that the majority of the residual HS converted to LS reverts back to HS, but given the esds, this is largely conjecture.

4.4 Conclusion

Compound **3** has been shown to undergo spin crossover in accordance with the magnetic susceptibility data. Crystallographic studies detailed here show that the behaviour of the Fe–N bond lengths and N–Fe–N angles are in keeping with those for similar compounds in the literature and with those discussed in Chapter 3.

In addition, in compound **3** there is disordered solvent pyridine. Although the high degree of disorder in the solvent makes it very difficult to draw concrete conclusions, it

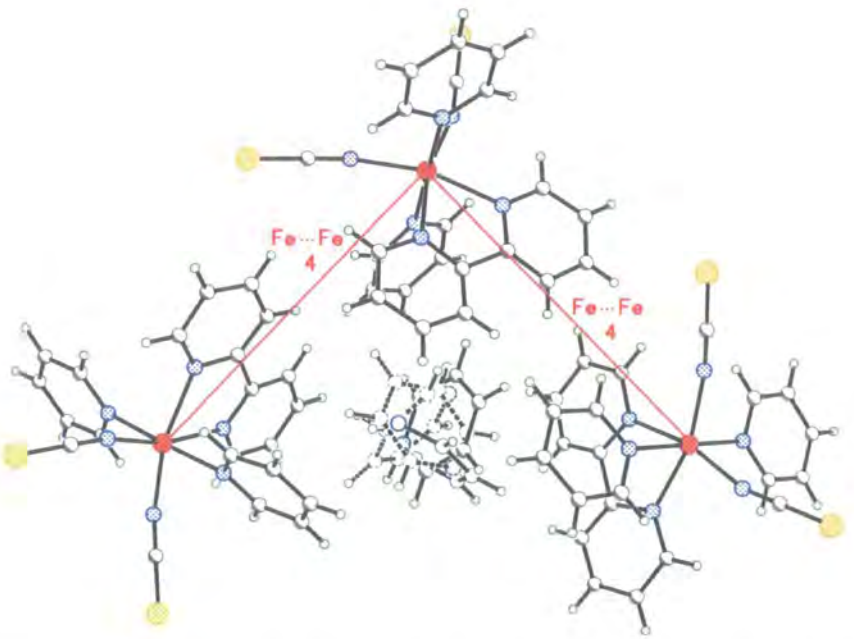

Figure 4.11: Compound **3** with the disordered pyrimidine solvent. Fe···Fe distance 4 is marked (Table 4.3).

is clear that there is a change in the relative positions of the different components. It is thought that on cooling the thermal motion of the solvent is reduced, leading to a reduction in the pyridine molecular volume. This contraction allows a slight shortening of one of the Fe$\cdots$Fe distances, which is shortened further by the contraction in the FeN_6 octahedra due to the spin transition. This contraction is coupled with a change in the size and shape of the solvent void and a change in the relative orientation of the disordered components.

On irradiation, the unit cell volume contracts in a process that is presumed to be a reverse-LIESST type effect. This reverse-LIESST is thought to involve a small amount of residual high spin present in the sample at 30 K that is converted to low spin on irradiation. This is far from conclusive as the esds of the cell parameters are large. In addition, the new low spin state is far from stable, with an increased unit cell volume once the irradiation has been discontinued. Although further work is required to confirm the nature of this unstable state, the studies carried out here suggest that this could be a fertile area for further research.

Chapter 5

Spin Crossover in Bithiazoline Complexes

5.1 Introduction

A considerable amount of work has been done on $Fe(Btz)_2(NCS)_2$, including magnetic susceptibility measurements,[10,50] infrared spectroscopy,[50,51] X-ray powder diffraction,[51] Electron Paramagnetic Resonance Spectroscopy (EPR),[178] calorimetry,[179] and Mössbauer spectroscopy.[51] All these techniques indicate that the SC transition takes place at approximately 175 K. The magnetic susceptibility data showed the transition to be very abrupt with a thermal hysteresis, i.e. $T_c = 171.2$ K on cooling and $T_c' = 180.9$ K on warming ($\Delta T = 9.7$ K). Calorimetry proved that the SC transition is first order in nature.

5.1.1 Polymorphism

In 1988, Ozarowski *et al.* identified two crystal polymorphs of the compound $Fe(Btz)_2(NCS)_2$, **A** and **B**.[178] Interestingly, only polymorph **A** undergoes SC, which allowed a study of the intermolecular interactions responsible for the SC phenomenon. In both cases, the thiocyanate ligands adopt a *cisoid* geometry around the iron centre (Figure 5.1).

Polymorph **A** was found to be triclinic with one molecule in the asymmetric unit, while polymorph **B** was found to be monoclinic ($C2/c$) with the molecule astride the two-fold axis that passes through the iron atom.[180]

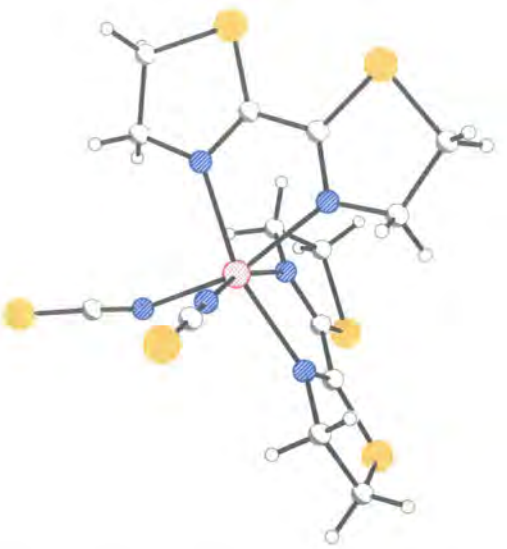

Figure 5.1: $Fe(Btz)_2(NCS)_2$ showing the *cisoid* conformation.

Thiocyanate Ligands

Polymorph **A** has shorter Fe–N bond lengths than **B**, an average of 2.158(10) Å compared with 2.175(10) Å. Comparing the thiocyanate ligand Fe–N distances shows that both distances in polymorph **B** are comparable with one Fe–NCS distance in polymorph **A**. The second Fe–N thiocyanate distance in polymorph **A** is fractionally shorter, 2.061(7) Å compared with 2.081(7) Å for polymorph **B**. Although these distances are within three esds, there is a considerable associated linearity of the corresponding Fe–N–C angle (178.1(7)°compared with 163.3(7)°and 159.7(6)°), suggesting that π-bonding is an important factor in this shorter average bond length. This short Fe–N bond could indicate a subtle increase in the ligand field strength accounting for the presence of the spin transition in **A** that is absent in **B**.[178]

Crystal Packing

Both polymorphs pack with the Btz rings stacking above each other leading to π–π interactions, however there is an increased separation in polymorph **B** (3.8 Å compared with 4.0 Å). This separation could be vital to the cooperativity which takes place through weak intermolecular electrostatic interactions like hydrogen bonds or π–π stacking interactions.

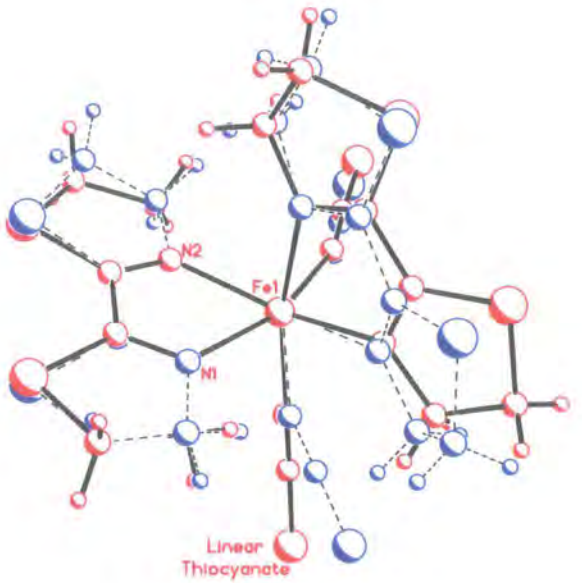

Figure 5.2: Overlay of the two polymorphs of $Fe(Btz)_2(NCS)_2$. Polymorph **A** is shown in red while polymorph **B** is shown in blue. The atoms labelled in red were used for the comparison, making the loss of planarity in the Btz ring in polymorph **B** clearly visible. The conformational differences and increased linearity of the thiocyanate ligand are also visible.

Increased planarity in the Btz rings in polymorph **A** (Figure 5.2) could be responsible for the closer packing, leading to the high degree of cooperativity indicated by the abruptness of the transition and its corresponding hysteresis.

5.1.2 A Dinuclear Spin Crossover Complex

Building on this mononuclear species, a dinuclear complex was synthesised.[181] Like $Fe(Btz)_2(NCS)_2$, $[Fe(Btz)(NCS)_2]_2Bpmd$ (compound **4**) has iron(II) centres ligated by bidentate bithiazoline and thiocyanate ligands. However, in compound **4**, one of the bithiazoline ligands is replaced with a 2,2′-bipyrimidine ligand (Bpmd), which forms a bridge between two iron centres (Figure 5.3).

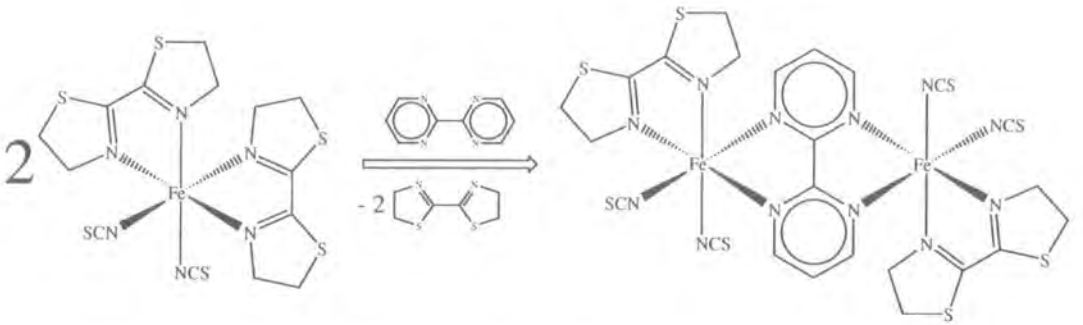

Figure 5.3: Schematic of the development of the dinuclear bithiazoline complex from the mononuclear species. The mononuclear complex (left) is extended by the addition of a bipyrimidine ligand to give a dinuclear complex (right), which necessitates the loss of two bithiazoline ligands.

5.1.3 Magnetic Susceptibility Data

SQUID magnetic susceptibility data for compound **4** indicate that the transition has a strange shape, which has been interpreted as a gradual transition centred around 197 K ending at a plateau between approximately 170 K and 180 K, followed by a second, more abrupt transition, centred around 163 K (Figure 5.4).[181]

The magnetic susceptibility of compound **4** has also been studied under pressure.[88] These experiments have shown that, in addition to making the transitions more gradual and increasing the transition temperature by about 50 K, the plateau is extended and enhanced by pressure.

Photomagnetic Data

This compound has been shown to undergo light-Induced Excited Spin-State Trapping at low temperature.[182] Photomagnetic data showing the time dependence of the high spin meta-stable state indicates that at temperatures below 40 K, the lifetime is enhanced (Figure 5.5).

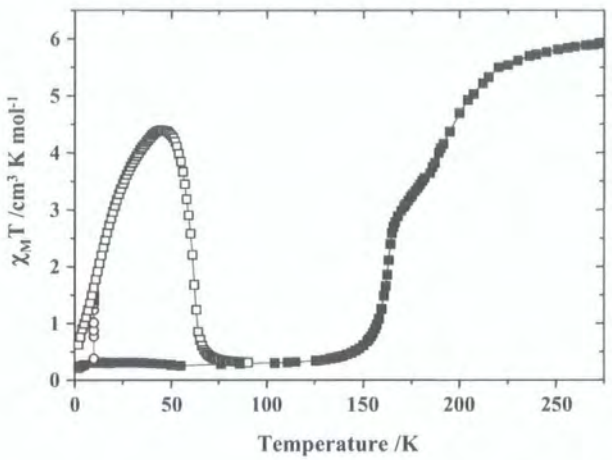

Figure 5.4: Magnetic susceptibility data for compound **4**.[182] The cooling curve is shown (■) together with irradiation at 10 K (○), and warming from 4 K to 100 K after irradiation (□).

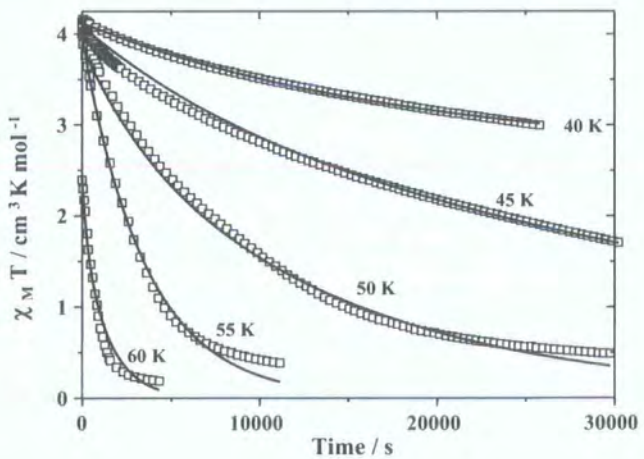

Figure 5.5: Time dependence of the high spin meta-stable state for compound **4**.[182] Below 40 K the lifetime is extended almost indefinitely.

Figure 5.6: Schematic of the small hexagonal twinned crystals of compound **4**.

5.1.4 Mössbauer Spectroscopy

Mössbauer spectroscopy indicates that at 305 K there is already approximately 9% LS present.[181,183] It is unclear whether this is because the transition is genuinely incomplete, or whether the transition is already under way. Considering a plot of the mole fraction of HS present (n_{HS}) suggests that the transition has reached a plateau by approximately 250 K, indicating than in all probability the former is the case. At low temperature, there is approximately 4% residual HS and the plateau between the two steps was found to be very close to 50% HS / 50% LS.

5.2 Single Crystal Diffraction Experiments

The crystals* had the form of small black hexagonal plates. These were shown not to be single as they would not index and when viewed through a microscope using reflected light, the boundaries between contact twins could be seen (Figure 5.6). This meant they could be cut to give wedges that were predominantly one single crystal.

5.2.1 Data Collection

A hexagonal plate was cut and the slice mounted in oil on a hair and quench cooled to 240 K using the Oxford Cryosystems Cryostream[130] mounted on the SMART-CCD 1000. A matrix was collected, which indexed as $a = 8.701(7)$ Å, $b = 9.409(8)$ Å, $c = 12.033(12)$ Å,

*Crystals courtesy of Prof. José A. Real, Dr. M. Carmen Muñoz and Dr. Ana B. Gaspar Pedrós[177] (Valencia).

$\alpha = 72.91(7)°$, $\beta = 79.76(6)°$, $\gamma = 67.05(6)°$, $V = 864.8(14)$ Å^3. A full sphere of data was collected at 16 s/frame, after which the crystal was cooled to 175 K at 120 K/hr.

Low Temperature Data

The matrix collected at 175 K initially gave problems indexing, but data were collected as at 240 K and the data indexed retrospectively to give a cell comparable to that seen at 240 K, but with a reduced volume of 838.4(19) Å^3.

On completion, the crystal was warmed to 245 K at 120K/hr, where another matrix yielded comparable results to those seen originally at 240 K. Therefore, the crystal was warmed to 285 K at 120 K/hr, after which it was removed and the Cryostream was replaced with the Oxford Cryosystems HeliX.[131] The crystal was returned to the diffractometer and cooled to 240 K at 120 K/hr, where another matrix yielded results in keeping with the previous two collected at similar temperatures, so the crystal was cooled to 30 K at 120 K/hr. A matrix at 30 K gave a comparable cell to that seen at 175 K, but reduced in volume still further to 804.5(6) Å. Another sphere of data was collected, identical to those at 240 K and 175 K.

At the end of the data collection, it was observed that the crystal was coated with what looked like ice, and a matrix collected after irradiating with the 15 mW red laser for about half an hour would not index. The crystal was then warmed up to 125 K at 360 K/hr, and the "ice" was observed to disappear at approximately 70 K, suggesting it was not water, but some other contaminant.[†] The crystal was cooled back to 30 K, with irradiation started during cooling, at 65 K. Another matrix collected after the laser was switched off would not index and the crystal diffracted poorly with evidence of loss of crystallinity. This was thought to be due to the damage caused by the crystal trying to expand while coated in the solid "ice", causing cracking. However, given the robustness of modern software, another sphere of data was collected, using the same regime as before.

[†]Carbon monoxide would appear to be the most likely contaminant as it freezes at approximately 68 K, however other possibilities include nitrogen (which is more abundant) and oxygen, which freeze at 63 K and 55 K respectively.

Irradiation

A new crystal fragment was mounted with glue on a hair and a matrix collected at 290 K using the SMART-CCD 1000, which indexed giving a comparable cell to the previous crystal. The crystal was then cooled to 30 K at 120 K/hr using the Oxford Cryosystems HeliX.[131] A matrix at 30 K indexed giving a similar cell to that seen for the first crystal at 30 K, after which the crystal was irradiated with the 25 mW red laser for approximately 4 mins. A matrix failed to index, but data were collected. However, indexing from the complete data gave a cell volume of 799.6(10) $Å^3$, indicating that the crystal was in its low spin state.

The above process was repeated with a third crystal, irradiating this time with the infrared laser for 5 mins, but again data after irradiating wouldn't index. The crystal was then warmed to 80 K at 360 K/hr to check the crystal quality and a matrix collected at 80 K indexed to give the expected LS cell with a volume of 804.3(7) $Å^3$. On cooling back to 30 K and irradiating again, it was still not possible to get a sensible cell, but nonetheless data were collected at 30 s/frame.

Comparing the first frame of matrix collections recorded before and after irradiation for these and previous matrix collections, suggested that there was some change, but this was not reflected in the cell parameters. It was thought that maybe the crystal was relaxing back to the low spin state, despite the magnetic susceptibility data which indicates that the lifetime of the meta-stable state at 30 K should be almost infinite. It was thought that this relaxation could be due to the difference between the poly-crystalline sample used for the magnetic susceptibility measurements and the single crystal used for structure determination. Another possibility is that the interaction with X-rays was causing relaxation, which would not be seen during SQUID measurements. Although the true cause was unknown, irradiating during the data collection could solve either problem. Since previous experiments using the red laser (λ = 633 nm) had caused considerable damage to the crystals, the near-infrared laser was used instead (λ = 830 nm). In order to irradiate during data collection, the laser was mounted using a custom-built attachment similar to that used in Chapter 4 (Section 4.2.1).

A fourth crystal was mounted in oil on a hair and quench cooled to 240 K where a matrix indexed giving the expected cell. The crystal was cooled to 30 K at 120 K/hr,

where a matrix indexed satisfactorily with a unit cell volume of 802.7(6) $Å^3$, indicating that the crystal was low spin. This was followed by a short data collection with 3° frames at 40 s/frame. The crystal was then rotated and irradiated for approximately 3 mins, after which a matrix was collected without irradiation. Once again the matrix would not index. However, using reflections from the matrix collection to refine the cell from the matrix prior to excitation, gave a cell volume of 810.9(10) $Å^3$ (compared with 802.7(6) $Å^3$ before irradiation). One of the most marked observations about the matrix collection however, is that the number of reflections found by the auto-indexing software was reduced to about half, suggesting that the crystal had suffered serious distress, thought to be caused by the irradiation.

Another matrix was collected, but the crystal was irradiated during data acquisition. Again indexing failed, however there was little further loss of intensity. Cell refinement using reflections from the matrix gave a cell of volume of 846(2) $Å^3$, but esds were very large so the cell needed further confirmation. The acquisition time was increased from 15 s/frame to 40 s/frame, which gave a similar cell with a volume of 845.5(9) $Å^3$. As much data as time allowed were collected, with the laser on and with 40 s/frame.

5.2.2 Data Analysis

In general, though the data did not index well, the cell parameters refined reasonably well. The raw data was of varying quality throughout, with all the data collected during and after irradiation noticeably worse than that collected before excitation. This is reflected in the figures of merit, which whilst not good for any of the data, are considerably worse for the data collected on the excited state. The poor quality is probably partly due to the strain caused by cutting the samples, though there may be other problems (including a minority twin component), which are exacerbated by the phase transitions. Irradiation seems to make all these problems even worse, with final values for R_{int} above 15%. Cell parameters for all the data were consistent (allowing for the changes due to the SC transitions).

The data were integrated in the usual fashion to a resolution of 0.73 Å. The structure was solved in $P\bar{1}$ from the 240 K data using direct methods and refined accordingly. The crystal faces were not visible due to the cutting and they could not be indexed.

However, although the crystals had an irregular shape due to the cutting process, they were reasonably isotropic in size, so the absorption corrections were carried out with SADABS only.[145]

The data at 175 K was scrutinised for the presence of super lattice reflections, but none were found. The structure was additionally solved in **P1**, but the figures of merit were no better than for the structure in $\mathbf{P\bar{1}}$ and there were no structural differences observed aside from the poor thermal ellipsoids caused by correlation effects.

5.2.3 Structure Refinement

At 240 K, 175 K and 30 K all non-hydrogen atoms were refined with anisotropic displacement parameters and although the hydrogen atoms could be located in the difference map, refinement of hydrogen positions led to an unreliable model, so the hydrogen atoms were added geometrically and refined using a riding model.

The short data collection on the fourth crystal at 30 K gave results consistent with those seen in the full data collection. However, the figures of merit were considerably worse, the esds were a lot larger and some of the thermal parameters were poorly defined, in the worst cases non-positive definite. All these difficulties could result from the wide frames, exacerbated by the inherent poor quality of the crystal and consequently only the iron and sulphur atoms were refined as anisotropic.[‡]

Irradiation

All the data collected after and during irradiation were of poor quality. The data for the third crystal gave very similar results to that for the first crystal, but were of a much lower quality, so were rejected.

All the data collected during and after irradiation, gave structures where there was a large amount of residual electron density close to the iron and sulphur atoms. Anisotropic

[‡]The data collected on the fourth crystal at 30 K with wide frames were recorded for structure confirmation and completion and the results are generally in keeping with the previous data collected at 30 K, though thermal parameters are very poor. Bond lengths, angles and other parameters discussed therefore, refer to the full dataset collected on the first crystal unless indicated otherwise.

	Mononuclear A	Dinuclear
a	8.521(8) Å	8.727(4) Å
b	11.063(9) Å	9.380(4) Å
c	12.598(6) Å	12.096(5) Å
α	96.83(5)°	73.052(10)°
β	91.81(6)°	79.508(11)°
γ	106.24(6)°	66.572(12)°
Volume	1120.5(12) Å^3	866.6(7) Å^3

Table 5.1: Cell parameters for the mononuclear complex (polymorph **A**) at room temperature[178] and the dinuclear analogue, compound **4**.

refinement of the carbon and nitrogen atoms led to poorly formed thermal ellipsoids, that were non-positive definite in the worst cases, so only the iron and sulphur atoms were refined anisotropically. Despite this, the geometry of the five and six membered rings is consistent with that prior to irradiation and no restraints were necessary. As with the data collected before irradiation, hydrogen atoms were added geometrically and refined using a riding model.

The program IVTON[174] was used to calculate the mean Fe–N bond lengths and the volumes for the iron octahedra in compound **4**.

5.3 Discussion

The dinuclear complex is chemically very different to the mononuclear analogue and would not be expected to have many structural features in common. However, there is a striking similarity between the unit cell parameters (Table 5.1) and this continues on a structural level.

5.3.1 Structural Analysis

Like polymorph **A** of the mononuclear complex, compound **4** is triclinic ($\mathbf{P\bar{1}}$). Prima facie, the structure appears very different, with only half the dinuclear molecule in the asymmetric unit (Figure 5.7). However, on close inspection of the mononuclear structure, it becomes clear that the inversion centre that relates two molecules, relates the two halves

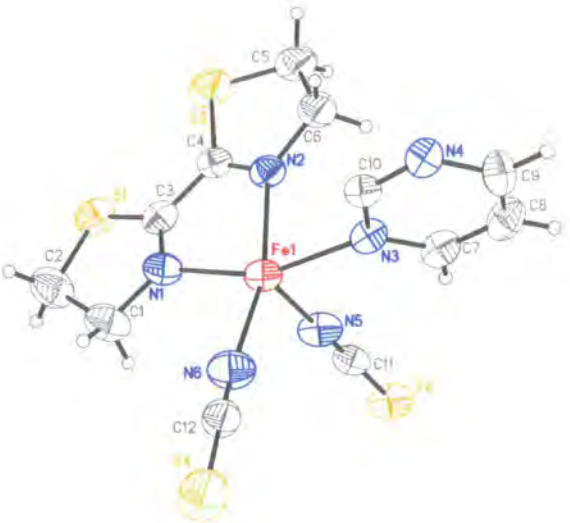

Figure 5.7: The asymmetric unit for compound **4** at 240 K, $a = 8.727(4)$ Å, $b = 9.380(4)$ Å, $c = 12.096(5)$ Å, $\alpha = 73.052(10)°$, $\beta = 79.508(11)°$, $\gamma = 66.572(12)°$, $V = 866.6(7)$Å^3 ($P\bar{1}$).

of the molecule in compound **4**. Thus, the dinuclear complex can be seen as a fusing of two mononuclear molecules, which is reflected in the cell parameters by a reduction in the cell volume.

Fe–N Distances

The thiocyanate Fe–N bond lengths are noticeably shorter than the other four Fe–N distances (2.050(5) Å and 2.066(5) Å compared with 2.151(6) Å, 2.217(4) Å, 2.193(5) Å and 2.223(5) Å). This is a trend that has been seen before in other thiocyanate complexes including compound **3** (see Section 4.3.1). However, despite the short thiocyanate Fe–N distances, the average Fe–N bond length of 2.142(10) Å indicates that at 240 K, compound **4** is high spin.

Packing and Short Contacts

Like compound **3**, there are no conventional hydrogen bonds, but there are weak C–H$\cdots$S interactions and, in this case, also S$\cdots$S close contacts.

The molecules pack together with Bpmd rings sitting in stacks along the a-axis (Fig-

ure 5.8). There are no π–π interactions however, because the Bpmd rings are in fact, slightly staggered and two of the thiocyanate ligands intrude, increasing the Bpmd–Bpmd distance to over 8 Å (Figure 5.8). The thiocyanate ligand points away from the iron centre towards the Bpmd ligand of the next molecule in the stack, so that the sulphur sits between the two rings. In this way, the stacks contain Bpmd rings alternating with sulphur atoms. This sulphur atom (S4), experiences a C–H$\cdots$S type interaction from one of the hydrogens on the Bpmd ligand in the adjacent stack, a relationship that is reciprocated (Figure 5.9).

Viewed down the c-axis (Figure 5.10), an overlap between the bithiazoline ligands can also be seen. Since Btz is not an aromatic ligand, π–π type interactions are not possible, but the distance between the planes of the overlapping Btz ligands is only 3.93(1) Å. This is probably caused by the weak S$\cdots$S interaction between one of the Btz sulphur atoms and S2 of one of the thiocyanate ligands (Figure 5.11).

5.3.2 Spin Crossover Transitions

On cooling to 175 K, there is a unit cell volume contraction of 3.4%, from 866.6(7) Å^3 to 837.5(4) Å^3, suggesting that there is a change in spin state. However, on cooling further to 30 K, there is a further contraction to 792.3(4) Å^3 which corresponds to an additional 5.2% (based on the unit cell at 240 K). The average Fe–N distance at 30 K is 1.958(4) Å indicating that the structure is clearly low spin. However, at 175 K the Fe–N average bond length of 2.052(11) Å, is exactly half way between the high and low spin values, suggesting that there is an intermediate phase.

Intermediate State

At the plateau, the magnetic data indicate that the intermediate state is half way between the high and low spin states, which is in keeping with the results from the average bond length. What is less clear, is the nature of this intermediate state. It is possible that the intermediate state is genuinely disordered HS/LS with two types of iron randomly ordered throughout the structure. However, in theory, it is more likely that cooperativity would lead to the formation of domains of high and low spin. The presence of these domains would lead to increased strain and probably deterioration in the crystal quality, which is

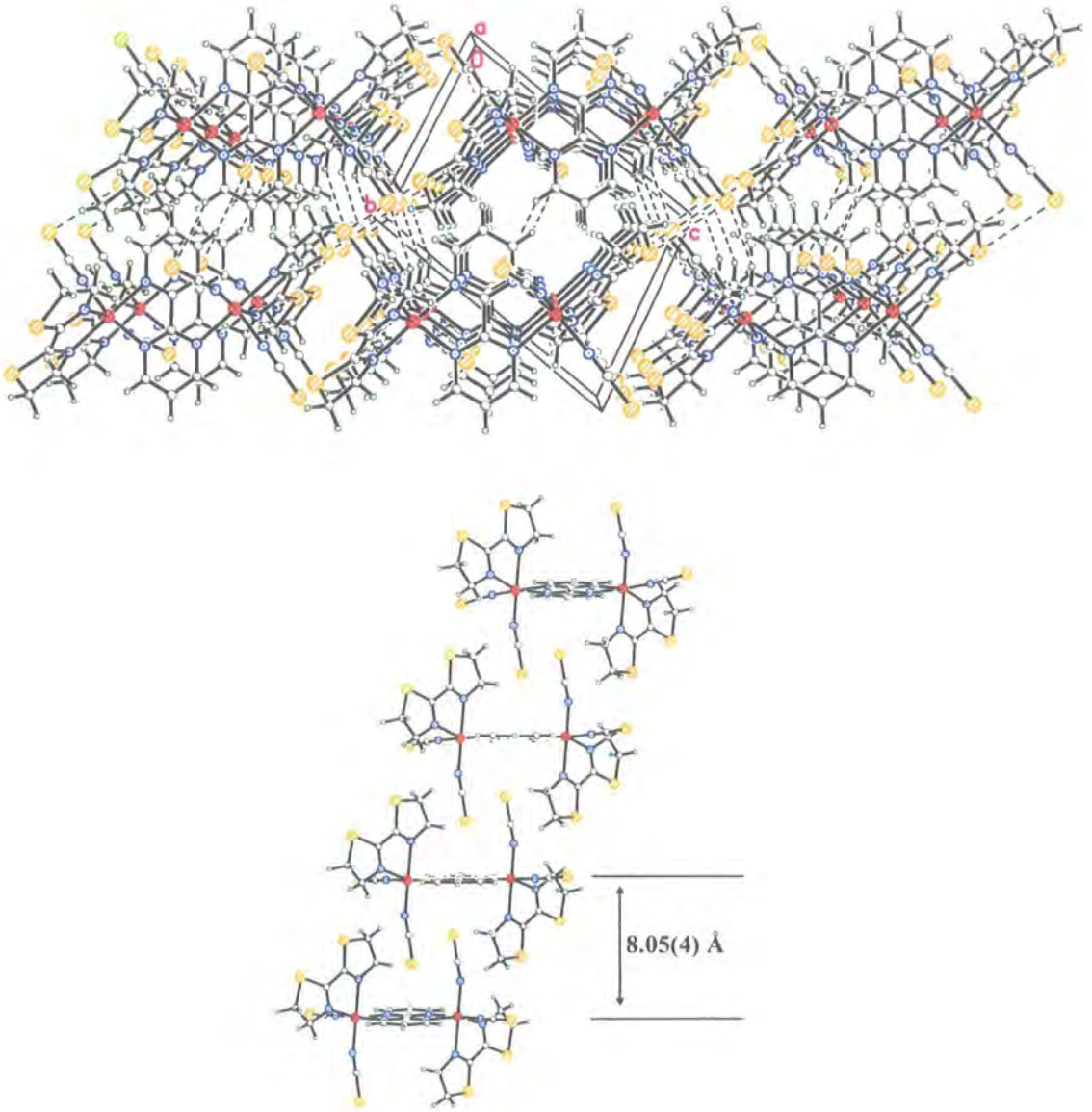

Figure 5.8: Packing and stacking in compound **4**. The stacking can clearly be seen in the packing diagram viewed down the *a*-axis (top), but the staggered nature of the stacking is better seen viewed from the side, where the Bpmd planes can clearly be seen (bottom). The distance between the Bpyd mean planes is 8.05(4) Å at 240 K.

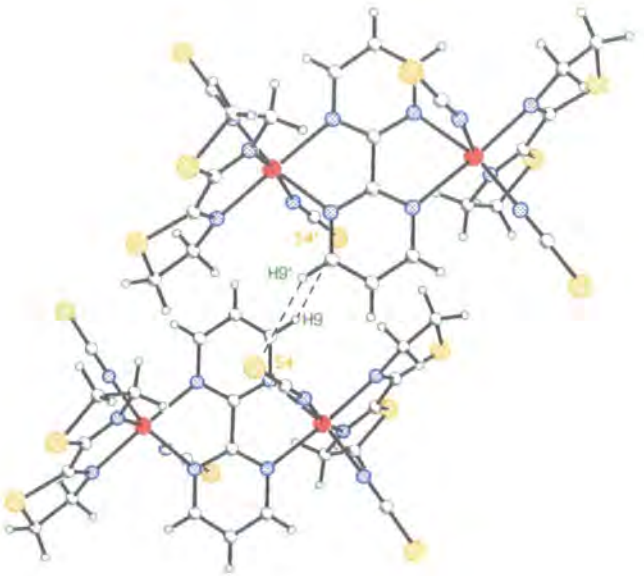

Figure 5.9: C–H···S interactions between thiocyanate ligand and bipyrimidine group. At 240 K the S4···H9′ distance is 2.818(4) Å.

not seen. It is more likely therefore, that the HS and LS iron(II) centres are ordered in some way, similar to $[Fe(Pic)_3]Cl_2.EtOH$ as discussed by Chernyshov *et al.*.[22] However, in $[Fe(Pic)_3]Cl_2.EtOH$ the super lattice reflections due to the differences between the HS and LS centres, were only visible with synchrotron radiation. In the case of compound **4**, only a laboratory X-ray source was used and the crystals were of such poor quality that super lattice reflections would be almost impossible to see. Thus it is impossible here to draw any further conclusions on the nature of the intermediate phase.

LIESST

Irradiating the crystal at 30 K and then collecting data gives a unit cell volume increase of only 2.3% to 810.7(3) $Å^3$. Irradiating for longer appears to make little difference to the unit cell volume, but collecting data while irradiating gives a considerable increase in the unit cell volume to 846.9(7) Å (a total increase of 6.9%). Comparing the two structures shows that a data collection after irradiation results in an increase in the average Fe–N distance to less than that of the intermediate state (2.009(8) Å). In contrast, data collected while irradiating show an increase in the average Fe–N bond length to that of the high

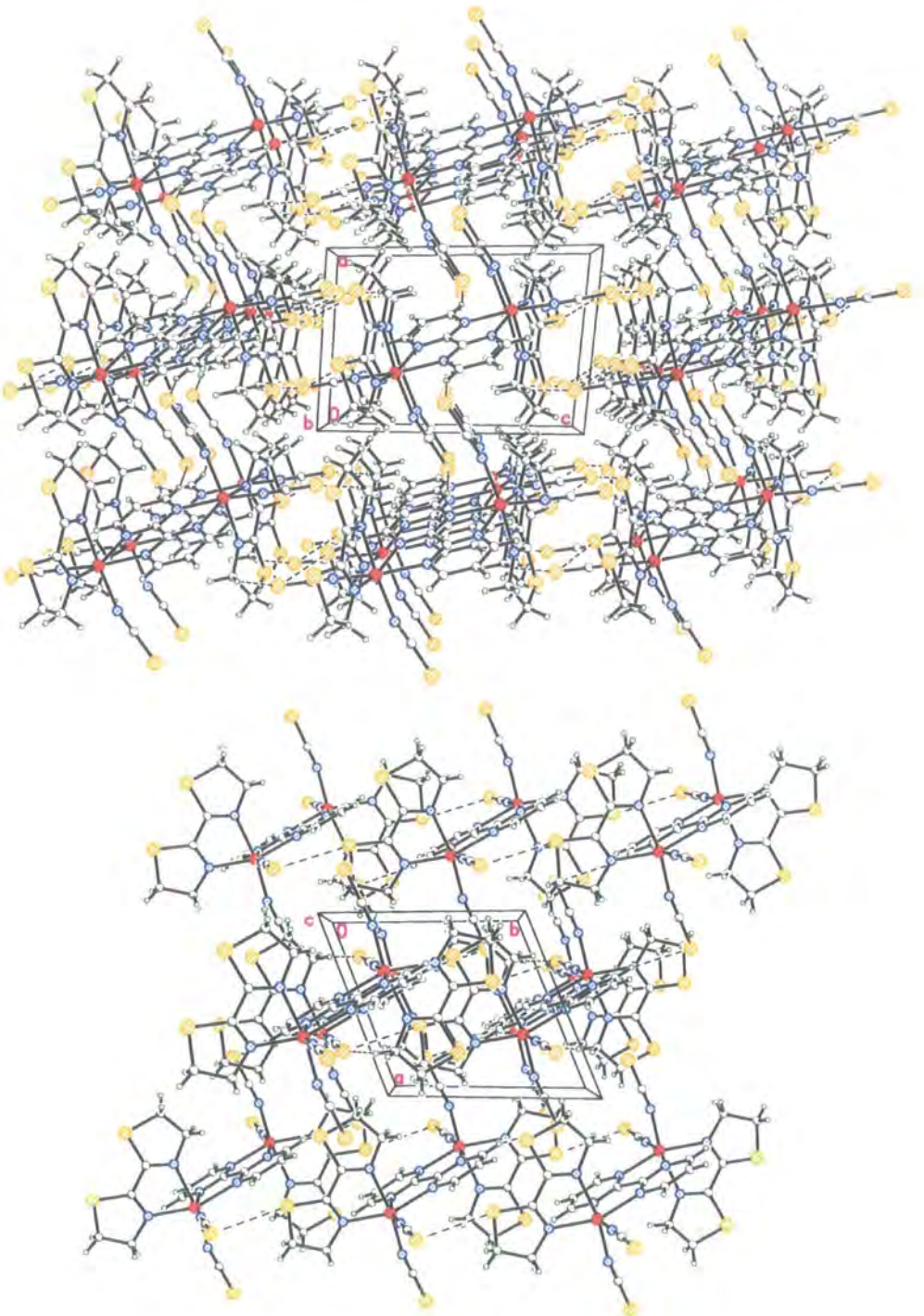

Figure 5.10: Packing in compound **4** viewed down the *b*-axis (top) and *c*-axis (bottom). The stacking of the molecules can be seen in the packing diagram viewed down the *b*-axis, while the Btz overlap can be seen in the packing diagram viewed down the *c*-axis.

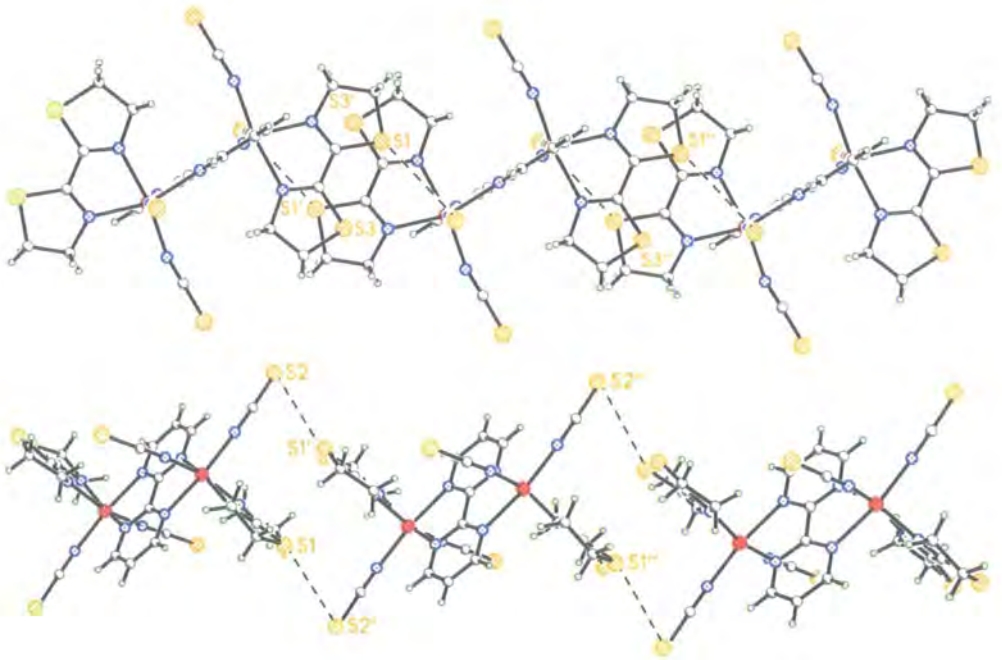

Figure 5.11: Bithiazoline ligand overlap (top, shown without perspective) and the S···S interactions in compound **4** (bottom). The perpendicular distance between adjacent Btz ligands is 3.93(1) Å and the S1···S2′ distance is 3.570(3) Å.

spin state, 2.145(5) Å compared with 2.142(10) Å at 240 K.

There are two possible reasons for the smaller increase in Fe–N distance on irradiating before data collection. Since irradiating during data collection gives Fe–N bond lengths comparable with that for the high spin state, irradiation must excite the low spin state to a meta-stable high spin state comparable to that seen at 240 K, which must be followed by relaxation. It is possible that after stopping irradiation, the crystal relaxes back to the low spin state gradually during the course of the data collection. This would make the structure appear to be similar to the intermediate state. However, matrix collections before the data collection (without irradiation) gave a similar volume to that from the full dataset, suggesting that there is little or no relaxation during the data collection. So the relaxation must take place as soon as the laser is switched off, or during the first couple of frames of data collection. Thus, the relaxation could be caused by the nature of the sample or interaction with X-rays during the data collection.

However, since the thermal transition takes place in two steps, it is possible that the relaxation also takes place in two steps. The first step of the relaxation could be rapid, and the lifetime of this intermediate state could be almost infinite at 30 K. If this were the case, it should be visible in the photo-magnetic data, but there is no evidence for a two step relaxation process. It is unclear therefore exactly what the cause of this relaxation is, but there are at least two more possibilities. Since the magnetic susceptibility data is collected on a micro crystalline powder, the relaxation could be a single crystal phenomenon, where the cooperativity within the crystal leads to rapid relaxation. Another possibility is that the X-rays could be stimulating a relaxation process.

Fe–N Distances and Octahedral Volumes

The individual Fe–N distances generally follow a similar pattern on cooling to that seen at 240 K, with the shortest Fe–N distance to the thiocyanate ligands (Table 5.2).

It is interesting to note however, that Fe1–N4 is the longest of the remaining four, while Fe1–N1 is by far the shortest, a situation that generally remains at all temperatures and both after and during irradiation.[§] Fe1–N2 and Fe1–N3 however, change their relative

[§]The only exception is Fe1–N3 on irradiation before data collection, where it is apparently shorter than

lengths with Fe1–N2 longer at 240 K, shorter at 30 K and Fe1–N2 and Fe1–N3 identical at 175 K. In other words, at 240 K, Fe1–N1 $\ll$ Fe1–N3 $<$ Fe1–N2 $<$ Fe1–N4, while at 175 K Fe1–N1 $\ll$ Fe1–N3 = Fe1–N2 $\ll$ Fe1–N4, which changes to Fe1–N1 $<$ Fe1–N2 $<$ Fe1–N3 = Fe1–N4 at 30 K, where the range is reduced. Thus Fe1–N2 experiences the largest contraction followed by Fe1–N4. Given the connection between the cooperativity and changes in bond length, this could indicate that the cooperativity takes place primarily along the directions of N2 and N4.

On irradiating, the esds are generally much larger making it more difficult to draw firm conclusions. However, the Fe–N bond length trends are generally the reverse of those seen on cooling, as would be expected.

The average Fe–N distance clearly indicates that the structure is high spin at 240 K, low spin at 30 K and an intermediate state on the plateau at 175 K. This is also reflected in the changes in the octahedral volumes, which show that the intermediate state is almost exactly half way between high and low spin (Table 5.2). The average Fe–N distances for the light excited states however, appear to show that simultaneously irradiating and collecting data gives a high spin state, while irradiating followed by collecting data gives a state approximately analogous to the intermediate state. This is also reflected in the octahedral volumes, which indicate that both excited states have a larger octahedral volume than prior to irradiation. However, it is apparent that the Fe–N bond lengths and octahedral volume from the data collected *after* irradiation are considerably smaller than those for the intermediate state recorded at 175 K. It is therefore apparent that this excited state has a large amount of residual low spin (relative to the intermediate and high spin states). This could be due to the choice of wavelength, and the green laser (λ = 532 nm), but this seems unlikely as this state depends on the relaxation rather than excitation.

Fe$\cdots$Fe Distances

The shortest Fe$\cdots$Fe distance is across the Bpmd ligand and at 240 K is 5.890(3) Å. In addition to this, each iron centre is surrounded by a number of other iron centres, but at 240 K, the next shortest Fe$\cdots$Fe distance is connected through the C9–H9$\cdots$S4

Fe1–N1, but the large esds make this result suspect.

interaction. Following that, there are two more short distance (less than 8.5 Å at 240 K), one connected through the Btz–Btz ligand overlap and the other is the distance between adjacent iron atoms in the stack along the *c*-axis (Figure 5.8, Table 5.3).

The intramolecular Fe···Fe distance behaves as would be expected, decreasing regularly as the crystal is cooled and the structure becomes low spin. However, the other distances are not as predictable. The distance between molecules in the stack increases by 0.068(5) Å on cooling from 240 K to 175 K, but undergoes almost no further change on cooling to 30 K. In contrast, the Btz Fe···Fe distance changes less between 240 K and 175 K than during the second step, undergoing changes of 0.151(5) Å and 0.228(5) Å respectively. Meanwhile, the C–H···S Fe···Fe distance changes by −0.113(5) Å during the first step and −0.078(5) Å between 175 K and 30 K.

The Fe···Fe distances for the irradiated structures look out of place at first glance. However, on closer inspection it becomes apparent that irradiating before collecting data generally gives values between those at 30 K and 175 K, and irradiating during data collection gives values between those seen at 175 K and 240 K. The only exception is the intrastack distances, which appear to contract. This may be an anomaly, but it could reflect cooperative interactions.

Thus, in general, the Fe···Fe distances reflect the change in spin state divorced from the thermal contraction, but the data quality makes it difficult to draw firm conclusions.

Intermolecular Interactions

Clearly the weak intermolecular interactions have a large effect on the transitions and this can be seen in the intermolecular close contact distances. On cooling to 175 K, it can be seen that of the shortest C–H···S contacts, three contract and three expand (Table 5.4) On cooling further to 30 K, all distances contract, ending shorter than for the high spin structure at 240 K.

	240 K	175 K	Contraction 1	30 K	Contraction 2	30 K - Irr.	30 K - Irr. During Collection
Fe1–N1	2.151(5) Å	2.057(5) Å	0.094(8) Å	1.945(6) Å	0.112(9) Å	2.027(14) Å	2.132(15) Å
Fe1–N2	2.217(4) Å	2.087(4) Å	0.130(7) Å	1.963(7) Å	0.124(9) Å	2.050(15) Å	2.239(16) Å
Fe1–N3	2.193(5) Å	2.089(4) Å	0.104(8) Å	1.978(6) Å	0.111(8) Å	2.007(14) Å	2.185(14) Å
Fe1–N4	2.223(5) Å	2.106(4) Å	0.117(8) Å	1.975(6) Å	0.131(8) Å	2.042(14) Å	2.227(15) Å
Fe1–N5	2.050(5) Å	1.981(5) Å	0.070(8) Å	1.935(6) Å	0.046(9) Å	1.956(16) Å	2.077(16) Å
Fe1–N6	2.066(5) Å	2.011(5) Å	0.055(8) Å	1.947(7) Å	0.064(10) Å	1.987(17) Å	2.059(16) Å
Average Fe–N Distance	2.142(10) Å	2.052(11) Å	0.090(15) Å	1.958(4) Å	0.094(12) Å	2.009(8) Å	2.145(5) Å
Octahedral Volume	12.80(4) $Å^3$	11.35(4) $Å^3$	1.45(6) $Å^3$	9.93(4) $Å^3$	1.42(6) $Å^3$	10.69(7) $Å^3$	12.81(7) $Å^3$

Table 5.2: Fe–N distances and octahedral volumes for compound **4**.

	240 K	175 K	30 K	30 K - Irr.	30 K - Irr. During Collection
Intramolecular	5.890(3) Å	5.638(2) Å	5.355(2) Å	5.465(6) Å	5.860(6) Å
Intermolecular					
Intra-stack	8.573(3) Å	8.641(3) Å	8.632(3) Å	8.598(6) Å	8.524(6) Å
Btz–Btz Interaction	8.267(3) Å	8.116(3) Å	7.888(3) Å	7.997(6) Å	8.249(6) Å
C–H$\cdots$S Interaction	8.069(3) Å	8.182(2) Å	8.260(3) Å	8.246(5) Å	8.122(6) Å

Table 5.3: Fe$\cdots$Fe distances for compound **4**.

Ignoring the bonds between the pairs of rings, the structure can be considered to consist of iron atoms each ligated by two thiocyanate ligands, two pyrimidine rings and two thiazole rings (Figure 5.12). The C–H···S contacts that contract between 240 K and 175 K are between the thiocyanate sulphur atom S2 and hydrogen atoms on the rings connected to N2, N4 and N3. In all cases except that of N3, the C–H···S interaction is in the same direction of the Fe–N bond. In the case of N3, the C–H···S interaction that contracts is *ortho* to the nitrogen. There is however, another C–H···S interaction which is *para* to N3 and is approximately co-linear with the Fe–N bond, but this C9–H9···S4 interaction extends slightly on cooling from 240 K to 175 K. The other C–H···S4 distance also expands slightly and is between S4 and H2A, which is connecting part of the ring containing N1. The final C–H···S distance is between S2 and H2B and also expands, but is the only S2 interaction to do so.

It is clear that the N2 and N4 rings and the S2 thiocyanate together with the weak intermolecular interactions between them, are critical to the transition. It is not surprising that this is the case, because the Fe–N distances for N2 and N4 contract the most. In addition, Fe1–N5 is consistently the shorter of the two thiocyanate Fe–N bonds and in the first step of the transition contracts more than Fe1–N6.

The other C–H···S interactions are between the sulphur atoms in the two thiazole rings and the pyrimidine of the bridging Bpmd ring. S1, which is part of the N1 thiazole ring, participates in a C–H···S with H7. The C7–H7···S1 interaction expands between 240 K and 175 K, but contracts by even more between 175 K and 30 K. In contrast, the short contact between the other thiazole sulphur atom S3 (part of the N2 ring), undergoes virtually no change on cooling through the first step, while it undergoes one of the largest expansions of all the short contacts between 175 K and 30 K. These changes are more difficult to understand, but appear to follow a similar sort of pattern. Thus, the S1···H7 interaction contracts more when the Fe1–N1 bond between the S1 ring and the central iron shortens most, which is in the second step. The S3 interaction on the other hand, expands during the second step, when the Fe1–N2 bond shows the least contraction.

The S···S interaction is even more difficult to understand, expanding slightly during the first step of the transition, then sharply contracting during the second step. The reason for this more complex behaviour is presumably due to the way it links the shorter

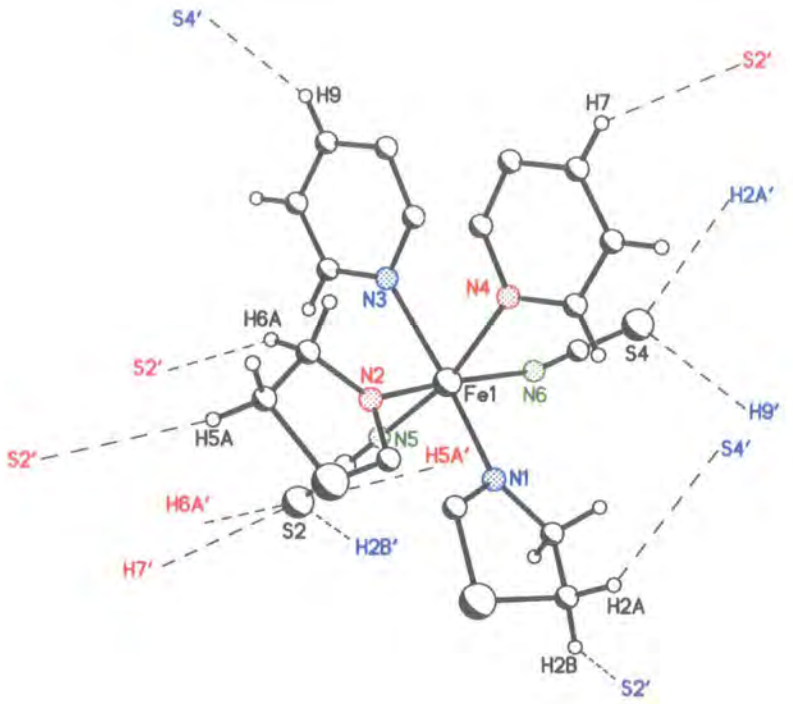

Figure 5.12: C–H···S interactions. The interactions labelled in red participate in bonds that contract between 240 K and 175 K. The thiocyanate nitrogen atoms are shown in green, N2 and N4 are shown in red to highlight their larger contraction and N1 and N3 are shown in blue.

Fe1–N5, thiocyanate ligand and the short Fe1–N1 thiazole ligand.

The short contact distances for the LIESST structures don't really fit into this pattern. This could be a reflection of the poor quality data, with the hydrogen positions riding on carbon atom positions that had to be refined as isotropic. However, the structure generated by irradiating before data collection has strikingly similar values for all the intermolecular contacts to those seen at 240 K. The data collected during irradiation give an even stranger result, with most distances longer than those at 240 K, suggesting that the structure is even *higher* spin than at 240 K. While the data are poor and it is not possible to draw any firm conclusions from these values, it is possible that there is another reason for these results, that could explain the unexpected relaxation of the LIESST state. However, without good quality data on both the LIESST states, further deductions are not possible.

	240 K	175 K	30 K	30 K - Irr.	30 K - Irr.
Thiocyanate					
S2···H6A	2.861(4) Å	2.840(3) Å	2.830(3) Å	2.861(6) Å	2.774(6) Å
S2···H2B	2.863(4) Å	2.911(3) Å	2.825(3) Å	2.863(6) Å	3.012(6) Å
S2···H7	2.977(4) Å	2.956(3) Å	2.921(3) Å	2.977(6) Å	3.037(6) Å
S2···H5A	3.049(4) Å	3.026(3) Å	2.998(3) Å	3.049(6) Å	3.117(6) Å
S4···H9	2.758(4) Å	2.779(3) Å	2.748(3) Å	2.758(6) Å	2.775(6) Å
S4···H2A	2.934(4) Å	2.955(3) Å	2.912(3) Å	2.924(6) Å	2.874(6) Å
Bithiazoline					
S1···H7	2.863(4) Å	2.912(3) Å	2.836(3) Å	2.863(6) Å	2.901(6) Å
S3···H8	3.188(4) Å	3.196(3) Å	3.276(3) Å	3.188(6) Å	3.090(6) Å
Bithiazoline–Thiocyanate					
S1···S2	3.504(7) Å	3.564(3) Å	3.494(3) Å	3.504(7) Å	3.480(7) Å

Table 5.4: Short intermolecular contact distances.

5.4 Conclusion

$[Fe(Btz)(NCS)_2]_2Bpmd$ is the first dinuclear spin crossover complex with a step transition that undergoes Light-Induced Excited Spin-State trapping, to be studied structurally. In general, the structural results agree with the magnetic susceptibility data, which show that the material has a plateau between transitions, where the HS/LS ratio is 50%. The structural data not only agree with these results, but also give some indication of the weak intermolecular interactions governing the transition. It has not been possible to find super-lattice reflections and a refinement in **P**1 did not change the bond lengths around the central iron atoms. However, it is possible that there is a super lattice, but the weak reflections were not visible because of their low intensity and the poor crystal quality. Indeed it is probable that there is HS/LS super-lattice order because without it the HS and LS atoms would be expected to form domains which would increase the internal strain in the crystal leading to crystal damage, but this is not seen.

Photo-magnetic data indicate that the structure has a light induced excited state that can be trapped for extended periods of time at 30 K, however, irradiating the crystal with red or infrared light gives only a partially excited state, with an average of less than half the molecules converted to high spin. With the custom-built apparatus for irradiating and collecting data simultaneously, a LIESST structure with Fe–N bond lengths and an

octahedral volume close to that seen at 240 K, has been identified. The data for both these excited states are poor however, which could be due to damage caused by irradiation. It is also possible though, that when the crystal relaxes suddenly from the excited state, there is no HS/LS order. Instead there could be domains of HS and LS introducing strain and causing crystal damage. If this is the case it suggests that the intermediate state at 175 K is ordered and should good quality crystals become available, a synchrotron study could lead to the location of super-lattice reflections alluded to above.

Chapter 6

A Dicyanamide Bridged, Dinuclear, Spin Crossover System

6.1 Introduction

$\{[N(CN)_2](FeBpl)_2\}(PF_6)_3$ (compound **5**) is an unusual dinuclear system with a dicyanamide ($N{\equiv}C{-}\bar{N}{-}C{\equiv}N$) bridge connecting the two iron centres. Each iron is encased in a novel pentadentate *N*-benzyl-*N*-pyridin-2-ylmethyl-*N'*-(2-pyridin-2-yl-1-pyridin-2-ylmethyl-ethyl)-ethane-1,2-diamine (Bpl) cage (Figure 6.1).

6.1.1 Magnetic Susceptibility Data

SQUID magnetic susceptibility data indicate that compound **5** has two gradual transitions over ranges of approximately 100–230 K and 310–400 K, with a step in between (Figure 6.2).[184]

6.2 Single Crystal Diffraction Experiments

At room temperature, the crystals* were small rectangular blocks that were red-orange in colour. This dichroic nature made it very difficult to see them extinguish and most

*Crystals courtesy of Prof. José A. Real, Dr. M. Carmen Muñoz, Prof. Rafael Moreno-Esparza and Ms. Norma Ortega Villar (Valencia and Mexico City).

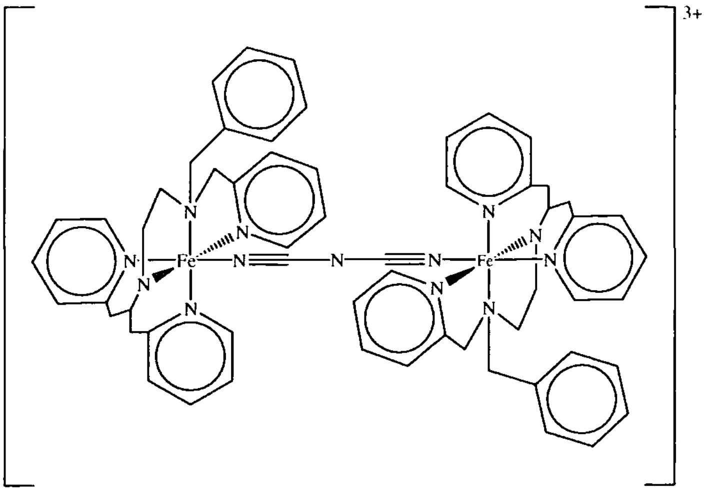

Figure 6.1: Molecular diagram of $[N(CN)_2](FeBpl)_2^{3+}$ (compound **5**).

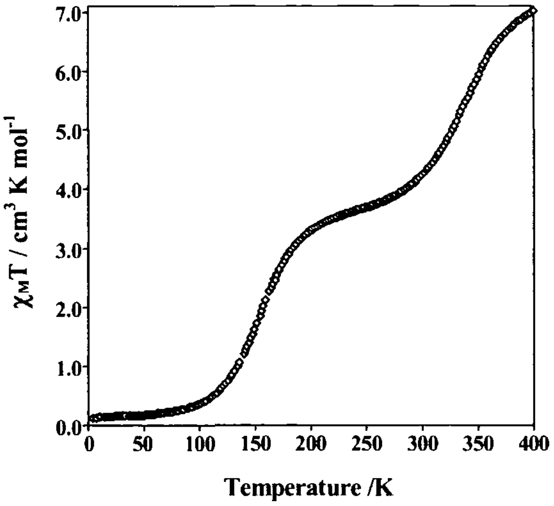

Figure 6.2: Magnetic susceptibility data for compound **5**. Only the cooling curve is shown, but the compound has no appreciable hysteresis.[184]

appeared to extinguish in parts suggesting the possibility of twinning. Initial attempts with these crystals resulted in high R-factors and extremely large residual electron density. GEMINI[147] clearly indicated that there was second component to the crystal, but all efforts to take this into account were unsuccessful. A twin law was determined using ROTAX,[146] but this refined to approximately 4 % and made very little difference to the overall refinement.

6.2.1 Data Collection

Eventually, a suitable crystal was found, and it was mounted on a hair with nail polish. Data were collected using the Bruker Proteum M diffractometer with the Bede Microsource®. This machine was selected as the crystals were small and weakly diffracting and the Bede Microsource® gives increased beam intensity compared with the conventional sealed tube X-ray sources. In addition, the instrument was fitted with the Series 700 Cryostream which can reach 400 K (compared with 360 K for the Series 600).[130]

At 290 K, a matrix data collection indexed as a = 9.437(5) Å, b = 16.502(8) Å, c = 20.706(8) Å, α = 104.82(3)°, β = 90.72(4)°, γ = 97.61(4)°, V =3085(3) Å^3 and was followed by warming to 400 K at 120 K/hr with photos taken before and after heating. Data were collected at 400 K with 60 s/frame. The crystal was then cooled at 120 K/hr to 290 K where a full data collection was recorded at 40s/frame.

The crystal was then cooled to 250 K at 120 K/hr, where another dataset was collected (30 s/frame), before cooling through the second transition to 90 K, where data were collected at 20 s/frame. The data collection had to be aborted after 100 frames due to the formation of ice on the hair and crystal, so the crystal was warmed to 400 K where it remained for 20 mins before it was cooled to 350 K at 120 K/hr, where a dataset was collected (50 s/frame). On completion, the crystal was cooled to 200 K at 120 K/hr where another matrix and dataset was collected (25 s/frame). When completed, the crystal was cooled to 150 K where the data collection was repeated (30 s/frame), before cooling to 90 K where another dataset was collected (30 s/frame). Finally, the crystal was warmed to 290 K and removed.

The data at 400 K were poor due to the inherent decrease in intensity caused by the thermal motion at high temperature. The crystal was returned to the diffractometer

therefore and heated to 400 K at 120 K/hr before a data collection was recorded with increased acquisition time (90 s/frame).

Variable Temperature Cell Parameters

Another crystal was selected and mounted as before. Using the Bruker Proteum M diffractometer, a matrix collection was recorded at 290 K, and the crystal was then warmed at 120 K/hr to 400 K where it was left for 30 mins. A matrix collection was carried out at 400 K, before cooling at 120 K/hr to 385 K, where a the cell determination was repeated. On completion, the crystal was cooled by a further 15 K (at 120 K/hr), where a matrix collection was recorded. Cells were determined in this fashion from 400 K to 100 K. The crystal was finally warmed to 290 K where another matrix collection was recorded.

6.3 Data Analysis

The final structures were all triclinic, $\mathbf{P\bar{1}}$. Initially however, the crystals chosen were twinned. With these crystals there were some indications that the cell was doubled along the *b*-axis on indexing. The structure solution however, suggested that the smaller cell was correct, with disorder present when the cell was doubled and when the structure was solved in **P**1. Structure refinement gave high *R*-factors and extraneous peaks of residual electron density. The crystal from which the results are discussed here was better, but being smaller had other problems and it is probable that there was still a small component of twinning present.

The data used indexed satisfactorily and were integrated in the usual manner. The faces were indexed, so numerical absorption corrections were carried out accordingly.

6.3.1 Structure Refinement

The initial data collection at 400 K was poor, because the intensity was reduced at high angle due to the high temperature. Consequently, SADABS[145] was unable to perform additional absorption corrections and some anisotropic displacement parameters were non-positive definite. In order to improve the quality of the results, the data were recollected with a longer data acquisition time and only integrated to 0.9 Å (instead of 0.75 Å as at all the other temperatures). Although this reduced the number of reflections used,

the relative intensity of the high angle data was increased by the longer collection time. Thus, absorption corrections were possible giving better statistics and improved thermal parameters. Despite the reduced number of reflections, the data to parameter ratio was still greater than 10:1.[†]

Disorder

Non-hydrogen atoms were refined as anisotropic in almost all cases except where disorder was present. For example, where there was disorder in a PF_6^- counter ion, the minor component was sometimes modelled using isotropic thermal parameters. In these cases, initially all the isotropic thermal parameters were constrained to a common value and the fractional occupancy of each component refined. When the refinement was stable, anisotropic thermal parameters were refined and the occupancies monitored. If the refinement was still stable, the occupancy was fixed to the refined value. Where the fractional occupancy for one component was very small, in most cases the refinement became unstable or the thermal ellipsoids were ridiculously shaped, so the minor component was modelled with isotropic thermal parameters.

There are three crystallographically inequivalent PF_6^- counter ions, P1, P2 and P3, numbered according to the central phosphorus atom. While the thermal motion is large at high temperature, P1 is modelled as ordered throughout, however P2 and P3 are both disordered. P2 is modelled with two orientations of equal occupancy at 400 K, decreasing fairly linearly to 85%/15% at 90 K (Figure 6.3). At room temperature and below, the minor component is modelled as isotropic.

The disorder in P3, was modelled as a rotational disorder around the F36–P3–F35 axis. Therefore, the two apical atoms were refined anisotropically with 100% occupancy at all temperatures, while the equatorial atoms were modelled as disordered in two positions. At room temperature and above, these were modelled as equally occupied, but below room temperature the occupancy of one component decreased approximately linearly to 75%/25% at 90 K. All P3 fluorine atoms were refined anisotropically except the minor component at 150 K and 90 K.

[†]Results from the second data collection are used in the discussion unless otherwise specified.

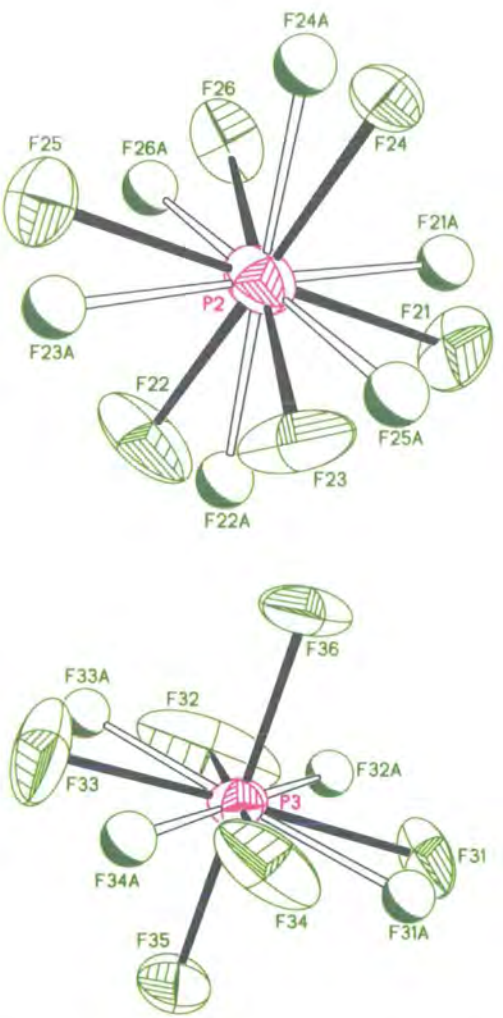

Figure 6.3: Disordered PF_6^- counter ions at 90 K. P2 is above and P3 below. The minor component atoms (15% and 25% occupancy respectively) are refined as isotropic and shown here as spheres with open bonds.

	400 K	**350 K**	**290 K**	**250 K**	**200 K**	**150 K**	**90 K**
s/frame	90	50	40	30	25	30	30
Independent Reflections	8986	14332	15057	14948	13667	14586	14396
Central Nitrogen	D(A)	D(A)	D(A)	D(A)	D(A)	D(A)	D(A)
Carbons in Bridge	O(A)	O(A)	D(I)	D(I)	D(I)	D(I)	D(A)
% age Disorder in P2	50(A)/50(A)	55(A)/45(A)	60(A)/40(A)	65(A)/35(I)	70(A)/30(I)	80(A)/20(I)	85(A)/15(I)
% age Disorder in P3	50(A)/50(A)	50(A)/50(A)	50(A)/50(A)	55(A)/45(A)	60(A)/40(A)	70(A)/30(I)	75(A)/25(I)
R_{int}	0.1390	0.0643	0.0573	0.0580	0.0528	0.0636	0.0571
R_1	0.0992	0.0721	0.0694	0.0753	0.0683	0.0750	0.0663
wR_2	0.2315	0.1211	0.1181	0.1278	0.1230	0.1335	0.1244
Goodness of Fit	0.820	0.908	0.913	0.948	0.934	0.943	0.946

Table 6.1: Summary of the data collection and structure refinement details for compound **5**. 'D' indicates modelled as disordered, 'O' indicates modelled as ordered, 'A' indicates refined as anisotropic and 'I' indicates refined as isotropic.

In all cases, restraints were necessary to maintain sensible octahedral geometries. These were usually restraining similar distances to be equal, for example, all P–F bonds in P2 were restrained, as were those in P3.

Dicyanamide Bridges

At all temperatures, the dicyanamide groups occupy positions around inversion centres, which generates half of each of the disordered anionic bridges. This disorder was modelled differently at different temperatures. At 400 K, the central nitrogen of the N≡C–N̄–C≡N bridge was modelled as 50% occupied and split into two symmetry related positions. On cooling to 350 K however, the disorder appears to be spreading to the adjacent carbon atoms, as they refine with larger thermal ellipsoids.

At 290 K and below, the bridge is modelled with two carbon positions each 50% occupied, with the second half of the dicyanamide group generated by symmetry. Since the two components of the disorder are so close together and in some cases overlapping, the anisotropic refinement is unstable. This results in poorly shaped thermal ellipsoids and in extreme cases, atoms that become non-positive definite. Thus the disordered carbon atoms are modelled isotropically until 90 K, where the thermal motion is sufficiently reduced to enable anisotropic refinement.

Although many of the hydrogen atoms were visible in the difference map, refinement was unreliable, so they were added geometrically and refined using a riding model. The program IVTON[174] was used to calculate the mean Fe–N bond lengths and the volumes for the iron octahedra in compound **5**.

6.4 Discussion

The structures were all triclinic ($\mathbf{P\bar{1}}$), with two half molecules in the asymmetric unit (Figure 6.4).

6.4.1 Structural Analysis

Both half molecules occupy a position such that an inversion centre in the middle of the dicyanamide bridge generates the other half of the molecule (Figure 6.5). Viewed down the *c*-axis, the molecules sit at 90° to each other and can be seen to cross at the bridge.

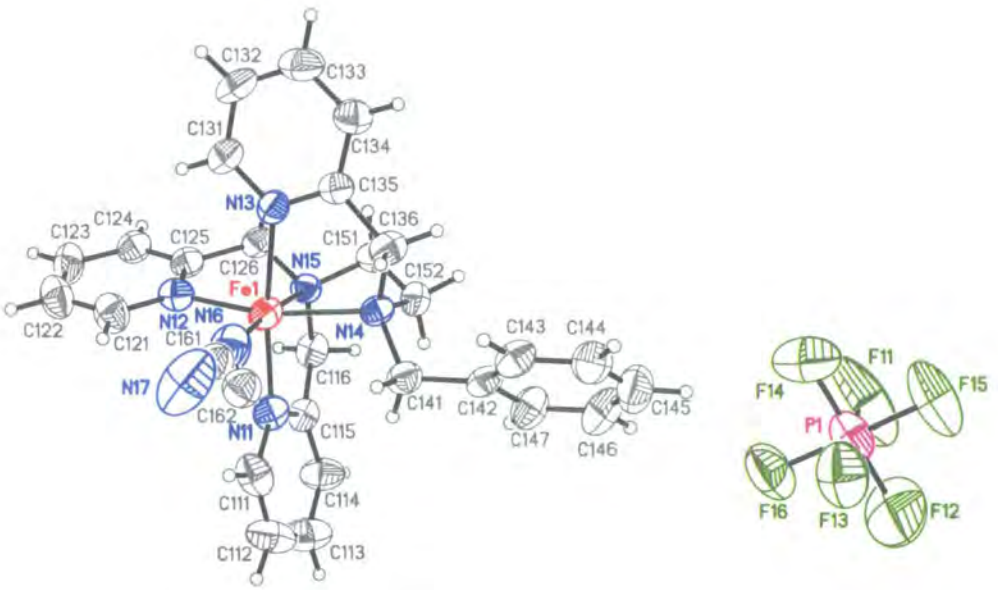

Figure 6.4: Part of the asymmetric unit for compound **5** at 290 K, a = 9.4161(7) Å, b = 16.4923(13) Å, c = 20.6515(15) Å, α = 104.691(2)°, β = 90.747(2)°, γ = 97.624(2)°, V =3071.1(4) Å^3 ($\mathbf{P\bar{1}}$). In the full asymmetric unit there is an additional half molecule and two extra PF_6^- counter ions.

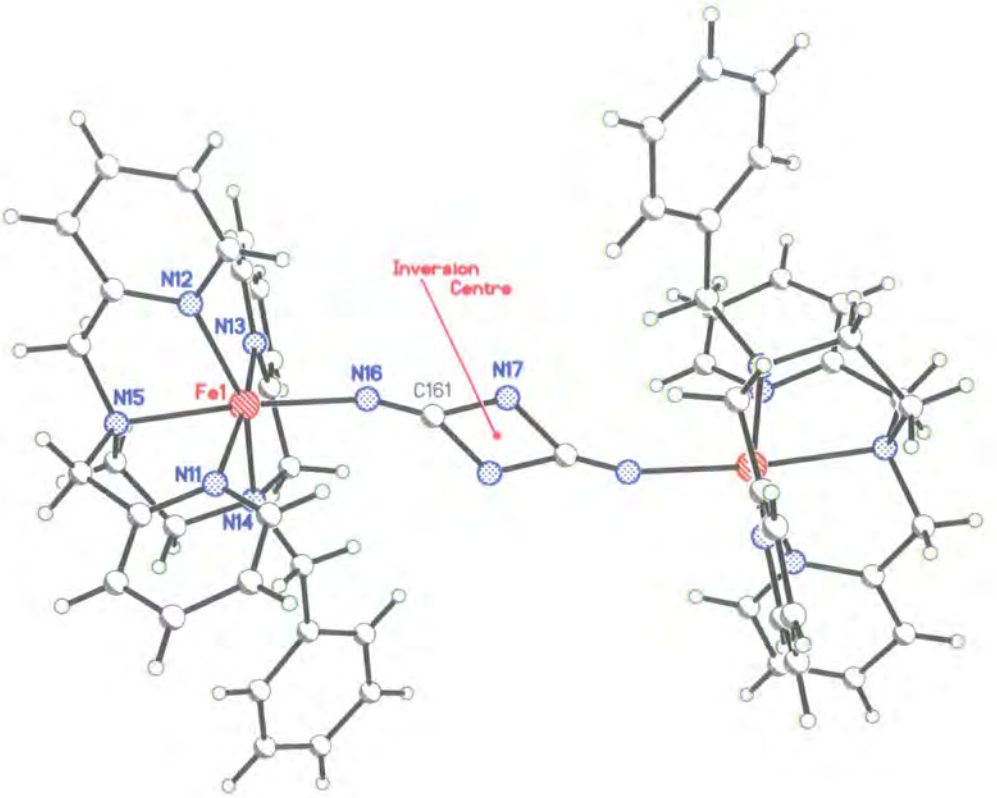

Figure 6.5: A molecule of $[N(CN)_2](FeBpl)_2^{3+}$ at 400 K.

Directly between the centre of the disordered bridges lies one of the PF_6^- counter ions (Figure 6.6).

Fe–N Distances

At 400 K the average Fe–N distances are 2.146(28) Å and 2.143(9) Å (for Fe1 and Fe2 respectively), indicating that the compound is predominantly high spin. Despite the large esds, Fe1–N16 and Fe2–N26 are clearly the shortest. These are the two nitrogen atoms that join the iron centres to their symmetry equivalents through dicyanamide bridges and are presumably shorter because of the anionic nature of the ligand.

In contrast, Fe1–N14 and Fe2–N24 are clearly the longest Fe–N bonds. N14 and N24 are two of four tertiary amide groups. The other tertiary amides' nitrogen atoms are N15 and N25, and although the Fe–N15 and Fe–N25 bond lengths are not as long as those to

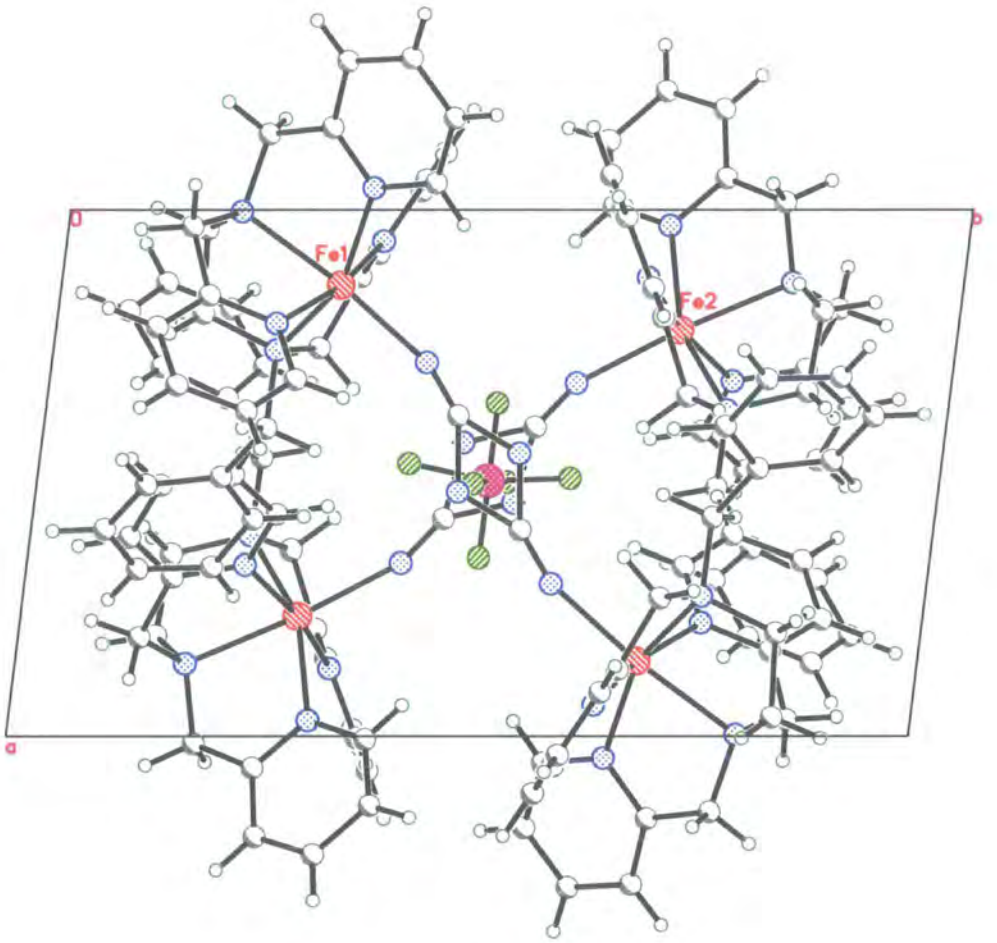

Figure 6.6: Two molecules of $[N(CN)_2](FeBpl)_2^{3+}$ at 400 K showing the crossing of the dicyanamide bridges with the PF_6^- between them.

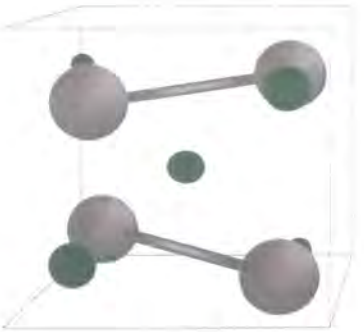

Figure 6.7: Schematic showing the idealised packing in compound **5**. The PF_6^- ions are shown as green spheres and the iron(II) cations are shown as grey dumbbells.

N14 and N24, they are longer than the average. The increased Fe–N distance in these four nitrogen atoms (N14, N15, N24 and N25) compared with the average, is probably due to steric effects.

Packing

The three PF_6^- counter ions lie between the two cations in staggered layers. One lies directly between the bridges, where they cross, forming a link between the molecules. The other two lie in the cavities formed by the cris-crossing of the two bulky molecules (Figure 6.7).

There are no conventional hydrogen bonding interactions, but there are weak C–H$\cdots$F interactions between each of the PF_6^- counter ions and the Bpl ligands (Figure 6.8). Although weak, this type of interaction is common in spin crossover materials and in many cases critical to the presence and type of transition. In this case, there is a plethora of H$\cdots$F interactions between 2.5 Å and 3.0 Å, but there are six H$\cdots$F contacts with distances of less than 2.5 Å. Of these, four involve P2, with one H$\cdots$F to each of the other anions. There are two particularly short contacts of 2.358(6) Å and 2.315(6) Å, involving F21 and F25 respectively.

6.4.2 Spin Crossover Transitions

There is a clear colour change between 400 K and 250 K, from yellow to dark orange, suggesting that there has been a spin transition. Although it is not as obvious, there is

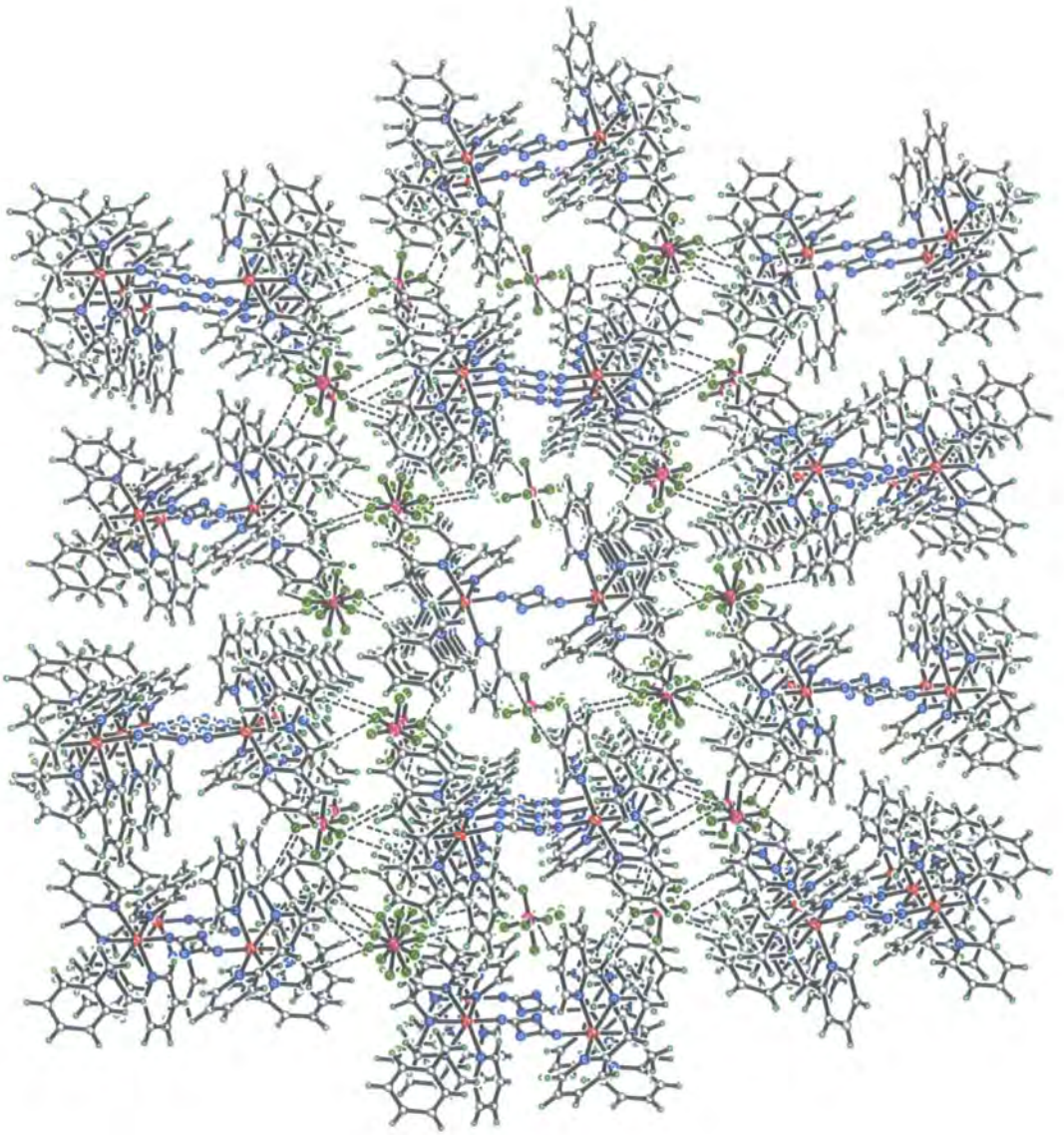

Figure 6.8: Crystal packing in compound **5**, viewed down the *a*-axis. Some of the C–H$\cdots$F interactions can be seen (shown with broken lines).

Figure 6.9: A crystal of compound **5**. At 400 K (left) the crystal is clear pale yellow, but on cooling to 250 K the colour darkens to a deep orange (centre) and cooling to 100 K gives a dark red colour (right).

also a change between 250 K and 100 K, from red-orange to deep red, (Figure 6.9).

Fe–N Distances

In addition to the colour change, the average Fe–N bond length changes from 2.145(28) Å at 400 K to 2.075(12) Å at 250 K and 2.004(15) Å at 90 K. This contraction is also seen in the octahedral volume which contracts from 12.80(6) $Å^3$ at 400 K to 10.62(4) $Å^3$ at 90 K indicating a transition from high to low spin. What is not immediately obvious is that the changes in the octahedral volumes follow the magnetic susceptibility curve, indicating the presence of a plateau in between 300 K and 200 K. At this plateau the molecules occupy an intermediate state half way between high and low spin (Figure 6.10). This was seen also in compound **3**, where the plateau was between two transitions both more abrupt than in compound **5** (Chapter 5).

It is important to note, that without Mössbauer spectroscopic data it is impossible to be certain that the spin transition in compound **5** is complete at either 400 K or 90 K. The octahedral volumes suggest there may be residual high spin at 90 K, but it is possible that this could be eliminated with further cooling. Similarly, there may be residual low spin at 400 K, which could be eliminated with additional heating, but the quality of a structure determined at 450 K would be very poor.

The distribution of bond lengths at 400 K is more or less repeated at each temperature with Fe1–N16 and Fe2–N26 generally shorter and Fe1–N14 and Fe2–N24 longer. However, what is not so clear from just looking at the raw data (Table 6.2) is that the step is also seen in the individual bond lengths. A plot showing the Fe–N bond lengths at the different temperatures clearly shows the plateau between 300 K and 200 K (Figure 6.11). On close

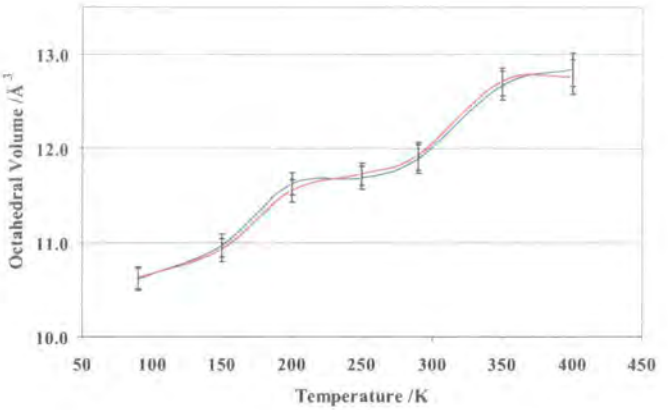

Figure 6.10: Plot of the octahedral volumes for compound **5**. Fe1 is shown in blue, Fe2 in red and the error bars show three estimated standard deviations. The plateau between 200 K and 300 K can be seen in both iron octahedral volumes.

inspection it can be seen that N11 to N15 and N21 to N25 all behave in the same way, with the step in the same place and comparable bond length changes. However, N16 and N26 follow a similar trend at higher temperatures, but during the second step, contract a lot less and therefore move from being the shortest Fe–N bonds to being short-intermediate bond lengths. Interestingly, N16 and N26 are both part of the anionic dicyanamide bridges.

Cell Parameters and Fe···Fe Distances

Comparing the cell parameters collected on cooling show that the cell contraction is very anisotropic. The majority of the contraction is in the a and b directions, with virtually no contribution from the c direction (Figure 6.12). The molecules run diagonally across the unit cell, almost entirely in the ab plane. However, the Fe···Fe distances within the molecules indicate that there is little change in the distance between the iron centres below 290 K. Between 290 K and 400 K, the Fe···Fe distance changes do not follow any obvious pattern, though this could be due to the data quality at high temperature (Table 6.3).

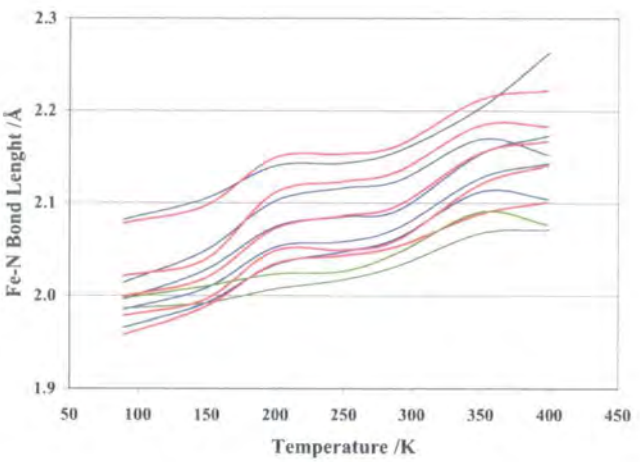

Figure 6.11: Plot of the Fe–N bond lengths for compound **5**. Fe1 is shown in blue and Fe2 in red, except for Fe1–N16 and Fe2–N26 which are dark and light green respectively.

		400 K	350 K	290 K	250 K	200 K	150 K	90 K
Fe1	N11	2.143(6) Å	2.127(5) Å	2.073(4) Å	2.058(5) Å	2.052(5) Å	2.008(5) Å	1.985(4) Å
	N12	2.104(6) Å	2.112(5) Å	2.062(5) Å	2.047(5) Å	2.033(5) Å	1.992(5) Å	1.966(4) Å
	N13	2.173(6) Å	2.153(5) Å	2.092(4) Å	2.085(5) Å	2.074(5) Å	2.028(4) Å	1.996(4) Å
	N14	2.263(10) Å	2.203(5) Å	2.156(4) Å	2.143(5) Å	2.140(5) Å	2.105(5) Å	2.082(4) Å
	N15	2.152(10) Å	2.169(5) Å	2.124(4) Å	2.116(4) Å	2.102(4) Å	2.049(4) Å	2.014(4) Å
	N16	2.071(14) Å	2.067(6) Å	2.032(6) Å	2.017(7) Å	2.007(7) Å	1.992(6) Å	1.986(4) Å
	Average	2.146(28) Å	2.134(13) Å	2.086(12) Å	2.073(10) Å	2.064(12) Å	2.027(13) Å	2.004(15) Å
	Volume	12.84(6) Å^3	12.67(5) Å^3	11.89(5) Å^3	11.69(4) Å^3	11.63(4) Å^3	10.97(4) Å^3	10.61(4) Å^3
Fe2	N21	2.141(7) Å	2.120(5) Å	2.060(5) Å	2.049(5) Å	2.048(5) Å	1.996(4) Å	1.978(4) Å
	N22	2.101(7) Å	2.088(5) Å	2.053(4) Å	2.043(5) Å	2.034(5) Å	1.988(4) Å	1.958(4) Å
	N23	2.167(7) Å	2.154(5) Å	2.097(4) Å	2.086(5) Å	2.072(5) Å	2.019(4) Å	1.999(4) Å
	N24	2.222(10) Å	2.212(5) Å	2.162(4) Å	2.153(5) Å	2.149(4) Å	2.097(4) Å	2.078(4) Å
	N25	2.183(9) Å	2.184(5) Å	2.134(4) Å	2.123(5) Å	2.111(4) Å	2.039(4) Å	2.021(4) Å
	N26	2.076(12) Å	2.090(7) Å	2.046(7) Å	2.026(8) Å	2.023(7) Å	2.010(5) Å	1.997(5) Å
	Average	2.143(9) Å	2.137(4) Å	2.088(11) Å	2.076(12) Å	2.069(12) Å	2.024(15) Å	2.004(13) Å
	Volume	12.76(6) Å^3	12.71(5) Å^3	11.92(5) Å^3	11.73(4) Å^3	11.55(4) Å^3	10.92(4) Å^3	10.63(4) Å^3

Table 6.2: Iron–nitrogen bond lengths at different temperatures.

	Distances			
Temperature	**Fe1···Fe1**	**Fe2···Fe2**	**N16···N16**	**N26···N26**
400 K	8.522(5) Å	8.589(5) Å	4.531(26) Å	4.582(22) Å
350 K	8.580(2) Å	8.605(2) Å	4.594(12) Å	4.542(13) Å
290 K	8.552(2) Å	8.572(2) Å	4.616(12) Å	4.584(12) Å
250 K	8.550(2) Å	8.566(2) Å	4.644(13) Å	4.615(15) Å
200 K	8.551(2) Å	8.563(2) Å	4.663(13) Å	4.619(14) Å
150 K	8.559(2) Å	8.572(2) Å	4.677(10) Å	4.640(10) Å
90 K	8.559(2) Å	8.569(2) Å	4.684(8) Å	4.654(8) Å

Table 6.3: Dicyanamide bridge distances at different temperatures.

Since the material undergoes SC from the high spin to the low spin state between 400 K and 100 K, there should be a contraction corresponding to the 0.4 Å from the shortening of the Fe–N bonds (0.2 Å from each end of the bridge), but this is not seen. Comparing the N16–N16/N26–N26 distances belonging to the dicyanamide bridges at different temperatures explains this anomaly. The Fe···Fe distance remains constant, because while the Fe–N distance contracts (due to the spin transition), the dicyanamide bridges are stretched (Table 6.3).

Disordered Dicyanamide Bridges

At all temperatures, the dicyanamide bridges are modelled as disordered around the inversion centre at $\frac{1}{2}\frac{1}{2}\frac{1}{2}$ (Figure 6.5). However, the level of this disorder is temperature dependant. At 350 K and 400 K the bridges are disordered with the central nitrogen atom split over two sites. On cooling, this disorder appears to spread to the adjacent carbon atoms which at 290 K and 250 K are also split over two sites. The electron density plots clearly show this separation of the two carbon sites (Figure 6.13 to 6.15). Cooling further, the two electron density peaks seem to coalesce again, and initially they were modelled as a single site at 90 K, but the thermal ellipsoids were still very elongated (Figure 6.16). A search of the CSD[1] suggests that the C–N–C expected angle in a dicyanamide ligand is generally close to 120° and the corresponding N–C–N angle approximates to linear (Figure 6.17). These angles are best attained when the dicyanamide carbons atoms are split over the two sites each with 50% occupancy, which was used for the final model.

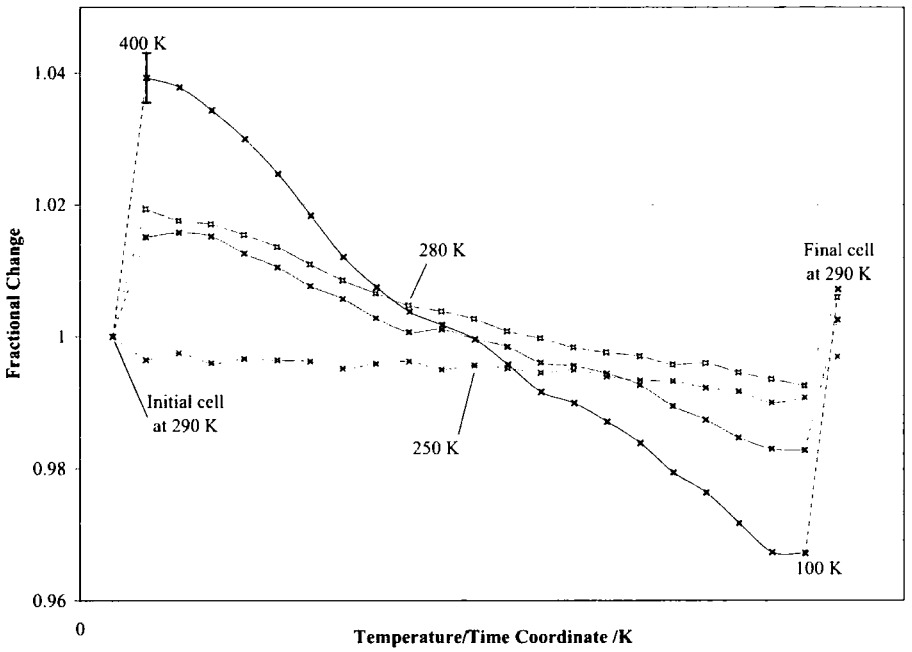

Figure 6.12: Selected cell parameters plotted as a fraction of the initial 290 K values. The cell volume is shown in black, a in blue, b in red and c in green. The reason for the difference between the initial and final cell parameters at 290 K is unclear as the difference is larger than the estimated standard deviations (the largest error is in the cell volume at 400 K and is shown). The magnetic data indicate that there is no hysteresis.

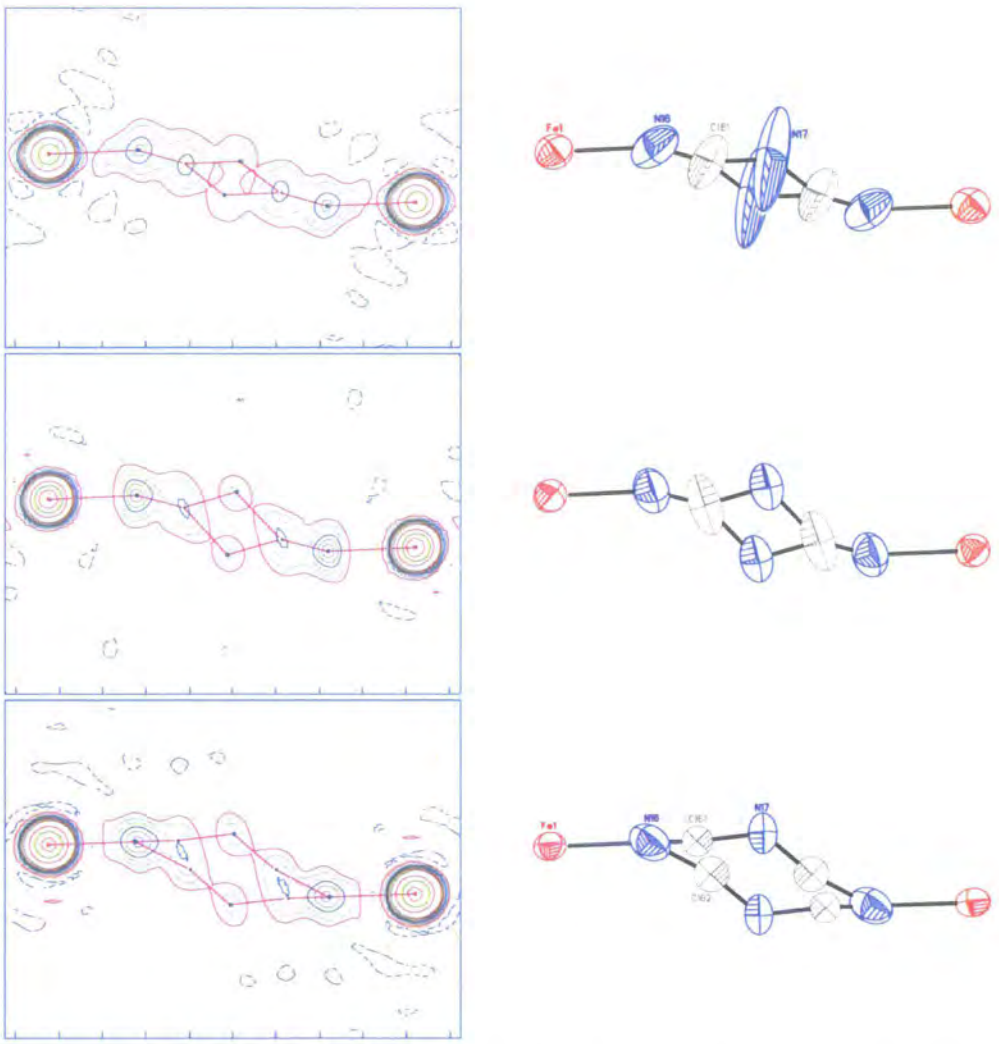

Figure 6.13: Observed electron density plots (left) and thermal ellipsoid plots (right) of the bridges between Fe1 and its symmetry equivalent. From the top to the bottom: 400 K, 350 K and 290 K. The contours are at every 1 e/Å^3 from 0 to 10 e/Å^3 and every 10 e/Å^3 thereafter. Negative electron density at every 1 e/Å^3 is shown with a broken line.

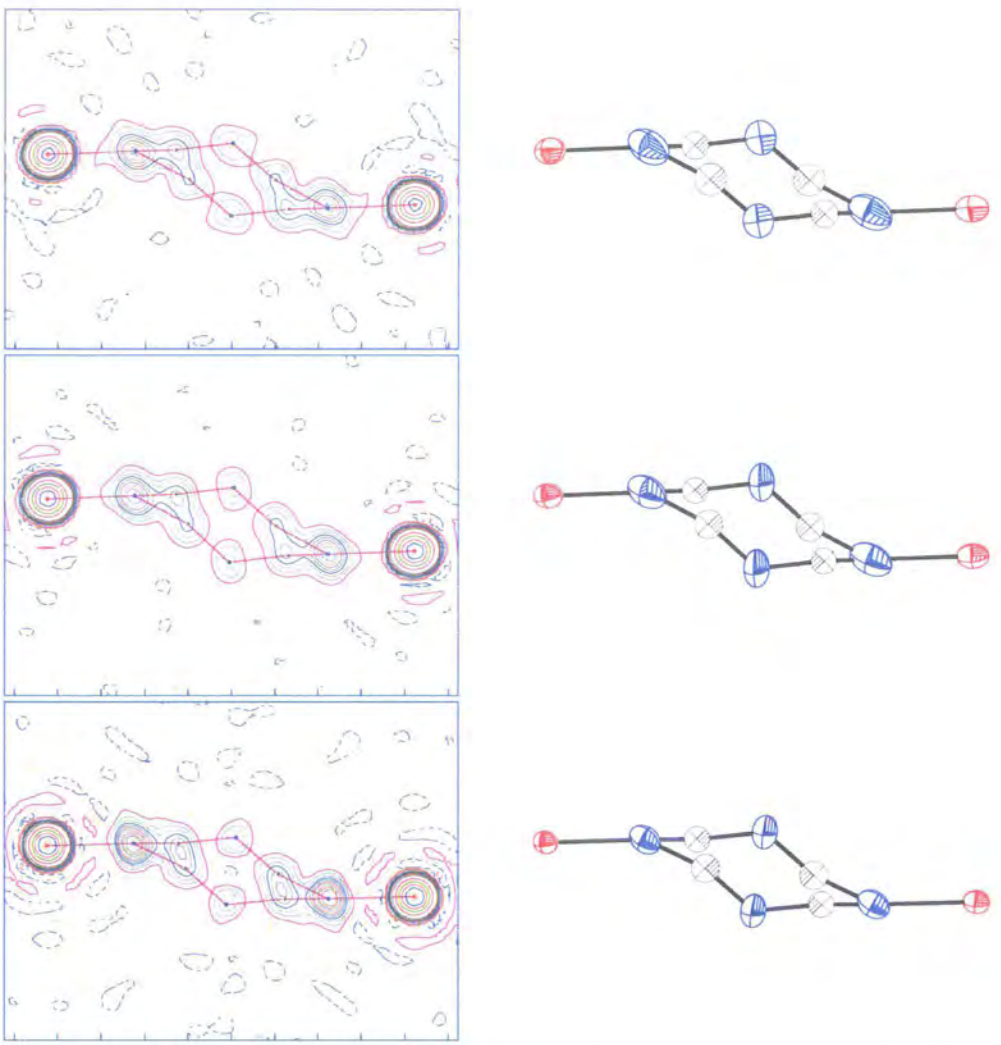

Figure 6.14: Observed electron density plots (left) and thermal ellipsoid plots (right) of the bridges between Fe1 and its symmetry equivalent. From the top to the bottom: 250 K, 200 K and 150 K. The contours are at every 1 e/Å^3 from 0 to 10 e/Å^3 and every 10 e/Å^3 thereafter. Negative electron density at every 1 e/Å^3 is shown with a broken line.

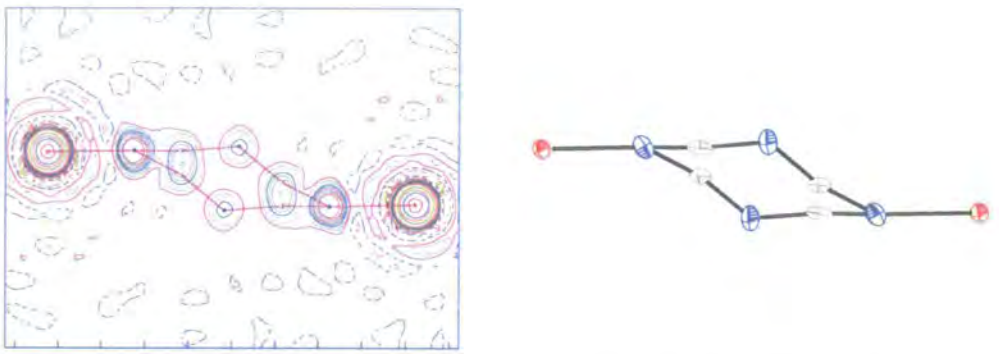

Figure 6.15: Observed electron density plots (left) and thermal ellipsoid plots (right) of the bridges between Fe1 and its symmetry equivalent at 90 K. The contours are at every 1 e/Å^3 from 0 to 10 e/Å^3 and every 10 e/Å^3 thereafter. Negative electron density at every 1 e/Å^3 is shown with a broken line.

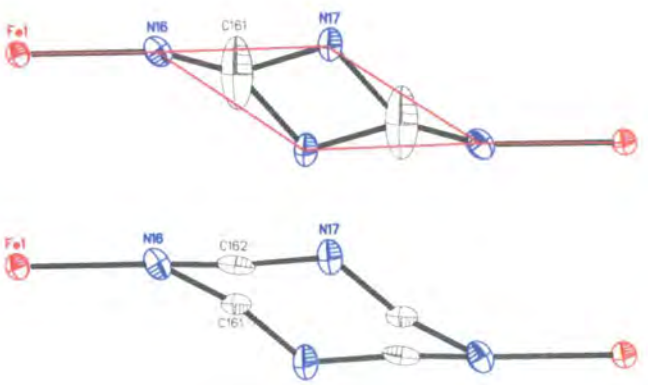

Figure 6.16: The dicyanamide bridge at 90 K with the carbon modelled as a single site with the suggested bonding overlayed in red (above). The bridge modelled with disordered carbon atoms is shown below.

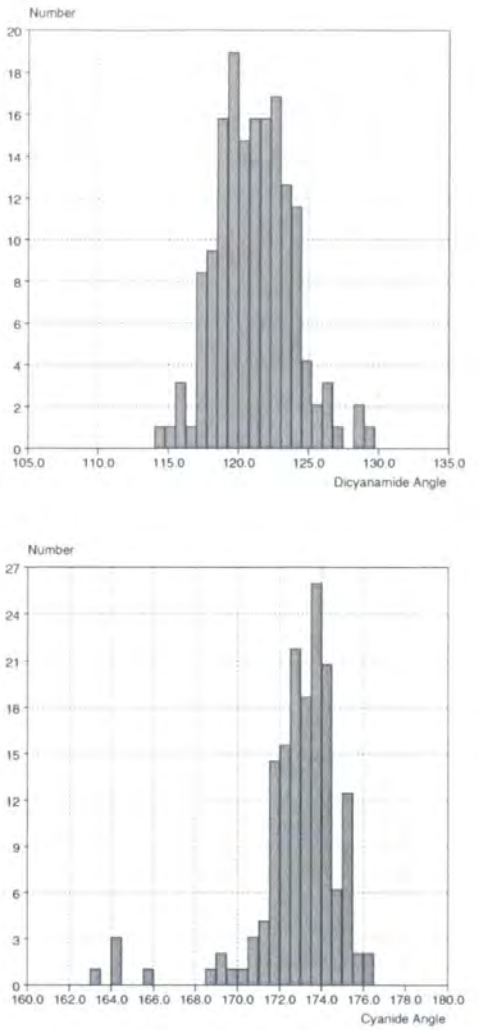

Figure 6.17: CSD[1] results for the C–N–C (above) and N≡C–N (below) angles in dicyanamide bridges. The mean average values are 121.15 and 172.95 with standard deviations of 2.71 and 2.09 respectively. The outliers below 170° in the N≡C–N histogram were all found to be disordered in the central nitrogen position of the dicyanamide bridge.

	Distances		
Temperature	N17···N17	N27···N27	Average
400 K	1.19(7) Å	1.26(7) Å	1.23(7) Å
350 K	1.47(3) Å	1.51(2) Å	1.49(3) Å
290 K	1.65(3) Å	1.74(3) Å	1.70(3) Å
250 K	1.69(3) Å	1.81(3) Å	1.75(3) Å
200 K	1.73(3) Å	1.81(3) Å	1.77(3) Å
150 K	1.62(3) Å	1.61(3) Å	1.62(3) Å
90 K	1.56(2) Å	1.59(2) Å	1.58(2) Å

Table 6.4: N–N distances at different temperatures.

On heating, the electron density plots show the electron density trough between the two sites of the central nitrogen atom disappearing. There are several possible explanations for this. Since the intensity falloff with respect to $\sin\theta/\lambda$ is increased at higher temperature, there is reduced intensity at high angle, a problem exacerbated by integrating to 0.9 Å. This reduced resolution has the effect of smearing the observed electron density which could account for the apparent merging of the two nitrogen sites. Another possibility is that the increased thermal energy leads to increased vibration along the dicyanamide bridge and an increase in electron density between the two nitrogen sites. A comparison of the N17···N17/N27···N27 distances between the two positions shows that it decreases on heating and it is possible that above 400 K it moves to occupy the inversion centre. This is certainly not the case at 400 K however, as refinement with N17 and N27 on the special positions not only leads to non-physical, huge thermal parameters, but also high R-indices. Refining the central nitrogen atoms away from the inversion centre at 400 K, gives prolate thermal ellipsoids, but viewing the situation along the bridge from the centre, suggests that the thermal motion is not trivial (Figure 6.18). The electron density maps suggest the central atom could be moving with a strange circular, toroidal motion, or librating to a huge degree, which could be caused by the large amount of thermal energy at 400 K. These are merely possibilities however, and concrete conclusions are not possible as the data collected at 400 K is of reduced quality, which could be artificially affecting the results.

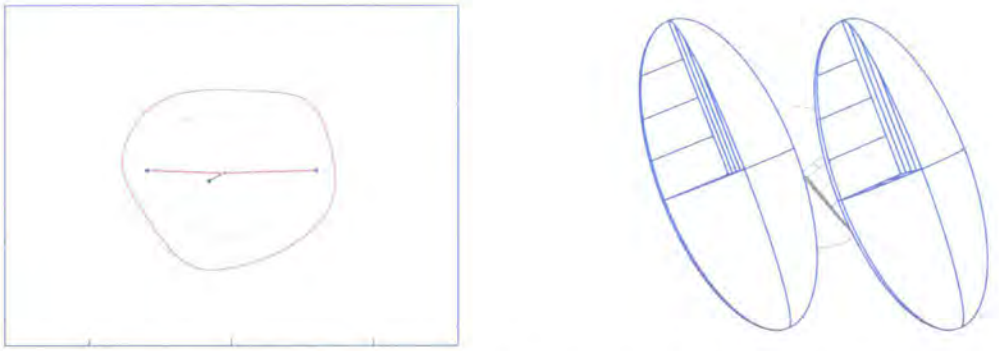

Figure 6.18: Observed electron density map and thermal ellipsoid plot viewed from the centre of the bridge between Fe1 and the symmetry equivalent at 400 K viewed towards Fe1. The contours are at every 1 e/Å^3 from 0 to 3 e/Å^3.

Atom	U_{eq}	Atom	U_{eq}
N11	0.0432(11)	N21	0.0454(11)
N12	0.0412(11)	N22	0.0444(11)
N13	0.0397(10)	N23	0.0432(11)
N14	0.0356(10)	N24	0.0391(10)
N15	0.0364(10)	N25	0.0370(10)
N16	0.0693(15)	N26	0.0726(16)

Table 6.5: Thermal values for the nitrogen ligand atoms for compound **5** at 290 K.

A comparison of the thermal parameters, U_{eq}[‡] for the ligating nitrogen atoms at room temperature shows that for N16 and N26 (the nitrogen atoms ligating the anionic bridges to the iron centres), the ADPs are considerably larger than for the other nitrogen atoms surrounding the iron centre (Table 6.5). Looking at the other temperatures, this trend is also apparent in the other results, but the effect is smaller at 90 K. Plotting the U_{eq} values with respect to temperature shows a very interesting phenomenon. Under normal conditions, thermal motion should increase linearly with temperature. Clearly, for N16 and N26 this is not the case (Figure 6.19). Above 150 K, the thermal motion is approximately linear, but there is a step between 90 K and 200 K.

[‡]U_{eq} is defined as one third of the trace of the orthogonalised U^{ij} tensor.

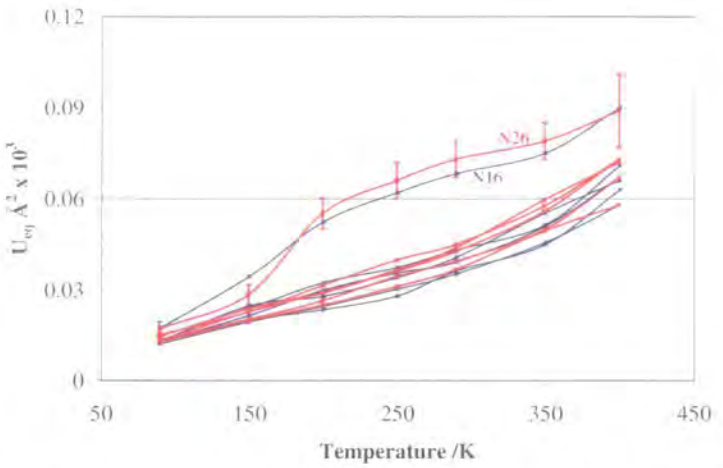

Figure 6.19: Variable temperature plot for the ligand nitrogen atoms. The Fe1 ligands are shown in blue and the Fe2 ligand atoms are shown in red. For clarity, errors are given for N26 only, but the other atoms are comparable or less.

It is possible that this is because the multi-dentate Bpl ligand, made up of a number of rigid pyridine rings, restricts the amount of movement making the ligating thermal parameters smaller. However, that doesn't explain the lack of linearity. It is more likely that the disorder in the dicyanamide bridges extends all the way along the bridge to include the ligand nitrogen atoms, N16 and N26, so that these are also disordered like the central nitrogen and carbon atoms. The fact that the two cyanide bond lengths are different and the nitrogen ellipsoids are slightly prolate supports this theory. On cooling, this disorder disappears indicating that it is dynamic in nature and it is probable that this corresponds to the completion of the spin transition. Refinement of the disorder at the higher temperatures was generally found to be unstable due to the extremely close proximity of the components and a corresponding large degree of overlap.

Disordered PF_6^-

P1 is relatively ordered throughout, though at higher temperatures the thermal parameters are very large and it is clear that there is a lot of thermal motion. P2 however, is clearly disordered throughout and is modelled with 50% occupancy in each orientation until the step, at which point the occupancy of one component gradually decreases. This suggests that the disorder is largely dynamic, with the less favourable orientation becoming less

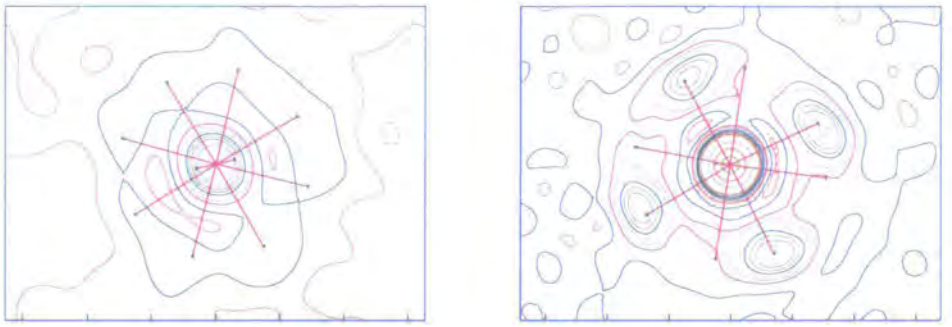

Figure 6.20: Electron density maps for the disordered P3 PF_6^- ion at 400 K (left) and 90 K (right) viewed down the *c*-axis. The contours are at every 1 e/Å^3 from 0 to 10 e/Å^3 and every 10 e/Å^3 thereafter. Negative electron density at every 1 e/Å^3 is shown with a broken line.

occupied on cooling.

P3 is also disordered, but the disorder is rotational in nature. P3 sits with four fluorine atoms in the *ab* plane. The rotation is around the F35–P3–F36 axis along the *c*-axis direction. This rotation is probably also dynamic, as the occupancy of the second component decreases on cooling through the transition from 50% at 400 K to 15% at 90 K (Figure 6.20).

Despite the fact that the PF_6^- ions are modelled as disordered, looking at the thermal parameters it is clear that at 400 K, the P2 and probably P3 are fairly freely rotating as would be expected at such a high temperature. On cooling however, the stronger of the C–H$\cdots$F interactions govern and P2 and P3 gradually become more ordered with a progressive reduction in the occupancy of the minor component.

6.5 Conclusion

At 400 K $\{[N(CN)_2](FeBpl)_2\}(PF_6)_3$ is high spin, while at 90 K it is low spin. However, in between these two temperatures, there are two gradual transitions with a plateau in between. The presence of this step transition seen in the magnetic data has been confirmed by comparison of octahedral volumes and Fe–N bond lengths recorded approximately every 50 K. These comparisons have shown some interesting effects in the anionic bridging

ligands. They indicate that where the Bpl cage-like ligands remain fairly static, undergoing only the contractions and reorganisations caused by the contraction of the Fe–N bonds, the dicyanamide bridges behave very differently. The two nitrogen atoms in the dicyanamide bridges ligating the iron cores (N16 and N26) have been shown to have much larger thermal parameters than the other ligating nitrogen atoms above 90 K. This effect is believed to be caused by disorder extending out from the centre of the bridge. This disorder leads to an explanation for the presence of the step transition. It is possible that above the plateau, the disorder in the centre of the bridge is dynamic, involving considerable movement, which may even be toroidal or similar to that of a rope turned by two children so that a third can skip. On cooling, this disorder is reduced and it is reasonable that at the plateau, the disorder at the centre of the bridge is becoming static. However, the two ends of the dicyanamide bridges remain disordered, only becoming more ordered at 90 K, suggesting that there may be a longitudinal disorder that may remain dynamic until the transition is complete and the complex is low spin.

A comparison of the Fe$\cdots$Fe distances and the length of the dicyanamide bridges indicate that there is a considerable degree of flexibility in the dicyanamide group which absorbs much of the change caused by the spin transition. It is this flexibility that could be responsible for the gradual nature of the transitions in this compound, in a way analogous to that discussed by van Koningsbruggen *et al.* with respect to triazole and tetrazole bridged polymers.[108] Van Koningsbruggen *et al.* explained how connecting iron centres together with triazole ligands to form polymer chains increased the strength of the elastic interactions between the SC active centres, increasing the cooperativity and making the transitions more abrupt. However, making the linking groups more flexible means the elastic interaction is effectively absorbed by the bridging ligands. Van Koningsbruggen *et al.* referred to this as a "tug of war between the elastic interaction and a shock-absorber effect." Similarly, the flexibility in the dicyanamide anionic bridging ligand in compound **5** could be acting as a kind of shock-absorber, preventing the transmission of elastic interactions along the bridge. This elastic flexibility is not present in the central ligand in compound **3**, which has more abrupt steps to the transition.

Part III

Spin Crossover in Coordination Polymer Networks

Chapter 7

Allosteric Reactions in Bistable Spin Crossover Networks

7.1 Introduction

The development of Hofmann type networks with spin crossover capability[112] has led to the use of metal cyanide anionic ligands in the design of complex, rigid networks.[125,185] Two such compounds use $[M(CN)_2]^-$ ligands to form bridges between iron centres (M = Au, Ag).

$\{Fe(Pmd)_2Fe(H_2O)_2[Au(CN)_2]_4\}.H_2O$ (compound **6**) and its silver analogue $\{Fe(Pmd)_2Fe(H_2O)_2[Ag(CN)_2]_4\}.H_2O$ (compound **7**) were synthesized by slow diffusion of two solutions containing stoichiometric amounts of $FeCl_2$/pyrimidine and $K[M(CN)_2]$ in an H-shaped vessel under argon, giving pale-yellow crystals. TGA data indicate three successive losses on heating, which correspond to water, pyrimidine and cyanide (Figure 7.1).

7.1.1 Magnetic Susceptibility Data

The materials have an abrupt spin transition (approximately 165 K and 218 K for compounds **6** and **7** respectively), both with a clearly defined hysteresis (Figure 7.2).[186] Heating to trap the dehydrated compound **6**, yields a material that remains paramagnetic throughout the temperature range (compound **8**). In contrast, on dehydrating compound **7** to give compound **9**, the spin transition is retained. The transition in the dehydrated compound **9** takes place at a lower temperature than in the hydrated material (approximately

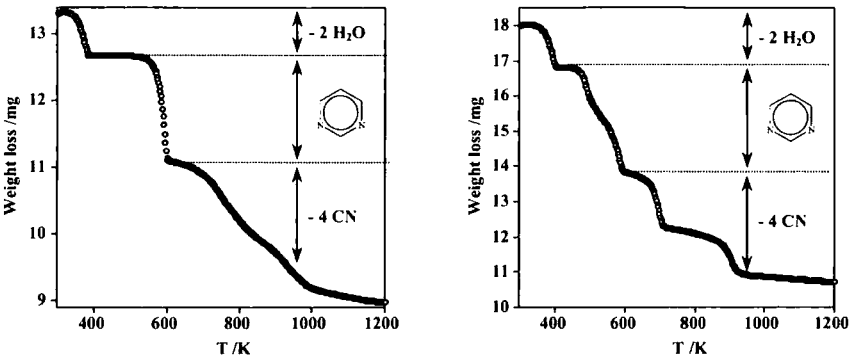

Figure 7.1: TGA data for compound **6** (left) and compound **7** (right) showing the loss of first water, then pyrimidine and finally cyanide on heating.[186]

125 K compared with 218 K for compound **7**).

7.2 Single Crystal Diffraction Experiments

Both compounds **6** and **7** were crystalline,* although the sample of the silver complex consisted of crystals that were much larger and more abundant. However, both samples contained specimens that were suitable for single crystal diffraction.

7.2.1 Data Collection

Single crystal data were collected on compounds **6** and **7** using the Bruker SMART-CCD 6000 and temperature was controlled using an Oxford Cryosystems Cryostream 600.[130]

$\{Fe(Pmd)_2Fe(H_2O)_2[Au(CN)_2]_4\}.H_2O$ (Compound 6)

The crystals for compound **6** were very small and many were intergrown. Consequently, a very small crystal of the gold compound was used (approximately 0.06 × 0.04 × 0.03 mm). The crystal was mounted in oil and quenched to 180 K. A matrix was collected at 180 K,

*Samples courtesy of Prof. José A. Real, Dr. M. Carmen Muñoz, Dr. Virginie Niel[187] and Ms. Ana G. Galet Domingo (Valencia).

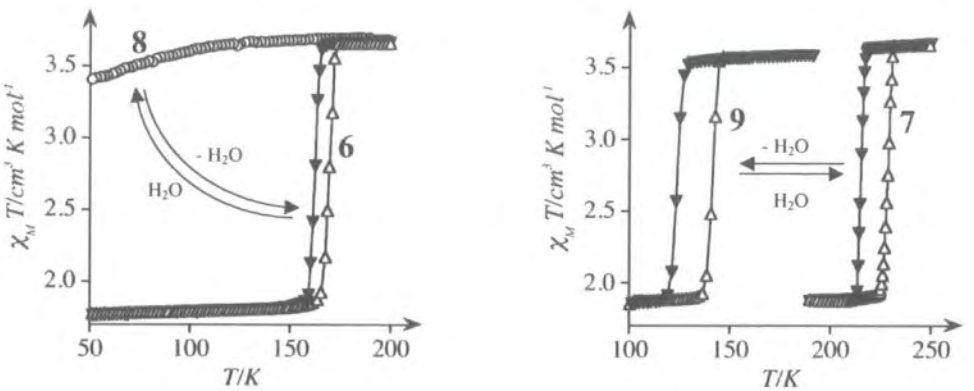

Figure 7.2: Magnetic susceptibility data for compounds **6** to **9**.[186] The SC transition in compound **6** takes place at approximately 165 K but on dehydration becomes paramagnetic (left). In compound **7** the transition moves to a lower temperature on dehydration (right). Both the cooling and warming modes are shown in each case (▼ and △) except for compound **6** which does not have a spin transition (○).

Figure 7.3: Compound **6** at 175 K (left) and 150 K (right).

followed by a full sphere data collection with 20 s/frame. The crystal was then cooled at 60 K/hr to 150 K, during which there was a dramatic colour change from yellow to red and where a matrix at 150 K indicated a sharp cell contraction. This was followed by cooling at 120 K/hr to 120 K where another matrix collection indicated the cell parameters were in keeping with those recorded at 150 K, so another full sphere of data was collected with 20 s/frame. Photographs were taken at 175 K and 150 K on cooling (Figure 7.3) and the faces were indexed on completion.

$\{Fe(Pmd)_2Fe(H_2O)_2[Ag(CN)_2]_4\}.H_2O$ (Compound 7)

For the silver compound, the crystals were much less intergrown and a much larger specimen was used (0.35 × 0.22 × 0.11 mm). Like compound **6**, the crystals were pale yellow at room temperature. The crystal was mounted using glue and a matrix collected at 290 K. The sample was then cooled at 360 K/hr to 230 K, then at 120 K/hr to 225 K. A second matrix was recorded and, allowing for thermal contraction, the cell was comparable with that at 290 K. The faces were indexed and a full sphere dataset was collected at 225 K, with 8 s/frame. Another matrix was collected after the data collection, before the sample was cooled to 205 K at 60 K/hr. The crystal which had been pale yellow had changed to deep red, so a matrix was recorded at 205 K, which indicated a significant cell contraction.

The sample was then cooled to 120 K at 120 K/hr where another matrix was collected. The cell was consistent with results at 205 K and a sphere of data was collected at 120 K at 6 s/frame. On completion, the sample was warmed to 217 K at 120 K/hr where a matrix was collected giving the same cell as at 120 K. The sample was then warmed to 225 K at 60 K/hr with pictures taken approximately every 0.5 K. By eye, a colour change was observed at approximately 220.7 K (Figure 7.4). A final matrix was collected at 225 K which indicated the same cell as at 290 K.

7.3 Data Analysis

In general, the data were of a high quality, and were treated in the usual manner. For both compound **6** and **7**, no additional reflections or suggestions of a change in symmetry were observed on cooling.

Figure 7.4: Compound **7** on warming. Photos taken at approximately 219.5 K, 220.0 K, 220.5 K, 220.7 K and 221.0 K (from left to right).

$\{Fe(Pmd)_2Fe(H_2O)_2[Au(CN)_2]_4\}.H_2O$ (Compound 6)

The data indexed satisfactorily and, in general, the data were integrated in the usual way to a resolution of 0.73 Å. The structure was solved as normal and refined well. Despite the small size of the crystal, the faces were visible and could be indexed. Thus, the absorption correction was carried out accordingly, followed by an additional absorption correction using SADABS.[145]

$\{Fe(Pmd)_2Fe(H_2O)_2[Ag(CN)_2]_4\}.H_2O$ (Compound 7)

Like compound **6**, the data indexed well and integration was carried out accordingly. The structure solved without difficulty and refined well. The faces were clearly visible so the absorption corrections were carried out as for the gold analogue.

7.3.1 Structure Refinement

All four structures refined satisfactorily and the high quality of the data is reflected in the final R-indices.

$\{Fe(Pmd)_2Fe(H_2O)_2[Au(CN)_2]_4\}.H_2O$ (Compound 6)

All non-hydrogen atoms were refined as anisotropic and the hydrogen atoms were located in the difference map. Full refinement led to unreasonable thermal parameters for some of the hydrogen atoms. For this reason, the thermal parameters were fixed, but the positions of the hydrogen atoms were allowed to refine freely. The water of crystallisation (including the hydrogen atoms) was visible in the difference map, but despite this, the refinements were unstable, hence the oxygen to hydrogen distances were restrained to a CSD average

value of 0.84 Å.[1]

The program IVTON[174] was used to calculate the mean Fe–N bond lengths and the volumes for the iron octahedra in compound **6**.

$\{Fe(Pmd)_2Fe(H_2O)_2[Ag(CN)_2]_4\}.H_2O$ (Compound 7)

All non-hydrogen atoms were fully refined whilst the hydrogen atoms were treated in the same way as those in compound **6**. As for the gold sample, IVTON[174] was used to calculate average Fe–N bond lengths and volumes for the iron octahedra.

7.4 Powder Diffraction Experiments

On heating, both compounds **6** and **7** lose water (to become compounds **8** and **9**) in a manner that is destructive to the crystals. However, whilst the crystal integrity is lost, the crystallinity of the sample is retained in both cases, as the single crystals become microcrystalline powders. Thus, due to the nature of the problem, powder diffraction techniques also had to be employed to examine these materials fully.

In order to study the spin transition, variable temperature powder data were also collected on compound **9** using the Bruker D8 Advance with the Oxford Cryosystems PheniX attachment.[152]

7.4.1 Data Collection

Both samples were studied using the Bruker D8 Advance and the Anton Paar HTK1200 environmental chamber.[150] Loss of water takes place at around 100 °C, so the temperatures required are at the bottom of the temperature range for the HTK1200. This attachment was chosen over the TTK450 however, as there is no crystalline background and this is preferable for structure solution.

$\{Fe(Pmd)_2Fe(H_2O)_2[Au(CN)_2]_4\}.H_2O$ (Compound 8)

Initially, four 1 hr scans (5–120° 2θ, 0.5 s/step, 0.0144° 2θ/step each), were collected at room temperature. The chamber was then evacuated and left for $\frac{1}{2}$ hr, before recording twelve 1 hr scans (as before). On completion, the sample was removed from the chamber

Step Number	Temperature	No. of 1 hr Scans	Vacuum
1	Room Temp.	4	-
2	Room Temp.	12	X
	1 hr in air		
3	Room Temp.	4	-
4	373 K	12	-
	1 hr in air		
5	Room Temp.	4	-

Table 7.1: Powder diffraction scans for $\{Fe(Pmd)_2Fe(H_2O)_2[Au(CN)_2]_4\}.H_2O$.

and left to stand in air for $\frac{1}{2}$ hr, before repeating the first set of four 1 hr scans, again at room temperature. The sample was then heated inside the furnace to 373 K at a rate of 0.05 K/s, where twelve 1 hr scans were recorded (5–120° 2θ, 0.5 s/step, 0.0144° 2θ/step as previously). Finally, the sample was removed from the furnace whilst hot and left to stand in air for 1 hr, before the four 1 hr scans were repeated (Table 7.1).

In each case, the first scan was compared with the last and there was found to be no difference. The short, separate scans were then combined using EVA,[149] to give five scans, suitable for structure refinement, one for each step (Table 7.1). EVA was also used to provide a peak list for indexing.

$\{Fe(Pmd)_2Fe(H_2O)_2[Ag(CN)_2]_4\}.H_2O$ (Compound 9)

Initial attempts at heating compound **7** resulted in samples that were very discoloured or had become amorphous and it was clear that the material was considerably more temperature sensitive than compound **7** (Figure 7.5). This was thought to result from temperature instability at the lower end of the temperature range of the HTK1200 and the relative readiness to loose pyrimidine compared with compound **6**, as shown by the TGA data (Figure 7.1).

In a similar fashion to the data collected on the gold sample, powder data were collected under vacuum using the Bruker D8 Advance with the HTK1200 furnace attachment, at room temperature. Initially, one 5 hr scan (5–120° 2θ, 2.0 s/step, 0.0144° 2θ/step) was collected at room temperature, under normal atmospheric conditions. On completion, the vacuum was switched on and after a 20 min wait, a series of five 5 hr scans (5–120° 2θ,

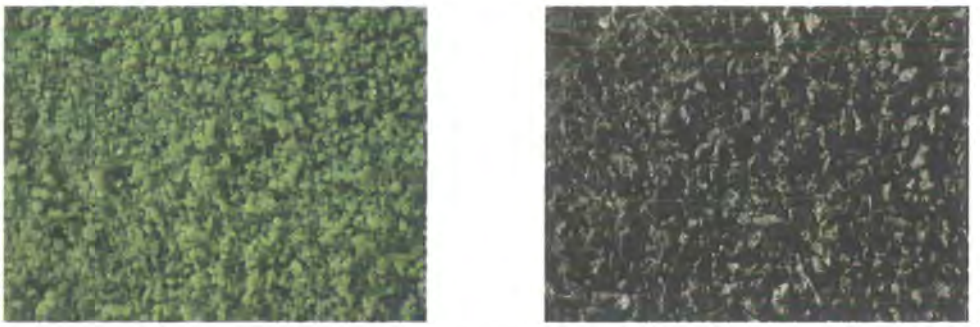

Figure 7.5: Photographs of compound **6** (left) and compound **7** (right) viewed under a microscope after heating in the HTK1200. Both samples started pale yellow in colour.

2.0 s/step, 0.0144° 2θ/step) were recorded followed by thirteen $\sim$ 1 hr scans (as for the longer scans, but 0.5 s/step).

The sample was then removed from the vacuum chamber and left in air for approximately $\frac{1}{2}$ hr, before another 5 hr scan was recorded (as before).

As for the gold sample, the scans under vacuum were compared to ensure the dehydration was complete and there was no time dependent change. The scans were then combined using EVA and a peak list was generated for indexing.

Variable temperature powder data were also collected on the Bruker D8 Advance using the Oxford Cryosystems PheniX attachment.[152] The sample was placed in the chamber and after a quick test scan, it was evacuated to approximately 1×10^{-2} mbar. Once the pressure was reasonably stable, the sample was cooled to 200 K where a $4\frac{1}{2}$ hr data collection was recorded (5–90° 2θ, 2.5 s/step, 0.0144° 2θ/step).

On completion, the PheniX was programmed to cool at 5 K/hr to 17 K while a total of twenty-seven scans were collected (each 5–60° 2θ, 1.2 s/step, 0.0144° 2θ/step). The scans were recorded approximately every 7.5 K, but the actual temperatures were recorded by the software. On reaching 17 K, another $4\frac{1}{2}$ hr scan was collected (as at 200 K), followed by two $\frac{1}{2}$ hr scans (0.3 s/step). The last two scans were over the same 2θ range and with the same step size as the previous scan so they could be combined for refinement.

On completion, the PheniX was warmed to room temperature at 540 K/hr then left for a total of approximately 1 hr 20 mins for the system to warm up and reduce the vacuum. The sample was then removed and placed in air for approximately $\frac{1}{2}$ hr to rehydrate, after

which another $4\frac{1}{2}$ hr scan was recorded (as before).

7.4.2 Data Analysis

Due to the fact that X-rays are scattered by electrons, heavy elements scatter considerably more than lighter elements. For this reason, the scattering in these materials is dominated by that of the gold or silver and to a lesser degree by the iron. Therefore, on the whole, these materials scattered well for molecular materials. In addition, the crystallinity of the gold sample was very good with peak widths of the order of 0.128°, a crystallinity that was retained when the sample was dehydrated. Compound **7** however, was not as crystalline, and the powder diffraction patterns were much noisier, requiring longer to get reasonable quality data. In addition, when the sample was dehydrated, the diffraction pattern was far more complicated than that for compound **8**, suggesting the structure was more complex.

$Fe_2(Pmd)_2[Au(CN)_2]_4$ (Compound 8)

Comparison of the room temperature powder pattern recorded under vacuum with that recorded prior to dehydration for the hydrated structure, indicated that the largest peak (200) moved from 12.3° 2θ to 14.5° 2θ (Figure 7.6). This corresponds to an a-axis contraction of approximately 2.5 Å. *Ab initio* indexing using DICVOL91[188] within CrysFire,[189] gave the monoclinic cell: a = 12.353 Å, b = 13.663 Å, c = 8.31 Å, β = 94.14°. Examination with CheckCell[190] gave the most likely space-group as $P2_1/c$ — the same as the hydrated compound **6**. This cell was then refined using Le Bail fitting within GSAS.[158,159] The cell parameters were also refined against the 373 K powder data, which gave similar results. For comparison, the shorter scans at room temperature recorded before, in between and after the two dehydration processes, were used to refine the hydrated cell obtained at 180 K, using single crystal diffraction (Table 7.2).

$Fe_2(Pmd)_2[Ag(CN)_2]_4$ (Compound 9)

Studying the raw data indicated that there is a considerable change during dehydration from the hydrated compound **7** to the dehydrated compound **9**. Although the overall appearance of the pattern is similar to that of compound **8**, it is apparent that the pattern is more complex and on close inspection some of the key peaks show a clear splitting. For

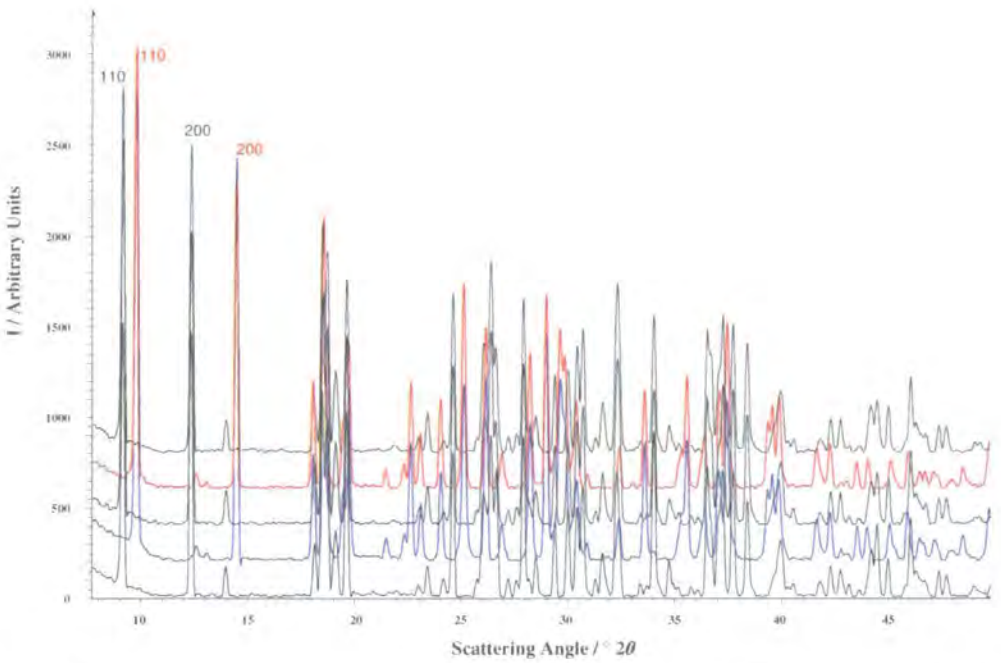

Figure 7.6: Powder patterns of compound **9** showing the reversible dehydration/hydration. The data collected under vacuum is shown in blue, the 373 K data in red and the data collected under ambient conditions before, between and after the dehydration steps are shown in black. The 110 and 200 peaks are marked to show the dramatic cell contraction.

	Room Temp. (1)	**Vacuum**	**Room Temp. (2)**	**373 K**	**Room Temp. (3)**
a	14.5229(3) Å	12.3829(3) Å	14.5236(4) Å	12.3728(3) Å	14.5226(4) Å
b	13.4235(3) Å	13.6746(3) Å	13.4324(3) Å	13.6791(3) Å	13.4339(3) Å
c	7.2957(2) Å	8.3317(2) Å	7.2955(2) Å	8.3374(2) Å	7.2960(2) Å
β	90.7821(2)°	94.148(2)°	90.772(2)°	94.148(2)°	90.770(2)°
V	1422.15(5) Å^3	1407.12(5) Å^3	1423.13(6) Å^3	1407.40(5) Å^3	1423.29(5) Å^3
R_p	0.0463	0.0427	0.0470	0.0361	0.0457
wR_p	0.0568	0.0626	0.0566	0.0483	0.0553
χ^2	1.515	2.231	1.251	1.966	1.245

Table 7.2: Cell parameters of compound **6** during repeated dehydration and rehydration.

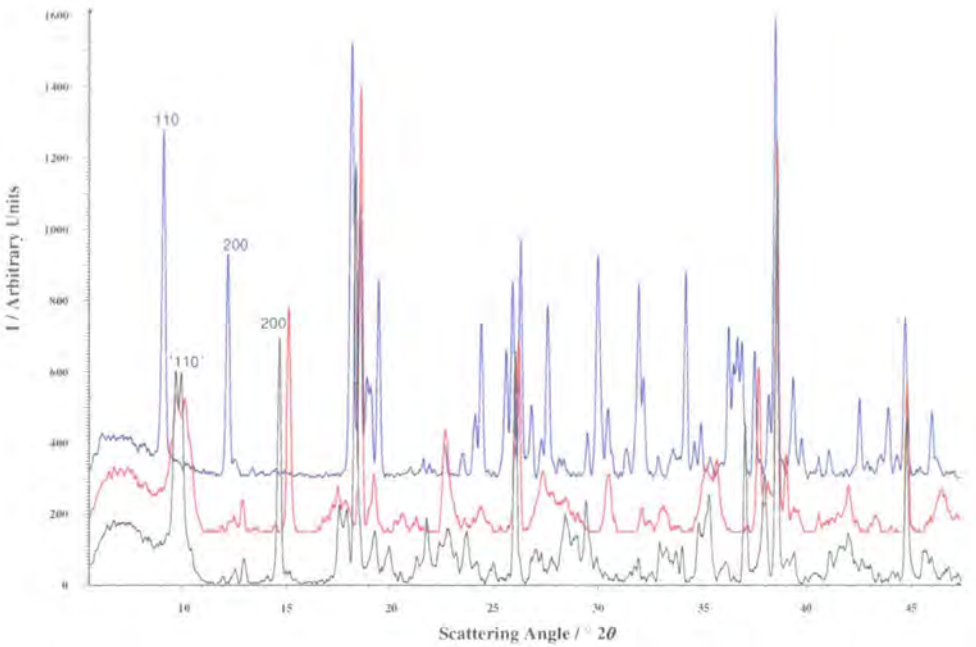

Figure 7.7: Powder patterns of compounds **7** and **9**. From bottom to top, the scan at 200 K is shown in black, 17 K in red and after rehydration in blue. The 200 peak moves from 12.2° under ambient conditions, to 14.6° under vacuum at 200 K and to 15.1° under vacuum at 17 K.

example, what would have been the 110 at approximately 9° has a definite split that is visible both at 200 K and at 17 K (Figure 7.7). In the hydrated compound **8**, this peak is not split and is the 110 which is equivalent to the Friedel, $\overline{1}\overline{1}0$. As the structure of compound **8** is monoclinic, the $110/\overline{1}\overline{1}0$ is also equivalent to the $\overline{1}10$ and the $1\overline{1}0$. Thus, splitting of this peak together with the appearance of systematic absences indicate that the symmetry of compound **9** is lower than that of compound **8**, suggesting a change from monoclinic to triclinic.

Attempts to index the data with CrysFire were unsuccessful, so DICVOL[188] within DASH[191] was used. Although the DICVOL indexing routine is broadly speaking the same within CrysFire and DASH, CrysFire requires a pre-prepared peak list (obtained in this case from EVA[149]) whereas DASH uses the raw data. Using the DASH version, the user selects a range in 2θ that contains a peak. The software then fits the peak, which enables a better identification of peak positions. In the case of compound **9** however, although

a number of possible cells were identified, none had a sensible volume and parameters similar to compound **7** or compound **8**.

The similarity between the powder data for compounds **8** and **9** however, suggest that the cells should be very similar. Using PowderCell,[192] the data for compound **9** were compared with simulated powder patterns for compound **9** based on the structure of compound **8** (discussed below). Replacing the gold atoms with silver atoms and adjusting the cell parameters, moving α and γ slightly away from 90°, led to a simulated pattern so similar to the data recorded under vacuum for compound **9**, that it could not be coincidence. Given this likeness, a refinement was attempted using GSAS.

The relative instability of Le Bail refinements meant Le Bail fitting was not possible without better cell parameters, so initially Rietveld refinement was used. The structure for compound **8** was used as the model, with the gold atoms replaced with silver atoms. In addition, it was necessary to generate one set of duplicate atoms to accommodate those that had been equivalent in $\mathbf{P2_1}/c$, but were not in $\mathbf{P\bar{1}}$. Initially, the cell parameters and sample shift were adjusted and refined alternately until the unit cell parameters and unit cell volume were sensible and the intensities approximately fitted the overall appearance of the collected data. Although the fit was very poor, as a starting model it looked promising.

The powder data collected before the vacuum was switched on, was used for a Le Bail refinement, which allowed reasonable identification of the sample height or "shift". This was then used together with the cell parameters from the starting model, enabling the Le Bail refinement of cell parameters and peak profile parameters.

The cell parameters for the hydrated structure were also refined against the data collected after rehydration, using Le Bail fitting. The sample height was refined and gave a slightly different value, but this is not surprising as the sample had been removed to allow rehydration and then replaced, which could affect the sample height.

Refining these cell parameters against the variable temperature powder data presented a severe correlation problem. Since the sample height and unit cell parameters are closely related, a refinement is not straight forward. In this case, a similar approach to that for the Le Bail fitting at room temperature was used. Since the rehydration had been carried out without removing the sample from the PheniX chamber, the sample position hadn't changed from start to finish. This meant that the sample height could be "calibrated" using

	Single Crystal	Ambient (1)	Vacuum	Ambient (2)
a	14.646(5) Å	14.6566(5) Å	12.1952(5) Å	14.6857(8) Å
b	13.344(6) Å	13.3474(4) Å	13.7185(7) Å	13.3565(6) Å
c	7.417(3) Å	7.4207(3) Å	8.5944(6) Å	7.4300(4) Å
α	90°	90°	87.940(4)°	90°
β	91.43(3)°	91.441(3)°	95.206(5)°	91.467(4)°
γ	90°	90°	88.429(4)°	90°
V	1449.1(8) Å^3	1451.24(10) Å^3	1430.32(10) Å^3	1456.90(15) Å^3
R_p	-	0.0525	0.0212	0.0488
wR_p	-	0.0676	0.0326	0.0631
χ^2	-	1.283	2.805	1.183

Table 7.3: Cell parameters of compound **7** during dehydration and rehydration. The data were taken from a single crystal matrix collection at room temperature and Le Bail refinements of powder data.

a refinement based on the data, after rehydration. This sample height was then used for the Le Bail refinements carried out against powder data collected in the PheniX. However, the "calibration" is only approximate as any contraction/expansion due to changes in temperature, leads to changes in sample height. Thus, the sample height difficulties build in a large error, making the magnitude of the contraction impossible to quantify accurately, but the presence of a contraction is beyond doubt.

The Le Bail refinements at 200 K and 17 K were reasonable considering the quality of the data available. An added complication however, was the aluminium background impurity from the sample holder. Initially, a second aluminium phase was included in the refinement which could then be used as an internal standard. However, there was considerable peak overlap and the amount of aluminium visible in the Le Bail fit was very small. For these reasons, the refinements were carried out with only the single phase (Table 7.4) and contaminated regions excluded.

Le Bail refinements of the shorter scans between 200 K and 17 K were attempted, but the data were much noisier, leading to increased peak overlap. This, together with the sample height difficulties meant that the refinements were unstable.

	Rehydrated	200 K	17 K
a	14.6725(7) Å	12.3255(5) Å	11.8922(8) Å
b	13.3550(4) Å	13.8532(7) Å	13.7431(10) Å
c	7.4310(3) Å	8.3166(4) Å	8.1098(6) Å
α	90°	86.571(4)°	84.038(5)°
β	91.369(3)°	97.019(4)°	96.682(5)°
γ	90°	88.455(4)°	88.842(5)°
V	1455.70(12) Å^3	1406.01(11) Å^3	1308.6(12) Å^3
R_p	0.0490	0.0598	0.0572
$_wR_p$	0.0632	0.0858	0.0839
χ^2	1.283	2.653	3.000

Table 7.4: Cell parameters of compound **9** from PheniX data.

7.4.3 Structure Solution and Refinement

Given the quality and complexity of the data for compound **9**, structure solution was not possible. The data for compound **8** was more approachable and given the success indexing the data collected under vacuum, structure solution was attempted.

$Fe_2(Pmd)_2[Au(CN)_2]_4$ (Compound 8)

Attempts were made to solve the structure with simulated annealing techniques using DASH.[168,191] DICVOL[188] within DASH was used to index the powder data independently and gave similar results to those obtained with CrysFire.[189] This cell was refined using the Pawley fitting routine within DASH. WebLab ViewerPro[193] was used to generate a model based on the single crystal structure without water. This consisted of the one iron centre connected to two anionic bridges together with a Pmd ligand. The starting temperature used (T_0) was 1000 K (the highest possible) with a cooling rate of 0.001 K (the lowest possible) and $N_1 = N_2 = 40$.

A sensible solution with this model was not found, so the fragments were rearranged, but results were still unconvincing. In order to give the program more freedom, two independent gold atoms and one iron atom were given as the model. The fit to the data was poor, but the solution was not entirely useless. The location of the gold atoms was very similar to those in the hydrated structure, i.e. approximately $\frac{1}{4}\frac{1}{2}0$ and $\frac{1}{4}\frac{3}{4}\frac{1}{4}$. The iron

atom location did not correspond, but as the scattering power of gold is approximately twice that of iron, it is not surprising that the software struggled to locate it. Adding the iron atoms on the inversion centres at $0\frac{1}{2}\frac{1}{2}$ and $\frac{1}{2}\frac{1}{2}\frac{1}{2}$ as in the hydrated structure, led to a considerably improved fit, so the hydrated structure was used to generate a model solution for the dehydrated structure.

The powder data collected under vacuum was used for the structure refinement, which was carried out in stages. Initially, the gold atoms were freely refined. Since the X-ray scattering factor for gold is considerably larger than that for any other element present, and the next largest is fixed by symmetry (the iron atoms), this was considered reasonably reliable. This fit was used to define the centre for rigid bodies for the $[Au(CN)_2]^-$ units. These were loosely modelled on the hydrated single crystal data, with the centre coincident with the atomic position of the gold atoms. Individually, the centres of these units were refined, then they were fixed while the rotations were refined. This had to be done in stages as refining the rigid body centre, at the same time as the rotations, resulted in the refinement becoming unstable. The Fe–N distances also had to be restrained and later, in order to improve the geometry, the N–N distances were also restrained, however, in each case these restraints resulted in subtle improvements to the figures of merit, suggesting that they improved the model.

Once the bridges had been refined satisfactorily, a rigid body for the ring was generated (also based on that in the hydrated structure). This ring position was refined and it immediately moved towards the second iron atom. This position was fixed and the gold bridges refined again, separately but in the same sequence as before. Once the bridges had been refined and the process repeated several times for each bridge, attention reverted to the ring. This process of refining the bridges and then the ring was repeated many times to ensure that the best fit possible was obtained. Towards the end, the ring was refined, but with restraints on two of the N–Fe–N angles (to maintain them close to 90°) and on all the Fe–ring angles to ensure that they remained close to 120°. There are several problems with the final refinement. For example, the sample appears to suffer from a small degree of preferred orientation and the $[Au(CN)_2]^-$ bridges are modelled as linear which is clearly not totally accurate (see page 205). However, the fit is reasonable and the statistics are good (Figure 7.8).

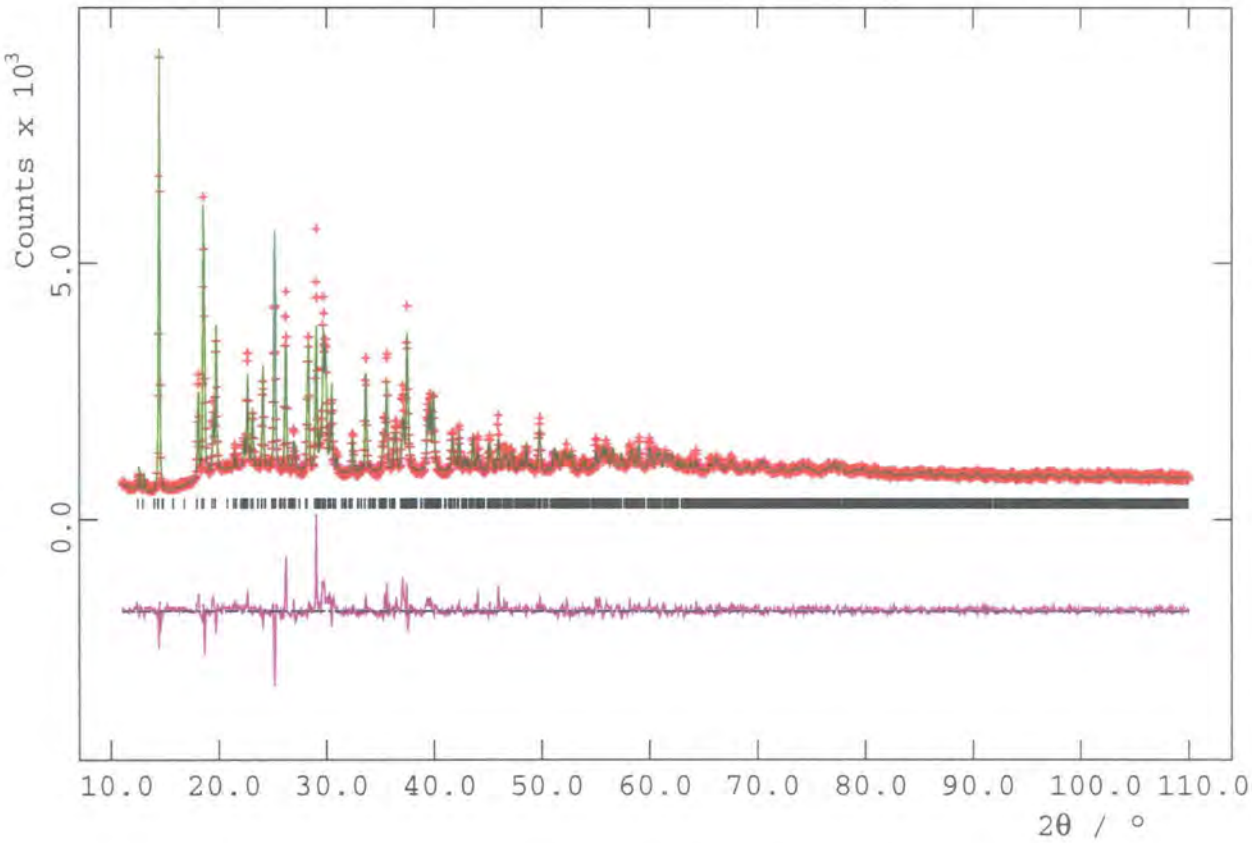

Figure 7.8: Fit for the Rietveld refinement of compound **8**. The data are shown as red crosses, the fit in green and the difference trace in purple. Goodness-of-fit (on F^2) = 2.52, χ^2 = 6.341, R_p = 0.0808 and wR_p = 0.1314 (R_p = 0.0505 and wR_p = 0.0718 excluding background).

7.5 Solid State ^{1}H Nuclear Magnetic Resonance Experiments

A sample of compound **7** was submitted for analysis by the Solid State NMR Service.[†] Since these materials are paramagnetic, NMR is difficult. The magnetism of the iron overpowers the magnetic field provided by the nuclear moment causing extreme broadening and smearing of the signal. However, in some cases it is possible to get some information.

7.5.1 Data Collection

The sample was crushed gently and placed in a 4 mm rotor (outside diameter) and data were collected with a Varian MAS probe, referencing with respect to tetramethylsilane. A single signal at approximately 13 ppm could be seen. The sample was heated in 10 °C steps, each followed by data acquisition. Initially, the temperature was controlled by the rotation speed, but above about 60 °C the sample heater was used. At approximately 383 K the signal disappeared and the sample was cooled back to room temperature where more data were acquired. The rotor was then removed and the sample left in air for $\frac{1}{2}$ hr, after which more data were collected. The signal had reappeared, however the intensity was considerably reduced, so the sample was left overnight in air. Further data were collected the following morning and although there appeared to be a small increase in intensity, the starting intensity was never fully regained (Figure 7.9).

7.5.2 Data Analysis

Prior to dehydration there was one clear signal (Figure 7.9) and it was assigned to the aqueous protons. At no point was there any evidence of any other signal, however the peak broadening due to the presence of the high spin iron, could explain the absence of signals from the aromatic protons which could be so broad that they disappear into the background.

[†]Work carried out with Dr. David Apperley and the EPSRC Solid-State NMR Service at Durham.

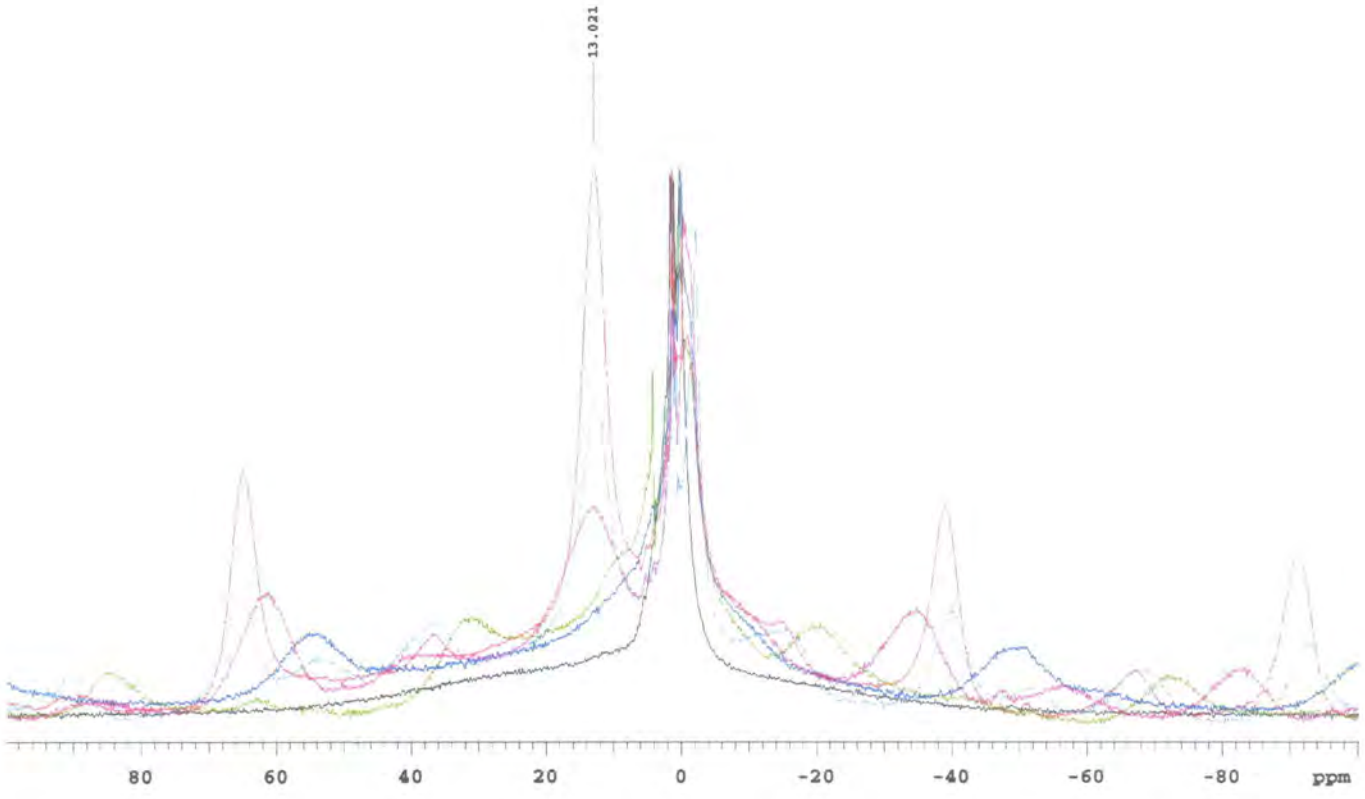

Figure 7.9: NMR data collected on compound **7**. The background from the rotor is shown in black and the initial room temperature data are shown in red with the peak at 13 ppm labelled. The extra peaks are spurious, as they depend on the data collection conditions. The data shown in green were collected at 383 K and the blue is room temperature after heating. The rehydrated data are shown in pink (after $\frac{1}{2}$ hr) and cyan (approximately 20 hr later).

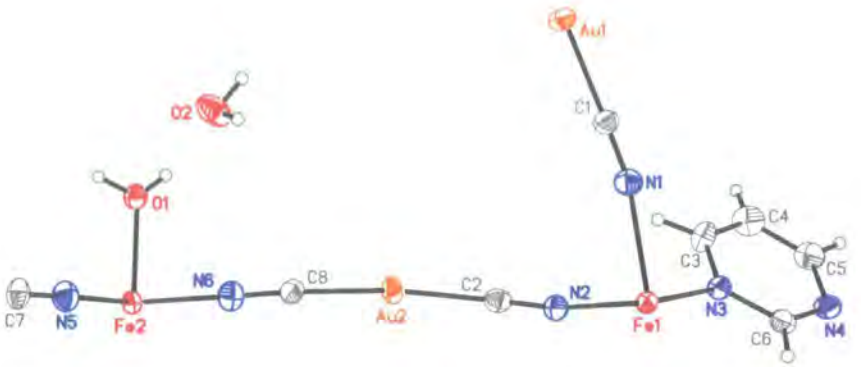

Figure 7.10: The asymmetric unit for compound **6** at 180 K, a = 14.6157(5) Å, b = 13.3075(5) Å, c = 7.2272(3) Å, β = 90.944(2)°, V = 1405.49(9) Å^3 ($\mathbf{P2_1/c}$).

On heating to 383 K the signal at 13 ppm disappeared, but on removing the sample and leaving in air, the signal reappeared. This was consistent with the assignment of the peak to the hydrogen atoms for the water, however on rehydration, the intensity was considerably reduced. Despite leaving the sample in air overnight, there was no further increase in intensity suggesting that the rehydration process had ceased.

7.6 Discussion

The hydrated structures consist of two six co-ordinate iron centres linked together by $[M(CN)_2]^-$ units. The asymmetric unit only contains 20 non-hydrogen atoms, but the two iron atoms occupy inversion centres so, by symmetry, a 3D network is generated (Figure 7.10 and 7.11).

7.6.1 Structural Analysis of Compound 6

Both iron atoms are ligated by cyanide groups in a square planar arrangement with the axial sites occupied by either pyrimidine or water (Fe1 and Fe2 respectively). Six of these iron centres connect to form a 2 × 3 rectangular motif (Figure 7.11). These rectangular motifs come together to form sheets which are connected together through $[Au(CN)_2]^-$ bridges at X and Y to give a three dimensional network. In the whole structure there are three such separate, interwoven networks. Viewed down the b-axis it is possible to see how

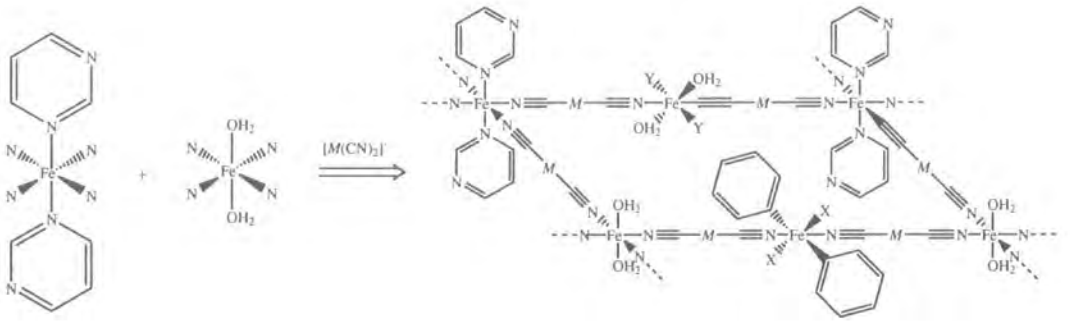

Figure 7.11: Schematic of the 3D networks, showing how the FeN_6 and FeN_4O_2 units form a 2×3 iron motif bridged by $[M(CN)_2]^-$ ligands.

these networks, separated by half a unit cell along the *b*-axis are interlaced (Figure 7.12). These three networks are connected together through aurophilic interactions and hydrogen bonds.

Hydrogen Bonding Networks

The nitrogen donor in the Pmd ring forms strong hydrogen bonds with the coordinated water making chains of alternating Fe1 and Fe2 octahedra (Figure 7.13). In addition to the coordinated water and nitrogen donor in the ring, there is water of crystallisation present. This solvent water sits in the cavity between two coordinated water molecules on two different Fe2 octahedra. The hydrogen bonds between these water molecules result in ordered solvent of crystallisation, which forms chains with the ligand water running along the *c*-axis. Because there is strong hydrogen bonding between the ligands and the solvent, the water in the cavity is ordered even in the high spin structures (Figure 7.13). In addition to hydrogen bonding to the solvent water (O2), the ligand water molecules (O1) also form a bridge between the two iron centres through strong hydrogen bonds to the second Pmd nitrogen. As such, the ligand water molecules join the two sets of hydrogen bonding chains, leading to the formation of a three dimensional network.

Dehydration of Compound 6

When the gold sample is dehydrated by heating or placing under vacuum, there is a significant contraction of the *a*-axis, which brings the free nitrogen of the pyrimidine within

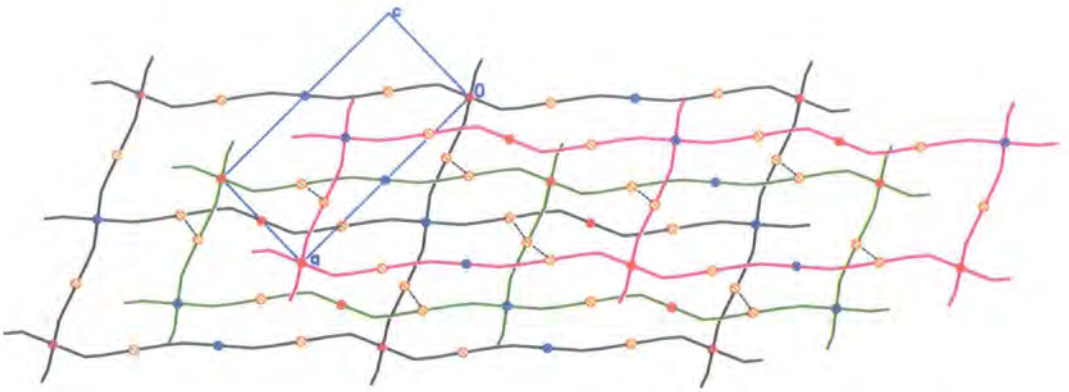

Figure 7.12: Three interpenetrating networks in compound **6**, shown in black, green and pink, viewed down the *b*-axis. Fe1 atoms are shown in red, Fe2 atoms are shown in blue, the aurophilic bonds are shown with broken black lines and the unit cell outline is shown in blue.

bonding distance of Fe2, thus maintaining the six-fold coordination sphere. Although this type of topochemical conversion is unusual, it is not unheard of. Ranford *et al.* reported similar behaviour in the dimeric hydrated species $[\{Zn(Sala)(H_2O)_2\}_2].2H_2O$ where $H_2(Sala)$ = *N*-(2-hydroxybenzyl)-L-alanine (salicylaldehyde).[194] They found that the zinc centre is a distorted square-pyramid, with the apical site occupied by a water molecule (Figure 7.14). The water forms strong hydrogen bonds with the salicylaldehyde of the next dimer unit. On heating, this water escapes through channels running through the structure and the free oxygen of the carboxylic acid moves to occupy the newly vacated site forming a rigid covalent network. In $[\{Zn(Sala)(H_2O)_2\}_2].2H_2O$ the dehydration is not reversible, and rehydration by displacing the ligating carboxylic acid oxygen does not occur. However, the irreversibility of the $[\{Zn(Sala)(H_2O)_2\}_2].2H_2O$ dehydration does not preclude the possibility of a similar reversible process in a different system.

On dehydrating compound **6**, the hydrogen bonding network is completely destroyed since not only is the solvent water lost, but also the vital bridging ligand water. This ligand is replaced by the nitrogen of the Pmd ring so while the hydrogen bonding network is lost, it is replaced by stronger covalent Fe–Pmd–Fe interactions.

In contrast, the three dimensional networks remain relatively unaltered, becoming slightly more regular in shape. The aurophilic interactions also remain intact, so the

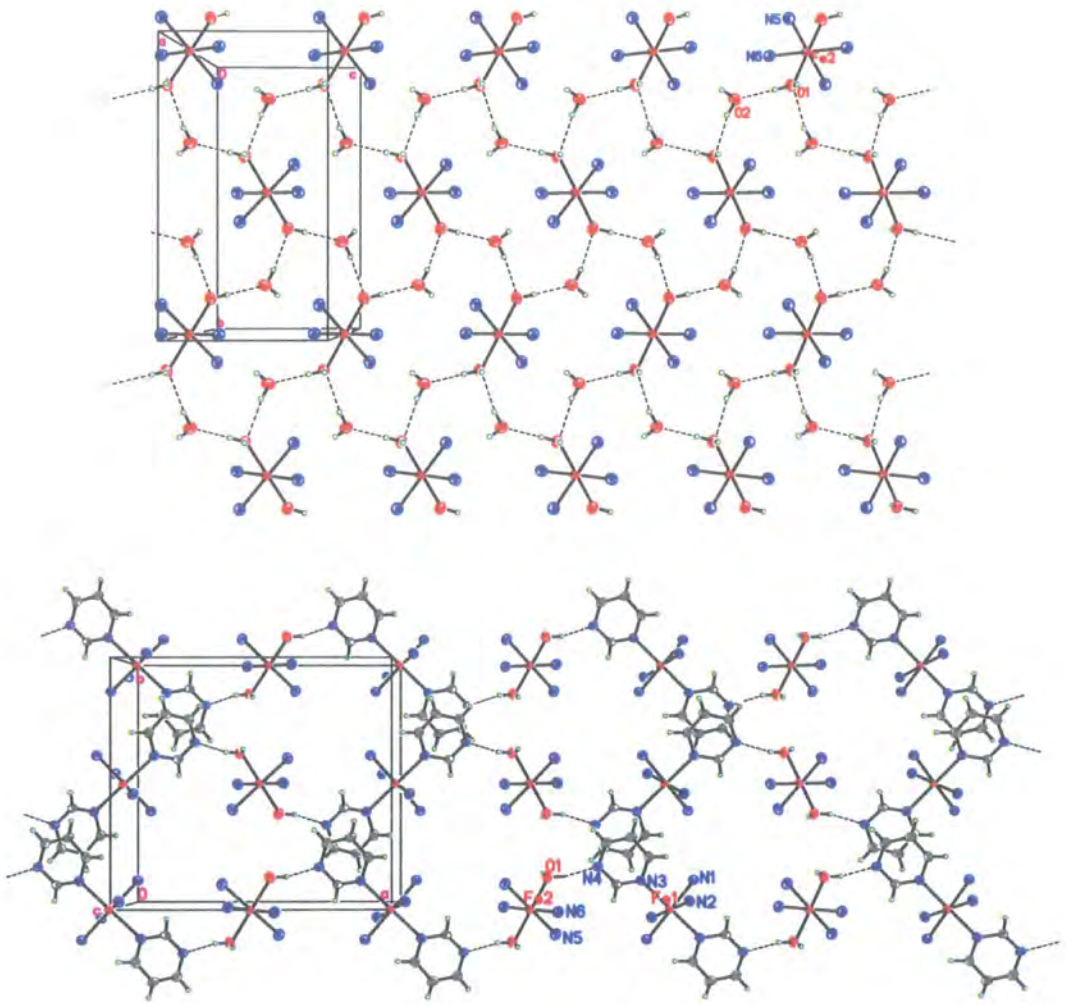

Figure 7.13: The hydrogen bonding compound **6** at 180 K. The ligand water molecules participate in both the hydrogen bonding chains with the solvent water (above) and form a bridge between the two iron centres (below).

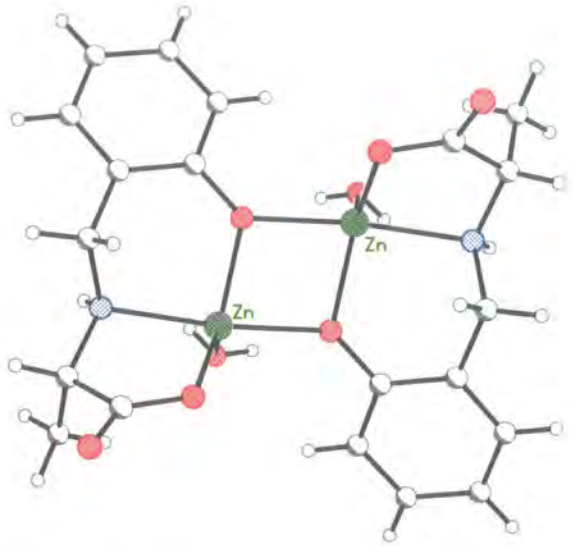

Figure 7.14: $[\{Zn(Sala)(H_2O)_2\}_2].2H_2O$.[194]

structure retains its bridges between the three separate covalent networks.

Compounds 8 and 9

Since compounds **6** and **7** are isostructural, the interpenetrating networks held together by M–M interactions and hydrogen bonds are also seen. Where the two compounds significantly differ is in their behaviour upon dehydration.

Like compound **6**, the silver sample also appears to lose water on heating or under vacuum. However, while the structure retains its crystallinity, it appears to undergo a loss of symmetry, so that the dehydrated material (compound **9**) is triclinic. The difference in the dehydrated structures must result from the difference between the gold and silver cyanide bridges and clearly is critical in explaining why compound **9** has a spin transition, but compound **8** does not.

7.6.2 Spin Crossover Transitions

The magnetic susceptibility data indicate that the degree of cooperativity is high in compounds **6** and **7** as they both undergo an abrupt transition with a clearly defined hysteresis. The dramatic colour change suggests that the transition is complete at 120 K in both com-

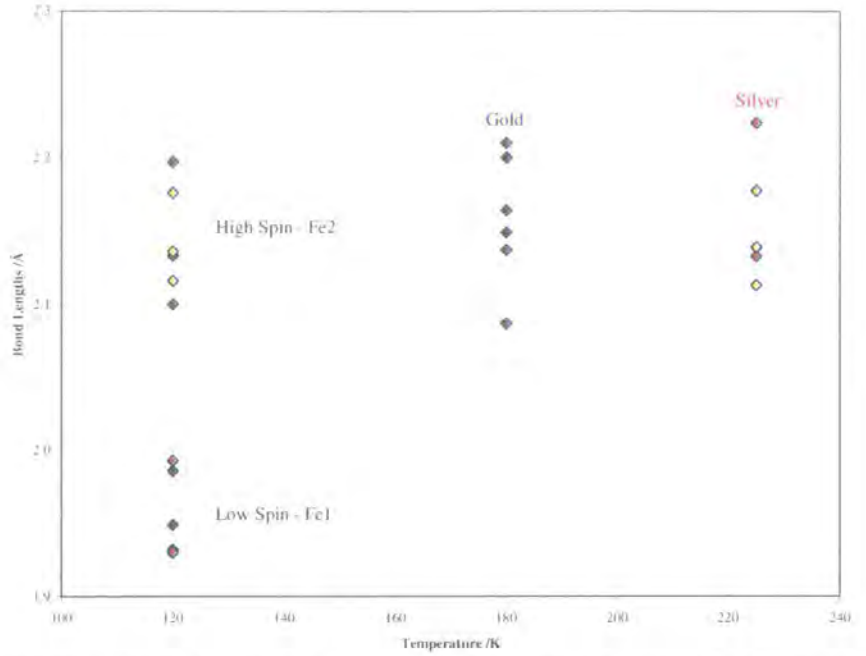

Figure 7.15: Fe–L bond lengths in compounds **6** and **7**. Compound **6** is shown in blue (Fe1) and green (Fe2) and compound **7** is shown in red (Fe1) and pink (Fe2). At 180 K (Compound **6**) and 225 K (Compound **7**) both iron centres are high spin. On cooling to 120 K however, only Fe1 becomes low spin and the change in Fe–N distances can clearly be seen in both compounds.

pounds. However, a close examination of the bond lengths and the SQUID data indicate that things are not as simple as that.

Fe–L Bond Lengths and Octahedral Volumes

A comparison of the bond lengths around the central iron atoms in compounds **6** and **7** indicates that only one of the iron centres undergoes a spin transition (Figure 7.15). The average Fe–N distance for Fe1 changes from 2.171(5) Å to 1.955(6) Å in compound **6** and 2.165(2) Å to 1.952(2) Å in compound **7**. However, there is very little change for Fe2 (less than 0.002 Å in both cases), indicating that it remains high spin.

Comparing the volumes of the octahedra clearly shows this effect (Table 7.5). Both iron atoms sit on inversion centres, so that the centres of the octahedra are coincident with the iron positions. The regularity of the network means the main octahedral distortions

	Compound 6		Compound 7	
	180 K	**120 K**	**225 K**	**120 K**
Fe1–N1	2.165(5) Å	1.949(7) Å	2.138(2) Å	1.932(3) Å
Fe1–N2	2.150(5) Å	1.930(6) Å	2.133(2) Å	1.930(3) Å
Fe1–N3	2.200(5) Å	1.986(7) Å	2.224(2) Å	1.993(3) Å
Fe2–N5	2.210(6) Å	2.197(7) Å	2.177(2) Å	2.176(3) Å
Fe2–N6	2.137(6) Å	2.133(7) Å	2.139(2) Å	2.136(3) Å
Fe2–O1	2.087(5) Å	2.100(6) Å	2.113(2) Å	2.116(3) Å
Fe1 Mean Bond length	2.171(23) Å	1.955(26) Å	2.165(46) Å	1.951(32) Å
Fe2 Mean Bond length	2.145(56) Å	2.143(44) Å	2.143(29) Å	2.143(27) Å
Fe1 Volume	13.61(4) Å^3	9.95(4) Å^3	13.49(4) Å^3	9.90(4) Å^3
Fe2 Volume	13.11(4) Å^3	13.09(4) Å^3	13.09(4) Å^3	13.09(4) Å^3
Fe1 Σ	20(1)°	15(1)°	20(1)°	13(1)°
Fe2 Σ	28(1)°	28(1)°	22(1)°	21(1)°

Table 7.5: Octahedron volumes and other selected results for compounds **6** and **7** in the high spin and low spin states.

are due to Jahn-Teller type effects. This can be seen in the extremely low values for Σ in both the high and low spin states (Table 7.5). The Jahn-Teller effects cause elongation in the Fe1 octahedra along the Pmd axis and compression along the water axis in the Fe2 octahedra.

The Fe2 centres are ligated by water which makes the ligand field weaker than that for the Pmd ligated Fe1 atoms. This prevents the Fe2 centres from undergoing spin crossover. This result agrees with the magnetic susceptibility data, which show that the transition is incomplete, with only half the iron centres participating in the spin transition.

While for both compounds the transitions are abrupt, they occur at significantly different temperatures. This can be explained in a number of ways. Firstly, the spin transition phenomenon is essentially entropy driven and the critical temperature where the HS and LS molar fractions are equal is $T_{\frac{1}{2}}$ (Equation 7.1). Calorimetric measurements show that ΔS is smaller for compound **6** than for compound **7** which should mean that the transition in the gold sample is at a higher temperature than in the silver analogue.[195] However, ΔH experiments indicate that there is a dramatic increase in ΔH when the gold is replaced with silver in compound **7**.[195] This explains why $T_{\frac{1}{2}}$ is lower for compound **6** than

compound **7**.

$$T_{\frac{1}{2}} = \frac{\Delta H}{\Delta S} \tag{7.1}$$

Thus, the spin transition in the hydrated phase as well as the magnetic behaviour, structure and water loss in the dehydrated phase, depend on the M centre.

Fe···Fe Distances

Each interpenetrating network consists of a 2 × 3 rectangular motif of units. The distance along the edge of this repeat unit changes with M and with spin state. There are two types of distance to be considered: the shorter Fe1···Fe2 distance and the longer Fe1···Fe1/Fe2···Fe2 distances. A comparison of these distances indicates that the Fe1···Fe2 distance contracts by the expected ∼ 0.2 Å caused by the spin transition in both compounds **6** and **7** (Table 7.6). However, the Fe1···Fe1/Fe2···Fe2 distances also contract by ∼ 0.2 Å, which is approximately half of what would be expected as the distance includes two Fe1–N2 bonds that each contract by over 0.2 Å in each case. This could be because the angle at which the cyanide groups ligate to Fe1 changes, becoming more linear on cooling in both compounds.

Since the iron atoms occupy the inversion centres in compounds **6** and **7** the Fe···Fe distances are independent of the refinement, depending only on the unit cell parameters. Therefore, the Fe···Fe distances can be determined not only for compound **8**, but also making a few assumptions, compound **9**. Compound **9** has been shown to be triclinic, so assuming the space group to be $\mathbf{P\bar{1}}$, the distance between the inversion centres and therefore the iron positions can be predicted. The space group is presumed to be $\mathbf{P\bar{1}}$ because **P1** is very rare, however it must be considered that **P1** is a possibility. If the space group were **P1**, the iron atoms would be unable to move far from the inversion centres because of the constraints caused by the network. Therefore, the Fe···Fe distances would remain similar, but could only be considered as a rough approximation.

The Fe···Fe distances in both compounds **8** and **9** are shorter than for their hydrated counterparts and the distances are shorter in compound **8** than compound **9**. This is also

	Fe1···Fe2	Fe1···Fe1	Fe1–N2–C2
Compound **6**			
180 K	10.5643(2) Å	20.3860(6) Å	152.0(5)°
120 K	10.3731(2) Å	20.1836(4) Å	166.7(6)°
Compound **7**			
225 K	10.6417(2) Å	20.5775(7) Å	155.3(2)°
120 K	10.4581(2) Å	20.3115(4) Å	169.1(3)°
Compound **8**			
290 K	10.306(1) Å	20.035(6) Å	-
Compound **9**			
290 K	10.357(5) Å	20.15(2) Å	-

Table 7.6: Fe···Fe distances in compounds **6**, **7**, **8** and **9**.

seen in the hydrated materials, where the Fe···Fe distances are 0.0774(4) Å and 0.192(2) Å shorter for the gold compound than the silver compound (Fe1···Fe2 and Fe1···Fe1 respectively, for the high spin structures). These differences appear to be smaller in the dehydrated materials (approximately 0.05(1) Å and 0.12(3) Å), but given the poor quality of the data for compound **9** it is not possible to be certain about the magnitude of the differences. However, the fact that the Fe···Fe distances are shorter suggest that the Fe–N–C angles are more distorted, or the bridges are more bent, or the Fe–N distance is shorter or a combination of all three.

Unit Cell Parameters

A comparison of the unit cell parameters of these materials at 120 K shows that the unit cell volume for compound **6** is less than that for compound **7** (Table 7.7). Initially, this would seem to be counterintuitive, as gold is below silver in the periodic table and therefore would normally be expected to give the larger volume. However, the electronegativity of gold according to the Pauling scale is 2.54 compared with 1.93 for silver, and comparisons of arsine complexes clearly show that the covalent radius for four coordinate Au(I) is approximately 6% shorter than that for four coordinate Ag(I).[196] Other work by the same group also supports this result[197,198] which can be explained by relativistic effects observed for heavy atoms.[199]

The increased electron affinity that gold has compared with silver means that the

	Compound 6	Compound 7	
a	14.0194(4) Å	14.2584(4) Å	(+1.70%)
b	13.1770(3) Å	13.0528(3) Å	(−0.94%)
c	7.4306(2) Å	7.4930(2) Å	(+0.84%)
β	91.3780(10)°	92.0550(10)°	(+0.74%)
V	1372.28(6) Å^3	1393.64(6) Å^3	(+1.56%)

Table 7.7: Cell parameters of compounds **6** and **7** at 120 K with the percentage increase for compound **7** given in parentheses.

$[Au(CN)_2]^-$ bridges in compound **6** are significantly shorter than the $[Ag(CN)_2]^-$ bridges in compound **7**.

The difference in percentage change in the cell parameters suggests that there is some directionality to this contraction (Table 7.7). The majority of the expansion on replacing gold with silver is along the a-axis, with a smaller component in the c direction. There is also a contraction along the b-axis of a similar magnitude to the expansion in the c direction.

While the $[M(CN)_2]^-$ bridges have a component in all directions, the M–M interactions are almost entirely in the bc plane (Figure 7.16). Comparing the M–M distances shows where the anisotropic contraction comes from. It would appear that there is an unit cell expansion on replacing gold with silver caused by the lengthening of the $[M(CN)_2]^-$ bridges. This affects all directions, but there is also an opposing contraction caused by a shortening of the M–M interactions. Thus, the majority of the unit cell expansion seen takes place in the a direction. These changes can best be seen by comparing the length of the $[M(CN)_2]^-$ bridges (N1$\cdots$N5 and N2$\cdots$N6) and the $M1$–$M2$ distances (Table 7.8).

Closed-Shell Interactions

For many years, gold(I) has been known to have a high affinity for itself, frequently forming bonds with itself, known as aurophilic or gold–gold interactions. These bonding interactions are of a similar strength to hydrogen bonds and as a result are now being used in crystal engineering.[200] Such interactions have also been shown to lead to the formation of nano-clusters of up to forty gold atoms, in a chiral helical arrangement.[201]

These interactions are not limited to gold however, and so called closed-shell or d^{10}-d^{10}

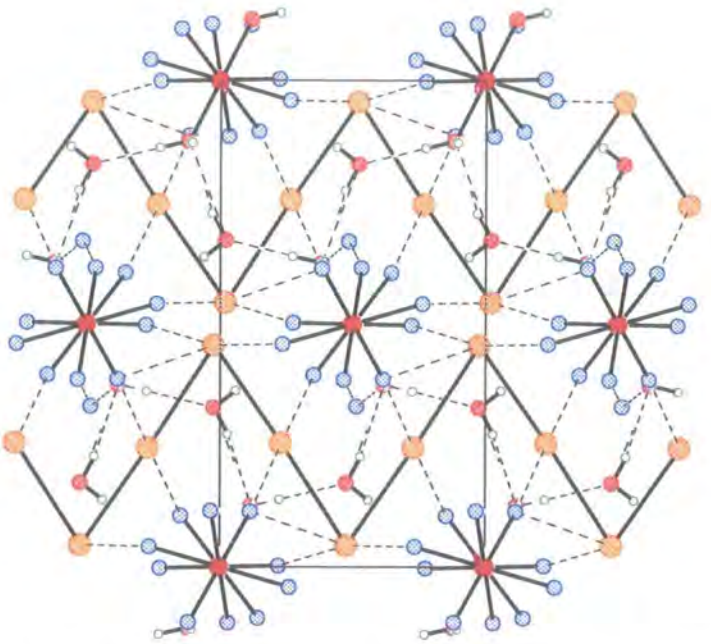

Figure 7.16: Au–Au interactions in compound **6**, viewed down the *a*-axis. The Au–Au bonds are shown in black zig-zagging from left to right, in the direction of the *c*-axis. The hydrogen bonding network can also be seen. (Carbon atoms and Pmd hydrogen atoms are omitted for clarity, the $[Au(CN)_2]^-$ bridges are shown with the Au–N as a broken line).

	Compound 6		**Compound 7**	
	180 K	**120 K**	**225 K**	**120 K**
*M*1–C1	1.988(6) Å	1.981(8) Å	2.062(3) Å	2.063(3) Å
*M*1–C7	1.995(6) Å	2.000(8) Å	2.061(3) Å	2.060(3) Å
C1–*M*1–C7	179.6(3)°	179.0(3)°	178.6(1)°	178.0(2)°
N1···N5	6.26(1) Å	6.28(1) Å	6.397(5) Å	6.412(6) Å
*M*2–C2	1.965(6) Å	1.976(7) Å	2.062(3) Å	2.060(3) Å
*M*2–C8	1.995(6) Å	1.976(7) Å	2.061(3) Å	2.064(3) Å
C2–*M*2–C8	171.9(3)°	171.1(3)°	166.8(1)°	164.9(2)°
N2···N6	6.21(1) Å	6.19(1) Å	6.328(5) Å	6.289(6) Å
*M*1–*M*2	3.2545(4) Å	3.3530(4) Å	3.1676(3) Å	3.1998(3) Å
	3.3257(4) Å	3.3380(4) Å	3.1950(3) Å	3.1606(3) Å

Table 7.8: Selected bond lengths and angles for compounds **6** and **7** at 120 K.

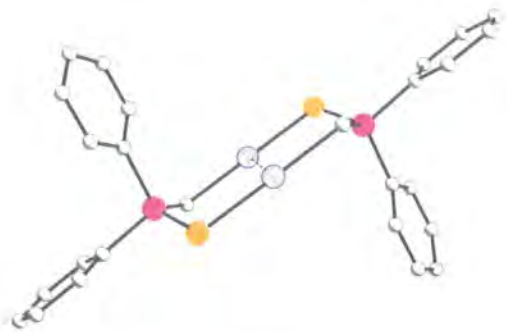

Figure 7.17: The eight membered ring of the methylenediphenylthiophosphinate silver complex occupies a chair type conformation.[204]

interactions have also been found in Cu(I) (cuprophilic interactions), Ag(I) (argentophilic interactions) and more recently mixed-metal heterometallic complexes have been shown to exhibit argento-aurophilic interactions.[202] Despite this, there are relatively few studies on isostructural compounds comparing the interactions. However, one such pair of compounds are the methylenediphenylthiophosphinate gold and silver compounds.[203,204] Both structures are in $C2/c$ with half a molecule in the asymmetric unit and an inversion centre generating the other half. The molecule consists of an eight membered ring constrained by a M–M interaction across the centre, so that it behaves like a six membered ring taking up a boat type conformation (Figure 7.17). The M–M interactions that extend across the ring, also continue between adjacent molecules creating a one dimensional pseudo-polymer (Figure 7.18).

In compounds **6** and **7**, the metal centres interact through long M–M bonds zig-zagging their way through the structure in the direction of the c-axis. These M–M bonds form important bridges linking the three dimensional networks together. Given the similarity between these weak M–M interactions and hydrogen bonds and π–π interactions, it was thought that these aurophilic/argentophilic bonds could play the same role in co-operativity. It is interesting to note that while the Au–C bonds are shorter than the Ag–C bonds, the Au–Au bonds are longer than the Ag–Ag. This mixture is also seen in the methylenediphenylthiophosphinate complexes, where the interaction across the ring is shorter in the silver compound than in the gold compound. However, while 'intermolecular' bonds are longer than the 'intramolecular' bonds, the Ag–Ag and Au–Au bonds are

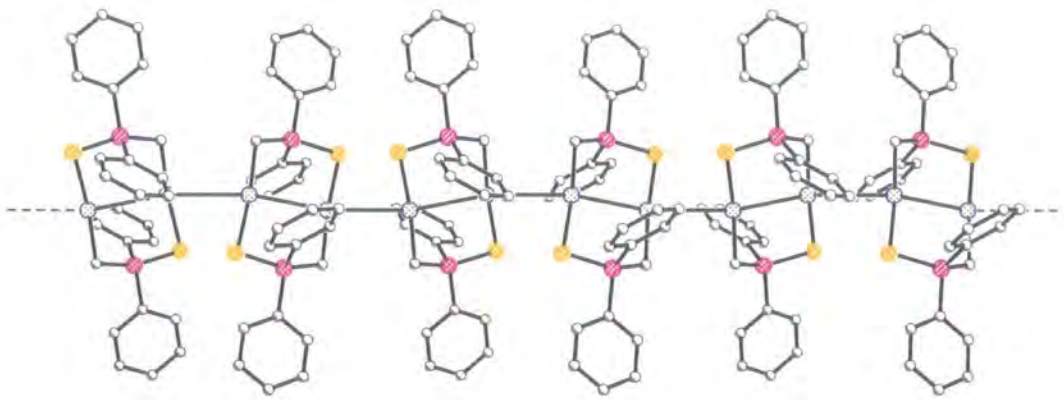

Figure 7.18: 'Pseudo-polymer' chains in a methylenediphenylthiophosphinate silver complex, caused by intermolecular interactions. The interactions across the ring (Au 3.040 Å, Ag 2.990 Å) are shorter than those between molecules (Au 3.222 Å, Ag 3.226 Å).

approximately the same length. This suggests that aurophilic and argentophilic interactions are similar to hydrogen bonds in their variety of length and strength, which can depend largely on the environment.

Non-linear Bridges

$[M(CN)_2]^-$ anions should be a completely linear building block.[205,206] However, for both compound **6** and **7**, one bridge deviates significantly from linearity. In both cases it is the same bridge and the N2–$M2$–N6 angles at 120 K are 166(1)° and 160(1)° (compared with 179(1)° and 177(1)°) for N1–$M1$–N5 for compounds **6** and **7** respectively. A close examination of the structure shows why this is the case. Viewed down the a-axis, the M–M interactions form a zig-zag motif (Figure 7.16). This zig-zag pattern has two different types of M site — central ($M1$) and apical ($M2$). The central position interacts with two apical sites and vice-versa. However, the geometry around the two M atoms is different.

The M atom that occupies the central site $M1$, approximates to square planar with the cyanide groups *trans* to each other. $M2$ on the other hand, has a seesaw ($TeCl_4$) type geometry with the cyanide groups *trans* with the M–M occupying the 'equatorial' sites (Figure 7.19). For this reason, the interactions of the two apical $M2$ atoms on the central position are equal and opposing, making the central $M1$ bridge linear. The interaction

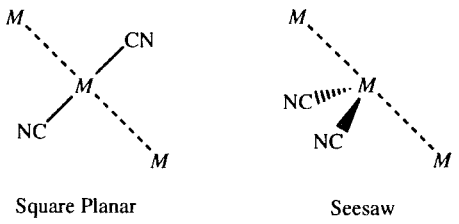

Figure 7.19: The two geometries for gold and silver found in compounds **6** and **7**.

of the two central $M1$ atoms on the apical $M2$ bridge however, are in the same direction which pulls the bridge away from linearity.

This non-linearity could also be used to explain the discrepancy in the length of the M–M interactions. The Ag–Ag bonds are noticeably and consistently shorter than the Au–Au bonds in both the high and low spin state (Table 7.8). According to the CSD,[1] the mean bond length for Ag–Ag interactions is 3.026(8) Å, which is longer than that for Au–Au interactions (2.944(6) Å).[‡] In compound **7**, the Ag–Ag bonds are shorter because the longer $[Ag(CN)_2]^-$ bridges have more flexibility than their gold counterparts and can therefore can bend more. This makes the structure of compound **6** slightly more strained than that of compound **7**. This is supported by the N–M–N and C–M–C angles which are closer to linear for the gold compound than the silver compound. The increased strain also explains why the iron cores in the gold complex are more distorted, as shown by the Σ values for compound **6** which are consistently higher than those for compound **7**.

On SC, both the Au–Au distances in compound **6** lengthen by approximately 0.1 Å, but the Ag–Ag distances only change by approximately 0.03 Å. These changes are in opposite directions, with the longer Ag–Ag distance contracting and the shorter Ag–Ag distance lengthening. This difference can be explained by the C–M–C angles, which for both the C–Au–C angles and the C1–Ag1–C7 angle undergo little change. The C2–Ag2–C8 angle however, which is 166.8(1)° at 225 K changes to 164.9(2)° at 120 K. This bending movement results in the lengthening of one Ag–Ag interaction, while shortening the other.

[‡]Both searches were carried out on version 5.24 of the CSD (November 2002), including only structures with no disorder, no errors and R-factors $< 10\%$.

	Compound 6		Compound 7	
	180 K	**120 K**	**225 K**	**120 K**
O_{Ligand}–H$\cdots$$O_{Solvent}$	2.689(3) Å	2.694(4) Å	2.692(2) Å	2.692(2) Å
$O_{Solvent}$–H$\cdots$$O_{Ligand}$	2.899(4) Å	2.890(5) Å	2.911(3) Å	2.875(3) Å
O_{Ligand}–H$\cdots$$N_{Pmd}$	2.762(5) Å	2.762(6) Å	2.805(3) Å	2.793(4) Å

Table 7.9: O$\cdots$O and O$\cdots$N distances for compounds **6** and **7**.

Hydrogen Bonding

There is a strong hydrogen bonding network, which takes the form of sheets of Fe2 atoms connected through the O–H$\cdots$O contacts between the solvent and ligand water molecules and chains of alternating Fe1 and Fe2 centres connected through O–H$\cdots$N interactions between the water and Pmd ligands (Figure 7.13).

Although there is no significant change in the hydrogen bond lengths on cooling, the $O_{Solvent}$–H$\cdots$$O_{Ligand}$ and O_{Ligand}–H$\cdots$$N_{Pmd}$ hydrogen bonds are longer for compound **7** than for compound **6** (Table 7.9). This could reflect the longer $[Ag(CN)_2]^-$ bridges, which force the iron atoms to be further apart, stretching the hydrogen bonds. This means that the distance from the unbound nitrogen in the Pmd ring to the water site that coordinates to Fe2 on dehydration, is slightly further in compound **7** than in compound **6**. It is probable that this minor difference together with the difference in the flexibility of the $[M(CN)_2]^-$ bridges, causes the structure of compound **7** to undergo a more drastic structural change on dehydration to form compound **9**, so that the Pmd can ligate to Fe2 as well as Fe1. This structural change could lead to subtly shorter Fe–Pmd distances in compound **9** compared with compound **8**, making the ligand field slightly stronger in the silver network allowing the spin transition to take place.

Transition Temperatures

This also leads to another explanation for the difference in the temperatures of the spin transitions in compounds **6** and **7**. The M–C distances are systematically shorter for the gold compound than the silver analogue (Table 7.8). This is because gold is more electron withdrawing than silver leading to a relative contraction along the $[M(CN)_2]^-$. This polarising makes $[Ag(CN)_2]^-$ a better electron donor and therefore a better ligand than

$[Au(CN)_2]^-$. This means that the ligand field and Fe–N bonds are stronger in compound **7**, stabilising the LS state with respect to the HS state, so that the transition takes place at a higher temperature in the silver compound than the gold compound.

This effect can be seen in the difference between the octahedral volumes in compounds **6** and **7**. In the silver compound, the high spin Fe1 octahedron is approximately 0.1 $Å^3$ smaller than the gold analogue. This difference is still apparent below the transition in the low spin state.

Since the donor capacity is reduced in the gold analogue (compound **6**), the ligand field in the gold compound is comparatively weaker which is supported by the fact that the equatorial Fe–N bonds are longer by 0.026 Å and 0.017 Å than in compound **7**. The weaker field results in a smaller energy difference between HS and LS for compound **6**, leading to a lower transition temperature for compound **6** than for compound **7**.

Compounds 8 and 9

According to the magnetic susceptibility data, the spin transition in the dehydrated silver compound takes place at 124 K on cooling and at 141 K on warming. By inspection, the powder data indicates that the transition takes place during the scan starting at 139.7 K (Figure 7.20). The transition is clearly sharp as this scan is comparable with those collected at higher temperatures apart from a slight residual peak at 14.6° 2θ (corresponding to the 200). The next scan was started at 132.2 K and overlaps well with the data recorded at lower temperatures (Figure 7.21). Since the transition must have taken place during the second half of the 139.7 K scan, most likely towards the end, this makes the transition temperature approximately 10 K higher than predicted by the magnetic susceptibility data. This difference could easily be due to differences in calibration between the two cooling devices.

The transition takes place at a lower temperature in compound **9** than in the hydrate, compound **7**. Recalling the differences in the Fe$\cdots$Fe distances, both dehydrated compounds had shorter Fe$\cdots$Fe distances than when hydrated, suggesting that the ligand field experienced by the iron centre is stronger in the anhydrate than in the hydrate. However, a stronger ligand field increases the gap between the e_g and t_{2g} levels increasing the difference between the HS and LS states, which should lead to an increase in the SC tran-

sition temperature. As this does not happen, either the results obtained from the powder diffraction data are inaccurate,[§] the octahedra undergo a distortion, or the $[M(CN)_2]^-$ bridging ligands bend so that the Fe–N bond lengths increase while the Fe···Fe distance decreases. It is probable that whatever happens affects the silver compound more than the gold compound as on dehydration compound **6** contracts by 0.258(2) Å, while compound **7** contracts by 0.285(7) Å. It has been shown that the $[Ag(CN)_2]^-$ bridges can bend more than $[Au(CN)_2]^-$ ligands as they are longer, which could enable the Pmd ligand to adopt a subtly different geometry changing the ligand field. This bending could be what is seen in the Fe···Fe distances. Given the poor quality of some of the powder diffraction data, a considerable amount of this discussion is conjecture, but it fits the facts well and until better data or more information is available, serves as a good working hypothesis. Attempts are underway to collect higher quality data, possibly including synchrotron data, in order to confirm or refute the theories discussed here.

Rehydration

The Le Bail refinements for the powder data were carried out for the hydrated phase, (compound **6**) before, between and after the dehydration steps, yielded very similar cells in all three cases and the data look almost identical when overlaid. This suggests that the rehydration is complete within the half hour allowed. However, although the cell parameters for compound **7** before dehydration and after rehydration are very similar, the intensities are slightly different. This intensity difference could be an artefact of the data caused by slight rearrangement of crystallites during the dehydration process leading to a change in the amount of preferred orientation[¶] or by some other peculiarity in the

[§]The Fe···Fe distance depends strongly on the cell parameters and the poor quality and complexity of the powder diffraction data for compound **9**, mean that the cell parameters determined are not as reliable as those for compounds **6**, **7** and **8**. Thus, the reliability of this result could be in doubt.

[¶]Preferred orientation is caused by crystallites lining up on the sample holder. It has the effect that some peaks are artificially increased in intensity and others reduced. However, it is most common in samples that have been packed tightly or pressed and where the crystallites are either plate or needle like. Although the samples could not be ground very finely in order to maintain the integrity of the networks, the samples were sprinkled on greased glass to avoid this problem.

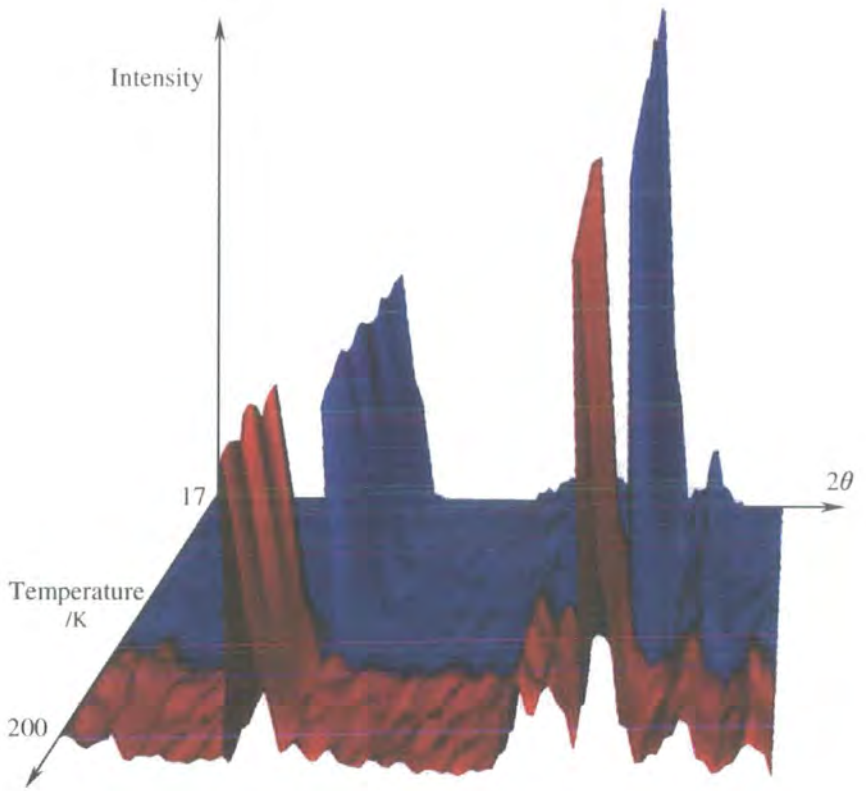

Figure 7.20: Three dimensional plot of powder diffraction data showing the spin crossover in compound **9**. The data collected above the transition is shown in red with the data below the transition in blue. The discontinuity shows the position of the transition, and takes place at approximately 134 K.

collection. As the data is not of as high a quality as that collected for compound **6**, it is not possible to be certain whether this is the case, however it is possible that there is also a structural explanation.

On rehydration, the *a* cell parameter expands and the other axes return to their former size, so Fe2 must be no longer coordinated by Pmd as the gap between the two iron centres is too large to bridged by a single Pmd ligand. Chemically, a four coordinate iron is unlikely, so the remaining iron coordination sites must be filled by water molecules. When compounds **6** and **7** are dehydrated there is a volume change consistent with the loss of only one water. Hence, the solvent water could conceivably be missing, or partially occupied, which would lead to very little change in the crystal lattice (as the solvent water fits into a cavity), and the intensity changes would also be small. Therefore, a vacant or partially occupied solvent void *could* lead to a compound with similar cell parameters to the initial hydrate. Thus, it is possible that the rehydration process that converts the triclinic structure back to the monoclinic phase, makes it more difficult for the water to access the cavities, so that rehydration is only partial and the free solvent water either takes longer to return or the site remains incompletely occupied.

Taking the XRPD data for the rehydration of compound **7** alone, the results are far from conclusive. However, although the NMR data are also far from reliable on their own, combined with the XRPD data the results are suggestive. Before dehydration the signal was approximately double that after rehydration. This change in the intensity could be put down to the paramagnetic iron disrupting the signal, however it is also possible that the rehydration could be incomplete. Again, the results are far from conclusive, but coupled with the XRPD results they suggest it is possible that rehydration is slower for compound **7** than compound **6**, or possibly only partial.

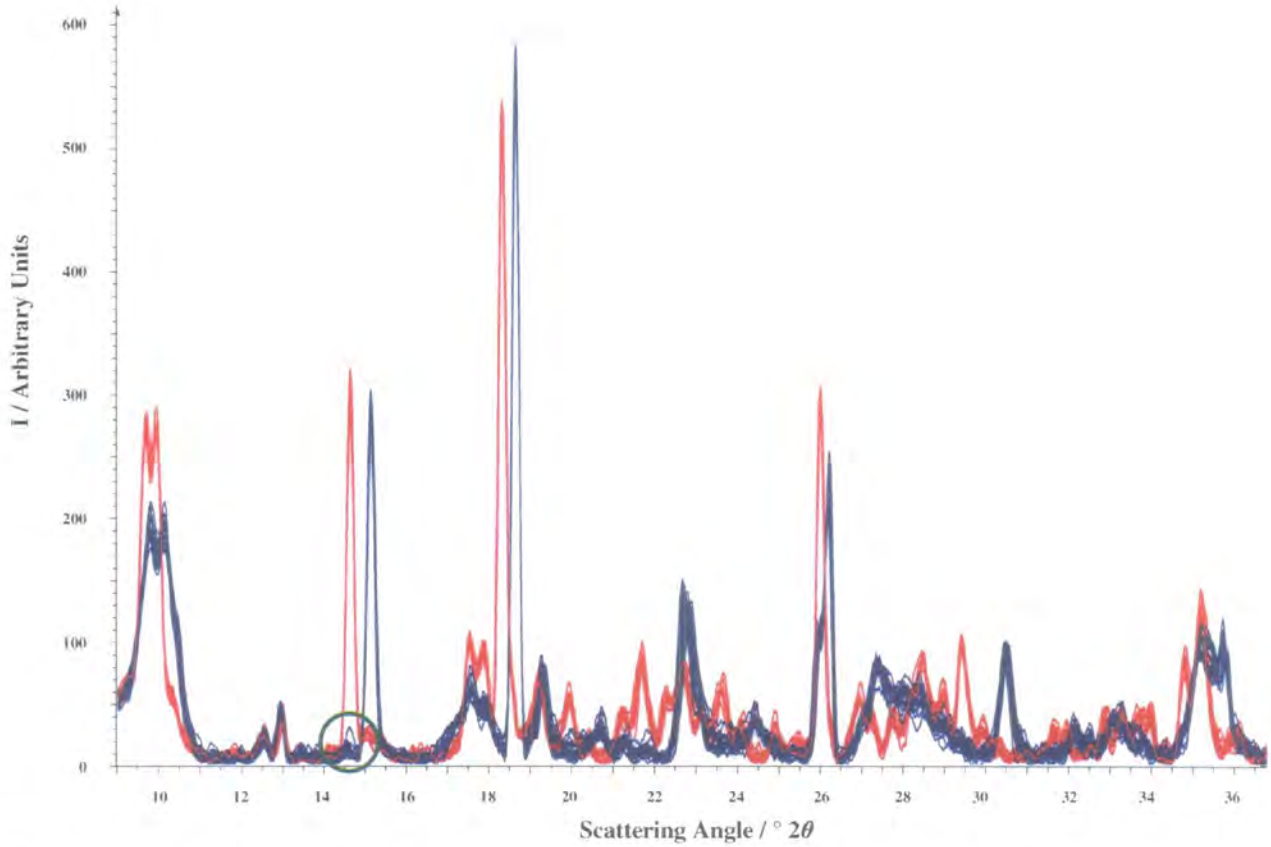

Figure 7.21: Overlay of powder diffraction data showing the spin crossover in compound **9**. The data collected above the transition are shown in red with the data below the transition in blue. The residual high spin peak in the scan that commenced at 139.7 K is highlighted in green.

7.7 Conclusion

Although structural studies on these compounds have answered many questions about these materials, the result is a number of new, unanswered questions.

In both compounds **6** and **7**, only one iron centre undergoes SC, which can be seen as effectively 'diluting' the spin transition in a similar way to doping with another element, i.e. the spin crossover active centres are being moved apart leading to a 'dilution', so the interactions are considerably weaker than for the hypothetical 100% active species. This makes the high degree of cooperativity seen in these compounds quite remarkable since the SC centres are spread out considerably more than was first thought.

While the compounds **6** and **7** are isostructural, compounds **8** and **9** are not. The difference between the electronegativity of the gold and silver centres holds the key to these differences. On dehydrating, compound **8** remains monoclinic and undergoes a sharp contraction in the a-axis to allow the free nitrogen of the Pmd ring to occupy the site vacated by the water ligand. Gold is more electronegative than silver, which makes the $[Au(CN)_2]^-$ bridges in compound **6** shorter than the $[Ag(CN)_2]^-$ bridges in compound **7**. The longer bridges in compound **7** move the iron centres further apart making it harder for the Pmd ligand to bridge the gap between them, so the structure has to change to maintain iron as a six-coordinate centre. This change is made possible by the larger flexibility in the longer $[Ag(CN)_2]^-$ bridges.

In compounds **6** and **7**, the difference in electronegativity affects the temperature of the phase transition. In compound **6**, the larger electronegativity is pulling the electrons away from the iron centre. This reduces the ligand field and stabilises the high spin state, resulting in a lower SC temperature for compound **6**.

This not only affects the magnetic behaviour of the hydrated form, but also affects the magnetic behaviour and the structures of the dehydrated materials. The longer bridges in compound **9** mean the Pmd ligands can't bridge the gap between the two iron centres without major structural change. It also results in a slightly stronger ligand field at the iron centre, leading to a retention of the SC transition in compound **9**, but at a lower temperature. This transition has a larger hysteresis suggesting increased cooperativity caused by the replacement of the weak hydrogen bonds by a stronger covalent network.

We have been unable to carry out a full structure determination for compound **9** due

to relatively poor crystallinity and increased complexity. Thus, the structural conclusions are based on results for compound **8**. In addition, there appears to be a possible difference between the hydrated and rehydrated powder diffraction patterns for compound **7**. This could be a function of the experiment, however a similar result is also seen in the NMR data, suggesting that the rehydration process may be slow or incomplete. Further work is required to confirm whether this is correct.

Although studies into counter ion and solvent replacement have indicated their importance to the presence or nature of SC, dedicated studies of dehydration and rehydration are rare, especially in the case of nanoporous framework SC materials. One such study carried out recently by Halder *et al.* followed the uptake and release of different solvent molecules in an azopyridine cross-linked iron(II) network.[207] However, in this case the solvent was uncoordinated, and the allosteric loss of the coordinated water in addition to the solvent water observed in compounds **6** and **7**, is believed to be unique. The reversibility of the allosterism, coupled with the retention of crystallinity, the strong thermo-chromism and the ability to control the spin transition, enhance the potential these nanoporous network materials may have in technological applications.

Chapter 8

Thermal and Light Induced Spin Transitions in a $[Cu(CN)_2]^-$ Bridged Coordination Polymer

8.1 Introduction

In a similar way to compounds **6** and **7** (Chapter 7), yellow crystals of $\{Fe(Pmd)_2[Cu(CN)_2]_2\}$ (compound **10**) were grown by slow diffusion of $Fe(BF_4)_2.6H_2O$ in pyrimidine with $((C_2H_5)_4N)[Cu(CN)_2]$ in methanol.[208] However, compound **10** has a completely different structure to compounds **6** and **7**, as there is no water present and the Pmd ligates both the iron centre and the copper centre.

8.1.1 Magnetic Susceptibility Data

SQUID magnetic susceptibility data indicate that compound **10** undergoes thermal and light induced transitions. The thermal transition occurs at 139 K on cooling with a 10 K hysteresis (Figure 8.1). On irradiating at 5 K, the compound undergoes Light-Induced Excited Spin-State Trapping (Figure 8.1) and magnetic studies on the decay of the metastable $^5T_2$ state indicate that at 30 K the lifetime is long (Figure 8.2).

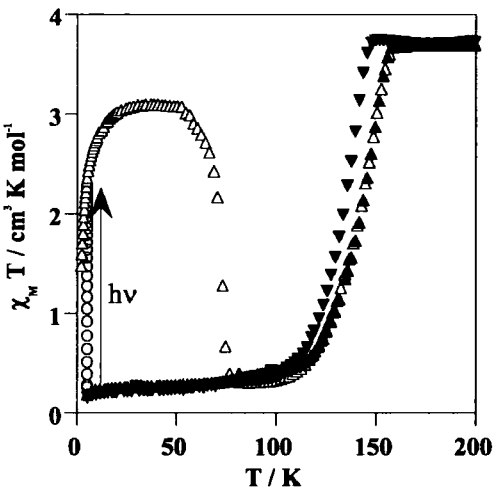

Figure 8.1: Magnetic Susceptibility Data for compound **10**.[208] The data indicate that the transition takes place at 139 K on cooling (▼) and 149 K on warming (▲), with the light induced meta-stable state (△) starting to revert to low spin at approximately 50 K, thence following the warming curve.

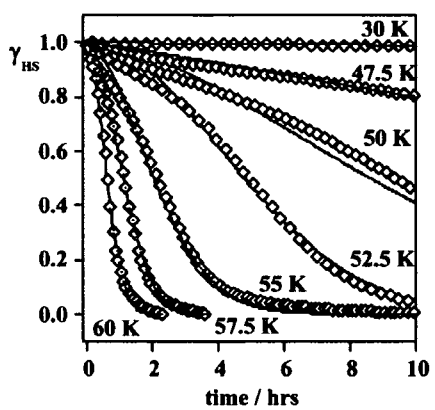

Figure 8.2: Time dependence of the high spin meta-stable state for compound **10**. By extrapolation, at 30 K the lifetime is extended indefinitely.[208]

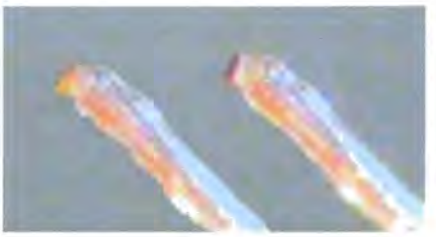

Figure 8.3: The crystal of compound **10**. There is a marked colour change associated with the spin transition and the crystal is pale yellow the high spin state (left) changing to dark red in the low spin state (right).

8.2 Single Crystal Diffraction Experiments

The crystals* were pale yellow-orange, but most did not extinguish light polarised under crossed polars. Since the quality of the crystals was generally so poor, it was thought that powder methods may be required, but after considerable searching a tiny triangular chip was broken off a larger lump. Despite the size of the fragment (0.06 × 0.05 × 0.03 mm), it could be seen to extinguish polarised light and diffracted reasonably well. Because of the size and the fact that the crystals had to be cut, it was necessary to mount the sample on a hair using oil (Figure 8.3). This was not the preferred method as data at room temperature was desired, and an initial matrix collected at 290 K did not index. However, cooling to 210 K (at 120 K/hr) yielded a matrix comparable to that given in the literature.[208]

8.2.1 Data Collection

Since the crystal was so small, data were collected using the Bruker Proteum M diffractometer (with the Bede Microsource®) fitted with the Series 700 Cryostream.[130]

*Crystals courtesy of Prof. José A. Real, Dr. M. Carmen Muñoz, Dr. Virginie Niel[187] and Ms. Ana G. Galet Domingo (Valencia).

Low Temperature Data

The crystal was cooled further from 210 K to 180 K at 120 K/hr where a full sphere of data were collected with 32 s/frame. On completion, a matrix data collection was recorded and the sample was cooled to 90 K at 120 K/hr. Another matrix collection was recorded, which gave a unit cell contraction of approximately 20 $Å^3$ (approximately 5%), suggesting the presence of a transition from high to low spin. A full sphere of data, also with 32 s/frame, was collected at 90 K. On completion the crystal was warmed to 290 K at 120 K/hr and removed from the diffractometer.

Light-Induced Excited Spin-State Trapping

The crystal was returned to the Bruker Proteum M diffractometer with the HeliX[131] in place. It was cooled to 210 K at 360 K/hr where a matrix collection yielded a similar unit cell to those collected previously. It was then cooled to 30 K at 120 K/hr where another matrix collection was in agreement with the low spin data collected at 90 K. There were already indications of a potential icing problem, so the sample was immediately irradiated for approximately 10 mins using the green laser (λ = 532 nm). Since the crystal was so tiny, it was rotated 90° every few minutes to ensure irradiation.

The matrix collection following irradiation was very poor and indexed very badly, but this was largely due to the presence of ice. Although the esds were large, the cell parameters suggested there was an increase in cell volume suggesting a SC transition had occurred. Data were collected, but due to instrument problems however, the data collection was terminated prematurely when it was less than $\frac{1}{3}$ complete.

8.2.2 Data Analysis

The data indexed very poorly, with up to one third of the reflections excluded from the unit cell refinement. However, the 180 K and 90 K data integrated well and the quality of the structure solution suggests that the rejected reflections came from a tiny secondary crystallite adhered to the primary crystal. Since the primary crystal was so small, this secondary crystallite would have been almost impossible to see. Since the larger of the crystals diffracted strongly for its size, it is understandable that diffraction from the tiny secondary crystallite was visible while the crystal was not. However, the data integrated,

solved and refined well, so it was assumed that there was little significant overlap between reflections from the two crystals.

The data were integrated in the usual manner to a resolution of 0.73 Å. The structure was solved in $P\bar{1}$ from the 90 K data using direct methods and refined accordingly. The crystal faces could not be indexed, so the absorption corrections were carried out with SADABS only.[145] Since the data collected at 30 K after irradiating contained so few reflections there were too few equivalents and SADABS could not be applied, so no absorption correction was carried out. Although the absorption coefficient for the sample (which contains copper and iron) is quite high, since the crystal was so very small and relatively isotropic in shape, it was felt that absorption effects would be minimal and would have a considerably smaller detrimental effect than some of the other problems.

8.2.3 Structure Refinement

At 180 K and 90 K all non-hydrogen atoms were refined with anisotropic displacement parameters and the hydrogen atoms were located in the difference map. Refinement of hydrogen positions led to an unrealistic model, so the hydrogens were added geometrically and refined using a riding model.

At 30 K after irradiation, refinement of anisotropic displacement parameters led to poorly shaped ellipsoids and in some cases, non-positive definite atoms, so all thermal motion was refined as isotropic. Since the structures at 180 K and 90 K refined well before absorption corrections had been applied, this was thought to result from the intrinsic quality of the data rather than an absorption effect, though it may also have been a contributing factor. Despite a relatively small amount of data (1939 unique reflections), only 106 parameters were refined as the asymmetric unit contains only twelve non-hydrogen atoms (Figure 8.4).

The program IVTON[174] was used to calculate the mean Fe–N bond lengths and the volumes for the iron octahedra in compound **10**.

8.3 Discussion

Although compound **10** was synthesised in a similar way to compounds **6** and **7**, the crystal structure is totally different, with compounds **6** and **7** monoclinic ($P2_1/c$) and

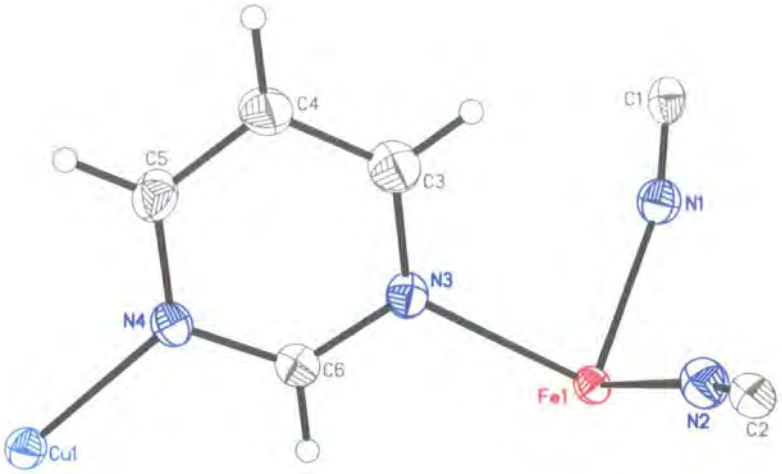

Figure 8.4: The asymmetric unit for compound **10** at 180 K, a = 6.7584(12) Å, b = 8.0796(15) Å, c = 7.9862(15) Å, α = 110.102(3)°, β = 108.500(4)°, γ = 99.272(4)°, V = 370.06(12) Å^3 ($\mathbf{P\bar{1}}$).

compound **10** triclinic ($\mathbf{P\bar{1}}$) with a cell volume that is less than a quarter of that for the silver and gold compounds. These differences are reflected in the structure and in the magnetic properties, with all compounds undergoing thermally induced transitions, but only compound **10** forming a meta-stable light induced state on irradiation at low temperature.

8.3.1 Structural Analysis

The structure consists of an octahedral iron atom and a three coordinate copper which are connected through bridging cyanide groups and Pmd ligands, forming a continuous three dimensional network.

Iron Environment

The octahedral iron centre is ligated by four $[Cu(CN)_2]^-$ ligands and two pyrimidine ligands (Pmd). The $[Cu(CN)_2]^-$ groups are arranged in a square planar geometry capped by two Pmd ligands forming an octahedron. The central iron atom sits on an inversion centre at 0 0 0 and the Fe–NC bond lengths are considerably shorter than the Fe–Pmd distances, so the iron atom occupies the centre of an elongated octahedron. The iron

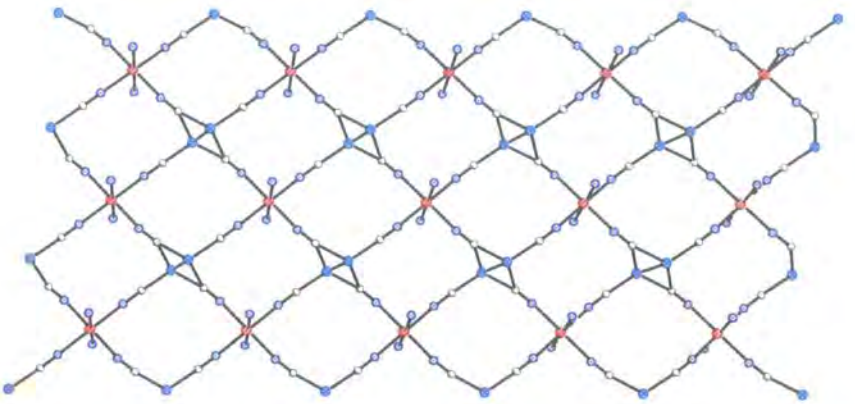

Figure 8.5: A two dimensional sheet of compound **10**.

centres together with the $[Cu(CN)_2]^-$ ligands form two dimensional sheets similar to those seen in compounds **6** and **7** (Figure 8.5). However, the second nitrogen atom of the Pmd ligand coordinates to the copper atom which is three coordinate in a pseudo trigonal planar arrangement.

Copper Atom Environment

There are effectively two types of copper coordination, the inner region and the outer region. The inner region consists of the two carbons from the cyanide groups and the Pmd nitrogen atom. These ligate the central copper atom in a distorted trigonal planar geometry with the copper sitting 0.418(1) Å out of the plane of the three coordinating atoms at 180 K. Thus the $[Cu(CN)_2]^-$ anionic ligands are bent with a N–Cu–N angle of approximately 110(3)°, dependant on the temperature.

This out of plane distortion is caused by secondary interactions between the copper atom and the atoms in the outer coordination region. A second $[Cu(CN)_2]^-$ ligand related by an inversion centre, forms a strongly bonded dimer linked by Cu–C interactions and cuprophilic interactions (Figure 8.6).

Cu···Fe Layers

The overall structure is made up of corrugated –$[Cu(CN)_2]$–Fe–$[Cu(CN)_2]$– layers which alternate with layers of Pmd ligands (Figure 8.7). The Pmd ligands form bridges be-

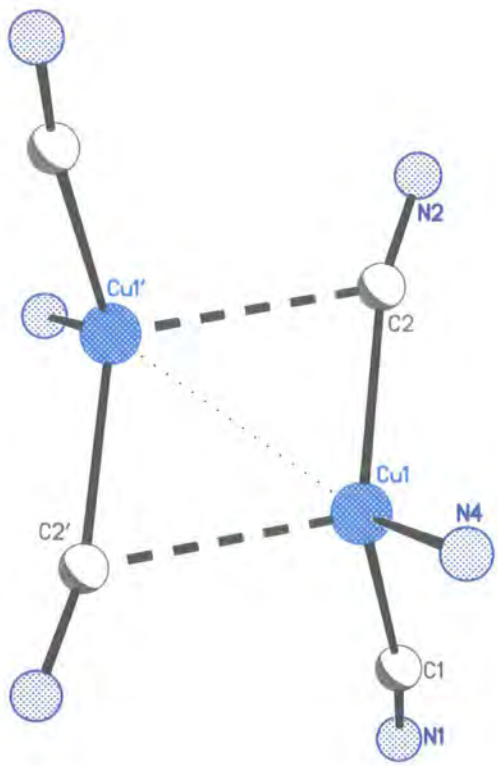

Figure 8.6: $[Cu(CN)_2]^-$ dimers showing the cuprophilic interaction with a dotted line and the Cu–C interaction as a broken line. At 180 K, this Cu–C distance is 2.334(4) Å compared with 1.935(4) Å, 1.975(4) Å and 2.065(3) Å for the inner region distances. The Cu–Cu distance is 2.5211(10) Å.

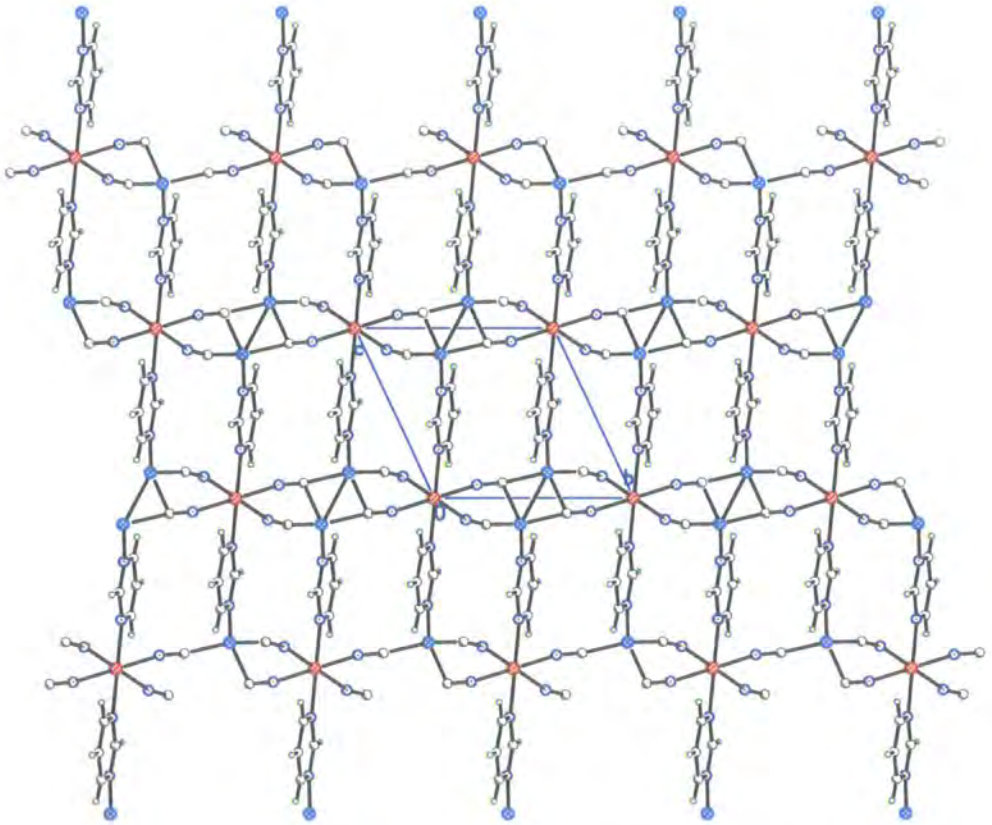

Figure 8.7: Corrugated layers in compound **10**. The cyanide ligands can be seen joining the iron and copper atoms (red and cyan respectively), leading to the formation of 'wavy' layers which are bridged by Pmd ligands.

tween the -[$Cu(CN)_2$]-Fe-[$Cu(CN)_2$]- layers, forming short Cu–Pmd–Fe–Pmd–Cu chains. These short chains are connected together by the Cu–Cu dimeric interactions, resulting in continuous chains stretching throughout the structure.

8.3.2 Spin Crossover Transitions

Between 180 K and 90 K, there is a contraction in the cell volume of over 18 $Å^3$ (nearly 5%), from 370.06(12) $Å^3$ to 352.00(11) $Å^3$. This is coupled with a change in colour (Figure 8.3) and shortening of the Fe–N bond lengths leading to a contraction of the iron octahedron.

		180 K	90 K	30 K (Irr)
$[Cu(CN)_2]^-$	Fe1–N1	2.116(4) Å	1.954(5) Å	2.127(26) Å
	Fe1–N2	2.142(4) Å	1.951(5) Å	2.167(39) Å
Pmd	Fe1–N3	2.256(4) Å	2.035(4) Å	2.260(28) Å
Average	Fe–N	2.17(7) Å	1.98(5) Å	2.18(7) Å
Octahedral Volume		13.62(2) $Å^3$	10.34(2) $Å^3$	13.87(8) $Å^3$

Table 8.1: Fe–N bond lengths for compound **10**. Although the values obtained for the LIESST structure have much larger esds, they are clearly in keeping with those obtained for the high spin state at 180 K, indicating that it too is high spin.

Bond Lengths and Octahedral Volumes

There are two distinct types of iron bond length — short Fe–N to the anionic $[Cu(CN)_2]^-$ ligands and long Fe–N to the neutral Pmd ligand. The longer Pmd bonds contract more than the $[Cu(CN)_2]^-$ bonds, but it is clear that there is also more contraction in the Fe–N2 bond than the Fe–N1 bond (Table 8.1). The octahedral volumes clearly reflect the change from high spin at 180 K to low spin at 90 K with a contraction of 3.3(4) $Å^3$.

LIESST

The data for the LIESST structure were very poor, compared with the data collected at 180 K and 90 K. Consequently, the esds are very large, making it difficult to infer any concrete results. However, there is a change in cell volume back to the high spin state on irradiation (volume = 371(6) $Å^3$), which is coupled with a clear change in the Fe–N bond lengths to values consistent with those seen at 180 K, indicating that the high spin state has been trapped by irradiation with light (Table 8.1).

Fe···Cu Distances

There are three unique, short Fe···Cu distances, two through cyanide bridging groups and one through the Pmd ligand, which as would be expected, is the longest (Table 8.2). The two cyanide Fe···Cu distances are noticeably separated by approximately 0.1 Å, a difference that occurs at all temperatures. The shorter of these Fe···Cu distance is via N1 and C1 (CN1). Close inspection of this ligand indicates that it is markedly more bent with

		180 K	90 K	30 K, Irr.
Fe···Cu	CN1	5.078(1) Å	4.974(1) Å	5.10(6) Å
	CN2	5.183(1) Å	5.007(1) Å	5.22(9) Å
	Pmd	5.862(2) Å	5.778(2) Å	5.86(12) Å
Fe–N–Cu	N1	158.3(2)°	163.9(2)°	157.5(7)°
	N2	166.2(2)°	165.5(2)°	166.7(5)°

Table 8.2: Fe···Cu distances and angles for compound **10**. Although the values obtained for the LIESST structure have much larger esds, they are clearly in keeping with those obtained for the high spin state at 180 K.

an Fe1–N1–Cu1 angle of 158.27(15)° compared with the Fe1–N2–Cu1 angle of 166.26(14)°, a difference that explains the difference in Fe···Cu distances.

Cooling through the spin transition leads to the expected shortening of all three Fe···Cu distances. However, it is notable that the CN1 Fe···Cu distance only shortens ~0.1 Å, compared with the ~0.2 Å for the CN2 Fe···Cu distance, bringing the Fe···Cu distances closer together (4.974(1) Å and 5.007(1) Å at 90 K). Comparing the Fe–N–Cu angles show that this is caused by a linearisation of the CN1 bridge, with the difference in angles reduced to only ~1.5° (compared with ~8.0° at 180 K).

The Pmd Fe···Cu distance also shortens less than the expected 0.2 Å with the spin transition. This is not surprising however, when it is considered that the contraction is along the Fe–N3 bond and has a component at right angles to the Fe···Cu direction (Figure 8.8). It is important to note however, that although the values for this and the Fe···Cu distances in the LIESST structure are clearly in keeping with those obtained for the high spin state at 180 K, the large esds mean it is not possible to infer anything further.

Fe···Fe Distances

There are four inequivalent Fe···Fe distances within the structure — two that could be described as *trans* with respect to the copper, and two that could be described as *cis* (Figure 8.9). The two *trans* distances are significantly longer than the two *cis* distances and *trans* A and *cis* A are longer than *trans* B and *cis* B (Table 8.3). *Trans* A contains two CN1 bridges while *trans* B contains two CN2 bridges. Although CN1 is shorter than

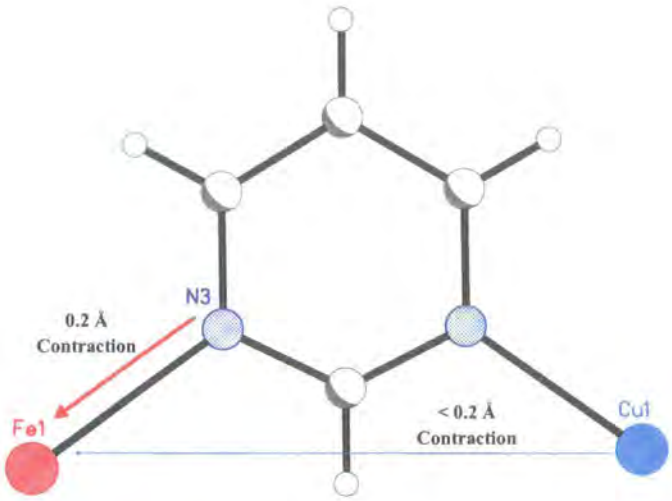

Figure 8.8: Fe1–N3 bond length contraction. The Fe1–N3 contraction is marked in red and the Fe1···Cu1 distance in cyan. The contraction in the Fe1–N3 bond of approximately 0.2 Å due to the spin transition, leads to a reduced contraction in the Fe1···Cu1 distance because the Fe1–N3 bond has a component perpendicular to the Fe1···Cu1 direction.

CN2, *trans* A is longer than *trans* B because *trans* B includes two copper atoms. On the other hand both *cis* A and *cis* B include CN1 and CN2 moieties, so the difference in Fe···Fe distance is caused by the geometry around the central copper atoms.

On cooling to the low spin state at 90 K, there is a shortening of ~0.20–0.25 Å in the *trans* Fe···Fe distances. The contraction in *trans* B is less than in *trans* A because the CN1 group becomes more linear in the low spin state. This effect is enhanced by the fact that the *trans* A distance includes two CN1 groups.

There is a much more marked contraction in the *cis* A Fe···Fe distance (nearly 0.4 Å), which is in contrast to the *cis* B Fe···Fe distance which undergoes a very small expansion of ~0.1 Å. This difference is caused by a combination of effects. In the case of the *cis* A Fe···Fe distance, the contraction is increased by a reduction in the C1–Cu1–C2A angle by nearly 3°. This change in the copper centre is subtle, but can probably be best seen by over laying the high and low spin copper dimers (Figure 8.10).

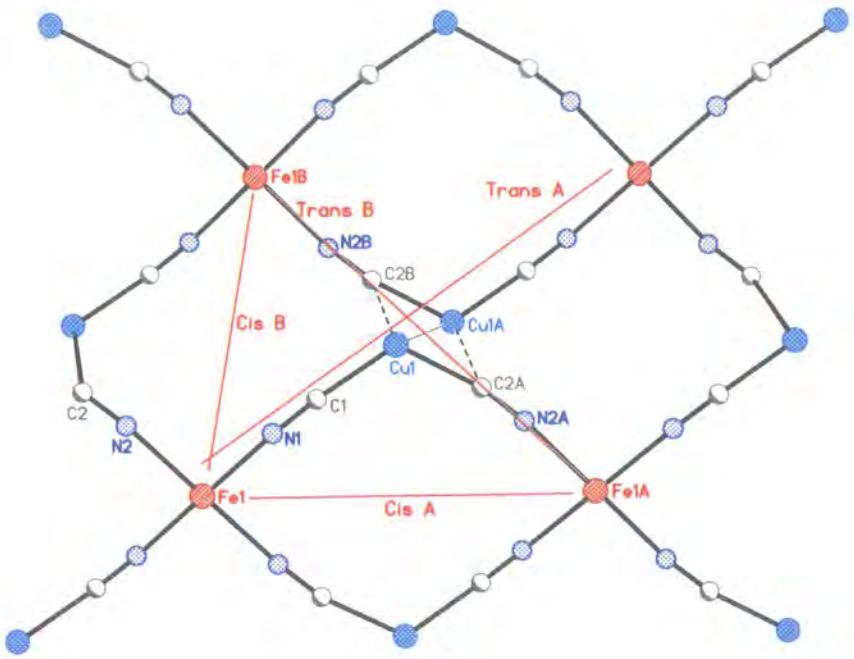

Figure 8.9: Fe···Fe distances.

		180 K	90 K	30 K, Irr.
Fe···Cu	*Trans* A	11.338(2) Å	11.075(2) Å	11.35(12) Å
	Trans B	9.662(2) Å	9.466(2) Å	9.70(13) Å
	Cis A	8.080(2) Å	7.701(2) Å	8.15(11) Å
	Cis B	6.758(2) Å	6.843(2) Å	6.71(3) Å
C–Cu1–C	C1/C2A	118.6(2)°	115.8(2)°	119.1(10)°
	C1/C2B	102.0(2)°	101.2(2)°	100.9(10)°
Cu1–C2B		2.334(5) Å	2.342(6) Å	2.33(2) Å

Table 8.3: Fe···Fe distances and C–Cu–C angles for compound **10**. Although the values obtained for the LIESST structure have much larger esds, they are clearly in keeping with those obtained for the high spin state at 180 K.

Figure 8.10: Overlay of the copper dimer at 180 K and 90 K. The high spin, 180 K structure is shown with dotted open circles and bonds drawn with a broken line. A subtle change in the orientation of the $[Cu(CN)_2]^-$ groups can clearly be seen.

8.4 Conclusion

The structure of compound **10** is very different from the silver and gold counterparts (compounds **6** and **7**) discussed previously. In this case, despite poor crystal quality and instrumentation problems, it has been clearly shown that the material undergoes spin crossover, under both thermal stimulus and on irradiation with green light, in keeping with the magnetic data reported.[208]

Structural changes that occur during the spin transition include a straightening of one cyanide group of the $[Cu(CN)_2]^-$ ligand, together with changes in the central C–Cu–C angle. These affect both the bond lengths and the change in bond lengths around the iron atom.

Given the difference between this compound and the silver and gold compounds, obviously the nature of the central atom in the $[Cu(CN)_2]^-$ ligand is critical to both the structure and the magnetic properties. In this case, subtle changes around the copper atom are integral to the transition.

Chapter 9

Cooperativity in an Intricate Iron(II) Network

9.1 Introduction

{Fe(Pmd)[$Ag(CN)_2$][$Ag_2(CN)_3$]} (compound **11**) was isolated as small, pale yellow needles from the reaction mixture that produced compound **7**.

9.1.1 Magnetic, Calorimetric and Absorption Data

Like compound **7**, compound **11** also undergoes spin crossover,[209] but magnetic, calorimetric and absorption data indicate that like the structure, the magnetic behaviour is more complex than that of compound **7**.

Magnetic Susceptibility Data

SQUID magnetic susceptibility data collected on small single crystals (20–30 mg) indicate that the transition has a step (Figure 9.1).[210] In addition to the step, photomagnetic studies indicate that the compound undergoes Light-Induced Excited Spin-State Trapping (LIESST). The sample was cooled to 10 K where it was irradiated with green light (550 nm) for 150 min, the time required to reach the saturation value of $\chi_M T = 1.70$ cm^3K/mol. The sample was then cooled to 2 K and then increased up to 200 K at 0.5 K/min where the magnetic susceptibility was measured as a function of temperature on warming.

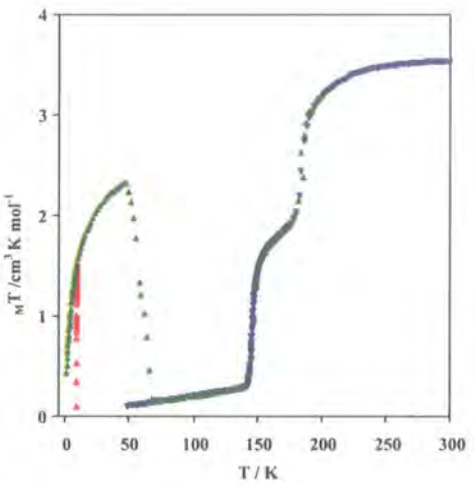

Figure 9.1: Magnetic susceptibility data for compound **11**.[209] The data indicate that the transitions take place at 185 K and 146 K on cooling (▼). Irradiating with a xenon lamp (▲) yields the meta-stable high spin LIESST state which reverts to low spin by 60 K thence following the cooling curve (▲).

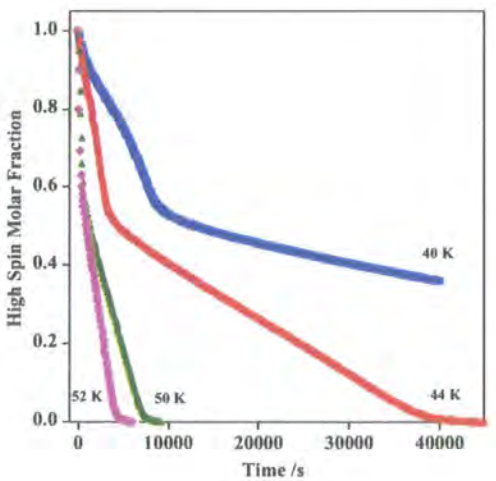

Figure 9.2: Time dependence of the high spin meta-stable state for compound **11**.[209] The relaxation is clearly a two step process with the first step more rapid than the second step. The lifetime of the meta-stable is considerably longer as the temperature is reduced.

From the magnetic susceptibility data, the relaxation temperature for the meta-stable state is between 50 K and 70 K after which there is a return to low spin. On further warming, the magnetic susceptibility data suggest the sample returns to the high spin state along the same path via the step. There is a narrow hysteresis loop (approximately 1.5 K) for the low-temperature step and the critical temperatures are 146 K on cooling and 147.5 K on warming. However, there is no appreciable thermal hysteresis for the high-temperature step.

Relaxation studies on the LIESST state show the occurrence of two relaxation processes, suggesting that there are two distinct iron(II) groups that relax at different rates and are characterized by different relaxation constants.

Differential Scanning Calorimetry (DSC)

Calorimetric measurements performed using a differential scanning calorimeter in the 120–300 K temperature range indicate the occurrence of two peaks — one for each step (T_c1 = 185.2 K and T_c2 = 147.7 K), which correspond with those obtained from the magnetic susceptibility data.[210] The temperature dependence of the anomalous heat capacity shows the presence of these two peaks very clearly (Figure 9.3). The overall enthalpy and entropy variations ΔH = 8.4 kJ mol^{-1} and ΔS = 53 J K^{-1} mol^{-1}, are within the experimental range observed for iron(II) SC compounds.[43]

Visible Absorption Spectroscopy

Visible absorption spectra were recorded between 450–750 nm using a spectrometer equipped with a CCD camera and light from a 50 W tungsten halogen source on a 21 μm thick crystal. The results indicate a band at approximately 525 nm that grows in intensity as the temperature is lowered. There is also an increase in the intensity just below ~500 nm so that the increase in intensity at ~525 nm appears as a shoulder. Variable temperature spectra were recorded on cooling and warming (Figure 9.4) and the HS molar fraction, was determined from the relative intensity of the absorption band characteristic of the LS state (Figure 9.5).

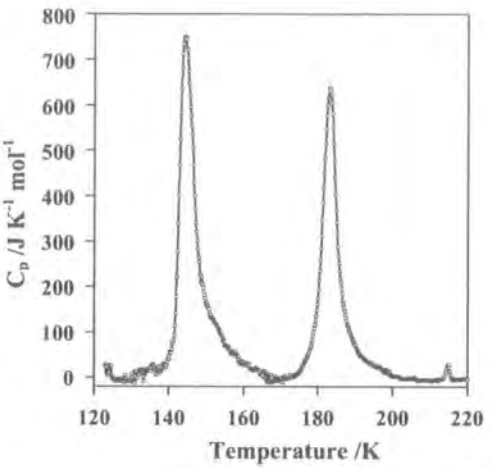

Figure 9.3: Heat Capacity data for compound **11**, showing the two peaks corresponding to the two steps of the transition, $T_c1 = 185.2$ K and $T_c2 = 147.7$ K.[209] The small peak at 218 K is due to a small degree of contamination caused by the presence of a minute quantity of compound **7**.

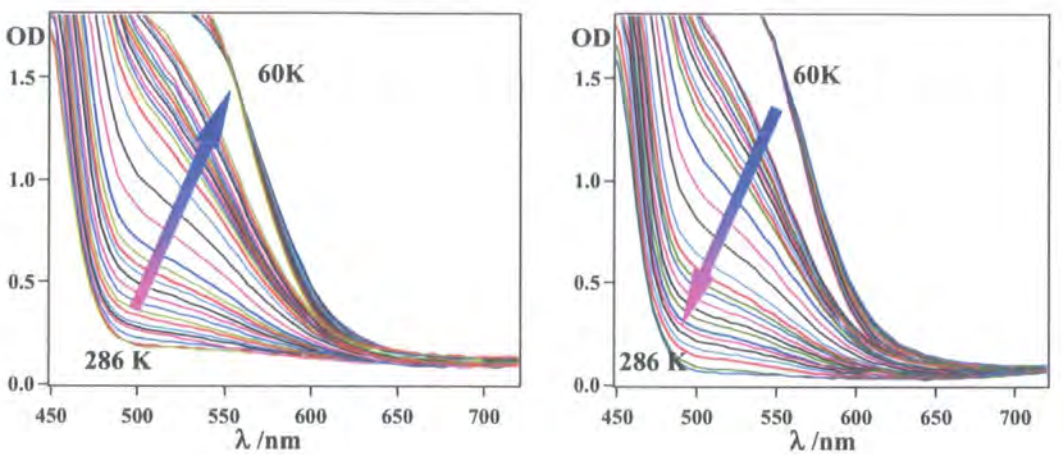

Figure 9.4: Variable temperature visible absorption spectra.[209] Data recorded on warming and cooling (left and right respectively), show the increase in intensity of the absorption bands at approximately 525 nm and below 500 nm indicative of the LS state.

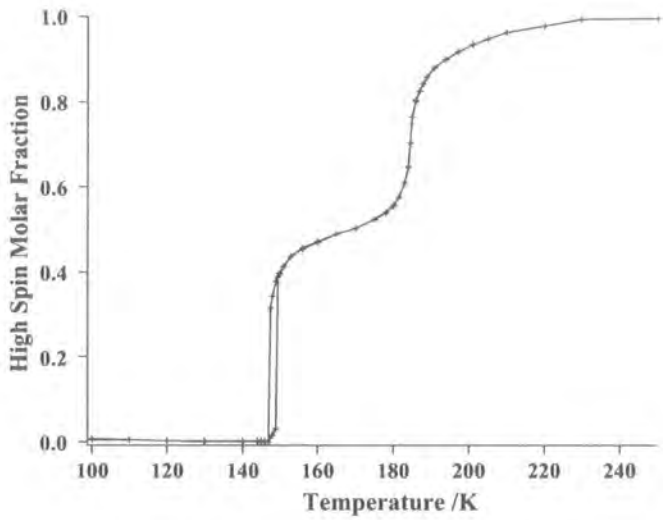

Figure 9.5: Temperature dependence of the high spin molar fraction determined from visible absorption spectroscopy, using the relative intensity of the absorption band characteristic of the LS state.[209] The hysteresis in the more abrupt low temperature step can be seen clearly.

9.2 Single Crystal Diffraction Experiments

The crystals* were small, yellow, flattened needles, but were all non-merohedral twins and this is reflected in the R-indices, which are high because the structure was refined using data for the major component only. The changes in the Fe–N bond lengths and octahedral volumes are still clearly visible however, and the fascinating nature of the material means that the insight gained from even twinned data is extremely valuable.

9.2.1 Data Collection

Single crystal data were initially collected using the Bruker SMART-CCD 6000 with an Oxford Cryosystems Cryostream 600,[130] but low temperature data were collected on the Bruker SMART-CCD 1000 with an Oxford Cryosystems HeliX.[131]

*Crystals courtesy of Prof. José A. Real, Dr. M. Carmen Muñoz, Dr. Virginie Niel[187] and Ms. Ana G. Galet Domingo (Valencia).

Variable Temperature Data

A typical crystal ($0.26 \times 0.10 \times 0.02$ mm) was selected and mounted on the Bruker SMART-CCD 6000. A matrix collection at 290 K indexed with a monoclinic unit cell with a volume of 6263(1) Å^3, so a full sphere of data were collected at 30 s/frame. On completion, the crystal was cooled at 120 K/hr to 220 K, where a matrix was collected. The crystal was then cooled to 170 K at 120 K/hr and a colour change from yellow to red was observed between 190 K and 180 K (Figure 9.6). At 170 K, a matrix indicated a contraction of over 3.5% to 6033(1) Å^3, so a full sphere of data was collected as at 290 K.

On completion, the crystal was cooled to 90 K at 120 K/hr during which the colour appeared to have deepened to a subtly darker shade of red. A matrix collection indicated a cell of 5775(1) Å^3, suggesting a further contraction of approximately 4% (based on the cell at 290 K). A sphere of data was recorded at 90 K as at the higher temperatures.

On completion, the crystal was warmed to 220 K and monitored for colour change. At 180 K the crystal was red, but by 190 K the crystal had changed back to yellow, with a pale red colour at 185 K. At 220 K, a matrix was collected that indicated a return to the high temperature state, where a fourth data collection was carried out (as before). After the data collection was complete, the crystal was warmed to 290 K, and removed from the instrument.

Light-Induced Excited Spin-State Trapping

The crystal was mounted on the Bruker SMART-CCD 1000 by flash cooling it to 230 K. It was then cooled at 100 K/hr to 30 K using the Oxford Cryosystems HeliX.[131] A matrix was collected at 30 K giving a unit cell volume of 5767(1) Å^3. This was followed by a collection of a hemisphere of data (30 s/frame). Unfortunately, the data collection was stopped during the experiment to set up the laser and in the process the crystal was irradiated briefly. A matrix collection confirmed that the unit cell volume had increased, so the crystal was irradiated for a further $2\frac{1}{2}$ hr using a red He-Ne laser (15 mW, $\lambda = 633$ nm). A matrix collection after irradiation indicated a return to the high temperature state with a unit cell volume of 6253(1) Å^3, so a hemisphere of data was collected as before.

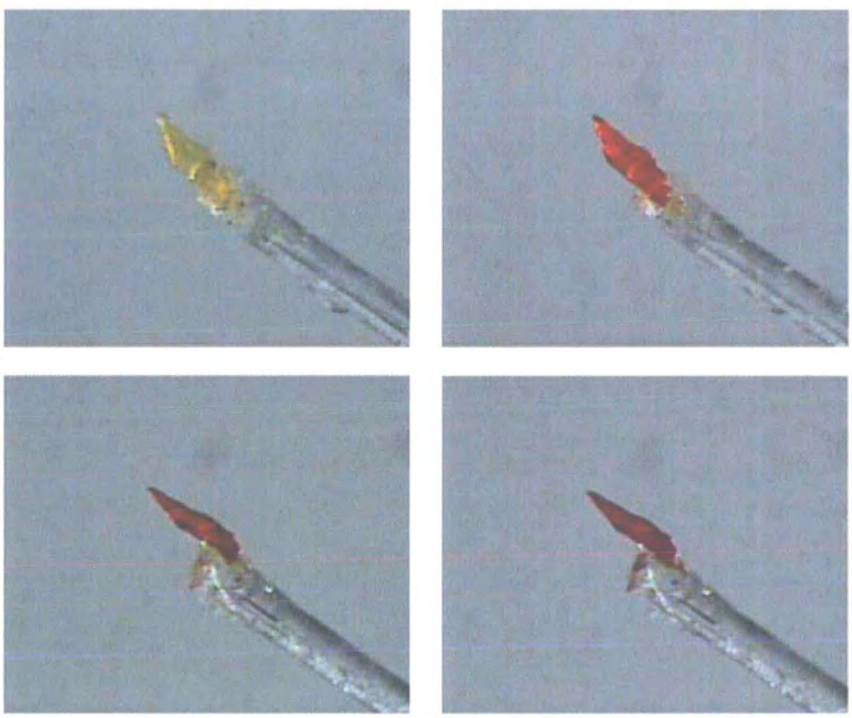

Figure 9.6: A crystal of compound **11** on cooling. The crystal is shown at 220 K (top left), 170 K (top right and bottom left) and 90 K (bottom right).

9.3 Data Analysis

While crystals of this compound are not very difficult to obtain they were apparently all twinned. The crystal used was also a non-merohedral twin, so the results are from structure refinements carried out against data from the main component with overlapping contamination of the second twin component in many of the reflections. Although efforts to use GEMINI[147] indexed the second component satisfactorily, refinement results were considerably worse. For this reason, the R-indices are high, there are large residual peaks and the esds are larger than would normally be the case. However, the structural changes are still clearly visible.

9.3.1 Structure Refinement

Cell parameters were determined and refined and the raw frame data were integrated in the usual fashion. The structures were solved using direct methods and refined by full-matrix least squares on F^2 using SHELXTL software.

Since the faces had been indexed, the data were corrected for absorption effects accordingly. Except for the data collected at 30 K, all non-hydrogen atoms were refined with anisotropic atomic displacement parameters, and hydrogen atoms were positioned geometrically and refined using a riding model.

Data collected at 30 K

Due to the premature irradiation of the crystal during the 30 K data collection there was a shortage of data, so the structure was refined with anisotropic displacement parameters for only the silver atoms, which were constrained together. In addition, the isotropic thermal parameters for groups of atoms were constrained to a single value. For example, all the thermal parameters for the cyanide nitrogen atoms were constrained to a single value, as were the thermal parameters for the cyanide carbon atoms.

The crystal quality deteriorated after irradiating the crystal, so only the metal atoms were refined with anisotropic displacement parameters. Thus, the carbon and nitrogen atoms were refined with isotropic displacement parameters, but further constraints were not necessary. For both 30 K structures, the hydrogen atoms were positioned geometrically and refined using a riding model.

The program IVTON[174] was used to calculate the mean Fe–N bond lengths and the volumes for the iron octahedra in compound **11**.

9.4 Discussion

No change in symmetry was observed and at all temperatures the structure is monoclinic ($\mathbf{P}2_1/c$), with five iron centres in the asymmetric unit (Figure 9.7). Despite the poor quality of the data which increases the esds, the spin transitions are clearly visible from the crystal structure results.

9.4.1 Structural Analysis

Like compounds **6**, **7**, **8**, **9** and **10**, the iron atoms are ligated by two apical pyrimidine rings and four equatorial cyanide ligands. Like compounds **7** and **9**, the cyanide ligands form part of silver cyanide bridges, but in this material, compound **11**, there are two different types. Both groups approximate to linear, but $[Ag_2(CN)_3]^-$ units (L_l) are approximately $1\frac{1}{2}$ times longer than the $[Ag(CN)_2]^-$ units (L_s). The five different iron centres include four different chemical environments. One iron centre is ligated by three L_l and one L_s and one is ligated by one L_l and three L_s. The other three iron centres are ligated by two of each, but one is in a *cis* conformation and the remaining two are in a *trans* conformation (Figure 9.8).

The 3D Network

The structure consists of iron layers and silver cyanide layers perpendicular to the x direction. Within the iron layers the iron centres are bridged by Pmd ligands, which lie flat within the iron planes forming chains within the layers. The silver cyanide groups form bridges between the iron centres in the different layers (Figure 9.9).

The crystal structure forms an intricate three dimensional network, with knots that are defined by the five crystallographically inequivalent iron atoms, which lie at the center of strongly distorted $[FeN_6]$ coordination units. These five crystallographically inequivalent iron centres are interconnected in a very complex way.

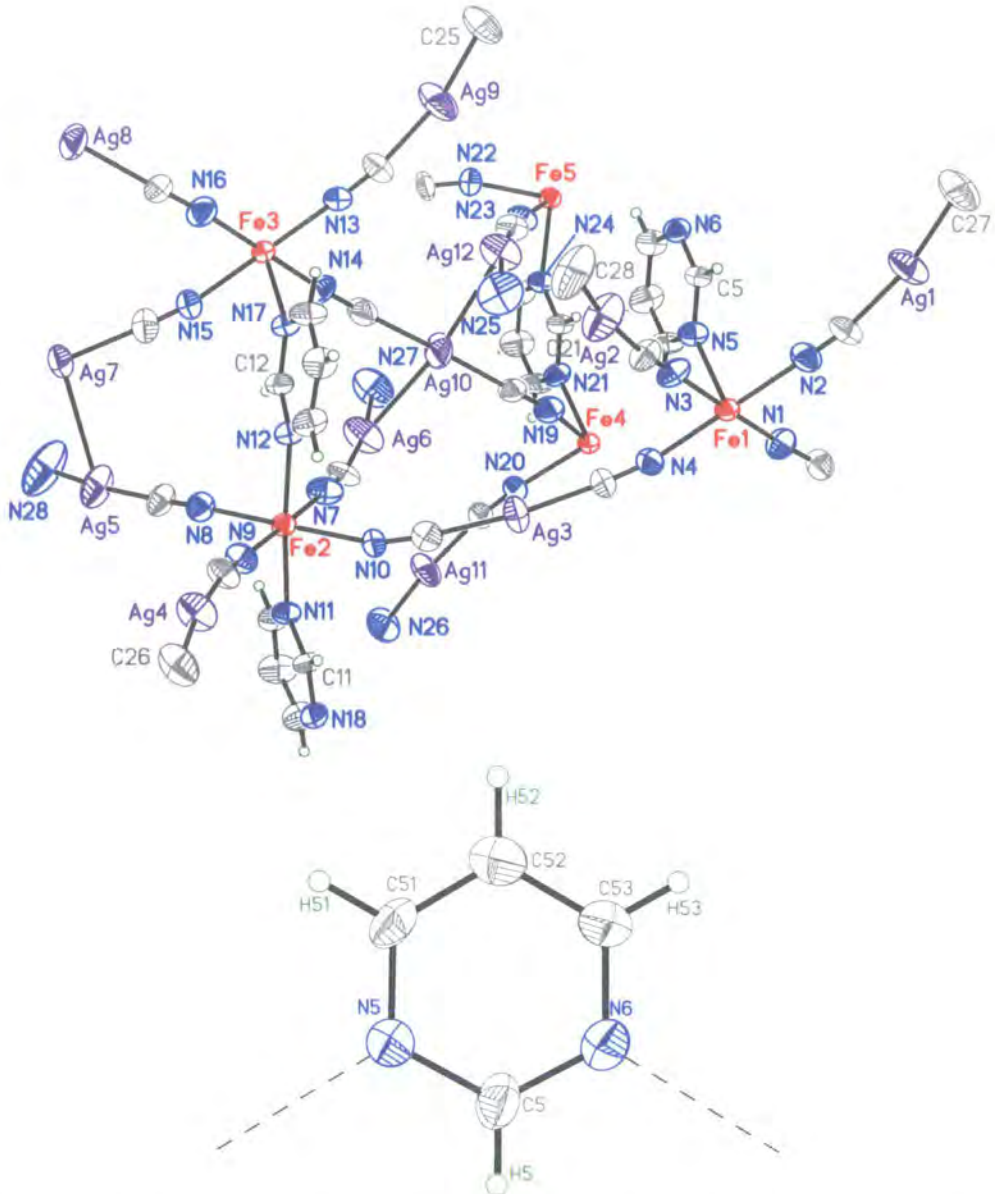

Figure 9.7: The asymmetric unit for compound **11** at 290 K (Top), $a = 6.7584(12)$ Å, $b = 8.0796(15)$ Å, $c = 7.9862(15)$ Å, $\alpha = 110.102(3)°$, $\beta = 108.500(4)°$, $\gamma = 99.272(4)°$, $V = 370.06(12)$ Å^3 ($\mathbf{P2_1/c}$). Only selected atoms are labelled because the structure is so complex. Cyanide carbon atoms have generally been labelled with the same number as their neighbouring nitrogen atom and the Pmd carbon atoms are labelled after the carbon atom between the two nitrogen atoms (bottom). Thus in this case, the rings are labelled after C5 (C51, C52 and C53), beginning at the side with the nitrogen atom with the lowest number (N5).

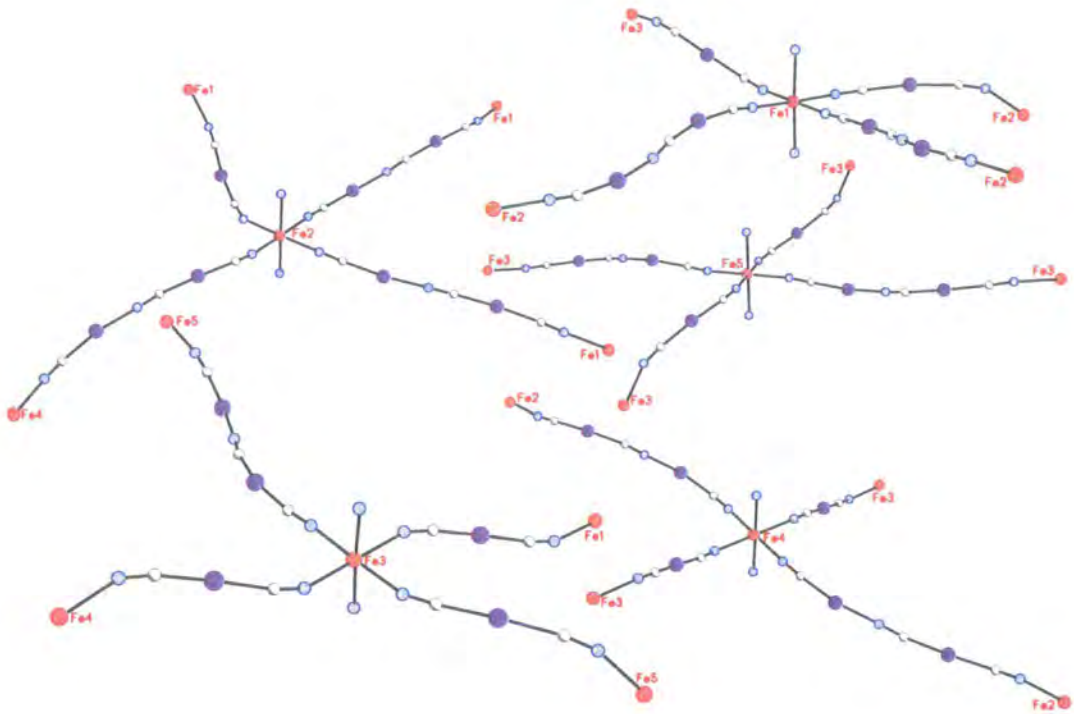

Figure 9.8: The environment around the five different iron centres.

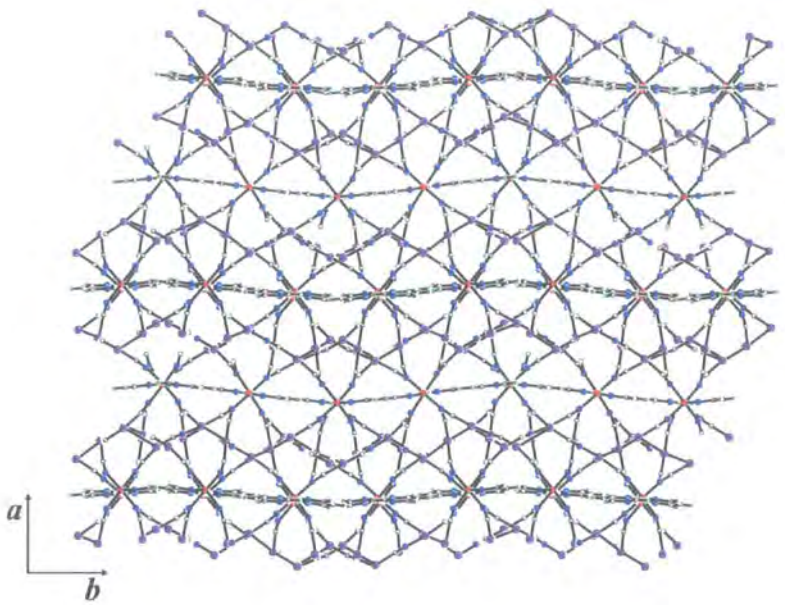

Figure 9.9: Layers within compound **11**. Silver is shown in purple and iron in red. The alternating layers connected by cyanide ligands can be seen.

Anionic $[Ag(CN)_2]^-$ and $[Ag_2(CN)_3]^-$ Ligands

The anionic groups $[Ag(CN)_2]^-$ and $[Ag_2(CN)_3]^-$, are defined by twelve crystallographically different silver atoms and all are close to linear.

Through the $[Ag(CN)_2]^-$ and $[Ag_2(CN)_3]^-$ groups (L_s and L_l), Fe1 connects to one equivalent of Fe3 via L_s and three equivalents of Fe2 (one via L_s and two via L_l). In turn: Fe2 connects once to Fe4 (L_l) and three times to Fe1 (one L_s and two L_l), Fe3 connects once to each Fe1 and Fe4 (both through L_s) and twice to Fe5 (one L_l, one L_s); Fe4 connects twice to Fe2 (both L_l) and twice to Fe3 (both L_s) and lastly Fe5 connects solely to Fe3 (two via L_s and two via L_l).

The equatorial bond lengths defined by the nitrogen atoms of the $[Ag(CN)_2]^-$ and $[Ag_2(CN)_3]^-$ groups are shorter than those of the axial positions occupied by the nitrogen atoms of the Pmd groups, which act as bridging ligands between the layers.

–[Fe–Pmd–Fe]$_\infty$– Chains

The Pmd bridges and the iron atoms form –[Fe–Pmd–Fe]$_\infty$– chains running along the *c*-axis. There are three different types of these chains in the structure. One is formed by all Fe1 iron atoms (with Fe1$\cdots$Fe1 = 6.150(1) Å at 290 K), and the others are formed by pairs of inequivalent iron atoms alternating along the chain (Fe2$\cdots$Fe3 = 6.177(2) Å and 6.154(1) Å and Fe4$\cdots$Fe5 = 6.150(1) Å, Figure 9.10).

Fe1 and Fe4$\cdots$Fe5 chains alternate along the *b*-axis, defining a two dimensional array of iron atoms lying in the *bc*-plane. A similar 2D array of iron atoms is defined by the Fe2$\cdots$Fe3 chains and these two different layers alternate along the *a*-axis (Figure 9.10). These layers formed by the different –[Fe–Pmd–Fe]$_\infty$– chains are organised in such a way that chains in consecutive layers are shifted along the *b*-axis by approximately half of the inter-chain separation (around 3.55 Å). The different iron layers are separated by layers of Ag atoms in which strong closed-shell argentophilic type interactions are observed. The shortest Ag$\cdots$Ag distances between $[Ag(CN)_2]^-$ and $[Ag_2(CN)_3]^-$ are in the range 2.99–3.02 Å (Tables 9.3 and 9.4) and are only slightly longer than in metallic silver (2.89(1) Å).[211]

9.4.2 Spin Transitions

Following the Fe–N bond lengths at different temperatures can give a key insight into cooperativity within the crystal.

Fe–N Bond Lengths and Octahedral Volumes

At 290 K, the shorter average equatorial Fe–N distances are all 2.14–2.15 Å while the longer average axial distances are 2.21–2.23 Å (Table 9.1). At 220 K, there is only a 0.4% decrease in the cell volume and the Fe–N distances change little. However, it is noticeable that while they are all still clearly high spin from the magnetic susceptibility data, both types of Fe–N distances are appreciably shorter for Fe5 than for the other four iron atoms.

Cooling still further to 170 K gives a sharp contraction of the cell (around 3.3%) accompanied by a marked change in colour from pale yellow to red (Figure 9.6), indicating that a spin transition has taken place. This colour change corresponds with a shortening of the Fe–N bonds around Fe3 and Fe5, consistent with a transition to the low spin state

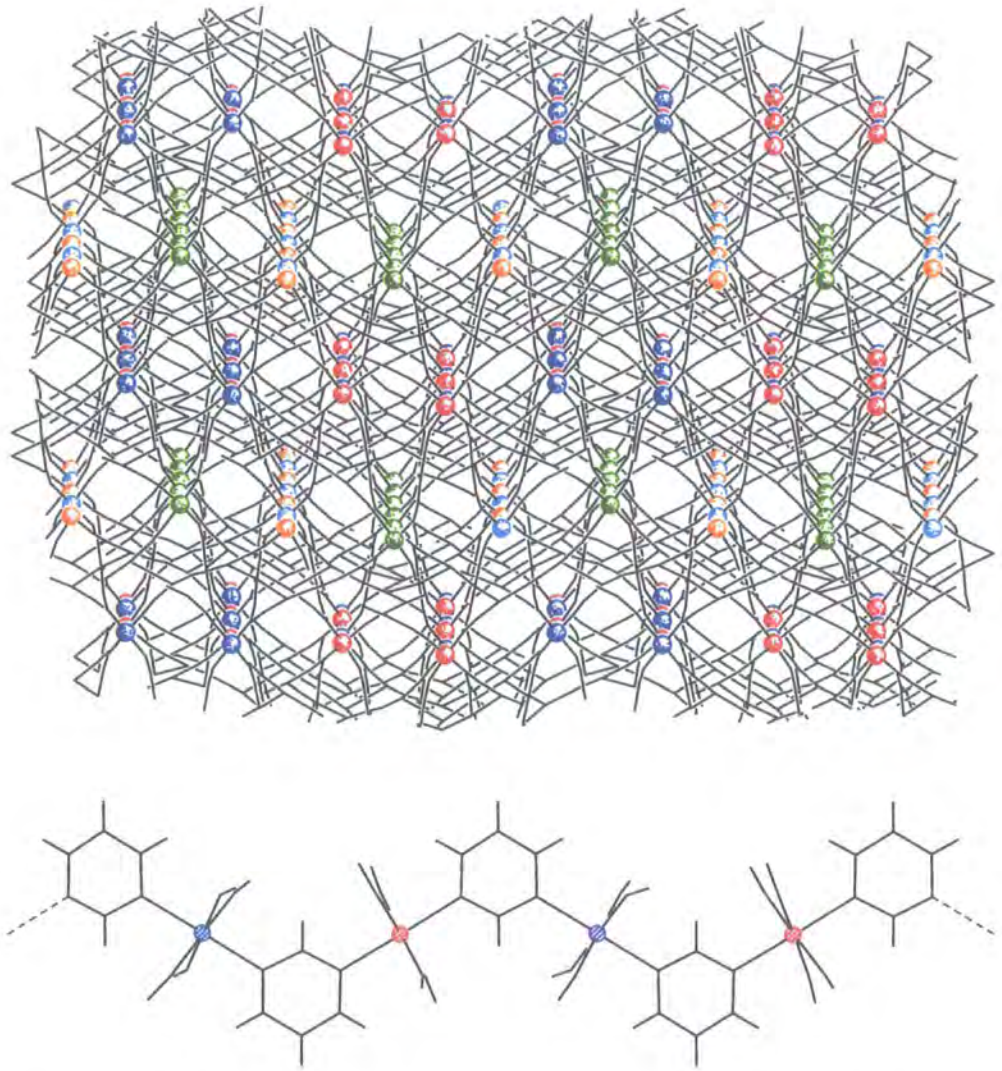

Figure 9.10: $-[Fe–Pmd–Fe]_{\infty}-$ chains in compound **11**. Three types of $-[Fe–Pmd–Fe]_{\infty}-$ chains can be seen running along the *c*-axis. Fe1 is shown in green, Fe2 in red, Fe3 in blue, Fe4 in cyan and Fe5 in orange. The Pmd rings are omitted and the silver cyanide ligands are shown as a black line for clarity. An example of a $-[Fe–Pmd–Fe]_{\infty}-$ chain is also shown.

for these iron atoms (i.e. approximately 0.2 Å).

Meanwhile, the Fe1 Fe–N distances are now intermediate. Since diffraction techniques see an average structure, this would seem to suggest that half of the Fe1 atoms change from high to low spin. If this change was ordered with alternating HS and LS iron centres super lattice peaks caused by a doubling of the *c*-axis should have been visible in the raw data. Although these were not seen, the raw data was not of the highest quality due to the presence of the non-merohedral twinning. In addition, the superstructure reflections arising from this doubling would be very weak and may not be visible, so the presence of an alternating chain of –HS–LS–HS– Fe1 ions cannot be discarded. However, a random distribution of half of these ions in different spin states within the crystal could produce strain which would lead to the deterioration in crystal quality, which was not observed.

The presence of two high spin, two low spin and one split HS–LS is in keeping with the magnetic susceptibility data, which indicates that there is a total half-spin conversion in the sample at 170 K.

On cooling to 90 K, there is a further contraction of 4.1% together with a corresponding darkening of the crystal colour indicating a further HS→LS transition. This is confirmed by the changes in Fe–N bond lengths, which indicate that all five iron centres have now become low spin.

Comparing the octahedral volumes for each iron centre at the different temperatures shows the same trend seen from following the bond lengths, but more clearly (Table 9.2). At first, the Fe5 octahedral volume decreases from 13.18(5) $Å^3$ to form an intermediate centre (12.11(5) $Å^3$). Then at the plateau at 170 K, Fe5 and Fe3 are low spin with Fe1 in an intermediate state (9.84(5) $Å^3$, 10.33(5) $Å^3$ and 11.56(5) $Å^3$ respectively). Finally, at 90 K and 30 K all iron centres are low spin.

On cooling from 90 K to 30 K, there is virtually no further change in the Fe–N distances or octahedral volumes, indicating that the spin transition is complete at 90 K. After irradiation with red laser light, there is a change in the unit cell volume of around 7.8% coupled with a colour change from red to yellow, indicating the presence of a low spin to high spin transition. This is also seen in the Fe–N bond lengths, which indicate that Fe1 to Fe4 are now high spin. Interestingly, Fe5 remains low spin (Table 9.1).

		Fe1	Fe2	Fe3	Fe4	Fe5
290 K	Equatorial Fe–N	2.14(3) Å	2.14(2) Å	2.15(2) Å	2.15(1) Å	2.12(1) Å
	Axial Fe–N	2.23(1) Å	2.23(1) Å	2.22(1) Å	2.22(1) Å	2.21(1) Å
220 K	Equatorial Fe–N	2.14(1) Å	2.14(2) Å	2.14(2) Å	2.14(2) Å	2.06(1) Å
	Axial Fe–N	2.21(1) Å	2.23(1) Å	2.20(1) Å	2.24(1) Å	2.15(1) Å
170 K	Equatorial Fe–N	2.04(3) Å	2.13(2) Å	1.96(2) Å	2.12(2) Å	1.93(2) Å
	Axial Fe–N	2.09(2) Å	2.23(2) Å	2.00(2) Å	2.22(2) Å	1.99(2) Å
90 K	Equatorial Fe–N	1.95(1) Å	1.94(1) Å	1.94(2) Å	1.94(2) Å	1.92(1) Å
	Axial Fe–N	2.00(1) Å	2.00(1) Å	1.98(2) Å	2.01(1) Å	2.02(1) Å
30 K	Equatorial Fe–N	1.94(3) Å	1.95(2) Å	1.94(2) Å	1.95(2) Å	1.93(1) Å
	Axial Fe–N	2.00(2) Å	1.99(2) Å	1.98(2) Å	2.01(2) Å	2.02(1) Å
30 K	Equatorial Fe–N	2.15(2) Å	2.13(2) Å	2.13(2) Å	2.13(1) Å	1.93(2) Å
(Irr.)	Axial Fe–N	2.20(1) Å	2.24(1) Å	2.19(1) Å	2.26(1) Å	2.01(1) Å

Table 9.1: Average Fe–N bond lengths for the five iron centres. Low spin iron distances are shown in blue, with intermediate Fe–N distances highlighted in red.

	Fe1	Fe2	Fe3	Fe4	Fe5
290 K	13.55(5) Å^3	13.53(5) Å^3	13.54(5) Å^3	13.71(5) Å^3	13.18(5) Å^3
220 K	13.43(5) Å^3	13.51(5) Å^3	13.34(5) Å^3	13.57(5) Å^3	12.11(5) Å^3
170 K	11.56(5) Å^3	13.41(5) Å^3	10.13(5) Å^3	13.26(5) Å^3	9.84(5) Å^3
90 K	10.00(5) Å^3	10.02(5) Å^3	9.94(5) Å^3	9.97(5) Å^3	9.81(5) Å^3
30 K	10.07(5) Å^3	10.03(5) Å^3	9.88(5) Å^3	10.14(5) Å^3	9.98(5) Å^3
30 K (Irr.)	13.47(5) Å^3	13.54(5) Å^3	13.25(5) Å^3	13.67(5) Å^3	10.02(5) Å^3

Table 9.2: Iron octahedral volumes.

–[Fe–Pmd–Fe]$_\infty$– Chains

There are three types of –[Fe–Pmd–Fe]$_\infty$– chains — Fe1$\cdots$Fe1, Fe2$\cdots$Fe3 and Fe4$\cdots$Fe5. At room temperature, the Fe$\cdots$Fe distances are very similar: Fe1$\cdots$Fe1 = 6.150(1) Å, Fe2$\cdots$Fe3 = 6.177(2) Å and 6.154(1) Å and Fe4$\cdots$Fe5 = 6.150(1) Å.

On cooling to 220 K, all Fe$\cdots$Fe distances shorten by approximately 0.2 Å, but cooling further to the step at 170 K shows a difference in the behaviour of the Fe$\cdots$Fe chains.

At 170 K, the average Fe2$\cdots$Fe3 distance (5.978(15) Å) is longer than both the Fe1$\cdots$Fe1 and Fe4$\cdots$Fe5 distances (both 5.965(1) Å). However, this is because one Fe2$\cdots$Fe3 distance is 0.03 Å longer (5.993(4) Å), while the other is in keeping with those for Fe1$\cdots$Fe1 and Fe4$\cdots$Fe5 (5.963(4) Å). On cooling to 90 K this distinction is lost, with all four chains within a range of 0.006 Å (Fe1$\cdots$Fe1 = 5.786(6) Å, Fe2$\cdots$Fe3 = 5.805(5) Å and 5.780(5) Å and Fe4$\cdots$Fe5 = 5.784(6) Å).

Irradiating leads to a further change, with one longer Fe2$\cdots$Fe3 distance (6.137(5) Å) compared with the other Fe$\cdots$Fe distances (Fe1$\cdots$Fe1 = 6.110(1) Å Fe2$\cdots$Fe3 = 6.117(5) Å and Fe4$\cdots$Fe5 = 6.109(1) Å).

9.4.3 Cooperativity

At first glance it might be thought that cooperativity would take place along the –[Fe–Pmd–Fe]$_\infty$– chains, but this is not the case. At 290 K, all five inequivalent iron atoms have a very similar octahedral volume with a value characteristic of a high spin state (in this case an average of 13.5(2) Å^3). At 220 K, it is clear that Fe1 to Fe4 are still in this high spin state (with an average volume of 13.45(13) Å^3), but Fe5 already shows a tendency towards a low spin configuration, with its octahedral volume of 12.1(5) Å^3. Clearly for some reason Fe5 has a lower energy barrier to the spin crossover than the other iron atoms.

The Intermediate Plateau

From the magnetic susceptibility measurements, the structural data collected at 170 K is coincident with the plateau between the two steps of the spin transitions, which is exactly halfway through the conversion. From the octahedral volumes, it is clear that both Fe2 and Fe4 remain high spin (13.35(10) Å^3) while Fe3 and Fe5 have crossed over to low spin (9.95(20) Å^3) with a change in volume that corresponds with the characteristic change

of around 0.2 Å in the Fe–N bond length. This means that in the two chains formed by inequivalent iron atoms (–Fe2–Pmd–Fe3–Pmd–Fe2– and –Fe4–Pmd–Fe5–Pmd–Fe4–), there is an alternating arrangement of –HS–LS–HS–LS– iron atoms (Figure 9.11).

From the octahedral volume, Fe1 appears to be in an intermediate state half way between the high and low spin states. It is thought that this is because the Fe1 site is HS/LS disordered, so that the crystal structure gives the average structure. It is possible that the disorder is random in nature since there is no evidence of any symmetry change or super-lattice reflections. However, the data are poor and any symmetry change would be subtle and therefore very hard to see. If the disorder is random, this would be expected to lead to the creation of HS and LS domains, which would lead to strain in the crystal which should be visible by increased R-indices and possibly even crystal damage. This is not seen, suggesting that the disorder is ordered and as the other chains are HS/LS disordered, it seems likely that the same could be true for the Fe1 chain.

Thus, studying the connectivity of the high and low spin ions at 170 K suggests that the cooperativity takes place, not through the Pmd ligands, but through the anionic silver cyanide bridges. Indeed, it seems reasonable that the anionic bridging ligands may play an important role in the stabilisation of the unlike-spin species in the step.

Ag–Ag Distances

Within the asymmetric unit there are twelve silver atoms, each of which are connected to one or two other silver centres by argentophilic silver-silver interactions. These Ag–Ag interactions form three distinct chains — two containing three silver atoms and one containing six silver atoms. All the Ag–Ag distances within the chains fall into two groups, long (3.2–3.3 Å) and short (~3.0 Å) and there are two pairs of short interactions: Ag1–Ag8 & Ag8–Ag–4 and Ag6–Ag10 & Ag10–Ag12 (Figure 9.12).

Similar patterns to those seen in the iron centres can also be seen in these two pairs of short argentophilic distances (Table 9.3). At 290 K and 220 K, all four of these distances are between 2.98 Å and 3.02 Å. On cooling to 170 K however, one pair of distances (Ag6–Ag10 and Ag10–Ag12) become noticeably shorter (2.96–2.97 Å). Cooling still further to the low spin state results in a further shortening coupled with shortening of the second pair, Ag7–Ag1 and Ag1–Ag8, so that all of the short Ag–Ag contacts are of a comparable

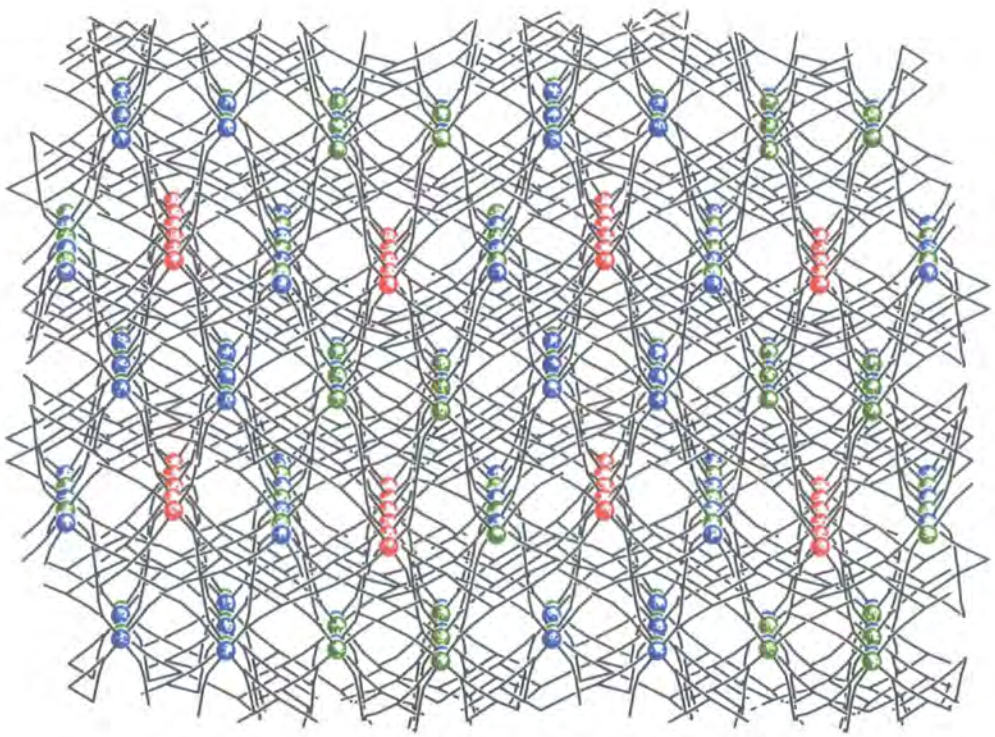

Figure 9.11: Alternating –HS–LS–HS– along the –[Fe–Pmd–Fe]$_\infty$– chains. HS is shown in green (Fe3 & Fe5), LS is shown in blue (Fe2 & Fe4) and the intermediate Fe1 is shown in red. The Pmd rings are omitted and the silver cyanide ligands are shown in black for clarity.

	Ag1–Ag8	Ag4–Ag8	Ag6–Ag10	Ag10–Ag12
290 K	2.989(2) Å	3.014(2) Å	2.996(2) Å	2.992(2) Å
220 K	2.993(2) Å	3.016(2) Å	2.994(2) Å	2.984(2) Å
170 K	2.991(3) Å	3.015(3) Å	2.963(3) Å	2.970(3) Å
90 K	2.944(2) Å	2.943(2) Å	2.942(2) Å	2.939(2) Å
30 K	2.947(3) Å	2.942(3) Å	2.942(3) Å	2.940(3) Å
30 K (Irr.)	3.007(3) Å	3.032(3) Å	3.008(3) Å	2.984(3) Å

Table 9.3: Short Ag–Ag bonds in compound **11**.

	Ag1–Ag7	Ag2–Ag3	Ag2–Ag9	Ag5–Ag7	Ag5–Ag11
290 K	3.200(2) Å	3.244(2) Å	3.266(2) Å	3.286(2) Å	3.237(2) Å
220 K	3.183(2) Å	3.228(2) Å	3.259(2) Å	3.261(2) Å	3.217(2) Å
170 K	3.177(3) Å	3.182(3) Å	3.265(3) Å	3.189(3) Å	3.227(2) Å
90 K	3.150(2) Å	3.095(2) Å	3.258(2) Å	3.108(2) Å	3.159(2) Å
30 K	3.138(3) Å	3.085(3) Å	3.241(3) Å	3.106(3) Å	3.147(2) Å
30 K (Irr.)	3.152(3) Å	3.173(3) Å	3.224(3) Å	3.208(3) Å	3.174(2) Å

Table 9.4: Long Ag–Ag bonds in compound **11**.

length (approximately 2.94 Å at 90 K).

The long Ag–Ag bonds do not follow any similar trend, generally contracting on cooling. The only irregularities are Ag2–Ag9 and Ag5–Ag11. These appear to be slightly longer at 170 K than 220 K, but since the data are poor, the esds are large so it is not possible to draw any conclusions.

LIESST

On irradiation, the structure clearly undergoes a spin transition, but not quite as expected. From the unit cell volume, it is clear that the LIESST phase is high spin and it would seem that the structure is completely high spin. This is supported by the change in crystal colour from red back to yellow. Despite this, although Fe1 to Fe4 have clearly returned to the HS state, Fe5 appears to remain LS.

So, from the structural data at 30 K after irradiation, Fe5 appears to remain in a LS state, despite other indications that all iron atoms should be in a HS state (i.e. the colour

and unit cell volume). This is explained by the time dependent magnetic susceptibility data which shows that there are two steps to the relaxation (Figure 9.2). The first section of the relaxation process lasts around 13 hr at 25 K[209,210] and shows a faster process than the second section. The X-ray data collection of the LIESST structure took around 13 hr, which means that there must have been some kind of relaxation during the data collection period. Since a diffraction experiment gives not only the structure averaged over the crystal, but also the structure averaged over time, it seems that what was measured was a time averaged structure of the first section of the relaxation process. Thus, Fe5 is thought to be relaxing faster than the time needed for a complete X-ray data collection. The photomagnetic data appears to indicate the involvement of half of the iron atoms, analogous to the thermally induced SC transition. Thus, the iron centres involved should also show some change, but this is not the case. The explanation for this is still unknown.

Connectivity and Cooperativity

It would seem that the Fe5 must have a larger energy difference between the HS and LS states and consequently a lower HS→LS energy barrier than the other iron atoms. Since Fe3 is LS at the plateau at 170K (and is the next iron atom to change its spin state on cooling together with half of the Fe1 atoms), a similar reasoning could be applied. Thus Fe3 should also have a relatively low HS→LS energy barrier.

However, cooperativity must be playing an important role in the magnetic behaviour of this material so there must be a structural reason to account for this. The silver cyanide anions interlink all iron atoms in all directions, but with four different coordination environments. Analysing the connectivity of Fe5, it can be seen that it is the only iron atom which by symmetry, is connected through the silver cyanide fragments to only one other kind of iron atom. Through all four of its equatorial ligands, it is connected to Fe3 where all other iron atoms are connected to either two or three other non-equivalent iron atoms.

Comparing the connectivity of the silver centres involved in the four shorter Ag–Ag interactions, shows that the two low spin centres at 170 K (Fe5 and Fe3), are ligated by silver cyanide ligands containing Ag7, Ag8, Ag9, Ag10 and Ag12. Of these, only Ag7 and Ag9 are not connected by a short Ag–Ag interaction. Notably, Ag10–Ag12 is one of the

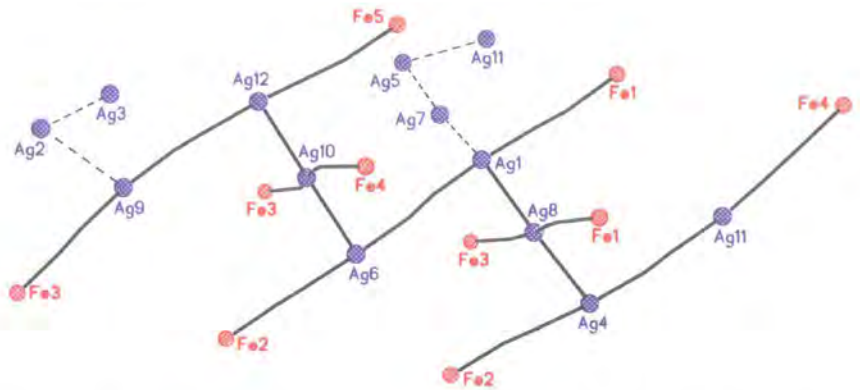

Figure 9.12: The silver chains in compound **11** with the long Ag–Ag interactions shown with a dotted line. Some of the connections between the iron atoms can also be seen.

two Ag–Ag bonds that have been shown to shorten at the intermediate plateau at 170 K. The other short Ag–Ag interaction that contracts also involves Ag10 and is to Ag6. Ag6 is part of one of the L_l ligands that binds to Fe1 (the intermediate iron centre at 170 K). This L_l ligand contains two silver atoms in the chain: Ag6 and Ag1. Ag1 is one of the central silver atoms in the long argentophilic silver chain (Figure 9.12). On the other hand, the other two short Ag–Ag interactions (Ag1–Ag8 and Ag8–Ag4) connect L_l silver cyanide ligands from Fe2 to Fe4 and Fe2 to Fe1 and these do not shorten between 290 K and 170 K corresponding with the absence of SC in Fe2 and Fe4. All of this demonstrates how the spin crossover transitions are reflected in the argentophilic interactions, which may even be critical to the propagation of the transition through the structure and therefore integral to the cooperativity.

Thus, it appears that Fe5 is the first iron to start changing its spin state and since it is communicating with Fe3 in a very efficient manner through the silver cyanide anions, it induces a transition in Fe3. This is followed by half of the Fe1 centres which yields the intermediate phase. All this suggests that the cooperativity takes place through the silver cyanide anions. The connectivity around the short Ag–Ag distances suggest that Fe2 may be next, though this is largely conjecture and there is no concrete evidence for this.

9.5 Conclusion

The structural data agree with the magnetic, calorimetric and absorption data, which shows the presence of two consecutive, thermally induced, spin crossover transitions. The structure, with five independent iron centres clearly undergoes a step transition, with two of the iron centres low spin for the intermediate phase, together with one iron centre which appears to be in an intermediate state, presumed to be half LS and half HS. On cooling, this and the remaining two iron centres become low spin forming a phase that can be used for Light-Induced Excited Spin-State Trapping. This meta-stable high spin state undergoes a multi-step relaxation process, which is thought to spread through the structure using similar cooperative mechanisms to the thermally induced transitions. The exact nature of this relaxation remains unknown, but further experiments are planned to follow the relaxation and associated structural changes.

The connectivity of the iron centres indicates that the cooperativity takes place through the anionic bridging silver cyanide ligands rather than through the Pmd groups. Thus, this has further demonstrated how effective metal cyanide bridges can be in transmitting the electronic changes associated with spin crossover transitions.

Chapter 10

Thermal and Light Induced Transitions in an Iron-Silver Spin Crossover Network

10.1 Introduction

Niel *et al.* recently reported three new silver cyanide networks with pyrazine, 4,4′-bipyridine and bispyridylethylene bridges (Pyz, Bpyn and Bpe).[185] All three materials are related to the previously discussed Hofmann-type clathrates, but to a lesser or greater degree. $\{Fe(Pyz)[Ag(CN)_2]_2.Pyz\}$ is closely related, forming a regular arrangement of flat layers bridged by Pyz ligands which form clathrates of the pyrazine solvent molecules. $\{Fe(Bpyn)_2[Ag(CN)_2]_2\}$ and $\{Fe(Bpe)_2[Ag(CN)_2]_2\}$ on the other hand have more puckered layers, but like $\{Fe(Pyz)[Ag(CN)_2]_2.Pyz\}$, the structures consist of two interpenetrating networks (Figure 10.1). More interesting however, is the variation in the magnetic properties caused by the differences between the three compounds.

10.1.1 Magnetic Susceptibility Data

$\{Fe(Pyz)[Ag(CN)_2]_2.Pyz\}$ and $\{Fe(Bpyn)_2[Ag(CN)_2]_2\}$ have been shown to be low and high spin respectively throughout the temperature range studied by Niel *et al.* (5 K to 300 K).[185] However, $\{Fe(Bpe)_2[Ag(CN)_2]_2\}$ (compound **12**) undergoes a spin transition that takes place between 150 K and 95 K on cooling. The transition levels off at

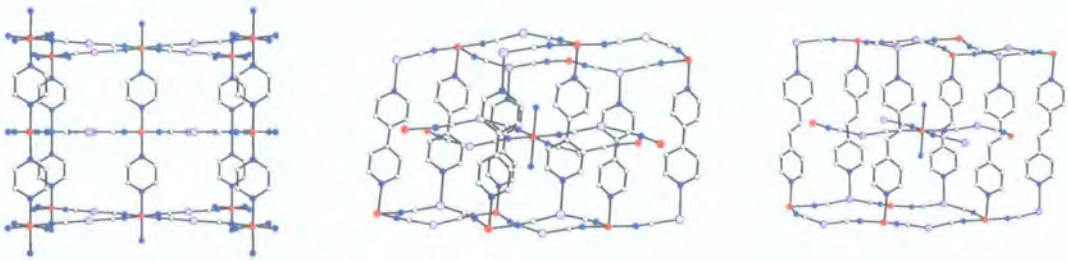

Figure 10.1: Three different three dimensional bimetallic networks with different magnetic properties, {Fe(Pyz)[Ag(CN)$_2$]$_2$.Pyz} (left, with the disordered solvent omitted for clarity), {Fe(Bpyn)$_2$[Ag(CN)$_2$]$_2$} (centre) and {Fe(Bpe)$_2$[Ag(CN)$_2$]$_2$} (right).[185] The interpenetrating nature of the Bpyn and Bpe networks can be seen.

1.1 cm^{3}K mol^{-1} indicating an incomplete transition, with about 30% residual high spin at 30 K.

Warming Modes

On warming, there is a small singularity in the magnetic susceptibility data which occurs between 100 K and 150 K, but the magnetic susceptibility data do not indicate a return to high spin until approximately 220 K, a hysteresis of approximately 95 K. The singularity manifests as a slight decrease in $\chi_M T$, followed by an abrupt increase and a slight wiggle back to a value comparable with that at 50 K (Figure 10.2).

Studies to investigate the anomaly involving warming the low spin complex to 180 K, then cooling, show that the anomaly has a hysteresis of about 4 K which is coupled with a secondary spin transition involving approximately half the trapped high spin iron centres. Warming back to room temperature and repeating the cycle with the same sample leads to an increase in the amount of trapped high spin at 30 K, with $\chi_M T$ values of 1.8 cm^{3}K mol^{-1}, 2.4 cm^{3}K mol^{-1} and 3.3 cm^{3}K mol^{-1} for the second, third and fourth cycles respectively.

Photomagnetic Studies

Niel *et al.* also showed through photomagnetic studies, that compound **12** undergoes Light-Induced Excited Spin-State Trapping (Figure 10.3). The dynamics of the LIESST relaxation were investigated over a temperature range of 55 K to 67 K, by the fitting of

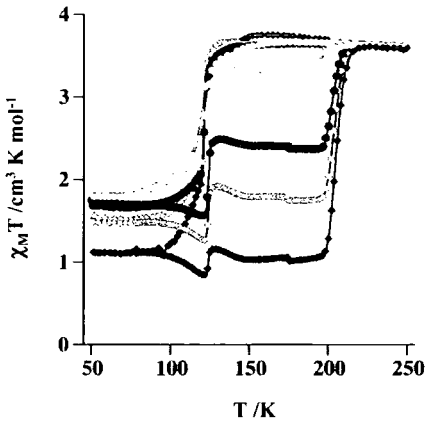

Figure 10.2: Magnetic data for compound **12**. The large hysteresis can clearly be seen in the first, second, third and fourth cooling/warming cycles (◆, ◇, • and ○ respectively), but there are changes to the anomaly and to the quantity of residual high spin.[185]

exponential curves relating the high spin molecular fraction (n_{HS}) to the relaxation rate $k(T)$ (Equation 10.1).

$$n_{HS} = e^{-k(T)t} \tag{10.1}$$

10.2 Single Crystal Diffraction Experiments

The red-orange crystals* were generally of good quality, being elongated blocks of a monoclinic habit, from approximately 0.2 × 0.1 × 0.1 mm in size and therefore highly suitable for single crystal X-ray diffraction.

*Crystals courtesy of Prof. José A. Real, Dr. M. Carmen Muñoz, Dr. Virginie Niel[187] and Ms. Ana G. Galet Domingo (Valencia).

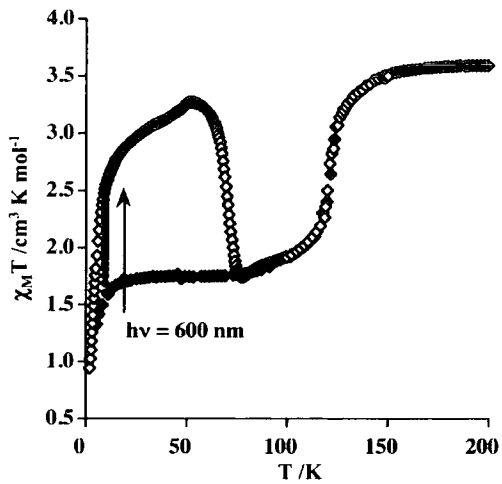

Figure 10.3: Photomagnetic data for compound **12**. Magnetic data were recorded on cooling to 10 K (◆) where the sample was irradiated (●) and then cooled to 4 K and warmed (◇).[185]

10.2.1 Data Collection

A typical crystal (0.22 × 0.10 × 0.10 mm) was selected and mounted in oil and quench-cooled to 160 K using the Oxford Cryosystems Cryostream 600[130] mounted on the Bruker SMART-CCD 1000.

Low Temperature Data

A matrix collection at 160 K resulted in a cell of a = 9.443(2) Å, b = 11.153(2) Å, c = 13.302(4) Å, β = 95.25(2)°, V = 1396.2(9) Å^3 which is comparable to that recorded in the literature.[185] A hemisphere of data was collected at 8 s/frame. On completion, the crystal was warmed at 360 K/hr to 260 K, where it was removed from the diffractometer. The cryostream was replaced with the Oxford Cryosystems HeliX and the crystal returned to the diffractometer, where it was cooled in stages to 30 K (300 K to 270 K at 120 K/hr, 270 K to 160 K at 360 K/hr and 160 K to 30 K at 120 K/hr).

A matrix collection at 30 K found a related, but different unit cell to that found at 160 K, with double the volume (a = 15.396(4) Å, b = 11.105(2) Å, c = 16.693(4) Å, β = 108.80(2)°, V = 2702(1) Å^3). Rejecting approximately 10% of the reflections, the

data could also be indexed to give the 160 K cell with a volume approximately 45 Å^3 smaller than that seen at 160 K. Data were collected as at 160 K, but with 6 s/frame. Ice formation on the crystal led to background scattering in the form of weak powder rings.

On completion, the crystal was irradiated with a red laser (15 mW, λ = 633 nm) for a total of approximately 25 mins, which gave a cell comparable with that seen at 160 K, but with a volume half way between those seen previously at 30 K and 160 K. Another dataset was collected at 30 K, as before.

Quenching

A second crystal of a similar size and shape to the first, was selected and mounted in oil on a hair. The Oxford Cryosystems HeliX[131] on the Bruker SMART-CCD 1000 was set to 30 K, but the cryostat was raised slightly so that the crystal could be mounted safely and the cryostat lowered as soon as possible, leading to extremely rapid cooling, or quenching.

A matrix was recorded at 30 K, which resulted in a unit cell volume comparable to that at 160 K, so a hemisphere of data was collected at 10 s/frame. On completion, the crystal was irradiated using the infrared laser, but there was no observed change in the cell parameters, so the crystal was warmed to 75 K at 120 K/hr and a matrix collected. The cell volume showed a contraction, but no cell change, so the crystal was returned to 30 K at 120 K/hr where another matrix was collected. The unit cell volume was comparable to that seen at 75 K, so another hemisphere of data was collected (16 s/frame).

On completion, the crystal was irradiated using a red laser (25 mW, λ = 633 nm) for approximately 2 mins after which a matrix was collected. An increase in cell volume indicated a return to the high spin state, so another hemisphere of data was collected (10 s/frame).

10.2.2 Data Analysis

The data indexed well and were integrated in the usual manner. The crystal was well formed, so the faces were indexed and absorption corrections were carried out accordingly.

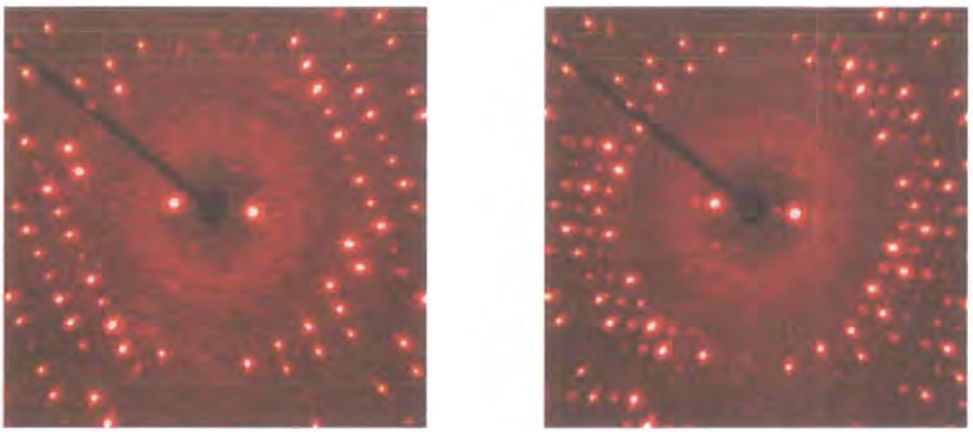

Figure 10.4: $h0l$ zones above and below the transition in compound **12**, with the high spin recorded at 130 K and the low spin recorded at 90 K on cooling (left and right respectively). The pseudo-**B**-centering that gives rise to the super-cell can be seen at 90 K.

30 K Data

The 160 K cell parameters and space group ($\mathbf{P}2_1/n$) agreed with the published data. However on cooling through the spin transition, additional reflections were observed (Figure 10.4). Indexing indicated that the unit cell was different from, but related to, the high spin cell. The cell volume clearly doubles from 130 K to 90 K, but the cell parameters indicate that the relationship is not as simple as the doubling of a single axis. Close inspection indicates that the matrix that converts the high spin primitive cell to the low spin pseudo-**B**-centred cell (Figure 10.5) and the inverse are:

$$\begin{pmatrix} -1 & 0 & 1 \\ 0 & -1 & 0 \\ 1 & 0 & 1 \end{pmatrix} \text{ and } \begin{pmatrix} -\frac{1}{2} & 0 & \frac{1}{2} \\ 0 & -1 & 0 \\ \frac{1}{2} & 0 & \frac{1}{2} \end{pmatrix}$$

This change in cell leads to a change in the space group with the n-glide plane becoming a c-glide.

10.2.3 Structure Refinement

Since the data were generally of a reasonable quality, all non-hydrogen atoms were refined as anisotropic at all temperatures. For the 160 K data, initially the hydrogen atoms were located in the difference Fourier map and refined satisfactorily, however for consistency

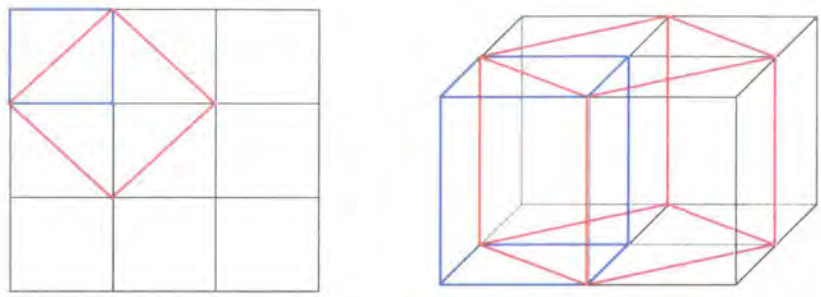

Figure 10.5: A schematic of the crystallographic phase change from primitive to pseudo-**B**-centering in compound **12**. The primitive high spin cell is shown in blue and the pseudo-**B**-centering low spin cell is shown in red.

with the other data, in the final refinement the hydrogen atoms were added geometrically and refined using a riding model.

30 K and LIESST Data

The 30 K doubled cell clearly led to twice the number of atoms in the asymmetric unit and consequently correlation was a serious concern. However, since there was a considerable change in other aspects of the structure, correlation was not a big problem. Two of the carbon atom thermal ellipsoids were poorly shaped, the residual peaks were a little large and the figures of merit although acceptable, were considerably higher than for the high spin state. This was initially thought to result from some kind of twinning, but close examination of the data did not confirm this and it was concluded that it was caused by other difficulties like residual high spin and absorption. Similar problems were seen in the LIESST data, suggesting that the problems were either caused by the extreme temperature or damage to the crystal caused by the structural changes or possibly the formation of ice on the crystal at 30 K.

Quenching

In contrast with the '120 K/hr cooled crystal' data, there were no problems with the refinement of the 'quenched' data, even after quench cooling, followed by two further spin transitions (relaxation to LS and irradiation back to HS). This suggested that the problems

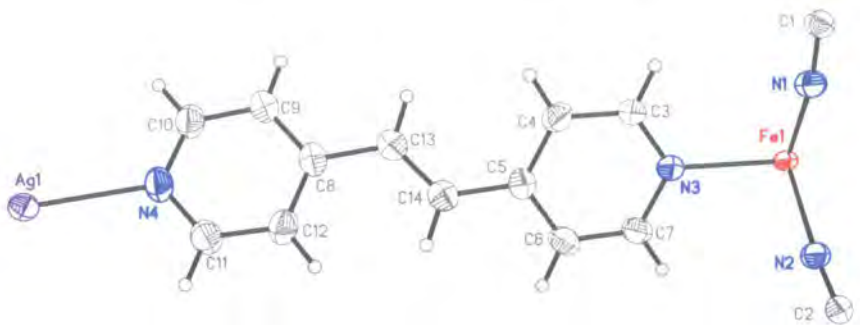

Figure 10.6: The asymmetric unit for compound **12** at 160 K, a = 9.4597(10) Å, b = 11.1484(13) Å, c = 13.3100(14) Å, β = 95.149(5)°, V = 1398.0(3) Å^3 ($\mathbf{P}2_1/n$).

experienced previously were related to the crystallographic phase change or the specific icing problems rather than the temperature.

The program IVTON[174] was used to calculate all the mean Fe–N bond lengths and volumes for the iron octahedra in compound **12**.

10.3 Discussion

At first glance compound **12** has much in common with compounds **6**–**11** (Chapters 7–9), but in practice it is very different.

10.3.1 Structural Analysis

The high spin structure of compound **12** is monoclinic ($\mathbf{P}2_1/n$) with half a formula unit in the asymmetric unit (Figure 10.6) and the iron atom Fe1, sitting on the inversion centre at $\frac{1}{2}$ $\frac{1}{2}$ $\frac{1}{2}$.

$Fe[Ag(CN)_2]$ Sheets

Like compounds **7**, **9** and **11**, compound **12** is made up of iron(II) centres linked by $[Ag(CN)_2]^-$ bridges. Unlike compounds **7**, **9** and **11**, compound **12** does not have argentophilic interactions running through the structure and in this and other ways is very different.

Like the $\{Fe(Pyz)[M(CN)_4].2H_2O\}$ compounds (M = Ni, Pd or Pt), the iron centres

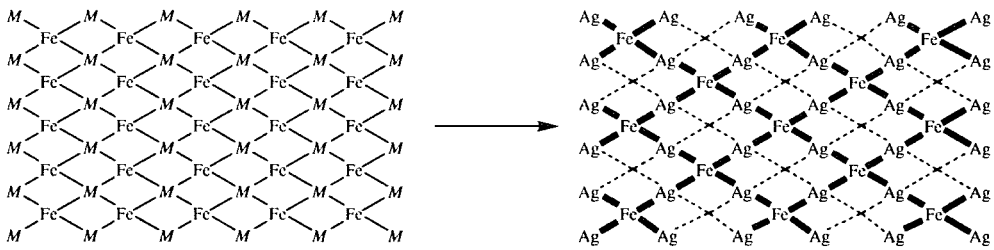

Figure 10.7: Schematic of the Fe–M nets in {Fe(Pyz)[M(CN)$_4$].2H$_2$O} compared with those seen in compound **12**. The loss of one iron centre on moving from a four coordinate, square planar M centre (left) to a two coordinate linear silver cyanide bridge (right) can be seen.

are ligated in a square planar motif by metal cyanide bridging ligands, which form sheets. However, in contrast to the {Fe(Pyz)[M(CN)$_4$].2H$_2$O} compounds where the M centre is four coordinate square-planar, the [Ag(CN)$_2$]$^-$ ligands approximate to linear, reducing the degree of connectivity within the sheets (Figure 10.7). Despite this, the magnetic susceptibility data indicate compound **12** has a very large hysteresis (70 K), suggesting that it is highly cooperative.

Interpenetrating Networks

Like the {Fe(Pyz)[M(CN)$_4$].2H$_2$O} compounds, the Fe–[Ag(CN)$_2$]$^-$ sheets are connected by bridging ligands, in this case Bpe ligands. The Bpe ligands occupy the axial sites around the iron atom with the nitrogen at the other end of the Bpe ligating the silver atom in the [Ag(CN)$_2$]$^-$ bridge. This silver atom is three coordinate in a T-shaped geometry with the cyanide groups approximately linear and the Bpe ligand at right angles to them.

There are two such, independent, interpenetrating networks within the structure. Recalling the comparison with the layers in the Fe(Pyz)[M(CN)$_4$].2H$_2$O compounds (Figure 10.7), it can be seen that there is one missing iron centre caused by substituting the four coordinate M for silver. The second network passes through these holes with two of the Bpe ligands sitting inside the vacant sites.

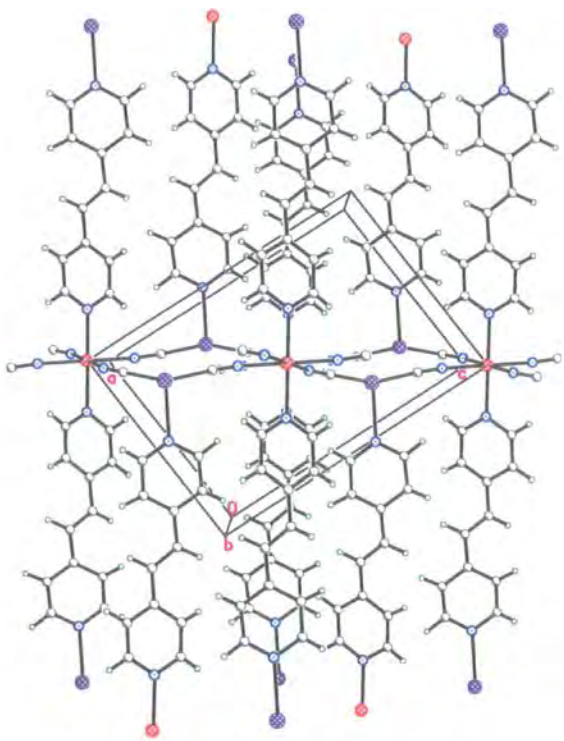

Figure 10.8: Sheets of Fe–$[Ag(CN)_2]^-$ linked together by Bpe ligands in compound **12**. The iron atoms sit on the inversion centre (at $\frac{1}{2}$ $\frac{1}{2}$ $\frac{1}{2}$ at 160 K) with the silver cyanide anion running along the diagonals from the centre to the corners of the unit cell.

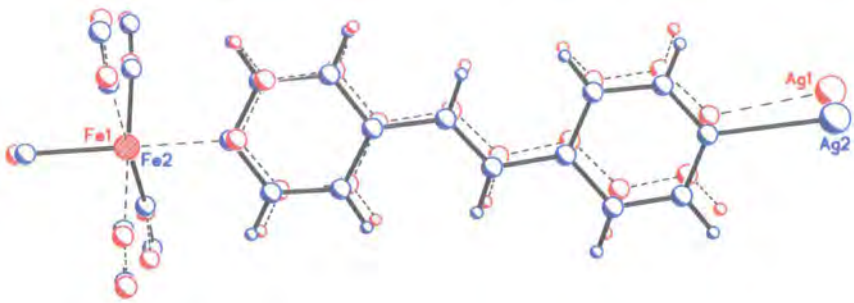

Figure 10.9: Overlay of the two iron centres in compound **12**, low spin **A**. The ligands joined to Fe1 are shown in red with bonds drawn with broken lines and the ligands joined to Fe2 are shown in blue with solid bonds.

10.3.2 Low Spin

From the magnetic susceptibility data, the transition takes place over a temperature range of approximately 55 K from 150 K to 95 K, becoming more gradual as it progresses (Figure 10.3). From the crystallographic data collected below the transition, there is a clear cell doubling coupled with the spin crossover (low spin structure **A**).

Structural Changes

The doubling of the cell volume is reflected in the contents of the asymmetric unit, which is also doubled, but there are other more subtle structural changes. The first most obvious difference is a change in bond lengths around the two now independent iron atoms (at 0 $\frac{1}{2}$ $\frac{1}{2}$ and $\frac{1}{2}$ 0 $\frac{1}{2}$). The Fe–N average bond lengths for each of the two iron atoms at 30 K are 2.15(4) Å and 2.00(3) Å (Fe1 and Fe2 respectively). These compare with 2.17(4) Å for the HS structure, indicating that while one iron (Fe2) converts almost entirely to low spin, Fe1 remains almost entirely high spin.

There is also a slight change in the orientation of the bridging pyridine rings, which break the symmetry, with angles of 5.9(1)° and 4.4(1)° between the two previously symmetrically equivalent rings (Figure 10.9). This is coupled with a slight lateral shift, which presumably reflects the slight change in the relative position of the layers.

10.3.3 Meta-Stable High Spin States

On quench-cooling, the crystal clearly doesn't have time to undergo the crystallographic phase change or complete the spin transition as the cell volume is 1367.0(2) Å^3, compared with 1398.0(3) Å^3 at 160 K and $\frac{2713.3(6)}{2}$ = 1356.6(6) Å^3 at 30 K cooled at 120 K/hr. This is confirmed comparing the average Fe–N bond length at 160 K (2.17(4) Å) with that when quenched to 30 K (2.15(4) Å).

Relaxation

Since the quench-cooled high spin state is essentially very similar in nature to a LIESST state, it was thought that it could be possible to access a low spin state by irradiation with infrared laser light or warming to a temperature where the relaxation rate was increased. Irradiation was unsuccessful, but warming to 75 K gave a cell volume of 1353(1) Å^3, indicating that relaxation had taken place, but without any crystallographic change leading to a new low spin structure, structure **B**. This was cooled to 30 K where a hemisphere of data indicated that the Fe–N average distance was indeed shorter (2.05(3) Å^3), indicative of a transition. This is also supported by the octahedral contraction from 13.22(2) Å^3 to 11.47(2) Å^3 which is between the volumes for the two iron centres for the other LS state structure **A** (13.27(2) Å^3 and 10.73(2) Å^3). This suggests that there is probably still residual high spin present, but in this case there is no distinction between the crystallographic sites.

The relaxation of the meta-stable, quenched, high spin state to the corresponding low spin structure is coupled with a twisting of the Bpe ligand. As seen in the slower cooled structure, there is a different degree of twisting for the two rings of the Bpe ligand. In this case, the ring ligating the iron atom only twists by 1.9(2)°, while the ring ligating the silver atom twists by 5.0(2)° (Figure 10.10).

This relaxation to the low spin structure **B** rather than structure **A**, is presumably related to the excitation effect seen in Chapter 3. In compound **2**, the spin crossover is coupled with a structural change, leading to a lower symmetry low spin state. On excitation with a red light at 30 K, the structure undergoes a transition to a meta-stable high spin state, but retains the low spin structure. It is thought that while the laser provides sufficient energy for the spin transition, there is not enough energy for the struc-

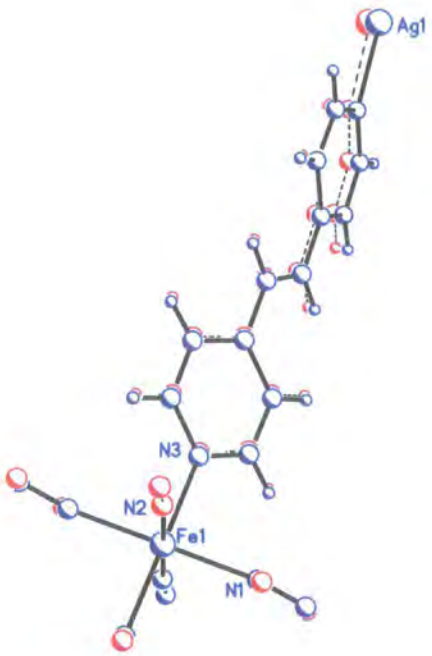

Figure 10.10: Overlay of the quenched low spin structure (**A**) with the high spin structure. The high spin structure is shown in red and the shortening of the Fe–N bonds can clearly be seen. On close inspection, the tilting of the Bpe rings can also be seen.

tural changes and at 30 K the temperature is too low for thermal energy to be available. Although the process is different, the effect is the same during the relaxation of the high spin compound **12**, where there is insufficient energy for the structural changes. It is unclear whether there is order in the HS–LS centres, or whether they are truly randomly distributed.

LIESST

Irradiating the structure **A** low spin state, left no evidence of the super-cell. The cell volume had undergone a relative expansion from $\frac{2713.3(6)}{2}$ = 1356.6(6) Å^3 to 1375.7(4) Å, which together with the change in Fe–N average bond length (to 2.17(4) Å) indicated a return to the high spin state.

Interestingly, irradiating the low spin structure **B** also led to an increase in cell volume from 1339.5(2) Å^3 to 1378.1(2) Å^3, a volume comparable with that of the LIESST state generated from the doubled cell, low spin structure. Overlaying the two indicates that there are no noticeable conformational differences between the two LIESST structures (Figure 10.11). Overlaying the quenched structure with the LIESST structure also shows that there is no observable difference between these two structures, indicating that all three routes lead to the same state. From this it can also be assumed that warming the meta-stable high-spin structure obtained via any of the three routes leads to the low spin structure **B** rather than the cell-doubled structure **A**.

10.3.4 Spin Crossover Transitions

So, a comparison of the Fe–N bond lengths and octahedral volumes for the six structures, clearly shows that there are four states (Table 10.1). These can be loosely described as high spin (160 K), low spin **A** (30 K), meta-stable high spin (quenched and LIESST) and low spin **B** (relaxed from the meta-stable high spin).

Octahedral Volumes

Low spin **A** has a doubled cell caused by the splitting of the iron centre into two, one high spin centre (Fe1) and an intermediate/low spin centre (Fe2). Comparing the octahedral volumes for Fe1 and Fe2 with those for the other structures, suggests that there may be a

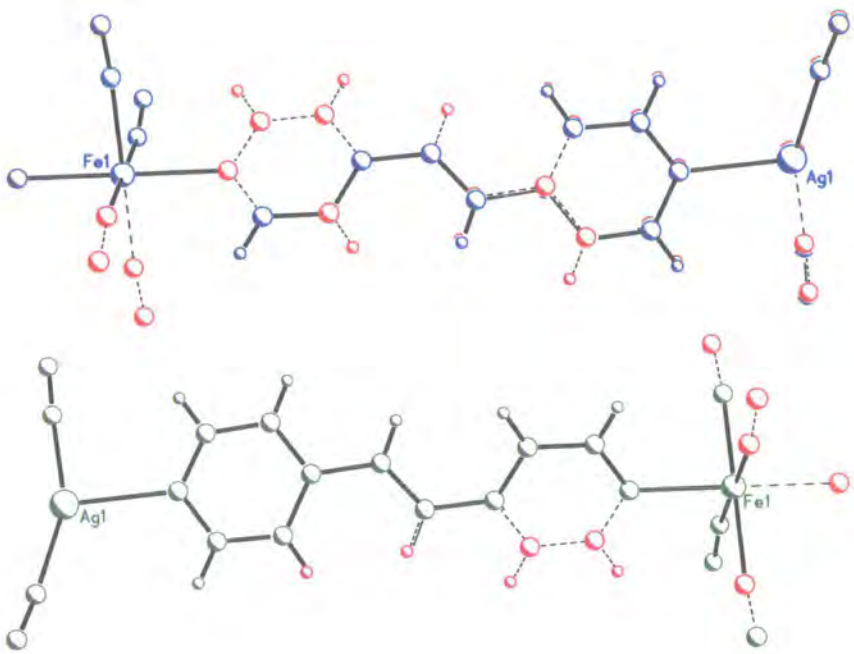

Figure 10.11: Overlays of the LIESST and the quenched structures. In both cases the quenched/irradiated structure is shown in red and the LIESST structure generated from the low spin structure **A** (cooling at 120 K/hr) is shown in blue (top) and low spin structure **B** (the quench cooled structure) is shown in green (bottom). Clearly there is no significant change in the conformation of the Bpe rings indicating that the structures are generally the same, with any differences seen only in the Fe–N bond lengths.

Temperature	Fe–N Distances				Octahedral
& Conditions	N1	N2	N3	Average	Volume
160 K	2.171(2) Å	2.129(2) Å	2.215(2) Å	2.17(4) Å	13.63(2) Å^3
30 K, Cooled (Fe1)	2.144(7) Å	2.114(7) Å	2.202(6) Å	2.15(4) Å	13.27(2) Å^3
30 K, Cooled (Fe2)	1.983(7) Å	1.986(7) Å	2.044(6) Å	2.00(3) Å	10.73(2) Å^3
30 K, Irr.	2.157(6) Å	2.134(6) Å	2.213(5) Å	2.17(4) Å	13.56(2) Å^3
30 K, Quenched	2.148(2) Å	2.111(2) Å	2.191(2) Å	2.15(4) Å	13.22(2) Å^3
30 K, Q/Warmed	2.049(2) Å	2.016(2) Å	2.089(2) Å	2.05(3) Å	11.47(2) Å^3
30 K, Q/W/Irr.	2.170(3) Å	2.131(3) Å	2.215(3) Å	2.17(4) Å	13.63(2) Å^3

Table 10.1: Fe–N distances in compound **12**.

very small amount of low spin on the HS Fe1 site, fitting in with the magnetic data, which indicates a total of only 30% residual high spin at 30 K. In contrast, the Fe2 octahedral volume clearly indicates that it is primarily low spin, but comparison with volumes for other iron centres (compounds **6** and **7** for example) suggests that there may also be a very small amount of residual high spin on the Fe2 site.[†]

On further inspection, the octahedral volume for Fe1 is very similar to that found for the quenched high spin structure suggesting that there may be a small amount of low spin present in both. Comparing the octahedral volumes for 30 K structure **B** with that for the "LS" Fe2 in **A** on the other hand, indicates that the iron atom in structure **B** is clearly HS/LS disordered.

Cyanide Groups

Studying the $Fe[Ag(CN)_2]_2$ sheets, it becomes apparent that there are two very different cyanide groups in the $[Ag(CN)_2]^-$ bridges. One ligates to the iron centre forming a linear bridge, while the other is distinctly bent (Figure 10.12). This is reflected in the Fe$\cdots$Ag distances which are 5.3581(5) Å and 5.1809(4) Å at 160 K (Table 10.2). The reason for this distortion of the grid is probably to allow two of the Bpe ligands to pass through the

[†]The HS/LS disorder on both iron sites could be in part responsible for the large residual electron density and poor figures of merit. Certainly, such a situation would lead to increased strain within the crystal which could cause damage leading to loss of crystal integrity and problems with the refinement.

"vacant" iron site in the $Fe[Ag(CN)_2]_2$ sheets. Since the iron atom sits on an inversion centre, the *trans* cyanide groups are related by symmetry. Consequently, there are two different types of CN–Fe–NC groups: CN_{bent}–Fe–NC_{bent} and CN_{linear}–Fe–NC_{linear}. These two different groups alternate throughout the structure, linked by silver atoms, forming chains.

In the case of the 30 K structure **A**, where there are two independent, alternating iron atoms, the alternating CN–Fe–NC groups coincide with the –LS–HS–LS– chains. Since all the iron centres are ligated by two CN_{bent} and two CN_{linear} in a trans configuration, in one direction the HS corresponds to the bent centre and the LS to the straight centre. In the chains running the other way however, this is reversed and the LS corresponds to the bent centre and the HS to the straight centre.

On undergoing spin crossover, the two Fe2–Ag distances shorten by 0.130(1) Å and 0.114(1) Å while the Fe1–Ag distances contract by 0.030(1) Å and 0.013(1) Å, reflecting the difference in the predominantly high spin Fe1 and low spin Fe2. As would be expected, intermediate values are seen for low spin **B**, illustrating the mixed HS/LS site.

What is not so clear is why the Fe$\cdots$Fe distance via the $[Ag(CN)_2]^-$ bridge is by far the shortest for low spin **B**. Since the iron centres in low spin **A** alternate –HS–LS–HS–LS– in all three directions, the Fe$\cdots$Fe distances are HS–LS, which might be expected to give an intermediate distance approximately 0.2 Å shorter than the HS–HS distance (compared with a LS–LS distance which should be 0.4 Å shorter than a HS–HS distance). This does not however, explain why the average HS–LS distance for low spin **B** is 0.050(1) Å shorter than that for low spin **A**. It is possible that the relaxed low spin state (**B**) has a smaller amount of residual high spin than the cooled low spin state (**A**), which would account of the shorter Fe$\cdots$Fe distance. Indeed, comparing the overall average of the octahedral volumes for low spin **A** (12.00(4) $Å^3$) with that of low spin **B** (11.47(2) $Å^3$) supports this, but this is far from conclusive. The Fe$\cdots$Ag distance (via the Bpe ligand) is also shorter for low spin **B** than for low spin **A**. This difference is probably caused by the conformational change in low spin **A**, leading to subtle changes in the Fe$\cdots$Ag distance, but could also result from a smaller amount of residual high spin present in low spin **B** than in low spin **A**.

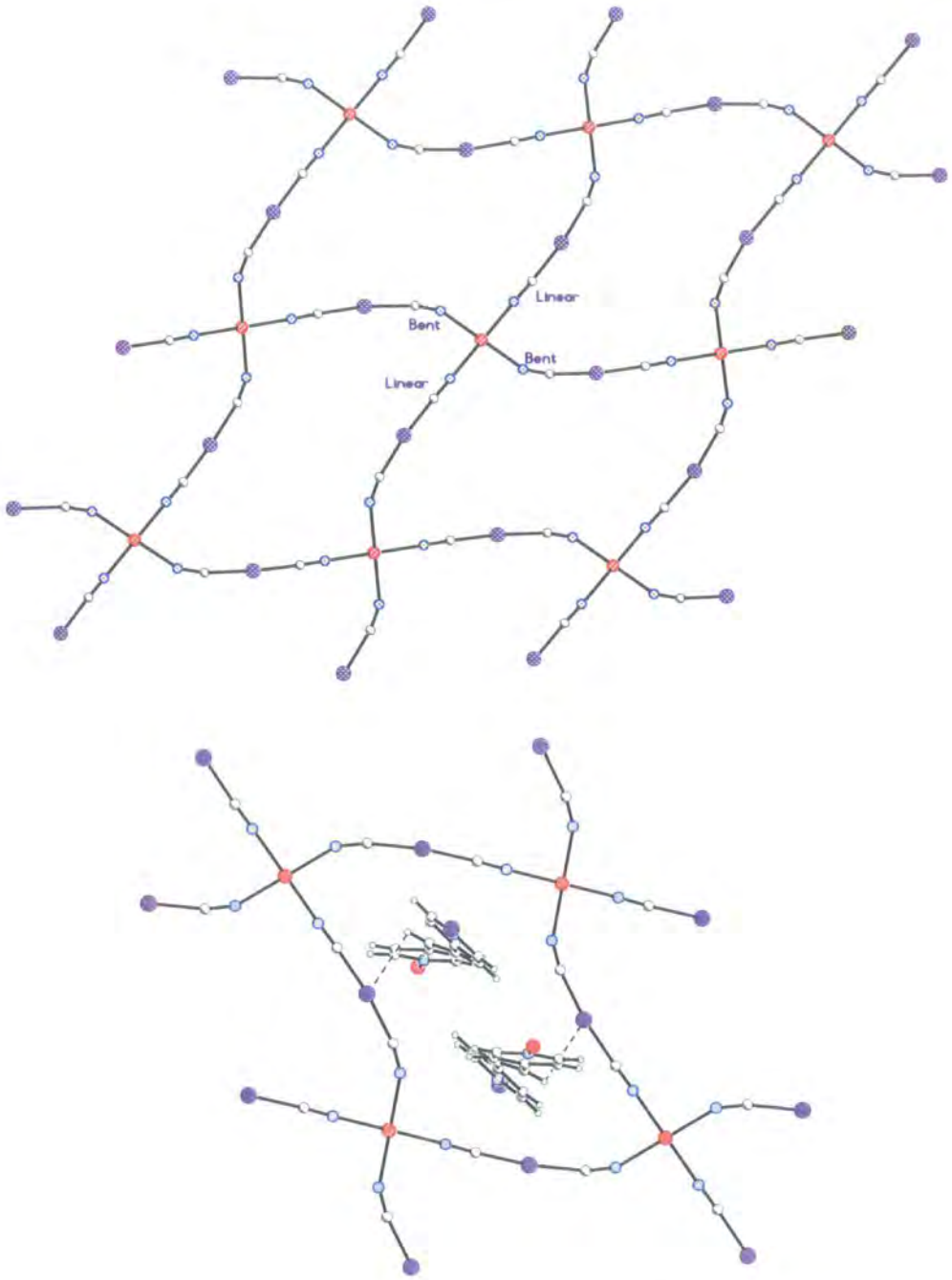

Figure 10.12: The $Fe[Ag(CN)_2]_2$ sheets in compound **12** at 160 K. The linear and bent cyanide groups are labelled (top) and the Bpe ligands of the second network can be seen passing through the "vacant" site in the $Fe[Ag(CN)_2]_2$ sheets (bottom). At 160 K, there is an Ag···H contact of 3.034(9) Å connecting the two interpenetrating networks, between Ag1 and H14A, shown with a dotted line.

Temperature & Conditions	Fe···Ag Distances (N1)	(N2)	(N3)	Fe···Fe
160 K	5.1809(4) Å	5.3581(5) Å	14.0989(13) Å	10.1677(7) Å
30 K, Cooled (Fe1)	5.1678(7) Å	5.3282(8) Å	14.0627(18) Å	10.0386(9) Å
30 K, Cooled (Fe2)	5.0673(7) Å	5.2286(8) Å	13.9598(17) Å	10.0386(9) Å
30 K, Irr.	5.1603(7) Å	5.3579(8) Å	14.0618(18) Å	10.1325(11) Å
30 K, Quenched	5.1446(3) Å	5.3404(3) Å	14.0369(8) Å	10.1034(5) Å
30 K, Q/Warmed	5.0889(4) Å	5.2498(4) Å	13.9568(8) Å	9.9887(5) Å
30 K, Q/W/Irr.	5.1635(4) Å	5.3637(4) Å	14.0764(9) Å	10.1391(5) Å

Table 10.2: Fe···Ag and Fe···Fe distances in compound **12**.

Low Spin Networks and Cooperativity

In low spin structure **A**, the high spin Fe1 centre is surrounded in a square planar arrangement by four Fe2, low spin centres. In the third direction, both Fe1 and Fe2 are ligated by Bpe ligands, which also ligate a silver atom. Although the silver atoms are also part of the next sheet, they are ligated in a T-shaped geometry and are "terminal" in the sense that there is no continuation in the same direction, so that they form short Ag–Bpe–Fe–Bpe–Ag chains. Since the iron atoms both sit on inversion centres, Fe1 is at the centre of an Ag1–Bpe–Fe1–Bpe–Ag1 chain and Fe2 is at the centre of a similar Ag2–Bpe–Fe2–Bpe–Ag2 chain. In addition to the Bpe ligands, both Ag1 and Ag2 are connected to one Fe1 and one Fe2 via cyanide groups, forming a bridge between the high and low spin centres.

Since the $[Ag(CN)_2]^-$ groups form bridges between the HS and LS centres, it is clear that in this compound cooperativity does not take place through the anionic ligands. There are two other possibilities, the first of which involves the Bpe ligands. It is conceivable that communication could take place through the linear side of the $[Ag(CN)_2]^-$ ligands via the Bpe ligand (Figure 10.13). Since this is a very long communication pathway, this seems unlikely and it also fails to explain communication between the two interpenetrating networks.

Another possible explanation also involves the Bpe ligands, but in a very different way. As explained earlier, pairs of the Bpe ligands occupy the "vacant" sites in the $Fe[Ag(CN)_2]_2$ sheets of the interpenetrating network. The bending of the cyanide ligands

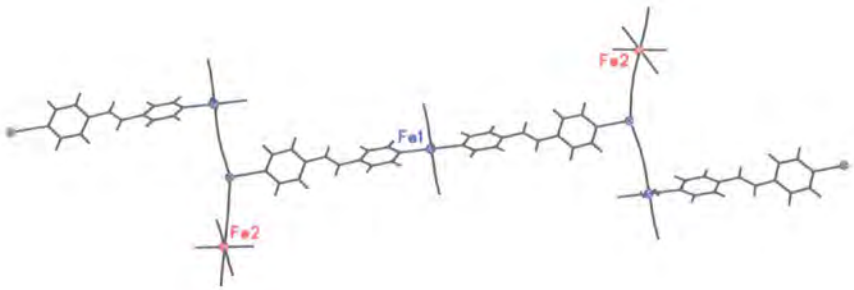

Figure 10.13: Ag1–Bpe–Fe1–Bpe–Ag1 chains in compound **12**. The carbon, nitrogen and hydrogen atoms are shown in black, Fe1 in blue and Fe2 in red for clarity. Similar Ag2–Bpe–Fe2–Bpe–Ag2 chains can also be seen.

brings the silver atoms of the $[Ag(CN)_2]^-$ anions into relatively close range of the ethylene part of the Bpe ligands, possibly close enough to allow a weak intermolecular interaction. Interestingly, the bent part of the $[Ag(CN)_2]^-$ anions ligates an iron centre in the same state as that connected to the closest Bpe ligand in the second network (Figure 10.14). This could explain how the two networks communicate, but unfortunately, though plausible, the explanation cannot be considered unequivocal as there are many short contacts of similar lengths within the structure, although these are the shortest.

10.4 Conclusion

Magnetically, compound **12** is a fascinating material, and structurally it has four distinct phases dependent on the physical treatment of the sample. These phases can be loosely described as high spin (160 K), low spin **A** (30 K), meta-stable high-spin (quenched and LIESST) and low spin **B** (relaxed from the meta-stable high spin). Low spin **A** is reached by cooling the high spin state through the spin transition at 120 K and is crystallographically different to the high spin state, with one predominantly high spin iron centre and one low spin centre.

In contrast, the meta-stable high spin state can be generated in a number of ways including quench cooling the high spin state and irradiating the low spin **A** with red light. Warming the meta-stable state appears to cause a relaxation to a different low spin state (**B**), which has a only one iron centre. This single site is believed to be HS/LS disordered

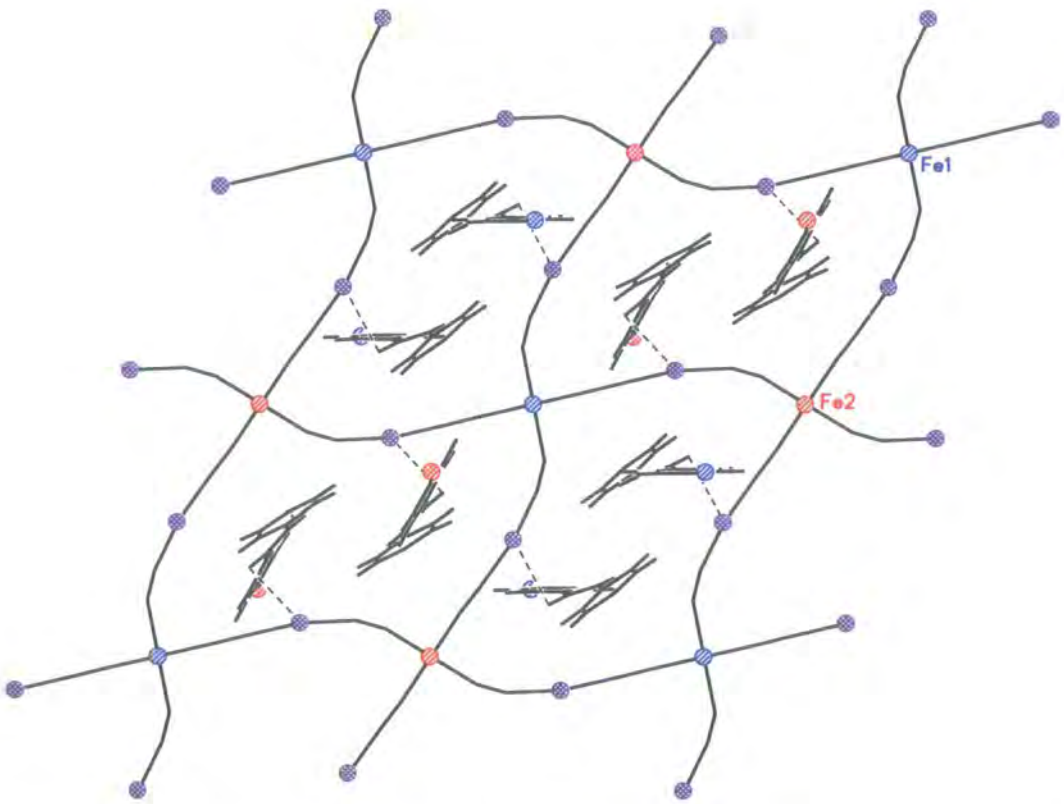

Figure 10.14: The $Fe[Ag(CN)_2]_2$ sheets, showing the Bpe ligands of the interpenetrating network in compound **12** at 30 K. The carbon, nitrogen and hydrogen atoms are shown in black, Fe1 in blue and Fe2 in red for clarity.

(approximately 75% HS from the ratio of the octahedral volumes), but it is important to note that the two different sites in low spin **A** are probably only visible because of other changes in the structure including the movement of the silver atoms, making the super lattice more visible. In the case of low spin **B** there may also be super lattice reflections, but these would be very weak making it impossible to see them without a stronger radiation source.[22]

Two possible cooperative mechanisms based on the low spin **B** structure have been discussed. Both these explanations rely on the differences between the linear and bent cyanide ligands. In the case of the cooperative Bpe chains, the bent Fe–NC prevents cooperativity, while in the interpenetrating network explanation, the bent ligand is critical to the communication. These descriptions are analogous to the "tug-of-war between elastic interactions and a shock-absorber effect" in the polymeric materials discussed by van Koningsbruggen *et al.*.[108] They describe how flexible linking groups within bridging ligands make transitions more gradual as they reduce the transmission of the vital elastic interactions through the structures. The elasticity of the bent Fe–NC group could be preventing the spread of the transition to the second site in the cooperative Bpe chain description. However, the bend in the Fe–NC ligand could lead to communication through the weak interactions between the networks. It is not clear which explanation is the most valid, but this study has given a valuable insight into this novel SC material.

Chapter 11

A Powder Diffraction Study of a Three Dimensional, Spin Crossover, Coordination Polymer

11.1 Introduction

One of the first Hofmann type spin crossover materials was Fe(Pyd)[Ni(CN)$_4$], which was first discussed in 1996.[120] Since then however, a number of related two and three dimensional materials have been synthesised and studied. Six such compounds have been compared, substituting the nickel atom in the centre of the anionic bridging ligands with palladium and platinum and replacing the pyrimidine ligand with pyrazine.[125] One of these compounds is the three dimensional spin crossover network {Fe(Pyz)[Pd(CN)$_4$].2H$_2$O} (compound **13**). This material consists of a three dimensional polymeric structure with iron octahedra connected through anionic bridges and pyrazine ligands (Pyz).

11.1.1 Magnetic Susceptibility Data

SQUID magnetic susceptibility data recorded for all of these materials generally show that converting a two dimensional material to a three dimensional network increases co-operativity and moves the spin transition to a higher temperature.[125] This can be seen by comparing compound **13** with its two dimensional counterpart, {Fe(Pyd)[Pd(CN)$_4$]} (Figure 11.1). In this case, the two dimensional pyridine containing material undergoes an

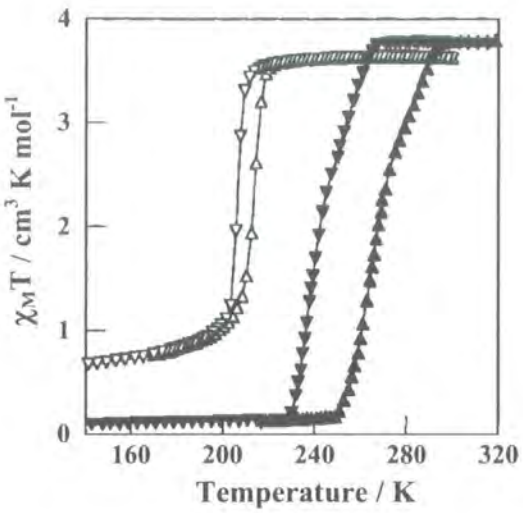

Figure 11.1: Magnetic susceptibility data for compound **13**. The transition in compound **13** takes place at approximately 220 K on cooling (▼) and at 240 K on warming (▲). In contrast, the two dimensional analogue has an incomplete transition with a reduced hysteresis and takes place at a lower temperature (▽ and △).[125]

abrupt but incomplete transition centred around 208 K on cooling, with an 8 K hysteresis. Increasing the dimensionality from 2D to 3D by replacing the pyridine with a bridging pyrazine increases the HS to LS conversion. The temperature of the transition is also increased by approximately 18 K and the hysteresis is increased by about 8 K. However, the nature of the transition also appears to change from a single step transition to a two step transition, with a slightly more gradual first step, but no plateau.

11.2 Powder Diffraction Experiments

All these compounds are microcrystalline powders and compound **13** is no exception. Therefore data were collected on the Bruker D8 Advance powder diffractometer, using the Oxford Cryosystems PheniX device to control the temperature.[152]

11.2.1 Data Collection

The sample* was sprinkled onto the aluminium sample plate, but was very soft, clumping together and did not cover the disc well. Despite a second attempt, large aluminium peaks were visible in the pattern, so these regions were excluded from the refinements (approximately 37–39° 2θ, 44–46° 2θ and 81–84° 2θ).

The PheniX was programmed to cool at 17 K/hr to 17 K while data were collected. Each scan took approximately $\frac{1}{2}$ hr, so a scan was recorded approximately every 10 K (8–65° 2θ, 0.4 s/step, 0.0144° 2θ/step). On reaching 17 K, a long scan was collected 10–120° 2θ, 1.5 s/step, 0.0144° 2θ/step, total approximately $3\frac{1}{2}$ hours. On completion, the PheniX was programmed to warm back to 300 K at 17 K/hr while more data were collected. This was followed by a long scan at 300 K (as at 17 K), for comparison.

11.2.2 Data Analysis

From inspection, there is a change in the patterns at around 260 K on cooling, with peaks moving to positive 2θ (Figure 11.2). This effect is indicative of the unit cell contraction caused by SC transitions. In the region around the transition, the data indicate the presence of two separate phases, thought to correspond to the high and low spin structures. No additional reflections or peak splitting were visible, so it was thought that there was no change in symmetry on cooling from the HS state to the LS state.

11.2.3 Structure Refinement

Compound **13** was thought to be isostructural with $\{Fe(Pyz)[Pt(CN)_4].2H_2O\}$ which is tetragonal ($\mathbf{P}4/m$), with $[Pd(CN)_4]^{2-}$ ligands forming sheets in the ab plane.[125] These sheets are linked by Pyz rings, which are disordered around a 4-fold axis in the c-direction. In addition, one of the solvent water molecules occupies a position on the 4-fold axis and mirror plane between the platinum atoms at 0 0 $\frac{1}{2}$, while the other occupies a position on the 2-fold axis and mirror plane between the Pyz rings at $\frac{1}{2}$ 0 $\frac{1}{2}$ (and 0 $\frac{1}{2}$ $\frac{1}{2}$).

*Sample courtesy of Prof. José A. Real, Dr. M. Carmen Muñoz, Dr. Virginie Niel[187] and Ms. Ana G. Galet Domingo (Valencia).

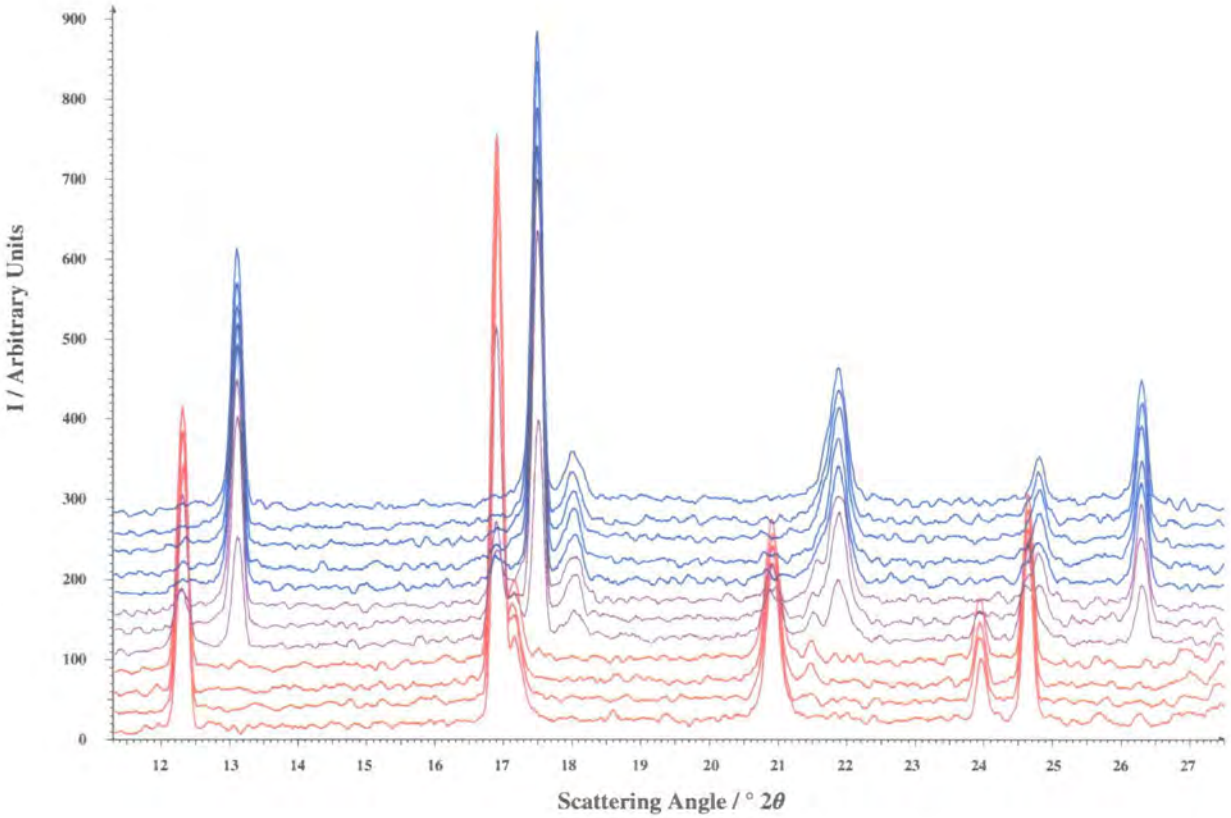

Figure 11.2: Powder diffraction patterns from compound **13** recorded at different temperatures. The first twelve scans are shown (from the bottom to the top). The scans before the transition are shown in red, the scans after the transition in blue and three obviously bi-phase scans which include both high spin and low spin states are shown in purple (5^{th}, 6^{th} and 7^{th} from the bottom, for which the average scan temperatures are 262 K, 254 K and 245 K).

Given the differences in scattering power between palladium, iron, oxygen, nitrogen and carbon, structure refinement was not thought to be reliable to identify Fe–N bond lengths. This was especially true given the quality of the data, which was collected in non-ideal conditions. However, in order to confirm the crystal structure, a refinement based on the structure of the known platinum analogue was refined against the 300 K long data collection. Since the data quality was less than ideal, restraints were required.[†]

As most of the atoms occupy special positions, the refinement involved only eight atomic positional parameters. As the refinement proceeded, the restraints were relaxed, the refinement of the atomic positional parameters was damped and the statistics and fit steadily improved while the bond lengths remained sensible. Finally, the Pyz hydrogen atom was added geometrically and the refinement repeated to convergence. The hydrogen atom was not refined nor were any of the thermal parameters.

Since data collection at 300 K was performed after cooling to 17 K, there was a second phase visible in the pattern, which was due to residual low spin. This LS phase was present as a very small impurity, so it was modelled using a second phase containing only the iron and palladium atoms. Since these metal atoms occupy special positions, it was presumed that positions would remain the same as in the LS state.

The structure was also refined against the 17 K data, but again regions had to be excluded and constraints were necessary.[‡] However, low R-indices and χ^2 values support the conclusion that there is no symmetry change.

Le Bail Fitting

Since information can be obtained from unit cell parameters, variable temperature Le Bail refinements were also carried out. For all data except that recorded around the transition, the Le Bail refinements were carried out as follows. Firstly, the background was refined using Rietveld refinement, using the proposed structure.[125] This was necessary because

[†]The values used for the constraints were standard bond lengths or values from the CSD[1] and the average Fe–N distances for compound **6** in the high spin state at 180 K.

[‡]The values used for the constraints were standard bond lengths or values from the CSD[1] as before, but the average Fe–N distances for compound **6** in the low spin state at 120 K were used.

the background refinement with Le Bail fitting was unstable, so Rietveld refinement was used to give a good, reliable baseline. This background was used in the Le Bail refinements where variables were added successively starting with the sample height, then the unit cell parameters, and finally profile parameters, a total of seven refinement variables.

Around the SC transition, the diffraction indicated the presence of a bi-phase material that clearly includes both the HS and LS states. Since the unit cell parameters for the HS and LS states are very different, the peak overlap in some of the strongest reflections was small enabling refinement of both phases in this temperature region (Figure 11.3). However, as Le Bail refinement effectively refines the structure factors, it is not possible to refine a scale factor. For this reason, a secondary Rietveld refinement was carried out with only the palladium and iron atoms included in each phase. This allowed the approximate determination of the phase fraction in the region around the transition, but only the background parameters, scale factors and phase fraction were refined in this way; the unit cell parameters were obtained from the Le Bail fit.

On cooling, the refinements were carried out with two phases against data that were collected between 262 K and 236 K (inclusive). The bi-phase refinements for the 271 K and 227 K data were unstable, so the refinements were carried out with only the one appropriate phase. Similarly, the refinements for the data collected around the transition on warming were refined with two phases, i.e. data recorded at 269 K and above.

11.3 Discussion

There are only eight atoms in the asymmetric unit (Figure 11.4), but the unit cell is small and the symmetry high (tetragonal, $\mathbf{P}4/m$), so a continuous network is generated.

11.3.1 Structural Analysis

These materials have been described as a type of clathrate or inclusion compound with water molecules residing in channels formed by the rigid networks (Figure 11.5). The channels are formed by $[Pd(CN)_4Fe]$ sheets which stack directly above each other, perpendicular to the c-axis. These $[Pd(CN)_4Fe]$ sheets are connected by rotationally disordered pyrazine ligands (Pyz), which lead to the formation of channels. These channels run along the a and b axes and contain water solvent (Figure 11.6).

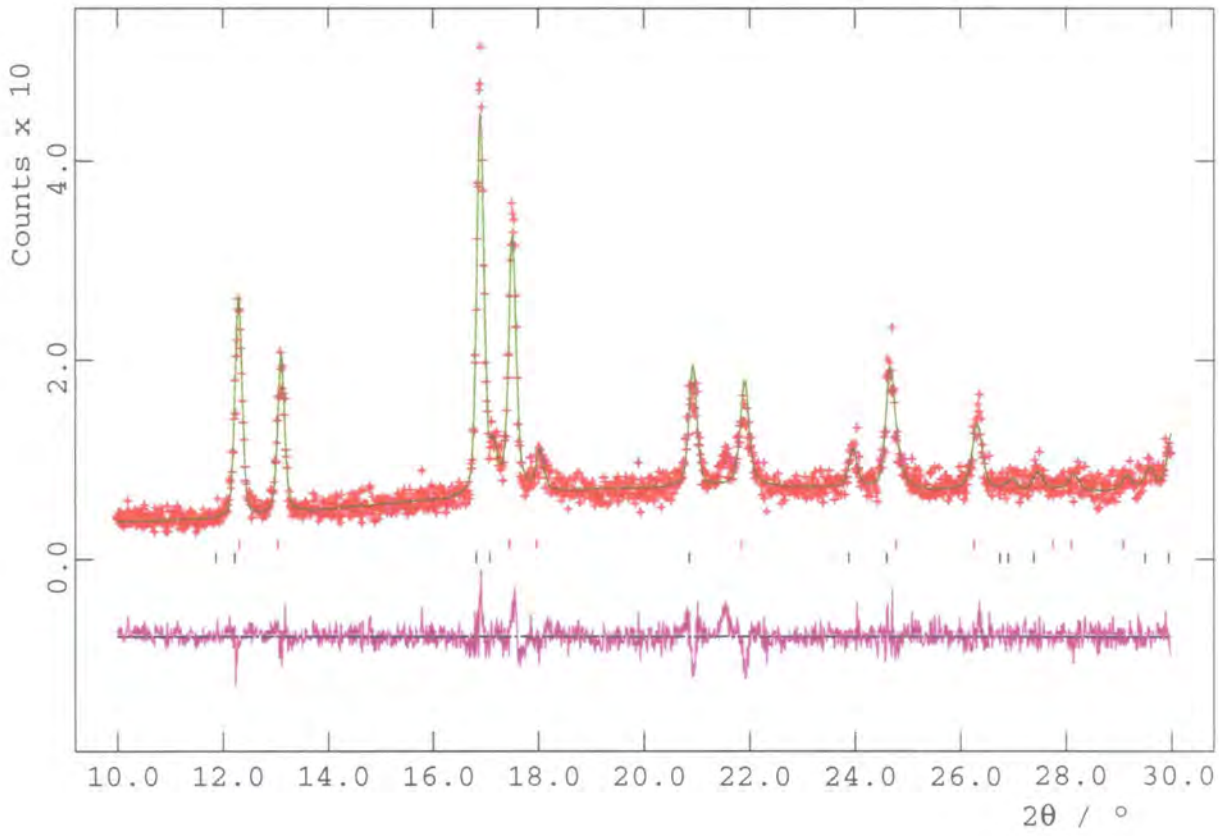

Figure 11.3: Fit for the Le Bail refinement of compound **13** at 262 K. The data are shown as red crosses, the fit in green and the difference trace in purple. Goodness-of-fit (on F^2) = 1.076, χ^2 = 1.158, , R_p = 0.0955 and wR_p = 0.1226, (R_p = 0.1087 and wR_p = 0.1350, excluding background).

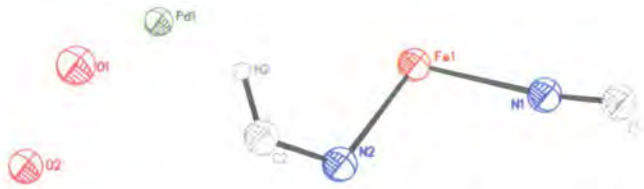

Figure 11.4: The asymmetric unit for compound **13** at 300 K, a = 7.4417(6) Å, c = 7.2389(7) Å, V =400.88(9) Å^3 (**P**4/m).

H-Bonding and Pd···O Interactions

The water molecules sit in the cavities made by the pyrazine rings, occupying special positions on the 2-fold and 4-fold axes and the mirror planes. The distance between the Pyz rings and the O1 water molecule (2.73(1) Å at 300 K) suggests that there may be C–H···O interactions between them (Figure 11.7). The second water molecule (O2) occupies a position between the square planar palladium atoms (Figure 11.8), at a distance equivalent to half the c cell dimension (3.619(1) Å at 300 K). This short Pd···O···Pd distance could be indicative of a weak Pd···H_2O···Pd interaction taking place in the c direction. However, as it is not possible to locate the hydrogen atoms, it is not possible to draw any conclusions as to the nature of this interaction. Indeed, the location exactly between the two palladium centres suggests that both lone pairs and hydrogens would be directed towards the palladium atoms, so the presence of an interaction is unclear.

11.3.2 Spin Crossover

On cooling there is a very large unit cell contraction of approximately 50 Å^3 from approximately 400 Å^3 to 350 Å^3 (12.5%) at approximately 250 K (Figure 11.9). This is one of the largest contractions due to spin crossover effects discussed here, or indeed reported in the literature. The contraction takes place over a range of approximately 20 K in agreement with the magnetic susceptibility data, however the temperature recorded for the transition is much higher than that determined from the SQUID data. It is possible that this is caused by a partial loss of water due to the vacuum necessary when using the PheniX (as seen with compounds **7**–**9**), however it is more likely that this results from calibration

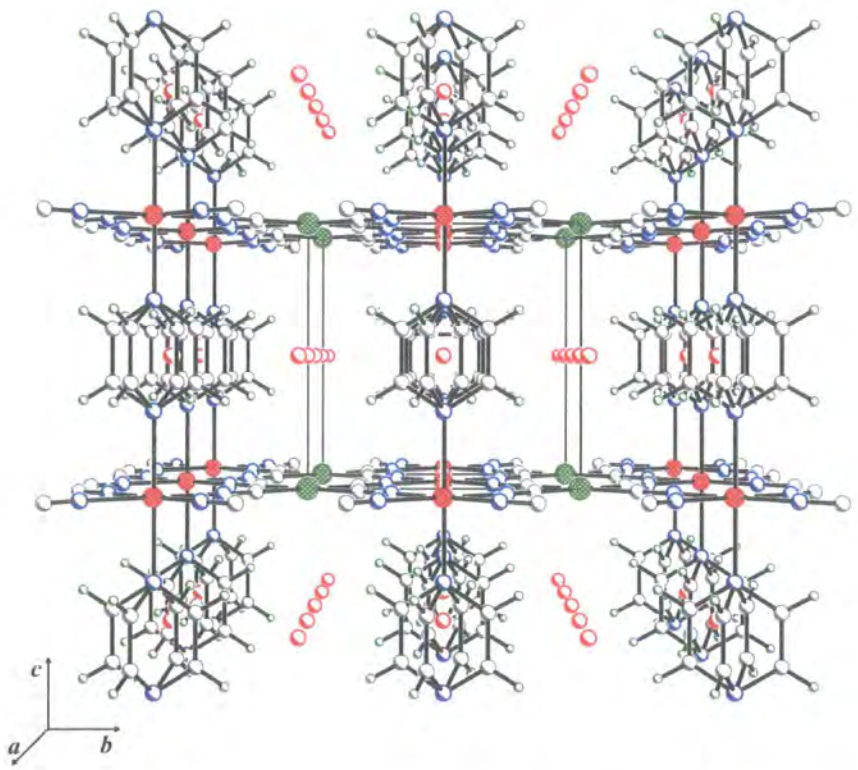

Figure 11.5: Compound **13** viewed down the *a*-axis showing the $[Pd(CN)_4Fe]$ sheets linked by disordered Pyz ligands.

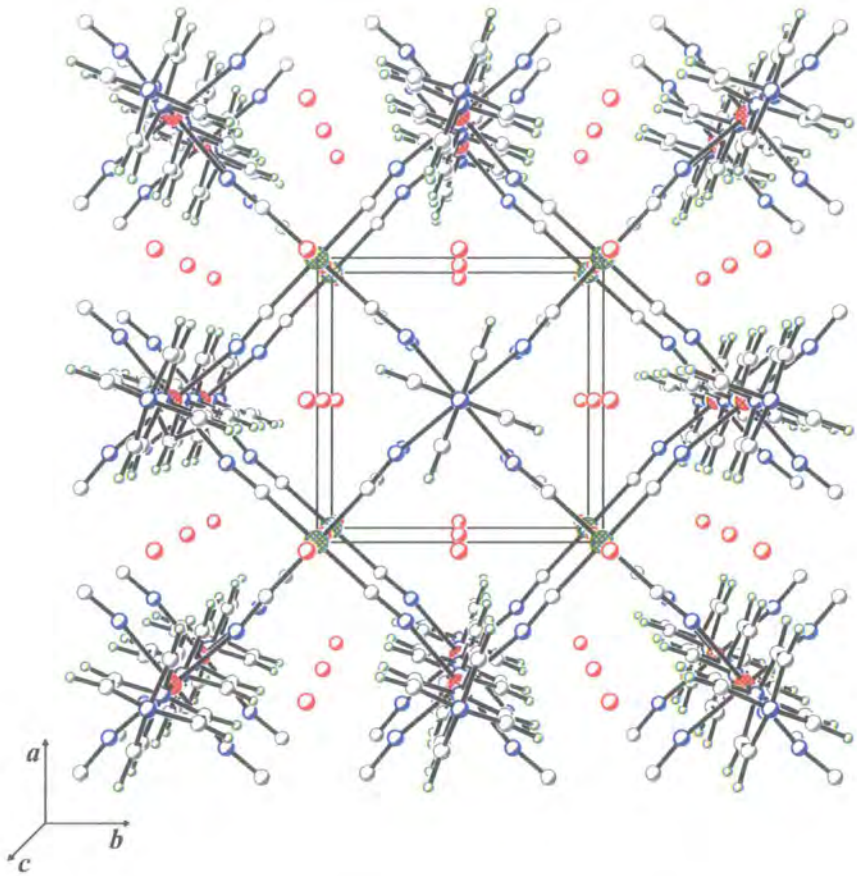

Figure 11.6: Compound **13** viewed down the *c*-axis showing the channels occupied by solvent water.

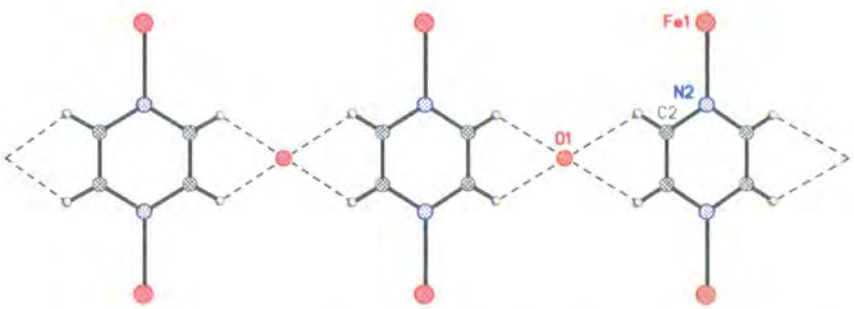

Figure 11.7: The Pyz···O hydrogen bonded chain. The C···O distance of 2.73(1) Å at 300 K suggests the presence of an interaction.

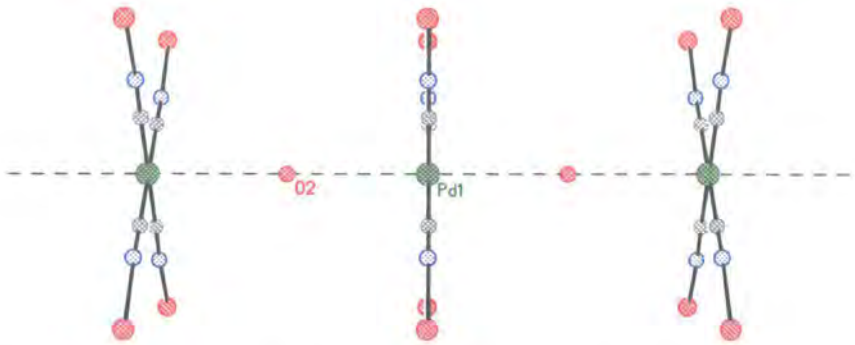

Figure 11.8: The Pd···O chain in compound **13**. The Pd···O distance of 3.619(1) Å at 300 K suggests there may be an interaction.

errors as there is no evidence of water loss in the powder data.[§] According to the powder diffraction results, the transition on cooling begins between 271 K and 262 K ($T_{1\downarrow}$) and is complete at 236 K ($T_{2\downarrow}$). On warming, the transition begins at between 260 K and 269 K ($T_{1\uparrow}$) and is incomplete at 300 K. Thus, the data collected during the transition has two phases; high spin and low spin.

Cell Parameter Changes

The data collected at 262 K on cooling is particularly interesting, because it contains both high and low spin states both in a large amount, enabling accurate determination of the cell parameters for both states at the same temperature (Table 11.1). The same effect can also be seen at 295 K, but as this is right at the top of the temperature range of the PheniX, the values could be less reliable.

The contraction in the c direction at 262 K is 0.447(3) Å, which corresponds with the contraction in the direction of the Pyz ligand. Since both the iron and nitrogen atom positions are constrained by symmetry, and there are two Fe–N_{Pyz} distances per asymmetric

[§]It is very difficult to prove the presence or absence of the solvent as the contribution to the diffraction from the water is very small compared with that of the iron and palladium atoms. Nevertheless, structure refinements carried out with the water molecules removed increased the R-indices, suggesting that either dehydration did not take place or was incomplete.

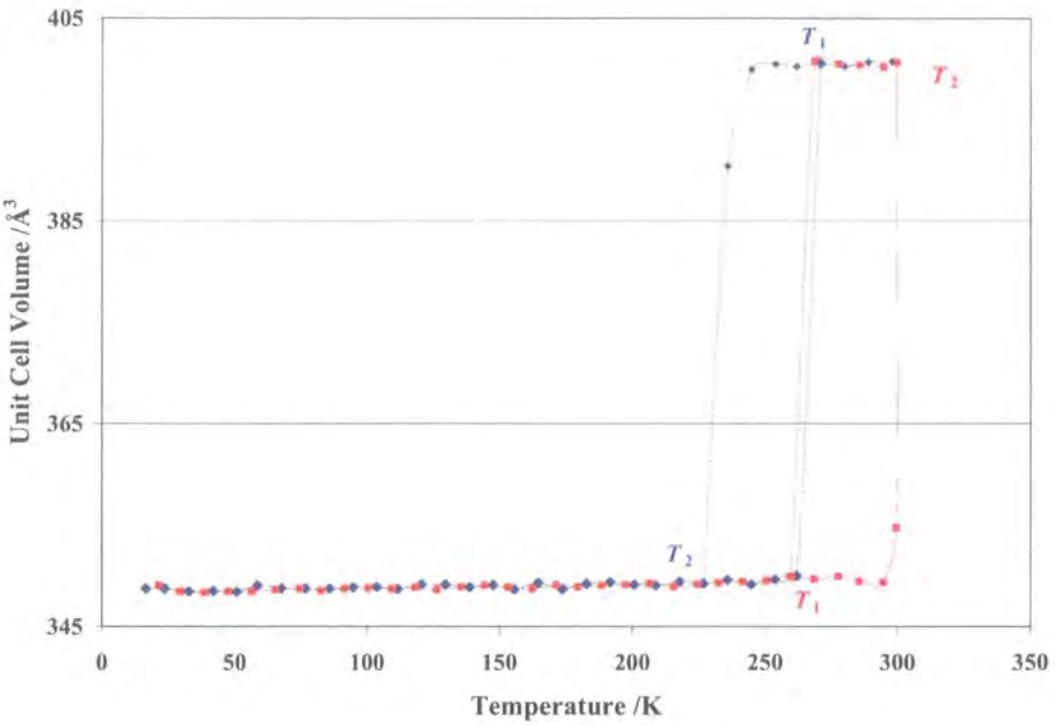

Figure 11.9: Unit cell volumes from powder diffraction data collected during cooling (blue) and warming compound **13** (red). It can be seen that the transitions on cooling and warming begin at the same temperature ($T_{1\downarrow} \approx T_{1\uparrow}$), but that the transition takes place over approximately 20–25 K ($T_{1\downarrow}$–$T_{2\downarrow}$) which is approximately the size of the hysteresis seen in the magnetic susceptibility data. The temperature of the transition is high on both warming and cooling compared with that seen in the magnetic susceptibility data, but the magnitude of the hysteresis agrees well. This suggests that the difference may result from calibration errors, however it is possible that the vacuum has removed some or all of the solvent.

unit, this enabled accurate determination of the Fe–Pyz contraction as 0.224(3) Å. The Fe–NC contraction is not quite so easy to quantify. The –Fe–NC–Pd–CN–Fe– chains run along the diagonal, but using trigonometry, the Fe–Pd distances for the HS and LS phases at 262 K can be calculated as 5.262(3) Å and 5.008(3) Å. Thus the difference is 0.254(4) Å, which would appear to be a very large contraction for an Fe–N bond in a spin crossover material. However, the possibility must be considered that the $[Pd(CN)_4]^{2-}$ ligand might not be planar or that the –Pd–C–N–Fe– groups may not be linear. Indeed, it is quite likely that there is distortion around the iron core in the HS state. However, according to the CSD, the $[Pd(CN)_4]^{2-}$ ligand should be close to planar and the site symmetry of the palladium atom is $4/m$ with the symmetry of the $[Pd(CN)_4]^{2-}$ moiety approximately D_{4h}. While it is possible that a loss of planarity breaks this symmetry (but could not be seen due to the poor quality data), it seems unlikely that this is the case. In addition, this would lead to a lengthening of the bonds rather than a shortening.

Thus, non-linear –Pd–C–N–Fe– groups seem more likely and recalling some of the $[Au(CN)_2]^-$ and $[Ag(CN)_2]^-$ ligands discussed previously, are quite possible. In the case of compound **13** however, steric repulsion suggests that the bending is more likely to be at the C–N–Fe angle than at the Pd–C–N angle. Typically, LS iron octahedra are more regular than HS octahedra, but bending of the C–N–Fe angle would not necessarily lead to change in the distortion. It is possible that the $[Pd(CN)_4]^{2-}$ moiety could rotate slightly around the Pd centre on cooling to the LS state (Figure 11.10). This would make the unit cell contract more, effectively reducing the amount of shortening of the Fe–N bond necessary to produce the same effect. The octahedral distortion would not increase as it is constrained by symmetry. The Fe–Pyz contraction has been given as 0.224(3) Å, which is in keeping with those seen in other materials, for example compounds **6** and **7**. In these compounds, the anionic bridging ligands lead to a comparable contraction, suggesting that there may be some additional structural change causing the large cell contraction of 12.5%. If there were a rotation of the $[Pd(CN)_4]^{2-}$ ligand, it would be nearly impossible to see with powder diffraction, but would be characterised by a change in the Fe–N–C angle.

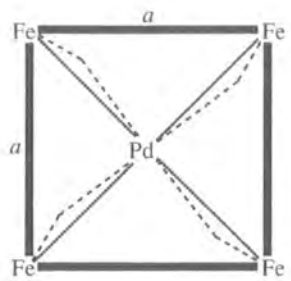

Figure 11.10: Schematic of the suggested distortion in compound **13** on cooling to the low spin state. The unit cell is shown in bold, and the possible distortion from linear in broken lines.

	High Spin	**Low Spin**	**Difference**
a	7.441(2) Å	7.183(2) Å	0.258(3) Å
c	7.230(2) Å	6.783(2) Å	0.447(3) Å
V	400.3(3) Å^3	349.9(2) Å^3	50.4(4) Å^3
wR_p	0.1226	-	-
R_p	0.0955	-	-
χ^2	1.158	-	-

Table 11.1: Cell parameters for the high and low spin states of compound **13** at 262 K, from data collected on cooling.

H-Bonding and Pd···O Interactions

The location of the solvent water molecules means the spin crossover transition will shorten their interactions with the main network. In the case of the Pd···O interaction, the distance will shorten by the same 0.224(1) Å that the Fe–Pyz bond contracts by. This means the distance changes from 3.615(3) Å to 3.392(3) Å (from the cell parameters at 262 K). It is harder to say how the C–H···O interactions change, as it is possible that the orientation of the ring changes. However, it is probable that this distance also changes. Given the importance of weak interactions on spin transitions, it is likely that the C–H···O and Pd···O interactions are important, but without more structural information, it is impossible to draw any further conclusions.

11.4 Conclusion

The spin crossover transition in compound **13** can be seen in both the raw powder data and in the change in unit cell parameters. Although there is very little thermal contraction, the contraction due to the SC transition is unusually large (~12.5%). This is primarily due to the high iron content in the sample, but may also be due to a change in orientation of the bridging $[Pd(CN)_4]^{2-}$ ligands.

Although powder X-ray diffraction is often considered to be the poor relation of single crystal diffraction, a considerable amount of information has been gained with a reasonable level of reliability, due to the high symmetry of the sample.

Part IV

Conclusion

Chapter 12

Closing Remarks

The results presented herein comprise one of the first comprehensive structural studies of spin crossover materials. It begins with mononuclear complexes and progresses onto the more unusual dinuclear complexes and novel bimetallic polymer networks. As such, it has brought to light a number of new phenomena.

Mononuclear and Dinuclear SC Complexes

$Fe(Phen)[H_2B(Pz)_2]_2$ (compound **2**) is thought to be the first example of a complex where the LIESST state is structurally different to the thermal HS state, as there is a symmetry change from $C2/c$ to the smaller primitive cell, $P\bar{1}$ (Chapter 3). Although compounds where the transition has a hysteresis often have an associated structural change, to our knowledge, the LIESST state of such a material has not before been studied. The comparison between compound **2** where there is a structural change and the Bpyd analogue compound **1**, where the three states (HS, LS and LIESST) are isostructural, gives a fascinating insight into the difference that can be made by the addition of two carbon atoms.

Dinuclear SC complexes are very rare, but the structures of two very unusual materials have been studied (Chapters 5 and 6). The first (compound **4**), involves a bipyrimidine bridged complex, which has been shown to undergo both a cooperative step transition and Light-Induced Excited Spin-State Trapping. However, despite magnetic susceptibility data that suggest the contrary, at 30 K the LIESST state appears to relax rapidly; an effect that might be X-ray stimulated. Irradiating during data collection using custom-built apparatus proved that the crystal remained intact and allowed a full structural

study, which to our knowledge, is the first such structure to be carried out under constant irradiation. In contrast, the second dinuclear complex (compound **5**) undergoes a more gradual step transition and does not undergo LIESST. The variable temperature structural study performed gives an indication of the causes for the separate steps of the transition.

Bimetallic Spin Crossover Networks

Structural studies of bimetallic polymeric SC compounds in the literature to date are few, as this is a relatively new field. However, $Fe(Pmd)_2Fe(H_2O)_2[Au(CN)_2]_4$ and $Fe(Pmd)_2Fe(H_2O)_2[Ag(CN)_2]_4$ (compounds **6** and **7**) are particularly interesting examples of this type of material (Chapter 7). The highly abrupt, cooperative transition accompanied by a dramatic colour change makes these compounds suitable for technological applications (e.g. displays). In addition, the loss of water coupled with the change in magnetic properties while retaining crystallinity, makes this type of material particularly interesting scientifically, as well as enhancing their industrial potential. For example this type of material could be used in devices for sensing humidity, where the temperature or presence of a colour change, indicates whether or not there is water present.

The copper analogue however (compound **10**, Chapter 8), although made in a similar way has a very different structure and has very different physical properties. Like compounds **6** and **7**, compound **10** undergoes a sharp SC transition without a structural change. However, not only does the transition take place at a much lower temperature, but the material can also be excited into a meta-stable high spin state using green light.

$\{Fe(Pmd)[Ag(CN)_2][Ag_2(CN)_3]\}$ (compound **11**, Chapter 9) was a bi-product of the reaction that gave compound **7**, but has yet another different structure and behaviour. This compound has five crystallographically unique iron centres, thought to be the first spin crossover material with such a high number of crystallographically inequivalent SC active centres. In compound **11** the iron atoms are connected by Pmd ligands to form chains, and through silver cyanide bridges forming a complex network. Despite the poor quality of the crystals, it has been possible to follow the progress of the spin transition, including a step transition and a meta-stable light induced HS state, through the changes in the FeN_6 octahedral volume. From this it was possible to identify the iron atoms responsible for the change in magnetic properties. Like compound **10**, compound **11** also

undergoes LIESST, but uniquely, the relaxation is a two step process.

The last silver cyanide compound studied was $\{Fe(Bpe)[Ag(CN)_2]_2\}$ (compound **12**, Chapter 10), which consists of $Fe[Ag(CN)_2]$ sheets connected by bis-pyridylethylene ligands to form two interpenetrating networks. This compound is one of the most unusual studied. Like compound **2**, it has a thermally induced structural transition coupled with the spin crossover. In the case of compound **12**, the LS state reached on cooling has a doubled cell volume. However, in contrast to compound **2**, irradiating at 30 K generates a high spin state with the *same* crystal structure as the thermal high spin state. This meta-stable HS structure can also be reached by quenching a single crystal to 30 K. On warming from this meta-stable high spin state though, a second low spin state, with a structure analogous to that of the high spin state is generated. This is another effect that has not been reported previously to our knowledge, and is related to the "light induced polymorphism" seen in compound **2**.

Thus, this is one of the first in depth, structural studies of thermal and light induced spin transitions and many of the light induced effects have not been seen in the literature. This includes the thermal and light induced polymorphism in compound **2**, the rapidly relaxing LIESST state in the bipyrimidine bridged dinuclear compound **4**, the unique two step relaxation seen in the complex iron-silver network of compound **11** and the unusual structural behaviour of compound **12**, which has two structural low spin states. This is in addition to a number of other materials which also exhibit a range of interesting properties including allosterism and thermo-chromism in addition to their notable magnetic properties.

This work has only scratched the surface of a fascinating field, but has highlighted a number of new properties with potential for use in technological applications.

Bibliography

[1] F. H. Allen, *Acta Cryst.*, **B58**, 380–388 (2002).

[2] I. J. Bruno, J. C. Cole, P. R. Edgington, M. Kessler, C. F. Macrae, P. McCabe, J. Pearson, and R. Taylor, *Acta Cryst.*, **B58**, 389–397 (2002).

[3] A. R. West, *Solid State Chemistry and its Applications*, John Wiley and Sons, 1984.

[4] O. Kahn, *Molecular Magnetism*, VCH Publishers Inc., New York., 1993.

[5] N. N. Greenwood and A. Earnshaw, *Chemistry of the Elements*, Butterworth-Heinemann, 1997.

[6] World Wide Web — http://www.everyscience.com/.

[7] P. Gütlich, Y. Garcia, and H. A. Goodwin, *Chem. Soc. Rev.*, **29**, 419–427 (2000).

[8] Y. Garcia, V. Ksenofontov, G. Levchenko, and P. Gütlich, *J. Mater. Chem.*, **10**, 2274–2276 (2000).

[9] B. Gallois, J. A. Real, C. Hauw, and J. Zarembowitch, *Inorg. Chem.*, **29**, 1152–1158 (1990).

[10] J. A. Real, B. Gallois, T. Granier, F. Suez-Panamá, and J. Zarembowitch, *Inorg. Chem.*, **31**, 4972–4979 (1992).

[11] Z. J. Zhong, J.-Q. Tao, Z. Yu, C.-Y. Dun, Y.-J. Liu, and X.-Z. You, *J. Chem. Soc., Dalton Trans.*, pages 327–328 (1998).

[12] A. Hauser, *Chem. Phys. Lett.*, **192**(1), 65–70 (1992).

[13] S. Decurtins, P. Gütlich, C. P. Köhler, H. Spiering, and A. Hauser, *Chem. Phys. Lett.*, **105**(1), 1–4 (1984).

[14] S. Decurtins, P. Gütlich, K. M. Hasselbach, A. Hauser, and H. Spiering, *Inorg. Chem.*, **24**, 2174–2178 (1985).

[15] A. Hauser, *Coord. Chem. Rev.*, **11**, 275–290 (1991).

[16] O. Kahn, J. Kröber, and C. Jay, *Adv. Mater.*, **4**(11), 718–728 (1992).

[17] O. Kahn and C. J. Martinez, *Science*, **279**, 44–48 (1998).

[18] J. C. Peltier, *Ann. Chimie*, **56**, 371–386 (1834).

[19] R. Damadian, *Science*, **171**, 1151–1153 (1971).

[20] R. N. Muller, L. V. Elst, and S. Laurent, *J. Am. Chem. Soc.*, **125**, 8405–8407 (2003).

[21] Abbess Instruments and Systems Inc., Technical Note: Magnetic Measuring Techniques — http://abbess.com/manuals/tech-note01.html.

[22] D. Chernyshov, M. Hostettler, K. W. Törnroos, and H.-B. Bürgi, *Angew. Chem. Int. Ed.*, **42**, 3825–3830 (2003).

[23] G. A. Renovitch and W. A. Baker, Jr, *J. Am. Chem. Soc.*, **1967**(89), 6377–6378.

[24] H. Köppen, E. W. Müller, C. P. Köhler, H. Spiering, E. Meissner, and P. Gütlich, *Chem. Phys. Lett.*, **91**(5), 348–352 (1982).

[25] M. Mikami, M. Konno, and Y. Saito, *Chem. Phys. Lett.*, **63**(3), 566–569 (1979).

[26] V. Petrouleas and J.-P. Tuchagues, *Chem. Phys. Lett.*, **137**(1), 21–25 (1987).

[27] D. Boinnard, A. Bousseksou, A. Dworkin, J.-M. Savariault, F. Varret, and J.-P. Tuchagues, *Inorg. Chem.*, **33**, 271–281 (1994).

[28] J. H. Takemoto and B. Hutchinson, *Inorg. Chem.*, **12**(3), 705–708 (1973).

[29] W. A. Baker, Jr and G. J. Long, *Chem. Commun.*, **15**, 368–369 (1965).

[30] A. Bousseksou, J. J. McGarvey, F. Varret, J. A. Real, J.-P. Tuchagues, A. C. Dennis, and M. L. Boillot, *Chem. Phys. Lett.*, **318**, 409–416 (2000).

[31] W. R. Scheidt and C. A. Reed, *Chem. Res.*, **81**, 543–555 (1981).

[32] M. F. Perutz, G. Fermi, and B. Luisi, *Acc. Chem. Res.*, **20**, 309–321 (1987).

[33] L. Cambi and A. Cagnasso, *Atti Acad. Naz. Lincei*, **13**, 809 (1931).

[34] L. Cambi and L. Szegö, *Ber. Dt. Chem. Ges.*, **64**, 2591–2598 (1931).

[35] L. Cambi and L. Szegö, *Chem. Ber.*, pages 656–661 (1933).

[36] J. G. Leipoldt and P. Coppens, *Inorg. Chem.*, **12**(10), 2269–2274 (1973).

[37] P. Gütlich, A. Hauser, and H. Spiering, *Angew. Chem. Int. Ed. Engl.*, **33**, 2024–2054 (1994).

[38] W. A. Baker, Jr and H. M. Bobonich, *Inorg. Chem.*, **3**(8), 1184–1188 (1964).

[39] E. König and K. Madeja, *J. Chem. Soc., Chem. Commun.*, (3), 61–62 (1966).

[40] R. Herber, *Inorg. Chem.*, **26**, 173–178 (1987).

[41] P. S. Rao, A. Reuveni, B. R. McGarvey, P. Ganguli, and P. Gütlich, *Inorg. Chem.*, **20**, 204–207 (1981).

[42] P. S. Rao, P. Ganguli, and B. R. McGarvey, *Inorg. Chem.*, **20**, 3682–3688 (1981).

[43] M. Sorai and S. Seki, *J. Phys. Chem. Solids*, **35**, 555–570 (1974).

[44] N. Shioyasu, K. Kagetsu, K. Mishima, M. K. Kubo, T. Tominaga, K. Nishiyama, and K. Nagamine, *Hyperfine Int.*, **84**, 477–481 (1994).

[45] T. Granier, B. Gallois, J. Gaultier, J. A. Real, and J. Zarembowitch, *Inorg. Chem.*, **32**, 5305–5312 (1993).

[46] M. Marchivie, P. Guionneau, J. A. K. Howard, G. Chastanet, J.-F. Létard, A. E. Goeta, and D. Chasseau, *J. Am. Chem. Soc.*, **124**(2), 194–195 (2002).

[47] C. Cartier, P. Thuery, M. Verdaguer, J. Zarembowitch, and A. Michalowitch, *J. Physique*, **47**(Suplément au nº 12, Colloque C8), 563–568 (1986).

[48] E. König and K. J. Watson, *Chem. Phys. Lett.*, **6**, 457–459 (1970).

[49] M. Konno and M. Mikami-Kido, *Bull. Chem. Soc. Jpn.*, **64**, 339–345 (1991).

[50] G. Bradley, V. McKee, S. M. Nelson, and J. Nelson, *J. Chem. Soc., Dalton Trans.*, pages 522–526 (1978).

[51] E. König, G. Gitter, W. Irler, and S. M. Nelson, *Inorg. Chim. Acta*, **37**, 169–179 (1979).

[52] M. Marchivie, P. Guionneau, J.-F. Létard, and D. Chasseau, *Acta Cryst.*, **B59**, 479–486 (2003).

[53] P. G. Sim and E. Sinn, *J. Am. Chem. Soc.*, **103**, 241–243 (1981).

[54] D. M. Halepoto, D. G. Holt, L. F. Larkworthy, G. J. Leigh, D. C. Povey, and G. W. Smith, *J. Chem. Soc., Chem. Commun.*, pages 1322–1323 (1989).

[55] P. L. Franke, J. G. Haasnoot, and A. P. Zuur, *Inorg. Chim. Acta*, **59**, 5–9 (1982).

[56] M. H. Klingele and S. Brooker, *Coord. Chem. Rev.*, **241**, 119–132 (2003).

[57] W. Hibbs, A. M. Arif, P. J. van Konningsbruggen, and J. S. Miller, *CrystEngComm*, **1**, 12–14 (article 4) (1999).

[58] J. Jeftić, R. Hinek, S. C. Capelli, and A. Hauser, *Inorg. Chem.*, **36**, 3080–3087 (1997).

[59] L. Wiehl, H. Spiering, P. Gütlich, and K. Knorr, *J. Appl. Cryst.*, **23**, 151–160 (1990).

[60] L. Wiehl, *Acta Cryst.*, **B49**, 289–303 (1993).

[61] J. Jung, F. Bruchhäuser, R. Feile, H. Spiering, and P. Gütlich, *Z. Phys. B*, **100**, 517–522 (1996).

[62] J. Jung, G. Schmitt, L. Wiehl, A. Hauser, K. Knorr, H. Spiering, and P. Gütlich, *Z. Phys. B*, **100**, 523–534 (1996).

[63] J. Jeftić and A. Hauser, *J. Phys. Chem. B*, **101**, 10262–10270 (1997).

[64] A. Hauser, J. Jeftić, H. Romstedt, R. Hinek, and H. Spiering, *Coord. Chem. Rev.*, **190–192**, 471–491 (1999).

[65] P. Poganiuch, S. Decurtins, and P. Gütlich, *J. Am. Chem. Soc.*, **112**, 3270–3278 (1990).

[66] J. Kusz, H. Spiering, and P. Gütlich, *J. Appl. Cryst.*, **34**, 229–238 (2001).

[67] L. Wiehl, G. Keil, C. P. Köhler, H. Spiering, and P. Gütlich, *Inorg. Chem.*, **25**, 1565–1571 (1986).

[68] M. Sorai, J. Ensling, K. M. Hasselbach, and P. Gütlich, *Chem. Phys.*, **20**, 197–208 (1977).

[69] A. M. Greenaway and E. Sinn, *J. Am. Chem. Soc.*, **100**(26), 8080–8084 (1978).

[70] A. M. Greenaway, C. J. O'Conner, A. Schrock, and E. Sinn, *Inorg. Chem.*, **18**(10), 2692–2695 (1979).

[71] B. A. Katz and C. E. Strouse, *J. Am. Chem. Soc.*, **101**(21), 6214–6221 (1979).

[72] E. C. Constable, *Adv. Inorg. Chem. Rad.*, **30**, 69–121 (1986).

[73] R. Hogg and R. G. Wilkins, *J. Chem. Soc.*, pages 341–350 (1962).

[74] S. Kremer, W. Henke, and D. Reinen, *Inorg. Chem.*, **21**, 3013–3022 (1982).

[75] B. N. Figgis, E. S. Kucharski, and A. H. White, *Aus. J. Chem.*, **36**, 1537–1561 (1983).

[76] P. Manikandan, K. Padmakumar, K. R. J. Thomas, B. Varghese, G. V. R. Chandramonli, and P. T. Manoharan, *Inorg. Chem.*, **40**, 6930–6939 (2001).

[77] J. Elhaïk, V. A. Money, S. A. Barrat, I. R. Kilner, C. A. Evans, and M. A. Halcrow, *Dalton Trans.*, pages 2053–2060 (2003).

[78] V. A. Money, I. R. Evans, M. A. Halcrow, A. E. Goeta, and J. A. K. Howard, *Chem. Commun.*, pages 158–159 (2003).

[79] J. R. Sams, J. C. Scott, and T. B. Tsin, *Chem. Phys. Lett.*, **18**(451–453) (1973).

[80] J. R. Sams and T. B. Tsin, *J. Chem. Soc., Dalton Trans.*, pages 488–496 (1976).

[81] A. W. Addison, S. Burman, C. G. Wahlgren, O. A. Rajan, T. M. Rowe, and E. Sinn, *J. Chem. Soc., Dalton Trans.*, pages 2621–2630 (1987).

[82] R. Boča, P. Baran, L. Dlháň, J. Šima, G. Weisinger, F. Renz, U. El-Ayaan, and W. Linert, *Polyedron*, **16**(1), 47–55 (1997).

[83] M. Hasegawa, F. Renz, T. Hara, Y. Kikuchi, Y. Fekuda, J. Okubo, T. Hoshi, and W. Linert, *Chem. Phys.*, **277**, 21–30 (2002).

[84] F. Cecconi, M. di Vaira, S. Midollini, A. Orlandini, and L. Sacconi, *Inorg. Chem.*, **20**, 3423–3430 (1981).

[85] E. König, G. Ritter, S. K. Kulshreshtha, J. Waigel, and L. Sacconi, *Inorg. Chem.*, **23**, 1241–1246 (1984).

[86] B. Kersting, M. J. Kolm, and C. Janiak, *Z. Anorg. Allg. Chem.*, **634**, 775–780 (1998).

[87] J. A. Real, J. Zarembowitch, O. Kahn, and X. Solans, *Inorg. Chem.*, **26**, 2939–2943 (1987).

[88] V. Ksenofontof, A. B. Gaspar, J. A. Real, and P. Gütlich, *J. Phys. Chem. B*, **105**, 12266–12271 (2001).

[89] A. B. Gaspar, V. Ksenofontov, J. A. Real, and P. Gütlich, *Chem. Phys. Lett.*, **373**, 385–391 (2003).

[90] S. Brooker, D. J. de Geest, R. J. Kelly, P. G. Plieger, B. Moubaraki, K. S. Murray, and G. B. Jameson, *J. Chem. Soc., Dalton. Trans.*, pages 2080–2087 (2002).

[91] S. Brooker, P. G. Plieger, B. Moubaraki, and K. S. Murray, *Angew. Chem. Int. Ed.*, **38**(3), 408–410 (1999).

[92] J. J. A. Kolnaar, M. I. de Heer, H. Kooijman, A. L. Spek, G. Schmitt, V. Ksenofontof, P. Gütlich, J. G. Haasnoot, and J. Reedijk, *Eur. J. Inorg. Chem.*, pages 881–886 (1999).

[93] D. W. Engelfriet, G. C. Verschoor, and W. den Brinker, *Acta Cryst.*, **B36**, 1554–1560 (1979).

[94] D. W. Engelfriet, G. C. Verschoor, and W. J. Vermin, *Acta Cryst.*, **B35**, 2927–2931 (1980).

[95] K. Ni-iya, A. Fuyuhiro, T. Yagi, S. Nasu, K. Kuzushita, S. Morimoto, and S. Kaizaki, *Bull. Chem. Soc. Jpn.*, **74**, 1891–1897 (2001).

[96] L. J. Charbonnière, A. F. Williams, C. Piguet, G. Bernardinelli, and E. Rivara-Minten, *Chem. Eur. J.*, **4**(3), 485–493 (1998).

[97] S. G. Telfer, B. Bocquet, and A. F. Williams, *Inorg. Chem.*, **40**, 4818–4820 (2001).

[98] G. Vos, R. A. le Fêbre, R. A. G. de Graaff, J. G. Haasnoot, and J. Reedijk, *J. Am. Chem. Soc.*, **105**, 1682–1683 (1983).

[99] G. Vos, R. A. G. de Graaff, J. G. Haasnoot, A. M. van derKraan, P. de Vaal, and J. Reedijk, *Inorg. Chem.*, **23**, 2905–2910 (1984).

[100] E. Breuning, M. Ruben, J.-M. Lehn, F. Renz, Y. Garcia, V. Ksenofontov, P. Gütlich, E. Wegelius, and K. Rissanen, *Angew. Chem. Int. Ed.*, **39**(14), 2505–2507 (2000).

[101] C. Janiak, *Dalton Trans.*, pages 2781–2804 (2003).

[102] L. G. Lavrenova, V. N. Ikorskii, V. A. Varnek, I. M. Oglezneva, and S. V. Larionov, *Koord. Khim. (Sov. J. Coord. Chem.)*, **12**(2), 207–215 (119–127) (1986).

[103] L. G. Lavrenova, V. N. Ikorskii, V. A. Varnek, I. M. Oglezneva, and S. V. Larionov, *Koord. Khim. (Sov. J. Coord. Chem.)*, **16**(5), 654–661 (349–355) (1990).

[104] E. Codjovi, L. Sommier, O. Kahn, and C. Jay, *New J. Chem.*, **20**(5), 503–505 (1996).

[105] O. Roubeau, J. G. Haasnoot, E. Codjovi, F. Varret, and J. Reedijk, *Chem. Mater.*, **14**, 2559–2566 (2002).

[106] P. J. van Koningbruggen, Y. Garcia, O. Kahn, L. Fournès, H. Kooijman, A. L. Spek, J. G. Haasnoot, J. Moscovici, K. Provost, A. Michalowicz, F. Rwnz, and P. Gütlich, *Inorg. Chem.*, **39**, 1891–1900 (2000).

[107] J. Schweifer, P. Weinberger, K. Mereiter, M. Boca, C. Reichl, G. Weisinger, G. Hilscher, H. van Koningsbruggen, P. Kooijman, M. Grunert, and W. Linert, *Inorg. Chim. Acta*, **339**, 297–306 (2002).

[108] P. J. van Koningbruggen, M. Grunnert, and P. Weinberger, *Mon. Chem.*, **134**, 183–198 (2003).

[109] G. de Munno, M. Julve, J. A. Real, F. Lloret, and R. Scopelliti, *Inorg. Chim. Acta*, **250**, 81–85 (1996).

[110] G. S. Matouzenko, G. Molnár, N. Bréfuel, M. Perrin, A. Bousseksou, and S. A. Borshch, *Chem. Matter.*, **15**, 550–556 (2003).

[111] M. Ohba and H. Ōkawa, *Coord. Chem. Rev.*, **198**, 313–328 (2000).

[112] K. R. Dunbar and R. A. Heintz, *Prog. Inorg. Chem.*, **45**, 283–391 (1997).

[113] W. Vreugdenhil, J. H. van Diemen, R. A. G. de Graaff, J. G. Haasnoot, J. Reedijk, A. M. van der Kraan, O. Kahn, and J. Zarembowitch, *Polyhedron*, **9**(24), 2971–2979 (1990).

[114] Y. Garcia, V. Ksenofontov, G. Levchenko, G. Schmitt, and P. Gütlich, *J. Phys. Chem. B*, **104**(21), 5045–5048 (2000).

[115] J. A. Real, E. Andrés, M. C. Muñoz, M. Julve, T. Granier, A. Bousseksou, and F. Varret, *Science*, **268**, 265–267 (1995).

[116] N. Moliner, M. C. Muñoz, S. Létard, X. Solans, N. Menendez, A. Goujon, F. Varret, and J. A. Real, *Inorg. Chem.*, **39**(23), 5390–5393 (2000).

[117] H. M. Powell and J. H. Rayner, *Nature*, **163**(4145), 566–567 (1949).

[118] J. H. Rayner and H. M. Powell, *J. Chem. Soc.*, **319–328** (1952).

[119] H. G. Bütner, G. J. Kearley, C. J. Howard, and F. Fillaux, *Acta Cryst.*, **B50**, 431–435 (1994).

[120] T. Kitazawa, Y. Gomi, M. Takahashi, M. Takeda, M. Enomoto, A. Miyazaki, and T. Enoki, *J. Mater. Chem.*, **6**(1), 119–121 (1996).

[121] S. Akyüz, A. B. Dempster, R. L. Morehouse, and S. Suzuki, *J. Mol. Struct.*, **17**, 105–125.

[122] K. Hosoya, T. Kitazawa, M. Takahashi, M. Takeda, J.-F. Meunier, G. Molnár, and A. Bousseksou, *Phys. Chem. Chem. Phys.*, **5**, 1682–1688 (2003).

[123] P. Gütlich, H. Köppen, and H. G. Steinhäuser, *Chem. Phys. Lett.*, **74**(3), 475–480 (1980).

[124] A. Bousseksou, L. Tommasi, G. Lemercier, F. Varret, and J.-P. Tuchagues, *Chem. Phys. Lett.*, **243**, 493–499 (1995).

[125] V. Niel, J. M. Martinez-Agudo, M. C. Muñoz, A. B. Gaspar, and J. A. Real, *Inorg. Chem.*, **40**, 3838–3839 (2001).

[126] Y. García, O. Kahn, L. Rabardel, B. Chansou, L. Salmon, and J. P. Touchagues, *Inorg. Chem.*, **38**, 4663–4670 (1999).

[127] P. J. Koningsbruggen, Y. García, H. Kooijman, A. L. Spek, J. G. Haasnoot, O. Kahn, J. Linares, E. Codjovi, and F. Varret, *J. Chem. Soc., Dalton Trans.*, pages 466–471 (2001).

[128] G. Molnár, V. Niel, J. A. Real, L. Dubrovinsky, A. Bousseksou, and J. J. McGarvey, *J. Phys. Chem. B*, **107**, 3149–3155 (2003).

[129] Photographs of unknown origin.

[130] J. Cosier and A. M. Glazer, *J. Appl. Cryst.*, **19**, 105–107 (1986).

[131] A. E. Goeta, L. K. Thompson, C. L. Sheppard, S. S. Tandon, C. W. Lehmann, J. Cosier, C. Webster, and J. A. K. Howard, *Acta Cryst.*, **C55**, 1243–1246 (1999).

[132] Photographs courtesy of Dr. A. E. Goeta.

[133] U. W. Arndt, J. V. P. Long, and P. Duncumb, X-ray Generator, **USP 6,282,263**, 2001.

[134] N. Loxley and L. Pina, X-ray Focusing Apparatus, **USP 6,504,901**, 2003.

[135] R. C. B. Copley, A. E. Goeta, C. W. Lehmann, J. C. Cole, D. S. Yufit, J. A. K. Howard, and J. A. Archer, *J. Appl. Cryst.*, **30**, 413–417 (1997).

[136] SAINT-NT, Data Reduction Software, Version 5.0., Bruker Analytical Instruments Inc., Madison, Wisconsin, U.S.A., 1999.

[137] SHELXTL, Structure Refinement and Solution Software, Version 5.1., Bruker Analytical Instruments Inc., Madison, Wisconsin, U.S.A., 1999.

[138] SMART-NT, Data Collection Software, Version 5.0., Bruker Analytical Instruments Inc., Madison, Wisconsin, U.S.A., 1999.

[139] A. L. Patterson, *Phys. Rev.*, **46**, 372–376 (1934).

[140] SHELXL-97, Program for the Refinement of Crystal Structures. G. M. Sheldrick, University of Göttingen, Germany., 1997.

[141] ATOMS. E. Dowty (http://www.shapesoftware.com/), 2000.

[142] ORTEP3. L. Farrugia (http://www.ornl.gov/sci/ortep/), 2000.

[143] enCIFer — CIF Checking, Editing and Visualisation software, Version 1.0., Cambridge Crystallographic Data Centre, 12, Union Road, Cambridge, CB2 1EZ, U.K. (http://www.ccdc.cam.ac.uk/), 2003.

[144] CheckCif. International Union of Crystallography, Abbey Square, Chester, CH1 2HU, England (http://www.iucr.org/).

[145] SADABS, Empirical Absorption Correction Program. G. M. Sheldrick, University of Göttingen, Germany, 1998.

[146] R. I. Cooper, R. O. Gould, S. Parsons, and D. J. Watkin, *J. Appl. Cryst.*, **35**, 168–174 (2002).

[147] GEMINI, Twinning Solution Program Suite, Version 1.0., Bruker Analytical Instruments Inc., Madison, Wisconsin, U.S.A., 1999/2000.

[148] Bruker DIFFRAC PLUS — editJob, Version 2.0., Bruker Analytical Instruments Inc., Madison, Wisconsin, U.S.A., 1995, 1996 & 1997.

[149] Bruker EVA MFC Application, Version 4.00.2., Bruker Analytical Instruments Inc., Madison, Wisconsin, U.S.A., 1996–1998.

[150] Anton Paar HTK1200. Anton Paar GmbH, Austria.

[151] Anton Paar TTK450. Anton Paar GmbH, Austria.

[152] The Oxford Cryosystems PheniX Oxford Cryosystems Ltd., Oxford, U.K., 2002.

[153] Photograph courtesy of Dr. S. Allen.

[154] Schematic taken from the Anton Paar HTK1200 Operating Manual.

[155] Photographs courtesy of Dr. S. Allen and from the Oxford Cryosystems literature.

[156] PDF-2, Version 4.0.70., International Centre for Diffraction Data, Newtown Square, Philadelphia, U.S.A., 1998.

[157] Bruker XCH, Version 3.02., Bruker Analytical Instruments Inc., Madison, Wisconsin, U.S.A., 1995 & 1998.

[158] GSAS — Generalised Structure Analysis System. A. C. Larson and R. B. Von Dreele, LAUR 86–748, LANSCE, MS-H805, Los Alamos National Laboratory, Los Alamos, NM 87545, California, U.S.A., 1987.

[159] B. H. Toby, *J. Appl. Cryst.*, **34**, 210–213 (2001).

[160] H. M. Ritveld, *Acta Cryst.*, **20**, 508–513 (1966).

[161] H. M. Ritveld, *Acta Cryst.*, **22**, 151–152 (1967).

[162] H. M. Ritveld, *J. Appl. Cryst.*, **2**, 65–71 (1969).

[163] G. S. Pawley, *J. Appl. Cryst.*, **14**, 357–361 (1981).

[164] L. M. D. Cranswick and A. L. Bail, *Acta Cryst.*, **A58(Supplement)**, C242 (2002).

[165] A. K. Cheetham and P. Wilkinson, *J. Phys. Chem. Solids*, **52**(10), 1199–1208 (1991).

[166] FULLPROF — A Program for Rietveld Refinement and Pattern Matching Analysis. J. Rodriguez-Carvajal, Abstracts of the Satellite Meeting on Powder Diffraction of the XV Congress of the IUCr, Toulouse, France, page 127., 1990.

[167] A. Le Bail, H. Duroy, and J. Fourquet, *Mat. Res. Bull.*, **23**, 447–452 (1988).

[168] W. I. F. David, K. Shankland, and N. Shankland, *Chem. Commun.*, pages 931–932 (1998).

[169] J. D. Oliver, D. F. Mullica, B. B. Hutchinson, and W. O. Milligan, *Inorg. Chem.*, **19**, 165–169 (1980).

[170] G. J. Long and B. B. Hutchinson, *Inorg. Chem.*, **26**, 608–613 (1987).

[171] F. Grandjean, G. J. Long, B. B. Hutchinson, L. Ohlhausen, P. Niell, and J. D. Holcomb, *Inorg. Chem.*, **28**(24), 4406–4414 (1989).

[172] J. A. Real, M. C. Muñoz, J. Faus, and X. Solans, *Inorg. Chem.*, **36**, 3008–3013 (1997).

[173] N. Moliner, L. Salmon, L. Capes, M. C. Muñoz, J.-F. Létard, A. Bouseksou, J.-P. Tuchagues, J. J. McGarvey, A. C. Dennis, M. Castro, R. Burriel, and J. A. Real, *J. Phys. Chem. B*, **106**, 4276–4283 (2002).

[174] T. Balić-Žunić and I. Vicković, *J. Appl. Cryst.*, **29**, 305–306 (1996).

[175] P. Guionneau, C. Brigouleix, Y. Barrans, A. E. Goeta, J.-F. Létard, J. A. K. Howard, J. Gaultier, and D. Chasseau, *C. R. Acad. Sci. Paris, Chemie*, **4**, 1–11 (2001).

[176] J. A. Real, *Private Communication.*

[177] A. B. Gaspar Pedros, *Transiciones de Espín en Compuestos de Hierro(II) y Cobalto(II) (Ph.D. Thesis)*, Departament de Química Inorgánica, Institut de Ciència Molecular, Facultat de Química, Universidad de València, 2002.

[178] A. Ozarowski, B. R. McGarvey, A. B. Sarkar, and J. E. Drake, *Inorg. Chem.*, **27**, 628–635 (1988).

[179] S. K. Kulshreshtha, R. Sasikala, and E. König, *Chem. Phys. Lett.*, **123**(3), 215–217 (1986).

[180] R. E. Marsh, *Inorg. Chem.*, **27**, 2902–2903 (1988).

[181] J. A. Real, H. Bolvin, A. Bousseksou, A. Dworkin, O. Kahn, F. Varret, and J. Zarembowitch, *J. Am. Chem. Soc.*, **114**(12), 4650–4658 (1992).

[182] J. A. Real, *Private Communication.*

[183] J. A. Real, I. Castro, A. Bousseksou, M. Verdaguer, R. Burriel, M. Castro, J. Linares, and F. Varret, *Inorg. Chem.*, **36**, 455–464 (1997).

[184] J. A. Real, *Private Communication.*

[185] V. Niel, M. C. Muñoz, A. B. Gaspar, G. Levchenko, and J. A. Real, *Chem. Eur. J.*, **8**(11), 2446–2453 (2002).

[186] V. Niel, A. L. Thompson, M. C. Munñoz, A. Galet, A. E. Goeta, and J. A. Real, *Angew. Chem. Int. Ed.*, **42**, 3760–3763 (2003).

[187] V. Niel, *Transiciones de Espín en Complejos de Hierro(II) Inducidas por la Acción de la Temperatura, la Presión y la Luz (Ph.D. Thesis)*, Departament de Química Inorgánica, Institut de Ciència Molecular, Facultat de Química, Universidad de València, 2002.

[188] A. Boultif and D. Louër, *J. Appl. Cryst.*, **24**, 987–993 (1991).

[189] R. Shirley, *The Crysfire 2002 System for Automatic Powder Indexing: User's Manual.*, The Lattice Press, 41 Guildford Park Avenue, Guildford, Surrey, GU2 7NL, England, 2002.

[190] CheckCell. J. Laugier and B. Bochu, Laboratoire des Matériaux et du Génie Physique, Ecole Nationale Supérieure de Physique de Grenoble (INPG), Domaine Universitaire, BP 46, 38402 Saint Martin d'Hères, France.

[191] W. I. F. David and K. Shankland, Dash, Program for Structure Solution from Powder Diffraction Data. Cambridge Crystallographic Data Centre, Cambridge, U.K., 2001.

[192] PowderCell for Windows, Version 2.4., W. Kraus and G. Nolze, Federal Intitute for Materials Research and Testing, Rudower Chaussee 5, 12489 Berlin, Germany, 200.

[193] WebLab ViewerPro, Version 3.20., Molecular Simulations Inc., 1998.

[194] J. D. Ranford, J. J. Vittal, and D. Wu, *Angew. Chem. Int. Ed.*, **37**, 1114–1116 (1998).

[195] J. A. Real, *Private Communication.*

[196] U. M. Tripathi, A. Bauer, and H. Schmidbauer, *J. Chem. Soc., Dalton Trans.*, pages 2865–2868 (1997).

[197] A. Bayler, G. A. Bowmaker, and H. Schmidbauer, *J. Am. Chem. Soc.*, **118**, 7006–7017 (1996).

[198] G. A. Bowmaker, H. Schmidbauer, S. Krüger, and M. Rösch, *Inorg. Chem.*, **36**, 1754–1757 (1997).

[199] D. R. McKelvey, *J. Chem. Educ.*, **60**, 112–116 (1983).

[200] D. B. Leznoff, B.-Y. Xu, R. J. Batchelor, F. W. B. Einstein, and B. O. Patrick, *Inorg. Chem.*, **40**, 6026–6034 (2001).

[201] *New Scientist*, (2381 (8 February)), 49 (2003).

[202] M. A. Rawashdeh-Omary, M. A. Omary, and J. P. Fackler, Jr, *Inorg. Chim. Acta*, **334**, 376–384 (2002).

[203] A. M. Mazany and J. P. Fackler, *J. Am. Chem. Soc.*, **106**(801–802) (1984).

[204] S. Wang, J. P. Fackler, and T. F. Carlson, *Organometallics*, **9**, 1973–1975 (1990).

[205] A. Rosenzweig and D. T. Cromer, *Acta Cryst.*, **12**, 709–712 (1959).

[206] J. L. Hoard, *Z. Krystallogr.*, **84**, 231–255 (1933).

[207] G. J. Halder, C. J. Kepert, B. Moubaraki, K. S. Murray, and J. D. Cashion, *Science*, **298**, 1762–1765 (2002).

[208] V. Niel, A. Galet, A. B. Gaspar, M. C. Muñoz, and J. A. Real, *Chem. Commun.*, pages 1248–1249 (2003).

[209] V. Niel, A. L. Thompson, A. E. Goeta, C. Enachescu, A. Hauser, A. Galet, M. C. Muñoz, and J. A. Real, *J. Am. Chem. Soc. — submitted.*

[210] J. A. Real, *Private Communication.*

[211] J. Spreadborough and J. W. Christian, *J. Scientific Instruments*, **36**, 116–118 (1959).

[212] S. Cornet, *Synthesis and Characterisation of Some Main-Group Compounds with Bulky Electron-Withdrawing Substituents (Ph.D. Thesis)*, Department of Chemistry, University of Durham, 2003.

[213] S. Bettington, *The Synthesis and Photophysical Studies of Cyclometalated Iridium(III) Complexes (Ph.D. Thesis)*, Department of Chemistry, University of Durham, 2003.

[214] S. R. Rutter, *Ph.D. Thesis, to be submitted*, Department of Chemistry, University of Durham, 2004.

Part V

Appendices

Appendix A

Crystallographic Information

A.1 Compound 1

A.1.1 Single Crystal Data

200 K

Empirical formula	C22 H24 B2 Fe N10
Formula weight	505.98
Temperature	200(2) K
Wavelength	0.71073 Å
Crystal system, space group	Monoclinic, $\mathbf{C}2/c$
Unit cell dimensions	a = 16.2215(15) Å α = 90°
	b = 15.0254(15) Å β = 114.858(4)°
	c = 11.0397(11) Å γ = 90°
Volume	2441.5(4) Å^3
Z	4
Density (calculated)	1.377 Mg/m^3
Absorption coefficient	0.650 mm^{-1}
F(000)	1048
Crystal size	0.20 x 0.10 x 0.07 mm
Theta range for data collection	2.35 to 30.51°
Index ranges	$-22 <= h >= 21$, $-21 <= k >= 19$, $-15 <= l >= 11$
Reflections collected	8856
Independent reflections	3510 [$R(int)$ = 0.0519]
Completeness to theta = 30.51°	93.7%
Absorption correction	None
Max. and min. transmission	0.9559 and 0.8810
Refinement method	Full-matrix least-squares on F^2
Data / restraints / parameters	3510 / 0 / 207
Goodness-of-fit on F^2	1.003
Final R indices [I>2sigma(I)]	R_1 = 0.0521, wR_2 = 0.0777
R indices (all data)	R_1 = 0.0987, wR_2 = 0.0886
Extinction coefficient	0
Largest diff. peak and hole	0.300 and −0.274 e.Å^{-3}

120 K

Empirical formula	C22 H24 B2 Fe N10
Formula weight	505.98
Temperature	120(2) K
Wavelength	0.71073 Å
Crystal system, space group	Monoclinic, $\mathbf{C}2/c$
Unit cell dimensions	a = 16.1373(8) Å α = 90°
	b = 14.6208(8) Å β = 113.775(2)°
	c = 10.8120(6) Å γ = 90°
Volume	2334.5(2) Å^3
Z	4
Density (calculated)	1.440 Mg/m^3
Absorption coefficient	0.680 mm^{-1}
F(000)	1048
Crystal size	0.20 x 0.10 x 0.07 mm
Theta range for data collection	2.41 to 30.47°
Index ranges	$-22 <= h >= 21$, $-20 <= k >= 18$, $-15 <= l >= 11$
Reflections collected	8408
Independent reflections	3351 [$R(int)$ = 0.0567]
Completeness to theta = 30.47°	93.9%
Absorption correction	None
Max. and min. transmission	0.9540 and 0.8760
Refinement method	Full-matrix least-squares on F^2
Data / restraints / parameters	3351 / 0 / 207
Goodness-of-fit on F^2	0.994
Final R indices [I>2sigma(I)]	R_1 = 0.0501, wR_2 = 0.0857
R indices (all data)	R_1 = 0.0951, wR_2 = 0.0962
Extinction coefficient	0
Largest diff. peak and hole	0.379 and −0.503 e.Å^{-3}

30 K

Empirical formula	C22 H24 B2 Fe N10
Formula weight	505.98
Temperature	30(2) K
Wavelength	0.71073 Å
Crystal system, space group	Monoclinic, $\mathbf{C}2/c$
Unit cell dimensions	a = 16.1106(11) Å $\alpha = 90°$
	b = 14.5909(10) Å $\beta = 113.895(3)°$
	c = 10.8281(8) Å $\gamma = 90°$
Volume	2327.2(3) Å^3
Z	4
Density (calculated)	1.444 Mg/m^3
Absorption coefficient	0.682 mm^{-1}
F(000)	1048
Crystal size	0.20 x 0.10 x 0.07 mm
Theta range for data collection	3.23 to 28.53°
Index ranges	$-20 <= h >= 19$, $-19 <= k >= 15$, $-14 <= l >= 11$
Reflections collected	6333
Independent reflections	2662 [$R(int) = 0.0606$]
Completeness to theta = 28.53°	89.6%
Absorption correction	None
Max. and min. transmission	0.9538 and 0.8757
Refinement method	Full-matrix least-squares on F^2
Data / restraints / parameters	2662 / 0 / 207
Goodness-of-fit on F^2	1.001
Final R indices [I>2sigma(I)]	$R_1 = 0.0491$, $wR_2 = 0.0823$
R indices (all data)	$R_1 = 0.0946$, $wR_2 = 0.0935$
Extinction coefficient	0
Largest diff. peak and hole	0.360 and −0.510 e.Å^{-3}

30 K — Irradiated

Empirical formula	C22 H24 B2 Fe N10
Formula weight	505.98
Temperature	30(2) K
Wavelength	0.71073 Å
Crystal system, space group	Monoclinic, $\mathbf{C}2/c$
Unit cell dimensions	a = 16.0350 Å α = 90°
	b = 14.9377(9) Å β = 114.986(2)°
	c = 11.0470(7) Å γ = 90°
Volume	2398.4(2) Å^3
Z	4
Density (calculated)	1.401 Mg/m^3
Absorption coefficient	0.662 mm^{-1}
F(000)	1048
Crystal size	0.20 x 0.10 x 0.07 mm
Theta range for data collection	3.22 to 28.32°
Index ranges	$-20 <= h >= 198$, $-19 <= k >= 15$, $-14 <= l >= 11$
Reflections collected	6071
Independent reflections	2700 [$R(int)$ = 0.0629]
Completeness to theta = 28.32°	89.9%
Absorption correction	None
Max. and min. transmission	0.9551 and 0.8790
Refinement method	Full-matrix least-squares on F^2
Data / restraints / parameters	2700 / 0 / 207
Goodness-of-fit on F^2	1.060
Final R indices [I>2sigma(I)]	R_1 = 0.0630, wR_2 = 0.0969
R indices (all data)	R_1 = 0.1089, wR_2 = 0.1073
Extinction coefficient	0
Largest diff. peak and hole	0.734 and −0.484 e.Å^{-3}

A.2 Compound 2

A.2.1 Single Crystal Data

200 K

Empirical formula	C24 H24 B2 Fe N10
Formula weight	530.00
Temperature	200(2) K
Wavelength	0.71073 Å
Crystal system, space group	Monoclinic, $C2/c$
Unit cell dimensions	a = 17.3607(16) Å α = 90°
	b = 16.0397(14) Å β = 121.617(3)°
	c = 10.5614(9) Å γ = 90°
Volume	2504.4(4) Å^3
Z	4
Density (calculated)	1.406 Mg/m^3
Absorption coefficient	0.637 mm^{-1}
F(000)	1096
Crystal size	0.28 x 0.10 x 0.02 mm
Theta range for data collection	1.87 to 29.12°
Index ranges	$-22 <= h >= 23$, $-21 <= k >= 17$, $-12 <= l >= 14$
Reflections collected	10201
Independent reflections	3370 [$R(int)$ = 0.0485]
Completeness to theta = 29.12°	99.9%
Absorption correction	Integration
Max. and min. transmission	0.9874 and 0.8417
Refinement method	Full-matrix least-squares on F^2
Data / restraints / parameters	3370 / 0 / 216
Goodness-of-fit on F^2	1.023
Final R indices [I>2sigma(I)]	R_1 = 0.0461, wR_2 = 0.0888
R indices (all data)	R_1 = 0.0807, wR_2 = 0.1003
Extinction coefficient	0
Largest diff. peak and hole	0.271 and −0.259 e.Å^{-3}

200 K — Short Collection

Empirical formula	C24 H24 B2 Fe N10
Formula weight	530.00
Temperature	200(2) K
Wavelength	0.71073 Å
Crystal system, space group	Monoclinic, $C2/c$
Unit cell dimensions	a = 17.347(13) Å α = 90°
	b = 16.021(12) Å β = 121.641(8)°
	c = 10.550(8) Å γ = 90°
Volume	2496(3) Å^3
Z	4
Density (calculated)	1.410 Mg/m^3
Absorption coefficient	0.639 mm^{-1}
F(000)	1096
Crystal size	0.15 x 0.12 x 0.08 mm
Theta range for data collection	2.76 to 29.10°
Index ranges	$-9 <= h >= 9$, $-21 <= k >= 21$, $-13 <= l >= 14$
Reflections collected	8158
Independent reflections	1889 [$R(int)$ = 0.1065]
Completeness to theta = 29.10°	56.4%
Absorption correction	Integration
Max. and min. transmission	0.9506 and 0.9102
Refinement method	Full-matrix least-squares on F^2
Data / restraints / parameters	1889 / 0 / 176
Goodness-of-fit on F^2	0.990
Final R indices [I>2sigma(I)]	R_1 = 0.0503, wR_2 = 0.0787
R indices (all data)	R_1 = 0.1116, wR_2 = 0.0954
Extinction coefficient	0
Largest diff. peak and hole	0.271 and −0.246 e.Å^{-3}

100 K

Empirical formula	C24 H24 B2 Fe N10
Formula weight	530.00
Temperature	100(2) K
Wavelength	0.71073 Å
Crystal system, space group	Triclinic, $\mathbf{P\bar{1}}$
Unit cell dimensions	a = 11.6730(13) Å α = 69.520(3)°
	b = 11.0458(13) Å β = 109.777(3)°
	c = 10.5651(12) Å γ = 93.368(3)°
Volume	1198.1(2) Å^3
Z	2
Density (calculated)	1.469 Mg/m^3
Absorption coefficient	0.666 mm^{-1}
F(000)	548
Crystal size	0.28 x 0.10 x 0.02 mm
Theta range for data collection	1.86 to 29.13°
Index ranges	$-15 <= h >= 15$, $-15 <= k >= 15$, $-11 <= l >= 14$
Reflections collected	11984
Independent reflections	6409 [$R(int)$ = 0.0539]
Completeness to theta = 29.13°	99.3%
Absorption correction	Integration
Max. and min. transmission	0.9868 and 0.8354
Refinement method	Full-matrix least-squares on F^2
Data / restraints / parameters	6409 / 3 / 430
Goodness-of-fit on F^2	1.033
Final R indices [I>2sigma(I)]	R_1 = 0.0628, wR_2 = 0.1296
R indices (all data)	R_1 = 0.1135, wR_2 = 0.1473
Extinction coefficient	0
Largest diff. peak and hole	1.379 and −0.662 e.Å^{-3}

30 K

Empirical formula	C24 H24 B2 Fe N10
Formula weight	530.00
Temperature	30(2) K
Wavelength	0.71073 Å
Crystal system, space group	Triclinic, $\mathbf{P\bar{1}}$
Unit cell dimensions	a = 11.655(2) Å α = 69.492(3)°
	b = 11.0156(19) Å β = 109.755(3)°
	c = 10.5664(18) Å γ = 93.280(3)°
Volume	1192.9(4) Å^3
Z	2
Density (calculated)	1.476 Mg/m^3
Absorption coefficient	0.669 mm^{-1}
F(000)	548
Crystal size	0.15 x 0.12 x 0.08 mm
Theta range for data collection	2.38 to 29.13°
Index ranges	$-15 <= h >= 15$, $-15 <= k >= 15$, $-14 <= l >= 12$
Reflections collected	8374
Independent reflections	5832 [$R(int)$ = 0.0546]
Completeness to theta = 29.13°	90.8%
Absorption correction	Integration
Max. and min. transmission	0.9484 and 0.9063
Refinement method	Full-matrix least-squares on F^2
Data / restraints / parameters	5832 / 0 / 407
Goodness-of-fit on F^2	0.915
Final R indices [I>2sigma(I)]	R_1 = 0.0545, wR_2 = 0.0894
R indices (all data)	R_1 = 0.0924, wR_2 = 0.0983
Extinction coefficient	0
Largest diff. peak and hole	1.048 and −0.635 e.Å^{-3}

30 K — Irradiated

Empirical formula	C24 H24 B2 Fe N10
Formula weight	530.00
Temperature	30(2) K
Wavelength	0.71073 Å
Crystal system, space group	Triclinic, $\mathbf{P\bar{1}}$
Unit cell dimensions	a = 10.727(7) Å α = 67.473(15)°
	b = 12.415(8) Å β = 110.377(15)°
	c = 10.712(6) Å γ = 93.505(11)°
Volume	1231.0(13) Å^3
Z	2
Density (calculated)	1.430 Mg/m^3
Absorption coefficient	0.648 mm^{-1}
F(000)	548
Crystal size	0.15 x 0.12 x 0.08 mm
Theta range for data collection	2.59 to 29.27°
Index ranges	$-14 <= h >= 8$, $-16 <= k >= 14$, $-12 <= l >= 14$
Reflections collected	5599
Independent reflections	5369 [$R(int)$ = 0.0302]
Completeness to theta = 29.27°	79.9%
Absorption correction	Integration
Max. and min. transmission	0.9500 and 0.9090
Refinement method	Full-matrix least-squares on F^2
Data / restraints / parameters	5569 / 6 / 350
Goodness-of-fit on F^2	1.014
Final R indices [I>2sigma(I)]	R_1 = 0.0798, wR_2 = 0.1620
R indices (all data)	R_1 = 0.1259, wR_2 = 0.1818
Extinction coefficient	0
Largest diff. peak and hole	1.152 and −0.999 e.Å^{-3}

A.3 Compound 3

A.3.1 Single Crystal Data

160 K

Empirical formula	C23.125 H19.125 Fe N6.225 S2
Formula weight	504.19
Temperature	160(2) K
Wavelength	0.71073 Å
Crystal system, space group	Tetragonal, $\mathbf{I}4_1/a$
Unit cell dimensions	a = 18.0482(5) Å α = 90°
	b = 18.0482(5) Å β = 90°
	c = 28.9962(10) Å γ = 90°
Volume	9445.2(5) Å^3
Z	16
Density (calculated)	1.418 Mg/m^3
Absorption coefficient	0.839 mm^{-1}
F(000)	4151
Crystal size	0.32 x 0.12 x 0.12 mm
Theta range for data collection	2.13 to 29.15°
Index ranges	$-23 <= h >= 23$, $-24 <= k >= 14$, $-32 <= l >= 39$
Reflections collected	24734
Independent reflections	6354 [$R(int)$ = 0.0427]
Completeness to theta = 29.15°	99.7%
Absorption correction	Integration
Max. and min. transmission	0.9060 and 0.7750
Refinement method	Full-matrix least-squares on F^2
Data / restraints / parameters	6354 / 0 / 287
Goodness-of-fit on F^2	1.023
Final R indices [I>2sigma(I)]	R_1 = 0.0471, wR_2 = 0.1187
R indices (all data)	R_1 = 0.0771, wR_2 = 0.1358
Extinction coefficient	0
Largest diff. peak and hole	0.672 and −0.688 e.Å^{-3}

100 K

Empirical formula	C23.125 H19.125 Fe N6.225 S2
Formula weight	504.19
Temperature	100(2) K
Wavelength	0.71073 Å
Crystal system, space group	Tetragonal, $I4_1/a$
Unit cell dimensions	a = 17.6203(4) Å α = 90°
	b = 17.6203(4) Å β = 90°
	c = 29.1010(9) Å γ = 90°
Volume	9035.1(4) Å^3
Z	16
Density (calculated)	1.483 Mg/m^3
Absorption coefficient	0.877 mm^{-1}
F(000)	4151
Crystal size	0.32 x 0.12 x 0.12 mm
Theta range for data collection	2.13 to 29.15°
Index ranges	$-24 <= h >= 23$, $-24 <= k >= 14$, $-36 <= l >= 39$
Reflections collected	29798
Independent reflections	6086 [$R(int)$ = 0.0507]
Completeness to theta = 29.15°	99.9%
Absorption correction	Integration
Max. and min. transmission	0.9020 and 0.7666
Refinement method	Full-matrix least-squares on F^2
Data / restraints / parameters	6086 / 0 / 287
Goodness-of-fit on F^2	1.036
Final R indices [I>2sigma(I)]	R_1 = 0.0455, wR_2 = 0.1098
R indices (all data)	R_1 = 0.0730, wR_2 = 0.1270
Extinction coefficient	0
Largest diff. peak and hole	0.870 and −0.887 e.Å^{-3}

A.4 Compound 4

A.4.1 Single Crystal Data

240 K

Empirical formula	C24 H22 Fe2 N12 S8
Formula weight	846.72
Temperature	240(2) K
Wavelength	0.71073 Å
Crystal system, space group	Triclinic, $\mathbf{P\bar{1}}$
Unit cell dimensions	a = 8.727(4) Å α = 73.052(10)°
	b = 9.380(4) Å β = 79.508(11)°
	c = 12.096(5) Å γ = 66.572(12)°
Volume	866.6(7) Å^3
Z	1
Density (calculated)	1.622 Mg/m^3
Absorption coefficient	1.357 mm^{-1}
F(000)	430
Crystal size	0.14 x 0.12 x 0.08 mm
Theta range for data collection	2.44 to 29.13°
Index ranges	$-11 <= h >= 11$, $-12 <= k >= 12$, $-15 <= l >= 16$
Reflections collected	7449
Independent reflections	4366 [$R(int)$ = 0.0454]
Completeness to theta = 29.13°	93.6%
Absorption correction	Semi-empirical from equivalents Max. and min. transmission
Max. and min. transmission	0.8992 and 0.8327
Refinement method	Full-matrix least-squares on F^2
Data / restraints / parameters	4366 / 0 / 208
Goodness-of-fit on F^2	1.031
Final R indices [I>2sigma(I)]	R_1 = 0.0687, wR_2 = 0.1474
R indices (all data)	R_1 = 0.1355, wR_2 = 0.1735
Extinction coefficient	0
Largest diff. peak and hole	0.460 and −0.546 e.Å^{-3}

175 K

Empirical formula	C24 H22 Fe2 N12 S8
Formula weight	846.72
Temperature	175(2) K
Wavelength	0.71073 Å
Crystal system, space group	Triclinic, $\mathbf{P\bar{1}}$
Unit cell dimensions	a = 8.606(3) Å α = 72.955(7)°
	b = 9.271(3) Å β = 80.170(7)°
	c = 11.950(4) Å γ = 67.038(8)°
Volume	837.5(4) Å^3
Z	1
Density (calculated)	1.679 Mg/m^3
Absorption coefficient	1.404 mm^{-1}
F(000)	430
Crystal size	0.14 x 0.12 x 0.08 mm
Theta range for data collection	2.46 to 29.13°
Index ranges	$-11 <= h >= 11$, $-12 <= k >= 12$, $-15 <= l >= 15$
Reflections collected	7173
Independent reflections	4223 [$R(int)$ = 0.0404]
Completeness to theta = 29.13°	93.3%
Absorption correction	Semi-empirical from equivalents Max. and min. transmission
Max. and min. transmission	0.8960 and 0.8277
Refinement method	Full-matrix least-squares on F^2
Data / restraints / parameters	4223 / 0 / 208
Goodness-of-fit on F^2	1.023
Final R indices [I>2sigma(I)]	R_1 = 0.0646, wR_2 = 0.1366
R indices (all data)	R_1 = 0.1097, wR_2 = 0.1514
Extinction coefficient	0
Largest diff. peak and hole	0.737 and −0.493 e.Å^{-3}

30 K

Empirical formula	C24 H22 Fe2 N12 S8
Formula weight	846.72
Temperature	30(2) K
Wavelength	0.71073 Å
Crystal system, space group	Triclinic, $\mathbf{P\bar{1}}$
Unit cell dimensions	a = 8.434(3) Å α = 72.338(5)°
	b = 9.075(3) Å β = 80.903(4)°
	c = 11.763(3) Å γ = 67.617(5)°
Volume	792.3(4) Å^3
Z	1
Density (calculated)	1.775 Mg/m^3
Absorption coefficient	1.484 mm^{-1}
F(000)	430
Crystal size	0.14 x 0.12 x 0.08 mm
Theta range for data collection	2.61 to 28.06°
Index ranges	$-10 <= h >= 9$, $-11 <= k >= 7$, $-12 <= l >= 15$
Reflections collected	3234
Independent reflections	2749 [$R(int)$ = 0.0241]
Completeness to theta = 28.06°	71.5%
Absorption correction	Semi-empirical from equivalents Max. and min. transmission
Max. and min. transmission	0.8905 and 0.8191
Refinement method	Full-matrix least-squares on F^2
Data / restraints / parameters	2749 / 0 / 208
Goodness-of-fit on F^2	1.070
Final R indices [I>2sigma(I)]	R_1 = 0.0555, wR_2 = 0.1275
R indices (all data)	R_1 = 0.0848, wR_2 = 0.1377
Extinction coefficient	0
Largest diff. peak and hole	0.622 and −0.598 e.Å^{-3}

30 K — Short Collection

Empirical formula	C24 H22 Fe2 N12 S8
Formula weight	846.72
Temperature	30(2) K
Wavelength	0.71073 Å
Crystal system, space group	Triclinic, $\mathbf{P\bar{1}}$
Unit cell dimensions	a = 8.46(2) Å α = 72.32(2)°
	b = 9.15(2) Å β = 80.854(18)°
	c = 11.79(3) Å γ = 67.42(2)°
Volume	802(3) Å^3
Z	1
Density (calculated)	1.754 Mg/m^3
Absorption coefficient	1.467 mm^{-1}
F(000)	430
Crystal size	0.12 x 0.10 x 0.10 mm
Theta range for data collection	2.61 to 28.07°
Index ranges	$-9 <= h >= 11$, $-9 <= k >= 11$, $-14 <= l >= 15$
Reflections collected	5029
Independent reflections	3301 [$R(int)$ = 0.1814]
Completeness to theta = 28.07°	84.6%
Absorption correction	Semi-empirical from equivalents Max. and min. transmission
Max. and min. transmission	0.8672 and 0.8436
Refinement method	Full-matrix least-squares on F^2
Data / restraints / parameters	3301 / 0 / 118
Goodness-of-fit on F^2	0.955
Final R indices [I>2sigma(I)]	R_1 = 0.1281, wR_2 = 0.1599
R indices (all data)	R_1 = 0.2955, wR_2 = 0.2190
Extinction coefficient	0
Largest diff. peak and hole	0.922 and −0.910 e.Å^{-3}

30 K — Irradiated

Empirical formula	C24 H22 Fe2 N12 S8
Formula weight	846.72
Temperature	30(2) K
Wavelength	0.71073 Å
Crystal system, space group	Triclinic, $\mathbf{P\bar{1}}$
Unit cell dimensions	a = 8.4994(16) Å α = 72.406(7)°
	b = 9.1551(19) Å β = 80.810(6)°
	c = 11.849(2) Å γ = 67.443(7)°
Volume	810.7(3) Å^3
Z	1
Density (calculated)	1.734 Mg/m^3
Absorption coefficient	1.451 mm^{-1}
F(000)	430
Crystal size	0.14 x 0.12 x 0.08 mm
Theta range for data collection	2.67 to 27.56°
Index ranges	$-10 <= h >= 10$, $-11 <= k >= 8$, $-15 <= l >= 15$
Reflections collected	5181
Independent reflections	3172 [$R(int)$ = 0.0404]
Completeness to theta = 27.56°	84.8%
Absorption correction	Semi-empirical from equivalents Max. and min. transmission
Max. and min. transmission	0.8928 and 0.8227
Refinement method	Full-matrix least-squares on F^2
Data / restraints / parameters	3172 / 0 / 118
Goodness-of-fit on F^2	1.258
Final R indices [I>2sigma(I)]	R_1 = 0.1709, wR_2 = 0.3253
R indices (all data)	R_1 = 0.2284, wR_2 = 0.3498
Extinction coefficient	0
Largest diff. peak and hole	1.346 and −1.120 e.Å^{-3}

30 K — Irradiated During Collection

Empirical formula	C24 H22 Fe2 N12 S8
Formula weight	846.72
Temperature	30(2) K
Wavelength	0.71073 Å
Crystal system, space group	Triclinic, $\mathbf{P\bar{1}}$
Unit cell dimensions	a = 8.639(4) Å α = 73.726(10)°
	b = 9.214(4) Å β = 80.388(8)°
	c = 12.041(6) Å γ = 67.295(8)°
Volume	846.9(7) Å^3
Z	1
Density (calculated)	1.660 Mg/m^3
Absorption coefficient	1.389 mm^{-1}
F(000)	430
Crystal size	0.12 x 0.10 x 0.10 mm
Theta range for data collection	2.46 to 29.13°
Index ranges	$-11 <= h >= 11$, $-12 <= k >= 12$, $-15 <= l >= 15$
Reflections collected	3351
Independent reflections	3008 [$R(int)$ = 0.1149]
Completeness to theta = 28.03°	73.3%
Absorption correction	Semi-empirical from equivalents Max. and min. transmission
Max. and min. transmission	0.8511 and 0.8736
Refinement method	Full-matrix least-squares on F^2
Data / restraints / parameters	3008 / 0 / 118
Goodness-of-fit on F^2	1.092
Final R indices [I>2sigma(I)]	R_1 = 0.1703, wR_2 = 0.3437
R indices (all data)	R_1 = 0.2780, wR_2 = 0.3918
Extinction coefficient	0
Largest diff. peak and hole	1.747 and −1.464 e.Å^{-3}

A.5 Compound 5

A.5.1 Single Crystal Data

400 K

Empirical formula	C56 H58 F18Fe2 N13 P3
Formula weight	1459.76
Temperature	400(2) K
Wavelength	0.71073 Å
Crystal system, space group	Triclinic, $\mathbf{P\bar{1}}$
Unit cell dimensions	a = 9.544(5) Å α = 104.381(12)°
	b = 16.632(9) Å β = 90.849(13)°
	c = 20.702(11) Å γ = 97.202(12)°
Volume	3155(3) Å^3
Z	2
Density (calculated)	1.537 Mg/m^3
Absorption coefficient	0.639 mm^{-1}
F(000)	1488
Crystal size	0.16 x 0.09 x 0.05 mm
Theta range for data collection	1.02 to 23.43°
Index ranges	$-6 <= h >= 10$, $-18 <= k >= 18$, $-23 <= l >= 22$
Reflections collected	14809
Independent reflections	8986 [$R(int)$ = 0.0.1390]
Completeness to theta = 23.43°	96.9%
Absorption correction	Integration
Max. and min. transmission	0.9688 and 0.9047
Refinement method	Full-matrix least-squares on F^2
Data / restraints / parameters	8986 / 375 / 833
Goodness-of-fit on F^2	0.820
Final R indices [I>2sigma(I)]	R_1 = 0.0992, wR_2 = 0.2315
R indices (all data)	R_1 = 0.2437, wR_2 = 0.2959
Extinction coefficient	0
Largest diff. peak and hole	0.831 and −0.840 e.Å^{-3}

350 K

Empirical formula	C56 H58 F18Fe2 N13 P3
Formula weight	1459.76
Temperature	350(2) K
Wavelength	0.71073 Å
Crystal system, space group	Triclinic, $\mathbf{P\bar{1}}$
Unit cell dimensions	a = 9.5126(9) Å α = 104.328(2)°
	b = 16.6366(16) Å β = 90.818(2)°
	c = 20.6718(19) Å γ = 97.211(2)°
Volume	3141.1(5) Å^3
Z	2
Density (calculated)	1.543 Mg/m^3
Absorption coefficient	0.641 mm^{-1}
F(000)	1488
Crystal size	0.16 x 0.09 x 0.05 mm
Theta range for data collection	1.02 to 27.50°
Index ranges	$-6 <= h >= 12$, $-21 <= k >= 21$, $-26 <= l >= 26$
Reflections collected	21477
Independent reflections	14332 [$R(int)$ = 0.0643]
Completeness to theta = 27.50°	99.1%
Absorption correction	Integration
Max. and min. transmission	0.9686 and 0.9043
Refinement method	Full-matrix least-squares on F^2
Data / restraints / parameters	14332 / 279 / 930
Goodness-of-fit on F^2	0.908
Final R indices [I>2sigma(I)]	R_1 = 0.0721, wR_2 = 0.1211
R indices (all data)	R_1 = 0.2396, wR_2 = 0.1716
Extinction coefficient	0
Largest diff. peak and hole	0.334 and −0.243 e.Å^3

290 K

Empirical formula	C56 H58 F18Fe2 N13 P3
Formula weight	1459.76
Temperature	290(2) K
Wavelength	0.71073 Å
Crystal system, space group	Triclinic, $\mathbf{P\bar{1}}$
Unit cell dimensions	a = 9.4161(7) Å α = 104.691(2)°
	b = 16.4923(13) Å β = 90.747(2)°
	c = 20.6515(15) Å γ = 97.624(2)°
Volume	3071.1(4) Å^3
Z	2
Density (calculated)	1.579 Mg/m^3
Absorption coefficient	0.656 mm^{-1}
F(000)	1488
Crystal size	0.16 x 0.09 x 0.05 mm
Theta range for data collection	1.02 to 28.27°
Index ranges	$-6 <= h >= 12$, $-21 <= k >= 21$, $-27 <= l >= 26$
Reflections collected	22169
Independent reflections	15057 [$R(int)$ = 0.0573]
Completeness to theta = 28.27°	98.8%
Absorption correction	Integration
Max. and min. transmission	0.9679 and 0.9023
Refinement method	Full-matrix least-squares on F^2
Data / restraints / parameters	15057 / 380 / 926
Goodness-of-fit on F^2	0.913
Final R indices [I>2sigma(I)]	R_1 = 0.0694, wR_2 = 0.1181
R indices (all data)	R_1 = 0.2109, wR_2 = 0.1605
Extinction coefficient	0
Largest diff. peak and hole	0.371 and −0.254 e.Å^3

250 K

Empirical formula	C56 H58 F18Fe2 N13 P3
Formula weight	1459.76
Temperature	250(2) K
Wavelength	0.71073 Å
Crystal system, space group	Triclinic, $\mathbf{P\bar{1}}$
Unit cell dimensions	a = 9.3841(7) Å α = 104.771(2)°
	b = 16.4442(12) Å β = 90.705(2)°
	c = 20.6515(14) Å γ = 97.763(2)°
Volume	3049.6(4) Å^3
Z	2
Density (calculated)	1.590 Mg/m^3
Absorption coefficient	0.661 mm^{-1}
F(000)	1488
Crystal size	0.16 x 0.09 x 0.05 mm
Theta range for data collection	1.02 to 28.28°
Index ranges	$-7 <= h >= 12$, $-21 <= k >= 21$, $-27 <= l >= 26$
Reflections collected	21998
Independent reflections	14948 [$R(int)$ = 0.0580]
Completeness to theta = 28.28°	98.7%
Absorption correction	Integration
Max. and min. transmission	0.9677 and 0.9017
Refinement method	Full-matrix least-squares on F^2
Data / restraints / parameters	14948 / 456 / 896
Goodness-of-fit on F^2	0.948
Final R indices [I>2sigma(I)]	R_1 = 0.0753, wR_2 = 0.1278
R indices (all data)	R_1 = 0.2106, wR_2 = 0.1721
Extinction coefficient	0
Largest diff. peak and hole	0.479 and −0.382 e.Å^3

200 K

Empirical formula	C56 H58 F18Fe2 N13 P3
Formula weight	1459.76
Temperature	200(2) K
Wavelength	0.71073 Å
Crystal system, space group	Triclinic, $\mathbf{P\bar{1}}$
Unit cell dimensions	a = 9.3569(7) Å α = 104.744(2)°
	b = 16.3681(12) Å β = 90.772(2)°
	c = 20.6038(14) Å γ = 97.872(2)°
Volume	3019.1(4) Å^3
Z	2
Density (calculated)	1.606 Mg/m^3
Absorption coefficient	0.667 mm^{-1}
F(000)	1488
Crystal size	0.16 x 0.09 x 0.05 mm
Theta range for data collection	1.02 to 27.49°
Index ranges	$-4 <= h >= 12$, $-21 <= k >= 21$, $-26 <= l >= 26$
Reflections collected	19610
Independent reflections	13667 [$R(int)$ = 0.0528]
Completeness to theta = 27.49°	98.7%
Absorption correction	Integration
Max. and min. transmission	0.9674 and 0.9008
Refinement method	Full-matrix least-squares on F^2
Data / restraints / parameters	13667 / 138 / 896
Goodness-of-fit on F^2	0.934
Final R indices [I>2sigma(I)]	R_1 = 0.0683, wR_2 = 0.1230
R indices (all data)	R_1 = 0.1730, wR_2 = 0.1574
Extinction coefficient	0
Largest diff. peak and hole	0.663 and −0.452 e.Å^3

150 K

Empirical formula	C56 H58 F18Fe2 N13 P3
Formula weight	1459.76
Temperature	150(2) K
Wavelength	0.71073 Å
Crystal system, space group	Triclinic, $\mathbf{P\bar{1}}$
Unit cell dimensions	a = 9.2824(7) Å α = 104.750(2)°
	b = 16.2859(13) Å β = 90.715(2)°
	c = 20.5636(16) Å γ = 98.076(2)°
Volume	2972.6(4) Å^3
Z	2
Density (calculated)	1.631 Mg/m^3
Absorption coefficient	0.678 mm^{-1}
F(000)	1488
Crystal size	0.16 x 0.09 x 0.05 mm
Theta range for data collection	1.03 to 28.28°
Index ranges	$-6 <= h >= 12$, $-21 <= k >= 21$, $-27 <= l >= 26$
Reflections collected	21461
Independent reflections	14586 [$R(int)$ = 0.0636]
Completeness to theta = 28.28°	98.7%
Absorption correction	Integration
Max. and min. transmission	0.9669 and 0.8993
Refinement method	Full-matrix least-squares on F^2
Data / restraints / parameters	14586 / 87 / 876
Goodness-of-fit on F^2	0.943
Final R indices [I>2sigma(I)]	R_1 = 0.0750, wR_2 = 0.1335
R indices (all data)	R_1 = 0.1834, wR_2 = 0.1717
Extinction coefficient	0
Largest diff. peak and hole	0.767 and −0.529 e.Å^3

90 K

Empirical formula	C56 H58 F18Fe2 N13 P3
Formula weight	1459.76
Temperature	90(2) K
Wavelength	0.71073 Å
Crystal system, space group	Triclinic, $\mathbf{P\bar{1}}$
Unit cell dimensions	a = 9.2331(7) Å α = 104.748(2)°
	b = 16.2139(12) Å β = 90.739(2)°
	c = 20.5275(15) Å γ = 98.473(2)°
Volume	2935.3(4) Å^3
Z	2
Density (calculated)	1.652 Mg/m^3
Absorption coefficient	0.686 mm^{-1}
F(000)	1488
Crystal size	0.16 x 0.09 x 0.05 mm
Theta range for data collection	1.03 to 28.29°
Index ranges	$-6 <= h >= 12$, $-21 <= k >= 21$, $-27 <= l >= 26$
Reflections collected	21187
Independent reflections	14396 [$R(int)$ = 0.0571]
Completeness to theta = 28.29°	98.7%
Absorption correction	Integration
Max. and min. transmission	0.9665 and 0.8981
Refinement method	Full-matrix least-squares on F^2
Data / restraints / parameters	14396 / 132 / 896
Goodness-of-fit on F^2	0.946
Final R indices [I>2sigma(I)]	R_1 = 0.0663, wR_2 = 0.1244
R indices (all data)	R_1 = 0.1460, wR_2 = 0.1521
Extinction coefficient	0
Largest diff. peak and hole	0.840 and −0.517 e.Å^3

A.6 Compound 6

A.6.1 Single Crystal Data

180 K

Empirical formula	C8 H8 Au2 Fe N6 O2
Formula weight	669.99
Temperature	180(2) K
Wavelength	0.71073 Å
Crystal system, space group	Monoclinic, $\mathbf{P}2_1/c$
Unit cell dimensions	a = 14.6157(5) Å α = 90°
	b = 13.3075(5) Å β = 90.944(2)°
	c = 7.2272(3) Å γ = 90°
Volume	1405.49(9) Å^3
Z,	4
Density (calculated)	3.166 Mg/m^3
Absorption coefficient	21.849 mm^{-1}
F(000)	1192
Crystal size	0.06 x 0.04 x 0.03 mm^3
Theta range for data collection	1.39 to 27.02°
Index ranges	$-18 <= h <= 18$, $-17 <= k <= 17$, $-9 <= l <= 9$
Reflections collected	15805
Independent reflections	3072 [$R(int)$ = 0.0540]
Completeness to theta = 27.02°	100.0%
Absorption correction	Integration
Max. and min. transmission	0.5602 and 0.3539
Refinement method	Full-matrix least-squares on F^2
Data / restraints / parameters	3072 / 4 / 199
Goodness-of-fit on F^2	0.926
Final R indices [I>2sigma(I)]	R_1 = 0.0241, wR_2 = 0.0447
R indices (all data)	R_1 = 0.0366, wR_2 = 0.0474
Extinction coefficient	0
Largest diff. peak and hole	1.433 and −1.131 eÅ^{-3}

120 K

Empirical formula	C8 H8 Au2 Fe N6 O2
Formula weight	669.99
Temperature	120(2) K
Wavelength	0.71073 Å
Crystal system, space group	Monoclinic, $\mathbf{P}2_1/c$
Unit cell dimensions	a = 14.0194(4) Å α = 90°
	b = 13.1770(3) Å β = 91.3780(10)°
	c = 7.4306(2) Å γ = 90°
Volume	1372.28(6) Å^3
Z	4
Density (calculated)	3.243 Mg/m^3
Absorption coefficient	22.377 mm^{-1}
F(000)	1192
Crystal size	0.06 x 0.04 x 0.03 mm^3
Theta range for data collection	1.45 to 28.28°
Index ranges	$-18 <= h <= 18$, $-17 <= k <= 17$, $-9 <= l <= 9$
Reflections collected	16756
Independent reflections	3401 [$R(int)$ = 0.1025]
Completeness to theta = 28.28°	99.9%
Absorption correction	Integration
Max. and min. transmission	0.5533 and 0.3470
Refinement method	Full-matrix least-squares on F^2
Data / restraints / parameters	3401 / 4 / 199
Goodness-of-fit on F^2	0.959
Final R indices [I>2sigma(I)]	R_1 = 0.0324, wR_2 = 0.0734
R indices (all data)	R_1 = 0.0442, wR_2 = 0.0767
Extinction coefficient	0
Largest diff. peak and hole	3.756 and −2.651 eÅ^{-3}

A.6.2 Powder Data

Before Dehydration

Empirical formula	C8 H8 Au2 Fe N6 O2
Formula weight	669.99
Temperature	293(2) K
Wavelength	1.540598 Å
Crystal system, space group	Monoclinic, $\mathbf{P2_1/c}$
Unit cell dimensions	a = 14.5229(3) Å α = 90°
	b = 13.4235(3) Å β = 90.782(2)°
	c = 7.2957(2) Å γ = 90°
Volume	1422.15(5) Å^3
Z	4
Index ranges	$0 <= h <= 16$, $0 <= k <= 15$, $-8 <= l <= 8$
Reflections collected	2037
Refinement method	Le Bail Refinement
Goodness-of-fit	1.053
χ^2	1.109
Final R indices	R_1 = 0.0482 wR_2 = 0.0611
R indices (- background)	R_1 = 0.0463 wR_2 = 0.0568

Rehydrated After Dehydration by Vacuum

Empirical formula	C8 H8 Au2 Fe N6 O2
Formula weight	669.99
Temperature	293(2) K
Wavelength	1.540598 Å
Crystal system, space group	Monoclinic, $\mathbf{P}2_1/c$
Unit cell dimensions	a = 14.5236(4) Å α = 90°
	b = 13.4324(3) Å β = 90.771(2)°
	c = 7.2955(2) Å γ = 90°
Volume	1423.13(7) Å^3
Z	4
Index ranges	$0 <= h <= 16$, $0 <= k <= 14$, $-8 <= l <= 8$
Reflections collected	2032
Refinement method	Le Bail Refinement
Goodness-of-fit	1.118
χ^2	1.251
Final R indices	R_1 = 0.0489 wR_2 = 0.0622
R indices (- background)	R_1 = 0.0470 wR_2 = 0.0566

Rehydrated After Dehydration by Heating

Empirical formula	C8 H8 Au2 Fe N6 O2
Formula weight	669.99
Temperature	293(2) K
Wavelength	1.540598 Å
Crystal system, space group	Monoclinic, $\mathbf{P2_1}/c$
Unit cell dimensions	a = 14.5226(4) Å α = 90°
	b = 13.4339(3) Å β = 90.770(2)°
	c = 7.2960(2) Å γ = 90°
Volume	1423.29(7) Å^3
Z	4
Index ranges	$0 <= h <= 17$, $0 <= k <= 15$, $-8 <= l <= 8$
Reflections collected	2041
Refinement method	Le Bail Refinement
Goodness-of-fit	1.116
χ^2	1.245
Final R indices	R_1 = 0.0481 wR_2 = 0.0617
R indices (- background)	R_1 = 0.0457 wR_2 = 0.0553

A.7 Compound 7

A.7.1 Single Crystal Data

225 K

Empirical formula	C8 H8 Ag2 Fe N6 O2
Formula weight	491.79
Temperature	225(2) K
Wavelength	0.71073 Å
Crystal system, space group	Monoclinic, $\mathbf{P}2_1/c$
Unit cell dimensions	a = 14.7035(5) Å α = 90°
	b = 13.2962(5) Å β = 91.441(2)°
	c = 7.3852(3) Å γ = 90°
Volume	1443.35(9) Å^3
Z	4
Density (calculated)	2.263 Mg/m^3
Absorption coefficient	3.683 mm^{-1}
F(000)	936
Crystal size	0.35 x 0.22 x 0.11 mm^3
Theta range for data collection	2.07 to 29.14°
Index ranges	$-20 <= h <= 20$, $-18 <= k <= 18$, $-10 <= l <= 10$
Reflections collected	19016
Independent reflections	3867 [$R(int)$ = 0.0245]
Completeness to theta = 29.14°	99.6%
Absorption correction	Integration
Max. and min. transmission	0.6875 and 0.3589
Refinement method	Full-matrix least-squares on F^2
Data / restraints / parameters	3867 / 4 / 199
Goodness-of-fit on F^2	1.064
Final R indices [I>2sigma(I)]	R_1 = 0.0219, wR_2 = 0.0517
R indices (all data)	R_1 = 0.0264, wR_2 = 0.0535
Extinction coefficient	0
Largest diff. peak and hole	0.809 and −0.688 eÅ^{-3}

120 K

Empirical formula	C8 H8 Ag2 Fe N6 O2
Formula weight	491.79
Temperature	120(2) K
Wavelength	0.71073 Å
Crystal system, space group	Monoclinic, $\mathbf{P}2_1/c$
Unit cell dimensions	a = 14.2584(4) Å α = 90°
	b = 13.0528(3) Å β = 92.0550(10)°
	c = 7.4930(2) Å γ = 90°
Volume	1393.64(6) Å^3
Z	4
Density (calculated)	2.344 Mg/m^3
Absorption coefficient	3.814 mm^{-1}
F(000)	936
Crystal size	0.35 x 0.22 x 0.11 mm^3
Theta range for data collection	2.12 to 29.13°
Index ranges	$-19 <= h <= 19$, $-17 <= k <= 17$, $-10 <= l <= 10$
Reflections collected	17709
Independent reflections	3744 [$R(int)$ = 0.0297]
Completeness to theta = 29.13°	99.7%
Absorption correction	Integration
Max. and min. transmission	0.6790 and 0.3487
Refinement method	Full-matrix least-squares on F^2
Data / restraints / parameters	3744 / 4 / 199
Goodness-of-fit on F^2	1.050
Final R indices [I>2sigma(I)]	R_1 = 0.0278, wR_2 = 0.0705
R indices (all data)	R_1 = 0.0327, wR_2 = 0.0730
Extinction coefficient	0
Largest diff. peak and hole	1.473 and −0.880 eÅ^{-3}

A.7.2 Powder Data

Room Temperature, Before Dehydration

Empirical formula	C8 H8 Ag2 Fe N6 O2
Formula weight	491.79
Temperature	293(2) K
Wavelength	1.540598 Å
Crystal system, space group	Monoclinic, $\mathbf{P2_1}/c$
Unit cell dimensions	a = 14.6566(5) Å $\alpha = 90°$
	b = 13.3474(4) Å $\beta = 91.441(3)°$
	c = 7.4207(3) Å $\gamma = 90°$
Volume	1451.24(10) Å^3
Z	4
Index ranges	$0 <= h <= 16$, $0 <= k <= 14$, $-8 <= l <= 8$
Reflections collected	2082
Refinement method	Le Bail Refinement
Goodness-of-fit	1.133
χ^2	1.283
Final R indices	$R_1 = 0.0525$ $wR_2 = 0.0676$
R indices (- background)	$R_1 = 0.0661$ $wR_2 = 0.1006$

Rehydrated After Dehydration Under Vacuum

Empirical formula	C8 H8 Ag2 Fe N6 O2
Formula weight	491.79
Temperature	293(2) K
Wavelength	1.540598 Å
Crystal system, space group	Monoclinic, $\mathbf{P2_1/c}$
Unit cell dimensions	a = 14.6857(8) Å α = 90°
	b = 13.3565(6) Å β = 91.4674(4)°
	c = 7.4300(4) Å γ = 90°
Volume	1456.89(15) Å^3
Z	4
Index ranges	$0 <= h <= 16$, $0 <= k <= 14$, $-8 <= l <= 8$
Reflections collected	2086
Refinement method	Le Bail Refinement
Goodness-of-fit	1.090
χ^2	1.183
Final R indices	R_1 = 0.0488 wR_2 = 0.0631
R indices (- background)	R_1 = 0.0519 wR_2 = 0.0703

Rehydrated After Dehydration Under Vacuum in PheniX

Empirical formula	C8 H8 Ag2 Fe N6 O2
Formula weight	491.79
Temperature	293(2) K
Wavelength	1.540598 Å
Crystal system, space group	Monoclinic, $\mathbf{P2}_1/c$
Unit cell dimensions	a = 14.6725(7) Å α = 90°
	b = 13.3550(4) Å β = 91.369(3)°
	c = 7.4310(3) Å γ = 90°
Volume	1455.70(12) Å^3
Z	4
Index ranges	$0 <= h <= 12$, $0 <= k <= 11$, $-6 <= l <= 6$
Reflections collected	557
Refinement method	Le Bail Refinement
Goodness-of-fit	1.137
χ^2	1.283
Final R indices	R_1 = 0.0490 wR_2 = 0.0632
R indices (- background)	R_1 = 0.0494 wR_2 = 0.0637

A.8 Compound 8

A.8.1 Powder Data

Room Temperature, Under Vacuum

Empirical formula	C8 H4 Au2 Fe N6
Formula weight	633.91
Temperature	293(2) K
Wavelength	1.540598 Å
Crystal system, space group	Monoclinic, $\mathbf{P2_1}/c$
Unit cell dimensions	a = 12.3853(6) Å $\alpha = 90°$
	b = 13.6752(6) Å β = 94.151(3)°
	c = 8.3347(4) Å $\gamma = 90°$
Volume	1408(3) Å^3
Z	4
Index ranges	$0 <= h <= 13$, $0 <= k <= 14$, $-8 <= l <= 8$
Reflections collected	1765
Absorption correction	None
Refinement method	Rietveld Refinement
Data / restraints / parameters	1765 / 27 / 34
Goodness-of-fit	2.518
χ^2	6.341
Final R indices	$R_1 = 0.0505$ $wR_2 = 0.0718$
R indices (- background)	$R_1 = 0.0808$ $wR_2 = 0.1314$

Room Temperature, Under Vacuum

Empirical formula	C8 H4 Au2 Fe N6
Formula weight	633.91
Temperature	293(2) K
Wavelength	1.540598 Å
Crystal system, space group	Monoclinic, $\mathbf{P2}_1/c$
Unit cell dimensions	a = 12.3829(3) Å $\alpha = 90°$
	b = 13.6746(3) Å $\beta = 94.148(2)°$
	c = 8.3317(2) Å $\gamma = 90°$
Volume	1407.12(7) Å^3
Z	4
Index ranges	$0 <= h <= 13$, $0 <= k <= 15$, $-9 <= l <= 9$
Reflections collected	2025
Refinement method	Le Bail Refinement
Goodness-of-fit	1.494
χ^2	2.231
Final R indices	$R_1 = 0.0332$ $wR_2 = 0.0456$
R indices (- background)	$R_1 = 0.0427$ $wR_2 = 0.0626$

373 K

Empirical formula	C8 H4 Au2 Fe N6
Formula weight	633.91
Temperature	373(2) K
Wavelength	1.540598 Å
Crystal system, space group	Monoclinic, $\mathbf{P}2_1/c$
Unit cell dimensions	a = 12.3728(3) Å α = 90°
	b = 13.6791(3) Å β = 94.148(2)°
	c = 8.3374(2) Å γ = 90°
Volume	1407.40(7) Å^3
Z	4
Index ranges	0 <= h <= 13, 0 <= k <= 15, -9 <= l <= 9
Reflections collected	2026
Refinement method	Le Bail Refinement
Goodness-of-fit	1.402
χ^2	1.966
Final R indices	R_1 = 0.0326 wR_2 = 0.0440
R indices (- background)	R_1 = 0.0361 wR_2 = 0.0483

A.9 Compound 9

A.9.1 Powder Data

Room Temperature, Under Vacuum

Empirical formula	C8 H4 Ag2 Fe N6
Formula weight	455.71
Temperature	293(2) K
Wavelength	1.540598 Å
Crystal system, space group	Monoclinic, $\mathbf{P\bar{1}}$
Unit cell dimensions	a = 12.1952(5) Å α = 87.940(4)°
	b = 13.7186(7) Å β = 95.206(5)°
	c = 8.5944(6) Å γ = 88.429(4)°
Volume	1430.32(10) Å^3
Z	4
Index ranges	$0 <= h <= 13$, $-15 <= k <= 15$, $-9 <= l <= 9$
Reflections collected	4119
Refinement method	Le Bail Refinement
Goodness-of-fit	1.675
χ^2	2.805
Final R indices	R_1 = 0.0212 wR_2 = 0.0326
R indices (- background)	R_1 = 0.0373 wR_2 = 0.0705

200 K, Under Vacuum

Empirical formula	C8 H4 Ag2 Fe N6
Formula weight	455.71
Temperature	200(2) K
Wavelength	1.540598 Å
Crystal system, space group	Monoclinic, $\mathbf{P2_1}/c$
Unit cell dimensions	a = 12.3255(5) Å α = 86.571(4)°
	b = 13.8532(7) Å β = 97.019(4)°
	c = 8.3166(4) Å γ = 88.455(4)°
Volume	1406.01(11) Å^3
Z	4
Index ranges	$0 <= h <= 10$, $-11 <= k <= 11$, $-6 <= l <= 6$
Reflections collected	1701
Refinement method	Le Bail Refinement
Goodness-of-fit	1.629
χ^2	2.653
Final R indices	R_1 = 0.0597 wR_2 = 0.0858
R indices (- background)	R_1 = 0.0607 wR_2 = 0.0871

17 K, Under Vacuum

Empirical formula	C8 H4 Ag2 Fe N6
Formula weight	455.71
Temperature	17(2) K
Wavelength	1.540598 Å
Crystal system, space group	Monoclinic, $\mathbf{P}2_1/c$
Unit cell dimensions	a = 11.8922(8) Å α = 84.038(5)°
	b = 13.7431(10) Å β = 96.682(5)°
	c = 8.1098(6) Å γ = 88.842(5)°
Volume	1308.6(12) Å^3
Z	4
Index ranges	$0 <= h <= 9$, $-11 <= k <= 11$, $-6 <= l <= 6$
Reflections collected	1588
Refinement method	Le Bail Refinement
Goodness-of-fit	1.732
χ^2	3.000
Final R indices	R_1 = 0.0572 wR_2 = 0.0839
R indices (- background)	R_1 = 0.0664 wR_2 = 0.1080

A.10 Compound 10

A.10.1 Single Crystal Data

180 K

Empirical formula	C12 H8 Cu2 Fe N8
Formula weight	447.19
Temperature	180(2) K
Wavelength	0.71073 Å
Crystal system, space group	Triclinic, $\mathbf{P\bar{1}}$
Unit cell dimensions	a = 6.7584(12) Å α = 110.102(3)°
	b = 8.0796(15) Å β = 108.500(4)°
	c = 7.9862(15) Å γ = 99.272(4)°
Volume	370.06(12) Å^3
Z	1
Density (calculated)	2.007 Mg/m^3
Absorption coefficient	3.824 mm^{-1}
F(000)	220
Crystal size	0.06 x 0.05 x 0.03 mm
Theta range for data collection	2.82 to 29.12°
Index ranges	$-9 <= h >= 8$, $-11 <= k >= 11$, $-10 <= l >= 10$
Reflections collected	3927
Independent reflections	1938 [$R(int)$ = 0.0524]
Completeness to theta = 29.12°	97.6%
Absorption correction	Semi-empirical from equivalents
Max. and min. transmission	0.8939 and 0.8030
Refinement method	Full-matrix least-squares on F^2
Data / restraints / parameters	1939 / 0 / 106
Goodness-of-fit on F^2	0.964
Final R indices [I>2sigma(I)]	R_1 = 0.0401, wR_2 = 0.0786
R indices (all data)	R_1 = 0.0625, wR_2 = 0.0829
Extinction coefficient	0
Largest diff. peak and hole	0.654 and −0.470 e.Å^{-3}

90 K

Empirical formula	C12 H8 Cu2 Fe N8
Formula weight	447.19
Temperature	90(2) K
Wavelength	0.71073 Å
Crystal system, space group	Triclinic, $\mathbf{P\bar{1}}$
Unit cell dimensions	a = 6.8434(13) Å α = 109.077(4)°
	b = 7.7006(14) Å β = 108.194(4)°
	c = 7.7696(15) Å γ = 99.021(4)°
Volume	352.00(11) Å^3
Z	1
Density (calculated)	2.110 Mg/m^3
Absorption coefficient	4.020 mm^{-1}
F(000)	220
Crystal size	0.06 x 0.05 x 0.03 mm
Theta range for data collection	2.92 to 29.13°
Index ranges	$-9 <= h >= 8$, $-10 <= k >= 10$, $-10 <= l >= 10$
Reflections collected	3761
Independent reflections	1864 [$R(int)$ = 0.0320]
Completeness to theta = 29.13°	98.0%
Absorption correction	Semi-empirical from equivalents
Max. and min. transmission	0.8889 and 0.7945
Refinement method	Full-matrix least-squares on F^2
Data / restraints / parameters	1864 / 0 / 106
Goodness-of-fit on F^2	1.178
Final R indices [I>2sigma(I)]	R_1 = 0.0471, wR_2 = 0.1140
R indices (all data)	R_1 = 0.0643, wR_2 = 0.1197
Extinction coefficient	0
Largest diff. peak and hole	1.160 and −0.653 e.Å^{-3}

30 K — Irradiated

Empirical formula	C12 H8 Cu2 Fe N8
Formula weight	447.19
Temperature	30(2) K
Wavelength	0.71073 Å
Crystal system, space group	Triclinic, $\mathbf{P\bar{1}}$
Unit cell dimensions	a = 6.71(4) Å α = 110.6(11)°
	b = 8.15(11) Å β = 108.1(13)°
	c = 7.98(7) Å γ = 99.2(10)°
Volume	371(6) Å^3
Z	1
Density (calculated)	2.004 Mg/m^3
Absorption coefficient	3.818 mm^{-1}
F(000)	220
Crystal size	0.06 x 0.05 x 0.03 mm
Theta range for data collection	3.09 to 29.10°
Index ranges	$-8 <= h >= 9$, $-7 <= k >= 9$, $-10 <= l >= 2$
Reflections collected	1259
Independent reflections	1259 [$R(int)$ = 0.0000]
Completeness to theta = 29.10°	63.6%
Absorption correction	Semi-empirical from equivalents
Max. and min. transmission	0.8941 and 0.8033
Refinement method	Full-matrix least-squares on F^2
Data / restraints / parameters	1259 / 0 / 46
Goodness-of-fit on F^2	0.983
Final R indices [I>2sigma(I)]	R_1 = 0.0803, wR_2 = 0.1784
R indices (all data)	R_1 = 0.1253, wR_2 = 0.1945
Extinction coefficient	0
Largest diff. peak and hole	1.734 and −2.154 e.Å^{-3}

A.11 Compound 11

A.11.1 Single Crystal Data

290 K

Empirical formula	C9 H4 Ag3 Fe N7
Formula weight	589.65
Temperature	290(2) K
Wavelength	0.71073 Å
Crystal system, space group	Monoclinic, $\mathbf{P2_1/c}$
Unit cell dimensions	a = 17.5595(6) Å α = 90°
	b = 29.2286(10) Å β = 97.410(2)°
	c = 12.2993(4) Å γ = 90°
Volume	6259.8(6) Å^3
Z	16
Density (calculated)	2.501 Mg/m^3
Absorption coefficient	4.601 mm^{-1}
F(000)	4384
Crystal size	0.084 x 0.070 x 0.020 mm
Theta range for data collection	1.17 to 28.28°
Index ranges	$-28 <= h >= 28$, $-38 <= k >= 38$, $-16 <= l >= 16$
Reflections collected	77042
Independent reflections	15546 [$R(int)$ = 0.0748]
Completeness to theta = 28.28°	99.9%
Absorption correction	Integration
Max. and min. transmission	0.917 and 0.492
Refinement method	Full-matrix least-squares on F^2
Data / restraints / parameters	15546 / 0 / 724
Goodness-of-fit on F^2	1.060
Final R indices [I>2sigma(I)]	R_1 = 0.0743, wR_2 = 0.2047
R indices (all data)	R_1 = 0.1413, wR_2 = 0.2403
Extinction coefficient	0
Largest diff. peak and hole	2.611 and −1.063 e.Å^{-3}

220 K

Empirical formula	C9 H4 Ag3 Fe N7
Formula weight	589.65
Temperature	220(2) K
Wavelength	0.71073 Å
Crystal system, space group	Monoclinic, $\mathbf{P}2_1/c$
Unit cell dimensions	a = 17.5596(8) Å α = 90°
	b = 29.2136(13) Å β = 97.300(2)°
	c = 12.2539(6) Å γ = 90°
Volume	6235.1(8) Å^3
Z	16
Density (calculated)	2.512 Mg/m^3
Absorption coefficient	4.621 mm^{-1}
F(000)	4384
Crystal size	0.084 x 0.070 x 0.020 mm
Theta range for data collection	1.17 to 28.29°
Index ranges	$-23 <= h >= 23$, $-38 <= k >= 38$, $-16 <= l >= 16$
Reflections collected	76323
Independent reflections	15479 [$R(int)$ = 0.0691]
Completeness to theta = 28.29°	99.8%
Absorption correction	Integration
Max. and min. transmission	0.917 and 0.491
Refinement method	Full-matrix least-squares on F^2
Data / restraints / parameters	15479 / 0 / 724
Goodness-of-fit on F^2	1.053
Final R indices [I>2sigma(I)]	R_1 = 0.0732, wR_2 = 0.2011
R indices (all data)	R_1 = 0.1212, wR_2 = 0.2271
Extinction coefficient	0
Largest diff. peak and hole	3.436 and −1.081 e.Å^{-3}

170 K

Empirical formula	C9 H4 Ag3 Fe N7
Formula weight	589.65
Temperature	170(2) K
Wavelength	0.71073 Å
Crystal system, space group	Monoclinic, $\mathbf{P}2_1/c$
Unit cell dimensions	a = 17.2561(10) Å $\alpha = 90°$
	b = 29.5042(18) Å $\beta = 96.875(2)°$
	c = 11.9308(7) Å $\gamma = 90°$
Volume	6030.6(10) Å^3
Z	16
Density (calculated)	2.597 Mg/m^3
Absorption coefficient	4.777 mm^{-1}
F(000)	4384
Crystal size	0.084 x 0.070 x 0.020 mm
Theta range for data collection	1.19 to 28.29°
Index ranges	$-23 <= h >= 23$, $-39 <= k >= 39$, $-15 <= l >= 15$
Reflections collected	69166
Independent reflections	14964 [$R(int)$ = 0.1002]
Completeness to theta = 28.29°	99.9%
Absorption correction	Integration
Max. and min. transmission	0.913 and 0.490
Refinement method	Full-matrix least-squares on F^2
Data / restraints / parameters	14964 / 0 / 724
Goodness-of-fit on F^2	1.075
Final R indices [I>2sigma(I)]	R_1 = 0.1012, wR_2 = 0.3078
R indices (all data)	R_1 = 0.1569, wR_2 = 0.3333
Extinction coefficient	0
Largest diff. peak and hole	5.343 and −2.022 e.Å^{-3}

90 K

Empirical formula	C9 H4 Ag3 Fe N7
Formula weight	589.65
Temperature	90(2) K
Wavelength	0.71073 Å
Crystal system, space group	Monoclinic, $\mathbf{P}2_1/c$
Unit cell dimensions	a = 17.1761(10) Å α = 90°
	b = 29.2567(17) Å β = 97.051(2)°
	c = 11.5799(7) Å γ = 90°
Volume	5775.1(10) Å^3
Z	16
Density (calculated)	2.712 Mg/m^3
Absorption coefficient	4.990 mm^{-1}
F(000)	4384
Crystal size	0.084 x 0.070 x 0.020 mm
Theta range for data collection	1.19 to 28.28°
Index ranges	$-22 <= h >= 22$, $-39 <= k >= 39$, $-15 <= l >= 15$
Reflections collected	62403
Independent reflections	14290 [$R(int)$ = 0.0775]
Completeness to theta = 28.28°	99.8%
Absorption correction	Integration
Max. and min. transmission	0.909 and 0.483
Refinement method	Full-matrix least-squares on F^2
Data / restraints / parameters	14290 / 0 / 724
Goodness-of-fit on F^2	1.135
Final R indices [I>2sigma(I)]	R_1 = 0.0834, wR_2 = 0.2152
R indices (all data)	R_1 = 0.1109, wR_2 = 0.2278
Extinction coefficient	0
Largest diff. peak and hole	4.427 and −2.231 e.Å^{-3}

30 K

Empirical formula	C9 H4 Ag3 Fe N7
Formula weight	589.65
Temperature	30(2) K
Wavelength	0.71073 Å
Crystal system, space group	Monoclinic, $\mathbf{P}2_1/c$
Unit cell dimensions	a = 17.214(3) Å α = 90°
	b = 29.252(5) Å β = 97.015(4)°
	c = 11.559(2) Å γ = 90°
Volume	5777(3) Å^3
Z	16
Density (calculated)	2.712 Mg/m^3
Absorption coefficient	4.989 mm^{-1}
F(000)	4384
Crystal size	0.084 x 0.070 x 0.020 mm
Theta range for data collection	2.65 to 28.12°
Index ranges	$-17 <= h >= 19$, $-36 <= k >= 38$, $-15 <= l >= 4$
Reflections collected	17731
Independent reflections	10368 [$R(int)$ = 0.0884]
Completeness to theta = 28.12°	73.5%
Absorption correction	Integration
Max. and min. transmission	0.909 and 0.525
Refinement method	Full-matrix least-squares on F^2
Data / restraints / parameters	10368 / 0 / 260
Goodness-of-fit on F^2	1.095
Final R indices [I>2sigma(I)]	R_1 = 0.1035, wR_2 = 0.2177
R indices (all data)	R_1 = 0.1637, wR_2 = 0.2390
Extinction coefficient	0
Largest diff. peak and hole	4.005 and −2.723 e.Å^{-3}

30 K — Irradiated

Empirical formula	C9 H4 Ag3 Fe N7
Formula weight	589.65
Temperature	30(2) K
Wavelength	0.71073 Å
Crystal system, space group	Monoclinic, $\mathbf{P}2_1/c$
Unit cell dimensions	a = 17.6506(19) Å α = 90°
	b = 29.281(3) Å β = 97.228(2°
	c = 12.2184(14) Å γ = 90°
Volume	6264.7(12) Å^3
Z	16
Density (calculated)	2.501 Mg/m^3
Absorption coefficient	4.601 mm^{-1}
F(000)	4384
Crystal size	0.084 x 0.070 x 0.020 mm
Theta range for data collection	1.17 to 28.28°
Index ranges	$-20 <= h >= 23$, $-37 <= k >= 38$, $-9 <= l >= 16$
Reflections collected	33203
Independent reflections	13630 [$R(int)$ = 0.1124]
Completeness to theta = 28.14°	88.8%
Absorption correction	Integration
Max. and min. transmission	0.917 and 0.451
Refinement method	Full-matrix least-squares on F^2
Data / restraints / parameters	13630 / 0 / 404
Goodness-of-fit on F^2	1.097
Final R indices [I>2sigma(I)]	R_1 = 0.1079, wR_2 = 0.2257
R indices (all data)	R_1 = 0.1704, wR_2 = 0.2490
Extinction coefficient	0
Largest diff. peak and hole	5.952 and −2.894 e.Å^{-3}

A.12 Compound 12

A.12.1 Single Crystal Data

160 K

Empirical formula	C28 H20 Ag2 Fe N8
Formula weight	740.11
Temperature	160(2) K
Wavelength	0.71073 Å
Crystal system, space group	Monoclinic, $\mathbf{P}2_1/n$
Unit cell dimensions	a = 9.4597(10) Å α = 90°
	b = 11.1484(13) Å β = 95.149(5)°
	c = 13.3100(14) Å γ = 90°
Volume	1398.0(3) Å^3
Z	2
Density (calculated)	1.758 Mg/m^3
Absorption coefficient	1.931 mm^{-1}
F(000)	728
Crystal size	0.22 x 0.10 x 0.10 mm
Theta range for data collection	2.39 to 29.14°
Index ranges	$-12 <= h >= 8$, $-15 <= k >= 15$, $-18 <= l >= 18$
Reflections collected	9714
Independent reflections	3688 [$R(int)$ = 0.0271]
Completeness to theta = 29.14°	98.1%
Absorption correction	Integration
Max. and min. transmission	0.9680 and 0.9024
Refinement method	Full-matrix least-squares on F^2
Data / restraints / parameters	3688 / 0 / 178
Goodness-of-fit on F^2	1.029
Final R indices [I>2sigma(I)]	R_1 = 0.0247, wR_2 = 0.0563
R indices (all data)	R_1 = 0.0336, wR_2 = 0.0593
Extinction coefficient	0
Largest diff. peak and hole	0.484 and −0.310 e.Å^{-3}

30 K

Empirical formula	C28 H20 Ag2 Fe N8
Formula weight	740.11
Temperature	30(2) K
Wavelength	0.71073 Å
Crystal system, space group	Monoclinic, $\mathbf{P}2_1/c$
Unit cell dimensions	a = 16.730(2) Å α = 90°
	b = 11.0991(13) Å β = 108.829(2)°
	c = 15.4382(19) Å γ = 90°
Volume	2713.3(6) Å^3
Z	2
Density (calculated)	1.812 Mg/m^3
Absorption coefficient	1.990 mm^{-1}
F(000)	1456
Crystal size	0.22 x 0.10 x 0.10 mm
Theta range for data collection	2.41 to 28.12°
Index ranges	$-19 <= h >= 21$, $-14 <= k >= 14$, $-13 <= l >= 20$
Reflections collected	13097
Independent reflections	5924 [$R(int)$ = 0.0477]
Completeness to theta = 28.12°	89.3%
Absorption correction	Integration
Max. and min. transmission	0.8258 and 0.6686
Refinement method	Full-matrix least-squares on F^2
Data / restraints / parameters	5924 / 0 / 355
Goodness-of-fit on F^2	1.086
Final R indices [I>2sigma(I)]	R_1 = 0.0621, wR_2 = 0.1803
R indices (all data)	R_1 = 0.1049, wR_2 = 0.2131
Extinction coefficient	0
Largest diff. peak and hole	2.651 and −3.676 e.Å^{-3}

30 K — Irradiated

Empirical formula	C28 H20 Ag2 Fe N8
Formula weight	740.11
Temperature	30(2) K
Wavelength	0.71073 Å
Crystal system, space group	Monoclinic, $\mathbf{P}2_1/n$
Unit cell dimensions	a = 9.4490(16) Å α = 90°
	b = 10.9580(19) Å β = 95.294(3)°
	c = 13.343(2) Å γ = 90°
Volume	1375.7(4) Å^3
Z	2
Density (calculated)	1.787 Mg/m^3
Absorption coefficient	1.963 mm^{-1}
F(000)	728
Crystal size	0.22 x 0.10 x 0.10 mm
Theta range for data collection	2.41 to 28.05°
Index ranges	$-6 <= h >= 11$, $-14 <= k >= 14$, $-16 <= l >= 17$
Reflections collected	6700
Independent reflections	3014 [$R(int)$ = 0.0339]
Completeness to theta = 28.12°	90.2%
Absorption correction	Integration
Max. and min. transmission	0.8279 and 0.6720
Refinement method	Full-matrix least-squares on F^2
Data / restraints / parameters	3014 / 0 / 178
Goodness-of-fit on F^2	1.206
Final R indices [I>2sigma(I)]	R_1 = 0.0554, wR_2 = 0.1162
R indices (all data)	R_1 = 0.0816, wR_2 = 0.1366
Extinction coefficient	0
Largest diff. peak and hole	3.924 and −1.472 e.Å^{-3}

30 K, Quenched

Empirical formula	C28 H20 Ag2 Fe N8
Formula weight	740.11
Temperature	30(2) K
Wavelength	0.71073 Å
Crystal system, space group	Monoclinic, $\mathbf{P}2_1/n$
Unit cell dimensions	a = 9.4431(7) Å α = 90°
	b = 10.9549(8) Å β = 95.270(1)°
	c = 13.2707(9) Å γ = 90°
Volume	1367.03(17) Å^3
Z	2
Density (calculated)	1.798 Mg/m^3
Absorption coefficient	1.975 mm^{-1}
F(000)	728
Crystal size	0.22 x 0.10 x 0.10 mm
Theta range for data collection	2.41 to 28.19°
Index ranges	$-12 <= h >= 11$, $-8 <= k >= 14$, $-16 <= l >= 17$
Reflections collected	7072
Independent reflections	2989 [$R(int)$ = 0.0185]
Completeness to theta = 28.19°	88.5%
Absorption correction	Integration
Max. and min. transmission	0.8269 and 0.6704
Refinement method	Full-matrix least-squares on F^2
Data / restraints / parameters	2989 / 0 / 178
Goodness-of-fit on F^2	1.037
Final R indices [I>2sigma(I)]	R_1 = 0.0210, wR_2 = 0.0492
R indices (all data)	R_1 = 0.0240, wR_2 = 0.0507
Extinction coefficient	0
Largest diff. peak and hole	0.798 and −0.770 e.Å^{-3}

30 K, Quenched—Warmed—Cooled

Empirical formula	C28 H20 Ag2 Fe N8
Formula weight	740.11
Temperature	30(2) K
Wavelength	0.71073 Å
Crystal system, space group	Monoclinic, $\mathbf{P}2_1/n$
Unit cell dimensions	a = 9.3388(7) Å α = 90°
	b = 11.0703(8) Å β = 94.7920(10)°
	c = 13.0018(10) Å γ = 90°
Volume	1339.47(17) Å^3
Z	2
Density (calculated)	1.835 Mg/m^3
Absorption coefficient	2.016 mm^{-1}
F(000)	728
Crystal size	0.22 x 0.10 x 0.10 mm
Theta range for data collection	2.42 to 28.31°
Index ranges	$-12 <= h >= 11$, $-9 <= k >= 14$, $-15 <= l >= 17$
Reflections collected	6979
Independent reflections	2932 [$R(int)$ = 0.0362]
Completeness to theta = 28.31°	87.9%
Absorption correction	Integration
Max. and min. transmission	0.8238 and 0.6654
Refinement method	Full-matrix least-squares on F^2
Data / restraints / parameters	2932 / 0 / 178
Goodness-of-fit on F^2	1.017
Final R indices [I>2sigma(I)]	R_1 = 0.0330, wR_2 = 0.0680
R indices (all data)	R_1 = 0.0512, wR_2 = 0.0731
Extinction coefficient	0
Largest diff. peak and hole	0.734 and −0.416 e.Å^{-3}

30 K, Quenched—Warmed—Cooled—Irradiated

Empirical formula	C28 H20 Ag2 Fe N8
Formula weight	740.11
Temperature	30(2) K
Wavelength	0.71073 Å
Crystal system, space group	Monoclinic, $\mathbf{P}2_1/n$
Unit cell dimensions	a = 9.4842(8) Å α = 90°
	b = 10.9423(9) Å β = 95.3620(10)°
	c = 13.3373(10) Å γ = 90°
Volume	1378.07(19) Å^3
Z	2
Density (calculated)	1.784 Mg/m^3
Absorption coefficient	1.959 mm^{-1}
F(000)	728
Crystal size	0.22 x 0.10 x 0.10 mm
Theta range for data collection	2.41 to 28.09°
Index ranges	$-12 <= h >= 12$, $-8 <= k >= 14$, $-16 <= l >= 17$
Reflections collected	7152
Independent reflections	3010 [$R(int)$ = 0.0427]
Completeness to theta = 28.09°	89.3%
Absorption correction	Integration
Max. and min. transmission	0.8282 and 0.6724
Refinement method	Full-matrix least-squares on F^2
Data / restraints / parameters	3010 / 0 / 178
Goodness-of-fit on F^2	1.028
Final R indices [I>2sigma(I)]	R_1 = 0.0312, wR_2 = 0.0705
R indices (all data)	R_1 = 0.0457, wR_2 = 0.0755
Extinction coefficient	0
Largest diff. peak and hole	0.666 and −0.515 e.Å^{-3}

A.13 Compound 13

A.13.1 Powder Data

300 K

Empirical formula	C8 H4 Fe N6 O2 Pd
Formula weight	374.37
Temperature	300 K
Wavelength	1.540598 Å
Crystal system, space group	Tetragonal, $\mathbf{P}4/m$
Unit cell dimensions (High Spin)	a = 7.4417(5) Å $\alpha = 90°$
	b = 7.4417(5) Å $\beta = 90°$
	c = 7.2389(7) Å $\gamma = 90°$
Volume	400.88(9) Å^3
Unit cell dimensions (Low Spin)	a = 7.2272(6) Å $\alpha = 90°$
	b = 7.2272(6) Å $\beta = 90°$
	c = 6.774(7) Å $\gamma = 90°$
Volume	353.8(6) Å^3
Z	1
Index ranges	$0 <= h >= 7$, $0 <= k >= 7$, $0 <= l >= 7$
Reflections collected	371
Absorption correction	None
Refinement method	Rietveld Refinement
Data / restraints / parameters	371 / 18 / 29
Goodness-of-fit on F^2	1.399
χ^2	1.958
Final R indices	R_1 = 0.0629, wR_2 = 0.0815
R indices (- background)	R_1 = 0.0977, wR_2 = 0.1319

17 K

Empirical formula	C8 H4 Fe N6 O2 Pd
Formula weight	374.37
Temperature	17 K
Wavelength	1.540598 Å
Crystal system, space group	Tetragonal, $\mathbf{P}4/m$
Unit cell dimensions	a = 7.1769(7) Å α = 90°
	b = 7.1769(7) Å β = 90°
	c = 6.7672(8) Å γ = 90°
Volume	348.6(1) Å^3
Z	1
Index ranges	0 <= h >= 7, 0 <= k >= 7, 0 <= l >= 7
Reflections collected	172
Absorption correction	None
Refinement method	Rietveld Refinement
Data / restraints / parameters	172 / 18 / 25
Goodness-of-fit on F^2	1.419
χ^2	2.013
Final R indices	R_1 = 0.0505, wR_2 = 0.0718
R indices (- background)	R_1 = 0.1010, wR_2 = 0.1408

262 K

Empirical formula	C8 H4 Fe N6 O2 Pd
Formula weight	374.37
Temperature	262 K
Wavelength	1.540598 Å
Crystal system, space group	Tetragonal, $\mathbf{P}4/m$
Unit cell dimensions (High Spin)	a = 7.4405(13) Å α = 90°
	b = 7.4405(13) Å β = 90°
	c = 7.2298(14) Å γ = 90°
Volume	400.3(3) Å^3
Unit cell dimensions (Low Spin)	a = 7.1828(13) Å α = 90°
	b = 7.1828(13) Å β = 90°
	c = 6.7828(14) Å γ = 90°
Volume	349.9(2) Å^3
Z	1
Index ranges	0 <= h >= 7, 0 <= k >= 7, 0 <= l >= 7
Reflections collected	149
Refinement method	Le Bail Refinement
Goodness-of-fit	1.076
χ^2	1.158
Final R indices	R_1 = 0.0955 wR_2 = 0.1226
R indices (- background)	R_1 = 0.1087 wR_2 = 0.1350

Appendix B

Conferences, Courses and Departmental Seminars

B.1 Conferences

Conference	Details
British Crystallographic Association Autumn Meeting 2000	Glaxo-Wellcome, Harlow, Essex, 16^{th} November, 2000
British Crystallographic Association Spring Meeting 2001	Reading University, Reading, UK, 7^{th}–10^{th} April, 2001
British Crystallographic Association Autumn Meeting 2001	Aston University, Birmingham, UK, 14^{th} November, 2001
Royal Society of Chemistry Farraday Division — General Discussion No. 122	Hulme Hall, University of Manchester, UK, 25^{th} -26^{th} June, 2002
XIX Congress of the International Union of Crystallography	Palexpo, Geneva, Switzerland, August 2002
British Crystallographic Association Autumn Meeting 2002	13^{th} November, 2002
Exemplar Chem.	Scientific Societies Lecture Theatre, New Burlington Place, London W1, UK, 29^{th} November, 2002
British Crystallographic Association Spring Meeting 2003	York University, Heslington, York, UK, 15^{th}–17^{th} April 2003

B.2 Courses

Course Title	Organisers/Sponsors & Location	Dates/Examinations
Condensed Matter Physics: X-rays and Neutrons	Dr. Thomas. P. A. Hase, University of Durham, UK	October, 2000
Condensed Matter Physics: Modern Magnetic Resonance	Prof. Robin K. Harris, University of Durham, UK	November, 2000
Diffraction & Scattering Methods	Dr. Andrés E. Goeta, University of Durham, UK	January/February, 2001. Examination 19^{th} March, 91% (pass)
Practical Electronic Structure Calculations	Dr. David J. Tozer, University of Durham, UK	February, 2001. Examination 15^{th} March, 63% (pass)
8^{th} BCA/CCG Intensive Course in X-ray Structure Analysis	British Crystallographic Association, Trevelyan College, Durham, UK	30^{th} March – 6^{th} April, 2001
7^{th} Oxford School on Neutron Scattering	Mansfield College, Oxford, UK	27^{th} August – 6^{th} September, 2001
Pupil Researcher Initiative Researcher in Residence Scheme Training	Sheffield Hallam University, Sheffield, UK. Newcastle University, Newcastle-upon-Tyne, UK	22^{th} September, 2001
ISIS Neutron Training Course	ISIS, Rutherford Appleton Laboratories, Didcot, Oxfordshire, UK.	19^{th}–28^{th} October, 2002
12^{th} Higher European Course for Users of Large Experimental Systems	ILL/ESRF Grenoble, France and LLB/LURE, Paris, France	17^{th} February – 28^{th} March, 2002
Magnetic Rietveld Course	Coseners House, Abingdon, UK	12^{th}–14^{th} December, 2002

B.3 Departmental and Other Seminars

Author	Title	Date
Dr. Victor Cristau	Recent Developments in OLED Technology: Organolanthanide Phosphors	11/10/00
Prof. Vickie McKee	Controlling Assemblies and Communicating Restraints	31/10/00
Dr. Jonathan P. L. Cox	Cosmic: A Universal DNA — Language for Communication with Aliens and Other Intelligent Life-forms	08/11/00
Dr. Wayne Hayes	Synthesis of Novel Dendrimers and Hyperbranched Polymers	22/11/00
Prof. Richard Compton	Dual Activation Approaches to Electroanalysis	06/12/00
Prof. Ashwini Nangia	A Cambridge Database Study of CH_3/CF_3 Exchange	07/12/00
Dr. Andrew de Mello	Chemical Integrated Circuits	24/01/01
Dr. Paul Wright	Making Space for Molecules	31/01/01
Dr. Sîan T. Howard	Analysis of Bonding Energy Distributions in Polyatomic Molecules	14/02/01
Dr. Nick Norman	Liquid Crystals of All Shapes and Sizes	21/02/01
Dr. David Keen	Probing Structural Disorder with Diffuse Neutron Scattering	14/03/01
Prof. John Richards	Proton Transfer in Water at Enzymes	28/03/01
Prof. Christopher Viney	Silk and Slime: Successful Supramolecular Science	15/05/01
Prof. David Sherrington	Why Not Design Heterogeneous Catalysts Logically	01/06/01
Prof. Roland Boese	The Melting Point Alternation of n-Alkanes and Derivatives	06/06/01
Prof. Mike Heineky	Structure and Dynamics of Transition Metal Hydrides	10/09/01
Dr. Sylvia Capelli	Molecular Motion from Multi-Temperature ADPs	04/10/01
Dr. Sergei Kozhuskov	Selected Chapter of Political Organic Chemistry: Fascinating Artificial Cyclopropane Architectures	08/11/01
Dr. Wilhelm Huck	Control Over Polymeric Materials on a Nano Level	23/01/02
Dr. Peter Hore	Chemistry in a Spin — Effects of Magnetic Fields on a Chemical Reaction	30/01/02
Prof. Peter Day	Some Supramolecular Chemistry of Magnets and Superconductors	31/01/02
Dr. Helen Aspinall	Defining Effective Chiral Binding Sites at Lanthanides — Enantioselectivity	13/02/02
Prof. David Nesbitt	Searching for Simplicity: Single Frequencies, Single Collisions, Single Molecules (RSc Bourke Medal Lecture)	24/04/02
Prof. Kenneth Harris	Understanding the Properties of Molecular Solids: Structure, Dynamics and Applied Aspects	07/05/02
Prof. Paul Madden	"Covalent" Effects in "Ionic" Materials	08/05/02
Prof. Vernon Gibson	Designing Catalysts for Polymer Synthesis	31/05/02
Dr. Gary McIntyre	Single Crystal Diffraction at the ILL: Science and Facilities	13/06/02
Prof. Paul Raithby	Adventures in Organometallic Polymer Chemistry	12/02/03
Dr. Patrick M. Woodward	Manipulating the Electronic Structure of Semiconducting Metal Oxides	21/03/03

Appendix C

Publications and Presentations

C.1 Lasers and Crystallography

short communications

Journal of Applied Crystallography

ISSN 0021-8898

Received 15th March 2004
Accepted 0 XXXXXXX 0000
Online 0 XXXXXXX 0000

Structural Studies of Light Induced Excited States

Amber L. Thompson, Andrew Beeby and Andrés E. Goeta *

Department of Chemistry, University of Durham, South Road, Durham, DH1 3LE, England. Correspondence e-mail: A.E.Goeta@durham.ac.uk

Over the last few years there has been a marked increase in the number of structural studies carried out on light induced excited states. Until now however, there has been no systematic approach to the irradiation of samples, which can make data collection difficult and results unreliable. Here we present a device for mounting a laser on a CCD diffractometer, which not only enables the collection of data without any constraints on the data collection strategy, but also simplifies alignment of the laser and can be left in place permanently.

1. Introduction

With the increasing interest in structure-property relationships there has been an increase in the variety of sample environments available, e.g. cryostats and pressure cells. In addition, the increase in the number of known materials that respond to light has led to considerable interest in studying the associated structural changes. One example of this is the short lived photo-induced state of the luminescent rhenium carbene complex, $[HNCH_2CH_2NHCRe(2,2'\text{-bipyridine})(CO)_3]Br$ (Cole *et al.* 2003). Similarly, irradiation can induce charge transfer (Gu *et al.* 2001) and structural studies have been carried out on the short lived laser-induced ferroelectric structure of tetrathiafulvalene-*p*-chloranil (Collet *et al.* 2003).

Examples of photo-switching involving more dramatic structural changes, like the reorganisation of ligand coordination, have also been reported. Complexes where there are different coordination modes that can be switched using light, include NO ligands in sodium nitroprussides (Coppens *et al.* 1998) and SO_2 ligands in ruthenium sulphur dioxide compounds (Kovalevsky *et al.* 2002). A further example of photo-induced structural changes, is sometimes to be found in iron(II) spin crossover complexes (Marchivie *et al.* 2002; Money *et al.* 2003; Niel *et al.* 2004; Thompson *et al.* 2004). These materials undergo structural modifications coupled with changes to the optical, magnetic and physical properties, which can be stimulated by temperature or pressure changes and sometimes, at low temperature, by irradiation with light (Light-Induced Excited Spin-State Trapping or LIESST, Decurtins *et al.* 1985).

To our knowledge, the structural study of light induced states has generally been a little haphazard, with a "point and fire" approach to irradiation, where the laser is pointed at the sample and aligned by eye. There are two key problems with this method: It is not certain that the sample is being completely irradiated and it is difficult to study structures under continuous irradiation, as movements of the diffractometer circles potentially changes the alignment and may lead to obstruction of the laser beam. This latter necessity and the number of samples we are currently working on, has led us to design a laser stand that not only enables the continuous irradiation of samples *during* data collection, but due to the robust nature of the apparatus, enables it to remain *in situ* as a permanent feature during routine experiments. Here we present the main characteristics of the apparatus that we are using to carry out structural studies on metastable light induced states of spin crossover complexes.

2. Design

The key aspect of the design hinges on the mounting of the laser on the detector arm, in such a way that the laser beam remains centred on the sample irrespective of movements of the diffractometer circles. Thence, the intense, collimated light from the laser is directed towards the crystal using a combination of mirrors and prisms. In the case of the work carried out in Durham, the requirement was for a device that could be used to continuously irradiate a single crystal at 30 K. Thus, the instrumentation initially dictated certain aspects of the design and this device was designed for an Oxford Cryosystems HeliX mounted on a three circle Bruker diffractometer. The nature of the HeliX means that the crystal resides inside a beryllium nozzle, so the laser must approach the sample from below. The only area that is never obstructed by the ϕ circle mount is the region in front of the detector, so the device consists of a series of mirrors and prisms mounted on a cradle attached to the front of the detector arm (Figure 1). Since it is a necessary requirement that the laser and mirrors move together, the laser is mounted vertically on the tail of the detector arm, behind the detector, pointing down. The mass of the lasers used is relatively low (less than 0.2 kg), so they place no significant extra load on the apparatus, leading to no damage to the instrument or introduction of any systematic error. From behind the detector, the laser beam passes vertically down past the tail of the detector arm and is reflected by a tilted mirror so that it passes alongside the detector (parallel to the detector arm). It then travels through a periscope made from two prisms, which deflect the beam to the front of the detector, so that it is travelling in the direction of the 2θ axis. Finally, a mirror mounted in front of the detector reflects the beam up, striking the crystal from beneath, so that it avoids the beryllium nozzle from the HeliX cryostat (Figure 2).

This laser device has been designed to fit both a Bruker SMART-1K and a Bruker APEX CCD area detector diffractometers, however with minor modifications, it could probably be adapted to fit almost any diffractometer. When using the older diffractometers, where the crystal is viewed using a microscope, it is not possible to see the crystal during irradiation

IUCr macros version 2.0.13: 2003/12/24

short communications

as focused laser light can cause serious damage to the eye. However, like most modern diffractometers, the APEX is fitted with a digital camera for crystal alignment. Scattered laser light is visible using the camera and causes no damage to it, and thus can be used to facilitate accurate laser alignment.

Within the described setup, the laser can be aligned before the start of the experiment and even without a crystal. This increases the likelihood of success by avoiding having to do the alignment when a precious sample is already at very low temperature and after having performed several multi-temperature data collections. In addition, the use of area detectors has reduced the data acquisition time, therefore reducing the cost of the experiment, particularly when an expensive cryogen like helium is needed to achieve the required temperatures. Coupling this with the increased accuracy of the alignment due to the presence of the digital camera makes light induced structural studies much more feasible.

3. Conclusion

Here we have presented schematics of a device designed to simplify the collection of data on light induced excited states. It is not only cheap and easy to use, but the two adjustable mirrors make it easy to align the laser should it be necessary (e.g. after changing the laser for one of a different wavelength). The device is also so stable and unobtrusive, that we have been able to leave it in place as a permanent feature and it is now common to carry out routine data collections with the laser mounted.

Acknowledgements

The authors would like to say a special thank-you to James Hodgson (Technical Workshop, Dept. of Chem., Durham) for his sterling efforts in bringing this work to fruition. ALT also thanks the EPSRC for a postgraduate fellowship.

References

Cole, J. M., Raithby, P. R., Wulff, M., Schotte. F., Plech, A., Teat, S. J., & Bushnell-Wye, G. (2003). *Faraday Discussions* **122**, 119–129.
Collet, E., Lemée-Cailleau, M.-H.,Buron-Le Cointe, M., Cailleau, H., Wulff, M., Luty, T., Koshihara, S.-Y., Meyer, M., Toupet, L., Rabiller, P., & Techert, S. (2003). *Science* **300**(5619), 612–615.
Coppens, P., Fomitchev, D. V., Carducci, M. D. & Culp, K. (1998). *J. Chem. Soc. Dalton Trans.*, 865–872.
Decurtins, S., Gütlich, P., Hasselbach, K. M., Hauser, A. & Spiering, H. (1985). *Inorg. Chem*, **24**(14), 2174–2178.
Gu, Z.-Z., Einaga, Y., Sato, O., Fujishima, A. & Hashimoto, K. (2001). *J. Solid State Chem.* **159**(2), 336–342.
Gütlich, P., Garcia, Y. & Woike, T. (2001). *Chem. Soc. Rev.* **219-221**, 839–879.
Kovalevsky, A. Yu., Bagley, K. A. & Coppens, P. (2002). *J. Am. Chem. Soc.*, **124**(31), 9241–9248.
Marchivie, M., Guionneau, P., Howard, J. A. K., Chastanet, G., Létard, J.-F., & Goeta, A. E. (2002). *J. Am. Chem. Soc.* **124**(2), 194–195.
Money, V. A., Evans, I. R., Halcrow, M. A., Goeta, A. E. & Howard, J. A. K. (2003). *Chem. Commun.*, 158–159.
Niel, V., Thompson, A. L., Goeta, A. E., Enachescu, C., Hauser, A. Galet, A., Muñoz, M. C. & Real, J. A. (2004). *J. Am. Chem. Soc. - Submitted.*
Thompson, A. L., Goeta, A. E., Real, J. A., Galet, A. & Muñoz, M. C. (2004). *Chem. Commun. - DOI:10.1039/<B403179B>*

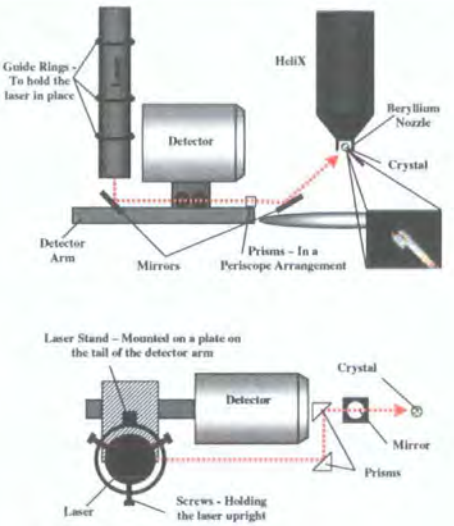

Figure 1
A schematic of the laser mounting and alignment device viewed in profile (top) and from above (bottom), with the path of the laser shown as a broken red line: the laser beam travels vertically down, and is reflected by a mirror so that it travels alongside the detector arm until two prisms redirect it to the front of the detector where a second mirror directs the beam up towards the sample. Minor adjustments to the alignment of the beam can be carried out using small screws to modify the angle of the mirrors. A photograph of a crystal on irradiation is shown inset.

Figure 2
The laser mount and guidance system with the laser beam path added in red (top) together with a close up of the goniometer, with the laser beam approaching the crystal from below (bottom). A 633 nm HeNe laser is shown, but 532 nm CW-Nd:YAG and 830 nm diode lasers have also been used. For these lasers the typical power at the sample is ~2 mW, which should lead to a temperature increase at the sample of less than 1 K. This indicates that the effects seen when using this device are photophysical rather than photothermal.

IUCr macros version 2.0.0: 2003/12/24

C.2 Thermal and Light Induced Polymorphism

COMMUNICATION

ChemComm www.rsc.org/chemcomm

Thermal and light induced polymorphism in iron(II) spin crossover compounds

Amber L. Thompson,[a] Andrés E. Goeta,*[a] José A. Real,*[b] Ana Galet,[c] and M. Carmen Muñoz[c]

[a] *Department of Chemistry, University of Durham, South Road, Durham, UK DH1 3LE. Fax: +44 191 386 1127; Tel: +44 191 324 2004; E-mail: A.E.Goeta@durham.ac.uk*

[b] *Institut de Ciencia Molecular/Departament de Química Inorgànica, Universitat de València, Doctor Moliner 50, Burjassot, Spain. E-mail: jose.a.real@uv.es*

[c] *Departament de Física Aplicada, Universitat Politècnica de València, Camino de Vera s/n, 46071, Valencia, Spain.*

Submitted for publication 1st March 2004.

The spin crossover complexes $\{Fe[H_2B(pz)_2]_2L\}$ ($[H_2B(pz)_2]^-$ = dihydrobis(pyrazolyl)borate, L = 2,2'-bipyridine (1), bipy and 1,10-phenanthroline, phen (2)) undergo both thermal and light induced spin crossover, but the structure of the low spin and light induced high spin states for 2 are different from that of the thermally induced high spin state and from those of 1.

The ability of spin crossover (SC) materials to change their magnetic, structural and optical properties stimulated by pressure or temperature, has led to increasing interest in their potential use in technological applications such as molecular switches, data displays, data storage devices and more recently as intelligent contrast agents for Magnetic Resonance Imaging.[1] The discovery that at low temperature is sometimes possible to photo-excite SC materials into a metastable high spin state[2] has enabled the study of high and low spin complexes without the added complication of thermal effects. This Light Induced Excited State Spin Trapping (LIESST) has also engendered significant interest in the optical properties of these materials.

While structural studies of thermally induced high and low spin complexes (HS and LS) are increasingly common, structure determinations of the metastable high spin state (MHS) are still very rare with only a handful reported in the literature.[3] In addition, to date, all structural studies on metastable light induced states have been carried out on materials where the LS, HS and MHS states are isostructural. Here we present the first structural study of a spin crossover complex, which exhibits thermal and light induced polymorphism.

Both $\{Fe[H_2B(pz)_2]_2bipy\}$ **(1)** and $\{Fe[H_2B(pz)_2]_2phen\}$ **(2)** undergo thermal induced SC (with characteristic temperatures of $T_{1/2}$ 160 K as well as light-induced SC.[4] The thermal transition in **2** is more cooperative than in **1** though, as shown by the more abrupt transition that takes place with hysteresis. Structural data have been reported previously for **1** above and below the SC transition, however, until now it had only been possible to collect data on **2** in the HS state as the crystal suffers structural damage on cooling through the transition.

Single crystal diffraction data† have been recorded for **1** at 200 K, 120 K, 30 K and at 30 K after irradiation with a red laser (λ = 633 nm). The crystal structure of the HS and LS states agree with the published data, where the structure is monoclinic (C2/c), with the molecule astride the two-fold rotation axis, which passes through the centre of the iron atom and between the rings of the bipy ligand. On cooling through the transition, there is a decrease in the average Fe-N bond length and the volume of the FeN_6 octahedron (Table 1), which is consistent with those seen previously for this and other SC compounds. After irradiation, the unit cell volume, the average Fe-N distance and octahedral volume all increase indicating that the photo-excited MHS state has been trapped.

Single crystal diffraction data† have also been recorded for **2** at 200 K, 100 K, 30 K and at 30 K after irradiation. The crystal was found to be in the C2/c monoclinic space group at 200 K (HS, same as in **1**), but to undergo a loss of symmetry to a related, primitive structure ($P\bar{1}$), with unit cell volume approximately half that of the high spin structure. This loss of lattice symmetry also leads to the loss of the C_2 molecular symmetry and this dramatic structural change explains the structural damage that previously led to difficulties in collecting data. The Fe-N bond lengths for **2** at 200 K and 100 K, clearly indicate a spin crossover transition coupled with the structural change (Table 1).

There is no further structural change on cooling **2** to 30 K. However, irradiation of **2** at 30 K leads to an increase in the unit cell volume from 1192.9(4) Å^3 to 1231.0(13) Å^3 (3.2%), and a corresponding increase in the octahedral volume from 10.53(2) Å^3 to 13.44(3) Å^3. Thus, the MHS state generated by irradiation with light has produced a second high spin polymorph, without the C_2 symmetry seen in the first. An overlay of the two HS molecules shows the conformational difference between the two polymorphs (Figure 1).

In addition to the loss of molecular symmetry, there is also a change in the crystal packing. The C2/c structures of **1** and **2** form stacks held together with π-π interactions between the interdigitating bipy/phen ligands (Figure 2). At 200 K, the phen-phen distance is 3.886(6) Å, which on cooling to 100 K, splits into two shorter, non-equivalent distances (3.657(9) Å and 3.528(9) Å). Between 100 K and 30 K, these distances contract (to 3.640(7) Å and 3.507(7) Å). While in **1** the bipy-bipy distance is 0.06 Å shorter for the MHS state than for the thermal HS state, the light induced expansion in **2** is highly asymmetric. In **2**, one phen-phen distance remains unchanged (3.638(10) Å) and the second expands by approximately 0.3 Å to 3.813(11) Å. This peculiar behaviour suggests that the light induced high spin polymorph is relatively unstable and only occurs because there is insufficient energy (supplied by the laser or available as thermal energy) to enable the structure to undergo a symmetry change to the preferred C2/c structure. This also explains why the relaxation temperature, as observed from the magnetic data, for

Table 1. Unit cell volumes, average Fe-N distances and octahedral volumes for **1** and **2**.

	Temperature	Unit Cell Volume	Fe-N Distance[a]	Octahedral Volume[a]
1	200 K	2441.5(4) Å^3	2.183(1) Å	13.67(2) Å^3
	120 K	2334.5(2) Å^3	2.004(9) Å	10.65(2) Å^3
	30 K	2327.2(3) Å^3	2.007(8) Å	10.69(2) Å^3
	30 K-Irr[b]	2398.4(2) Å^3	2.187(2) Å	13.74(2) Å^3
2	200 K	2504.4(4) Å^3	2.180(1) Å	13.63(2) Å^3
	100 K	1198.1(2) Å^3	1.998(6) Å	10.56(2) Å^3
	30 K	1192.9(4) Å^3	1.996(9) Å	10.53(2) Å^3
	30 K-Irr[b]	1231.0(13) Å^3	2.171(8) Å	13.44(3) Å^3

[a] Calculated using IVTON.[5]
[b] After irradiation at 30 K with red light (λ = 633 nm).

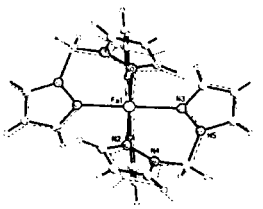

Fig. 1. Overlay of the two high spin polymorphs of **2**, showing the loss of C_2 molecular symmetry. The light induced state is shown with a broken line.

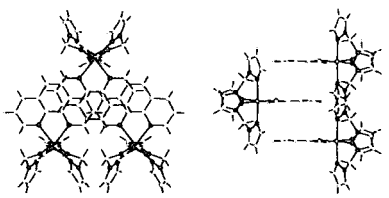

Fig. 2. π-π interactions in **2** at 200 K, showing the overlapping ligands (left) and the stacking (right).

the MHS states for **1** and **2** are 52 K and 44 K respectively. This is unusual because the thermal transition for **2** on cooling begins at a slightly lower temperature than that for **1**, and in general, higher temperature thermal SC transitions yield lower temperature relaxations for the LIESST state. The thermal HS state for **2** is marginally more stable than that for **1**, suggesting that the light induced MHS state for **2** should also be more stable, and consequently the relaxation from the MHS state should take place at a higher temperature for **2** than for **1**. The light induced polymorphic behaviour of **2** explains why this is not the case, and in practice the C2/*c* MHS state of **1** is more stable than the triclinic light induced high spin polymorph of **2**.

The authors would like to thank The Royal Society for a Study Visit and a Joint Project award, the EPSRC for a postgraduate fellowship (ALT), the Universitat Politécnica de València for a predoctoral fellowship (AG), and Ministerio Español de Ciencia y Tecnología for financial assistance of the (MCM & JAR, project BQU 2001-2928).

Notes and references

† The crystals of **1** were synthesised as discussed previously in the literature.[4] A typical red crystal was chosen 0.20 x 0.10 x 0.07 mm, mounted in fluoropolyether oil on a hair and quench cooled to 200 K using an Oxford Cryosystems Cryostream 600 series open flow N_2 cooling device.[6] Using a Bruker SMART-CCD 1000 area detector diffractometer, with graphite-monochromated Mo-Kα radiation (λ = 0.71073 Å), several sets of ω-scans (0.3°/frames) at different φ settings were collected. On completion, the crystal was cooled to 120 K at 240 K/hr, where the data collection was repeated. The crystal was then warmed to 200 K at 180 K/hr then to 290 K at 360 K/hr where the crystal was removed. The Cryostream was then replaced with an Oxford Cryosystems HeliX open flow helium cryostat,[7] and the crystal was cooled to 30 K in stages. At 30 K a hemisphere of data was collected (ω-scans, 0.9°/frames), after which the crystal was irradiated for approximately 30 mins with a 25 mW red laser (λ = 633 nm) after which data were collected as at 200 K and 120 K. Cell parameters were determined and refined using the SMART software[8] and raw frame data were integrated using the SAINT program.[9] The structures were solved by direct methods and refined by full-matrix least squares on F^2 using SHELXTL software[10] (crystal data are listed below). Reflection intensities were corrected for absorption effects by numerical integration based on measurements and indexing of the crystal faces (using SHELXTL software). Non-hydrogen atoms were refined anisotropically and hydrogen atoms were located in the difference map and refined with isotropic displacement parameters. *Single Crystal Data*: $C_{22}H_{24}B_2FeN_{10}$, M_r = 505.98, monoclinic, C2/*c*. **30 K** – a = 16.1106(11) Å, b = 14.5909(10) Å, c = 10.8281(8) Å, β = 113.895(3)°, V = 2327.2(3) Å, Data/restraints/parameters – 2662/0/207, R_{int} = 0.0606, Final R_1 = 0.0491, wR_2 = 0.0823 (I>2 (I)). **30 K-Irr** – a = 16.0350(9) Å, b = 14.9377(9) Å, c = 11.0470(7) Å, β = 114.986(2)°, V = 2398.4(2) Å, Data/restraints/parameters – 2700/0/207, R_{int} = 0.0629, Final R_1 = 0.0630, wR_2 = 0.0969 (I>2 (I)). $\Delta\rho_{min,max}$<=1 e.Å^3 in all cases.

‡ The crystals of **2** were synthesised as discussed previously in the literature.[4] A typical red crystal was chosen (0.28 x0.10x0.02 mm), mounted in epoxy resin (Araldite®) on a hair and quench cooled to 200 K using an Oxford Cryosystems Cryostream 600 series open flow N_2 cooling device.[6] Using a Bruker SMART-CCD 6000 area detector diffractometer, with graphite-monochromated Mo-Kα radiation (λ = 0.71073 Å), data were collected as for **1**. On completion, the crystal was cooled to 100 K at 360 K/hr, where the data collection was repeated. A second red crystal (0.28 x 0.10 x 0.02 mm) was selected and quenched to 200 K using an Oxford Cryosystems HeliX.[7] Cell parameters recorded using a Bruker ProteumM diffractometer with Bede Microsource® (Mo-Kα radiation, λ = 0.71073 Å), agreed with those seen previously at 200 K, so the crystal was cooled to 30 K at 360 K/hr, where a hemisphere was collected (as before). On completion, the crystal was irradiated for approximately 2 mins with a 25 mW red laser (λ = 633 nm) after which another hemisphere was collected. The data treatment was carried out as for **1**, except that hydrogen atoms were positioned geometrically and refined using a riding model. *Single Crystal Data*: $C_{22}H_{24}B_2FeN_{10}$, M_r = 505.98. **200 K** – monoclinic, C2/*c*, a = 17.3607(16) Å, b = 16.0397(14) Å, c = 10.5614(9) Å, β = 121.617(4)°, V = 2504.4(4) Å, Data/restraints/parameters – 3370/0/216, R_{int} = 0.0485, Final R_1 = 0.0461, wR_2 = 0.0888 (I>2 (I)). **100 K** – triclinic, P$\bar{1}$, a = 11.6730(13) Å, b = 11.0458(13) Å, c = 10.5651(12) Å, α = 69.520(3)°, β = 109.777(3)°, γ = 93.368(3)°, V = 1198.1(2) Å, (the related larger cell: a = 16.5354(14) Å, b = 15.5923(13) Å, c = 10.5651(12) Å, α = 89.688(4)°, β = 118.202(3)°, γ = 93.168(3)°, V = 2396.2(3) Å) Data/restraints/parameters – 6409/0/403, R_{int} = 0.0539, Final R_1 = 0.0628, wR_2 = 0.1296 (I>2 (I)). **30 K** – triclinic, P$\bar{1}$, a = 16.655(2) Å, b = 11.0156(19) Å, c = 10.5664(8) Å, α = 69.492(3)°, β = 109.755(3)°, γ = 93.280(3)°, V = 1192.9(4) Å, Data/restraints/parameters – 5832/0/407, R_{int} = 0.0546, Final R_1 = 0.0545, wR_2 = 0.0894 (I>2 (I)). **30 K-Irr** – triclinic, P$\bar{1}$, a = 10.727(7) Å, b = 12.415(8) Å, c = 10.712(6) Å, α = 67.473(15)°, β = 110.377(15)°, γ = 93.505(11)°, V = 1231.0(13) Å, Data/restraints/parameters – 5369/0/350, R_{int} = 0.0302, Final R_1 = 0.0798, wR_2 = 0.1620 (I>2 (I)). $\Delta\rho_{min,max}$<=1.2 e.Å^3 in all cases. All structures have been deposited with the CCDC (Nos X-Y). See http://www.rsc.org/suppdata/cc/b0/b000000a/ for crystallographic data in CIF format.

1 O. Kahn, J. Kröber, and C. Jay, *Adv. Mater.*, 1992, **4**(11), 718; O. Kahn and C. J. Martinez, *Science*, 1998, **279**, 44; O. Kahn, Molecular Magnetism, VCH Publishers Inc., New York., 1993.

2 S. Decurtins, P. Gütlich, K. M Hasselbach, H. Spiering and A. Hauser, *Inorg. Chem.*, 1985, **24**, 2174.

3 J. Kusz, H. Spiering and P. Gütlich, *J. Appl. Cryst.* 2001, **34**, 229; M. Marchivie, P. Guionneau, J. A. K. Howard, G. Chastanet, J-F. Létard, A. E. Goeta, D. Chasseau, *J. Am. Chem. Soc.*, 2002, **124**, 194; V. A. Money, I. R. Evans, M. A. Halcrow, A. E. Goeta, J. A. K. Howard, *Chem. Commun.*, 2003, 158.

4 J. A. Real, M. C. Muñoz, J. Faus, X. Solans, *Inorg. Chem.*, 1997, **36**, 3008; N. Moliner, L. Salmon, L. Capes, M. C. Muñoz, J.-F. Létard, A. Bouseksou, J.-P. Tuchagues, J. J. McGarvey, A. C. Dennis, M. Castro, R. Burriel, and J. A. Real, *J. Phys. Chem. B*, 2002, **106**, 4276.

5 T. Balic-Zunic and I. Vickovic, *J. Appl. Cryst.*, 1996, **29**, 305.

6 J. Cosier and A. M. Glazer, *J. Appl. Cryst.*, 1986, **19**, 105.

7 A. E. Goeta, L. K. Thompson, C. L. Sheppard, S. S. Tandon, C. W. Lehmann, J. Cosier, C. Webster and J. A. K. Howard, *Acta Cryst.*, 1999, **C55**, 1243; Oxford Cryosystems Newsletter, Issue 2, August 2003.

8 SMART-NT, Data Collection Software, Version 5.0; Bruker Analytical X-ray Instruments Inc., Madison, WI, USA, 1999.

9 SAINT-NT, Data Reduction Software, Version 5.0., Bruker Analytical Instruments Inc., Madison, Wisconsin, U.S.A., 1999.

10 SHELXTL, Structure Refinement and Solution Software, Version 5.1., Bruker Anaytical Instruments Inc., Madison, Wisconsin, U.S.A., 1999.

C.3 A Pyridyl-Bridged Dinuclear Palladium Complex

PAPER

NJC www.rsc.org/njc

A new precatalyst for the Suzuki reaction—a pyridyl-bridged dinuclear palladium complex as a source of mono-ligated palladium(0)

Andrew Beeby,*[a] Sylvia Bettington,[a] Ian J. S. Fairlamb,*[b] Andrés E. Goeta,[a] Anant R. Kapdi,[b] Elina H. Niemelä[b] and Amber L. Thompson[a]

[a] *Department of Chemistry, University of Durham, South Road, Durham, UK DH1 3LE. E-mail: andrew.beeby@durham.ac.uk; Fax: +44 (0)191 384 4737; Tel: +44 (0)191 334 2023*

[b] *Department of Chemistry, University of York, Heslington, York, UK YO10 5DD. E-mail: ijsf1@york.ac.uk; Fax: +44 (0)1904 432516; Tel: +44 (0)1904 434091*

Received (in Durham, UK) 22nd January 2004, Accepted 3rd March 2004
First published as an Advance Article on the web

A dinuclear pyridyl-bridged palladium complex, *trans*-(*P*,*N*)-[PdBr(μ-C_5H_4N-C^2,N)(PPh_3)]$_2$ **1**, was obtained from material isolated from the Suzuki cross-coupling reaction of 2-bromopyridine with 2,4-difluorophenylboronic acid in the presence of catalytic $(PPh_3)_4Pd$. Complex **1** is an effective precatalyst for the Suzuki cross-coupling reactions of a variety organoboronic acids and aryl bromides, and represents a useful source of mono-ligated palladium(0), "$(Ph_3P)Pd(0)$".

Introduction

Palladium-catalyzed C–C and C–X bond forming processes are amongst the most important reactions in organic synthesis.[1] The Pd-catalyzed cross-coupling reaction of organohalides with organoboronic acids, the Suzuki reaction, represents a key transformation in both academic and industrial sectors.[2] The catalyst of choice, particularly in natural product synthesis, is *still* $(Ph_3P)_4Pd(0)$, even though a significant step change in the field has been recently observed in the development of highly active, electron rich Pd-catalysts, possessing increased catalytic lifetimes.[3] The nature of the 'catalytically active' species, in particular, the number of phosphine ligands necessary to aid transmetallation, reductive elimination and to stabilize the Pd-centre, has often been questioned.[4] Classically it has been assumed that *two* phosphine ligands are required for catalyst activity, but studies with electron rich, bulky ligands, such as $(t\text{-Bu})_3P$ and $(t\text{-Bu})_2$-(biphenyl)P, have demonstrated that it is very likely that only one ligand remains on Pd.[5] It would be interesting to study Pd-precursors that allow for the generation of mono-ligated Pd-species in the absence of dibenzylideneacetone (dba).[6] Herein we describe the use of *trans*-(*P*,*N*)-[PdBr(μ-C_5H_4N-C^2,N)(PPh_3)]$_2$ **1** in the Suzuki reaction, which is expected to give "$(Ph_3P)Pd(0)$". Our findings, suggesting **1** as a suitable precursor catalyst, are discussed.

Results and discussion

Our initial studies were concerned with a side-product obtained from the Suzuki reaction of 2-bromopyridine **2** with 2,4-difluorophenylboronic acid **3** catalyzed by $(Ph_3P)_4Pd$ (Scheme 1, eqn. [1]). The expected cross-coupled product **4** was isolated in 82% yield; however, we were somewhat curious about the presence of a yellow component obtained from chromatography, which crystallized on evaporation to give pale brown diamond crystals in 0.11% yield. Suitable crystals for X-ray diffraction studies were chosen, which revealed the component to be a co-crystal of **1** and **4** (Fig. 1).†

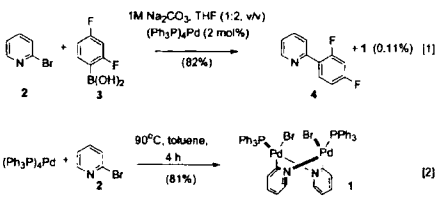

Scheme 1 Eqn. [1], first isolation of **1** Suzuki reaction of **2** and **3**. Eqn. [2], direct reaction of **2** with $(Ph_3P)_4Pd$ to give **1**.

Each palladium atom exhibits a square-planar geometry with the bromide and carbon bonds in a *trans* configuration. The Pd–Pd interatomic distance is 3.2338(4) Å and is consistent with the structure reported[8] (3.194(2) Å) and the chlorine analogue[9] (3.165(3) Å), previously published. This suggests that the interaction may be weak; although a search of the Cambridge Structural Database[10] (Version 1.5, November 2002, 272 066 entries) using ConQuest[11] shows that similar species occupy a range of 2.543–3.315 Å with a mean average of 2.795 Å. The central ring of our structure possesses two pyridine rings bridging the palladium atoms with the nitrogen *trans* to triphenylphosphine and carbon *trans* to bromine in both cases. These planes are inclined at an angle of 81.2° forming a six-membered ring in a boat conformation. The oxidative

† Chemical formula: $C_{46}H_{38}Br_2N_2P_2Pd_2$, $0.5(C_{11}H_7NF_2)$, M_r = 1148.93, T = 120 K, triclinic ($P\bar{1}$), a = 10.4525(4) Å, b = 13.0911(5) Å, c = 17.7535(6) Å, α = 81.5170(10)°, β = 78.849(2)°, γ = 70.8180(10)°, V = 2241.84(14) Å^3, Z = 2, μ = 2.699 mm^{-1}, Data/restraints/parameters = 11754/1/561, R_{int} = 0.0418, Final R_1 = 0.0431 wR_2 = 0.0898 [$I > 2\sigma(I)$]. CCDC reference number 207524. See http://www.rsc.org/suppdata/nj/b4/b401077a/ for crystallographic data in .cif or other electronic format.

DOI: 10.1039/b401077a

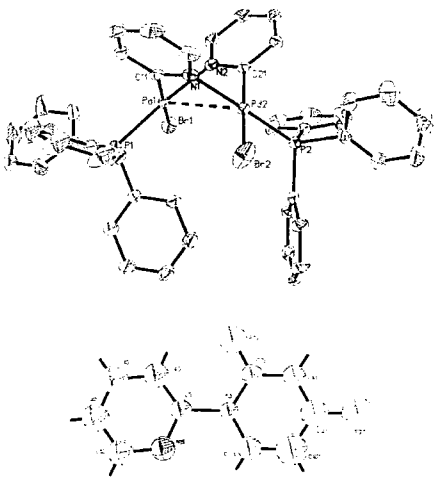

Fig. 1 Crystal structure of **1** with thermal ellipsoids at 50%. The structure of 2-(2,4-difluorophenyl)pyridine, **4**, with which **1** is co-crystallised, is also shown. The disorder is omitted for clarity.

addition of 2-, 3- and 4-bromopyridines to $(Ph_3P)_4Pd$ results in the formation of dimeric metallated pyridine species, such as **1**.[8] Complex **1** was thus synthesised by direct reaction of $(Ph_3P)_4Pd$ with **2** to give **1** in 81% yield, possessing identical ^1H, ^{31}P NMR spectroscopic and ESI spectrometric data to the material isolated in the reaction of **2** and **3** (Scheme 1, eqn. [2]).

We questioned whether **1** represented an intermediate catalyst resting state in the reaction of **2** and **3**, which led us to study **1** as a general precatalyst for the Suzuki cross-coupling reaction.[12] In the first reaction, **1** (0.2 mol%) was added to a mixture of **2** and phenylboronic acid **6a** in THF–1 M Na_2CO_3 at 80°C (Scheme 2, eqn. [1]). After 15 h the reaction was judged complete (TLC), with workup and purification by flash chromatography, affording the cross-coupled product **4a** in 68% yield.

Reaction of 6-methoxy-2-bromopyridine **2a** with **6a** under the same conditions gave the cross-coupled product **4b** in 77% yield (Scheme 2, eqn. [1]). We subsequently found that the reaction of **2** with **6a** could be conducted at 60 °C, proceeding in slightly higher yield (74%). Room temperature reactions with these substrates in the presence of **1** were sluggish, but encouraged by our results, we investigated the cross-coupling reactions of several aryl bromides and aryl boronic acids in the presence of **1** at 60 °C (Table 1).

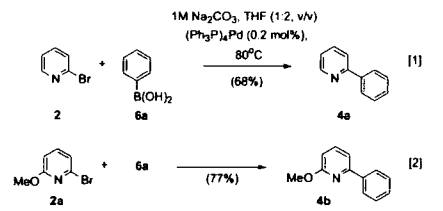

Scheme 2 Eqn. [1], use of **1** as a precatalyst for reaction of **2** and **6a**. Eqn. [2], use of **1** as a precatalyst for reaction of **2a** and **6a**.

Bromobenzene **5a** reacts with **6a**, 4-methylbenzeneboronic acid **6b**, 4-formylbenzeneboronic acid **6c** and 4-chlorobenzeneboronic acid **6d** in yields between 62–75% (entries 1–4). The turnover numbers per hour for these reactions were good (206–250 TON h^{-1}). 4-Bromoacetophenone **5b** couples effectively with **6a–d** in yields of 64–76% (entries 5–8). The turnover numbers per hour were lower than seen in reactions with **5a** (107–127 TON h^{-1}). A similar observation is apparent with the activated substrate, 4-nitro-1-bromobenzene **5c** (108–122 TON h^{-1}, entries 9–12). Methyl benzoate **5d** couples satisfactorily with **6a–d** (52–72% yields, entries 13–16). The less activated substrate, 2-methyl-1-bromobenzene **5e** couples well with **6a–d** (62–75% yields, entries 17–20), with surprisingly higher values observed for the turnover numbers per hour (207–250 TON h^{-1}). Indeed, 2-methoxy-1-bromobenzene **5f** couples equally well (74–81% yields, entries 21–24) in good turnover numbers (123–135 TON h^{-1}). The sterically hindered, deactivated substrate 2,6-dimethyl-1-bromobenzene **5g** (50–71% yields, entries 25–28) gave the lowest turnover numbers per hour seen in this series (21–30 TON h^{-1}). However, the fact that the unactivated substrates **5e** and **5f** couple more effectively than the more activated substrates **5b** and **5c** is an interesting observation.

The effect of additional Ph_3P on the reaction rate was probed systematically (Table 2). We chose 2-bromopyridine **2** as the substrate for reaction with phenylboronic acid **6a** under identical conditions to those given in Table 1. All reactions were stopped after 3 h (quenched by passing the mixture through a plug of silica gel).[13] The Ph_3P ligand (1, 2 and 4 equivalents of Ph_3P were added per equivalent of **1**; from a stock solution in dry THF) was added *via* microsyringe prior to addition of **1** to the reaction mixture. An obvious trend was seen in these reactions, where additional Ph_3P clearly reduces the turnover numbers per hour (entries 1–4, Table 2). In the absence of the additional Ph_3P, the cross-coupled product **4a** was produced in 74% after 3 h (entry 1, 123 TON h^{-1}). In the presence of 1 equivalent of Ph_3P (0.5 equivalent per Pd), **4a** was produced in 69% (entry 2, 115 TON h^{-1}). On increasing to 2 equivalents of Ph_3P (1 equivalent per Pd), **4a** was produced in 62% (entry 3, 103 TON h^{-1}). Finally, increasing the amount of Ph_3P to 4 equivalents (2 equivalents per Pd), **4a** was produced in 51% (entry 4, 85 TON h^{-1}). A comparison of entries 1, 3 and 4 formally allows us to correlate the effect of mono-ligated palladium(0) (Ph_3P-Pd(0)), bis-ligated palladium(0) ($(Ph_3P)_2Pd(0)$) and tris-ligated palladium(0) ($(Ph_3P)_3Pd(0)$). Thus in these reactions, excess Ph_3P slows down catalysis.

Complex **1** has previously been employed as a precatalyst for the cross-coupling reaction of chloropyridine with methylmagnesium bromide.[14] The occurrence of the reaction was rationalised generally by displacement of the bromide ligand from a monomeric species by an incoming nucleophile (Nu), to generate $[Pd(Nu)(\eta^1\text{-}C_5H_4N\text{-}C^n)(PPh_3)_2]$ (where $n = 3$ or 4).[15] Reductive elimination provides $Nu\text{-}C_5H_4N$ as the cross-coupled product and regenerates $(Ph_3P)_2Pd$ as the active catalytic species. However, such a proposal would have to occur through disproportionation of Ph_3P from the mono-phosphine palladium species to give the bis-phosphine palladium and a naked palladium species, which presumably would aggregate and precipitate out of solution. In our reactions we do not observe the formation of palladium black.[16]

Given our results, we propose that a mono-ligated phosphine species (Ph_3P-Pd(0)) is essential for higher turnover numbers. A precatalytic cycle based on the classical mechanism is proposed from precatalyst **1** (Fig. 2).[17] The dimeric precatalyst **1** is expected to be in equilibrium with a 14-electron monomeric species **1'**.[18] Transmetallation with an activated arylboronic acid will then occur through formal displacement of bromide to give Pd(II) intermediate **1**. Reductive elimination will then generate the cross-coupled product **4a** and give the

Table 1 Suzuki cross-coupling of aryl bromides and aryl boronic acids catalysed by pyridyl complex **1**

Entry	Aryl bromide	Arylboronic acid	Product	Time/h	Yield (%)[b]	TON h^{-1}[c]
1	 **5a**	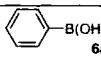 **6a**	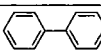 **7a**	1.5	62	206
2	**5a**	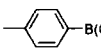 **6b**	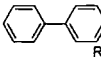 R = Me, **7b**	1.5	63	210
3	**5a**	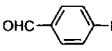 **6c**	R = CHO, **7c**	1.5	75	250
4	**5a**	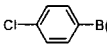 **6d**	R = Cl, **7d**	1.5	74	247
5	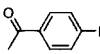 **5b**	**6a**	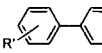 R' = 4-$COCH_3$, R = H, **7e**	3	64	107
6	**5b**	**6b**	R' = 4-$COCH_3$, R = Me, **7f**	3	69	115
7	**5b**	**6c**	R' = 4-$COCH_3$, R = CHO, **7g**	3	71	118
8	**5b**	**6d**	R' = 4-$COCH_3$, R = Cl, **7h**	3	76	127
9	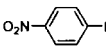 **5c**	**6a**	R' = 4-NO_2, R = H, **7i**	3	65	108
10	**5c**	**6b**	R' = 4-NO_2, R = Me, **7j**	3	66	110
11	**5c**	**6c**	R' = 4-NO_2, R = CHO, **7k**	3	68	113
12	**5c**	**6d**	R' = 4-NO_2, R = Cl, **7l**	3	73	122
13	 **5d**	**6a**	R' = 2-CO_2Me, R = H, **7m**	4	62	78
14	**5d**	**6b**	R' = 2-CO_2Me, R = Me, **7n**	4	52	65
15	**5d**	**6c**	R' = 2-CO_2Me, R = CHO, **7o**	4	71	89
16	**5d**	**6d**	R' = 2-CO_2Me, R = Cl, **7p**	4	72	90
17	 **5e**	**6a**	R' = 2-Me, R = H, **7q**	1.5	63	210
18	**5e**	**6b**	R' = 2-Me, R = Me, **7r**	1.5	62	207
19	**5e**	**6c**	R' = 2-Me, R = CHO, **7s**	1.5	74	247
20	**5e**	**6d**	R' = 2-Me, R = Cl, **7t**	1.5	75	250
21	 **5f**	**6a**	R' = 2-OMe, R = H, **7u**	3	76	127
22	**5f**	**6b**	R' = 2-OMe, R = Me, **7v**	3	81	135
23	**5f**	**6c**	R' = 2-OMe, R = CHO, **7w**	3	74	123
24	**5f**	**6d**	R' = 2-OMe, R = Cl, **7x**	3	77	128
25	 **5g**	**6a**	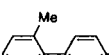 R = H, **7y**	12	63	26
26	**5g**	**6b**	R = Me, **7z**	12	50	21
27	**5g**	**6c**	R = CHO, **7a'**	12	61	25
28	**5g**	**6d**	R = Cl, **7b'**	12	71	30

[a] *Reaction conditions*: aryl bromide (1.05 eq.), aryl boronic acid (1.0 eq.), **1** (0.2 mol%), 1 M Na_2CO_3–THF (1 : 2 v/v), 60 °C with magnetic stirring. [b] Isolated yields after chromatography. [c] TON h^{-1}: calculated by considering the number of moles of desired product produced per mole of catalyst used per hour.

Table 2 Effect of excess triphenylphosphine on Suzuki coupling of **2** with **5a** using precatalyst

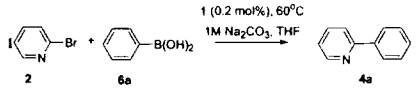

2 **6a** **4a**

Entry	Additional Ph_3P (%)[b]	Time/h	Yield (%)[c]	TON h^{-1}[d]
1	0	3	74	123
2	0.1	3	69	115
3	0.2	3	62	103
4	0.4	3	51	85

[a] Reactions performed with 0.2 mol% catalyst using the conditions and reagents described in Table 1. [b] Ph_3P stock solutions were prepared using dry THF and the appropriate aliquot added to the reaction mixture at $t = 0$. [c] Yields calculated from the ^1H NMR spectra of the isolated material (crude). [d] TON h^{-1}: calculated by considering the number of moles of desired product produced per mole of catalyst used per hour.

mono-ligated species **II**. This species can now proceed into the standard catalytic cycle. Standard oxidative addition with the appropriate organohalide gives **III**. Transmetallation of **III** with the activated arylboronic acid affords **IV**, which then undergoes reductive elimination to reveal the cross-coupled product, regenerating the monomeric palladium(0) species **II** as a consequence.

Support for the precatalytic cycle comes by following the reaction of 4-nitrobromobenzene **5c** with phenylboronic acid **6a**, in the presence of precatalyst **1** (5 mol%) at 60 °C, by GC-MS analysis. The first turnover should produce 2-phenylpyridine **4a**. After *ca.* 1 min of the reaction, **4a** is produced, *via* the precatalyst cycle. The formation of **7i** and disappearance of **5c** is then observed (over 3 h), which is expected if mono-ligated palladium(0) species **II** then enters the standard catalytic cycle.

To summarise, we have conducted the first Suzuki cross-coupling reactions employing precatalyst **1**. A great advantage of this complex is its stability under ambient conditions (air and moisture stable), unlike other commonly employed Pd(0) catalysts, *e.g.* $(Ph_3P)_4Pd$, which are readily oxidised to Pd(II) species in air. Complex **1** is easily synthesised in high yield and may be used at low catalyst loadings (0.2 mol%), under relatively mild conditions (60 °C). Investigations into the effect of additional phosphine on the rate of reaction demonstrated an interesting trend. Here it was shown that excess phosphine (> 1 Ph_3P per Pd) slows downs catalysis, which is presumably associated with transmetallation and reductive elimination steps, key events that are ultimately dependant on ligand dissociation. Finally, this study demonstrates how important it is to isolate every component from a reaction mixture—by doing this we have ultimately been led to the identification of a new precatalyst for the Suzuki reaction.

Experimental

THF was dried over sodium–benzophenone ketyl (distilled prior to use). All reactions were conducted under an inert atmosphere of Ar or N_2 on a Schlenk line. $Pd(PPh_3)_4$ was prepared by reduction of $(Ph_3P)_2PdCl_2$ with hydrazine.[19] $(PPh_3)_2PdCl_2$ was prepared from $PdCl_2$ (provided by Johnson Matthey as a loan) in refluxing DMSO and PPh_3 (2 eq.) using a known procedure.[20] Melting points were recorded on an electrothermal IA9000 Digital Melting Point Apparatus and are uncorrected. TLC analysis was performed on Merck 5554 aluminium backed silica gel plates and compounds visualized by ultraviolet light (254 nm), phosphomolybdic acid solution (5% in EtOH), or 1% ninhydrin in EtOH. ^1H NMR spectra were recorded at 270 MHz using a JEOL EX270 spectrometer or at 400 MHz using a JEOL ECX400 spectrometer: ^{13}C NMR spectra at 67.9 or 100.5 MHz. Chemical shifts are reported in parts per million (δ) downfield from an internal tetramethylsilane reference. Coupling constants (J values) are reported in hertz (Hz), and spin multiplicities are indicated by the following symbols: s (singlet), d (doublet), t (triplet), q (quartet), qn (quintet), sx (sextet), m (multiplet), br (broad).

The following compounds were characterized by ^1H, ^{13}C NMR and mass spectrometry and compared to the known

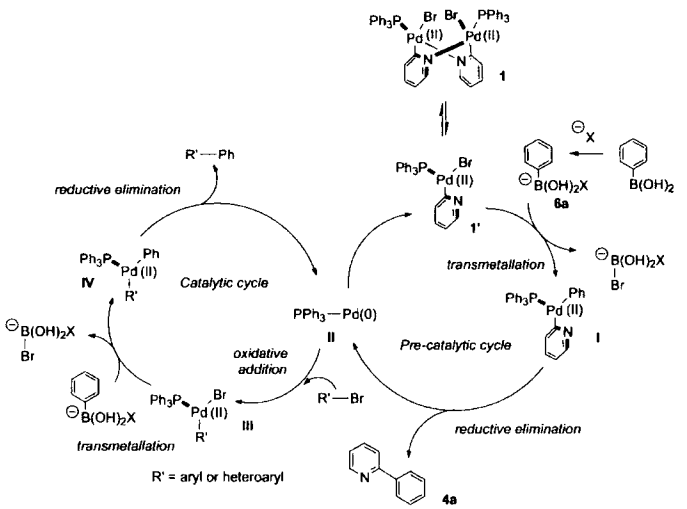

Fig. 2 The catalytic cycle employing precatalyst **1** in Suzuki cross-coupling reactions.

literature data: 4-acetylbiphenyl **7c**,[21] biphenyl **7a**,[22] 4-nitrobiphenyl **7i**,[23] 2,6-dimethylbiphenyl **7y**,[24] 2-methoxycarbonylbiphenyl **7m**,[25] 2-methylbiphenyl **7q**,[26] 2-methoxybiphenyl **7u**,[27] 4-methylbiphenyl **7b**,[22] 4-acetyl-4′-methylbiphenyl **7f**,[28] 2,6-dimethyl-4′-methylbiphenyl **7z**,[21] 2-methoxycarbonyl-4′-methylbiphenyl **7n**,[29] 2,4′-dimethylbiphenyl **7r**,[28] 2-methoxy-4′-methylbiphenyl **7v**,[21] 4′-formylbiphenyl **7c**,[26] 4-acetyl-4′-formylbiphenyl **7g**,[30] 2-methyl-4′-formylbiphenyl **7s**,[26] 4′-chlorobiphenyl **7d**,[26] 4-acetyl-4′-chlorobiphenyl **7h**,[31] 4-nitro-4′-chlorobiphenyl **7l**,[32] 2,6-dimethyl-4′-chlorobiphenyl **7b′**,[33] 2-methoxycarbonyl-4′-chlorobiphenyl **7p**,[32] 2-methyl-4′-chlorobiphenyl **7t**,[33] 2-methoxy-4′-chlorobiphenyl **7x**[26] and 2-methoxycarbonyl-4′-formylbiphenyl **7p**.[34]

1-Phenyl-2-bromopyridine 4a

δ_H (300 MHz, $CDCl_3$) 8.66 (1H, dt, J = 4.2 Hz, *CH*), 7.91 (2H, m, 2 × *CH*), 7.70 (2H, m, 2 × *CH*), 7.42 (3H, m, 3 × *CH*), 7.21 (1H, m, *CH*); MS (ES+): 156.1 $(M+H)^+$.

1-Phenyl-2-bromo-6-methoxypyridine 4b

δ_H (300 MHz, $CDCl_3$) 8.09 (2H, d, J = 7.2 Hz, 2 × *CH*), 7.65 (1H, t, J = 7.5 Hz, *CH*), 7.45 (4H, m, 4 × *CH*), 6.73 (1H, d, J = 8.1 Hz, *CH*), 4.08 (3H, s, CH_3); MS (ES+): 186.1 $(M+H)^+$.

4-Nitro-4′-methylbiphenyl 7j

δ_H (400 MHz, $CDCl_3$) 8.22 (2H, d, J = 7.9 Hz, *CH*), 7.66 (2H, d, J = 7.9 Hz, 2 × *CH*), 7.64 (2H, d, J = 8.1 Hz, *CH*), 7.24 (2H, d, J = 8.1 Hz, 2 × *CH*), 2.35 (3H, s, CH_3); δ_C (100 MHz, $CDCl_3$) 149.05, 139.05, 135.91, 132.60, 129.88, 127.45, 127.19, 124.07, 21.19; MS (EI) m/z 213 (M^-, 100), 75, 152, 115, 165, 183.

4-Nitro-4′-formylbiphenyl 7k

δ_H (400 MHz, $CDCl_3$) 10.08 (1H, s, *CHO*), 8.10 (2H, d, J = 8.8 Hz, 2 × *CH*), 8.01 (2H, d, J = 8.8 Hz, 2 × *CH*), 7.98 (2H, d, J = 8.5 Hz, 2 × *CH*), 7.66 (2H, d, J = 8.5 Hz, 2 × *CH*); MS (EI) m/z 227 (M^-, 78), 152, 210, 76.

2,6-Dimethyl-4′-formylbiphenyl 7a′

δ_H (400 MHz, $CDCl_3$) 9.98 (1H, s, *CHO*), 7.36 (2H, d, J = 6.7 Hz, 2 × *CH*), 7.34 (1H, d, J = 7.1Hz, *CH*), 7.33 (2H, m, 2 × *CH*), 7.29 (2H, m, 2 × *CH*), 1.93 (6H, s, 2 × CH_3).

2-Methoxy-4′-formylbiphenyl 7w

δ_H (400 MHz, $CDCl_3$) δ 10.00 (1H, s, *CHO*), 7.85 (2H, d, J = 8.2 Hz, 2 × *CH*), 7.42 (2H, d, J = 8.2 Hz, 2 × *CH*), 7.23–7.13 (4H, m, 4 × *CH*), 2.208 (3H, s, OCH_3); δ_C (100 MHz, $CDCl_3$) 192.31, 148.70, 140.88, 135.19, 130.20, 129.27, 128.34, 128.22, 127.57, 127.50, 56.38.

Original isolation of *trans*-(P,N)-[PdBr-(μ-C_5H_4N-C^2,N)(PPh_3)]$_2$ (1)

2,4-Difluorophenylboronic acid **3** (5g, 32 mmol), 2-bromopyridine **2** (5.5 g, 3.3 mL, 35 mmol. 1.1 eq.), Na_2CO_3 (1M aq., 50 mL), THF (100 mL) and $Pd(PPh_3)_4$ (0.75 g, 0.6 mmol, 2 mol %) were heated overnight in a nitrogen atmosphere at 80 °C with continuous stirring. The reaction was cooled to room temperature and water (200 mL) was added. The resulting mixture was extracted with ethyl acetate (5 × 100 mL), dried ($MgSO_4$), filtered and evaporated *in vacuo*. Flash chromatography afforded 2-(2,4-difluorophenyl)pyridine **4**, as a pale yellow liquid (5.0 g, 82%). Complex **1** was isolated from a fraction containing the impure product as pale brown diamond shaped crystals (20 mg, 1.1 × 10^{-3}%). δ_H (400 MHz, $CDCl_3$) 8.58 (1H, m), 7.85 (6H, m), 7.36 (3H, m), 7.28 (6H, m), 6.61 (1H, m), 6.49 (2H, m); δ_P (121 MHz, $CDCl_3$) 30.79. Electrospray mass spectrometry in acetonitrile gives similar results to those reported previously.[15]

Direct preparation of *trans*-(*P*,*N*)-[PdBr-(μ-C_5H_4N-C^2,N)(PPh_3)]$_2$(1)

Tetrakistriphenylphosphine palladium(0) (600 mg, 0.48 mmol) was dissolved in toluene (40 mL) to produce a bright clear yellow solution. 2-Bromopyridine (137 mg, 0.87 mmol, 1.8 eq.) was then added. The resulting mixture was heated to 90 °C for 4 h, during which time the solution became cloudy and a pale green-yellow colour. The reaction mixture was cooled to room temperature and filtered. The green-yellow precipitate was collected and washed thoroughly with diethyl ether (5 × 10 mL) and subsequently dissolved in chloroform. The filtrate was evaporated to dryness and the solid recrystallized from chloroform and *n*-hexane to give the pure product as a green-yellow crystalline solid (205 mg, 81%). δ_H and δ_P data were identical to that given above.

Typical Suzuki reaction

Phenylboronic acid (50 mg, 0.41 mmol), 2-bromopyridine (71.3 mg, 0.45 mmol, 1.1 eq.), Na_2CO_3 (1 M (aq.), 1 ml), THF (1.5 mL) and Pd-dimer crystals (1 mg, 0.95 μmoles, 0.21 mol%) were degassed *via* three 'freeze–pump–thaw' cycles. The resulting mixture was heated at 60 °C overnight during which the clear solution became bright yellow in colour. The reaction mixture was allowed to cool to room temperature after which water (10 mL) was added. The mixture was then extracted with dichloromethane (3 × 10 mL) and the organic extracts dried ($MgSO_4$), filtered and concentrated *in vacuo*. Purification by flash chromatography gave the pure cross-coupled product, 2-phenylpyridine, as a pale yellow liquid (43 mg, 68%). ^{1}H NMR 300 MHz ($CDCl_3$) δ: 8.66 (1H, dt, J = 4.2 Hz), 7.91 (2H, m), 7.70 (2H, m), 7.42 (3H, m), 7.21 (1H, m); MS (ES+): 156.1 $(M+H)^+$.

Crystal structure determination of *trans*-(P,N)-[PdBr(μ-C_5H_4N-C^2,N)(PPh_3)]$_2$†

Single crystal X-ray diffraction experiments were carried out at 120 K using graphite monochromated Mo Kα radiation (λ = 0.71073 Å) on a Bruker SMART-CCD 1K area detector diffractometer. The temperature was controlled using a Cryostream N_2 open-flow cooling device.[35] Five series of narrow ω-scans (0.3°) were performed at several φ-settings to cover a sphere of data to a maximum resolution of between 0.70 and 0.77 Å. Cell parameters were initially determined using the SMART software,[36] and raw frame data were integrated and cell parameters refined using the SAINT program. The structure was solved by direct methods and refined by full-matrix least squares on F^2 using the SHELXTL software.[37] The reflection intensities were corrected by numerical integration based on measurements and indexing of the crystal faces (using SHELXTL software). The structure is of a co-crystal of **1** and **4**. Both **1** and **4** have disorder which is modeled. For **1**, one of the phenyl rings from the each PPh_3 ligand is disordered such that there are two positions, each with 50% occupancy. All non-hydrogen atoms were refined with anisotrpic displacement parameters. **4** occupies a possition on an inversion centre, which relates the two components. Anisotropic refinement of **4** is unstable, so all atoms were refined with isotropically. Hydrogen atoms for both **1** and **4** were refined using a riding model.

Acknowledgements

We would like to thank EPSRC (SLB and ALT) for their financial support and Professor T. B. Marder for his helpful discussions and suggestions. IJSF thanks for the University of York for financial assistance and Johnson Matthey for a generous loan of palladium salts.

References

1 (*a*) *Metal-catalyzed Cross-coupling Reactions*, eds. F. Diederich and P. J. Stang, Wiley-VCH, New York, 1998; (*b*) J. Tsuji, *Palladium Reagents and Catalysts, Innovations in Organic Synthesis*, Wiley, New York, 1995.
2 N. Miyaura and A. Suzuki, *Chem. Rev.*, 1995, **95**, 2457–2483.
3 A. F. Littke and G. C. Fu, *Angew. Chem., Int. Ed.*, 2002, **41**, 4176–4211 and references cited therein..
4 A. F. Littke, C. Dai and G. C. Fu, *J. Am. Chem. Soc.*, 2000, **122**, 4020–4028.
5 The bridged dimer $[(t\text{-Bu})_3P(Br)Pd]_2$ is a suitable source of "$(t\text{-Bu})_3PPd$", however the corresponding Ph_3P complex is not known, see: R. Vilar, D. M. P. Mingos and C. J. Cardin, *J. Chem. Soc., Dalton Trans.*, 1996, 4313–4314. T-shaped 14-electron mono-phosphine Pd(II) intermediates, containing $(t\text{-Bu})_3P$ have been isolated and characterized, see: J. P. Stambuli, M. Buhl and J. F. Hartwig, *J. Am. Chem. Soc.*, 2002, **124**, 9346–9347.
6 Dibenzylideneacetone (DBA) is assumed to play a non-innocent role in Pd-catalyzed cross-coupling reactions; see: C. Amatore, G. Broeker, A. Jutand and F. Khalil, *J. Am. Chem. Soc.*, 1997, **119**, 5176–5185.
7 Complete crystallographic data for **1** have been deposited at the Cambridge Crystallographic Data Centre (deposit number, CCDC 207524).
8 K. Nakatsu, K. Kinoshita, H. Kanda, K. Isobe, Y. Nakamura and S. Kawaguchi, *Chem. Lett.*, 1980, 913–914.
9 T. A. Anderson, R. J. Barton and B. E. Robertson, *Acta. Crystallogr., Sect. C*, 1985, **C41**, 1171–1173.
10 F. H. Allen, *Acta Crystallogr., Sect. B*, 2002, **B58**, 380–388.
11 I. J. Bruno, J. C. Cole, P. R. Edgington, M. Kessler, C. F. Macrae, P. McCabe, J. Pearson and R. Taylor, *Acta Crystallogr., Sect. B*, 2002, **B58**, 389–397.
12 The use of dimeric 2-pyridyl Pd(II) complexes as effective catalysts for Suzuki cross-coupling reactions has *not* been reported.
13 It is important that enough silica-gel is used to ensure that trace quantities of palladium are not carried through into the analysis sample. We have found that the reaction can still turnover on passing larger quantities of material through silica gel. In cases where larger samples are required it is possible to add two equivalents (per Pd) of 1,1′-diphenylphosphinoethane (dppe) to the crude reaction which irreversibly inhibits catalysis: E. H. Niemela, A. F. Lee and I. J. S. Fairlamb, *Org. Lett.*, 2004, submitted for publication (21/01/04).
14 K. Isobe and S. Kawaguchi, *Heterocycles*, 1981, **16**, 1603–1612.
15 C. H. C. Clavius, J. S. L. Yeo, Z. H. Loh, J. J. Vittal, W. Henderson and T. S. A. Hor, *J. Chem. Soc. Dalton. Trans.*, 1998, 3777–3784.
16 If the reactions are opened up to air, palladium black is produced in <0.5 h.
17 It is appreciated that an anionic cycle could be operative from **1** by which the mono-ligated palladium(0) species is generated (such as $(Ph_3P\text{-}Pd(0)\text{-}Br(-))$. For detailed information related to this type of cycle see the work by Amatore and Jutand: (*a*) C. Amatore and A. Jutand, *Acc. Chem. Res.*, 2000, **33**, 314–321; (*b*) C. Amatore and A. Jutand, *J. Organomet. Chem.*, 1999, **576**, 254–278.
18 N. W. Alcock, J. M. Brown and D. I. Hulmes, *Tetrahedron*, 1993, **4**, 743–756.
19 (*a*) D. R. Coulson, *Inorg. Synth.*, 1972, **13**, 121–124; (*b*) R. B. King and P. N. Kapoor, *Inorg. Chem.*, 1972, **11**, 1524–1527.
20 F. G. Mann and D. Purdie, *J. Chem. Soc.*, 1935, 1549–1551.
21 J. P. Wolfe, R. A. Singer, B. H. Yang and S. L. Buchwald, *J. Am. Chem. Soc.*, 1999, **121**, 9550–9561.
22 C. J. Mathews, P. J. Smith and T. Welton, *Chem. Commun.*, 2000, 1249–1250.
23 N. E. Leadbeater and M. Marco, *Org. Lett.*, 2002, **4**, 2973–2976.
24 C. Griffiths and N. E. Leadbeater, *Tetrahedron Lett.*, 2000, **41**, 2487–2490.
25 Y. Kobayashi, A. D. William and R. Mizojiri, *J. Organomet. Chem.*, 2002, **653**, 91–97.
26 N. Kataoka, Q. Shelby, J. P. Stambuli and J. F. Hartwig, *J. Org. Chem.*, 2002, **67**, 5553–5566.
27 N. Miyaura, T. Yanagi and A. Suzuki, *Synth. Commun.*, 1981, **11**, 513–519.
28 A. F. Littke and G. C. Fu, *J. Am. Chem. Soc.*, 2001, **123**, 6989–7000.
29 K. Inada and N. Miyaura, *Tetrahedron*, 2000, **56**, 8657–8660.
30 A. G. M. Barrett, P. A. Procopiou and U. Voigtmann, *Org. Lett.*, 2001, **3**, 3165–3168.
31 J. P. Idoux, G. E. Kiefer, G. R. Baker, W. E. Puckett and F. J. Spence, *J. Org. Chem.*, 1980, **45**, 441–444.
32 I. Klement, M. Rottlaender, C. E. Tucker, T. N. Majid and P. Knochel, *Tetrahedron*, 1996, **52**, 7201–7220.
33 H. C. Bell, J. R. Kalman, J. T. Pinhey and S. Sternhell, *Tetrahedron Lett.*, 1974, **15**, 857–860.
34 C. G. Blettner, W. A. König, W. Stenzel and T. Schotten, *Synlett*, 1998, 295–297.
35 J. Cosier and A. M. Glazer, *J. Appl. Cryst.*, 1986, **19**, 105–107.
36 SMART-NT, Data Collection Software, version 5.0, Bruker Analytical X-ray Instruments Inc, Madison, Wisconsin, USA, 1999.
37 SHELXL, version 5.1, Bruker Analytical Instruments Inc, Madison, Wisconsin, USA, 1999.

C.4 Magnetic Dimensionality of $Y_{(2-x)}Dy_xBaCuO_5$

ELSEVIER

Available online at www.sciencedirect.com

SCIENCE DIRECT®

Solid State Communications 130 (2004) 387–390

solid state communications

www.elsevier.com/locate/ssc

Magnetic dimensionality of $Y_{(2-x)}Dy_xBaCuO_5$

L.A. Baum[a], A.E. Goeta[b], R.C. Mercader[a,*], A.L. Thompson[b]

[a]*Departamento de Física, IFLP, Facultad de Ciencias Exactas, Universidad Nacional de La Plata, C.C.67, 1900 La Plata, Argentina*
[b]*Department of Chemistry, University of Durham, South Road, Durham DH1 3LE, UK*

Received 27 January 2004; accepted 13 February 2004 by A. Zawadowski

Abstract

In this communication, we report the effect that doping Y_2BaCuO_5 with Dy has on its two-dimensional (2D) magnetic structure. Pure samples at both ends of the series, as well as samples doped with 1, 5, 10 and 25% dysprosium, have been characterised using X-ray diffraction, and AC susceptibility together with neutron diffraction studies on the 1 and 5% samples, which were used to measure the magnetic ordering at low temperatures. The results show that 1% Dy is enough to disrupt the 2D magnetic ordering turning it into a 3D array. The low dysprosium concentration indicates that the 3D ordering is achieved without the existence of a rare earth magnetic sublattice. The change in the ordering temperature from 27 K for the pure Y_2BaCuO_5 to 16 K for the 1 and 5% Dy compounds, together with the parameters from the AC susceptibility fittings, reveal that the effect of the Dy doping affects the electronic structure of the Cu ions that become involved in the superexchange pathways. The discrepancy between the parameters obtained by the Curie–Weiss fittings of the real part of the AC susceptibility and the neutron diffraction results, shows that the exchange mechanism deviates from the mean field model for all dysprosium concentrations.

PACS: 75.30.Cr; 75.30.Et

Keywords: A. Magnetically ordered materials; D. Exchange and superexchange; E. Magnetic susceptibility; E. Neutron scattering

1. Introduction

Since the constituent elements of Y_2BaCuO_5 are the same as those of the high T_c superconducting cuprates, there is a great deal of interest in fully grasping the details of their magnetic behavior. This is enhanced by the fact that there is also a similarity between the electronic structures of the copper centre in the orthorhombic (*Pnma*) R_2BaCuO_5 (where R = Y or rare earth), and that of the copper in the CuO_2 planes of the tetragonal $YBa_2Cu_3O_7$ high T_c superconductor (also known as the 1:2:3 phase) [1].

Although Y_2BaCuO_5 (*Pnma*), has been studied for some time by different techniques [2,3], some doubts remain regarding its magnetic structure. Indeed, there is still some dispute as to its true magnetic structure at low temperature [4]. Most DC susceptibility and neutron diffraction studies indicate that the array of magnetic pathways is two-dimensional (2D), however, some authors [5] believe that they may be one-dimensional (1D). The low temperature neutron diffraction studies have been unable to verify this unambiguously. Isomorphous *Pnma* R_2BaCuO_5 compounds generally display an antiferromagnetic 3D array [6], however, in the series R_2BaMO_5 (M = transition metal) diverse structures with 3D, 2D and 1D magnetic orderings have been observed [6]. In particular some 1D R_2BaMO_5 materials have been shown to undergo magnetic excitations of the Haldane gap type [7].

The type of interactions that lead to the magnetic ordering is also not completely understood. Approximately 10 years ago, when most of the series of compounds were synthesized [8–10], several publications claimed that the ordering of the M sublattice induces the ordering of the rare

* Corresponding author. Tel.: +54 (221) 424-6054; fax: +54 (221) 425-2006.
E-mail address: rcm@fisica.unlp.edu.ar (R.C. Mercader).

0038-1098/$ - see front matter © 2004 Elsevier Ltd. All rights reserved.
doi:10.1016/j.ssc.2004.02.026

388 L.A. Baum et al. / Solid State Communications 130 (2004) 387–390

earth sublattice [11,12]. However, several examples have been found subsequently, where Cu was replaced by a non-magnetic metal, like Zn, and the 3D ordering still could be observed [13]. Nevertheless, to our knowledge, the detailed way that the interaction between the rare earth and the transition metal ions influence the ordering has not been determined to date.

In order to obtain a better understanding of the role of the R–M interaction in the magnetic ordering of the *Pnma* series of green phases, we have doped the low-dimensional Y_2BaCuO_5 with 1, 5, 10 and 25% Dy and studied its magnetic properties by AC susceptibility and neutron diffraction measurements.

2. Experimental

Six samples of $Y_{(2-x)}Dy_xBaCuO_5$ were prepared with different concentrations of Dy, namely, 0, 1, 5, 10, 25 and 100% (calculated based on the molecular weight such that $x = 0.02, 0.10, 0.20, 0.50$ and 2.0). The method used was a solid–solid standard reaction starting from the stoichiometric appropriate quantities of Y_2O_3, CuO, $BaCO_3$, and Dy_2O_3. The compounds were ground in an agate mortar, heated to 600 C for 12 h before being left to cool to room temperature. On completion, the sample was pressed into pellets and successively annealed at 900 and 950 C for 24 h, with grinding and repressing between the heating stages. The phases obtained were checked by X-ray diffraction. No impurities could be detected, but the AC susceptibility showed, through a kink in the $\chi'(T)$ curve at 92(1) K, the existence of small quantities of the high T_c superconductor $YBa_2Cu_3O_{7-\delta}$. This was removed by repeatedly annealing at 1000 C for 24 h.

The AC susceptibility measurements were carried out in a LakeShore 7130 AC susceptometer with an excitation field of 1 Oe at a frequency of 825 Hz. Measurements taken at other excitation frequencies displayed the same thermal dependence for the susceptibility. The error in the real part of the susceptibility, χ', was typically of $\approx 3\%$ and the temperature uncertainty was within ± 1 K.

The neutron diffraction experiments were performed on the 1 and 5% Dy samples, on station D20 at the Institut Laue–Langevin (Grenoble). Data were collected at 1.6, 10 and 35 K with shorter scans recorded approximately every 1 K.

3. Results and discussion

Fig. 1 displays the thermal dependence of $\chi'(T)$, the real part of the AC susceptibility, for pure Y_2BaCuO_5 together with its inverse, $\chi'^{-1}(T)$ (inset). The solid line is a Curie–Weiss fit to the experimental data. Fig. 2 shows $\chi'^{-1}(T)$ for the doped compounds at the concentrations indicated.

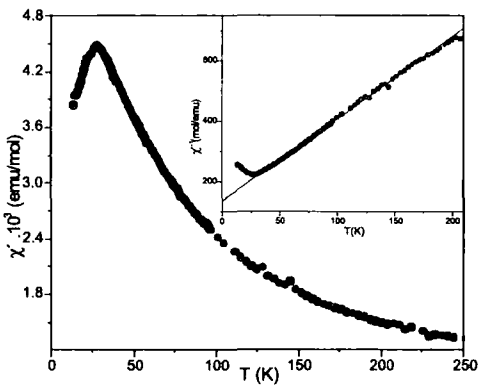

Fig. 1. The thermal dependence of the real part of the AC susceptibility for the pure Y_2BaCuO_5 compound. The inverse susceptibility data fitted to a Curie–Weiss law (solid line) as described in the text is shown inset.

Because in the low temperature region the curve clearly cannot be fitted appropriately to a Curie–Weiss dependence, the fitting was performed from $T = 2T(\chi'_{max})$ for the pure, 1 and 5% Dy doped samples.

All the data of the curves shown in Fig. 2 were also fitted to a Curie–Weiss law and the values of the Curie constant, C, and the Weiss temperature, θ_w, are displayed in Table 1. These values have been plotted versus the dysprosium concentration in Fig. 3. The Curie constant grows linearly with the concentration of dopant, which follows the increase in the number of magnetic atoms per unit volume in the sample. However, the Weiss temperature displays a different dependence in the high and the low concentration regions, indicating that when the concentration varies, the functional relationship of the susceptibility with the exchange integral (J) changes. This suggests that the 3D

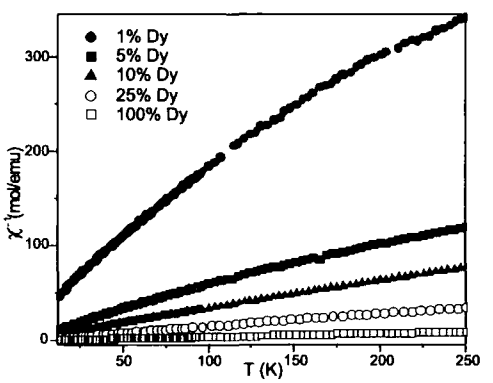

Fig. 2. The thermal dependence of the inverse of the real part of the AC susceptibility for the Dy-doped Y_2BaCuO_5 compounds at the concentrations indicated.

Table 1
Curie constant, C, and Weiss temperature, θ_w, yielded after fitting a Curie–Weiss law to the inverse AC susceptibility data for Dy-doped Y_2BaCuO_5 samples

	1% Dy	5% Dy	10% Dy	25% Dy	100% Dy
C (JK)	0.8(6)	2.2(1)	3.3(9)	7.4(3)	28.0(1)
θ_w (K)	37(1)	29(1)	11(1)	10.1(1)	9(1)

character of the Curie–Weiss law does not seem to reflect the ordering mechanism in the $Y_{(2-x)}Dy_xBaCuO_5$ system.

To take into account the anisotropies shown in the above results, we have simulated the $\chi'(T)$ curve using a planar (2D) Heisenberg model. The fittings were performed using the Levenberg–Marquardt, non-linear, least-squares method, following the high temperatures series expansion described by Lines [14]. The fitting to the pure sample susceptibility shown as the solid line in Fig. 4, yielded a value $J = 29(1)$ K. The 2D character of the magnetic array is confirmed when this value is fed into the expression: $\chi'_{max}T(\chi'_{max})/C$, derived by de Jongh [15]. This test involves the maximum value of the susceptibility and the temperature at which it occurs. The series expansion was also used to simulate the $\chi'(T)$ curve for the 1% Dy doped sample. If variations of 5% were allowed in the resulting series coefficients (to keep them within the convergence values of the series), it was possible to obtain a suitable fitting that yields $J = 16(1)$ K.

It was not possible to repeat this procedure for the other dysprosium concentrations without obtaining a divergence in the series. This indicates that the high temperature series is inappropriate to describe the thermal dependence of the susceptibility for any concentration but the lowest ones.

The neutron diffraction data measured at 1.6 and 35 K for the 1% Dy sample are shown in Fig. 5. The inset shows the detail of the magnetic peak at 16° (8.8 Å, $\lambda = 2.4$ Å), as

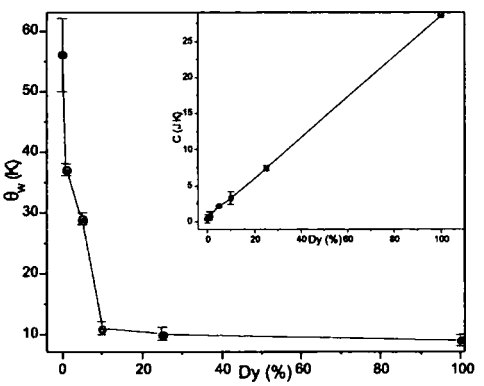

Fig. 3. The dependence of the Curie constant, C, and Weiss temperature, θ_w on Dy-doping concentration, obtained after fitting the data in Fig. 2 and shown in Table 1 to a Curie–Weiss law.

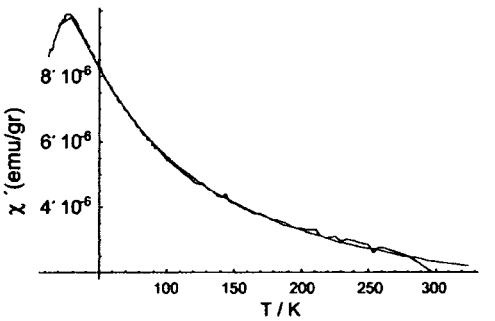

Fig. 4. Thermal dependence of the real part of the AC susceptibility for the pure Y_2BaCuO_5 compound fitted to a series expansion using a planar Heisenberg Hamiltonian.

previously observed in Y_2BaCuO_5 by Chattopadhyay et al. [2]. The intensity of the peak at 16° obtained from the neutron diffraction results as a function of the measurement temperature are shown in Fig. 6 and the inset shows the neutron diffraction data expanded around 16° for the 5% Dy-doped Y_2BaCuO_5 sample at the temperatures indicated. Both samples display an ordering temperature of about 16 K.

These results indicate that doping with only 1% of Dy is enough to change the ordering temperature of the Y_2BaCuO_5 system from 27 to 16 K, although there is no possibility of finding a suitable Hamiltonian to obtain a good fit with a high-temperature series expansion. The fact that only 1% Dy is also enough to change the magnetic dimensionality of the system, indicates that this change cannot be attributed to a rare earth magnetic sublattice, but that the rare earth dopant is influencing the electronic properties of the copper in such a way as to modify its behavior in the superexchange mechanism.

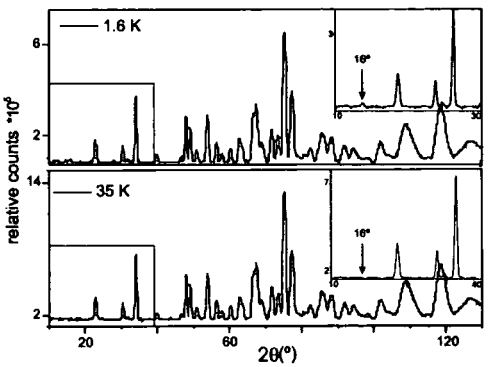

Fig. 5. The neutron diffraction data for the 1% Dy-doped Y_2BaCuO_5 sample, measured at 1.6 and 35 K. An expanded region at low angles shows the behavior of the magnetic peak at 16° in detail (inset).

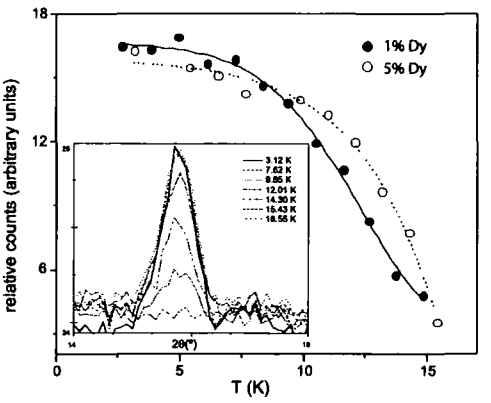

Fig. 6. The dependence on the measurement temperature of the integrated intensity of the magnetic peak at 16° obtained from the neutron diffraction data. The points are joined by a line to guide the eye. The inset shows the expanded neutron diffraction data in the region around this magnetic peak for the 5% Dy-doped Y_2BaCuO_5 sample at the temperatures indicated.

Moreover, it has recently been reported that doping the Y_2BaCuO_5 system with small concentrations of magnetic ions (Er, Fe, or Gd) results in susceptibility curve peaks at roughly the same temperature of 16 K [16]. This agreement between the literature results and the T_N obtained in the present study for the lowest concentrations of Dy, is a further support for the influence of the dopant on the electronic orbitals of Cu, making them change their interactions along the superexchange pathways responsible for the magnetic ordering.

4. Conclusions

We have demonstrated that the thermal dependence of the susceptibility of Y_2BaCuO_5 can be fitted to a planar Hamiltonian and that the high-temperature series coefficients are good fitting parameters, confirming its 2D magnetic ordering.

For the 1% Dy doped sample, the same development could be used and the neutron diffraction data agreed with the Néel temperature, T_N.

The 5% and higher Dy concentrations displayed orderings that could not be fitted in the same way as for the pure Y_2BaCuO_5 and 1% Dy samples.

Applying systematically the Curie–Weiss model to all the Dy concentrations shows a variation of the Weiss temperature, θ_w, which does not agree with the T_N found by neutron diffraction measurements. This also reveals that the Curie–Weiss model does not describe the magnetic behavior of the system even for low Dy concentrations.

The coincidence of the Néel temperatures for different magnetic dopants at about 16 K evidences that the existence of a rare earth ion, even in small concentrations, modifies the electronic structure of the copper ions.

Acknowledgements

The authors would like to acknowledge Clemens Ritter of the Institut Laue–Langevin for his assistance with the neutron data and EPSRC for funding for ALT. RCM is member of the 'Carrera del Investigador Científico,' CONICET, Argentina. LAB thanks the 'Fundación Rocca', Techint, Argentina, for financial support. Partial economic support by grant *CONICET PIP 2853/01* is acknowledged.

References

[1] R.H. Buttner, E.N. Maslen, Acta Cryst. B 49 (1993) 62.
[2] T. Chattopadhyay, P.J. Brown, U. Köbler, M. Wilhelm, Europhys. Lett. 8 (1989) 685.
[3] O.D. Kolotii, V.A. Blinkin, Soy. Phys. Solid State 34 (1992) 774.
[4] I.V. Golosovsky, P. Böni, P. Fischer, Solid State Commun. 87 (1993) 1035.
[5] E.W. Ong, B.L. Ramakrishna, Z. Iqbal, Solid State Commun. 66 (1988) 171.
[6] R. Sáez-Puche, J. Hernández-Velasco, Adv. Mater. Res. 1 (1994) 65.
[7] J.F. DiTusa, G. Aeppli, S.W. Cheong, J.H. Park, C. Broholm, C.T. Chen, Phys. Rev. Lett. 73 (1994) 1857.
[8] R. Sáez-Puche, J.M. Martín-Llorente, J.M. Coronado, J. Less-Common Met. 175 (1991) 131.
[9] R. Sáez-Puche, J.M. Coronado, C.L. Otero-Díaz, J.M. Martin-Llorente, J. Solid State Chem. 93 (1991) 461.
[10] A. Salinas-Sánchez, R. Sáez-Puche, M.A. Alario-Franco, Solid State Commun. 78 (1991) 112.
[11] R. Burriel, M. Castro, C. Piqué, A. Salinas-Sánchez, R. Sáez-Puche, J. Magn. Magn. Mater. 104 (1992) 627.
[12] J. Hernández-Velasco, A. Salinas, F. Fernández, R. Sáez-Puche, J. Alloys Compd. 203 (1994) 15.
[13] G.F. Goya, R.C. Mercader, L.B. Steren, R.D. Sánchez, M.T. Causa, M. Tovar, J. Phys.: Condens. Matter 8 (1996) 4529.
[14] M.E. Lines, J. Phys. Chem. Solids 31 (1979) 101.
[15] L.J. de Jongh, Magnetic Properties of Transition Metal Compounds, Kluwer Academic Publishers, Amsterdam, 1990, p. 1.
[16] M.N. Popova, E. Antic-Fidancev, P. Porcher, J. Solid State Chem. 162 (2001) 42.

C.5 Boron Compounds Containing Ar, Ar′ & Ar″ Ligands

FULL PAPER

Dalton
www.rsc.org/dalton

Synthesis and characterisation of some new boron compounds containing the 2,4,6-$(CF_3)_3C_6H_2$ (fluoromes = Ar), 2,6-$(CF_3)_2C_6H_3$ (fluoroxyl = Ar′), or 2,4-$(CF_3)_2C_6H_3$ (Ar″) ligands†

Stéphanie M. Cornet, Keith B. Dillon,* Christopher D. Entwistle, Mark A. Fox,* Andrés E. Goeta, Helen P. Goodwin, Todd B. Marder and Amber L. Thompson
Chemistry Department, University of Durham, South Road, Durham, UK DH1 3LE. E-mail: k.b.dillon@durham.ac.uk

Received 14th August 2003, Accepted 4th September 2003
First published as an Advance Article on the web 26th September 2003

Several new boron compounds containing the 2,4,6-$(CF_3)_3C_6H_2$ (fluoromes = Ar), 2,6-$(CF_3)_2C_6H_3$ (fluoroxyl = Ar′) or 2,4-$(CF_3)_2C_6H_3$ (Ar″) ligands have been synthesised from reactions of ArLi, Ar′Li or Ar″Li with BCl_3, and characterised by ^{19}F and ^{11}B NMR spectroscopy. Chlorine/fluorine exchanges are evident in these reactions. The crystal and molecular structures of Ar_2BF, Ar''_3B, $Ar_2B(OH)$, $Ar'B(OH)_2$ and Mes_2BF (Mes = 2,4,6-$Me_3C_6H_2$) have been determined by single crystal X-ray diffraction. Ar''_3B represents the first example of a compound containing three Ar″ ligands to be structurally characterised. Molecular geometries and GIAO-NMR shifts for several new boron compounds have been calculated at the HF/6-31G* level of theory, and compared with the available experimental results.

Introduction

Although the chemistry of 2,4,6-$(CF_3)_3C_6H_2$ (fluoromes = Ar), 2,6-$(CF_3)_2C_6H_3$ (fluoroxyl = Ar′) and 2,4-$(CF_3)_2C_6H_3$ (Ar″) has been well-developed over the last 15 years,[1-6] little has been published about the ability of these ligands to stabilise group 13 elements. Schluter *et al.* described the syntheses of indium and gallium derivatives containing the 2,4,6-$(CF_3)_3C_6H_2$ (Ar) ligand.[6,7] Bardaji *et al.* reported the formation of a thallium derivative, Ar_3Tl.[8] No syntheses of aluminium derivatives of these ligands have been reported to date.

However, the most studied group 13 element involving the ligands Ar, Ar′ or Ar″ is boron. A preliminary conference report mentioned the formation of $ArBCl_2$ **7** and Ar_2BCl **1** from reaction of ArLi with BCl_3, and the occurrence of Cl/F exchange.[2] Ishihara *et al.* explored the arylboronic acid $ArB(OH)_2$ **12** as a catalyst for amidination of carboxylic acids, and the acid $Ar''B(OH)_2$ **21** as a catalyst precursor in the asymmetric allylation of aldehydes with allyltrimethylsilanes.[9,10] Gibson *et al.* reported the preparation of Ar_2BCl **1** from the reaction of ArLi with boron trichloride, and its hydrolysis to give the boronic acid $Ar_2B(OH)$ **2**, as shown in Scheme 1.[11] A lithium complex of type $[LiOBAr_2]$ **3** and a molybdenum complex **4** were synthesised from this acid **2**. The synthesis of Ar_2BN_3 **5** from Ar_2BCl and Me_3SiN_3 was described by Fraenk *et al.*, and an X-ray structure of the partially hydrolysed product, a 1 : 1 $Ar_2BN_3 \cdot Ar_2B(OH)$ complex **6**, was obtained.[12]

Here we report in detail the separate reactions of ArLi and an Ar′Li/Ar″Li mixture with BCl_3. The numerous boron species formed have been characterised by ^{19}F and ^{11}B NMR solution-state spectroscopy. These reactions clearly involve intriguing fluorine/chlorine exchanges. We show that compound Ar_2BCl **1**, reported as the major product[11,12] from the reaction of ArLi and BCl_3, is in fact the boron–fluorine compound Ar_2BF **8**. This has been confirmed by single crystal X-ray diffraction. The molecular structure of the known[13] dimesitylfluoroborane Mes_2BF **22** (Mes = 2,4,6-$Me_3C_6H_2$) has been similarly ascertained, to compare with that of **8**. The structures of $Ar_2B(OH)$ **2**, Ar''_3B **16** and $Ar'B(OH)_2$ **17** have also been determined by low-temperature X-ray crystallography. In addition, molecular geometries and GIAO-NMR shifts for several boron compounds have been calculated at the HF/6-31G* level of theory, and compared with the experimental results, where available.

Results and discussion

Synthesis and solution-state NMR spectroscopy

Slow addition of ArLi to a $BCl_3 \cdot OEt_2$ solution in diethyl ether, keeping the boron reagent in excess (Scheme 2), gave rise to a mixture of $ArBCl_2$ **7** and Ar_2BF **8**, identified from their ^{19}F and ^{11}B NMR spectroscopic data (Table 1). Ar_2BF **8** was isolated and fully characterised by X-ray crystallography. In addition, boron trihalide–diethyl etherate adducts were observed in solution ($BFCl_2 \cdot OEt_2$ **9**, $BF_2Cl \cdot OEt_2$ **10** and $BF_3 \cdot OEt_2$ **11**, Table 1). Their NMR data are very similar to literature results.[14]

When the reaction was carried out by addition of $BCl_3 \cdot OEt_2$ to excess ArLi, the products observed were $ArBF_2 \cdot OEt_2$ **13** and Ar_2BF **8** (Scheme 3). ^{19}F and ^{11}B NMR data for **13** are included in Table 1. Adducts **9–11** were not detected in this instance.

Fluorine-19 NMR spectroscopy shows for the three compounds **7**, **8** and **13** the characteristic signals of the Ar ligand: a resonance at around −57 ppm for the *ortho*-CF_3 groups, and a singlet at about −64 ppm corresponding to the *para*-CF_3 groups. (Table 1) The couplings in the ^{19}F NMR spectra of a triplet (−56.2 ppm, $^5J_{F-F}$ 15.4 Hz) and a doublet (−57.4 ppm, $^5J_{F-F}$ 14.3 Hz) for $ArBF_2 \cdot OEt_2$ **13** and Ar_2BF **8**, respectively arise from the fluorines attached to the boron atoms. The latter signal has been confirmed as a doublet by recording the ^{19}F spectrum at two frequencies (188.18 and 376.35 MHz). In both sets of ^{19}F NMR data reported in the literature[11,12] for the incorrectly characterised compound **1**, the two peaks assigned to the *ortho*-CF_3 groups are in fact a doublet, and this compound is really Ar_2BF **8**.

For the diaryl compound **8**, a weak broad multiplet (arising from both spin–spin coupling and the quadrupolar nature of boron) is observed at −9.1 ppm, assigned to the boron-bound fluorine. A similar value of −14.5 ppm is found for the related dimesitylfluoroborane **22**. The ^{19}F signal for the fluorines bound to boron in $ArBF_2 \cdot OEt_2$ occurs at −145.9 ppm, at significantly lower frequency than those reported for other arylboron difluorides.[15] This difference probably arises from the

† Electronic supplementary information (ESI) available: rotatable 3-D molecular structure diagrams of experimental structures of **2**, **8**, **16**, **17** and **22** and of HF/6-31G* optimised geometries in CHIME format and tables of data for the HF/6-31G* optimized geometries. See http://www.rsc.org/suppdata/dt/b3/b309820f/

DOI: 10.1039/b309820f

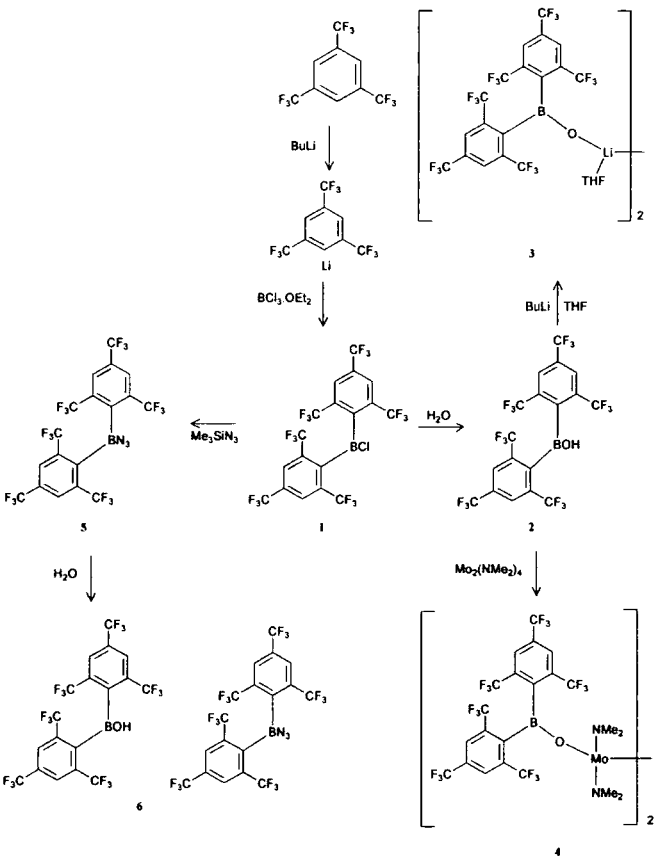

Scheme 1

electron-withdrawing nature of the Ar group, resulting in stronger coordination of Et_2O, as confirmed by the ^{11}B NMR shift of −2.4 ppm. For the similar compound $(C_6F_5)_2BF{\cdot}OEt_2$, a ^{19}F signal at −150.0 ppm for the fluorine bound to boron and an ^{11}B shift of 12.4 ppm have been reported.[16] Very recently, dimethyl[8-(difluoroborolyl)naphthalen-1-yl]amine was found to show clear evidence for formation of an intramolecular 'ate'-complex by donation from N to B of the BF_2 group, with an ^{11}B NMR shift of 10 ppm, and a ^{19}F shift of −149 ppm.[17]

The presence of $ArBF_2{\cdot}OEt_2$ **13** and Ar_2BF **8** (and also the adducts **9–11**) can be explained by chlorine/fluorine exchange while the reaction is taking place. This phenomenon has also been observed in the reaction of ArLi with $SiCl_4$.[4,18] The only source of fluorine atoms in the solution is the CF_3 groups in the ArLi compound. No F/Cl exchange between ArH and BCl_3 was found, even after refluxing for 2 h, indicating that exchange does not take place until the aryl group is attached to Li or B. The driving force for this exchange may arise from the relative bond energies. The sum of a C–F and a B–Cl bond energy term (taken from data for the halides[19]) is −929 kJ mol^{-1}, while that for a B–F and a C–Cl bond energy term is −963 kJ mol^{-1}. It is thus energetically favourable for exchange to occur, by −34 kJ mol^{-1}. A similar explanation has been proposed for the observation of F/Cl exchange in Ar, Ar′ and Ar″ silicon derivatives, but not in their germanium or tin analogues.[18] This cannot be the full explanation, however, since similar thermodynamic considerations would apply to a reaction between ArH and BCl_3, where no exchange was detected. It seems probable that a two-stage process is involved. Coordination of the aromatic group to boron brings at least one fluorine from a CF_3 group into close proximity to B, as noted in the crystal structures described below, thus facilitating an intramolecular exchange between F on C and Cl on B. This exchange would generate a species with a $-CF_2Cl$ group in the *ortho*-position of the aromatic moiety, which is not observed in the isolated product. An intermolecular exchange is now possible, however, between Ar_2BCl and the intramolecular exchange product, similar to that seen between $BCl_3{\cdot}OEt_2$ and $BF_3{\cdot}OEt_2$, which is known to be facile,[14] thus allowing the formation of Ar_2BF.

The known[11,12] boronic acid $Ar_2B(OH)$ **2** was obtained by slow hydrolysis of Ar_2BF **8**. The structure of the hydroxy-compound **2** was ascertained by single-crystal X-ray diffrac-

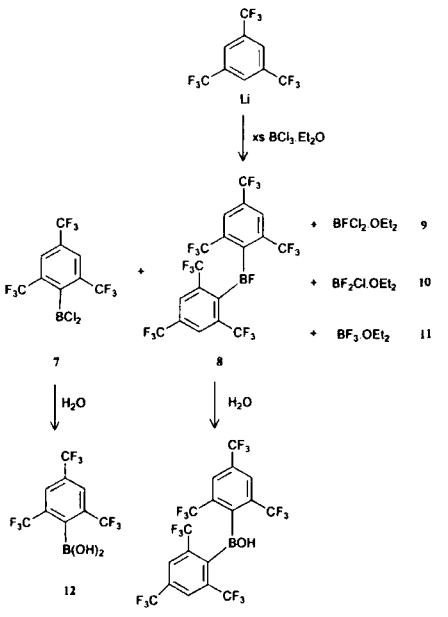

Scheme 2

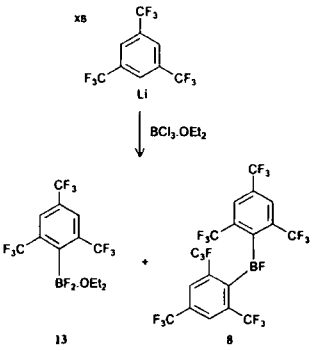

Scheme 3

tion. Facile hydrolysis of $ArBCl_2$ **7** to $ArB(OH)_2$ **12** was observed. ^{19}F and ^{11}B NMR data for these Ar derivatives are included in Table 1. The ^{11}B resonance becomes more shielded on replacing an aryl group with a chlorine atom, and even more so with hydroxy or fluorine substituents, due to increasing π back donation into the vacant orbital on the three-coordinate boron atom.[20]

Reaction of Ar′Li/Ar″Li with BCl_3. A solution containing a mixture of Ar′Li/Ar″Li, obtained from lithiation of 1,3-bis-(trifluoromethyl)benzene Ar′H, was added to excess of a BCl_3 solution in diethyl ether. The ^{19}F and ^{11}B NMR spectra (Table 1) indicated new compounds in solution $Ar'BCl_2$ **14** and Ar'_2BF **15**, identified by comparison with the closely related

Table 1 Experimental and computed fluorine and boron NMR data (ppm) for boron compounds in this study

		$\delta(^{19}F)$	$\delta(^{19}F)$ (calc.)[a,b]	$\delta(^{11}B)$	$\delta(^{11}B)$ (calc.)[a]
Ar_2BOH	**2**	−56.2 (s, 12F, *o*-CF_3), −63.8 (s, 6F, *p*-CF_3)	−79 (*o*-CF_3), −86 (*p*-CF_3)	44.8	40.7
$ArBCl_2$	**7**	−56.4 (s, 6F, *o*-CF_3), −64.0 (s, 3F, *p*-CF_3)	−80 (*o*-CF_3), −85 (*p*-CF_3)	56.8	59.1
Ar_2BF	**8**	−57.4 (d, $^5J_{F-F}$ 14.3 Hz, 12F, *o*-CF_3), −64.0 (s, 6F, *p*-CF_3), −9.1 (m, 1F, BF)	−78 (*o*-CF_3), −86 (*p*-CF_3), −21 (BF)	46.6	43.6
BCl_2·OEt_2				10.7	16.8
$BFCl_2$·OEt_2	**9**	−114.3 (q, $^1J_{B-F}$ 57.6 Hz)	−118	7.9 (d, $^1J_{B-F}$ 58.1 Hz)	10.8
BF_2Cl·OEt_2	**10**	−128.4 (q, $^1J_{B-F}$ 30.0 Hz)	−134	3.9 (t, $^1J_{B-F}$ 29.0 Hz)	4.4
BF_3·OEt_2	**11**	−151.2 (s)	−157	0	−0.4
$ArB(OH)_2$	**12**	−56.6 (s, *o*-CF_3), −63.8 (s, *p*-CF_3)	−83 (*o*-CF_3), −85 (*p*-CF_3),	26.0	26.1
$ArBF_2$·OEt_2	**13**	−56.2 (t, $^5J_{F-F}$ 15.4 Hz, 6F, *o*-CF_3), −63.8 (s, 3F, *p*-CF_3), −145.9 (m, 2F, BF)	−81 (*o*-CF_3), −85 (*p*-CF_3), −144 (BF)	−2.4	5.3
$Ar'BCl_2$	**14**	−56.9 (s)	−77	57.5	59.3
Ar'_2BF	**15**	−57.2 (d, $^5J_{F-F}$ 14.7 Hz, 6F, CF_3), −12.1 (m, 1F, BF)	−79 (*o*-CF_3), −23 (BF)	46.1	44.1
Ar''_3B	**16**	−56.7 (s, 9F, *o*-CF_3), −63.9 (s, 9F, *p*-CF_3)	−77/−79 (*o*-CF_3), −88/−86 (*p*-CF_3)	73.6	68.1/67.2
$Ar'B(OH)_2$	**17**	−56.8	−83	26.7	26.4
Ar'_2BF·OH_2	**18**	−58.8 (d, $^5J_{F-F}$ 22.5 Hz, 6F, CF_3), −189.9 (m, 1F, BF)	−78 (*o*-CF_3), −145 (BF)	5.7	13.0
Ar'_2BOH	**19**	−56.3	−79	45.1	41.2
Ar'_2BF·OEt_2	**20**	−58.4 (d, $^5J_{F-F}$ 24.6 Hz, 6F, *o*-CF_3), −63.2 (s, 6F, *p*-CF_3), −200.6 (m, 1F, BF)	−81 (*o*-CF_3), −85 (*p*-CF_3), −153 (BF)	8.2	17.3
Mes_2BF	**22**	−14.5	−30	53.0	49.1

[a] At the GIAO-HF/6-31G*//HF/6-31G* level. [b] The computed fluorine shifts are averaged where applicable. [c] From conformation B/conformation A of optimised geometries, respectively.

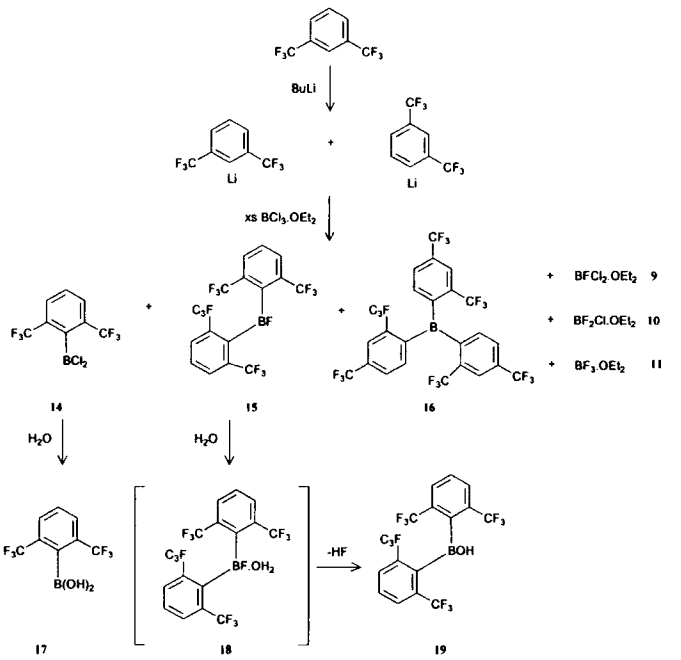

Scheme 4

compounds $ArBCl_2$ **7** and Ar_2BF **8**, respectively. Another new compound Ar''_3B **16** and the known species $BFCl_2{\cdot}OEt_2$ **9**, $BF_2Cl{\cdot}OEt_2$ **10** and $BF_3{\cdot}OEt_2$ **11** (Table 1) were also observed (Scheme 4). The new compounds **14–16** were separated by distillation under reduced pressure.

With an excess of Ar′Li/Ar″Li, products **14**, **15** and **16** were again identified in solution, together with the adduct $Ar''_2BF{\cdot}OEt_2$ **20** (Scheme 5, Table 1). The halogen-exchanged derivatives of $BCl_3{\cdot}OEt_2$ were not detected. Hydrolysis of $Ar'BCl_2$ **14** in air gave rise to the formation of $Ar'B(OH)_2$ **17** crystals, which were studied by single-crystal X-ray diffraction. Hydrolysis of Ar'_2BF with H_2O in ether led eventually to $Ar'_2B(OH)$ **19**, via an intermediate **18** retaining a B–F bond according to the NMR spectra. Comparison of the ^{19}F and ^{11}B NMR shifts with theoretical calculations, as discussed below, suggests that this intermediate **18** is probably $Ar'_2BF{\cdot}(OH_2)$, although the anionic species $[Ar'_2BF(OH)]^-$ cannot be entirely discounted on the basis of the results.

The ^{19}F NMR spectrum of Ar''_3B **16** consisted of a singlet at −56.6 ppm (9F, *o*-CF_3) and a singlet at −63.8 ppm (9F, *p*-CF_3) ppm. In order to investigate the rotation of the ring with respect to the B–C bond, ^{19}F NMR spectra of Ar''_3B were recorded in toluene-d_8 between 90 and −80 °C (Fig. 1). No changes were observed until −40 °C, where a new set of signals started to appear. The spectrum at −80 °C showed signals corresponding to two conformations of Ar''_3B (Fig. 2), *i.e.* two singlets at −56.6 and −63.8 ppm, and two singlets at −56.2 and −62.2 ppm, in an overall 5.5 : 1 ratio. At this temperature, by comparison with the variable temperature ^{19}F NMR results for $(2\text{-}CF_3C_6H_3)_3B$,[21] where two signals were only detected at −100 °C in a 0.7 : 1 ratio, it is clear that both conformations **A** and **B** exist in solution, although one of these is dominant. The crystal structure

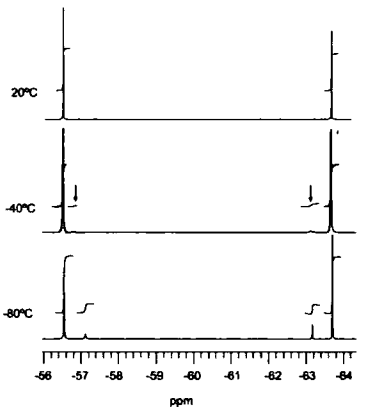

Fig. 1 Variable-temperature ^{19}F NMR spectra of Ar''_3B **16**

determined at −153 °C, discussed in more detail below, shows that the molecule is in conformation **B**, unlike $(2\text{-}CF_3C_6H_4)_3B$ which is in conformation **A** from single-crystal X-ray diffraction at −80 °C.[21] It is thus probable that **B** is the preferred conformation of **16** at −80 °C. Theoretical calculations described below indicate that there is only a very small energy difference between conformations **A** and **B**, with **B** being slightly more stable in each case, thus providing a reasonable

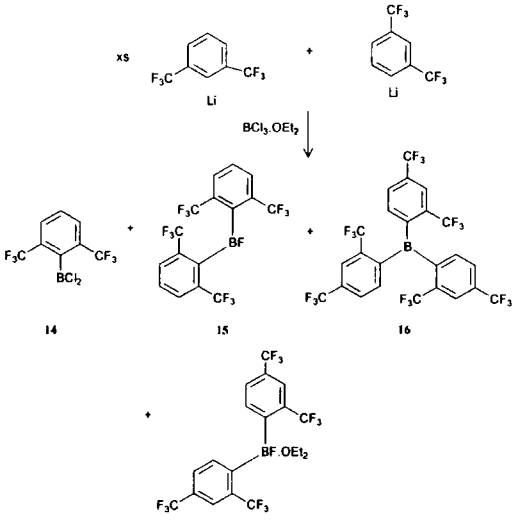

Scheme 5

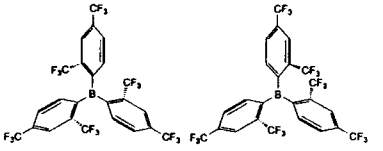

Fig. 2 Different conformations for Ar″$_3$B 16

explanation for the low-temperature results. Unfortunately, because of solvent limitations, we were unable to extend these studies to lower temperatures, where further restriction of rotation would be expected, giving rise to two sets of signals in a 2 : 1 ratio from conformation **B**.

X-Ray crystallography

Single-crystal X-ray diffraction studies were carried out at 120 K for compounds $Ar_2B(OH)$ **2**, Ar_2BF **8**, Ar″$_3$B **16**, and Mes_2BF **22**, and at 100 K for Ar′$B(OH)_2$ **17**. Their molecular structures are illustrated sequentially in Figs. 3–7, respectively. Selected bond distances and angles are listed in Table 2. Rotational disorder was found for the *para*-CF_3 group in Ar_2BF

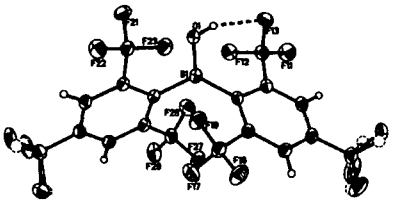

Fig. 3 Molecular geometry of $Ar_2B(OH)$ **2** (atomic displacement ellipsoids in this and the following Figures are drawn at the 50% probability level).

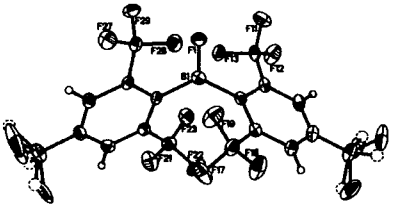

Fig. 4 Molecular geometry of Ar_2BF **8**.

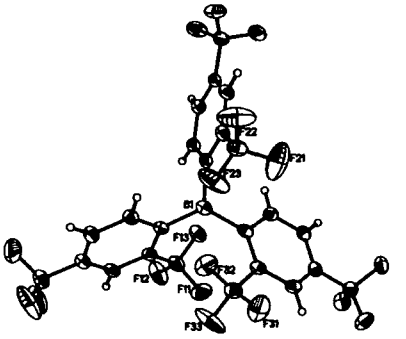

Fig. 5 Molecular geometry of Ar″$_3$B **16**.

and $Ar_2B(OH)$, as is often observed in compounds containing these ligands.[3,5,18,22]

The structure of $Ar_2B(OH)$ **2** at 200 K has been determined previously by Fraenk *et al* in the 1 : 1 complex of Ar_2BN_3 and Ar_2BOH **6**.[12] Their results are very similar to those obtained at 120 K for **2** in the present work. The O(1)–B(1)–C(21) angle is 112.65(13)° at 120 K, whereas O(1)–B(1)–C(11) is 121.62(14)°.

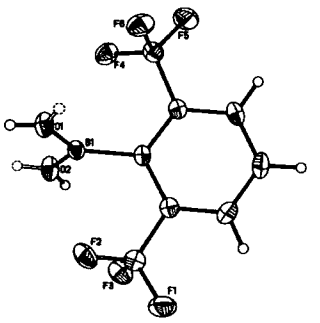

Fig. 6 Molecular geometry of Ar′B(OH)$_2$ **17**. The hydrogens of the –OH groups are disordered over two positions with *ca.* 50% occupancy.

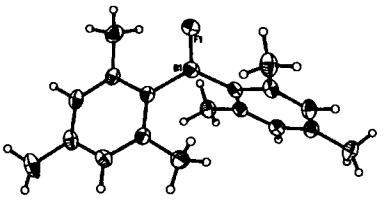

Fig. 7 Molecular geometry of Mes$_2$BF **22**

An intramolecular OH ··· F bridge is found between the hydrogen atom of the OH group and one fluorine atom of a CF_3 group (Fig. 3). The OH distance is 0.78(2) Å, while the H(1) ··· F(13) and H(1) ··· F(12) distances are 2.184(24) and 2.731(23) Å, respectively. The B–C distances in **2** and **8** are similar to those in the 1 : 1 $Ar_2BN_3{\cdot}Ar_2B(OH)$ complex (1.620(6) and 1.599(7) Å for the two Ar_2B components).[13] C–B–C angles in **2** and **8** (125.73(13) and 128.5(2)°, respectively) are similar to that found in $Mes_2B(OH)$,[23] and larger than the ones of 123.1(2)° in 2,6-$(F_2C_6H_3)_2BCl$[12] and of 123.3(4)° in $(C_6F_5)_2BCl$.[24] This is due to the presence of a bulky group such as CF_3 or CH_3 in the *ortho* position.

Comparison between Ar_2BF **8** (Fig. 4) and Mes_2BF **22** (Fig. 7) shows that the C–B–C angles are similar, reflecting similar steric bulk for Ar and Mes groups. The B–C distances, however, are approximately 0.02 Å longer and the B–F distance is *ca.* 0.03 Å shorter in Ar_2BF than the corresponding bond lengths in Mes_2BF. This is presumably due to reduction of the electron density on the boron atom by the electron-withdrawing Ar groups, thus increasing the π back-donation from the fluorine atom.

A compound containing three Ar″ ligands, Ar″$_3$B **16**, has been structurally characterised for the first time (Fig. 5). Like (2-$CF_3C_6H_4)_3B$,[21] the triaryl compound Ar″$_3$B exists in a propeller-like geometry, with the three aryl groups twisted out of the plane defined by the three carbons attached to boron. The three rings are twisted by 46.7, 53.7 and 68.9° towards the reference plane made by the three carbons bonded to the boron atom, C(11), C(21) and C(31). These angles are larger than those observed in triphenylborane (28.3°)[25] and [(3,5-$CF_3)_2C_6H_3]_3B$ (33.3–38.3°),[26] but are similar to those in (2-$CF_3C_6H_4)_3B$ (40°–55°)[21] and trimesitylborane Mes_3B (40–60°),[27] reflecting the steric size of the *ortho*-substituents. The molecular structure of **16** (Fig. 5) shows that it is in the more stable conformation **B** (Fig. 2), unlike (2-$CF_3C_6H_4)_3B$ which has conformation **A**. The C–B–C angles in **16** are 117.6(2), 117.0(2) and 124.7(2)°, respectively, for C(11)–B(1)–C(21), C(21)–B(1)–C(31) and

Table 2 Selected bond lengths (Å) and angles (°) for compounds determined by X-ray crystallography

2		**8**		**16**		**17**		**22**	
B(1)–C(11)	1.618(2)	B(1)–C(11)	1.594(4)	B(1)–C(11)	1.582(4)	B(1)–C(1)	1.597(2)	B(1)–C(11)	1.570(2)
B(1)–C(21)	1.608(2)	B(1)–C(21)	1.588(4)	B(1)–C(21)	1.582(4)	B(1)–O(1)	1.355(2)	B(1)–C(21)	1.568(2)
B(1)–O(1)	1.340(2)	B(1)–F(1)	1.313(3)	B(1)–C(31)	1.582(4)	B(1)–O(2)	1.360(2)	B(1)–F(1)	1.339(2)
C(11)–B(1)–C(21)	125.73(13)	C(11)–B(1)–C(21)	128.5(2)	C(11)–B(1)–C(21)	117.6(2)	C(1)–B(1)–O(1)	120.82(14)	C(11)–B(1)–C(21)	125.39(14)
O(1)–B(1)–C(11)	112.65(13)	F(1)–B(1)–C(11)	115.5(2)	C(11)–B(1)–C(31)	124.7(2)	C(1)–B(1)–O(2)	121.03(14)	F(1)–B(1)–C(11)	117.79(14)
O(1)–B(1)–C(21)	121.62(14)	F(1)–B(1)–C(21)	116.0(2)	C(21)–B(1)–C(31)	117.0(2)	O(1)–B(1)–O(2)	118.15(14)	F(1)–B(1)–C(21)	116.82(14)

Table 3 Short B ··· F contacts (Å)

	$Ar_2B(OH)$ 2	Ar_2BF 8	Ar''_3B 16	$Ar'B(OH)_2$ 17
B–F	2.829–2.914	2.763–2.796	2.800–2.815	2.622–2.634
No. of contacts	4	4	3	2
No. of *ortho*-fluorines	12	12	9	6

C(1)–B(1)–C(31), a distorted trigonal planar geometry of the boron atom. The bond angles at C(11), C(21), and C(31) reveal a significant bending deformation, for example C(12)–C(11)–B(1) 126.7(2)° and C(16)–C(11)–B(1) 116.8(2)°. These significant values are due to close packing between two molecules of **16** in the crystal. There is no such distortion in the reported X-ray structure of $(2\text{-}CF_3C_6H_4)_3B$.[21]

The B–O distances in $Ar'B(OH)_2$ **17** (Fig. 6) are similar to those in the crystal structure of $2,6\text{-}F_2C_6H_3B(OH)_2$, with values of 1.355(2) and 1.360(2) Å in **17**, 1.341(4) and 1.351(4) Å in the difluoro compound,[27] and 1.34(3) and 1.35(3) Å in $3,5\text{-}(CF_3)_2C_6H_3B(OH)_2$, H-bonded in a complex with a carboxylate anion.[28] The angles around boron are close to trigonal in both $Ar'B(OH)_2$, ranging from 118.15(14) to 121.03(14)°, and $2,6\text{-}F_2C_6H_3B(OH)_2$ (118.1(2) to 122.5(2)°),[27] showing that the presence of just one Ar′ group has little effect on the stereochemistry. The B–C distance of 1.597(2) Å in $Ar'B(OH)_2$ **17** is slightly longer than the B–C bond length of 1.578(4) Å reported in $2,6\text{-}F_2C_6H_3B(OH)_2$,[27] and that of 1.56(2) Å in the $3,5\text{-}(CF_3)_2C_6H_3B(OH)_2$ complex.[28] The hydrogens of the –OH groups appear to be disordered over two positions (Fig. 6), with approximately 50% occupancy of each site. Intermolecular hydrogen bonding in the crystal of $Ar'B(OH)_2$ **17** implies that, if a particular hydrogen occupies one such position, this fixes the positions of the three hydroxyl hydrogens forming a repeating unit, as shown by the dotted lines in Fig. 8. While the pattern is not necessarily the same in the next dotted rectangle, there will be a preference for the same orientation, resulting from electrostatics, and giving a symmetrical repeating unit. The O(1) ··· H ··· O(1′), O(2) ··· H ··· O(2′) and O(1) ··· H ··· O(2) (intermolecular) distances are 2.7508(25), 2.7532(25) and 2.6801(16) Å, respectively. Similar hydrogen bonding has been reported for the complex containing the boronic acid $3,5\text{-}(CF_3)_2C_6H_3B(OH)_2$ and a carboxylate anion, with O ··· H ··· O distances of 2.67(2) and 2.64(2) Å.[28]

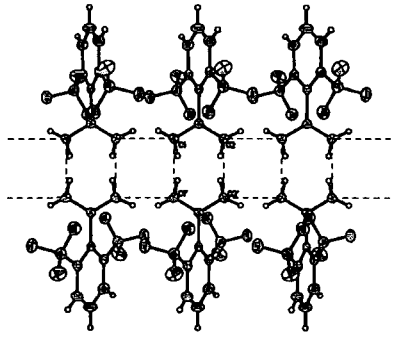

Fig. 8 Repeating pattern *via* hydrogen bonds in crystal of $Ar'B(OH)_2$ **17**

As often described for compounds containing Ar, Ar′ or Ar″ groups,[10,21,22] short contacts between the central atom and some fluorine atoms of the *o*-CF_3 substituents are apparent (Table 3). These compare well with B ··· F contact distances of 2.845(3), 2.816(4) and 2.763(3) Å in $(2\text{-}CF_3C_6H_4)_3B$, even with different conformations of the compounds.[21] The number of contacts depends on the number of trifluoromethyl groups in the *ortho* position. B ··· F contacts are shorter in compounds containing only one aryl ring (Table 3). In $Ar_2B(OH)$ the range of values is somewhat broader, probably because of the F ··· H interaction mentioned above.

Computations

A series of *ab initio* calculations has been performed to provide optimised gas-phase structures and NMR shift data for the boron compounds made here. Use of the computationally intensive MP2/6-31G* level of theory gave excellent agreements between observed and optimised geometries for Mes_2BF (see Table S1, ESI† for details). Removal of the *para*-methyl group did not significantly affect the geometry around the boron atom or the calculated boron shifts. The lower level of theory, HF/6-31G*, gave reasonable agreements between observed and computational data for Mes_2BF. Since there is little justification in using the MP2/6-31G* level of theory here, calculations were carried out at the HF/6-31G* level of theory for the compounds described. Selected parameters for the optimised and experimental geometries of the compounds structurally characterised in this work are also listed in the ESI. The agreement between computed and optimised geometries is very good. As shown from X-ray crystallography, short B ··· F contacts are found. The optimised geometry of $Ar'B(OH)_2$ also shows the presence of an intramolecular F ··· H bridge.

Both conformations (**A** and **B**) of Ar''_3B were optimised at HF/6-31G*, with **B** found to be lower in energy than **A** by *ca.* 4 kJ mol^{-1}. This energy difference is substantially less than 15.5 kJ mol^{-1} reported[21] for the closely related $(2\text{-}CF_3C_6H_4)_3B$ using the AM1 level of theory. The latter borane – a model for Ar''_3B – was computed at the HF/6-31G* level of theory here to give more realistic energy values. Conformation **B** is 2 kJ mol^{-1} lower in energy than **A** in $(2\text{-}CF_3C_6H_4)_3B$ and the rotational barrier between **A** and **B** is 28.9 kJ mol^{-1} with respect to **B**. The rotational barrier between the two enantiomers of **B** is 16.8 kJ mol^{-1}. All these calculated values at the *ab initio* level are in good agreement with the observed ^{19}F NMR data at low temperatures for $(2\text{-}CF_3C_6H_4)_3B$ and Ar''_3B. It is therefore not surprising to find either conformation (**A** or **B**) in the solid-state for $(2\text{-}CF_3C_6H_4)_3B$ and Ar''_3B, considering the very similar energies computed for both conformations.

Since good agreement is found between computed and experimental geometries, geometries for compounds not structurally determined in this work were also optimised at the HF/6-31G* level of theory. The boron environments in optimised geometries for $ArB(OH)_2$, Ar'_2BF and Ar'_2BOH are virtually identical to those in $Ar'B(OH)_2$, Ar_2BF and Ar_2BOH, respectively, showing the *para*-CF_3 group to have little effect on the environment surrounding the boron atom. The neutral chlorides, $ArBCl_2$ and $Ar'BCl_2$, have similar parameters to those found in $ArB(OH)_2$ and $Ar'B(OH)_2$.

Selected parameters from optimised geometries of the adducts, $ArBF_2{\cdot}OEt_2$, $Ar'_2BF{\cdot}OH_2$, $Ar''_2BF{\cdot}OEt_2$ and $BF_{3-x}Cl_x{\cdot}OEt_2$ are shown in the ESI.† The adducts all have four-coordinate boron with similar boron environments. There are only two reported examples of arylborane ether adducts structurally characteried, namely $Ph_3B{\cdot}THF$[29] and $Ph_2BCl{\cdot}THF$.[30] Since they are four-coordinate boron compounds, the accuracy of the HF/6-31G* level of theory was examined by comparing the optimised geometry with the X-ray data for $Ph_2BCl{\cdot}THF$. It is clear from the results that the agreement is poor with respect

to the B–O bond length. It is known that the geometries of boron adducts in the gas phase differ considerably from geometries in the solid state, particularly for the bond distances between the boron atom and the Lewis base.[31] The optimised geometries for the adducts made here are therefore expected in the gas-phase and in solution. A different level of theory such as the self-consistent reaction field would be needed for probable solid-state geometries of these adducts.[32] Reported optimised geometries of $BF_3{\cdot}OMe_2$ and $BCl_3{\cdot}OMe_2$ at *ab initio* levels are in good agreement with $BF_3{\cdot}OEt_2$ and $BCl_3{\cdot}OEt_2$ geometries here.[33] The B–O bond distances shorten on going from $BF_3{\cdot}OEt_2$, $BF_2Cl{\cdot}OEt_2$, $BFCl_2{\cdot}OEt_2$ to $BCl_3{\cdot}OEt_2$ as expected from the ligand close-packing theory.[34] Fig. 9 shows an optimised geometry for the adduct $ArBF_2{\cdot}OEt_2$ at the HF/6-31G* level of theory.

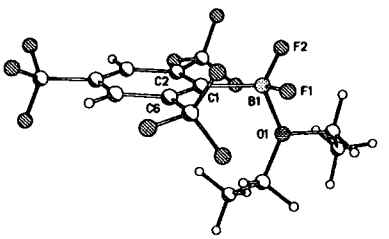

Fig. 9 Optimised molecular geometry for the adduct $ArBF_2{\cdot}OEt_2$ **13**.

Computed boron and fluorine NMR shifts generated from the optimized geometries for all compounds synthesised here are listed in Table 1. These values are in acceptable agreement with observed shifts, apart from the B–F fluorine shifts for $Ar'_2BF{\cdot}OH_2$ and $Ar''_2BF{\cdot}OEt_2$. A related derivative $(C_6F_5)_2BF{\cdot}OEt_2$ was subjected to computations, in order to see whether the presence of two aryl groups in an adduct would give poor computed ^{19}F shifts. The calculated shifts were −149 (*o*-CF), −154 (BF), −170 (*p*-CF), −186 ppm (*m*-CF) for ^{19}F and 13.0 ppm for ^{11}B, in good agreement with reported data (−134 (*o*-CF), −150 (BF), −155 (*p*-CF), −163 ppm (*m*-CF) for ^{19}F and 12.4 ppm for ^{11}B).[16] Selected parameters for the optimized geometry of $(C_6F_5)_2BF{\cdot}OEt_2$ are also shown in Table S2 (ESI†). Possible alternatives to $Ar'_2BF{\cdot}OH_2$ and $Ar''_2BF{\cdot}OEt_2$ such as Ar'_2BFOH^- anion and $Ar''BClF{\cdot}OEt_2$, respectively, were also examined by computations, and neither gave significantly better agreement in the NMR shifts. At present, identification of $Ar'_2BF{\cdot}OH_2$ and $Ar''_2BF{\cdot}OEt_2$, with the four groups attached to boron in these adducts collectively very bulky, is tentative.

Experimental

All manipulations, including NMR sample preparation, were carried out either under an inert atmosphere of dry nitrogen or *in vacuo*, using standard Schlenk procedures or in a glovebox. Chemicals of the best available commercial grades were used, in general without further purification. ^{19}F NMR spectra were recorded on Varian Mercury 200, Varian VXR 400, or Varian Inova 500 Fourier-transform spectrometers at 188.18, 376.35, and 470.26 MHz, respectively. ^{11}B NMR spectra were recorded on the Varian Mercury 300 or Varian Inova 500 spectrometers at 96.22 and 160.35 MHz, respectively. ^1H and ^{13}C NMR spectra were recorded on the Varian VXR 400 instrument at 400 and 100.57 MHz, respectively, for Ar''_3B only. Ambient-temperature NMR spectra were obtained using $CDCl_3$ as solvent for isolated compounds; the NMR spectra of reaction mixtures were recorded in the solvent(s) used for the reaction, with a little $CDCl_3$ added to provide the deuterium lock. Chemical shifts were measured relative to external $CFCl_3$ (^{19}F) or $BF_3{\cdot}Et_2O$ (^{11}B), with the higher frequency direction taken as positive. Mass spectra for isolated samples were recorded on a VG Micromass 7070E instrument under EI conditions at 70 eV and for impure samples on a Fisons VG Trio 1000 mass spectrometer coupled directly to a Hewlett Packard 5890 Series II gas chromatograph (Column: HP-1; 25 m; 0.25 mm I.D.; 0.32 μm film thickness). Mes_2BF was synthesised according to the literature.[13]

Synthesis of $ArBCl_2$ 7 and Ar_2BF 8. A solution of ArLi was prepared by adding BuLi (28 ml, 1.6 M in hexanes, 44.8 mmol) dropwise to a stirred solution of ArH (12.8 g, 45.4 mmol) in 100 ml of Et_2O at −78 °C and leaving the mixture to warm to room temperature for 5 h. Fluorine NMR spectroscopy on a sample of the solution revealed two peaks corresponding to ArLi at −62.6 (*o*-CF_3) and −62.8 (*p*-CF_3) ppm, and a small peak at −63.7 ppm assigned to ArH. To the yellow ArLi solution was added dropwise *via* cannula a BCl_3 solution (100 ml, 1 M in heptane, 100 mmol) in diethyl ether (50 ml) at −78 °C. The reaction mixture was allowed to warm to room temperature for 6 h with stirring, leaving a yellow solution and a white precipitate. The solution was then filtered and solvents were removed *in vacuo*, leaving a yellow oil and a white solid. This mixture was vacuum distilled at 60 °C/0.05 Torr to give a fraction containing $ArBCl_2$ **7** (0.8 g, 5% yield) and the adducts $BF_xCl_{3-x}{\cdot}OEt_2$ (2.6 g). The residue was then sublimed at 95 °C under vacuum to give a white solid identified as Ar_2BF **8** (3.2 g, 24% yield). Crystals of Ar_2BF were obtained by recrystallisation from dichloromethane.

$ArBCl_2$: ^1H NMR: 8.07 (s) ppm. ^{13}C NMR: 134.6 (q, $^2J_{C\text{-}F}$ 35.1 Hz), 132.7 (q, $^2J_{C\text{-}F}$ 32.7 Hz), 125.6 (septet, $^3J_{C\text{-}F}$ 3.0 Hz, CH), 123.0 (q, $^1J_{C\text{-}F}$ 273.8 Hz), 122.7 (q, $^1J_{C\text{-}F}$ 274.2 Hz) ppm. GC-MS: *m/z* 362 (M, calc. for $C_9H_2F_9BCl_2$: 362, with expected pattern at 361–364 from ^{10}B, ^{11}B, ^{35}Cl and ^{37}Cl isotopes), 327 (M − Cl).

Ar_2BF: ^1H NMR: 8.17 (s) ppm. ^{13}C NMR: 137.2 (q, $^2J_{C\text{-}F}$ 38.0 Hz), 134.5 (q, $^2J_{C\text{-}F}$ 34.4 Hz), 134.1 (CB), 126.6 (septet, $^3J_{C\text{-}F}$ 3.0 Hz, CH), 122.8 (q, $^1J_{C\text{-}F}$ 275.2 Hz), 122.3 (q, $^1J_{C\text{-}F}$ 273.0 Hz) ppm. EI-MS: *m/z* – (M, calc. for $C_{18}H_4F_{19}B$ 592), 573 (M–F, pattern at 572–574 from ^{10}B, ^{11}B and ^{13}C), 505 (M − CF_4 + H).

Synthesis of $Ar'BCl_2$ 14, Ar'_2BF 15 and Ar''_3B 16. A solution of Ar′/Ar″Li was generated by adding BuLi (28 ml, 1.6 M in hexanes, 44.8 mmol) dropwise to a stirred solution of Ar′H (10.5 g, 49.1 mmol) in 100 ml of Et_2O at −78 °C and left to warm to room temperature for 4 h. Fluorine NMR spectroscopy on a sample of the solution revealed two peaks corresponding to Ar″Li at −61.9 (*o*-CF_3) and −62.8 (*p*-CF_3) ppm, a peak corresponding to Ar′Li at −62.1 ppm and a small peak at −63.7 ppm assigned to Ar′H. The ^{19}F peak integrals indicate the solution to contain a Ar′Li : Ar″Li ratio of 3 : 4. To the dark brown solution of Ar′/Ar″Li was added dropwise *via* cannula, a solution of BCl_3 (100 ml, 1 M in heptane, 100 mmol) in Et_2O (50 ml) at −78 °C. The reaction mixture was allowed to warm to room temperature for 3 h, leaving a brown solution and a white precipitate. The solution was filtered and the solvents removed *in vacuo*, leaving a brown oil, which was distilled under reduced pressure (0.05 Torr). A fraction containing $Ar'BCl_2$ **14** (1.8 g, 14% yield) and the adducts $BF_xCl_{3-x}{\cdot}OEt_2$ (3.2 g) was collected at 48 °C. A second colourless fraction was collected at 92 °C and identified as Ar'_2BF **15** (0.5 g, 5% yield). The white solid remained in the flask was sublimed under vacuum at 120 °C, affording Ar''_3B **16** as a white crystalline solid (1.6 g, 17% yield). A crystal of Ar''_3B suitable for X-ray study was obtained by recrystallization from hexane.

$Ar'BCl_2$: ^1H NMR: 7.88 (d, J_{HH} 7.8 Hz, 2H), 7.73 (t, J_{HH} 7.8 Hz, 1H) ppm. ^{13}C NMR: 132.7 (q, $^2J_{C\text{-}F}$ 33.0 Hz), 130.8 (s, CH), 129.5 (q, $^3J_{C\text{-}F}$ 2.9 Hz, CH), 123.7 (q, $^1J_{C\text{-}F}$ 272.7 Hz) ppm.

Table 4 Crystal data and structure refinement parameters

	Ar′$_2$B(OH) 2	Ar$_2$BF 8	Ar″$_3$B 16	Ar′B(OH)$_2$ 17	Mes$_2$BF 22
Empirical formula	$C_{18}H_3BF_{18}O$	$C_{18}H_4BF_{19}$	$C_{24}H_9BF_{18}$	$C_8H_7BF_6O_2$	$C_{18}H_{22}BF$
M_r	590.03	592.02	650.12	257.93	268.17
Crystal system	Triclinic	Monoclinic	Triclinic	Orthorhombic	Monoclinic
Space group	$P\bar{1}$	$P2_1/n$	$P\bar{1}$	$P2_12_12$	$P2_1/c$
Crystal size/mm	0.38 × 0.24 × 0.18	0.20 × 0.20 × 0.05	0.50 × 0.20 × 0.10	0.43 × 0.20 × 0.10	0.30 × 0.22 × 0.20
T/K	120(2)	120(2)	120(2)	100(2)	120(2)
a/Å	9.1587(3)	8.9564(6)	10.1795(7)	14.0859(14)	8.2080(5)
b/Å	10.1298(3)	9.4751(6)	11.0533(8)	14.4620(14)	7.8003(5)
c/Å	12.5200(4)	23.6514(15)	11.4719(8)	5.0028(5)	24.0891(16)
α/°	112.5700(10)	90	94.9440(10)	90	90
β/°	99.9530(10)	98.494(1)	108.3620(10)	90	90.3380(10)
γ/°	102.5760(10)	90	94.5490(10)	90	90
V/Å^3	1003.60(5)	1985.1(2)	1212.75(15)	1019.12(17)	1542.27(17)
Z	2	4	2	4	4
D_c/g cm^{-3}	1.953	1.981	1.78	1.681	1.155
μ/mm^{-1}	0.234	0.241	0.200	0.187	0.072
R_{int}	0.0274	0.0736	0.0365	0.0283	0.0388
Observed data [$I > 2\sigma(I)$]	3844	2748	3840	2209	2719
R_1 index [$I > 2\sigma(I)$]	0.0359	0.0469	0.0528	0.0305	0.0528
R_1 index (all data)	0.0447	0.0982	0.0741	0.0333	0.0795
wR_2 index [$I > 2\sigma(I)$]	0.0914	0.0924	0.1255	0.0717	0.1274
wR_2 index (all data)	0.0981	0.1113	0.1362	0.0735	0.1418
Goodness of fit (S)	1.022	1.026	1.057	1.122	1.025
No. of variables	386	381	388	169	269

GC-MS: *m/z* 294 (M, calc. for $C_6H_3F_6BCl_2$ 294), 259 (M − Cl, isotope pattern at 258–261).

Ar′$_2$BF: ^{1}H NMR: 7.97 (d, J_{HH} 8.0 Hz, 2H), 7.78 (t, J_{HH} 8.0 Hz, 1H) ppm. ^{13}C NMR: 133.7 (q, $^2J_{C\text{-}F}$ 34.5 Hz), 131.5 (s, CH), 129.2 (q, $^3J_{C\text{-}F}$ 3.0 Hz, CH), 123.3 (q, $^1J_{C\text{-}F}$ 275.2 Hz) ppm. EI-MS: *m/z* 456 (M, calc. for $C_{16}H_6F_{12}B$ 456), 369 (M–CF_4 + H, isotope pattern at 368–370).

Ar″$_3$B: ^{1}H NMR: 8.00 (s, 1H), 7.80 (d, J_{HH} 7.6 Hz, 1H), 7.41 (d, J_{HH} 7.6 Hz, 1H) ppm. ^{13}C NMR: 143.7 (CB), 135.4 (s, CH), 133.6 (q, $^2J_{C\text{-}F}$ 34.3 Hz), 133.5 (q, $^2J_{C\text{-}F}$ 33.7 Hz), 127.3 (q, $^3J_{C\text{-}F}$ 3.6 Hz, CH) 123.1 (septet, $^3J_{C\text{-}F}$ 3.0 Hz, CH), 123.1 (q, $^1J_{C\text{-}F}$ 274.5 Hz), 122.9 (q, $^1J_{C\text{-}F}$ 273.0 Hz) ppm. EI-MS: *m/z* 650 (M, calc. for $C_{24}H_9F_{18}B$ 650), 631 (M − F, isotope pattern at 630–632), 436 (M − Ar″ − H).

Synthesis of Ar$_2$BOH 2. Distilled water (5 ml) was added dropwise to a stirred solution of Ar$_2$BF (0.5g, 0.85 mmol) in ether (30 ml). The ether layer was separated and dried *in vacuo* to yield a white solid Ar$_2$BOH **2** (0.4 g, 80%). This solid was recrystallized from dichloromethane to yield crystals suitable for X-ray crystallography.

Ar$_2$BOH: ^{1}H NMR: 8.15 (CH, 4H, s), 7.87 (OH, 1H, s) ppm. ^{13}C NMR: 138.5 (CB), 136.8 (q, $^2J_{C\text{-}F}$ 35.2 Hz), 133.4 (q, $^2J_{C\text{-}F}$ 34.4 Hz), 126.6 (septet, $^3J_{C\text{-}F}$ 3.0 Hz, CH), 123.0 (q, $^1J_{C\text{-}F}$ 275.2 Hz), 122.4 (q, $^1J_{C\text{-}F}$ 273.1 Hz) ppm.

Synthesis of Ar′$_2$BOH 19. The method for the synthesis of Ar$_2$BOH was also used to convert Ar′$_2$BF into Ar′$_2$BOH in a similar yield. Fluorine and boron NMR spectra on an aliquot of the ether layer after 30 min stirring revealed an intermediate, presumed to be Ar′$_2$BF·OH$_2$. The NMR data for the intermediate were recorded from a $CDCl_3$ solution of Ar′$_2$BF with a drop of water and two drops of ether added.

Ar′$_2$BOH: ^{1}H NMR: 7.94 (d, J_{HH} 8.0 Hz, 2H), 7.69 (t, J_{HH} 8.0 Hz, 1H) ppm. ^{13}C NMR 132.5 (q, $^2J_{C\text{-}F}$ 34.2 Hz), 130.5 (s, CH), 129.6 (q, $^3J_{C\text{-}F}$ 3.7 Hz, CH), 123.6 (q, $^1J_{C\text{-}F}$ 275.2 Hz) ppm.

Syntheses of Ar′B(OH)$_2$ 17 and ArB(OH)$_2$ 12. A portion of the distilled fraction containing Ar′BCl_2 and the adducts BF_xCl_{3-x}·OEt_2 in ether was left exposed to air. After two days, white crystals were formed and identified by X-ray crystallography as Ar′B(OH)$_2$. A solid was obtained from slow exposure to air of a sample of $ArBCl_2$ and the adducts BF_xCl_{3-x}·OEt_2, and tentatively identified by NMR as ArB(OH)$_2$.

Reaction of BCl_3 with excess ArLi. A solution of ArLi was made by adding BuLi (28 ml, 1.6 M in hexanes, 44.8 mmol) dropwise to a stirred solution of ArH (12.8 g, 45.4 mmol) in 100 ml of Et_2O at −78 °C and left to warm to room temperature overnight. The light brown solution was slowly treated with BCl_3 (6 ml, 1 M in heptane, 6 mmol) at −78 °C, and left to warm to room temperature for 1 h. Fluorine and boron NMR spectra were obtained from a sample of the reaction mixture which showed $ArBF_2$·OEt_2 to be the major product. Ar$_2$BF and a substantial amount of unreacted ArLi were also present. To the reaction mixture was then added a further 6 ml of BCl_3 (1 M in heptane, 6 mmol) at −78 °C. After warming the mixture to room temperature, ^{19}F and ^{11}B NMR data on an aliquot of the solution gave Ar$_2$BF as the major component and $ArBF_2$·OEt_2 as the only other significant compound. On removing the ether and heptane *in vacuo*, the residue contained a yellow oil and a white solid. NMR data on the yellow oil revealed Ar$_2$BF but no $ArBF_2$·OEt_2. It is presumed the latter adduct dissociated into $ArBF_2$ and Et_2O on removing the ether *in vacuo*. Vacuum sublimation of the residue at 93 °C gave a white solid identified as Ar$_2$BF (3.3 g, 46% yield).

Reaction of BCl_3 with excess Ar′Li. A solution of Ar′/Ar″Li was generated by adding BuLi (28 ml, 1.6 M in hexanes, 44.8 mmol) dropwise to a stirred solution of Ar′H (10.5 g, 49.1 mmol) in 100 ml of Et_2O at −78 °C and left to warm to room temperature overnight. The brown solution was slowly treated with BCl_3 (6 ml, 1 M in heptane, 6 mmol) at −78 °C and left to warm to room temperature for 1 h. Fluorine and boron NMR spectra obtained from a sample of the reaction mixture revealed Ar″$_3$B to be the major product. Ar″$_2$BF·OEt_2 and unreacted Ar′Li were also present. The reaction mixture was then treated with a further 6 ml of BCl_3 (1 M in heptane, 6 mmol) at −78 °C. After warming the mixture to room temperature, ^{19}F and ^{11}B NMR data on an aliquot of the solution gave Ar″$_3$B and Ar′$_2$BF as the major components. Ar″$_2$BF·OEt_2 and Ar′BCl_2 were also observed. On removing the ether and heptane *in vacuo*, the residue contained a yellow oil and a white solid. NMR data on the yellow oil revealed only Ar″$_3$B and Ar′$_2$BF. The fates of Ar″$_2$BF·OEt_2 and Ar′BCl_2 are not clear.

Crystallography. Single crystal structure determinations were carried out from data collected at 100 or 120 K, using graphite monochromated Mo-Kα radiation (λ = 0.71073 Å) on a Bruker

SMART-CCD detector diffractometer equipped with a Cryostream N_2 flow cooling device.[35] In each case, series of narrow ω-scans (0.3°) were performed at several ϕ-settings in such a way as to cover a sphere of data to a maximum resolution between 0.70 and 0.77 Å. Cell parameters were determined and refined using the SMART software,[36] and raw frame data were integrated using the SAINT program.[37] The structures were solved using direct methods and refined by full-matrix least squares on F^2 using SHELXTL.[38] Relevant parameters for data collection and structure solution are given in Table 4

CCDC reference numbers 217588–217592.

See http://www.rsc.org/suppdata/dt/b3/b309820f/ for crystallographic data in CIF or other electronic format.

Computational methods. All *ab initio* computations were carried out with the Gaussian 98 package.[39] All geometries discussed here were optimised at the HF/6-31G* level with no symmetry constraints. Frequency calculations were computed on these optimised geometries at the HF/6-31G* level for imaginary frequencies; none was found for geometries where the *para* CF_3 group is absent. Theoretical ^{11}B chemical shifts at the GIAO-HF/6-31G*//HF/6-31G* level have been referenced to B_2H_6 (16.6 ppm)[40] and converted to the usual $BF_3{\cdot}OEt_2$ scale: $\delta(^{11}B) = 123.4 - \sigma(^{11}B)$. For Mes_2BF, the HF/6-31G* optimised geometry in Table 4 was then optimised at the MP2/6-31G* level of theory, and the ^{11}B shift of 55.4 ppm was computed from the MP2 optimised geometry at the GIAO-B3LYP/6-311G* level of theory with the scale: $\delta(^{11}B) = 102.84 - \sigma(^{11}B)$. Unlike the excellent agreements between observed and computed ^{11}B NMR shifts of fluoroboranes, computed ^{19}F NMR shifts have not been shown to be as accurate.[41,42] Here, calculated ^{19}F chemical shifts at the GIAO-HF/6-31G*//HF/6-31G* level have been referenced to HF and converted to the usual $CFCl_3$ scale: $\delta(^{19}F) = (237.7 - \sigma(^{19}F))/0.911$. Computed NMR shifts (GIAO-HF/6-31G*//HF/6-31G*) for Ar*BFCl·OEt_2: ^{11}B 12.0 ppm; ^{19}F −84 (*o*-CF_3), −86 (*p*-CF_3), −135 (BF) ppm; for Ar'_2BFOH^-: ^{11}B 3.8 ppm; ^{19}F −78 (CF_3), −158 (BF) ppm; for dimethyl[8-(difluoroborolyl)naphthalen-1-yl]amine: ^{11}B 9.9 ppm; ^{19}F −146 ppm.[17] Cartesian coordinates for the optimised geometries obtained are available in the ESI.†

Acknowledgements

We thank the EPSRC for the award of studentships (to S. M. C., C. D. E., H. P. G., and A. L. T.), for an Advanced Research Fellowship (to M. A. F.), and C. F. Heffernan, A. M. Kenwright and I. P. McKeag for assistance in recording some of the NMR spectra.

References

1 G. E. Carr, R. D. Chambers, T. F. Holmes and D. G. Parker, *J. Organomet. Chem.*, 1987, **325**, 13; M. Scholz, H. W. Roesky, D. Stalke, K. Keller and F. T. Edelmann, *J. Organomet. Chem.*, 1989, **366**, 73; H. Grutzmacher, H. Pritzkow and F. T. Edelmann, *Organometallics*, 1991, **10**, 23; S. Brooker, J. Buijink and F. T. Edelmann, *Organometallics*, 1991, **10**, 25; M. Abe, K. Toyota and M. Yoshifuji, *Chem Lett.*, 1992, **12**, 259; K. B. Dillon and H. P. Goodwin, *J. Organomet. Chem.*, 1992, **429**, 169; K. B. Dillon and H. P. Goodwin, *J. Organomet. Chem.*, 1994, **469**, 125; F. T. Edelmann, *Comments Inorg. Chem.*, 1992, **12**, 259; M. Belay and F. T. Edelmann, *J. Organomet. Chem.*, 1994, **479**, C21; J.-T. Alhemann, H. W. Roesky, M. Noltemeyer, H.-G. Schmidt, L. N. Markovsky and Y. G. Shermolovich, *J. Fluorine Chem.*, 1998, **87**, 87; C. Bartolomé, P. Espinet, F. Villafañe, S. Giesa, A. Martín and A. G. Orpen, *Organometallics*, 1996, **15**, 2019; K. B. Dillon, V. C. Gibson, J. A. K. Howard, L. J. Sequeira and J. W. Yao, *Polyhedron*, 1996, **15**, 4173; V. C. Gibson, C. Redshaw, L. J. Sequeira, K. B. Dillon, W. Clegg and M. R. J. Elsegood, *Chem. Commun.*, 1996, 2151; K. B. Dillon, V. C. Gibson, J. A. K. Howard, C. Redshaw, L. Sequeira and J. W. Yao, *J. Organomet. Chem.*, 1997, **528**, 179; M. G. Davidson, K. B. Dillon, J. A. K. Howard, S. Lamb and M. D. Roden, *J. Organomet. Chem.*, 1998, **550**, 481; P. Espinet, S. Martin-Barrios, F. Villafañe, P. G. Jones and A. K. Fisher, *Organometallics*, 2000, **19**, 290; A. S. Batsanov, K. B. Dillon, V. C. Gibson, J. A. K. Howard, L. J. Sequeira and J. W. Yao, *J. Organomet. Chem.*, 2001, **631**, 18; A. S. Batsanov, S. M. Cornet, L. A. Crowe, K. B. Dillon, R. K. Harris, P. Hazendonk and M. D. Roden, *Eur. J. Inorg. Chem.*, 2001, 1729.

2 K. B. Dillon, H. P. Goodwin, T. A. Straw and R. D. Chambers, *Euchem. Conf. Phosphorus, Silicon, Boron and Related Elements in Low Coordinated States*, Paris-Palaiseau, 1988.

3 K. H. Whitmire, D. Labahn, H. W. Roesky, M. Noltemeyer and G. M. Sheldrick, *J. Organomet. Chem.*, 1991, **402**, 55.

4 J. K. Buijink, M. Noltemeyer and F. T. Edelmann, *J. Fluorine Chem.*, 1993, **61**, 51.

5 N. Burford, C. L. B. Macdonald, D. J. LeBlanc and T. S. Cameron, *Organometallics*, 2000, **19**, 152.

6 R. D. Schluter, H. S. Isom, A. H. Cowley, D. A. Atwood, R. A. Jones, F. Olbritch, S. Corbelin and R. J. Lagow, *Organometallics*, 1994, **13**, 4058.

7 R. D. Schluter, A. H. Cowley, D. A. Atwood, R. A. Jones, M. R. Bond and C. J. Carrano, *J. Am. Chem. Soc.*, 1993, **115**, 2070.

8 M. Bardaji, P. G. Jones, A. Laguna, A. Moracho and A. K. Fischer, *J. Organomet. Chem.*, 2002, **648**, 1.

9 K. Ishihara, S. Ohara and H. Yamamoto, *J. Org. Chem.*, 1996, **61**, 4196.

10 K. Ishihara, M. Mouri, Q. Gao, T. Maruyama, K. Furuta and H. Yamamoto, *J. Am. Chem. Soc.*, 1993, **115**, 11490.

11 V. C. Gibson, C. Redshaw, W. Clegg and M. R. J. Elsegood, *Polyhedron*, 1997, **16**, 2637.

12 W. Fraenk, T. M. Klapötke, B. Brumm, P. Mayer, H. Nöth, H. Piotrowski and M. Suter, *J. Fluorine Chem.*, 2001, **112**, 73.

13 A. Pelter, K. Smith and H. C. Brown, *Borane Reagents: Best Synthetic Methods*, Academic Press, London, 1988, p. 428.

14 K. Sasakura, Y. Terui and T. Sugasawa, *Chem. Pharm. Bull.*, 1985, **33**, 1836.

15 H. J. Frohn, H. Franke, P. Fritzen and V. V. Bardin, *J. Organomet. Chem.*, 2000, **598**, 127.

16 R. Duchateau, S. J. Lancaster, M. Thornton-Pett and M. Bochmann, *Organometallics*, 1997, **16**, 4995.

17 R. L. Giles, J. A. K. Howard, L. G. F. Patrick, M. R. Probert, G. E. Smith and A. Whiting, *J. Organomet. Chem.*, 2003, **680**, 257.

18 A. S. Batsanov, S. M. Cornet, K. B. Dillon, A. E. Goeta, A. L. Thompson and B. Y. Xue, *Dalton Trans.*, 2003, 2496.

19 *Thermodynamical Properties of Individual Substances*, ed. I. V. Gurvich, I. V. Veits and S. B. Alcock, Hemisphere Publ. Corp., Washington DC, USA, 4th edn., 1991, vol. 2, pt. 1; *Handbook of Chemistry and Physics*, ed. D. R. Lide, CRC Press, Boca Raton, FL, USA, 76th edn., 1995–1996; S. S. Batsanov, *Strukturnaya Khimiya*, Dialog MGU, Moscow, 2000.

20 M. E. Schwarz and L. C. Allen, *J. Am. Chem. Soc.*, 1970, **92**, 1466.

21 S. Toyota, M. Asakura, M. Öki and F. Toda, *Bull. Chem. Soc. Jpn.*, 2000, **73**, 2357.

22 A. S. Batsanov, S. M. Cornet, K. B. Dillon, A. E. Goeta, P. Hazendonk and A. L. Thompson, *J. Chem. Soc., Dalton Trans.*, 2002, 4622.

23 K. J. Weese, R. A. Bartlett, B. D. Murray, M. M. Olmstead and P. Power, *Inorg. Chem.*, 1987, **26**, 2409.

24 W. E. Piers, R. E. v. H. Spence, L. R. MacGillivray and M. J. Zaworotko, *Acta Crystallogr., Sect. C*, 1995, **51**, 1688.

25 W. V. Konze, B. L. Scott and G. J. Kubas, *Chem. Commun.*, 1999, 1807.

26 J. F. Blount, P. Finocchiaro, D. Gust and K. Mislow, *J. Am. Chem. Soc.*, 1973, **95**, 7019.

27 D. C. Bradley, I. S. Harding, A. D. Keefe, M. Motevalli and D. H. Zheng, *J. Chem. Soc., Dalton Trans.*, 1996, 3931.

28 M. T. Reetz, J. Huff, J. Rudolph, K. Töllner, A. Deeze and R. Goddard, *J. Am. Chem. Soc.*, 1994, **116**, 11588.

29 W. J. Evans, J. L. Shreeve and J. W. Ziller, *Acta Crystallogr., Sect. C*, 1996, **52**, 2571; M. Niehues, G. Erker, O. Meyer and R. Frohlich, *Organometallics*, 2000, **19**, 2813.

30 W. I. Cross, M. P. Lightfoot, F. S. Mair and R. G. Pritchard, *Inorg. Chem.*, 2000, **39**, 2690.

31 K. R. Leopold, M. Canagaratna and J. A. Phillips, *Acc. Chem. Res.*, 1997, **30**, 57.

32 H. Jiao and P. v. R. Schleyer, *J. Am. Chem. Soc.*, 1994, **116**, 7429.

33 V. Jonas, G. Frenking and M. T. Reetz, *J. Am. Chem. Soc.*, 1994, **116**, 8741.

34 B. D. Bowsell, R. J. Gillespie and G. L. Heard, *Inorg. Chem.*, 1999, **38**, 4659.

35 J. Cosier and A. M. Glazer, *J. Appl. Crystallogr.*, 1986, **19**, 105.

36 SMART-NT, Data Collection Software, version 5.0, Bruker Analytical X-ray Instruments Inc., Madison, WI, 1999.

37 SAINT-NT, Data Reduction Software, version 6.0, Bruker Analytical X-ray Instruments Inc., Madison, WI, 1999.
38 SHELXTL, version 5.1, Bruker X-ray Analytical Instruments Inc., Madison, WI, 1999.
39 M. J. Frisch, G. W. Trucks, H. B. Schlegel, G. E. Scuseria, M. A. Robb, J. R. Cheeseman, V. G. Zakrzewski, J. A. Montgomery, Jr., R. E. Stratmann, J. C. Burant, S. Dapprich, J. M. Millam, A. D. Daniels, K. N. Kudin, M. C. Strain, O. Farkas, J. Tomasi, V. Barone, M. Cossi, R. Cammi, B. Mennucci, C. Pomelli, C. Adamo, S. Clifford, J. Ochterski, G. A. Petersson, P. Y. Ayala, Q. Cui, K. Morokuma, D. K. Malick, A. D. Rabuck, K. Raghavachari, J. B. Foresman, J. Cioslowski, J. V. Ortiz, B. B. Stefanov, G. Liu, A. Liashenko, P. Piskorz, I. Komaromi, R. Gomperts, R. L. Martin, D. J. Fox, T. Keith, M. A. Al-Laham, C. Y. Peng, A. Nanayakkara, C. Gonzalez, M. Challacombe, P. M. W. Gill, B. G. Johnson, W. Chen, M. W. Wong, J. L. Andres, M. Head-Gordon, E. S. Replogle and J. A. Pople, GAUSSIAN 98 (Revision A.9), Gaussian, Inc., Pittsburgh, PA, 1998.
40 T. P. Onak, H. L. Landesman and R. E. Williams, *J. Phys. Chem.*, 1959, **63**, 1533.
41 T. Onak, M. Diaz and M. Barfield, *J. Am. Chem. Soc.*, 1995, **117**, 1403.
42 M. A. Fox, R. Greatrex and D. L. Ormsby, *Chem. Commun.*, 2002, 2052.

C.6 Allosteric Effects in Spin Crossover Networks

Angewandte Chemie

Communications

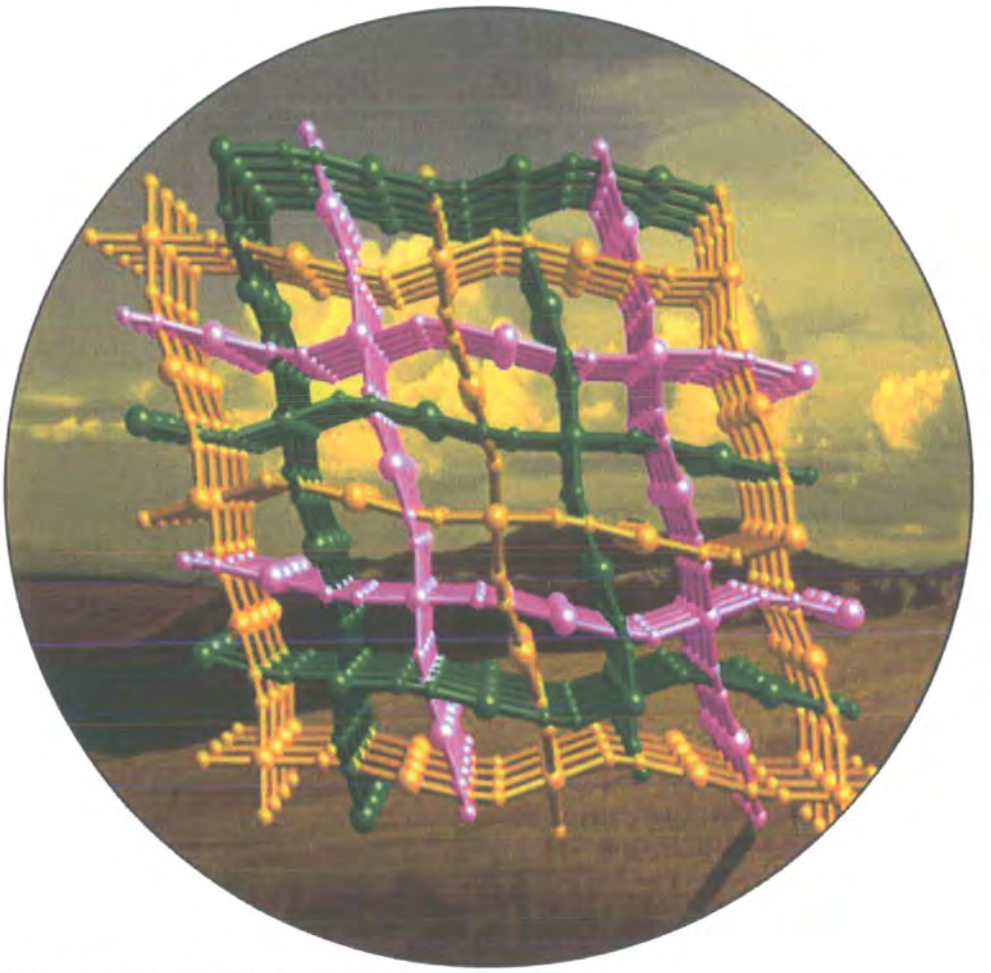

The three interpenetrated independent 3D spin-crossover networks in $[Fe(pdm)(H_2O)\{Ag(CN)_2\}_2]\cdot H_2O$ transform into a single 3D network upon losing the coordinated water molecules. This process is reversible and is accompanied by drastic modifications of the spin-crossover switching properties. For more information see the following communication by J. A. Real and co-workers.

Angew. Chem. Int. Ed. 2003, *42*, 3759 DOI: 10.1002/anie.200351853

Communications

Hysteresis in Fe-CN-Ag/Au Networks

Crystalline-State Reaction with Allosteric Effect in Spin-Crossover, Interpenetrated Networks with Magnetic and Optical Bistability**

*Virginie Niel, Amber L. Thompson, M. Carmen Muñoz, Ana Galet, Andrés E. Goeta, and José A. Real**

The versatility of metal–organic chemistry offers a unique opportunity to construct multifunctional materials based on the assembly of molecular building blocks. Such an approach can lead to the design of coordination polymers with specific network topologies and potentially interesting properties.[1] Incorporation of iron(II) spin crossover (SCO) building blocks in such framework structures is particularly suitable for these purposes as the labile electronic configurations of the iron units may be switched between the high- (HS) and low-spin (LS) states. This switching leads to distinctive changes in magnetism, color, and structure, which may be induced by variation of temperature and/or pressure and by light irradiation.[2] Strong signal generation and hysteresis (memory effect) may be achieved when rigid linkers, which allow communication between the SCO centers, propagate the structural changes cooperatively to the whole framework conferring a bistable character to the material.[3-5] The construction of sensory and memory devices is the ultimate goal.

Hofmann-like open frame coordination polymers have been the subject of much research for many years.[6] Nevertheless, incorporation of iron(II) SCO building blocks in such systems is relatively recent.[7] Following this strategy we have shown the suitability of cyano-metallate complexes as connectors between iron(II) SCO centers to build highly cooperative thermo-, piezo-, and photo-switchable two- and three-dimensional coordination polymers.[8-10] A further important aspect for developing multifunctional materials based on these polymers stems from their porous nature,[11] which opens opportunities for investigating the interplay between inclusion chemistry and SCO signal generation.[12,13] Herein we report on the incorporation of electronic SCO, molecular recognition, and crystalline-state reaction[14] switching events and their cooperative interactions in $[Fe(pmd)(H_2O)\{M(CN)_2\}_2]\cdot H_2O$ (**1**) (pmd = pyrimidine; M = Ag (**1Ag**) or Au (**1Au**)). This is a cyanide-based bimetallic coordination polymer made up of triple interpenetrated, 4-connected, three-dimensional, open-frame networks.

Compound **1** is monoclinic (space group $P2_1/c$) whatever the spin state (the structural parameters reported below correspond to the HS state).[15] Two distinct iron atoms, Fe(1) and Fe(2) (see Figure 2), which define the inversion center of an elongated $\{Fe(1)N_6\}$ and a compressed $\{Fe(2)N_4O_2\}$ coordination octahedron, respectively, constitute the building blocks of the structure. The four equatorial positions are occupied by the cyanide nitrogen atoms of the $[M(CN)_2]^-$ groups while the apical positions are occupied by two nitrogen atoms of two pmd ligands (Fe(1)) and by two water molecules (Fe(2)). The $[M(CN)_2]^-$ groups link the Fe(1) and Fe(2) atoms generating {Fe(1)-NC-M(1)-CN-Fe(2)-NC-M(2)-CN-} groups which connect to form rectangular motifs. These rectangles have edges Fe(1)···Fe(1) = 20.5775(7) (**1Ag**), 20.3860(6) Å (**1Au**) and Fe(1)···Fe(2) = 10.6417(2) (**1Ag**), 10.5643(2) Å (**1Au**). The edge sharing rectangles define an infinite set of parallel layers pillared by $[M(CN)_2]^-$ groups. The resulting 4-connected 3D network corresponds to the expanded version of the prototypical $CdSO_4$ net decorated by the coordinating water molecules and the pmd ligands (Figure 1a).[16,17] The much larger intraframework spaces are occupied by two other identical but independent networks, which interpenetrate the first network and each other (Figure 1b). Communication between the three covalently bonded nets is through weaker metallophilic M···M interactions (average Ag···Ag and Au···Au distances 3.1813(3) and 3.2901(4) Å, respectively) and hydrogen bonds between the coordinated water molecules and the uncoordinated nitrogen atom of the pmd ligands (N(pmd)···H_2O = 2.805(3) Å (**1Ag**) and 2.762(6) Å (**1Au**); (Figure 2a, b). This arrangement accounts for the close proximity of the Fe(2) atom and the uncoordinated nitrogen atom, Fe(2)-OH_2···N(pmd), which provides favorable conditions for a topochemical reaction to take place (Figure 2a).

Complete and rapid loss of both ligated and nonbonded water molecules occurs simultaneously in the temperature range 345–399 K (**1Ag**) and 323–382 K (**1Au**). X-ray powder diffraction spectra (XRPD) were recorded on **1Au** at 290 K and 373 K at ambient pressure and at 290 K under vacuum. The data obtained clearly confirms that at 290 K at ambient pressure the sample is in the hydrated state, in agreement with results obtained from single-crystal measurements. The X-ray spectra taken at 373 K at ambient pressure and at 290 K under vacuum are essentially identical though different to the spectra of the hydrated sample, thus revealing the structural changes caused by the loss of the water molecules. Ab initio indexing of the powder pattern of the dehydrated sample clearly shows the massive cell-contraction (ca. 2.5 Å) taking place along the *a* axis, previously assumed from the observed shift of the 200 reflection from 12.3(2)° to 14.5(2)° (Supporting Information). This large and reversible structural modification involving not only the loss of an unbound water

[*] Prof. Dr. J. A. Real, Dr. V. Niel
Institut de Ciencia Molecular/Departament de Química Inorgànica
Universitat de València
Doctor Moliner 50, 46100 Burjassot, València (Spain)
Fax: (+34) 96-386-4322
E-mail: jose.a.real@uv.es
A. L. Thompson, Dr. A. E. Goeta
Department of Chemistry
University of Durham
South Road, Durham, DH1 3LE (UK)
Prof. Dr. M. C. Muñoz, A. Galet
Departament de Física Aplicada
Universitat Politécnica de València
Camino de Vera s/n, 46071 València (Spain)

[**] We are grateful for financial assistance from the Ministerio Español de Ciencia y Tecnología (project BQU 2001-2928), The Royal Society for a Study Visit and a Join Project awards. ALT thanks EPSRC for a Postgraduate Fellowship. AG thanks to the Universitat Politècnica de València for a predoctoral fellowship.

Supporting information for this article is available on the WWW under http://www.angewandte.org or from the author.

  DOI: 10.1002/anie.200351853

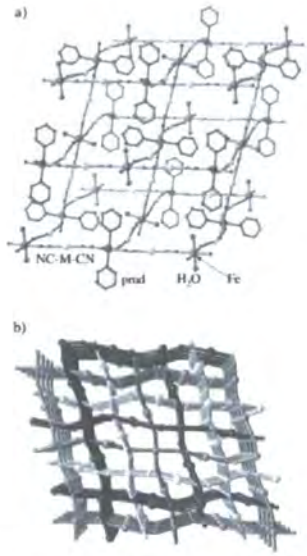

Figure 1. a) Fragment of the 3D network of **1** displaying the expanded version of the $CdSO_4$ structure. b) Perspective view of the three interlocked networks.

molecule but more importantly the loss of a coordinating water molecule, affects the integrity of the single crystals of **2** (they crack and become effectively a polycrystalline powder) precluding the in situ structure determination from single-crystal diffraction techniques. The structure determination of **2Au** was then carried out from a rigid-body Rietveld refinement of the hydrated model, excluding the water molecules, using the newly determined cell parameters.[18] No change in space group has been observed following the **1**↔**2** transformation. There are two crystallographically distinct $\{FeN_6\}$ distorted octahedrons in **2** whose Fe(1) and Fe(2) sites can be unambiguously identified with those corresponding to **1**. However, in contrast to **1**, the pmd ligand now bridges directly the Fe(1) and Fe(2) atoms defining a system of infinite chains {-Fe(1)-pmd-Fe(2)} running parallel to the *a* axis (Fe(1)···Fe(2) = 6.1927(4) Å) in **2**. The $[M(CN)_2]^-$ groups of one chain link with the equatorial positions of the iron centers, connecting adjacent chains and defining a single 3D network (Figure 2c, d). These significant structural changes are a consequence of the cooperative topochemical ligand substitution, which involves the concerted loss of the bonded water generating double coordination unsaturation at the Fe(2) centers and the coordination of the uncoordinated pmd nitrogen atom belonging to adjacent networks. A first example of topochemical conversion of a hydrogen-bonded into a covalent bonded supramolecular network was described for the binuclear $[\{Zn(sala)(H_2O)_2\}_2]\cdot 2H_2O$ compound (H_2sala = *N*-(2-hydroxybenzyl)-L-alanine), but this process was irreversible.[19] In contrast, when **1Au** and **1Ag** are exposed to an atmosphere of H_2O, selective absorption of this vapor induces the inverse reaction at the Fe(2) sites, regenerating the three independent 3D networks (Figure 2c, d). The system does not suffer any noticeable fatigue after repeating several **1**↔**2** cycles.

X-ray powder diffraction spectra of **1Ag** have also been recorded and it can be clearly observed that the behavior is similar to that described for the **1Au** compound. In spite of this, there are clear differences between **2Ag** and **2Au**, which point to either a different unit cell or a loss of symmetry from monoclinic to triclinic in **2Ag**. Further work is in progress to establish the cell parameters and space group for **2Ag**, with the aim of solving its crystal and molecular structure.

Figure 3 shows the temperature dependence of the $\chi_M T$ product for **1Ag** and **1Au**, χ_M being the molar magnetic susceptibility and T the temperature. At room temperature,

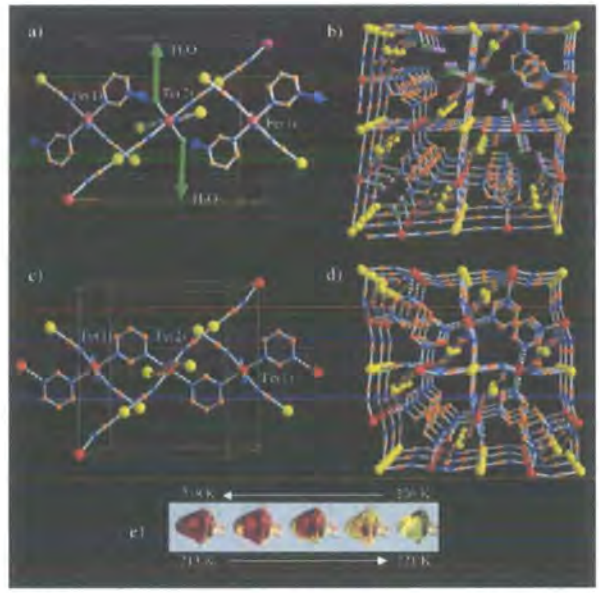

Figure 2. a) Unit cell of **1** showing fragments of three networks. Arrows on the uncoordinated nitrogen atoms (blue) and coordinated water molecules (green) indicate the dynamic event, which takes place during the topochemical solid-state reaction. b) Perspective view, [001], of the three nets showing the N(pmd)···H_2O hydrogen-bond system. c) Unit cell of **2Au** displaying the infinite chains defined by the bridging mode of the pmd ligand (striped bonds represent the new coordination bonds generated after dehydration. d) Perspective view of the new 3D network **2Au**. e) Photographs showing the color change of a **1Ag** single crystal around the critical region (yellow and deep red colors correspond to the high- and low-spin states, respectively).

Communications

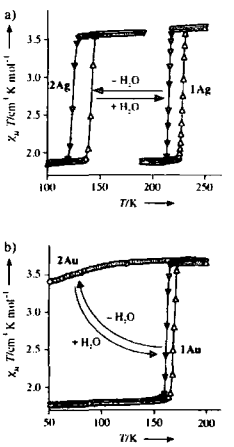

Figure 3. Magnetic susceptibility measurements displaying the first-order spin transition for a) **1Ag/2Ag** and b) **1Au/2Au**.

$\chi_M T$ is 3.7 for **1Ag** and 3.6 cm^3 K mol^{-1} for **1Au**. These values are consistent with the iron(II) ion in the HS state. Upon cooling, $\chi_M T$ remains almost constant up to 218 K (**1Ag**) and 165 K (**1Au**), below these temperatures the $\chi_M T$ value undergoes a sharp decrease that is characteristic of a first order SCO transition. The $\chi_M T$ value drops to 1.8 (**1Ag**) and 1.7 (**1Au**) cm^3 K mol^{-1} at 213 K and 159 K, respectively. The warming mode reveals the occurrence of thermal hysteresis. The critical temperatures for the cooling (T_c^{down}) and warming (T_c^{up}) modes (215 and 223 K (**1Ag**) and 163 and 171 K (**1Au**) respectively), indicate the occurrence of approximately 8 K wide hysteresis loops. At temperatures below T_c, the $\chi_M T$ value indicates that 50% of the iron(II) ions remains in the HS state for both compounds. As expected from their coordination environments, Fe(1) undergoes the HS↔LS transition while Fe(2) remains HS, which is in agreement with the structural data obtained at 120 K for both derivatives.

The temperature dependence of $\chi_M T$ was measured for the dehydrated **2Ag** and **2Au** forms (Figure 3a, b). For **2Ag** $\chi_M T$ is 3.6 cm^3 K mol^{-1} at room temperature and remains constant down to 125 K, which indicates that the iron(II) ion is in the HS state in **2Ag**. The subsequent sharp decrease of $\chi_M T$ to a value of 1.9 cm^3 K mol^{-1} is due to the occurrence of a spin transition. The warming mode reveals the occurrence of a 17 K wide thermal hysteresis loop. The critical temperatures are $T_c^{down} = 124$ K and $T_c^{up} = 141$ K. Compound **2Ag** has a hysteresis loop twice the width of **1Ag**, which denotes the expected increase of cooperativity when replacing the hydrogen-bonding internetwork interactions in **1** by stronger coordination bonds in the more rigid framework **2**. Compound **2Au** does not undergo a spin transition in the whole temperature range ($\chi_M T$ has a constant value of around 3.8 cm^3 K mol^{-1} between room temperature and 120 K). This difference in the behavior of **2Ag** and **2Au** may be supported by the differences in the diffraction patterns observed for each of the compounds upon dehydration, see above. The marked down shift of T_c in **2Ag** and disappearance of SCO in **2Au** indicate a decrease of the ligand-field strength at the Fe(1) site and may be ascribed to the bridging mode of the pmd ligand. Recovery of the original SCO behavior of **1Ag** and **1Au** occurs when **2Ag** and **2Au** are left in air atmosphere.

Compounds **1Ag**, **1Au**, and **2Ag** undergo a dramatic change of color from pale yellow (HS state) to deep red (LS state) accompanying the SCO (Figure 2c). This thermochromic effect, observed in other 2D and 3D Fe^{II}–M^{II} (M = Ni, Pd, Pt) Hofmann-like SCO compounds, is a consequence of the increase in intensity of the metal-to-ligand charge transfer (MLCT) band around 550 nm, associated with the electron delocalization from the t_{2g} orbitals of the iron(II) ion to the π^* orbitals of the ligands which is enhanced by the HS→LS spin change.[8]

In summary, the coordination polymers **1Au** and **1Ag** undergo thermally induced first-order, spin-crossover transitions with magnetic and chromatic bistability. They also participate in a controlled and fully reversible crystalline-state ligand substitution, involving coordination/uncoordination of gaseous water and pmd. This induces expansion/contraction of the nanoporous framework and the repeated allosteric transformation of the three interpenetrated nets into a single three-dimensional net (**2Ag** and **2Au**) without affecting their crystallinity but altering their SCO behavior significantly. Such a cooperative combination, in the same lattice, of different molecular events, such as recognition, allosterism, and electronic bistability is of fundamental significance for the generation of new switchable, multiproperty materials.

Experimental Section

1Ag: was synthesized by slow diffusion, under an argon atmosphere, of two aqueous solutions containing stoichiometric amounts of $Fe(BF_4)_2 \cdot 6H_2O$ (0.185 mmol, 2 mL)/pyrimidine (0.374 mmol, 2 mL) in one side and $K[Ag(CN)_2]$ (0.374 mmol, 2 mL) in the other side of an H-shaped vessel. Pale yellow prismatic crystals were separated three weeks later. Yield approximately 50%. Elemental analysis (%) calcd for $C_8H_8N_6Ag_2O_2Fe$: C 19.54, H 1.61, N 17.09; found: C 20.05, H 1.98, N 16.76.

1Au: to an aqueous solution containing $FeCl_2$ (0.087 mmol, 4 mL) and pyrimidine (0.173 mmol, 4 mL) was added a water solution of $K[Au(CN)_2]$ (0.173 mmol, 6 mL). The resulting solution was stirred for 10 min and left at room temperature to evaporate under an argon stream. Pale yellow crystals were separated one week later. Yield approximately 70%. Elemental analysis (%) calcd for $C_8H_8N_6Au_2O_2Fe$: C 14.34, H 1.20, N 12.54; found: C 14.95, H 1.50, N 12.03.

2Ag and **2Au**: Dehydrated samples **2Ag** and **2Au** were prepared from **1Ag** and **1Au** in the SQUID sample holder. Hydrated samples placed in sealed containers in the SQUID sample holder and their magnetism checked. Small holes were then made in the lids of the sample containers and the samples left standing for 30 min at 380 K, dehydration under these conditions is confirmed by the thermogravimetric analysis (see Supporting Information).

Received: May 9, 2003 [Z51853]
Published online: July 28, 2003

Keywords: allosterism · cooperative effects · crystalline-state reactions · N ligands · spin crossover

[1] a) J. M. Lehn, *Science* **2002**, *295*, 2400; b) M. D. Hollingsworth, *Science* **2002**, *295*, 2410.
[2] P. Gütlich, A. Hauser, H. Spiering, *Angew. Chem.* **1994**, *106*, 2109; *Angew. Chem. Int. Ed. Engl.* **1994**, *33*, 2024.
[3] J. A. Real, A. B. Gaspar, V. Niel, M. C. Muñoz, *Coord. Chem. Rev.* **2003**, *236*, 121.
[4] W. Vreugdenhill, J. H. Van Diemen, R. A. G. De Graaff, J. G. Haasnoot, J. Reedijk, A. M. Van der Kraan, O. Kahn, J. Zarembowitch, *Polyhedron* **1990**, *9*, 2971.
[5] O. Kahn, C. J. Martinez, *Science* **1998**, *279*, 44.
[6] T. Iwamoto in *Inclusion Compounds, Vol. 5* (Eds.: J. L. Atwood, J. E. D. Davies, D. D. MacNicol), Oxford University Press, London, UK, **1991**, p. 177.
[7] T. Kitazawa, Y. Gomi, M. Takahashi, M. Takeda, A. Enemoto, T. Miyazaki, T. Enoki, *J. Mater. Chem.* **1996**, *6*, 119.
[8] V. Niel, J. M. Martinez-Agudo, M. C. Muñoz, A. B. Gaspar, J. A. Real, *Inorg. Chem.* **2001**, *40*, 3838.
[9] V. Niel, M. C. Muñoz, A. B. Gaspar, A. Galet, G. Levchenko, J. A. Real, *Chem. Eur. J.* **2002**, *8*, 2446.
[10] V. Niel, A. Galet, A. B. Gaspar, M. C. Muñoz, J. A. Real, *Chem. Commun.* **2003**, 1248.
[11] a) B. Chen, M. Eddaoudi, S. T. Hyde, M. O'Keeffe, O. M. Yaghi, *Science* **2001**, *291*, 1021; b) O. M. Yaghi, G. Li, H. Li, *Nature* **1995**, *378*, 703.
[12] P. J. Langley, J. Hulliguer, *Chem. Soc. Rev.* **1999**, *28*, 279.
[13] a) G. J. Halder, C. J. Kepert, B. Moubaraki, K. S. Murray, J. D. Cashion, *Science* **2002**, *298*, 1762; b) J. A. Real, E. Andrés, M. C. Muñoz, M. Julve, T. Granier, A. Bousseksou, F. Varret, *Science* **1995**, *268*, 265.
[14] M. Albrecht, M. Lutz, A. L. Spek, G. van Koten, *Nature* **2000**, *406*, 970.
[15] Crystal for **1Ag**: Monoclinic, space group $P2_1/c$, $a = 14.7035(5)$, $b = 13.2962(5)$, $c = 7.3852(3)$ Å, $\beta = 91.441(2)°$, $Z = 4$, $V = 1443.35(9)$ Å^3, $T = 225$ K, $\rho_{calcd} = 2.263$ mg m^{-3}, $\mu = 3.683$ mm^{-1}, 19016 reflections measured, 3867 unique ($R_{int} = 0.0245$) which were used in all calculations and 3425 greater than $2\sigma(I)$. The final $R(F)$ was 0.0219 ($I > 2\sigma(I)$ data) and the $wR(F^2)$ was 0.0535 (all data). Crystal data for **1Au**: Monoclinic, space group $P2_1/c$, $a = 14.6157(5)$, $b = 13.3075(5)$, $c = 7.2272(3)$ Å, $\beta = 90.944(2)°$, $V = 1405.49(9)$ Å^3, $\rho_{calcd} = 3.166$ mg m^{-3}, $T = 180$ K, $\mu = 21.849$ mm^{-1}, 15805 reflections measured, 3072 unique ($R_{int} = 0.0545$) which were used in all calculations and 2441 greater than $2\sigma(I)$. The final $R(F)$ was 0.0241 ($I > 2\sigma(I)$ data) and the $wR(F^2)$ was 0.0474 (all data). CCDC-209792–209795 contain the supplementary crystallographic data for this paper. These data can be obtained free of charge via www.ccdc.cam.ac.uk/conts/retrieving.html (or from the Cambridge Crystallographic Data Centre, 12 Union Road, Cambridge CB2 1EZ, UK; fax: (+44) 1223-336-033; or deposit@ccdc.cam.ac.uk).
[16] L. Carlucci, G. Ciani, P. Macchi, D. M. Proserpio, *Chem. Commun.* **1998**, 1837.
[17] M. O'Keeffe, M. Eddaoudi, H. Li, T. Reineke, O. M. Yaghi, *J. Solid State Chem.* **2000**, *152*, 3.
[18] Crystal data for **2Au**: Monoclinic, space group $P2_1/c$, $a = 12.3855(7)$, $b = 13.6751(6)$, $c = 8.3348(4)$ Å, $\beta = 94.150(3)°$, $V = 1407.98(15)$ Å^3, $Z = 4$, $T = 293$ K. Final $wR_p = 7.46\%$, $R_F = 5.15\%$, GooF = 2.61, $\chi^2 = 6.827$ (see Supporting Information for structure refinement).
[19] J. D. Ranford, J. J. Vittal, D. Wu, *Angew. Chem.* **1998**, *110*, 1159; *Angew. Chem. Int. Ed.* **1998**, *37*, 1114.

 DOI: 10.1002/anie.200351246

C.7 Group 14 Compounds Containing Ar, Ar′ & Ar″ Ligands

FULL PAPER

Dalton
www.rsc.org/dalton

The synthesis and characterisation of some Group 14 compounds containing the 2,4,6-$(CF_3)_3C_6H_2$, 2,6-$(CF_3)_2C_6H_3$ or 2,4-$(CF_3)_2C_6H_3$ ligands

Andrei S. Batsanov, Stéphanie M. Cornet, Keith B. Dillon,* Andrés E. Goeta, Amber L. Thompson and Bao Yu Xue
Chemistry Department, University of Durham, South Road, Durham, UK DH1 3LE

Received 5th March 2003, Accepted 15th April 2003
First published as an Advance Article on the web 9th May 2003

New $(aryl)_2ECl_2$ and $(aryl)ECl_3$ compounds [E = Si, Ge or Sn; aryl = 2,4,6-$(CF_3)_3C_6H_2$ (Ar), 2,6-$(CF_3)_2C_6H_3$ (Ar′) and/or 2,4-$(CF_3)_2C_6H_3$ (Ar″)] were prepared by reactions of ECl_4 with 2 equivalents of ArLi or of a Ar′Li/Ar″Li mixture. The latter gives predominantly the less sterically hindered product Ar''_2ECl_2 for E = Si or Ge, but Ar'_2SnCl_2 for the larger central atom. The products were characterised by elemental analysis, ^{19}F and (where appropriate) ^{119}Sn NMR spectroscopy, and single-crystal X-ray diffraction for Ar''_2SiCl_2, $ArGeCl_3$, Ar_2GeCl_2, Ar''_2GeCl_2, Ar_2SnCl_2 and Ar'_2SnCl_2. For E = Si the synthesis is complicated by Cl/F exchange: besides Ar'_2SiCl_2 and Ar''_2SiCl_2, ^{19}F NMR spectroscopy identified in solution Ar''_2SiF_2 and Ar'_2SiF_2. The latter was isolated and its X-ray structure determined. In all compounds, the E atom has a strongly distorted tetrahedral coordination, supplemented by short intramolecular E ··· F contacts (secondary coordination) with *o*-CF_3 group(s).

Introduction

The 'fluoromes' ligand 2,4,6-$(CF_3)_3C_6H_2$ (henceforth, Ar) is known for its stabilising influence in the compounds of transition metals[1,2] and main group[3] elements, including phosphorus[4] and arsenic.[5] This is due to the high electronegativity (compared with most aryl ligands) of this group, combined with some ability for M→C π back donation and the steric demands of the two *ortho* trifluoromethyl groups, which can hinder rotation of the ligands as well as favour low coordination numbers by protecting vacant coordination sites. The 'fluoroxyl' 2,6-$(CF_3)_2C_6H_3$ group (Ar′), possessing similar advantages, is used much less,[4b,f,6-8] partly because lithiation of its precursor 1,3-bis(trifluoromethyl)benzene (Ar′H) can proceed in two different positions, leading to a mixture of Ar′ and 2,4-$(CF_3)_2C_6H_3$ (Ar″) derivatives.[4f,7,8] Recently we undertook a systematic study of a series of Group 15 compounds with Ar, Ar′ and/or Ar″ ligands.[8] The corresponding derivatives of tetravalent Group 14 elements (Si, Ge and Sn), remain comparatively unexplored, particularly simple halides and/or hydrides. Attempts to prepare Ar_2SiCl_2 from reaction of ArLi with $SiCl_4$, were frustrated by fluorine/chlorine exchange, yielding only Ar_2SiF_2.[9] Similarly, Ar_2SiHF was obtained from reaction between $HSiCl_3$ and ArLi.[10] Ar_2GeH_2 was synthesised from the germanium(II) precursor Ar_2Ge,[11] while $ArSnPh_3$ was similarly prepared from ArLi and Ph_3SnCl.[12] Various other derivatives containing Ar groups, often produced by reaction between an E(II) precursor Ar_2E (E = Ge or Sn) and oxidising agents, have been structurally characterised,[4e,13-16] but none containing Ar′ or Ar″ groups, although Ar′$SnMe_3$,[7b] Ar″-$SnMe_3$[7b] and Ar'_2Sn[17] have been prepared. X-Ray structures of these compounds consistently reveal intramolecular E ··· F separations shorter than the sums of the van der Waals radii, indicative of additional weak ("secondary") coordination, or attractive electrostatic interactions, which can play an important role in stabilisation of these molecules.

In the present work we have synthesised a series of the Ar, Ar′ and Ar″ derivatives of Group 14 elements (*i.e.* Si, Ge and Sn), which have been characterised by elemental analysis, ^{19}F and (where appropriate) ^{119}Sn NMR solution-state spectroscopy. X-Ray crystal structures of seven products have been determined at low temperatures.

Results and discussion

All the chloro-derivatives were prepared by reaction of the corresponding Group 14 tetrachloride ECl_4, with 2 equivalents of ArLi (from ArH), or with a mixture of Ar′Li and Ar″Li (to the total of 2 equivalents), obtained by lithiation of Ar′H (Scheme 1). In agreement with earlier reports,[9,10] the synthesis of Ar_2SiCl_2 (**1a**) was frustrated by chlorine/fluorine exchange and the only product isolated was Ar_2SiF_2 (**2**). For Ar′ and Ar″ derivatives, the Cl/F exchange was slower, and the compounds Ar'_2SiCl_2 (**3a**), Ar''_2SiCl_2 (**4a**), Ar'_2SiF_2 (**5**) and Ar''_2SiF_2 (**6**) were all detected in solution by means of ^{19}F NMR spectroscopy (see Table 1). Of the two isomeric chlorides, the less sterically hindered **4a** was present in larger amount than **3a**, but interestingly, the opposite was observed for the fluorides: **5** was more abundant than **6**. Probably, **3a** undergoes faster Cl/F exchange than **4a**, with the overall order of exchange rates

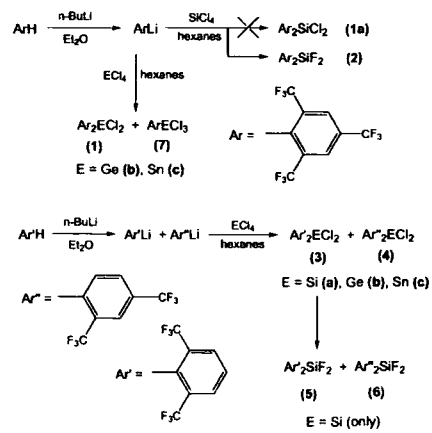

Scheme 1 Synthetic reactions (all performed at −78 °C).

DOI: 10.1039/b302544f

Table 1 ^{19}F NMR spectra for Si(IV) compounds

	o-CF_3		p-CF_3	Si–F	
	δ/ppm	$^5J_{F-F}$/Hz	δ/ppm	δ/ppm	$^5J_{F-F}$/Hz
2	−57.3 t (12F)	12.8	−64.2 s (6F)	−124.5 m (2F)	12.8
3a	−58.9 s (12F)				
4a	−57.9 s (6F)		−64.2 s (6F)		
5	−57.5 t (12F)	12.3		−125.5 m (2F)	12.5
6	−59.2 t (6F)	12.4	−64.1 s (6F)	−133.0 septet (2F)	12.3

decreasing in the sequence Ar_2SiCl_2 > Ar'_2SiCl_2 > Ar''_2SiCl_2. A possible mechanism for this exchange is presented in Scheme 2. Products **4a** and **5** were isolated as colourless crystalline solids, and their X-ray structures were ascertained.

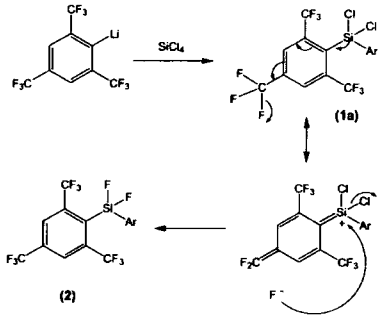

Scheme 2 Possible mechanism of Cl/F exchange in Si derivatives.

No F/Cl exchange was observed for the germanium and tin derivatives. This difference possibly arises because the bond energy terms are more favourable for exchange in the case of silicon. The sum of a C–Cl and an Si–F bond energy term (taken from values in tetrahalides[18]) is 912 kJ mol^{-1}, whereas the sum of a C–F and an Si–Cl term is 887 kJ mol^{-1}. Thus the exchange should give a net energy gain of 25 kJ mol^{-1}. The corresponding sums for germanium are 792 and 827 kJ mol^{-1} and for tin, 730 and 803 kJ mol^{-1}, respectively, giving in both cases a negative balance, −35 kJ mol^{-1} for Ge and −73 kJ mol^{-1} for Sn. Although the actual bond energies can be somewhat different in the present compounds because of different ligand environment, it is evident from the general trend that the Cl/F exchange is energetically more profitable, the only source of fluorine in each instance being the dissociation of a C–F bond.

The reaction of ArLi with $GeCl_4$ yielded a mixture of Ar_2GeCl_2 (**1b**) and $ArGeCl_3$ (**7b**) in a *ca.* 2 : 1 ratio. Both products were isolated and characterised by X-ray crystallography. The Ar′Li/Ar*Li mixture reacted similarly with $GeCl_4$ to give a solution containing predominantly $Ar^*_2GeCl_2$ (**4b**), according to the ^{19}F NMR spectra. This compound, too, was recrystallised and characterised by X-ray crystallography. A single ^{19}F resonance at −53.8 ppm was tentatively assigned to the symmetrical disubstituted isomer Ar'_2GeCl_2 (**3b**), particularly in view of the similarity of its shift to those of the fluorines in the o-CF_3 groups of **1b** (−54.4 ppm) and **7b** (−52.9 ppm). There were other small impurity peaks present, however, and the possibility that the signal at −53.8 ppm could arise from the monosubstituted precursor $Ar'GeCl_3$, which should also give a single ^{19}F resonance, cannot be entirely discounted.

Reaction of ArLi with $SnCl_4$ in a 2 : 1 molar ratio led to the isolation of mainly Ar_2SnCl_2 **1c**, together with a small quantity of $ArSnCl_3$ **7c**. Similar treatment of the Ar′Li/Ar″Li mixture with $SnCl_4$ yielded a solution containing mainly the more

Table 2 ^{19}F and ^{119}Sn NMR spectra (δ/ppm) for Ge(IV) and Sn(IV) compounds

	o-CF_3	$^4J_{Sn-F}$/Hz	p-CF_3	^{119}Sn
1b	−54.4 s (12F)		−64.1 s (6F)	
3b	−53.8 s (12F)[a]			
4b	−58.7 s (6F)		−64.1 s (6F)	
7b	−52.9 s (6F)		−63.5 s (3F)	
1c	−56.9 s (12F)[b]	10.0	−63.9 s (6F)	−146.7
3c	−56.7 s (12F)[b]	10.0		−141.1
4c	−58.9 s (6F)[c]		−63.8 s (6F)	−97.4
7c	−55.9 s (6F)[b]	19.2	−63.0 s (3F)	−140.7

[a] See Text. [b] (singlet) with Sn satellites. [c] Weak signal, Sn satellites unobserved.

Table 3 Selected bond distances (Å) and angles (°) in **7b**

Ge–C(1)	1.981(2)	C(1)–Ge–Cl(1)	113.72(4)
Ge–Cl(1)	2.1277(4)	C(1)–Ge–Cl(2)	111.89(6)
Ge–Cl(2)	2.1117(8)	Cl(1)–Ge–Cl(2)	108.46(2)
Ge ··· F(1)	2.909(2)	Cl(1)–Ge–Cl(1′)	99.82(3)
		Cl(1′)–Ge ··· F(1)	168.1(1)

sterically hindered disubstituted product Ar'_2SnCl_2 (**3c**), which has also been characterised crystallographically. The less hindered isomer $Ar^*_2SnCl_2$ (**4c**) was identified in solution from its ^{19}F and ^{119}Sn NMR spectra. The larger size of the Sn atom relative to Si and Ge must reduce the steric hindrance between ligands in these ψ-tetrahedral structures, which probably explains the reversal in isomeric ratio between **3** and **4**. ^{19}F and ^{119}Sn NMR data for new Ge and Sn compounds are listed in Table 2.

Molecular structures studied by single-crystal X-ray crystallography are shown in Figs. 1–4, while selected bond distances and angles are compared in Tables 3 and 4. It is noteworthy

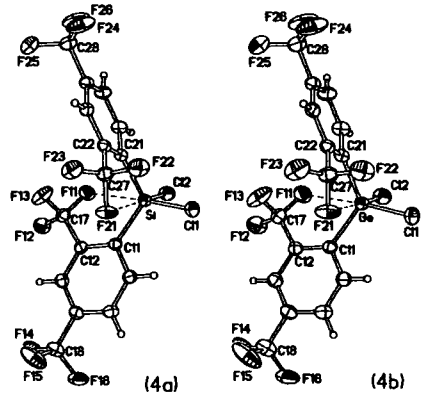

Fig. 1 Molecular structures of $Ar^*_2SiCl_2$ (**4a**) and $Ar^*_2GeCl_2$ (**4b**). Henceforth atomic displacement ellipsoids are drawn at 50% probability level.

Table 4 Selected bond distances (Å) and angles (°)

Compound E	4a Si	5 Si	1b Ge	4b Ge	1c Sn	3c Sn
E–C(11)	1.884(2)	1.899(2)	1.997(3)	1.958(2)	2.183(6)	2.177(2)
E–C(21)	1.884(2)	1.895(2)	2.017(3)	1.957(2)	2.195(6)	2.183(2)
E–Cl(1)	2.050(1)	1.579(1)[a]	2.1513(9)	2.1484(7)	2.326(2)	2.3266(7)
E–Cl(2)	2.048(1)	1.569(1)[a]	2.1174(9)	2.1496(7)	2.298(2)	2.3372(7)
C(11)–E–C(21)	117.47(8)	115.53(8)	120.07(12)	119.95(10)	120.3(2)	115.73(7)
C(11)–E–Cl(1)	108.88(6)	113.17(8)[a]	113.46(9)	107.77(7)	119.0(2)	120.66(6)
C(11)–E–Cl(2)	108.22(7)	105.27(7)[a]	103.34(9)	108.65(7)	96.1(2)	98.18(6)
C(21)–E–Cl(1)	108.00(7)	104.65(7)[a]	96.65(9)	108.26(7)	103.8(2)	100.96(6)
C(21)–E–Cl(2)	109.29(6)	113.76(7)[a]	118.17(9)	108.21(7)	113.9(2)	121.53(6)
Cl(1)–E–Cl(2)	104.17(5)	104.06(6)[a]	104.33(4)	102.64(3)	102.58(7)	100.11(3)
E ··· F(11)	2.901(2)	2.793(1)	2.757(2)	2.860(2)	2.720(4)	2.686(2)
E ··· F(21)	2.882(2)	2.745(1)	2.809(2)	2.848(2)	2.799(4)	2.768(1)
E ··· F(14)	–	–	3.379(2)	–	3.344(4)	–
E ··· F(15)	–	3.054(1)	3.399(2)	–	3.382(4)	3.203(2)
E ··· F(25)	–	3.073(1)	3.010(2)	–	2.979(3)	3.002(2)
Cl(1)–E ··· F(11)	174.30(4)	172.60(6)	167.77(5)	172.45(5)	170.6(1)	168.26(5)
Cl(2)–E ··· F(21)	176.92(4)	173.14(5)	169.32(5)	177.20(4)	170.3(1)	169.33(3)
C(11)–E ··· F(25)	–	160.3(1)	164.5(1)	–	164.6(2)	160.69(6)
C(21)–E ··· F(15)	–	160.5(1)	152.6(1)	–	154.1(2)	153.91(6)

[a] F ligands instead of Cl.

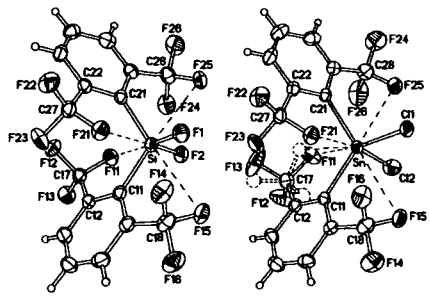

Fig. 2 Molecular structures of Ar'_2SiF_2 (5) and Ar'_2SnCl_2 (3c), showing the disorder of one *o*-CF_3 group in 3c.

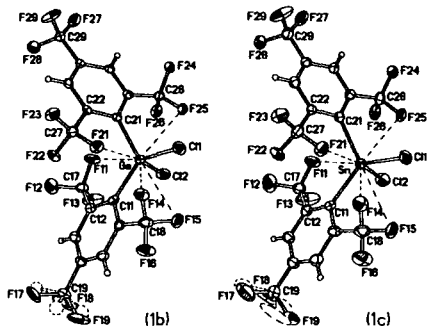

Fig. 3 Molecular structures of Ar_2GeCl_2 (1b) and Ar_2SnCl_2 (1c), showing the disorder of one *p*-CF_3 group.

that compound 4a is crystallographically isostructural (isomorphous) with 4b, and 1b with 1c. In molecules 1b and 1c, the *para*-CF_3 group of *one* Ar ligand is rotationally disordered;

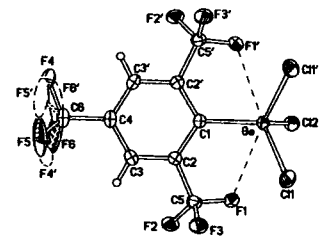

Fig. 4 Molecular structure of $ArGeCl_3$ (7b), showing the disorder of the *p*-CF_3 group. Atoms generated by the mirror plane are primed.

such disorder has been frequently observed for both Group 14[10,14c] and Group 15[3c,d,8] derivatives of Ar. In 3c, one *ortho*-CF_3 group is rotationally disordered.

Molecules of all the diaryl-dihalo compounds have no crystallographic symmetry and show a distorted tetrahedral coordination of the central atom (E), with the C–E–C bond angle the widest and the Cl–E–Cl angle (or F–E–F in 5) the smallest. This distortion can be explained by the steric repulsion between bulky aryl groups. However, the difference between these two angles is higher in 4b than in 4a, and in 1c than in 1b, *i.e.* the distortion *increases* with the increase of the E atom size, which should apparently relieve the steric overcrowding. It is also noteworthy that in Ar″ derivatives 4a and 4b all four Cl–E–C angles are similar, while in Ar and Ar′ derivatives 1b,c and 3c two Cl–E–C angles are much wider than the other two. The F–E–C angles in 5 show a similar, but more regular, distortion. These distortions are obviously due to the fact that both Ar and Ar′ ligands have two CF_3 groups in *ortho* positions to E and thus cause more steric overcrowding than Ar″, which has only one *ortho*-CF_3. Similar asymmetry has been observed earlier for $Ar_2EX(Y)$ compounds, where E = Si or Sn, X = F or Cl, and Y is a unidentate ligand.[9,10,14] Thus, in Ar_2SiF_2 the F–Si–C angles vary from 102.8(2) to 112.8(2)°,[9] and in Ar_2SiHF from 105.9(1) to 112.5(1)°.[10] Even larger variations occur in $Ar_2Sn(Cl)(\mu_2O)Sn(Cl)Ar_2$ (Cl–Sn–C angles 99.1(1)–119.7(1)°)[14a] and in $Ar_2Sn(F)L$, where L = *N*-(1-adamantyl)-[(pentafluoro-2-propenyl)thio]amine, $C_{13}H_{15}F_5NS$ (C–Sn–F angles 90.1(2)–107.7(2)°).[14c]

Molecule **7b** lies on a crystallographic mirror plane normal to the benzene ring and passing through the Ge, Cl(2), C(1) and C(4) atoms. Here the Ge atom also has distorted tetrahedral coordination and the CF_3 group in the *para*-position to the Ge is disordered between two orientations (related in this case by the mirror plane).

The E–F and E–Cl bonds in diaryldihalogenides are 0.03–0.05 Å longer than in the corresponding Group 14 tetrahalogenides, *viz.* SiF_4 (1.540(1) Å),[19a] $SiCl_4$ (2.008(1) Å),[19b] $GeCl_4$ (2.096(2) Å in the crystal,[20] 2.113(3) Å in the gas phase[21]) and $SnCl_4$ (2.279(3) Å).[22] The lengthening is obviously due to the replacement of the halogen by a less electronegative aryl ligand, and correspondingly the effect is smaller in the monoaryltrichloride **7b** (*ca.* 0.02 Å) than in the diaryl analogue **1b**, and it increases with decreasing number of electron-withdrawing CF_3 groups (compare **1b** with **4b**, and **1c** with **3c**).

Structural studies of Group 14 compounds containing *only* aryl and halogen ligands, are scarce, especially for Si and Ge. The Si–C bonds in Ph_3SiCl (1.862 Å)[23] are slightly shorter than in **4a** (1.884(2) Å), while still shorter Si–C bonds (*ca.* 1.84 Å) were found in two compounds where Si atoms are incorporated into fused-ring systems, *viz.* 9,9,10,10-tetrachloro-9,10-disila-9,10-dihydroanthracene[24] and 9,9-dichloro-9-sila-9-hydrofluorene.[25] The mean Si–C bond distance in **5** (1.897(2) Å) can be compared with those in **2** (1.901(5) Å),[9] Ar_2SiHF (1.906(5) Å),[10] and *o*-Tol_3SiF (1.861 Å).[26] Finally, comparison can be made with tetraaryl derivatives, *e.g.* $SiPh_4$[27] and $Si(p\text{-}Tol)_4$[28] with Si–C distances 1.877 and 1.873(3) Å, respectively. Thus halogeno ligands have no definite effect on the Si–C(aryl) bonds, while CF_3 substituents in the aryl ligands tend to weaken them, probably by diminishing the electron density on the benzene ring and hence the π back-donation.

No compound with Ge–C(aryl) *and* Ge–Cl bonds has been structurally characterised before, except 10,10-dichloro-10-germa-9-oxa-9,10-dihydroanthracene,[29] where the Ge–C bonds of 1.890 Å are incorporated into a fused-ring system. The Ge–C bonds in Ar derivative **1b** are 0.05 Å longer than in its Ar″ analogue **4b**, and in the latter nearly the same as in tetra-aryl compounds $GePh_4$[30] (1.957(4) Å) and $Ge(p\text{-}Tol)_4$[28] (1.948(5) Å). On the other hand, the Sn–C(Ar) bonds in **1c** are less than 0.01 Å longer than Sn–C(Ar′) in **3c**, and in both cases are substantially weaker than in Ph_2SnCl_2 (2.113(5) Å),[31] or $(mes)_2SnCl_2$, a non-fluorinated analogue of **1c** (2.117 Å).[32] Thus a CF_3 group in an *ortho* position affects an E–C bond much more than one in a *para* position, which can be attributed to higher steric overcrowding and direct $CF_3 \cdots E$ interactions (see below), rather than to mere electron withdrawing by this group. Indeed, bulkier *ortho*-substituents cause similar Sn–C(aryl) bond lengths even in the absence of fluorination, *e.g.* in $(2,4,6\text{-}Pr^i_3C_6H_2)_2SnCl_2$ (2.147(4) Å)[33] and $(2,4,6\text{-}Bu^t_3C_6H_2)_2SnCl_2$ (2.198(4) Å).[34]

Indeed, a salient feature of all the compounds studied herein is short intramolecular E ··· F contacts with *o*-CF_3 groups of the aryl ligands. Such contacts have been observed earlier in numerous Group 14 derivatives,[3a,9–16] as well as in some Group 15 compounds.[8] Although the van der Waals radii of Group 14 elements are difficult to determine directly (because these atoms are seldom exposed sufficiently to participate in intramolecular contacts), a variety of indirect techniques gives consistent values of 2.1 Å for Si and Ge and 2.25 Å for Sn.[35] Thus (assuming a radius of 1.5 Å for F), each molecule contains 2 to 5 E ··· F contacts well below the sum of the van der Waals radii, which are listed in Tables 3 and 4. These contacts can be compared also with the sums of "equilibrium" radii, the sums of which correspond to the minimum of the atom–atom potential curve and hence the point of zero van der Waals force,[36] *viz.* 2.26 Å (Si), 2.32 Å (Ge), 2.46 Å (Sn) and 1.65 Å (F).[35] Thus, insofar as van der Waals forces are concerned, the E ··· F interactions should be substantially repulsive. They, however, can be counterbalanced by electrostatic attraction (E and F carrying opposite charges) and/or weak ("secondary") coordination, *i.e.* donation of lone electron pairs of F into the outer-shell orbitals of E. The latter interpretation agrees with relatively high chemical stability of the compounds. It is also noteworthy that the Ge ··· F distances in **4b** are *shorter* by 0.04 Å than Si ··· F in the isostructural **4a**, which contradicts the simple repulsive model (the Ge atom is larger than Si), but can be explained by a weakly-bonding model (the outer orbitals of Ge are more diffuse and hence more suitable for interaction with F).

In the Ar″ derivatives **4a** and **4b**, the coordination of Si and Ge is complemented to (4 + 2) by the F(11) and F(21) atoms (belonging to different Ar″ ligands), approximately in *trans* positions to the chloro ligands; there is no other E ··· F contact within 3.7 Å. A similar pair of short E ··· F contacts exists in each of the bis-Ar and bis-Ar′ derivatives also (which can be regarded as evidence of specific character of these interactions), but the presence of two more *o*-CF_3 groups gives rise to additional, somewhat longer, E ··· F contacts. In the Ar′ derivatives **5** and **3c**, these "additional" *o*-CF_3 groups contribute one contact each, *viz.* E ··· F(15) and E ··· F(25), both approximately in *trans* positions to E–C bonds. The resulting (4 + 4) coordination of E can be described as a tetrahedron capped on each face. The same description was applied previously to the structures of Ar_2SiF_2[9] and Ar_2SiHF.[10] In **5**, the E ··· F(15) and E ··· F(25) distances are almost equal, while in **3c** they differ by 0.2 Å. This non-equivalence is obviously connected with strongly asymmetric distortions of bond angles (between covalent bonds) at the Sn atom, the causes of which are unclear. In **1b** and **1c**, one of the *o*-CF_3 groups adopts a different orientation: instead of one F atom pointing roughly towards the E atom, there are two longer contacts, E ··· F(14) and E ··· F(15), the E atom lying close to the bisectral plane of the F(14)C(18)F(15) angle.

Molecule **7b** contains two (symmetrically related) Ge ··· F(1) contacts in *trans* positions to Cl(1) and its equivalent. It is noteworthy that the Ge–Cl(1) bond is 0.016 Å longer than Ge–Cl(2), which suggests a certain (if small) covalent character of the Ge ··· F(1) interaction.

Experimental

All manipulations, including NMR sample preparation, were carried out either under an inert atmosphere of dry nitrogen or *in vacuo*, using standard Schlenk procedures or a glovebox. Chemicals of the best available commercial grades were used, in general without further purification. ^{19}F NMR spectra were recorded on a Varian Mercury 200, Varian VXR 400, or Varian Inova 500 Fourier-transform spectrometer at 188.18, 376.35, and 470.26 MHz, respectively. ^{119}Sn NMR spectra were recorded on the Varian Inova 500 spectrometer at 186.37 MHz. Chemical shifts were measured relative to external $CFCl_3$ (^{19}F) or Me_4Sn (^{119}Sn), with the higher frequency direction taken as positive. Microanalyses were performed by the microanalytical services of the Department of Chemistry, University of Durham.

Syntheses

Lithiation reactions were carried out as described previously.[4,8,37] **WARNING**: It is important in these reactions to keep a slight excess of the hydrocarbon (ArH or Ar′H) to *n*-butyllithium at all times, to avoid any attack on a CF_3 group and the possible **explosive** formation of LiF.

Ar_2SiF_2 (2). A solution of ArLi (100 ml, 30 mmol) in diethyl ether was added dropwise to a solution of $SiCl_4$ (2.5 g, 1.72 ml, 15 mmol) in hexanes at −78 °C. The solution was allowed to warm to room temperature and stirred for 5 h. A precipate formed. The solution was filtered and solvents were removed

under vacuum, leaving a yellow oil. This oil was distilled under reduced pressure (0.01 Torr), giving a yellow oil, bp 85 °C. Yield 1.8 g (19% based on ArH). Anal. Calc. for $C_{18}H_4F_{20}Si$: C 34.41, H 0.64. Found: C 32.9, H 0.75%.

Ar''_2SiCl_2 (4a). An Ar′Li/Ar″Li (50 ml, 20 mmol) solution in diethyl ether was added dropwise to a solution of $SiCl_4$ (1.7 g, 10 mmol) in pentane at −78 °C. The solution was allowed to warm to room temperature and stirred for 3 h. The precipitated LiCl was filtered off and the solvents and excess $SiCl_4$ were removed under vacuum, leaving a yellow sticky oil which was distilled under reduced pressure (0.01 Torr). The fraction collected at 120 °C was recrystallised from pentane, yielding 1.8 g (32.4%) of **4a**. Anal. Calc. for $C_{16}H_6Cl_2F_{12}Si$: C 36.6, H 1.15. Found: C 36.8, H 1.24%.

Ar'_2SiF_2 (5). An Ar′Li/Ar″Li (50 ml, 40 mmol) solution in diethyl ether was added dropwise to a solution of $SiCl_4$ (3.39 g, 2.3 ml, 20 mmol) in hexanes at −78 °C. The solution was allowed to warm to room temperature and stirred for 3 h. The precipitated LiCl was filtered off, and the solvents and excess $SiCl_4$ were removed under vacuum, leaving a yellow oil (**4a**) and a white solid. The solid was washed three times with hexanes and purified by sublimation under vacuum, giving white crystals of **5**. Yield: 2.5 g (12.7%). Anal. Calc. for $C_{16}H_6F_{14}Si$: C 39.04, H 1.23. Found: C 38.3, H 1.24%.

Ar_2GeCl_2 (1b) and $ArGeCl_3$ (7b). An ArLi (50 ml, 30 mmol) solution in diethyl ether was added dropwise to a $GeCl_4$ solution (3.2 g, 1.71 ml, 15 mmol) in hexanes at −78 °C. The solution was allowed to warm to room temperature and stirred for 4 h. A white precipitate of LiCl appeared and was filtered off. The solvents and excess $GeCl_4$ were removed under vacuum, leaving a yellow oil and a white solid. The oil was filtered and then distilled under reduced pressure (0.01 Torr), giving a colourless oil, bp 85 °C. Analysis showed that this was impure but contained mainly **7b**. Yield: 2.6 g (19%). After one month, fine crystals of **7b** formed. There was insufficient material for further analysis but a single-crystal X-ray structure determination was carried out. The filtered-off solid was washed three times with hexanes, yielding 3.17 g (30%) of **1b**. Crystals were grown from dichloromethane. Anal. Calc. for $C_{18}H_4Cl_2F_{18}Ge$: C 30.64, H 0.57. Found C: 30.59, H 0.58%

Ar''_2GeCl_2 (4b). A solution of Ar′Li/Ar″Li (60 ml, 40 mmol) in diethyl ether was added dropwise to a solution of $GeCl_4$ (4.29 g, 2.6 ml, 20 mmol) in diethyl ether at −78 °C. The solution was allowed to warm to room temperature and stirred for 2 h. A white precipitate of LiCl formed. The solution was filtered and the solvents were removed under vacuum, leaving a black oil. The oil was distilled under reduced pressure (0.01 Torr), and a fraction was collected at 80–90 °C. Yield: 5.8 g (51%). After one week, small crystals formed. Anal. Calc. for $C_{16}H_6Cl_2F_{12}Ge$: C 33.7, H 1.06, Cl 12.45. Found: C 32.4, H 1.53, Cl 12.8%.

Ar_2SnCl_2 (1c) and $ArSnCl_3$ (7c). An ArLi (50 ml, 30 mmol) solution in diethyl ether was added slowly to a solution of $SnCl_4$ (3.90 g, 2.75 ml, 15 mmol) in hexanes. The solution was then allowed to warm to room temperature and stirred for 5 h. A white precipitate of LiCl appeared. The solution was filtered and the solvents were removed under vacuum, leaving a brown oil and a solid. The oil was filtered and distilled under reduced pressure, giving a yellow oil of **7c** (bp 85 °C) in a small quantity. The solid (**1c**) was washed three times with hexanes, dried under vacuum and recrystallised from diethyl ether. Yield 3.8 g (51%). Anal. Calc. for $C_{18}H_4Cl_2F_{18}Sn$: C 28.76, H 0.54. Found: C 28.60, H 0.78%.

Ar'_2SnCl_2 (3c) and Ar''_2SnCl_2 (4c). An Ar′Li/Ar″Li (250 ml, 94 mmol) solution in diethyl ether was added dropwise to

Table 5 Crystallographic data

Compound	**4a**	**5**	**1b**	**4b**	**7b**	**1c**	**3c**
CCDC No.	205552	205553	205554	205556	205555	205557	205558
Formula	$C_{16}H_6Cl_2F_{12}Si$	$C_{16}H_6F_{14}Si$	$C_{18}H_4Cl_2F_{18}Ge$	$C_{18}H_4Cl_2F_{18}Ge$	$C_6H_2Cl_4F_4Ge$	$C_{18}H_4Cl_2F_{18}Sn$	$C_{18}H_4Cl_2F_{18}Sn$
Formula weight	525.20	492.30	705.70	569.70	460.05	751.80	615.80
Crystal system	Monoclinic	Triclinic	Monoclinic	Monoclinic	Orthorhombic	Monoclinic	Triclinic
Space group	$P2_1/n$ (no. 14)	$P\bar{1}$ (no. 2)	$P2_1/n$ (no. 14)	$P2_1/n$ (no. 14)	*Pnma* (no. 62)	$P2_1/c$ (no. 14)	$P\bar{1}$ (no. 2)
Crystal size /mm	0.40 × 0.40 × 0.26	0.32 × 0.25 × 0.12	0.34 × 0.20 × 0.08	0.4 × 0.12 × 0.12	0.40 × 0.28 × 0.28	0.46 × 0.22 × 0.06	0.5 × 0.4 × 0.38
T/K	120	120	120	150	120	150	150
a/Å	10.429(7)	8.221(2)	8.3893(6)	10.547(2)	11.284(1)	8.465(1)	8.783(2)
b/Å	11.534(7)	9.644(2)	30.043(2)	11.661(2)	12.541(1)	30.409(4)	9.095(2)
c/Å	16.608(10)	12.267(3)	8.6373(6)	16.636(3)	9.710(3)	8.724(1)	12.162(3)
α/°	90.00	98.48(1)	90.00	90.00	90.00	90.00	81.697(4)
β/°	107.84(2)	100.30(1)	96.433(1)	108.21(1)	90.00	96.635(2)	83.970(4)
γ/°	90.00	112.50(1)	90.00	90.00	90.00	90.00	82.135(4)
V/Å^3	1902(2)	858.8(4)	2163.2(3)	1943.7(6)	1374.1(5)	2230.6(5)	948.7(4)
Z	4	2	4	4	4	4	2
D_c/g cm^{-1}	1.834	1.904	2.167	1.947	2.224	2.239	2.156
μ/mm^{-1}	0.520	0.284	1.826	1.964	2.906	1.543	1.744
Reflections, total	17420	6314	16108	14919	11660	11861	7949
Reflections, unique	5059	3601	4795	5376	1921	4298	5003
R_{int}	0.032	0.022	0.042	0.033	0.022	0.052	0.015
Refls. with $I > 2\sigma(I)$	4018	2970	3860	3900	1745	3130	4708
$R[I > 2\sigma(I)]$	0.036	0.034	0.041	0.036	0.022	0.052	0.025
$wR_2(F^2)$, all data	0.094	0.084	0.085	0.087	0.056	0.117	0.069
No. of variables	304	280	365	304	125	345	299

a solution of $SnCl_4$ (12.24 g, 8.63 ml, 47 mmol) at room temperature. The solution was stirred for 4 h. A white precipitate of LiCl appeared. The brown solution was filtered and solvents and excess $SnCl_4$ were removed under vacuum, leaving a brown sticky oil and a brown solid. The oil (**4c**) was filtered, the solid washed with pentane and dichloromethane and dried *in vacuo*, giving a beige solid (**3c**), which was recrystallised from pentane and diethyl ether. Yield (**3c**) 3.48 g (57%). Anal. Calc. for $C_{16}H_6Cl_2F_{12}Sn$: C 31.21, H 0.98. Found C 29.7, H 1.26%.

X-Ray crystallography

Single crystal X-ray diffraction experiments were carried out at low temperature, 120 or 150 K, using graphite-monochromated Mo-Kα radiation (λ = 0.71073 Å) on a Bruker SMART (CCD 1 K area detector) diffractometer equipped with a Cryostream N_2 open-flow cooling device.[38] Series of narrow ω-scans (0.3°) were performed at several ϕ-settings in such a way as to cover a sphere of reciprocal space to a maximum resolution between 0.70 and 0.77 Å. Cell parameters were determined and refined using the SMART software,[39] and raw frame data were integrated using the SAINT program.[40] The structures were solved by direct methods and refined by full-matrix least squares on F^2 using SHELXTL software.[41] Crystal data and experimental details are listed in Table 5. For structure **4b**, the reflection intensities were corrected by numerical integration based on measurements and indexing of the crystal faces (using SHELXTL software).[41] For the remaining structures, the absorption corrections were carried out by the multi-scan method, based on multiple scans of identical and Laue equivalent reflections (using the SADABS software).[42] Non-hydrogen atoms were refined anisotropically, except for the disordered component of structure **1b**. For structures **4a,b** and **7b** the hydrogen atoms were found in difference Fourier maps. For structures, **1b,c**, **3c** and **5** the hydrogen atoms were positioned geometrically and refined using a riding model.

CCDC reference numbers 205552–205558.

See http://www.rsc.org/suppdata/dt/b3/b302544f/ for crystallographic data in CIF or other electronic format.

Acknowledgements

We thank the EPSRC for the award of studentships (to S. M. C. and A. L. T.), the CVCP for an ORS award (to B. Y. X.), and A. M. Kenwright, C. F. Hefferman and I. H. McKeag for assistance in recording some of the NMR spectra.

References

1 (*a*) R. D. Schluter, A. H. Cowley, D. A. Atwood, R. A. Jones, M. R. Bond and C. J. Carrans, *J. Am. Chem. Soc.*, 1993, **115**, 2070; (*b*) R. D. Schluter, H. S. Isom, A. H. Cowley, D. A. Atwood, R. A. Jones, F. Olbrick, S. Corbelin and R. J. Lagow, *Organometallics*, 1994, **13**, 4058; (*c*) K. B. Dillon and H. P. Goodwin, *J. Organomet. Chem.*, 1994, **469**, 125; (*d*) M. Belay and F. T. Edelmann, *J. Organomet. Chem.*, 1994, **479**, C21; (*e*) C. Bartolomé, P. Espinet, J. Villafañe, S. Giesa, A. Martin and A. G. Orpen, *Organometallics*, 1996, **15**, 2019; (*f*) P. Espinet, S. Martin-Barrios, J. Villafañe, P. G. Jones and A. K. Fischer, *Organometallics*, 2000, **19**, 290.

2 (*a*) V. C. Gibson, C. Redshaw, L. J. Sequeira, K. B. Dillon, W. Clegg and M. R. Elsegood, *Chem. Commun.*, 1996, 2151; (*b*) K. B. Dillon, V. C. Gibson, J. A. K. Howard, L. J. Sequeira and J. W. Yao, *Polyhedron*, 1996, **15**, 4173; (*c*) K. B. Dillon, V. C. Gibson, J. A. K. Howard, C. Redshaw, L. J. Sequeira and J. W. Yao, *J. Organomet. Chem.*, 1997, **528**, 179; (*d*) A. S. Batsanov, K. B. Dillon, V. C. Gibson, J. A. K. Howard, L. J. Sequeira and J. W. Yao, *J. Organomet. Chem.*, 2001, **631**, 181.

3 (*a*) H. Grützmacher, H. Pritzkow and F. T. Edelmann, *Organometallics*, 1991, **10**, 23; (*b*) S. Brooker, J.-K. Buijink and F. T. Edelmann, *Organometallics*, 1991, **10**, 25; (*c*) K. H. Whitmire, D. Labahn, H. W. Roesky, M. Noltemeyer and G. M. Sheldrick, *J. Organomet. Chem.*, 1991, **402**, 55; (*d*) N. Burford, C. L. B. Macdonald, D. J. LeBlanc and T. S. Cameron, *Organometallics*, 2000, **19**, 152.

4 (*a*) M. Scholz, H. W. Roesky, D. Stalke, K. Keller and F. T. Edelmann, *J. Organomet. Chem.*, 1989, **366**, 73; (*b*) M. Abe, K. Toyota and M. Yoshifuji, *Chem. Lett.*, 1992, 2349; (*c*) K. B. Dillon and H. P. Goodwin, *J. Organomet. Chem.*, 1992, **429**, 169; (*d*) M. G. Davidson, K. B. Dillon, J. A. K. Howard, S. Lamb and M. D. Roden, *J. Organomet. Chem.*, 1998, **550**, 481; (*e*) K. B. Dillon, H. P. Goodwin, T. A. Straw and R. D. Chambers, *Proc. Euchem. PSIBLOCS Conf.*, Paris-Palaiseau, 1998; (*f*) A. S. Batsanov, S. M. Cornet, L. A. Crowe, K. B. Dillon, R. K. Harris, P. Hazendonk and M. D. Roden, *Eur. J. Inorg. Chem.*, 2001, 1729.

5 J.-T. Ahlemann, A. Künzel, H. W. Roesky, M. Noltemeyer, L. Markovskii and H.-G. Schmidt, *Inorg. Chem.*, 1996, **35**, 6644.

6 J. Escudié, C. Couret, H. Ranaivonjatovo, M. Lazraq and J. Satgé, *Phosphorus Sulfur*, 1987, **31**, 27.

7 (*a*) L. Heuer, P. G. Jones and R. Schmutzler, *J. Fluorine Chem.*, 1990, **46**, 243; (*b*) H.-J. Kroth, H. Schumann, H. G. Kuivila, C. D. Schaeffer, Jr. and J. J. Zuckerman, *J. Am. Chem. Soc.*, 1975, **97**, 1754.

8 A. S. Batsanov, S. M. Cornet, K. B. Dillon, A. E. Goeta, P. Hazendonk and A. L. Thompson, *J. Chem. Soc., Dalton Trans.*, 2002, 4622.

9 J.-K. Buijink, M. Noltemeyer and F. T. Edelmann, *J. Fluorine Chem.*, 1993, **61**, 51.

10 J. Braddock-Wilking, M. Schieser, L. Brammer, J. Huhmann and R. Shaltout, *J. Organomet. Chem.*, 1995, **499**, 89.

11 J. E. Bender IV, M. M. Banaszak Holl, A. Mitchell, N. J. Wells and J. W. Kampf, *Organometallics*, 1998, **17**, 5166.

12 A. Vij, R. L. Kirchmeier, R. D. Willett and J. M. Shreeve, *Inorg. Chem.*, 1994, **33**, 5456.

13 (*a*) H. Grützmacher and H. Pritzkow, *Angew. Chem., Int. Ed. Engl.*, 1991, **30**, 1017; (*b*) H. Grützmacher, S. Freitag, R. Herbst-Irmer and G. S. Sheldrick, *Angew. Chem., Int. Ed. Engl.*, 1992, **31**, 437; (*c*) V. Lay, H. Pritzkow and H. Grützmacher, *J. Chem. Soc., Chem. Commun.*, 1992, 260; (*d*) H. Grützmacher and H. Pritzkow, *Chem. Ber.*, 1993, **126**, 2409; (*e*) H. Grützmacher, W. Deek, H. Pritzkow and M. Sander, *Angew. Chem., Int. Ed. Engl.*, 1994, **33**, 456.

14 (*a*) S. Brooker, F. T. Edelmann and D. Stalke, *Acta Crystallogr., Sect. C*, 1991, **47**, 2527; (*b*) J. F. Van der Maelen Uria, M. Belay, F. T. Edelmann and G. M. Sheldrick, *Acta Crystallogr., Sect. C*, 1994, **50**, 403; (*c*) S. Freitag, R. Herbst-Irmer, J. T. Ahlemann and H. W. Roesky, *Acta Crystallogr., Sect. C*, 1995, **51**, 631.

15 (*a*) J. E. Bender IV, M. M. Banaszak Holl and J. W. Kampf, *Organometallics*, 1997, **16**, 2743; (*b*) J. E. Bender IV, A. J. Shusterman, M. M. Banaszak Holl and J. W. Kampf, *Organometallics*, 1999, **18**, 1547.

16 K. W. Klinkhammer, T. F. Fassler and H. Grützmacher, *Angew. Chem., Int. Ed.*, 1998, **37**, 124.

17 M. P. Bigwood, P. J. Corvan and J. J. Zuckerman, *J. Am. Chem. Soc.*, 1981, **103**, 7643.

18 (*a*) *Thermodynamical Properties of Individual Substances*, ed. L. V. Gurvich, I. V. Veits and S. B. Alcock, Hemisphere Publ. Corp., Washington DC, 4th edn., 1991, vol. 2, pt. 1; (*b*) *Handbook of Chemistry and Physics*, ed. D. R. Lide, CRC Press, Boca Raton, FL, USA, 76th edn., 1995–1996; (*c*) S. S. Batsanov, *Strukturnaya Khimiya*, Dialog MGU, Moscow, 2000 (in Russian).

19 (*a*) D. Mootz and L. Kortle, *Z. Naturforsch., Teil B*, 1984, **39**, 1295; (*b*) L. N. Zakharov, M. Yu. Antipin, Yu. T. Struchkov, A. V. Gusev, A. M. Gubin and N. V. Zhernenkov, *Kristallografiya*, 1986, **31**, 171.

20 K. Merz and M. Driess, *Acta Crystallogr., Sect. C*, 2002, **58**, i101.

21 Y. Morino, Y. Nakamura and T. Iijima, *Chem. Phys.*, 1960, **95**, 643.

22 H. Reuter and R. Pawlak, *Z. Anorg. Allg. Chem.*, 1999, **626**, 925.

23 E. B. Lobkovskii, V. N. Fokin and K. N. Semenenko, *Zh. Strukt. Khim.*, 1981, **22**(4), 152.

24 V. A. Sharapov, A. I. Gusev, Yu. T. Struchkov, N. G. Komalenkova, L. N. Shamshin and E. A. Chernyshev, *Zh. Strukt. Khim.*, 1980, **21**(6), 114.

25 Y. Liu, T. C. Stringfellow, D. Ballweg, I. A. Guzei and R. West, *J. Am. Chem. Soc.*, 2002, **124**, 49.

26 S. Dell, D. M. Ho and R. A. Pascal, Jr., *J. Org. Chem.*, 1999, **64**, 5626.

27 V. Gruhnert, A. Kirfel, G. Will, F. Wallrafen and K. Recker, *Z. Kristallogr.*, 1983, **163**, 53.

28 M. Charisse, S. Roller and M. Drager, *J. Organomet. Chem.*, 1992, **427**, 23.

29 A. I. Udel'nov, V. E. Shklover, N. G. Bokii, E. A. Chernyshev, T. L. Krasnova, E. F. Shchipanova and Yu. T. Struchkov, *Zh. Strukt. Khim.*, 1974, **15**, 83.

30 A. Karipides and D. A. Haller, *Acta Crystallogr., Sect. B*, 1972, **28**, 2889.

31 P. T. Greene and R. F. Bryan, *J. Chem. Soc. A*, 1971, 2549.

32 T. Krauter and B. Neumuller, *Z. Naturforsch., Teil B*, 1998, **53**, 503.
33 H. K. Sharma, F. Cervantes-Lee, J. S. Mahmoud and K. H. Pannell, *Organometallics*, 1999, **18**, 399.
34 M. Weidenbruch, K. Schafers, S. Pohl, W. Saak, K. Peters and H. G. von Schnering, *J. Organomet. Chem.*, 1988, **346**, 171.
35 S. S. Batsanov, *Inorg. Mater.*, 2001, **37**, 871.
36 N. L. Allinger, *Adv. Phys. Org. Chem.*, 1976, **13**, 1.
37 G. E. Carr, R. D. Chambers, T. F. Holmes and D. G. Parker, *J. Organomet. Chem.*, 1987, **325**, 13.
38 J. Cosier and A. M. Glazer, *J. Appl. Crystallogr.*, 1986, **19**, 105.
39 SMART-NT, Data Collection Software, version 5.0; Bruker Analytical X-ray Instruments Inc., Madison, WI, USA, 1999.
40 SAINT-NT, Data Reduction Software, version 5.0; Bruker Analytical X-ray Instruments Inc., Madison, WI, USA, 1999.
41 SHELXTL, version 5.1, Bruker Analytical Instruments Inc., Madison, WI, USA, 1999.
42 G. M. Sheldrick, SADABS, Empirical Absorption Correction Program, University of Göttingen, Germany, 1998.

C.8 Group 15 Compounds Containing Ar, Ar′ & Ar″ Ligands

DALTON
FULL PAPER

New group 15 compounds containing the 2,4,6-$(CF_3)_3C_6H_2$ (fluoromes = Ar), 2,6-$(CF_3)_2C_6H_3$ (fluoroxyl = Ar′) or 2,4-$(CF_3)_2C_6H_3$ (Ar″) ligands

Andrei S. Batsanov,[a] Stéphanie M. Cornet,[a] Keith B. Dillon,*[a] Andrés E. Goeta,[a] Paul Hazendonk[b] and Amber L. Thompson[a]

[a] *Chemistry Department, University of Durham, South Road, Durham, UK DH1 3LE*
[b] *Department of Chemistry and Biochemistry, University of Lethbridge, 4401 University Drive, Lethbridge, Alberta, Canada T1K 3M4*

Received 25th July 2002, Accepted 2nd October 2002
First published as an Advance Article on the web 11th November 2002

Several new P or As compounds containing the 2,4,6-$(CF_3)_3C_6H_2$ (Ar), 2,6-$(CF_3)_2C_6H_3$ (Ar′) and/or 2,4-$(CF_3)_2C_6H_3$ (Ar″) ligands have been synthesised, and characterised by multinuclear NMR spectroscopy and (for all isolated compounds) elemental analysis. The crystal and molecular structures of $ArPBr_2$ **1**, Ar_2PCl **2**, Ar''_2PCl **3**, Ar''_2PBr **4**, Ar′Ar″AsCl **5**, Ar′Ar″AsBr **6** and Ar′Ar″AsH **7** have been determined by single-crystal X-ray diffraction. A particularly interesting feature of these structures is close contacts between *ortho*-fluorines and the P or As atoms, as observed previously in Ar′Ar″PCl and Ar_2AsCl.

Introduction

The ability of the 2,4,6-$(CF_3)_3C_6H_2$ (fluoromes = Ar) group to stabilise both main group and transition metal species is well-documented.[1–25] Comparatively little has been published about the 2,6-$(CF_3)_2C_6H_3$ (fluoroxyl = Ar′) group as a substituent, however,[6,24,26–28] partly because there are complications in the chemistry of the precursor 1,3-bis(trifluoromethyl)benzene, Ar′H.[24,27,28] This can lithiate in two positions, giving rise to a mixture of 2,6-$(CF_3)_2C_6H_3$ (Ar′) and 2,4-$(CF_3)_2C_6H_3$ (Ar″) derivatives. The latter ligand is unlikely to stabilise low-coordinate species such as diphosphenes, because of only one bulky substituent in the *ortho*-position. In group 15, the hydrides and halides $ArPH_2$,[1,2] $ArPCl_2$,[1,2] ArPClF,[1] $ArPF_2$,[1] $Ar'PH_2$,[26] $Ar'PCl_2$,[26] Ar_2PH,[20] Ar_2PCl,[1] Ar′Ar″PCl,[24] Ar′Ar″PF,[27] Ar''_2PF,[27] $ArAsCl_2$,[16] Ar_2AsH,[2] Ar_2AsCl,[22] Ar_2AsF,[2] $ArSbCl_2$,[1] Ar_2SbCl,[1,21,22] Ar_2BiCl[5] and Ar_3Bi[5] have been reported. Of these, only Ar′Ar″PCl,[24] Ar_2AsCl,[22] Ar_2SbCl,[22] Ar_2BiCl[5] and Ar_3Bi[5] have been characterised crystallographically. In a very recent paper we described the synthesis, X-ray crystal structure and a detailed multinuclear NMR study in both solid state and solution of Ar′Ar″PCl.[24] In the present work, we report the synthesis and characterisation of several new group 15 derivatives containing Ar, Ar′ and/or Ar″ substituents. The X-ray crystal and molecular structures have been determined at low temperature for $ArPBr_2$ **1**, Ar_2PCl **2**, Ar''_2PCl **3**, Ar''_2PBr **4**, Ar′Ar″AsCl **5**, Ar′Ar″AsBr **6** and Ar′Ar″AsH **7**.

Results and discussion

The halogeno-derivatives were synthesised by reaction of the appropriate group 15 trihalide with the lithiated materials ArLi (from ArH) or a mixture of Ar′Li/Ar″Li (from Ar′H), as shown in Schemes 1 and 2, respectively. Even when an excess of the halide was used, some of the twice-substituted derivative Ar_2EX (except for Ar_2PBr), Ar′Ar″EX or Ar''_2EX (E = P or As; X = Cl or Br) was isolated, as described for Ar′Ar″AsCl **5** and Ar''_2PCl **3**. No evidence was found in the Ar′Li/Ar″Li reactions for the formation of the more sterically hindered second substitution product Ar'_2EX. The compounds could be identified by means of their ^{19}F and (where appropriate) ^{31}P NMR solution-state spectra (Experimental section). The hydrido-species

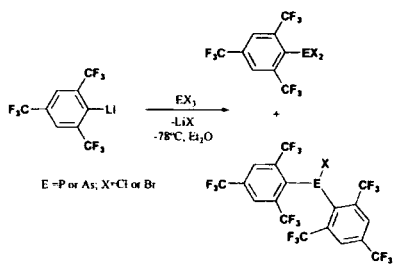

Scheme 1 Reaction of ArLi with EX_3 (E = P or As; X = Cl or Br).

Ar′Ar″PH **8** and Ar′Ar″AsH **7** were prepared by $LiAlH_4$ reduction of the corresponding chlorides; the synthesis of Ar′Ar″PCl, and its X-ray crystal structure, have been described in a previous paper.[24]

A mixture of the chloro-derivatives ArAr′PCl **9** and ArAr″PCl **10** was also prepared by reaction of Ar′Li/Ar″Li with $ArPCl_2$ in an overall 1:1 molar ratio. Both compounds could be distinguished by their ^{19}F and ^{31}P NMR solution spectra, but they could not be separated by distillation.

A very notable feature of the room temperature ^{19}F NMR spectra for all compounds with one Ar″ substituent and one Ar or Ar′ substituent was the occurrence of a broad, unresolved resonance for the two *ortho*-CF_3 groups of the Ar or Ar′ moiety. Similar observations have been reported previously by us for Ar′Ar″PCl,[24] and in the literature for Ar′Ar″PF[27] and Cp*ArPCl,[29] with $^4J_{PF}$ not resolved, although interestingly a $^4J_{PF}$ value of 31.6 Hz was recorded for Cp*ArPH.[29] These results suggest strongly that there is a rotational barrier present in the more sterically hindered species. A detailed ^{19}F NMR temperature-dependence study is in progress, together with theoretical calculations, and these results will be reported elsewhere when complete.[30]

Eight of the compounds have been isolated as solids, and low-temperature X-ray crystal structures have been determined for seven of these. The only failure was Ar′Ar″PH **8**, for which

 DOI: 10.1039/b207327g

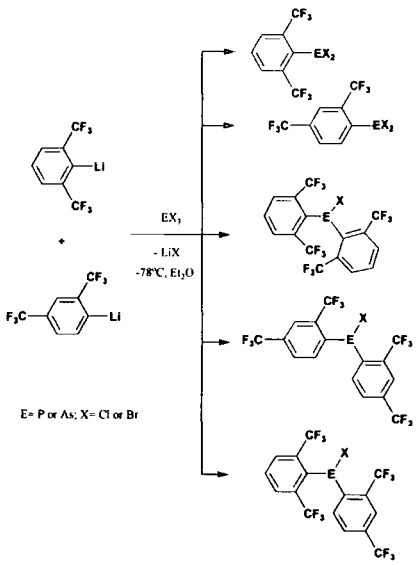

Scheme 2 Reaction of Ar′Li/Ar″Li with EX_3 (E = P or As; X = Cl or Br).

data were collected but the structure could not be solved, because of poor crystal quality. The crystal and molecular structures have been established for $ArPBr_2$ **1**, Ar_2PCl **2**, Ar''_2PCl **3**, Ar''_2PBr **4**, Ar′Ar″AsCl **5**, Ar′Ar″AsBr **6** and Ar′Ar″-AsH **7**; these are illustrated in Figs. 1–7, respectively. Selected

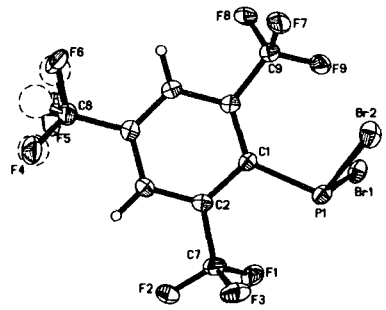

Fig. 1 Thermal ellipsoid drawing of $ArPBr_2$ **1**, showing 50% probability displacement ellipsoids for non-H atoms, and the disorder in the *p*-CF_3 group.

bond distances and angles are listed in Table 1 for phosphorus compounds and in Table 2 for arsenic derivatives. It is noteworthy that the crystals of **3** and **4** are isomorphous, while **5** is isomorphous with **6**.

Compound **1** crystallises with two independent molecules in the asymmetric unit, as shown in Fig. 1 and Table 1. The October 2001 release of the Cambridge Structural Database (Version 5.22)[31] contains only three structures of $RPBr_2$ compounds, *viz.* $Ph_3P{=}C(Me)PBr_2$,[32] $Ph_3P{=}C(SiMe_3)PBr_2$[32] and

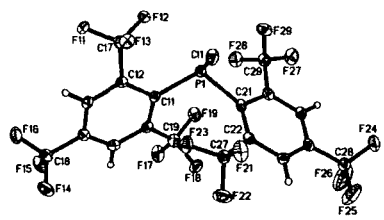

Fig. 2 Thermal ellipsoid drawing of Ar_2PCl **2**, showing 50% probability displacement ellipsoids for non-H atoms.

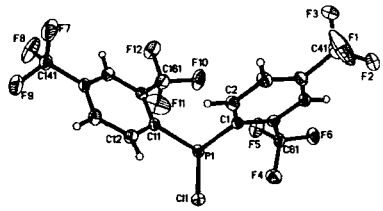

Fig. 3 Thermal ellipsoid drawing of Ar''_2PCl **3**, showing 50% probability displacement ellipsoids for non-H atoms.

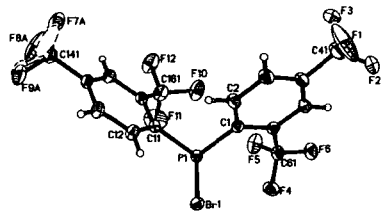

Fig. 4 Thermal ellipsoid drawing of Ar''_2PBr **4**, showing 50% probability displacement ellipsoids for non-H atoms, and the disorder in one of the *p*-CF_3 groups.

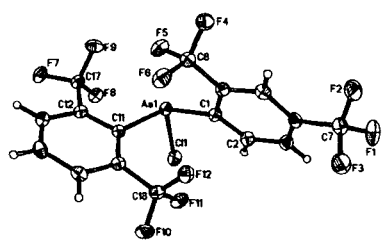

Fig. 5 Thermal ellipsoid drawing of Ar′Ar″AsCl **5**, showing 50% probability displacement ellipsoids for non-H atoms.

$C_5H(CHMe_2)_4PBr_2$.[33] The Br–P–Br angle in these compounds is smaller than in **1**, ranging from 93.5(1) to 96.06(7)°,[32] it is noteworthy, however, that the sum of the bond angles around phosphorus is also larger in **1** (*ca.* 310°) compared with the first two compounds above, where it varies from 295.8[32] to 305.7°,[31,33] reflecting the greater steric demands of the *ortho*-CF_3 groups. The P–Br bond lengths in **1** and **4** are slightly shorter than usually found in organophosphorus bromides (*e.g.* values between 2.268(2) and 2.489(3) Å),[32–38] although shorter

Table 1 Selected bond distances (Å) and angles (°) for phosphorus compounds 1–4

$ArPBr_2$ 1				Ar_2PCl 2			Ar''_2PCl 3			Ar''_2PBr 4		
P(1)–Br(1)	2.2228(8)	P(2)–Br(3)	2.2166(8)	P(1)–Cl(1)	2.0628(10)		P(1)–Cl(1)	2.0619(9)		P(1)–Br(1)	2.2340(5)	
P(1)–Br(2)	2.2153(8)	P(2)–Br(4)	2.2194(8)	P(1)–C(11)	1.882(3)		P(1)–C(1)	1.854(2)		P(1)–C(1)	1.8572(18)	
P(1)–C(1)	1.879(3)	P(2)–C(11)	1.887(3)	P(1)–C(21)	1.885(3)		P(1)–C(11)	1.857(2)		P(1)–C(11)	1.8591(17)	
C(1)–P(1)–Br(2)	102.10(8)	C(11)–P(2)–Br(4)	102.41(8)	C(11)–P(1)–C(21)	109.87(12)		C(1)–P(1)–C(11)	100.37(10)		C(1)–P(1)–C(11)	100.51(8)	
C(1)–P(1)–Br(1)	102.52(9)	C(11)–P(2)–Br(3)	103.22(8)	C(11)–P(1)–C(1)	103.68(9)		C(1)–P(1)–C(1)	97.38(7)		C(1)–P(1)–Br(1)	96.99(6)	
Br(2)–P(1)–Br(1)	105.35(3)	Br(3)–P(2)–Br(4)	104.90(3)	C(21)–P(1)–C(1)	92.95(9)		C(11)–P(1)–C(1)	100.95(7)		C(11)–P(1)–Br(1)	101.63(6)	

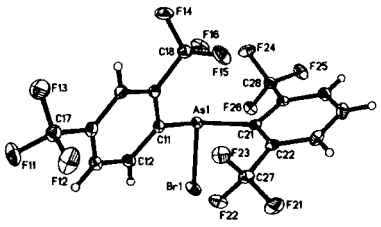

Fig. 6 Thermal ellipsoid drawing of Ar′Ar″AsBr **6**, showing 50% probability displacement ellipsoids for non-H atoms.

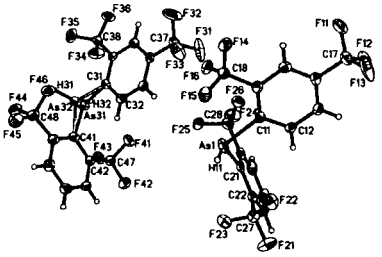

Fig. 7 Thermal ellipsoid drawing of Ar′Ar″AsH **7**, showing 50% probability displacement ellipsoids for non-H atoms; both independent molecules in the asymmetric unit are shown, because of the disorder in one As atom position.

P–Br distances of 2.203(3)–2.212(3) Å have been observed in PBr_3 complexes with $Cr(CO)_5$[39,40] and $W(CO)_5$.[40] This parallels the observation of a fairly short P–Cl bond in Ar′Ar″PCl of 2.061(1) Å, which was attributed to the electron-withdrawing properties of the CF_3 groups,[24] and of 2.063(1) Å in **2** and 2.062(1) Å in **3** (Table 1).

One striking feature of the crystal structure of **2** is the very marked asymmetry in the C–P–Cl bond angles, which differ by more than 10°. Similar observations have been reported in the literature for Ar_2AsCl (which exists in two different crystalline modifications, orthorhombic at 130 K and monoclinic at 296 K, with similar structures[22]), Ar_2SbCl[22] and Ar_2BiCl,[5] as shown in Table 3, although no comments thereon were included in these reports. This asymmetry probably arises as a consequence of secondary interactions between the group 15 element and fluorines of the *ortho*-CF_3 groups, as discussed in more detail below. Only minor differences in the C–E–X (E = P or As; X = Cl or Br) angles are apparent for the less sterically hindered compounds Ar′Ar″PCl,[24] Ar''_2PCl **3**, Ar''_2PBr **4**, Ar′Ar″AsCl **5** and Ar′Ar″AsBr **6**, with a maximum value of *ca.* 3.7° in **4**, as shown in Tables 1 and 2.

The As–Cl bond length in **5** of 2.2074(5) Å is similar to that in the orthorhombic modification of Ar_2AsCl (2.1920(12) Å),[22] and slightly shorter than in $AsCl_3$,[41] or other organo-derivatives with one As–Cl bond.[42–44] The As–Br distance of 2.3530(3) Å in **6** also appears normal, lying between the values of 2.31 Å for $AsBr_3$[45] and 2.40(1) Å for Ph_2AsBr,[46] and is similar to the corresponding bond length in Mes_2AsBr of 2.34(2) Å at low temperature and 2.3846(4) Å at higher temperature.[47] In structure **7**, there are two distinct molecules in each asymmetric unit, one of which has the arsenic atom disordered over two almost equally-populated sites (55 and 45% occupation, respectively). Data for the non-disordered As(1) atom are quoted in Table 2. The As–C distances are very similar in all instances, ranging from 1.980(4) to 2.007(6) Å, but even for As(1) it is not possible

Table 2 Selected bond distances (Å) and angles (°) for arsenic compounds 5–7

Ar′Ar″AsCl 5		Ar′Ar″AsBr 6		Ar′Ar″AsH 7[a]	
As(1)–Cl(1)	2.2074(5)	As(1)–Br(1)	2.3530(3)	As(1)–H(11)	See text
As(1)–C(1)	1.9880(18)	As(1)–C(11)	1.9827(19)	As(1)–C(11)	1.980(5)
As(1)–C(11)	2.0182(17)	As(1)–C(21)	2.0099(19)	As(1)–C(21)	1.995(5)
C(1)–As(1)–C(11)	102.98(7)	C(11)–As(1)–C(21)	103.15(8)	C(11)–As(1)–C(21)	98.11(18)
C(1)–As(1)–Cl(1)	100.08(6)	C(11)–As(1)–Br(1)	101.43(6)	C(11)–As(1)–H(11)	See text
C(11)–As(1)–Cl(1)	98.84(5)	C(21)–As(1)–Br(1)	98.91(5)	C(21)–As(1)–H(11)	See text

[a] Data for As(1): see text for further discussion.

Table 3 Comparison of key bond distances (Å) and angles (°) for Ar_2ECl (E = P, As, Sb or Bi)

Compound	Ar_2PCl	Ar_2AsCl[a]	Ar_2SbCl	Ar_2BiCl
E–Cl	2.0628(10)	2.1920(12)	2.358(11)	2.463(3)
E–C(1)	1.882(3)	2.023(4)	2.22(3)	2.356(8)
E–C(2)	1.885(3)	2.016(4)	2.25(3)	2.338(7)
C(1)–E–C(2)	109.87(12)	107.53(16)	107.0(12)	106.9(3)
C(1)–E–Cl	103.68(9)	100.57(12)	101.3(9)	99.5(2)
C(2)–E–Cl	92.95(9)	92.04(11)	88.4(9)	87.8(2)
Reference	This work	22	22	5

[a] Data for the orthorhombic modification at 130 K.

to be precise about distances or bond angles involving the H atom attached to As. The results indicate 1.37(6) Å for As(1)–H(11), and in the disordered molecule 1.42(10) Å for As(32)–H(32), and 1.63(12) Å for As(31)–H(31). These compare with 1.484(18) Å in a primary organoarsine,[48] a calculated value of 1.519 Å in AsH_3,[49] 1.520 Å in $[Cp^*Mn(CO)_2]AsH$,[50] and 1.5(2) Å in $Cp_2Nb(HAsEt_2)(H_3BAsEt_2)$.[51]

Disorder was found for the *para*-CF_3 groups in $ArPBr_2$ **1** and Ar″PBr **4**. This is often observed in compounds with these substituents, for example in Ar_2AsCl,[22] Ar_2SbCl,[22] Ar_2BiCl[5] and Ar_3Bi.[5] In all of the compounds studied there appear to be secondary interactions between the group 15 element and some of the fluorines of the *ortho*-CF_3 groups, as observed previously in Ar_2AsCl (both forms),[22] Ar_2SbCl[22] and Ar′Ar″PCl.[24] This is illustrated in Table 4, where the range of short E ··· F contacts (E = P, As or Sb), and number of such contacts, are listed, together with the number of fluorines in *ortho*-CF_3 groups. (There are often further E ··· F contacts at only slightly longer distances.) At least three such interactions are found for six fluorines in *o*-CF_3 groups, four for nine fluorines, and five for the only example studied here with twelve fluorines, *i.e.* Ar_2PCl **2**. The distances are shorter in all instances than the sum of the empirical van der Waals radii of P (1.91 Å) and F (1.40 Å),[52] as well as the theoretical ones (estimated as 2.05 and 1.42 Å respectively[53]). Since the van der Waals radii of As and Sb are expected to be larger than that of P, this deduction applies *a fortiori* to the heavier elements. These secondary interactions are expected to play a vital role in stabilising the structures, and almost certainly account for the large asymmetry in C–E–Cl bond angles in Ar_2ECl, described above. Similar interactions of fluorines from *ortho*-CF_3 groups in Ar ligands with the transition metals V,[18] Cr[19,25] and Mo[25] have also been reported.

Experimental

All manipulations, including NMR sample preparation, were carried out either under an inert atmosphere of dry nitrogen or *in vacuo*, using standard Schlenk procedures or a glovebox. Chemicals of the best available commercial grades were used, in general without further purification. The ^{31}P NMR spectra of phosphorus-containing starting materials were checked, to confirm the absence of any major impurities. ^{19}F NMR spectra were recorded on a Varian Mercury 200, Varian VXR 400, or Varian Inova 500 Fourier-transform spectrometer at 188.18, 376.35, and 470.26 MHz, respectively. ^{31}P NMR spectra were recorded on the same instruments at 80.96, 161.91 or 202.32 MHz. Chemical shifts were measured relative to external $CFCl_3$ (^{19}F) or 85% H_3PO_4 (^{31}P), with the higher frequency direction taken as positive. Microanalyses were performed by the microanalytical services of the Department of Chemistry, University of Durham.

Solutions containing ArLi or a mixture of Ar′Li/Ar″Li were prepared as described previously.[24,54]

Synthesis of $ArPBr_2$ 1

A solution of ArLi (100 ml, 48 mmol) was added to a PBr_3 (2.25 ml, 24 mmol) solution in diethyl ether (100 ml) at −78 °C. The solution was allowed to warm to room temperature and stirred for 2 h. A white precipitate of LiBr appeared. The solution was filtered and the solvents and excess PBr_3 were removed *in vacuo* leaving an orange oil. This oil was distilled under reduced pressure (0.03 Torr) giving colourless crystals. Yield (based on ArH): 4.80 g (20.3%).

Elemental analysis for $C_9H_3Br_2F_9P$ (M = 472). Calc: C 22.88, H 0.4%. Found: C 22.76, H 0.45%.

Table 4 Short E–F contacts (E = P, As or Sb)

Compound	Range (Å)		No. of contacts	No. of fluorines	Ref.
$ArPBr_2$ 1	P(1)	2.865–3.208	3	6	This work
	P(2)	2.877–3.217	3	6	
Ar_2PCl 2		2.843–3.111	5	12	This work
Ar′Ar″PCl		2.890–3.25	4	9	24
Ar''_2PCl 3		2.874–3.124	3	6	This work
Ar''_2PBr 4		2.887–3.122	3	6	This work
Ar_2AsCl	130(2) K	2.991–3.012	3	12	22
	296(1) K	2.935–3.110	3	12	22
Ar′Ar″AsCl 5		2.701–3.292	4	9	This work
Ar′Ar″AsBr 6		2.707–3.277	4	9	This work
Ar′Ar″AsH 7	As(1)	2.934–3.186	4	9	This work
	As(31)	2.859–3.326	4	9	
	As(32)	2.880–3.247	4	9	
Ar_2SbCl		2.821–3.107	4	12	22

^{31}P NMR ($CDCl_3$): δ 130.1 (septet, $^4J_{P-F}$ 62.3 Hz); ^{19}F NMR ($CDCl_3$): δ −53.1 (d, $^4J_{P-F}$ 62.4 Hz, 6F, *o*-CF_3), −64.1 (s, 3F, *p*-CF_3).

Synthesis of Ar_2PCl 2

A solution of ArLi (100 ml, 48 mmol) was added dropwise to a solution of PCl_3 (2.09 ml, 24 mmol) in diethyl ether at −78 °C. The solution was allowed to warm to room temperature and stirred for 2 h. A white precipitate of LiCl appeared. The solution was filtered and the solvents and excess PCl_3 were removed under vacuum leaving a yellow oil, which was distilled under reduced pressure (0.01 Torr). Fractions were collected at 60 °C ($ArPCl_2$; ~65% of distillate) and 100 °C (Ar_2PCl; ~35% of distillate). Crystals were grown by recrystallisation from dichloromethane.

Elemental analysis for $C_{18}H_4ClF_{18}P$ (M = 628.5). Calc.: C 34.36, H 0.6%. Found: C 34.1, H 0.6%.

^{31}P NMR ($CDCl_3$): δ 74.9 (m, $^4J_{P-F}$ 41.9 Hz); ^{19}F NMR ($CDCl_3$): δ −54.4 (d, $^4J_{P-F}$ 41.2 Hz, 12F, *o*-CF_3), −64.1 (s, 6F, *p*-CF_3).

Synthesis of Ar''_2PCl 3

A solution of Ar′Li/Ar″Li (100 ml, 94 mmol) in diethyl ether was added dropwise over 20 min to a solution of PCl_3 (25.2 g, 16 ml, 162 mmol) in diethyl ether (100 ml) at −78 °C. This solution was allowed to warm to room temperature and stirred for 4 h. A white precipitate of LiCl appeared. The solution was filtered through a fine sinter, and solvent and PCl_3 in excess were removed *in vacuo* giving a brown oil. The product was purified by distillation under vacuum (0.02 Torr) and two different fractions were collected at 86 °C ($Ar'PCl_2$/$Ar''PCl_2$; yield 9.2 g, 31% based on Ar′H) and 140 °C (Ar''_2PCl). Crystals of Ar''_2PCl were obtained by recrystallisation from hexanes. Yield (based on Ar′H) 11.68 g (25%).

Elemental analysis for $C_{16}H_5ClF_{12}P$ (M = 492.5). Calc.: C 38.97, H 1.22%. Found: C 38.96, H 1.35%.

^{31}P NMR ($CDCl_3$) δ 68.3 (septet, $^4J_{P-F}$ 65.5 Hz); ^{19}F NMR ($CDCl_3$) δ −57.3 (d, $^4J_{P-F}$ 65.8 Hz, 6F, *o*-CF_3), −63.7 (s, 6F, *p*-CF_3); ^{13}C NMR (C_7D_8) δ 140.3 (d, $^1J_{P-C}$ 56.8 Hz), 133.1 (q, $^2J_{F-C}$ 33.9 Hz), 129.1 (s), 123.7 (br s), 123.6 (d, $^3J_{P-C}$ 1.9 Hz), 123.6 (q, $^1J_{F-C}$ 275.8 Hz), 123.4 (qd, $^1J_{P-C}$ 273.1 Hz, $^3J_{P-C}$ 1.74 Hz).

Synthesis of Ar''_2PBr 4

A solution of Ar′Li/Ar″Li (100 ml, 94 mmol) was added slowly to a PBr_3 (8 ml, 85 mmol) solution in diethyl ether (100 ml) at −78 °C. The solution was allowed to warm to room temperature and stirred for 5 h. A white precipitate of LiBr appeared. The solution was filtered and the solvents and excess PBr_3 were removed *in vacuo* leaving a brown oil. This oil was distilled under reduced pressure (0.01 Torr), fractions were collected at 60 °C ($Ar'PBr_2$/$Ar''PBr_2$; ~65% of distillate) and 120 °C (Ar''_2PBr; ~35% of distillate). Yield (based on Ar′H): 4.52 g (9%).

Elemental analysis for $C_{16}H_4BrF_{12}P$ (M = 537). Calc.: C 35.78, H 1.13%. Found: C 35.69, H 1.15%.

^{31}P NMR ($CDCl_3$): δ 57.4 (septet, $^4J_{P-F}$ 65.8 Hz); ^{19}F NMR ($CDCl_3$) δ −57.7 (d, $^4J_{P-F}$ 65.8 Hz, 6F, *o*-CF_3), −63.7 (s, 6F, *p*-CF_3).

Synthesis of Ar′Ar″AsCl 5

A solution of Ar′Li/Ar″Li (100 ml, 94 mmol) in diethyl ether was added dropwise to a solution of $AsCl_3$ (13.5 ml, 160 mmol) in hexanes (100 ml) over a period of 20 min at −78 °C. The mixture was allowed to warm to room temperature and stirred for 4 h. A precipitate of LiCl formed. This was filtered off and the solvents and excess $AsCl_3$ removed *in vacuo*, leaving a brown oil. This oil was distilled under reduced pressure (0.01 Torr), and three different fractions were collected at 100 °C ($Ar'AsCl_2$; ~30% of distillate), 115 °C ($Ar''AsCl_2$; ~20% of distillate) and 145 °C (Ar′Ar″AsCl; ~50% of distillate). Ar′Ar″AsCl was purified by recrystallisation from hexanes. Yield (based on Ar′H): 4.5 g (9%)

Elemental analysis for $C_{18}H_6AsClF_{12}$ (M = 536.4). Calc.: C 35.79, H 1.12%. Found: C 35.33, H 1.10%.

^{19}F NMR ($CDCl_3$): δ −54.8 (br s, 6F, *o*-CF_3 in Ar′), −58.8 (s, 3F, *o*-CF_3 in Ar″), −63.5 (s, 3F, *p*-CF_3); ^{1}H NMR ($CDCl_3$): δ 8.1 (d, $^3J_{H-H}$ 8 Hz), 7.7 (s), 7.28 (d, $^3J_{H-H}$ 8 Hz), 7.26 (d, $^3J_{H-H}$ 7.6 Hz), 6.6 (t, $^3J_{H-H}$ 7.6 Hz).

Synthesis of Ar′Ar″AsBr 6

An Ar′Li/Ar″Li (20 ml, 19 mmol) solution in diethyl ether was added dropwise to a solution of $AsBr_3$ (3.2 g, 10.2 mmol) in hexanes at room temperature. The solution was stirred for 4 h, giving a brown solution. Solvents were removed under vacuum leaving a brown oil which was distilled under reduced pressure (0.01 Torr). Fractions were collected at 81 °C ($Ar'AsBr_2$/$Ar''AsBr_2$; ~60% of distillate) and 110 °C (Ar′Ar″AsBr/Ar''_2AsBr; ~40% of distillate).

The Ar′Ar″AsBr/Ar''_2AsBr mixture was dissolved in hexanes and left in the freezer. After one month colourless crystals of Ar′Ar″AsBr appeared. Yield 0.98 g (31%).

Elemental analysis for $C_{16}H_6AsBrF_{12}$ (M = 581.03). Calc.: C 33.08, H 1.04%; Found: C 33.46, H 1.04%.

^{19}F NMR ($CDCl_3$): δ −54.9 (br s, 6F, *o*-CF_3 in Ar′), −58.8 (s, 3F, *o*-CF_3 in Ar″), −63.5 (s, 3F, *p*-CF_3).

Synthesis of Ar′Ar″AsH 7

$LiAlH_4$ (0.2 ml, 1 M in diethyl ether, 0.2 mmol) was slowly added at 0 °C to an Ar′Ar″AsCl (0.2 g, 0.4 mmol) solution in hexanes. The solution was left to warm to room temperature and stirred for four days. Solvents were removed *in vacuo* and the resulting white solid washed three times with hexanes (3 × 2 mL). Crystals were grown by sublimation under vacuum. Yield 0.15 g (71%).

Elemental analysis for $C_{16}H_7AsF_{12}$ (M = 502.1). Calc.: C 38.27, H 1.41%. Found: C 37.98, H 2.03%

^{19}F NMR (C_7D_8): δ −58.2 (d, $^5J_{F-H}$ 7.1 Hz, 6F, *o*-CF_3 in Ar′), −61.2 (s, 3F, *o*-CF_3 in Ar″), −63.8 (s, 3F, *p*-CF_3); ^{1}H NMR (C_7D_8): δ 8.06 (d, $^3J_{H-H}$ 8 Hz), 7.9 (s), 7.7 (t, $^3J_{H-H}$ 8 Hz), 7.4 (d, $^3J_{H-H}$ 8 Hz), 6.9 (t, $^3J_{H-H}$ 7.6 Hz), 5.99 (br s, As–H).

Synthesis of Ar′Ar″PH 8

$LiAlH_4$ (0.09 ml, 1.0 M in diethyl ether, 0.09 mmol) was added to an Ar′Ar″PCl (0.08 g, 0.18 mmol) solution in diethyl ether (5 ml). The solution was stirred for one day. A white precipitate of LiCl appeared; the solution was then filtered and solvents were removed under vacuum leaving a white solid, which was washed three times with diethyl ether (3 × 2 ml). Yield 0.05 g (60%).

Elemental analysis for $C_{16}H_7PF_{12}$ (M = 458.2). Calc.: C 41.90, H 1.54%. Found: C 39.95, H 2.12%.

^{19}F NMR ($CDCl_3$): δ −57.7 (br s, 6F, *o*-CF_3 in Ar′), −61.2 (d, $^4J_{P-F}$ 43.7 Hz, 3F, *o*-CF_3 in Ar″), −63.4 (s, 3F, *p*-CF_3); ^{31}P{^{1}H} NMR (C_7D_8): δ −67.2 (m); ^{31}P(^{1}H coupled) NMR (C_7D_8): δ −67.6 (dm, $^1J_{P-H}$ 240.7 Hz); ^{1}H NMR (C_7D_8): δ 7.5–6.2 (aromatic region), 5.7 (d, $^1J_{P-H}$ 240.4 Hz, P–H).

Synthesis of ArAr′PCl 9/ArAr″PCl 10

A solution of Ar′Li/Ar″Li (20 ml, 6.6 mmol) was added dropwise to a solution of $ArPCl_2$ (2.52 g, 6.6 mmol) in diethyl ether. A precipitate of LiCl immediately formed. The solution was filtered and distilled under reduced pressure (0.01 Torr) giving a yellow oil, bp 110 °C.

^{19}F NMR ($CDCl_3$): ArAr′PCl 9: δ −54.1 (d, $^4J_{P-F}$ 42.1 Hz, 6F, *o*-CF_3), −54.3 (d, $^4J_{P-F}$ 42.1 Hz, 6F, *o*-CF_3), −64 (s, 3F,

Table 5 Crystal data and structure refinement parameters

	ArPBr$_2$ **1**	Ar$_2$PCl **2**	Ar″$_2$PCl **3**	Ar″$_2$PBr **4**	Ar′Ar″AsCl **5**	Ar′Ar″AsBr **6**	Ar′Ar″AsH **7**
Empirical Formula	$C_9H_2Br_2F_9P$	$C_{18}H_4ClF_9P$	$C_{16}H_6ClF_{12}P$	$C_{16}H_6BrF_{12}P$	$C_{16}H_6AsClF_{12}$	$C_{16}H_6AsBrF_{12}$	$C_{16}H_7AsF_{12}$
M_r	471.90	628.63	492.63	537.09	536.4	581.04	502.14
Crystal system	Triclinic	Monoclinic	Monoclinic	Monoclinic	Monoclinic	Monoclinic	Monoclinic
Space group	$P\bar{1}$	$P2_1/n$	$I2/a$	$I2/a$	$P2_1/c$	$P2_1/c$	$P2_1/c$
Crystal size/mm	0.42 × 0.26 × 0.22	0.10 × 0.08 × 0.01	0.22 × 0.16 × 0.10	0.40 × 0.50 × 0.75	0.18 × 0.20 × 0.40	0.35 × 0.30 × 0.2	0.30 × 0.10 × 0.05
T/K	110(2)	120(2)	100(2)	103(2)	100(2)	120(2)	120(2)
a/Å	8.000(1)	8.0347(6)	18.734(6)	19.0725(13)	13.436(3)	13.7761(8)	8.1315(10)
b/Å	10.501(1)	8.5325(6)	8.170(3)	8.2148(6)	9.055(1)	8.9308(5)	14.9159(18)
c/Å	16.153(2)	29.833(2)	23.559(7)	23.6350(15)	14.644(3)	14.6416(8)	28.272(4)
α/°	101.39(1)	90.00	90.00	90.00	90.00	90.00	90.00
β/°	98.48(1)	94.572(2)	96.820(5)	97.447(4)	100.98(1)	99.6590(10)	96.389(2)0
γ/°	90.91(1)	90.00	90.00	90.00	90.00	90.00	90.00
V/Å^3	1314.3(3)	2038.7(3)	3580.2(19)	3671.8(4)	1749.0(6)	1775.84(17)	3407.7(7)
Z	4	4	8	8	4	4	8
D_c/g cm^{-3}	2.385	2.048	1.828	1.943	2.043	2.173	1.957
μ/mm^{-1}	6.385	0.436	0.423	2.444	2.219	4.285	2.119
R_{int}	0.0247	0.0486	0.0507	0.0354	0.0303	0.0324	0.0565
Observed data [$I > 2\sigma(I)$]	5691	3233	3420	4504	3749	3532	5199
R_1 [$I > 2\sigma(I)$]	0.0287	0.0430	0.0435	0.0294	0.0257	0.0220	0.0592
R_1 (all data)	0.0385	0.0761	0.0656	0.0325	0.0326	0.0294	0.0888
wR_2 [$I > 2\sigma(I)$]	0.0727	0.0952	0.1053	0.0713	0.0647	0.0472	0.1203
wR_2 (all data)	0.0755	0.1087	0.1158	0.0732	0.0687	0.0494	0.1329
Goodness of fit (S)	1.065	1.044	1.037	1.040	1.048	1.067	1.139
No. of variables	399	343	295	280	295	271	536

p-CF_3); ArAr″PCl **10**: δ −55.5 (br s, 6F, *o*-CF_3 in Ar), −58.6 (d, $^4J_{P-F}$ 58.3 Hz, 3F, *o*-CF_3 in Ar″), −63.6 (s, 3F, *p*-CF_3), −64.1 (s, 3F, *p*-CF_3); ^{31}P NMR ($CDCl_3$): ArAr′PCl **9**: δ 76.6 (m);ArAr″PCl **10**: δ 69.9 (m).

X-Ray crystallography

Single crystal X-ray diffraction experiments were carried out at low temperature, 100–120 K (see Table 5), using graphite monochromated Mo-Kα radiation (λ = 0.71073 Å) on a Bruker SMART (CCD 1 K area detector) diffractometer equipped with a Cryostream N2 flow cooling device.[55] Series of narrow ω-scans (0.3°) were performed at several ϕ-settings in such a way as to cover a sphere of data to a maximum resolution between 0.70 and 0.77 Å. Cell parameters were determined and refined using the SMART software,[56] and raw frame data were integrated using the SAINT program.[57] The structures were solved by direct methods and refined by full-matrix least squares on F^2 using SHELXTL software.[58] Crystal data and structure refinement parameters are shown in Table 5.

The reflection intensities were corrected by numerical integration based on measurements and indexing of the crystal faces for **4** and **5** (using SHELXTL software).[58] For the remaining structures, the absorption corrections were carried out by the multi-scan method, based on multiple scans of identical and Laue equivalent reflections (using the SADABS software).[59]

Non-hydrogen atoms were refined anisotropically, except in some cases where there was disorder (see Results and discussion). For structures **1**, **3** and **5** the hydrogen atoms were found in difference Fourier maps and in the case of **1** constrained accordingly. For structures **2**, **4** and **6**, the hydrogen atoms were positioned geometrically and refined using a riding model. In the special case of Ar′Ar″AsH **7**, the hydrogen atoms were found in the Fourier difference map, one constrained and the other allowed to refine freely. The remaining hydrogen atoms were positioned geometrically and refined using a riding model.

CCDC reference numbers 189700–189706.

See http://www.rsc.org/suppdata/dt/b2/b207327g/ for crystallographic data in CIF or other electronic format.

Acknowledgements

We thank the EPSRC for the award of studentships (to S. M. C. and A. L. T), and A. M. Kenwright and C. F. Heffernan for assistance in recording some of the NMR spectra.

References

1 K. B. Dillon, H. P. Goodwin, T. A. Straw and R. D. Chambers, *Proc. Euchem. PSIBLOCS Conf.*, Paris-Palaiseau, 1988.
2 M. Scholz, H. W. Roesky, D. Stalke, K. Keller and F. T. Edelmann, *J. Organomet. Chem.*, 1989, **366**, 73.
3 H. Grutzmacher, H. Pritzkow and F. T. Edelmann, *Organometallics*, 1991, **10**, 23.
4 S. Brooker, J.-K. Buijink and F. T. Edelmann, *Organometallics*, 1991, **10**, 25.
5 K. H. Whitmire, D. Labahn, H. W. Roesky, M. Noltemeyer and G. M. Sheldrick, *J. Organomet. Chem.*, 1991, **402**, 55.
6 M. Abe, K. Toyota and M. Yoshifuji, *Chem. Lett.*, 1992, 2349.
7 F. T. Edelmann, *Comments Inorg. Chem.*, 1992, **12**, 259.
8 K. B. Dillon and H. P. Goodwin, *J. Organomet. Chem.*, 1992, **429**, 169.
9 R. D. Schluter, A. H. Cowley, D. A. Atwood, R. A. Jones, M. R. Bond and C. J. Carrans, *J. Am. Chem. Soc.*, 1993, **115**, 2070.
10 R. D. Schluter, H. S. Isom, A. H. Cowley, D. A. Atwood, R. A. Jones, F. Olbrick, S. Corbelin and R. J. Lagow, *Organometallics*, 1994, **13**, 4058.
11 K. B. Dillon and H. P. Goodwin, *J. Organomet. Chem.*, 1994, **469**, 125.
12 F. T. Edelmann, *Main Group Met. Chem.*, 1994, **17**, 67.
13 F. T. Edelmann, *ACS Symp. Ser. (Inorg. Fluorine Chem.)*, 1994, **555**, 309.
14 M. Belay and F. T. Edelmann, *J. Organomet. Chem.*, 1994, **479**, C21.
15 C. Bartolomé, P. Espinet, J. Villafañe, S. Giesa, A. Martin and A. G. Orpen, *Organometallics*, 1996, **15**, 2019.
16 J.-T. Ahlemann, A. Künzel, H. W. Roesky, M. Noltemeyer, L. Markovskii and H.-G. Schmidt, *Inorg. Chem.*, 1996, **35**, 6644.
17 K. B. Dillon, V. C. Gibson, J. A. K. Howard, L. J. Sequeira and J. W. Yao, *Polyhedron*, 1996, **15**, 4173.
18 V. C. Gibson, C. Redshaw, L. J. Sequeira, K. B. Dillon, W. Clegg and M. R. Elsegood, *Chem. Commun.*, 1996, 2151.
19 K. B. Dillon, V. C. Gibson, J. A. K. Howard, C. Redshaw, L. J. Sequeira and J. W. Yao, *J. Organomet. Chem.*, 1997, **528**, 179.
20 M. G. Davidson, K. B. Dillon, J. A. K. Howard, S. Lamb and M. D. Roden, *J. Organomet. Chem.*, 1998, **550**, 481.
21 J.-K. Buijink, M. Noltemeyer and F. T. Edelmann, *J. Fluorine Chem.*, 1993, **61**, 51.
22 N. Burford, C. L. B. Macdonald, D. J. LeBlanc and T. S. Cameron, *Organometallics*, 2000, **19**, 152.
23 P. Espinet, S. Martin-Barrios, J. Villafañe, P. G. Jones and A. K. Fischer, *Organometallics*, 2000, **19**, 290.
24 A. S. Batsanov, S. M. Cornet, L. A. Crowe, K. B. Dillon, R. K. Harris, P. Hazendonk and M. D. Roden, *Eur. J. Inorg. Chem.*, 2001, 1729.
25 A. S. Batsanov, K. B. Dillon, V. C. Gibson, J. A. K. Howard, L. J. Sequeira and J. W. Yao, *J. Organomet. Chem.*, 2001, **631**, 181.
26 J. Escudié, C. Couret, H. Ranaivonjatovo, M. Lazraq and J. Satgé, *Phosphorus Sulfur*, 1987, **31**, 27.
27 L. Heuer, P. G. Jones and R. Schmutzler, *J. Fluorine Chem.*, 1990, **46**, 243.
28 H.-J. Kroth, H. Schumann, H. G. Kuivila, C. D. Schaeffer Jr. and J. J. Zuckerman, *J. Am. Chem. Soc.*, 1975, **97**, 1754.
29 H. Voelker, D. Labahn, F. M. Bohnen, R. Herbst-Irmer, H. W. Roesky, D. Stalke and F. T. Edelmann, *New J. Chem.*, 1999, **23**, 905.
30 S. M. Cornet, K. B. Dillon, P. Hazendonk, in preparation.
31 F. H. Allen, *Acta Crystallogr., Sect. A*, 1998, **54**, 758.
32 A. Schmidpeter, H. Nöth, G. Jochem, H.-P. Schrödel and K. Karaghiosoff, *Chem. Ber.*, 1995, **128**, 379.
33 Y. Ehleiter, G. Wolmershäuser, H. Sitzmann and R. Boese, *Z. Anorg. Allgm. Chem.*, 1996, **622**, 923.
34 N. Burford, A. I. Dipchand, B. W. Royan and P. S. White, *Inorg. Chem.*, 1990, **29**, 4938.
35 A. N. Chernega, A. A. Korkin, N. E. Aksinenko, A. V. Ruban and V. D. Romanenko, *J. Gen. Chem. USSR*, 1990, **60**, 2201.
36 G. Jochem, A. Schmidpeter, M. Thomann and H. Nöth, *Angew. Chem., Int. Ed. Engl.*, 1994, **33**, 663.
37 H.-P. Schrödel, A. Schmidpeter, H. Nöth and M. Schmidt, *Z. Naturforsch., Teil B*, 1996, **51**, 1022.
38 R. Pietschnig, J. Ebels, M. Nieger, N. Zoche, M. Jansen and E. Niecke, *Bull. Soc. Chim. Fr.*, 1997, **134**, 1039.
39 H. Jelinek-Fink, E. N. Duesler and R. T. Paine, *Acta Crystallogr., Sect. C*, 1987, **43**, 635.
40 M. S. Davies, M. J. Aroney, I. E. Buys, T. W. Hambley and J. L. Calvert, *Inorg. Chem.*, 1995, **34**, 330.
41 P. Kisluik and C. H. Townes, *J. Chem. Phys.*, 1950, **18**, 1109.
42 J. Trotter, *Can. J. Chem.*, 1962, **40**, 1590.
43 A. Camerman and J. Trotter, *J. Chem. Soc.*, 1965, 730.
44 J. E. Stuckey, A. W. Cordes, L. B. Handy, R. W. Perry and C. K. Fair, *Inorg. Chem.*, 1972, **11**, 8.
45 J. Trotter, *Z. Kristallogr.*, 1965, **122**, 230.
46 J. Trotter, *J. Chem. Soc.*, 1962, 2567.
47 H. Nöth and R. Waldhör, *Z. Naturforsch., Teil B*, 1999, **54**, 603.
48 B. Twamley, C.-S. Hwang, N. J. Hardman and P. P. Power, *J. Organomet. Chem.*, 2000, **609**, 152.
49 G. S. Blevins, A. W. Jache and W. Gordy, *Phys. Rev.*, 1955, **97**, 684.
50 W. A. Hermann, B. Koumbouris, A. Schafer, T. Zahn and M. L. Ziegler, *Chem. Ber.*, 1985, **118**, 2472.
51 G. I. Nikonov, A. J. Blake, J. Lorberth, D. A. Lemonovskii and S. Wocadlo, *J. Organomet. Chem.*, 1997, **547**, 235.
52 Yu. V. Zefirov and P. M. Zorkii, *Russ. Chem. Rev.*, 1989, **58**, 421.
53 M. Franck, R. F. Hout Jr. and W. J. Hehre, *J. Am. Chem. Soc.*, 1984, **106**, 563.
54 G. E. Carr, R. D. Chambers, T. F. Holmes and D. G. Parker, *J. Organomet. Chem.*, 1987, **325**, 13.
55 J. Cosier and A. M. Glazer, *J. Appl. Crystallogr.*, 1986, **19**, 105.
56 SMART-NT, Data Collection Software, version 5.0; Bruker Analytical X-ray Instruments Inc., Madison, WI, USA, 1999.
57 SAINT-NT, Data Reduction Software, version 6.0; Bruker Analytical X-ray Instruments Inc., Madison, WI, USA, 1999.
58 SHELXTL, version 5.1; Bruker Analytical X-ray Instruments Inc., Madison, WI, USA, 1999.
59 G. M. Sheldrick, SADABS, Empirical Absorption Correction Program, University of Göttingen, Germany, 1998.

C.9 Structural Phase Transitions in $CsInF_4$

Acta Cryst. (2002). A58 (Supplement), C341

STRUCTURAL PHASE TRANSITIONS IN $CsInF_4$

A. L. Thompson[1] A. E. Goeta[1] C. C. Wilson[2] A. Ayala[3] C.W.A. Paschoal[3] I Guedes[3] J-Y Gesland[4]
[1]University of Durham, Department of Chemistry, Science Laboratories, South Road, DURHAM DH1 3LE UK [2]ISIS, Rutherford Appleton Laboratory, Didcot, Oxon, UK. [3]Departamento de Fisica, Universidade Federal do Ceara, CP 6030, 60455-760 Fortaleza (CE) Brasil. [4]Universite du Maine - Cristallogenese, 72025 - Le Mans CEDEX 09 - France

In the past 20 years many studies have been devoted to the structural characterization of cubic perovskite compounds, of the form ABX_3. This has been mainly due to the wide variety of potentially important technological properties shown by these materials, e.g. Ferroelectricity, ionic conductivity, superconductivity, etc. Phase transitions on these materials are thought to be caused by tilts of rigid BX_6 octahedra, even in the case of large tilt angles. If rigid BX_6 octahedra are so important for understanding the behavior of these materials, it is clear that the study of systems involving phase transitions with rigid octahedra forming only a 2-dimensional array, could provide additional insight on the theory of phase transitions. Moreover, it will help towards understanding issues like the displacive character of ferroelastic transitions, as it simplifies the problem. 2-Dimensional arrays of octahedra like the ones mentioned previously are found, for example, in tetrafluoroaluminates $MAlF_4$ (M=Tl, Rb,K,NH_4), where several phase transitions are observed. In this communication we will be introducing $CsInF_4$, a new material of the ABX_4 family. $CsInF_4$ appears to have a number of temperature dependent phase transitions based on the tilting of the InF_6 octahedra. Dielectric measurements clearly show the presence of four distinct phases with transitions at 280 K, 380 K and 415 K. In addition, the transitions have been verified and further characterized by Differential Scanning Calorimetry (DSC), variable temperature X-ray powder diffraction and single crystal neutron diffraction experiments. Results and conclusions drawn from these experiments will be presented.

Keywords: CSINF4 PEROVSKITES (2 DIMENSIONAL) ABX4

C.10 A Novel Fe(II) Framework Structure

Acta Cryst. (2002). A58 (Supplement), C204

A NOVEL Fe(II) FRAMEWORK STRUCTURE: CORRELATIONS TO ITS THERMAL AND LIGHT INDUCED SPIN TRANSITIONS

A.E. Goeta[1] A.L. Thompson[1] J.A. Real[2] V. Niel[2] A.B. Gaspar[2] M.C. Munoz[3]
[1]Department of Chemistry, University of Durham, DURHAM DH1 3LE, UK
[2]Departament de Quimica Inorganica/Institut de Ciencia Molecular, Universitat de Valencia, Doctor Moliner 50, E-46100 Burjassot, Valencia, Spain
[3]Departament de Fisica Aplicada, Universitat Politecnica de Valencia, Camino de Vera s/n, E-46071, Valencia, Spain

New opportunities for the development of novel electronic devices may arise from the control of the spin crossover phenomenon. Widely studied in iron(II) molecular complexes, it can be produced by a change of temperature, pressure or by light irradiation. The latter is a most promising feature of the spin transition, with potential applicability in optical storage devices. However, up to now, the LIESST effect (Light Induced Excited Spin State Trapping) has been only observed at very low temperatures. It is then crucial, for useful applications, to determine and study the molecular factors that will predispose a material to undertake a photoconversion at ambient temperatures. In this context, cooperativity appears to be very important and considerable effort is currently being devoted to understanding how the spin transition is propagated through a crystal. Strong cooperativity would be expected to be most likely, and indeed has been observed, in polymeric and 3D extended systems. We present here an iron(II) complex, in which we have tried to enhance cooperativity through interactions via $[Ag(CN)_2]^-$ anions. The resulted compound was found to be Fe_2 (pyrimidine) $[Ag_2(CN)_3]^-$ $[Ag(CN)_2]^-$ and it presents a two-step (at 185 K and 150 K) spin transition showing also the LIESST effect at temperatures below 70 K. X-ray diffraction data has been collected at 290 K, 220 K, 170 K, 90 K, 30 K and at 30 K after irradiating the crystal with a 638 nm He-Ne laser. Fascinating structure-property correlations have been obtained from a molecular structure that shows an unprecedented packing arrangement for a spin crossover compound.

Keywords: LOW TEMPERATURE CRYSTALLOGRAPHY, SPIN CROSSOVER, LIESST EFFECT

C.11 Synthesis & Characterisation of $Bi_2YO_4Cu_2Se_2$

COMMUNICATION

ChemComm www.rsc.org/chemcomm

Synthesis and characterisation of the new oxyselenide $Bi_2YO_4Cu_2Se_2$†

John S. O. Evans,* Edward B. Brogden, Amber L. Thompson and Richard L. Cordiner
Department of Chemistry, University of Durham, Science Site, Durham, UK DH1 3LE. E-mail: john.evans@durham.ac.uk

Received (in Cambridge, UK) 24th January 2002, Accepted 12th March 2002
First published as an Advance Article on the web 26th March 2002

In this communication we report the synthesis, structure and preliminary characterisation of $Bi_2LnO_4Cu_2Se_2$ (Ln = Y, Gd, Sm, Nd, La) phases; these materials are members of a new family of layered oxychalcogenides.

The range of technologically important applications of mixed metal oxides and mixed metal chalcogenides is vast. They have been exploited (*inter alia*) for their conductivity, magnetic, catalytic, optical, energy storage and structural properties. In contrast, the amount of work on oxychalcogenides, materials that contain both oxide and chalcogenide anions, is relatively sparse. This is, of course, partially due to the propensity of such materials to decompose to species containing oxyanions (SO_4^{2-}, SO_3^{2-}, *etc.*) in which the chalcogen has been oxidised. There are, however, a number of such phases known ranging from simple species such as ZrOS[1] and natural minerals such as kermesite and sarabauite (Sb_2OS_2 and $CaSb_{10}S_6O_{10}$);[2,3] three-dimensional phases such as $La_2Ta_2S_2O_8$[4] and $LaCrOS_2$;[5] layered materials such as $Na_2Cu_4OSe_2$,[6] $(LaO)_4Sn_2S_6$[7] and $Sr_2Cu_2CoO_2S_2$[8] and very recently Ruddlesden–Popper phases such as $Ln_2Ti_2O_5S_2$ (Ln = Pr, Nd, Sm–Er, Y) and their alkali metal intercalates.[9–11] Such phases are of interest in that they offer potential control of material properties *via* the anion rather than the cation sublattice.

In this communication we report the synthesis and structural characterisation of a new family of layered oxyselenides of general formula $Bi_2LnO_4Cu_2Se_2$. These phases were targeted using a simple 'building block' strategy[12,13] and were anticipated to contain the stable $[Cu_2Se_2]^{n-}$ building block and oxide layers related to those in other oxide/mixed anion phases.

$Bi_2LnO_4Cu_2Se_2$ phases were prepared by heating a stoichiometric mixture of Ln_2O_3, Bi_2O_3, Cu, Bi and Se in an evacuated sealed silica ampoule to a temperature of 850 °C for 24 h. Lower temperatures resulted in the predominance of the stable BiOCuSe,[14,15] whilst higher temperatures or longer reaction times led to higher impurity levels (presumably due to side reactions with the silica ampoule) and sample decomposition.

Initial inspection of laboratory powder X-ray diffraction data of $Bi_2YO_4Cu_2Se_2$ suggested that the material had the structure type anticipated. This was confirmed by Rietveld refinement of laboratory X-ray powder data and time of flight neutron diffraction data collected on the SEPD diffractometer at the Intense Pulsed Neutron Source (IPNS) at the Argonne National Laboratory, USA. Refinement results are shown in Fig. 1 and Table 1.‡ The structure of $Bi_2YO_4Cu_2Se_2$ is shown in Fig. 2. It has space group *I4/mmm* with $a = b = 3.864$ Å, $c = 24.428$ Å and can be described as formally containing layers of $[Cu_2Se_2]^{-}$ Cu centred edge sharing tetrahedra interspersed with $[Bi_2YO_4]^{+}$ oxide layers. Similar $[Cu_2Se_2]^{n-}$ blocks are found in materials such as $TlCu_2Se_2$, BiOCuSe[14,15] and others. We note that if one assumes formal oxidation states of Cu^{1+} and Se^{2-} there must be holes present in the valence band.[16] The oxide slabs contain Y in a pseudo-cubic coordination environment (8 × O at 2.378 Å) with a *c/a* ratio of the YO_8 unit of 1.015. Bi adopts a coordination enviromnment typical of a lone pair cation with four short bonds to oxygen (4 × 2.232 Å) and four longer bonds to Se (4 × 3.431 Å) of the Cu_2Se_2 layers. A similar oxide building block can be found in Bi_2LaO_4Cl.[17]

Other members of this family with Ln = Y, Gd, Sm, Nd and La have been prepared and characterised. Their unit cell

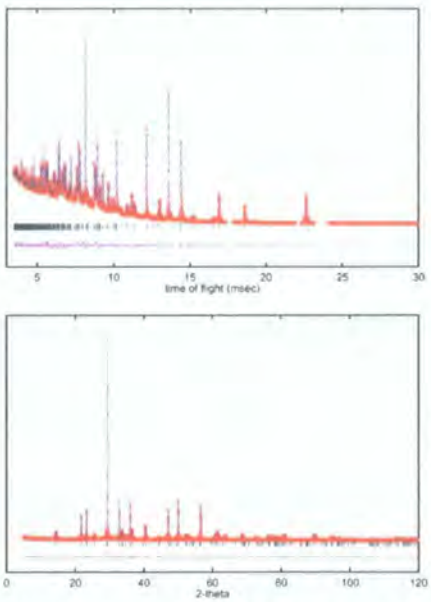

Fig. 1 Results of (a) neutron and (b) X-ray Rietveld refinements. Red points show the observed data, blue line the calculated pattern and the lower pink line the difference curve. Vertical tick marks show positions of allowed reflections. Minor impurity regions have been excluded from neutron data.

Table 1 Fractional atomic coordinates determined by combined refinement of X-ray and neutron diffraction data[a]

Atom	*x/a*	*y/b*	*z/c*	$100U_{eq}$/Å^2
Bi	0.5	0.5	0.89748(6)	0.87(3)
Y	0.5	0.5	0.5	0.45(5)
O	0.0	0.5	0.94322(8)	0.94(5)
Cu	0.0	0.5	0.25	1.39(4)
Se	0.5	0.5	0.31254(7)	1.24(4)

[a] Space group *I4/mmm*, 293 K, $a = b = 3.86463(3)$, $c = 24.428(4)$ Å.

† Electronic supplementary information (ESI) available: fractional atomic coordinates from Rietveld refinement of $Bi_2Ln_4O_4Cu_4Se_2$ phases. See http://www.rsc.org/suppdata/cc/b2/b200892k/

DOI: 10.1039/b200892k

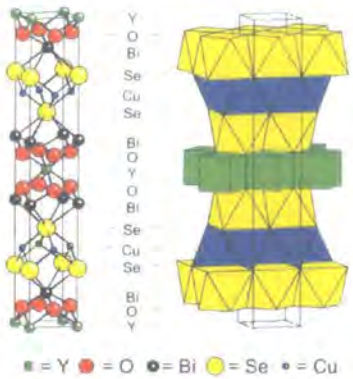

Fig. 2 Structure of $Bi_2YO_4Cu_2Se_2$ in ball and stick and polyhedral representations.

Table 2 Cell parameters of $Bi_2LnO_4Cu_2Se_2$ phases determined by X-ray diffraction data

Atom	a	c	V/Å^3
Y	3.8631(5)	24.4227(5)	364.47(1)
Gd	3.88631(8)	24.4535(6)	369.33(1)
Sm	3.89976(7)	24.4620(6)	372.02(1)
Nd	3.91795(10)	24.5001(8)	376.09(2)
La	3.95319(29)	24.6314(23)	384.93(5)

parameters are included in Table 2§ and show the expected trends with Ln radius.

Preliminary measurements of electrical resistivity were carried out on pellets of $Bi_2YO_4Cu_2Se_2$ using evaporated In contacts in a conventional four-probe arrangement. Current-voltage measurements confirmed that the contacts were ohmic. Resistivity (ρ)–temperature (T) characteristics were measured under constant current conditions over the temperature range 77–300 K using an Oxford Instruments DN107 liquid nitrogen crysostat controlled by an Oxford Instruments ITC4 controller. Room temperature values of resistivitiy were $\sim 2 \times 10^{-2}$ Ω cm and were found to vary linearly with temperature, implying that conduction was essentially metallic in character. The temperature coefficient was $\sim 4 \times 10^{-5}$ Ω cm K^{-1}.

Further studies on the properties and chemistry of this family of materials are in progress.

We wish to thank J. D. Jorgensen and S. Short of Argonne National Laboratory for access to neutron diffraction facilities, Dr Andrew Brinkman for conductivity measurements and the EPSRC, Royal Society of Chemistry and University of Durham for funding.

Notes and references

‡ Neutron diffraction data were recorded on a 4.9 g sample on the SEPD diffractometer of the Intense Pulsed Neutron Source at Argonne National Laboratory. Data were collected and analysed over a time of flight range of 3–30 ms (d = 0.47–4.01 Å). This sample contained small impurities (not present in smaller scale syntheses) which were excluded from the refinement. X-Ray diffraction data were collected from 10–120° 2θ on a Siemens d5000 diffractometer equipped with a graphite diffracted beam monochromator. A step size of 0.02° and a time per step of 10 s were used. To obtain high precision fractional coordinates a combined refinement of neutron and X-ray data was performed in the GSAS software suite.[18] A total of 33 variables were refined (2 scale factors, 2 cell parameters, 3 fractional coordinates, 5 temperature factors, 8 profile coefficients, 6 background terms per phase). Final agreement factors were χ^2 = 3.0, $R(F^2)$ = 9.78/7.74%, wR_p = 11.09/8.23% (X-ray/neutron). Fig. 1 contains X-ray data of a higher purity sample refined on the same structural model that gave χ^2 = 2.0, $R(F^2)$ = 8.69%, wR_p = 9.85%.

§ Cell parameters were determined by Rietveld refinement of data collected from 5–120° 2θ with a step size of 0.02° and a collection time per step of 9 s. Fractional coordinates derived from these refinements have been deposited as ESI.†

1 G. A. Eisman, J. S. Swinnea and H. Steinfink, *J. Solid State Chem.*, 1985, **56**, 397.
2 P. Bonazzi, S. Menchetti and C. Sabelli, *Neues Jahrb. Mineral.-Monatsh.*, 1987, 557.
3 I. Nakai, K. Nagashima, K. Koto and N. Morimoto, *Acta Crystallogr., Sect. B*, 1978, **34**, 3569.
4 T. D. Brennan and J. A. Ibers, *J. Solid State Chem.*, 1992, **98**, 82.
5 J. Dugue, T. Vovan and J. Villers, *Acta Crystallogr., Sect. B*, 1980, **36**, 1291.
6 Y. B. Park, D. C. Degroot, J. L. Schindler, C. R. Kannewurf and M. G. Kanatzidis, *Chem. Mater.*, 1993, **5**, 8.
7 M. Guittard, S. Benazeth, J. Dugue, S. Jaulmes, M. Palazzi, P. Laruelle and J. Flahaut, *J. Solid State Chem.*, 1984, **51**, 227.
8 W. J. Zhu, P. H. Hor, A. J. Jacobson, G. Crisci, T. A. Albright, S. H. Wang and T. Vogt, *J. Am. Chem. Soc.*, 1997, **119**, 12398.
9 C. Boyer, C. Deudon and A. Meerschaut, *C. R. Acad. Sci. Ser. IIC*, 1999, **2**, 93.
10 M. Goga, R. Seshadri, V. Ksenofontov, P. Gutlich and W. Tremel, *Chem. Commun.*, 1999, 979.
11 S. G. Denis and S. J. Clarke, *Chem. Commun.*, 2001, 2356.
12 Y. Tokura and T. Arima, *Jpn. J. Appl. Phys.*, 1990, **29**, 2388.
13 M. T. Weller and C. S. Knee, *J. Mater. Chem.*, 2001, **11**, 701.
14 P. S. Berdonosov, A. M. Kusainova, L. N. Kholodkovskaya, V. A. Dolgikh, L. G. Akselrud and B. A. Popovkin, *J. Solid State Chem.*, 1995, **118**, 74.
15 A. M. Kusainova, P. S. Berdonosov, L. G. Akselrud, L. N. Kholodkovskaya, V. A. Dolgikh and B. A. Popovkin, *J. Solid State Chem.*, 1994, **112**, 189.
16 G. V. Vajenine and R. Hoffmann, *Inorg. Chem.*, 1996, **35**, 451.
17 C. J. Milne, P. Lightfoot, J. D. Jorgensen and S. Short, *J. Mater. Chem.*, 1995, **5**, 1419.
18 A. C. Larson and V. Dreele, *Los Alamos Internal Report No. 86-748*, 1994.

C.12 Poster Presentations

Presented to The British Crystallographic Association, Spring 2003

STRUCTURE-PROPERTY CORRELATIONS OF NOVEL SPIN CROSSOVER MATERIALS. A. L. Thompson and A. E. Goeta, Department of Chemistry, University of Durham, UK; J. A. Real and V. Niel, Departament de Quimica, Universitat de Valencia, Spain; M. C. Muñoz Departament de Fisica Aplicada, Universitat Politecnica de Valencia, Spain.

Spin transition materials have a wide range of potential technological uses from molecular switches to data storage devices. [1]

Here we will be reporting two novel iron (II) coordination polymers showing sharp spin transitions with a pronounced hysteresis accompanied by a dramatic colour change. All these are important characteristics indicative of a high degree of cooperativity within the systems, which is vital for technological applications. In addition, these new materials undergo a controlled, complete and fully reversible crystalline-state dehydration involving both ligated and non-bonded water molecules. This topochemical conversion leads to fundamental changes in the structural network and coordination environment of the iron centres (shown below), directly affecting the magnetic properties of the materials. This rare combination of allosteric behaviour and electronic bistability achieved by the unique coexistence of nanoporosity and spin crossover could lead the way to a new generation of switching materials.

Our studies of these materials both in the hydrated and dehydrated forms, using a variety of techniques including variable temperature single crystal and powder diffraction will be presented. The results lead to an insight into the structural changes that occur during these fascinating phenomena.

1. Kahn, Kröber & Jay (1992), *Adv. Mater.*, 4, No. 11, p718.

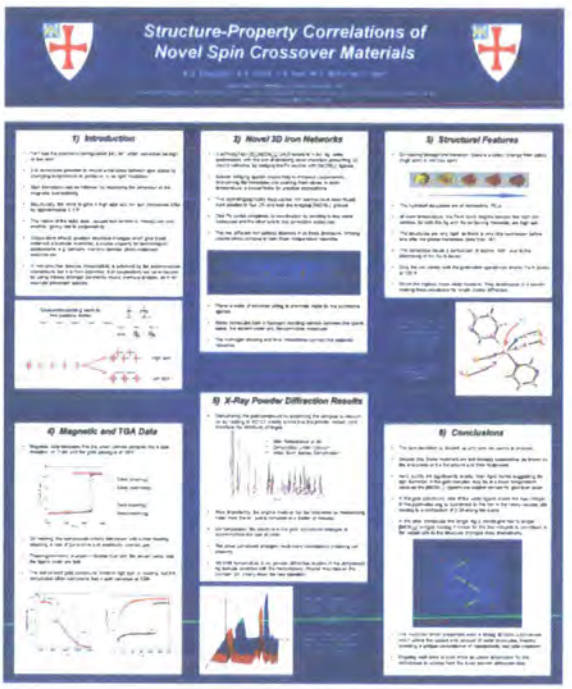

HOW SMALL IS THE LABORATORY LIMIT? Judith A.K. Howard, Andres E. Goeta, Andrei Batsanov, Amber L. Thompson, Department of Chemistry, University of Durham, Durham DH1 3LE; John Wall, Bede Scientific Instruments Ltd, Belmont Business Park, Belmont, Durham DH1 1TW.

Smaller and smaller crystals are what the crystallographers are getting from chemists. Faster and faster data collections are what the crystallographers and the chemists both would like to see happening in the laboratory. The two demands have seemingly opposed each other for a very long time and more recently the problem has been addressed primarily by improving detector technology. 'Improving' the source of X-rays is the other option and at Durham we have recently installed a new diffractometer equipped with a Bruker-Nonius detector and a Bede molybdenum target Microsource® X-ray generator with glass polycapillary X-ray optics. The Microsource is a 60W microfocus X-ray generator which requires very low electrical power requirements and cooling water flow rate. This is in huge contrast to our Fddd cryogenic diffractometer [1] running on a 15kW Mo rotating anode generator.

We have been exploring just how small and how poor a crystal we can measure data from, now that we have the Mo Microsource working in the laboratory at Durham.

We have recorded data from tiny crystals from a variety of molecular compounds, inorganic mixed metal oxides and large molecular weight supramolecular and co-ordination compounds, at room temperature and at low temperatures. The details of these data collections and the results of the molecular structures will be presented at the meeting in York. We have also recorded comparison studies between the new diffractometer and the older in-house 1K and 6K SMART diffractometers.

Below is just one example of the result from a tiny, twinned and disordered crystal in a pseudo-tetragonal space group with a unit cell volume of almost 6000$Å^3$. The crystal size was ~ 0.0007 mm^3.

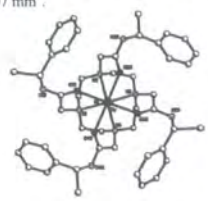

1. R.C.B.Copley, A.E.Goeta, C.W.Lehmann, J.C.Cole. D.S.Yufit, J.A.K.Howard, J.A.Archer. (1997) J. Appl .Cryst. **30**, 413-7

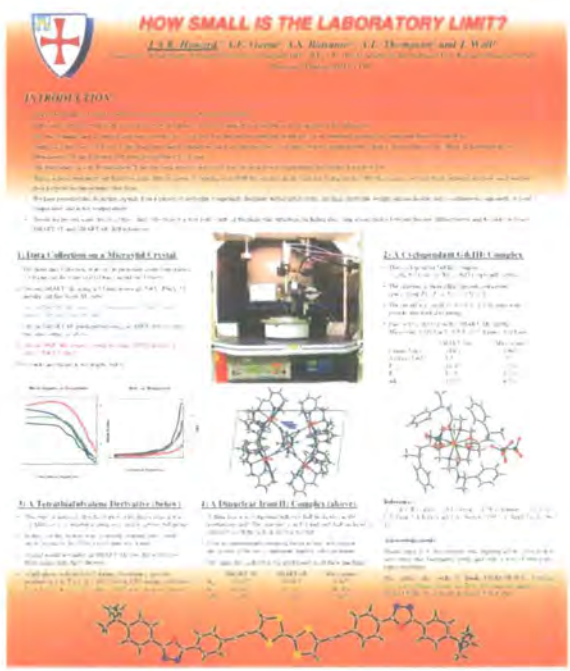

(Presented by Prof. J. A. K. Howard).

Presented to The Department of Chemistry, University of Durham, UK, January 2003

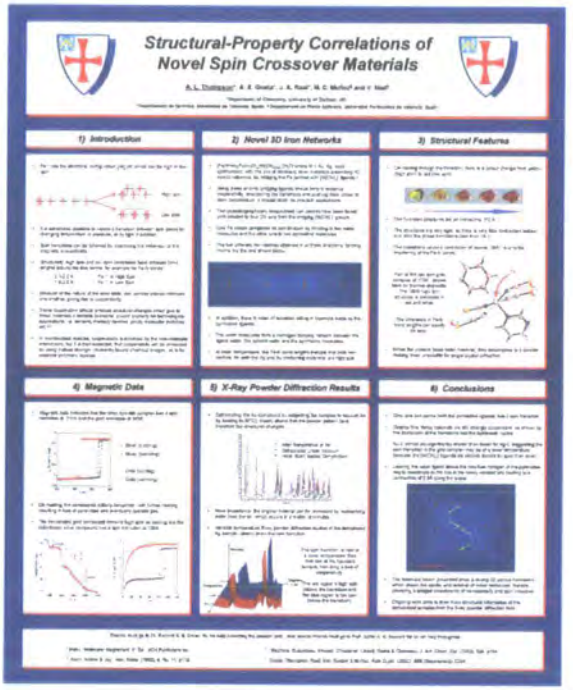

Presented to The International Union of Crystallography, 2002

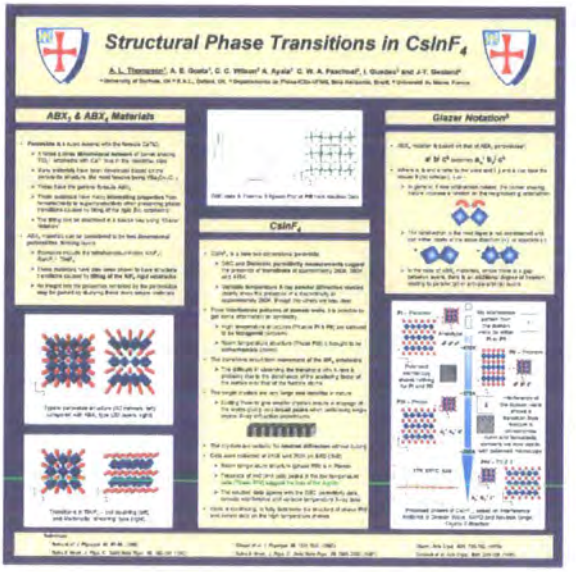

Presented to The 12^{th} Higher European Course for Users of Large Experimental Systems, 2002

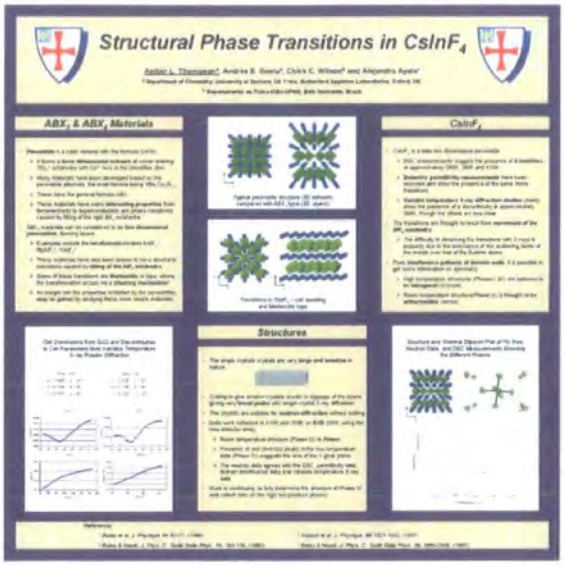

Presented to The British Crystallographic Association, Spring 2001

POLYMORPHISM IN $LiNH_4SO_4$, A. E. Goeta and A. L. Thompson, Department of Chemistry, University of Durham.

Phase transitions within the series of $LiMAO_4$ compounds (M=K, Na, Rb, Cs, NH_4 and A=S, Cr, Mo, W) lead to a series of very complex structural changes which give rise to interesting physical properties. For example, the most widely studied member of this group, $LiKSO_4$, is known to be ferroelectric, ferroelastic, pyroelectric, and a fast-ionic conductor in different phases.

These compounds are based on either corner or edge-sharing LiO_4 and AO_4 tetrahedra and their observed phase changes are known to be a result of very subtle distortions in this flexible framework.

$LiNH_4SO_4$ has two known polymorphs, both of which are stable at room temperature. On one hand, β-$LiNH_4SO_4$ has a hexagonal arrangement of tetrahedra like $LiKSO_4$ and $LiNaSO_4$, and has been well studied over the years. On the other hand, α-$LiNH_4SO_4$ has been less well studied. New results on the molecular and crystal structure of three polytypes of the alpha form will be discussed in this presentation.

The hexagonal nature of the $LiMAO_4$ materials is shown here with lithium in the centre of the pale grey tetrahedra, sulphur in the centre of the dark tetrahedra and the cations in the interstices.

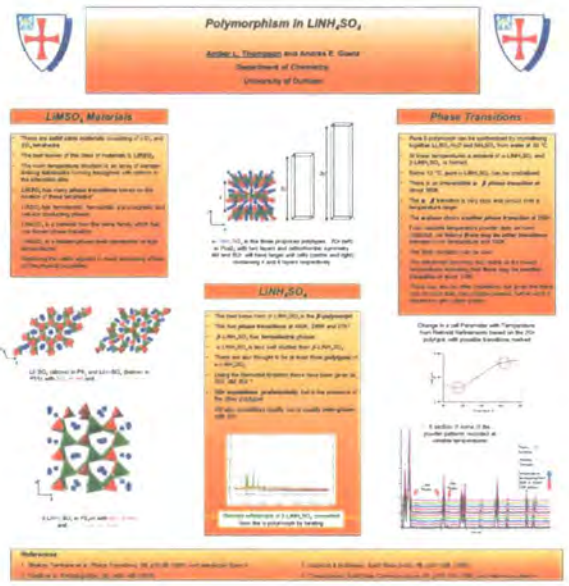

C.13 Other Presentations and Reports

Structure-Property Correlations in Novel Fe(II) Spin Crossover Networks

Department of Chemistry Graduate Symposium, University of Durham, UK, 9^{th} July 2003.

Electron Density Determination Of Hexafluorobenzene (C_6F_6)

3^{rd} European Charge Density Meeting, University of Aarhus, Sandbjerg, Denmark, 24^{th}–29^{th} June 2003 (poster, presented by Dr. R. Goddard).

Correlaciones Magneto-Estructurales en Complejos de Transición de Spin

National Atomic Energy Commission, Department of Solid State Materials, Buenos Aires, Argentina, April 2003 (presented by Dr. A. E. Goeta).

Cyclic Triphosphenium Ions and Related Species

University of Bremen, Germany, 30^{th} October 2002; University of Braunschweig, Germany, 30^{th} October 2002 and the Technical University of Munich, Germany, 4^{th} November 2002 (presented by Dr. K. B. Dillon).

Two Step Spin Transition in {Fe(Pmd)[Ag(CN)$_2$][Ag$_2$(CN)$_3$]}, a Bewildering Complex 3D Network

8^{th} International Conference on Molecule-based Magnets, Valencia, Spain, 5^{th}–10^{th} October 2002 (poster, presented by A. Galet).

Synthesis, Structure and Magnetic Properties of New Dinuclear Iron(II) Compounds

8^{th} International Conference on Molecule-based Magnets, Valencia, Spain, 5^{th}–10^{th} October 2002 (poster, presented by N. Ortega-Villar).

A Novel Fe(II) Framework Structure: Correlations to it's Thermal and Light Induced Spin Transitions

19^{th} Congress and General Assembly of the International Union of Crystallography, Geneva, Switzerland, 12^{th} August, 2003 (presented by Dr. A. E. Goeta).

Experimental Report RB12910 (carried out at ISIS, September 2001)

ISIS Experimental Report **Rutherford Appleton Laboratory**		RB Number: 12910 Date of Report: 4 June 2002	
Title of Experiment:	Anharmonic thermal motion analysis based on the single crystal structure of hexafluorobenzene	Local Contact:	M. Gutmann
Principal Proposer: Affiliation:	Christian W. Lehmann Max-Planck-Institut fuer Kohlenforschung, Germany	Instrument:	SXD
Experimental Team:	A. Thompson (Durham Univ.), C. W. Lehmann	Date of Experiment:	Sept. 2001

While the crystal structure of hexafluorobenzene has been first described in references [1] and [2], the charge distribution (experimental electron or deformation density) has not been reported previously. It is of particular interest in comparison to benzene and d6-benzene because of the reversed electronegativities of the ring carbons and the substituents. We have collected several high resolution X-ray diffraction data sets of hexafluorobenzene, using different area-detector diffractometers and data integration software packages. Data were collected from a single crystal of hexafluorobenzene grown under low temperature conditions from the melt ex-situ as well as from a single crystal of hexafluorobenzene grown in-situ on the diffractometer. All data sets were analysed using the multipole model of Coppens and Hansen [3] as implemented in the XD package [4]. Despite the rather different data collection and integration approaches, virtually identical deformation density maps were obtained. However, these maps show rather asymmetric deformation density distributions around the fluorine atoms.

In order to test the hypothesis that the asymmetric deformation densities around the fluorines originate from anharmonic thermal motion of these atoms in the crystal, a single crystal neutron diffraction experiment was carried out. - A simultaneous refinement, using X-ray data, of anharmonic displacement parameters expressed through a Gram-Charlier expansion in the multipole model and the refinement of spherical harmonics describing the atom centered electron density deformations is not possible, because both functions are highly correlated. Although anharmonic motion can in principle be deduced from multi-temperature X-ray diffraction studies [5], we made the observation that above 200 K diffuse scattering is rather strong, limiting the useful temperature in the laboratory to just 100 K.

A single crystal of hexafluorobenzene was grown by careful annealing of liquid hexafluorobenzene just below the melting point in a cylindrical glass tube of 5 mm diameter. The crystal was rapidly transferred into a pre-cooled vanadium can and mounted on the cold finger of a closed cycle helium refrigerator. After cooling to 100 K diffraction images revealed, that the crystal had disintegrated into three components. Bragg peaks belonging to the major component were indexed and a data set was obtained. The preliminary results of a conventional least-squares refinement are given below. A complete analysis of anharmonic displacement effects is still pending.

Empirical formula	C_6F_6
Temperature	100 K
Crystal system	monoclinic
Space group	$P2_1/n$, (no. 14)
Unit cell dimensions	a = 5.88680(10) Å. b = 9.0177(2) Å = 93.9626(11)°. c = 16.7248(3) Å.
Volume	885.72(3) Å^3
Z	6
Independent reflections	1696
Parameters	163
Goodness-of-fit on F2	1.058
Final R indices [I>2 (I)]	R1 = 0.0730
R indices (all data)	wR^2 = 0.1986

1) N.Boden, P.P.Davis, C.H.Stam, G.A.Wesselink, Mol.Phys., 25, 81, 1973
2) M.D.Bertolucci, R.E.Marsh, J.Appl.Crystallogr., 7, 87, 1974
3) N.K.Hansen, P.Coppens, Acta Cryst. A34, 909, 1978
4) T.Koritsanszky, S.T.Howard, Z.Su, P.R.Mallinson, T.Richter, N.K.Hansen, XD.Computer Program Package for Multipole Refinement and Analysis of Electron Density from Diffraction Data, Free University of Berlin, Germany, 1997
5) R.Restori, D.Schwarzenbach, Acta Cryst A52, 369,1996

Experimental Report 5-31-1373 (carried out at ILL, November 2002)

EXPERIMENTAL REPORT

EXPERIMENT N° 5-31-1373 INSTRUMENT D20

DATES OF EXPERIMENT 6^{th}-8^{th} November 2002

TITLE Magnetic structure of Dy doped Y_2BaCuO_5 compounds

EXPERIMENTAL TEAM (names and affiliation)

GOETA, Andrés (Department of Chemistry, University of Durham, U.K.)
THOMPSON, Amber (Department of Chemistry, University of Durham, U.K.)
BAUM, Lorena (Departamento de Física, Universidad de La Plata, Argentina.)
MERCADER, Roberto (Departamento de Física, Universidad de La Plata, Argentina.)

LOCAL CONTACT Clemens Ritter

Date of report 21^{st} January 2004

Although Y_2BaCuO_5 (**P***nma*), has been studied for some time by different techniques [1, 2], some doubts remain regarding its magnetic structure [3]. Most DC susceptibility and neutron diffraction studies indicate that the array of magnetic pathways is two-dimensional (2D), however some authors believe that they may be one-dimensional (1D) [4]. The low temperature neutron diffraction studies have been unable to verify this unambiguously. Isomorphous **P***nma* R_2BaCuO_5 (R = rare earth) compounds generally display an antiferromagnetic 3D array [5], however in the series R_2BaMO_5 (M = transition metal) diverse structures with 3D, 2D and 1D magnetic orderings have been observed [6, 5]. In particular some 1D R_2BaMO_5 materials have been shown to undergo magnetic excitations of the Haldane gap type [7]. In order to understand the relevant parameters that lead to the 2D and 3D magnetic arrays, and to investigate in detail the nature of the R–M interactions in the **P***nma*-type compounds, we plan to dope the yttrium sites of the Y_2BaCuO_5 "green phase" with different magnetic ions, e.g. Dy, Eu, Sm, Ho, Tm, etc.. This report covers an initial experiment that was accepted through the FAST access procedure in order to verify whether it was worth starting a long term project on the subject. Thus, the high flux D20 instrument was chosen to rapidly map the temperature dependent magnetic behaviour of two dysprosium doped Y_2BaCuO_5 samples.

From susceptibility studies, we found that 10% Dy causes the destruction of the 2D arrays. Hence, we studied samples containing 1% and 5% Dy. The purity of the samples was confirmed by powder X-ray diffraction measurements and susceptibility studies (4–300K). Neutron powder diffraction data were collected on D20 (λ = 2.4 Å) on both the 1% and 5% Dy samples, at 2 K, 10 K and 35 K together with shorter scans between these temperatures collected approximately every 1 K during warming. The raw data showed the appearance of two magnetic peaks at approximately 16° and 28° (approximately 8.8 Å and 5.0 Å respectively), in keeping with the results reported by Chattopadhyay *et al.* (Figure 1) [1]. The intensity of the peak at 16° 2θ as a function of temperature, clearly shows that the onset of the ordering takes place at around 16 K for both samples (Figure 2).

Page 2 of Report on Experiment N° 5-31-1373

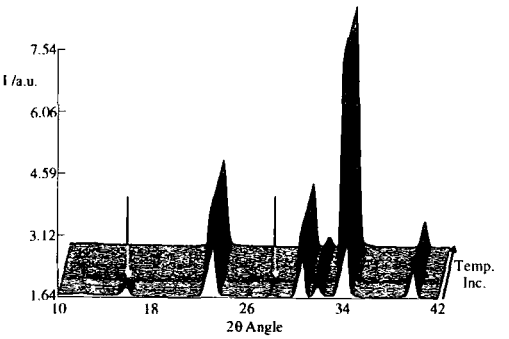

Figure 1. Neutron powder diffraction data for 1% Dy doped Y_2BaCuO_5. The appearance of additional peaks due to the magnetism at 16° and 28° are marked with red arrows.

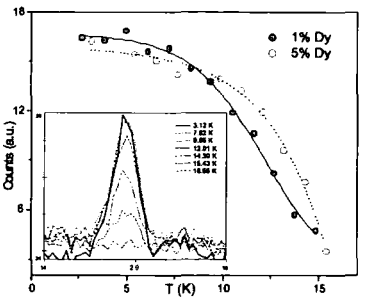

Figure 2. The temperature dependence of the integrated intensity of the magnetic peak at 16° together with this magnetic peak for the 5% Dy doped sample at different temperatures (inset).

The results from the neutron diffraction data are in keeping with results obtained from AC susceptibility measurements and shows that doping with 1% is enough to change the ordering temperature of the Y_2BaCuO_5 system from 27 K to 16 K.

Although magnetic structure refinements have not yet been completed, further work is under way and the experiment is considered to have been very successful. This work is the basis of further research and an article including these preliminary results has been submitted for publication to *Solid State Communications* [8].

References

[1] T. Chattopadhyay, P. Brown, U. Köbler, and M. Wilhelm, *Europhys. Lett.*, **8**, 685 (1989).

[2] O. D. Kolotii and V. Blinkin, *Sov. Phys. Solid State*, **34**, 774 (1992).

[3] I. V. Golosovsky, P. Böni, and P. Fischer, *Solid State Comm.*, **87**, 1035 (1993).

[4] E. Ong, B. Ramakrishna, and Z. Iqbal, *Solid State Comm.*, **66**, 171 (1988).

[5] R. Sáez-Puche and J. Hernández-Velasco, *Adv. Mater. Res.*, **1**, 65 (1994).

[6] G. F. Goya, R. C. Mercader, L. B. Steren, R. D. Sánchez, M. T. Causa, and M. Tovar, *J. Phys.,: Condens. Matter*, **8**, 4529 (1996).

[7] J. DiTusa, G. Aeppli, S. Cheong, J. Park, C. Broholm, and C. Chen, *Phys. Rev. Lett.*, **73**, 1857 (1994).

[8] L. A. Baum, A. E. Goeta, R. C. Mercader, and A. L. Thompson, *Solid State Comm., submitted* (2004).

Work Published Elsewhere

Other work has been included in the thesis of Stéphanie Cornet including a number of novel platinum stabilised phosphine complexes.[212] In addition, structural work has been carried out on a range of cyclometallated iridium complexes together with their separate ligands. These materials are for potential use in light emitting devices and have been included in Sylvia Bettington's thesis.[213] A number of rigid rod type molecules have also been structurally characterised and will be included in Simon Rutter's thesis.[214]